Earth Abundant Transition Metal Molecular Complexes for Water Splitting

by

Virginia Larson

A dissertation submitted in partial fulfillment
of the requirements for the degree of
Doctor of Philosophy
(Chemistry)
in the University of Michigan
2024

Doctoral Committee:

       Professor Nicolai Lehnert, Chair
       Professor Stephen Maldonado
       Associate Professor Charles McCrory
       Assistant Professor Nirala Singh

Virginia A. Larson

vlarson@umich.edu

ORCID iD: 0000-0002-7094-6286

Dedication

This thesis is dedicated with love to my mom, my dad, and my sister.

Acknowledgements

Thank you to Nicolai Lehnert, for your support and instruction, for providing opportunities and for guiding my PhD research. Thank you to my other committee members for your support and encouragement.

Thank you to those who encouraged me early on to become a chemist, thank you especially to Ms. Schifsky, Dr. Lovaason, Dr. Burden, Dr. Walhout, and Dr. Eggimann. Thank you to Prof. Tonks for starting me on chemistry research and for your encouragement.

Thanks to everyone I overlapped with in the Lehnert lab for making experimental research more fun, for all the coffee runs, and nights out! Thanks to Lizzie for being a friend and fun desk mate in your own unique way. Thanks to Jill for being a great spectroscopy partner. Thanks to Victor, Jill, Garrett and Faridat for all the tennis and racquetball adventures. Thanks to Victor and Jill for being great mentors and friends. Many thanks to Molly who taught me so much about the electrocatalysis project and how to be a graduate student in general! Esmee, thanks for being such a great undergrad to work with, I can't wait to see you succeed wherever you end up next. Thanks to Luis for your humor and joy, it was lovely to be in the same subgroup as you. Thanks to Lily for being a fun and intelligent REU student, I can't wait to see what cool science you do! Thanks to Dana for all your hard work and for being so quick to learn! Thanks to Michael for being a dedicated lab member and for being eerily good at predicting defense dates. Thanks to Bloom for being a joy to be around. Thanks to Felipe for always being up for anything. Thank you also to Andrew, Brad, Hai, Corey, Hannah, Abby, Ally, Sophia, Caelan, and Daniel.

Thank you to those of you who started as classmates in inorganic chemistry at the same time as me and who became close friends. Lizzie, Isaac, Emily, Jess, Cheyanne, I wish you all the best.

Thank you to the McCrory lab members, especially Maiko, Kevin, (Luis), and Faridat for your help with the GC and for chatting. Thanks to the Pecoraro, Maldonado, and Bartlett labs for kindly letting me use instruments and borrow things. Thank you to the many others in chemistry who made this a great department to work in!

Thank you to everyone who went climbing with me at planet rock and outside! Thank you to John and Aaron, to Julie, Kelly, Derek, and James, to Zechariah, Exequiel, Wami, Chris, to Jonathon and Taylor.

Thank you to those of you I had the privilege of living with. Thanks to Surabhi for trusting a stranger to be an apartment mate our first year. Thanks to Edith, Kali, Daphne, Christina, and Agnes thanks for all the fun times at Brookridge Ct. and for improving Covid isolation!

Thank you to George and Mary Lindquist, whose hospitality and kindness is unmatched. Thanks for inviting me to your home, first for Tuesday night dinners, and then as a houseguest. Thanks to everyone at those dinners for all the conversation, laughter, and community. Thank you especially to Meleah for your friendship over these last few months.

Thank you to everyone in GC for the first years of my time at Michigan. Thanks for the fellowship, friendship, and community. Thanks especially to Edith and Janelle. Thank you to everyone at Redeemer, thank you for welcoming me, for the encouragement, and for all you do.

Thank you to those whose friendships started before my time at Michigan and continue to be a wonderful source of fun and support! Thank you to those of you in or associated with the Pheonix house, it has been great to see you all virtually and in person throughout the years. Thanks

especially to Kathryn, Jade, Basil, Francesca, and Hayley for all the fun times in Chicago and letting me stay with you at such short notice. Thank you to other Wheaties as well, especially Erica for being a great friend and for eating ice cream with me. Thank you to Elisa, for years of friendship and catching up every time we were both in MN.

Thank you to my family: my mom Linda, dad George, and sister Helen. Thank you for always caring for me and for all the fun adventures. Thank you Grandma for your encouraging emails every morning, letting us all know you are ok! Thank you to my cousins, aunts, and uncles for your care and support throughout my life.

Thanks and glory to God who gives us the universe and the ability to study it.

Thank you again to everyone above, and to anyone who, by accident, I neglected to mention here, you really made this PhD journey better!

Table of Contents

List of Tables

List of Figures

Figure 2.10. Raman spectra of GO films before reduction, and the resulting RGO films after electrochemical reduction with or without catalyst, as indicated. Electrochemical reduction was conducted with 15 CV scans between 0 and -1.2 V vs Ag|AgCl at 200 mV/s in 0.1 M KPF$_6$ solution; the working electrode was a GO or **GO-1** film on glassy carbon; carbon felt was used as the counter electrode; Ag|AgCl in saturated KCl was used as the reference electrode. A two compartment cell with half cells separated by Nafion was used, under N$_2$. The standard deviation

Abstract

Further development and understanding of the chemistry of earth-abundant transition-metal molecular catalysts for water splitting will aid development of a sustainable hydrogen economy. If dihydrogen can be produced sustainably, such as by water splitting, dihydrogen can assist in our transition to a sustainable society, as it is a promising as a clean fuel, for energy storage, and for ammonia and other chemical syntheses.

On the reductive side of water splitting, Chapters 2 and 3 of this thesis study cobalt bis(benzenedithiolate) type catalysts for the hydrogen evolution reaction (HER). This family of catalysts is highly active for HER and our group has previously studied their immobilization through physisorption to graphitic electrode surfaces. However, in these studies the catalytic activity declined over time, and this was thought to be due to the catalyst dissociating from the electrode surface. Chapter 2 describes the synthesis and characterization of a new amine modified cobalt bis(benzenedithiolate) catalyst, which is then covalently attached to graphene oxide. The drop-cast thin films of this material are shown to be highly active for HER and more durable than the physisorbed analog, confirming that dephysisorption is a decay method for the physisorbed systems. Detailed electrocatalysis investigations expand our understanding of thin film electrocatalysis. Controlled potential electrolysis experiments show slow decline in catalytic activity over 8 hours, primarily due to demetallation. To further understand how this highly active catalyst family performs HER and how they decay, their mechanism was further investigated in Chapter 3. It was previously proposed that the starting Co(III) catalyst, when reduced by one electron distorted from square planar to tetrahedral which would promote de-physisorption during catalysis. Instead, this Co(II) complex is shown to be a $S_t = 1/2$ square planar complex. This suggests that dephysisorption of this intermediate is not the primary reason for deactivation of the physisorbed catalyst systems. Reactivity studies suggest that Co(II) bis(benzenedichlorodithiolate) reacts with acid, but under the explored conditions does not make hydrogen, suggesting Co bis(benzenedithiolate)s could be useful catalysts beyond HER.

On the oxidative side of water splitting, in collaborative studies, Chapters 4, 5, and 6 spectroscopically and theoretically investigate transition metal complexes with reactive metal-oxygen moieties. First, with the Nam Group in Seoul Korea, in Chapter 4, a reactive formal Ni(IV)-oxo species is shown to be best described as a $S_t = 1$ Ni(III)-oxyl species. The radical nature of this species may contribute to its high reactivity, while simultaneously avoiding the infamous "oxo-wall". Second, in Chapter 5, with the Ray Group in Berlin Germany, a Fe(II)-phenoxyl radical species is characterized with in-depth spectroscopy and theoretical calculations. Interestingly, this unusual species maintains an Fe(II) oxidation state in the presence of an oxidizing phenoxy radical ligand, due to electronically tuning of its co-ligand. This shows that careful ligand tuning can temporarily stabilize reactive radicals at low-valent metal centers for further reactivity. Finally, in Chapter 6, with the Nam group, a series of Fe(III)-peroxide complexes with drastically different reactivity are characterized spectroscopically and theoretically. Electronic structure calculations allow the assignment of the main characteristic electronic transition, which shows the smaller co-ligand ring size correlates to a stronger Fe-peroxide bond. These investigations on reactive intermediates provide spectroscopic markers and chemical information for future studies and inform our understanding of the oxidative side of water splitting, hydrogen fuel cell reactions, and oxidative reactions in bioinorganic chemistry.

Chapter 1 Introduction

This introduction is partially adapted from a review article and research paper referenced here.[1,2]

1.1 Catalytic Water Splitting and Introduction to Sustainability

The negative impacts of climate change are already being seen around our planet and necessitate stepping away from fossil fuels as the primary energy source to make our lives and industries more sustainable.[3,4] The Intergovernmental Panel on Climate Change (IPCC) reports a 1.1 °C increase in global surface temperature from the 1850-1900 baseline. This causes harm to our human civilization and to the natural world we inhabit, increasing natural disaster rate,[5,6] stressing our food supply,[7,8] and decreasing biodiversity.[9] Together, we must reduce our environmental harm and instead work for a sustainable society. A more sustainable future is possible, when industries move towards sustainable and even regenerative practices.[3] Major sustainability efforts include closed cycle consumerism, replacing carbon-based energy sources with renewable energy, decreasing pollution, and regenerative agriculture.[8,9] Chemists can participate the shift to a sustainable in using more abundant and ethically sourced chemicals, optimizing reactions to create less waste, and developing the chemistry needed to provide renewable energy and sustainable medicine and materials.[10,11] There are many subfields in chemistry that are contributing to the advancement of green science. Here, the use and storage of clean energy, specifically where hydrogen gas can contribute is discussed.

1.1.1 Solar Energy Conversion and Storage

The sun is the ultimate source of energy on earth, through photosynthesis in ages past providing energy stored in fossil fuels, and through solar panels today. If enough of the sun's energy could be captured, we could sustainably meet the growing demands of our civilization. This can occur in a few methods; first solar energy can generate electricity through photovoltaic solar panels. Second, solar rays can be directed into architectures to warm and cool buildings

appropriately to the local climate. Third, the sun can be used in agriculture to grow raw plant materials for biofuels and sustainable chemical feedstocks.[12] Fourth, solar energy capture can be coupled directly (photochemical and photoelectrochemical, see Figure 1.1) or indirectly (electrochemical with sustainably sourced electricity) to power chemical reactions that produce desired commodity and specialty chemicals for industrial use. Fifth, similar photo(electro)chemical processes can be used to drive endothermic chemical reactions to generate solar "fuels" that store solar energy.

Storing clean energy is necessary for a society that will hopefully thrive on only renewable energy. There are times when the production of renewable energy outpaces its use, as has already been seen for solar energy on sunny days in California.[13] Storing this excess energy during peak production is helpful in meeting later energy demands, for example at times of the day when renewable energy is not available as a primary energy source, such as days of low solar energy flux.[14] One set of chemical reactions that are driven uphill are flow batteries where a redox reaction (electrolysis) takes place and the high energy products are stored in solutions where then they can come together at a later time and release energy. Other options are the synthesis of a chemical fuel. Fuel synthesis creates a high energy chemical that is later burned with oxygen to release useful energy. The type of fuel dictates how it can be burned, if synthetic hydrocarbon fuels mimicking gasoline could be made, those could be burned in a traditional combustion engine. Hydrogen is the simplest chemical fuel with high energy density and can be burned cleanly in a hydrogen fuel cell, only producing water.

1.1.2 Hydrogen's Role in a Sustainable Society

Hydrogen is a promising aid for our transition to a sustainable society as a promising clean fuel for transportation and as a temporary storage mechanism for excess renewable energy. Hydrogen is already a high demand commodity chemical, as it is needed in the Haber-Bosch process for ammonia production for fertilizers, in the Fisher-Tropsch process where CO and H_2 are reacted to yield hydrocarbons, in refining oil, and in the synthesis of fine chemicals.[15,16] In addition, it is a promising clean fuel for transportation as it burns cleanly (producing only water vapor as a product), is energy dense, and able to be sourced renewably.[17,18] Hydrogen could join chemical redox flow batteries and mechanical energy storage as proposed solutions to renewable energy storage, but only if it can be produced cheaply and effectively via water splitting.[19] In all,

hydrogen can fill many niches in the energy ecosystem, lowering our reliance on fossil fuels.[19,20] Yan and co-workers suggest that hydrogen could replace carbon-based energy sources for 18% of our energy needs.[21] The US Department of Energy (DOE) recognizes the need for sustainable hydrogen and has published a goal of "$1 per 1 kilogram in 1 decade" to spur development of clean hydrogen production technology.[22] Japan, the UK, India, and France also have plans in place to scale up hydrogen use as a power source in their transitions to a more sustainable society.[16]

1.1.3 Types of and Reactions in Water Splitting

Producing hydrogen by the hydrogen evolution reaction (HER, see Equation 1, and Figure 1.1) is a promising way to cleanly make hydrogen. Water splitting uses an applied potential to split water into dioxygen and (di)hydrogen gas.

$$2H^+ + 2\ e^- \rightarrow H_2 \qquad\qquad \textbf{Equation 1}$$

$$H_2O \rightarrow 2H^+ + \tfrac{1}{2}\ O_2 + 2\ e^- \qquad\qquad \textbf{Equation 2}$$
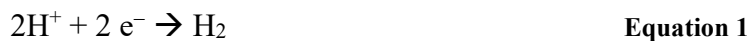
Reducing protons from water gives hydrogen gas, this is known as the hydrogen evolution reaction (HER), Eq. 1. On the other side of water splitting, water is oxidized to make oxygen gas, as shown in Eq. 2. Research on HER is extensive, but hydrogen is still not able to be sustainably and commercially produced from water. Water oxidation, or oxygen evolution (OER), involves the transfer of 4 e$^-$ and 4 H$^+$ and so is often more challenging than HER. OER and the reverse reaction, O_2 reduction, needed to "burn" hydrogen in fuel cells, involves several intermediates with metal ions interacting with oxygen-based species. The electronic structures and reactivities of these intermediates are discussed further in Section 1.3.
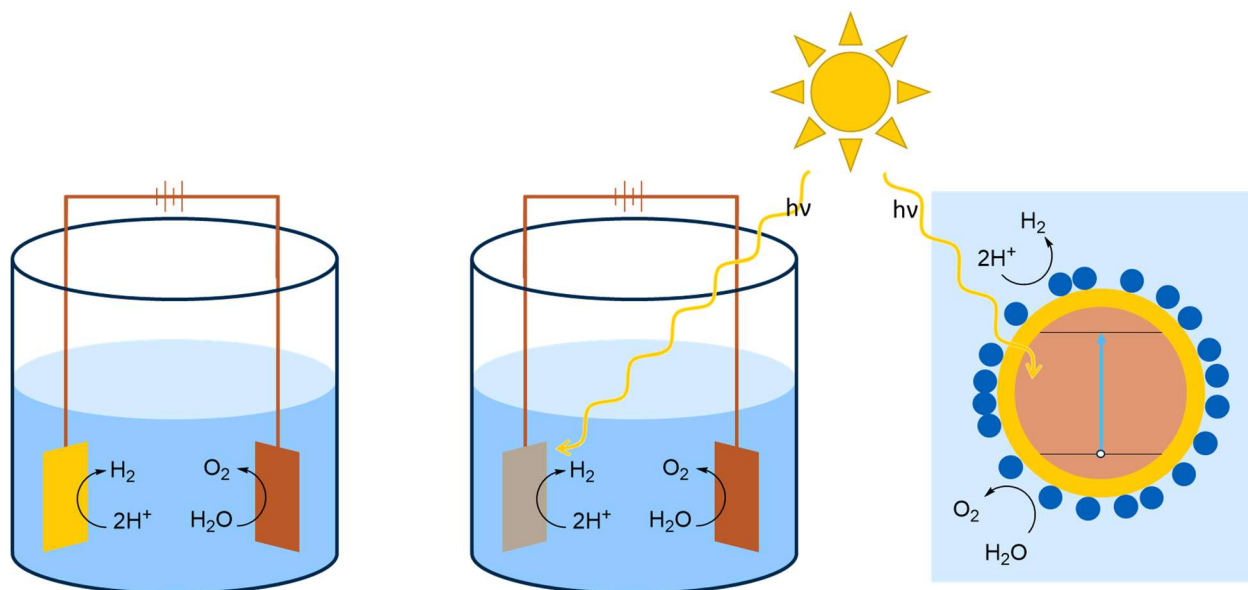
Figure 1.1. Three types of solar-powered water splitting: (left) electrocatalytic, powered by solar electricity, (center) photoelectrochemical, using light-absorbing semiconductor electrodes, (right) photocatalytic, shown here with a catalyst (schematically shown as a blue dot) on a light-absorbing quantum dot.

There are three main variations of water splitting catalytic systems, see Figure 1.1. In the first, electrocatalytic water splitting, the necessary high energy electrons for water splitting can come from electricity, ideally renewable sourced electricity. In this case, HER occurs at the cathode and OER at the anode. The sun's energy can also be used more directly to excite electrons in a photovoltaic semiconductor, as is the case for photoelectrocatalytic water splitting, or a photosensitizer in solution, as is the case for photocatalytic water splitting. In Figure 1.1 and the discussion so far, HER is coupled to OER; however, HER could also be coupled with a different, more useful oxidation reaction, such as methanol reforming, the oxidation of small molecules, or biomass conversion to value added chemicals.[23–25]

1.1.4 Hydrogen Evolution Reaction: Catalysts and Catalysis
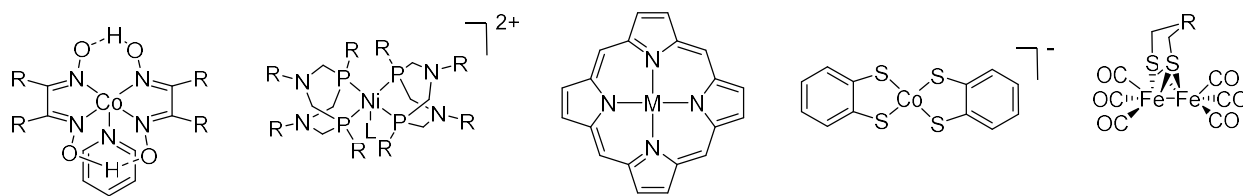
Figure 1.2. General chemical structures of common molecular catalysts for hydrogen evolution, from left to right: cobaloxime type catalysts, DuBois type catalysts, metalloporphyrins, cobalt bis(benzenedithiolate) complexes, and FeFe hydrogenase models.

A catalyst is useful to lower the overpotential and allow more efficient use of the applied electric energy. An ideal catalyst is efficient, cheap, and durable. Using earth abundant molecular catalysts immobilized on electrode surfaces is an approach that has the potential to fulfill these goals. Molecular catalysts have the benefits of easy and precise characterization by established spectroscopic methods, rational synthesis, and rational modification/tuning of the catalyst properties.[26,27] Using earth abundant metals allows for the catalysts to be cheaper and more easily scaled than catalysts based on rare earth metals.[28] Fe, Co, and Ni are popular abundant metals for HER catalysts.[26,29,30] These metal ions are then paired with suitable ligands to tune their catalytic properties, and many corresponding catalyst systems have been reported.[26] Important families of HER catalysts include cobaloximes,[31–36] Dubois-type catalysts,[37–40] metalloporphyrins,[41,42] metal complexes with dithiolene type ligands,[43–48] and FeFe and NiFe hydrogenase models (See Figure 1.2).[49–55] The structures of these synthetic catalysts are partially inspired by the design of nature's HER catalysts: hydrogenases.[18,50] The hydrogenase models are clearly the closest mimics of the enzyme, but other catalysts take inspiration from these enzymes as well, by the inclusion of sulfur based ligands, other non-innocent ligands, and the incorporation of second coordination sphere groups.

1.2 Cobalt Bis(benzenedithiolate) Type Catalysts for Hydrogen Production

Cobalt bis(benzenedithiolate) type catalysts are an ideal catalyst family for the development of hydrogen evolution systems as they are highly active and can be easily immobilized onto graphitic electrode surfaces.

1.2.1 History

Benzenedithiolate (bdt) transition metal complexes were first used for the quantification of metals in solution as they easily form colored metal complexes.[56] For instance in the 1930's,

tolyldithiolate was used to quantify Sn^{II} in solution, as it reacts to form a pink complex.[57,58] In the 1960's bis(bdt) type complexes and other dithiolene transition metal complexes were studied by Gray and Billig, among others, for their interesting electronic properties, with the benzenedithiolates serving as non-innocent ligands.[59–61] The non-innocent nature of these complexes has been further studied in the mid-2000s. Detailed studies on Co(bdt)$_2$ derivatives have shown that the ground states of these complexes are best described as being composed of 50-70% Co^{III}(L)$_2$ and 50-30% Co^{II}(L˙)(L) character, showing partial oxidation of the bdt ligand.[62,63] This is due to the close energy match of the Co d and dithiolate π orbitals, causing good orbital overlap and very covalent bonding. See also Section 1.3.4 for discussion on bonding inversion in first row transition metals. The non-innocent property of the benzenedithiolate-type ligands may contribute to their ability to function as redox active catalysts, allowing reactivity at the sulfurs and storage of electron density through-out the complex.[48] Notably some of the complexes dimerize, forming metal sulfur bonds between two metal bis(dithiolene) monomers such that each of the metals are five coordinate. However, dimerization is not observed for the Co bis(tolyldithiolate) and Co bis(benzenedichlorodithiolate) complexes discussed here-in.[47,60]

These Co(bdt)$_2$ and derivatives were first shown to be active for HER by the Eisenberg group in the early 2010's. Co(bdt)$_2$ was first studied for homogeneous electrocatalytic HER and homogeneous photocatalytic HER with Ru(bpy)$_3{}^{2+}$ as a photosensitizer.[46] The effects of modification of the ligand on the catalytic activity of the complexes was also investigated.[47] Further, when paired with CdSe nanocrystals as the photosensitizer, these were shown to be durable photocatalytic systems, active for 300,000 turn over numbers (TON) over 60 hr.[64] Our group then showed these catalysts could be immobilized on electrode surfaces by physisorption, see Section 1.2.4. Benzenedithiolate and dithiolene type catalysts with various metals are still being actively developed and explored as HER catalysts.[48,60]

1.2.2 Mechanism

The HER mechanism involves four nominal steps, two protonation (chemical steps, or "C") and two electron transfer steps ("E"). For Co bis(benzenedithiolate) types of catalysts, the first mechanistic step is known to be reduction, as these catalysts are not observed to be protonated at reasonable acid concentrations, and the catalytic wave is observed at more negative potentials than the Co^{III}/Co^{II} couple. The second step is known to be protonation, as the Co^{II}/Co^{I} couple is not

observed in the absence of acid within a reasonable potential window. This shows that the first two steps are EC, and so the full mechanism is then ECCE or ECEC. The following steps have not yet been observed experimentally, but have been investigated computationally in support of an ECCE mechanism.[65] According to calculations by Solis and Hammes-Schiffer, after reduction, the complex is protonated at S_{bdt}. Then a second protonation occurs at another S_{bdt}. Finally, reduction occurs, one of the H-S_{bdt} is transferred to the Co^{I} to give a Co^{III}-hydride, and then dihydrogen is eliminated intramolecularly.

1.2.3 Immobilization of Molecular Catalysis on Electrode Surfaces

There is great interest in immobilizing earth abundant transition metal molecular catalysts on electrode surfaces,[66,67] as catalyst immobilization onto electrode surfaces adds the benefits of heterogenous catalysis to those of molecular catalysts. The application of heterogenized molecular catalysts allows for (a) the use of less catalyst compared to homogenous solution, (b) easy separation of the catalyst from the electrolyte solution, and (c) it also limits cross contamination between half-cell reactions, while maintaining most of the benefits of the molecular catalyst systems. While attaching molecular catalysts to electrode surfaces has many benefits, potential issues include the identification of the active species on the surface and possible degradation pathways upon attachment to the surface or under catalytic conditions.[68] To develop molecular catalysts into HER active films on electrode surfaces, researchers have explored different immobilization approaches including physisorption to carbon nanotubes and other graphitic materials,[69–76] incorporation into reduced graphene oxide thin films[77,78] and into polymer matrices,[79] covalent attachment to carbon nanotubes[72,80,81] and edge plane graphite (EPG),[55,82,83] chemical modification of glassy carbon (GC),[84,85] and incorporation into metal organic frameworks (MOFs)[86–92] and into MOFs embedded with carbon nanotubes.[92–94] Similar to the immobilization of molecular catalysts onto electrode surfaces, many groups have integrated single metal ions into (often graphitic) electrode surfaces, which often yields effective catalysts but also comes with a number of challenges, including the control and full characterization of the metal coordination sites.[95]

1.2.4 Cobalt Bis(Benzenedithiolate) Type Catalysts Physisorbed to Graphitic Electrode Surfaces.

Previous studies from our group took advantage of the fact that Co bis(benzenedithiolate) type catalysts have planar structures, which allows them to π-stack well with graphitic materials. Physisorption allows heterogenization of these catalysts in a straightforward way, and the resulting, functionalized electrodes show high HER activity when the catalysts are physisorbed to reduced graphene oxide (RGO)[96] or a variety of other graphitic surfaces.[73] The effects of ligand modification on the adsorption, retention, and HER activity of the physisorbed catalysts was also studied.[97] Remarkably, these cobalt bis(benzenedithiolate) type catalysts have been shown to have higher turnover frequencies (TOFs) in the surface-bound state than in solution.[96]

Physisorption to graphitic surfaces allows simple preparation of HER active electrodes, by simply soaking the electrode in a solution of the catalyst.[96] Cobalt bis(benzenedithiolate) type catalysts have been physisorbed to a wide variety of graphitic electrode surfaces, including well defined Highly Ordered Pyrolytic Graphite (HOPG), and inexpensive graphite, but also thin films of graphitic materials, like graphene and RGO, that have been deposited on other (benign) electrodes.[73,96] Additionally, these catalysts can be embedded inside of a (multilayer) graphitic film, such as RGO films.[78] These RGO films are made from graphene oxide (GO). GO is an oxidized, exfoliated form of graphite and has the benefit of being solution processable. GO can be reduced to RGO, which then returns many of the structural and chemical properties of graphene, including the conductivity. Drop-casting GO films with embedded catalysts and then reducing the GO in situ to RGO films is another convenient method to prepare HER active thin films on benign electrodes.[78,98]

There have been additional notable examples of heterogeneous catalysts derived from cobalt bis(benzenedithiolate)s. In particular, Marinescu and co-workers have developed 1D and 2D MOFs with active sites of cobalt bis(benzenedithiolate)s.[88–91] Additionally, a cobalt dithiolene complex has been recently reported as HER active catalyst when physisorbed to carbon nanotubes on carbon paper.[76]

1.2.5 State of the Art

Making direct comparisons to other examples from the literature is challenging due to variations in film thickness in these systems, but by comparing catalyst loading on the surface broadly, one can roughly compare activities between these systems (see Table 1.1). A 2019 review nicely summarizes electrocatalytic HER abilities of 3rd row transition metal molecular catalysts

immobilized on surfaces.[26] A full review is not attempted here, but relevant and top examples in the field are highlighted.

Physisorbing molecular catalysts to graphitic thin films, such as multiwalled carbon nanotubes, can give catalyst loadings on the order of 1-10 nmol/cm^2. If the catalysts are not prone to physisorption on their own, covalent attachment to pyrene can help catalysts to physisorb on the surface.[69,71,72,74–76,80] Unfortunately, in many examples from the literature the film thickness is not reported, and so the density of the catalyst in the film is unknown, and a further, detailed comparison with these systems is not suitable. Yet, with these systems, current densities ranging from 0.5 to 4 mA/cm^2 are typical, and these current densities allow TONs on the order of 10^5-10^6 for the best performing systems. Coordination polymers, such as those reported by Marinescu and co-workers, allow much higher metal ion density on the electrode surface, on the order of µmol/cm^2. But despite the higher density of electrochemically active Co on the surface, similar current densities for HER are observed, likely due to the fact that the catalysts deeper in the film cannot participate in HER.[88,99] Further afield, immobilization of hydrogenase enzymes allows for a quite high TON ($7 \cdot 10^6$ in 16 hr), and with a specially designed highly porous electrode surface, 0.2 nmol/cm^2 in a 12 µm thick film has been accomplished.[100]

Table 1.1. Comparison of various earth abundant HER catalysts immobilized on electrode surfaces. Note: here "/" is used to indicate physisorption, and "-" is used to note chemisorption/covalent bonding to the electrode surface.

System*	Thickness of film (nm)	Surface Density of electrochemically active species nmol/cm² (% of total catalyst on surface)	TON (CPE time)	Initial current density mA/cm²	Conditions	Ref
Graphite/Co(bdtCl₂)₂		14.1	2.18E5 (8h)	78	pH 0.3, -0.5 V vs SHE	[73]
HOPG/Co(bdtCl₂)₂		0.260	9.10E6 (8h)	65	pH 0.3, -0.5 V vs SHE	[97]
MWCNT-NiP		1.5 ± 0.5	1E5 (10h)	4	pH 0.3, -0.3 V vs NHE	[80]
MWCNT/pyrene-NiP		2 ± 0.5	8.5E4 (6hr)	4	pH 0.3, -0.3 V vs NHE	[74]
MWCNT-(Co diimine-dioxime)		4.5 ± 0.2	5.5E4 (7hr)	2	pH 4.5, -0.59 V vs RHE	[72]
MWCNTs/pyrene-Co(glyoxime)		150	420 (24 hr)	0.34	pH 6.5, -0.7 V vs SHE	[75]
SWNH(horns)/pyrene-CoTPA		2.0 ± 0.4	9180 (12 hr)	0.33	pH 7.4, at -0.96 V vs NHE	[71]
MWCNTs/FeFe hydrogenase mimic-pyrene		7.6 ± 0.9 (80%)	4 ± 2 E3 (20 hr)	−0.71±0.2	pH 7, at -0.49 V vs RHE	[69]
MWCNT/dimeric cobalt dithiolene		12.1 (23%)	5.1E5 (16hr)		pH 7, at -0.6 V vs RHE	[76]
carbon cloth/C60-(Co diimine-dioxime)		260	190 (1 hr)	2.7	pH 4.5, at -0.8 V NHE	[101]
RGO/CoPorph		no couple observed	tested by repeat CV, at pH 14, currents >30 mA/cm2 observed over 1000 cycles			[77]
GCox-CoPorph		n.r. (95 ± 6%)				[85]
EPG/FeFe hydrogenase		0.039	4.9 ± 0.1 E5 (9 hr)	0.42	pH 4, -0.8 V vs SHE	[82]
P(VP-St)/Co(Pc)	1,000	n.r.	2E5 (1hr)		pH 1.0, -0.90 V vs Ag|AgCl	[102]
PTTB/CoSalen	223	0.169 (10%)	1.1E5 (2 hr)	1	pH 4.5, -0.75 V vs RHE	[79]
Co dithiolene 2D coordination polymer	360±40	3700±400		6-7	pH 2.6, -0.65 V vs SHE	[88]
Ni dithiolene coordination polymer		680		3	pH 1.3, at -0.8 V vs SHE	[99]
Co porphyrin MOF-MWCNT/Nafion		5 (32%)	3.2E4 (1/2 hr)	3	pH 1, -0.715 V vs RHE	[93]
Cobaloxime MOF	1,000	70 (54%)	2.1 E4 (18 hr)	1.7	pH 4, at -0.45 V vs RHE	[86]
hydrogenase-mesoporous ITO	12,000	0.2		1.5	pH 6, -0.6 V vs NHE	[100]

*Abbreviations: MWCNT = multiwalled carbon nanotubes, SWNH = single walled carbon nanohorns, Porph = porphyrin, GCox = oxidized glassy carbon, EPG = edge plane graphite, P(VP-St) = Poly(4-Vinylpyridine-Co-Styrene), PTTB = polythiophene analogue, MOF = metal organic framework, and ITO = indium–tin oxide.

As mentioned above, the US DOE would like to have the cost of H_2 gas at \$1/kg. This will require durable and cheap catalysts that can produce H_2 with a high current density. As an exercise, if one had a 100 cm^2 electrode that could run consistently with a current density of 100 mA/cm^2, it would take 111 days of constant electrolysis to produce 1 kg of H_2. While the catalysts listed in Table 1.1 are promising, there are quite a lot of improvements necessary before earth abundant transition metal molecular catalysts in thin films will meet our goals for industrial hydrogen production. To improve molecular earth abundant HER catalysis it is not only crucial to develop new catalysts and new immobilization methods but to understand these catalysts' mechanisms, and thermodynamic and kinetic catalytic parameters to better learn their chemistry and apply lessons learned in the design of new, high-performing catalysts.
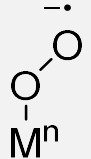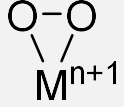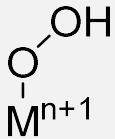
1.3 Metal-Oxygen species

Transition metals are used as catalysts not only for reductive reactions, like hydrogen evolution, see above, but also for a variety oxidative reactions in nature's catalysts, enzymes, and chemistry's synthetic catalysts; many of these reactions are relevant to renewable energy processes.[103,104,113–118,105–112] In the catalytic reduction of dioxygen, the oxidation of water to dioxygen, and the use of oxygen related species in C-H activation and other oxidation reactions, the transition metal mediates O–O bond formation and cleavage.[115,117,118] Several of the reaction intermediates are oxygen derived ligands bound to a transition metal ion: metal-oxo, -peroxo, -superoxo, species. Under carefully chosen conditions, such intermediates can sometimes be isolated and further characterized. Relevant reactions and their mechanisms for water splitting and common enzymatic reactions are described in more detail in Sections 1.3.1 and 1.3.2, respectively.

Table 1.2 shows a summary of such species, especially those discussed in this thesis, and their charge, spin, and common vibrational spectroscopic markers. Upon binding and one electron reduction of dioxygen gas, an end-on bound metal-superoxo moiety can be formed. Further reduction (here assumed to be from the metal) can form a side-on bound peroxo moiety. Protonation of one of the oxygen atoms can then form a hydroperoxo type moiety. Further protonation and removal of water can give a terminal metal-oxygen species. Valence tautomerization of this species can yield a metal-oxyl species, which weakens the M-O bond, and which is a key intermediate proposed for water oxidation. High-valent metal(IV)-O species can also be obtained in the laboratory by reacting an O-atom donor with a metal(II) species, specifically

yielding a $M^{IV}=O$ or $M^{III}-O^{\bullet}$. These terminal metal-O species are crucial reactive intermediates in oxidation reactions. The electronic structure of such M-O species is discussed in further detail below (Section 1.3.3).

Table 1.2. Summary of oxygen derived species and select properties.

Species	dioxygen	superoxo	peroxo	hydroperoxo	oxo	oxyl
Structure	$O{=}O$	$\overset{-\bullet}{O}$ bonded to $O-M^n$	$O-O$ bridging M^{n+1} (peroxo)	$O{-}OH$ on M^{n+1}	$O{=}M^{IV}$ (double bond)	$O^{\bullet}$ on M^{III}
Charge on oxygen moiety	0	-1	-2	-1	-2	-1
Spin on oxygen moiety	1	½	0	0	0	½
Vibrational spectroscopic marker(s)		O-O stretch near 1100 cm^{-1}	O-O stretch near 800 cm^{-1}	Deuterium sensitive vibrations, O-O stretch near 800 cm^{-1}	M-O stretch, around 500-900 cm^{-1}	Relatively weaker M-O stretch

1.3.1 Relevance to Water Splitting and Renewable Energy Reactions

On the anodic side of water splitting, water is oxidized to make (di)oxygen gas. Catalyzing the four electron, four proton transformation of OER is a challenge that often limits the activity of overall water splitting systems.[117] This reaction is challenging for earth abundant transition metal molecular catalysts, yet chemists have designed several such catalysts most of which feature multidentate or macrocyclic ligands with nitrogen coordination to the metal.[117] Many molecular OER catalysts take design inspiration from nature's enzymes, especially photosystem II (PSII), the function and mechanism of which is described further below.[118,119] The reverse reaction, oxygen reduction reaction (ORR), is needed to "burn" hydrogen in fuel cells. As in water splitting, the ORR involves transferring four electrons and four protons and limits the overall efficiency of the cell.[118] The proposed catalytic cycles for both these reactions often involve several intermediates with metal ions interacting with oxygen-based species. Especially relevant are the high-valent metal-oxo intermediates that are often proposed as key intermediates in catalytic cycles, yet they are rarely observed and characterized.[1,117,118] Understanding how oxygen related species, such as -oxo, -peroxo, and -superoxo moieties, interact with such metal complexes in further detail could enable chemists to design catalysts with higher reactivity and durability.

1.3.2 Relevance in Biology

In biology, O–O bond formation and cleavage transformations mainly occur at Fe and Mn sites because these metals are abundantly available, readily bind oxygenic species and exhibit rich redox chemistry.[114,120] As described above, dioxygen activation and the reverse O-O coupling reaction often involve proposed metal-superoxo, -peroxo, -oxo and/or -oxyl intermediates as described in Section 1.3.[115] High-valent metal–oxo complexes are especially common reactive intermediates. Collectively, these findings inspired the synthesis of Mn–O and Fe–O systems, which have recently been joined by similar systems featuring late transition metals. For example, the O–O bond-formation step preceding O_2 evolution at the oxygen-evolving complex in PSII is proposed to occur via a putative Mn–O intermediate.[121–125] In the case of PSII, detailed experimental and theoretical studies that aimed to discern between these two mechanisms have yielded controversial results,[126,127] although recent work favors a coupling mechanism:[128,129] this mechanism requires the oxygenic ligands to have distinct radical oxyl ($O^{\bullet-}$) character instead of being oxo (O^{2-}) groups. In the context of high-valent metal complexes, this is possible by the valence tautomerism $M^{n+1}{=}O^{2-} \leftrightarrow M^n{-}O^{\bullet-}$. Nevertheless, the major flaw in our understanding of PSII remains the lack of data on the intermediates directly preceding O–O bond formation, which means that unambiguous assignment of the mechanism is not possible.

The microscopic reverse of O–O bond formation is O_2 activation, wherein a M–O_2(H) complex converts into a high-valent metal–O intermediate through homolytic or heterolytic O–O bond cleavage. This activation process is better understood[113–116] on account of trapping and in-depth spectroscopic characterization of high-valent Fe–O cores in heme and non-heme oxygenases, which perform hydroxylations, O-atom transfers and other reactions[114,129–131]. Yet there are still uncertainties in specific mechanisms, for instance, a dinuclear $Fe^{IV}_2O_2$ species is believed to be the active oxidant in the hydroxylation of CH_4 by soluble methane monooxygenase (sMMO),[132,133] but the exact identity of this active species has been the subject of much controversy.

The uncertainty related to the O–O bond formation mechanism in PSII and the nature of the reactive intermediates in many Fe- and Cu-containing oxygenases have inspired bioinorganic chemists to synthesize and characterize model complexes as an indirect means to probe the structures of reactive intermediates and the plausible mechanisms. By studying how molecular complexes perform O–O bond formation and cleavage, we can perhaps better understand the way

in which the reactions proceed in biology. These synthetic molecular complexes need not be restricted to those featuring nature's choice of metals, namely, Mn, Fe and Cu. Thus, a wide variety of bioinspired and biomimetic Cr, Mn, Fe, Co, Ni and Cu complexes have been prepared,[111,114–116,130,134–137] some of which have proven to be valuable spectroscopic models for the enzyme active sites.

1.3.3 Terminal Metal–Oxygen Species and the 'Oxo Wall'

Specifically, terminal high-valent metal-oxos, such as Mn–O, Fe–O, Co–O, Ni–O and Cu–O cores, are known to have high reactivity towards O–O bond formation, H-atom transfer (HAT) and oxygen-atom transfer (OAT) reactions. In the case of Ni and Cu, evidence for such high-valent intermediates is more speculative.

We can obtain information regarding the reactivity and stability of terminal metal–O cores directly from ligand-field theory. To understand the bonding between a metal center and an oxo ligand, we first need to consider which metal and ligand frontier orbitals are involved in bonding. For the oxo dianion (O^{2-}), the occupied O(2p) orbitals can participate in σ-donor and π-donor bonding to the metal center. For a first-row transition-metal ion M^{n+}, it is the 3d orbitals that are the most relevant for bonding, especially for highly oxidized metal centers. These d orbitals become nondegenerate when M^{n+} experiences a ligand field. In the case of an octahedral (O_h) ligand field, the d_{z2} and d_{x2-y2} orbitals that overlap directly with the ligands are raised in energy relative to the d_{xy}, d_{xz} and d_{yz} orbitals. This O_h symmetry is lowered if one of the M–ligand bonds is significantly stronger than the other ones, as is the case when the M–O fragment is present. Loss of an xy mirror plane results in effective C_{4v} (tetragonal) symmetry, wherein the M–O bond is collinear with the z-axis. Relative to the d_{xy} orbital, the d_{xz} and d_{yz} orbitals are higher in energy owing to their π-antibonding interactions with the oxo group. Likewise, the d_{z2} energy is raised owing to a strong M–O σ-antibonding interaction (Figure 1.3a). In most cases, the d_{xy} orbital is essentially non-bonding with respect to all ligands. By contrast, the d_{x2-y2} orbital participates in σ bonding with ligands in the xy plane, whose electron-donating or electron-withdrawing abilities affect the properties of the M–O complex, such that altering these ligands can tune spin states and reactivity.
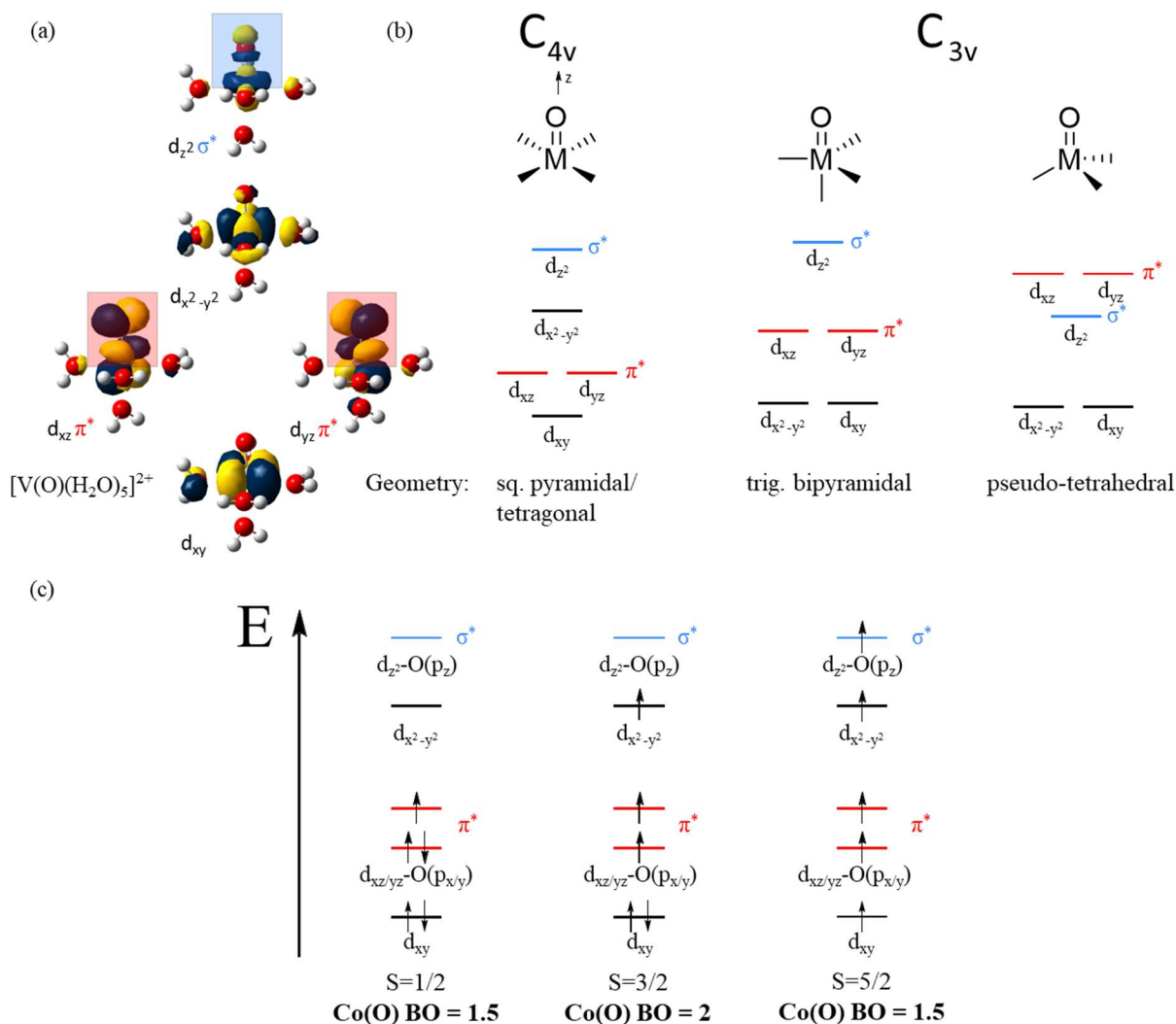
Figure 1.3. Coordination geometry, d-electron counts, and spin state govern M–O bond order. a) Molecular orbitals calculated for $[V(O)(H_2O)_5]^{2+}$ in tetragonal (C_{4v}) symmetry, indicating σ-bonding and π-bonding interactions involved in the V–O linkage. The V–O σ-antibonding and π-antibonding interactions are highlighted. Here, the M–O bond coincides with the z-axis. b) The relative energies of valence d orbitals of a M–O complex depend on its symmetry. c) The spin state of a complex, here a tetragonal Co^{IV}–O ($3d^5$) species, affects the formal M–O bond order. With respect to the M–O interaction, the black orbitals are non-bonding, the blue ones σ* and the red ones π*.

The average energy of the d orbitals, which depends on the effective nuclear charge of the transition-metal cation, decreases on moving left to right across the first row and with increasing metal oxidation state. This means that, for an early metal M–O complex, the filled O(2p) orbitals are much lower in energy than the M(3d) orbitals. In terms of the orbitals associated with the M–O fragment, the bonding combinations are mostly localized on the O center and the antibonding

15

combinations have dominant M(3d) character (see Figure 1.3a and Figure 1.4). As one moves left-to-right across the periodic table, the d-orbital energies decrease to values more comparable with the O(2p) orbitals, resulting in more covalent M–O bonding, and eventually bonding inversion, discussed below.

In the frontier molecular orbital diagram for a M–O complex in C_{4v} symmetry (Figure 1.3b, left) a pair of electrons of the oxo group formally occupies each one of the σ-bonding and π-bonding M–O orbitals (at lower energy and not shown). The number of electrons in the d orbitals then depends entirely on the nature and oxidation state of the metal. Using $[V(O)(H_2O)_5]^{2+}$ as an example, a complex initially studied by Ballhausen and Gray in 1962,[138] the V^{IV} center has a single d electron in the non-bonding d_{xy} orbital. This gives a formal V≡O triple bond, with the six bonding electrons coming exclusively from the oxo ligand. Advancing across the first row increases the 3d electron count for a given oxidation state. In a tetragonal $Cr^{IV}O$ (d^2) complex, the d_{xy} orbital would be doubly occupied, giving an unchanged M–O bond order of 3. For $Mn^{IV}O$ (d^3), one electron now populates the M–O antibonding π* orbitals (d_{xz}/d_{yz}), decreasing the formal M–O bond order to 2.5 and causing a Jahn–Teller distortion. In the case of $Fe^{IV}O$ (d^4), which is a key intermediate in C–H bond activation by high-valent heme and non-heme Fe–O intermediates, the famous Fe^{IV}=O double bond results. Then, one arrives at group 9. Indeed, by advancing from Fe^{IV} to Co^{IV} (d^5), another electron populates an M–O π* antibonding orbital, decreasing the bond order to 1.5, which destabilizes the oxo ligand and makes it more basic and nucleophilic. The M–O unit becomes much more reactive, such that it can undergo protonation and/or afford bridged M–O–M complexes. When suitable substrates are available, this likely increases reactivity for OAT and HAT. The effect of decreasing bond order becomes more drastic when one adds additional M–O π* antibonding electrons for Ni^{IV} and Cu^{IV}. See Section 4.1.2 for literature examples of proposed high-valent terminal Ni-O complexes. This growing instability of the M–O group and the corresponding increased reactivity was first noted by Ballhausen and Gray and is now widely known as the 'oxo wall'.[105,139] This term was coined by Harry Gray in the 1990s and first used in his advanced inorganic chemistry course.[140]

Our discussion has, so far, focused on low-spin complexes. There is, however, a possibility to break the oxo wall if higher spin states are considered, at least in the case of Co^{IV}. Let us illustrate this concept with simplified molecular orbital diagrams of formally tetragonal Co^{IV}–O complexes in different spin states (Figure 1.3c). A Co^{IV} center in an intermediate spin state ($S_t = 3/2$) can form

a Co=O double bond — a direct violation of the oxo wall. One example for such a complex is $[Co(13\text{-}TMC)(O)]^{2+}$ (13-TMC= 1,4,7,10-tetramethyl-1,4,7, 10-tetraazacyclotridecane).[141] In the case of a Ni^{IV}–oxo complex in a high-spin state ($S_t = 2$), a maximum Ni–O bond order of 1.5 could still be achieved, see Figure 4.1. However, whether this latter type of complex can be accessed experimentally is unclear. Aside from perturbing the spin state, another strategy to circumvent the oxo wall is to change the symmetry of the complex. The oxo wall declares the instability of late-transition-metal–oxo species of tetragonal symmetry but does not refer to other symmetries, despite erroneous literature claiming so. For example, a trigonal-bipyramidal (TBP) complex with an apical M–O moiety has C_{3v} symmetry and a different splitting pattern of the d orbitals (Figure 1.3b, middle). Here, the lowest-energy d orbitals are $d_{x2\text{-}y2}$ and d_{xy}, both of which are orthogonal to the M–O bond. Hence, a low-spin complex can store four electrons in these d orbitals without affecting the (formal) M–O bond order. In the case of Co^{IV} and Ni^{IV} complexes, one and two additional electrons are added to the π-antibonding d_{xz} and d_{yz} orbitals, which leads to formal M–O bond orders of 2.5 and 2, respectively. With Cu^{IV}, a third electron is added to these orbitals, destabilizing the M–O interaction such that the maximum formal bond order is 1.5.

If one begins with TBP symmetry featuring an apical oxo group and removes the other apical ligand, this allows the three remaining co-ligands to bend down, giving rise to pseudo-tetrahedral (PTD) C_{3v} symmetry (Figure 1.3b, right). A complex with PTD geometry has a similar orbital ordering as TBP, but the d_{z2} orbital may mix with the M(4s) and M(4p) orbitals, as proposed for an Fe–nitrido complex, such that the d_{z2} level drops in energy between the $d_{x2\text{-}y2}/d_{xy}$ and d_{xz}/d_{yz} pairs.[142] However, density functional theory (DFT) calculations on PTD V–O and Cr–O complexes predict d_{z2} to be the highest-energy 3d orbital in PTD symmetry,[143] so this point requires further study. If the d_{z2} energy does indeed fall between the $d_{x2\text{-}y2}/d_{xy}$ and d_{xz}/d_{yz} pairs, then low-spin Co^{IV}–O and Ni^{IV}–O complexes would have electron density in the σ-antibonding d_{z2} orbital and not in the π-antibonding d_{xz}/d_{yz} orbitals, which would be a truly unique bonding situation for a metal–oxo complex (weak σ-bonding and strong π-bonding). The synthesis and characterization of $[Ir^{V}(O)(mesityl)_3]$, a heavy late-transition-metal complex in this symmetry, was reported in 1993.[144]

Importantly, the electronic structures of such complexes play important roles in their reactivities. These complexes are often unstable, as predicted using ligand field diagrams, but have long been claimed as intermediates in reactions and catalytic cycles. Recently, chemists have

stabilized and characterized a few putative late-transition-metal–oxo complexes past the oxo wall. The syntheses of these complexes typically involve low-coordinate, non-tetragonal species and/or complexes with bulky ligands that may prevent bimolecular-decay pathways involving the highly basic oxo ligands of two M–O cores. If the M–O core is taken to be apical, then the equatorial donation of the supporting ligands can be tuned to stabilize this core, even if the metal element M is beyond the oxo wall in group 9 or higher.

1.3.4 Bonding Inversion

Fe: 56%
O: 29%

Co: 47%
O: 44%

Ni: 23%
O: 69%

Cu: 6%
O: 85%
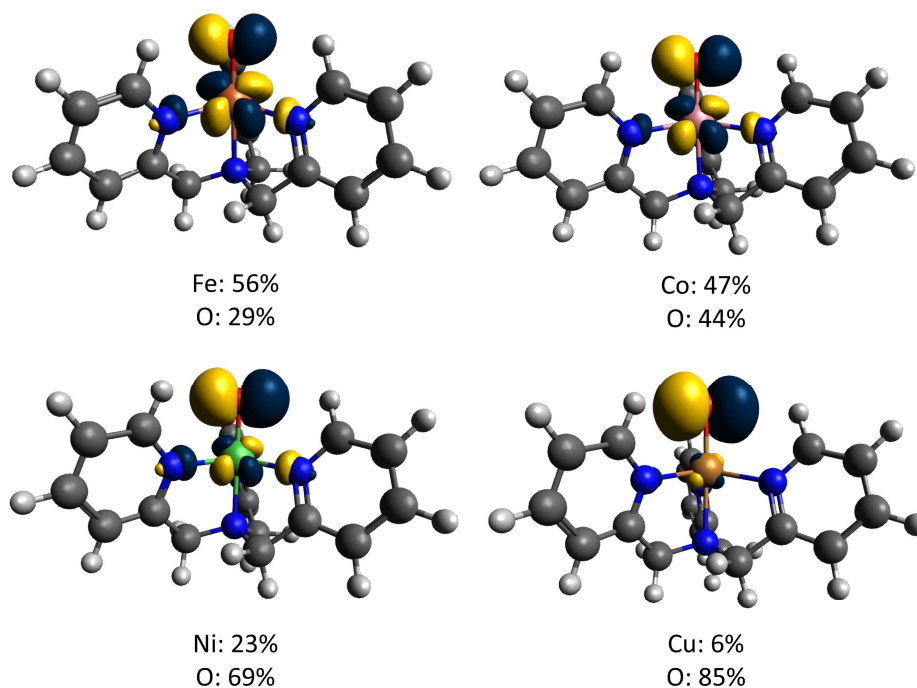
Figure 1.4. Inversion in a π-antibonding MO for a series of metal-oxo complexes from Fe through Cu for a series of M(O)[TBA]$^{n+}$ complexes. The percentage of metal and oxygen character of the MO shown is listed for each. The MOs were calculated in ORCA with PBE0/TZVP and visualized in Avogadro after optimization with PBE0/TZVP in Gaussian.

Another factor that can contribute to the instability of the late-transition-metal–oxo complexes is valence tautomerization. Thus, an oxo complex $Mn^{+1}=O^{2-}$ can exist as the corresponding oxyl species $Mn–O^{\bullet-}$, which is expected to be much more reactive.[145,146] This is particularly likely for late transition M–O complexes, in which the d orbitals are already very low in energy. If the d-orbital energies drop below those of occupied O(2p) orbitals, an inversion in bonding results, which means that the M–O bonding orbital combinations now have more

dominant M(d) character, and the antibonding orbital combinations have more O(2p) contributions.[146,147] In such an inverted ligand field, the oxo ligand acquires distinct radical (oxyl) character, weakening M–O bonding and likely activating the M–O group for reactions with substrates. This is illustrated by the metal decreasing and oxygen character increasing in a π-antibonding molecular orbital (MO) from Fe to Cu as calculated and visualized in Figure 1.4. The π-antibonding MO for Fe, top left, shows majority Fe character, as expected in traditional ligand field theory. However, this π-antibonding MO for Cu shows hardly any Cu character and nearly all O character, showing that the bond is fully inverted. The bonding MO is not shown but would have nearly all Cu character.

1.4 Scope of Thesis

The research described herein brings us closer to sustainable hydrogen production by investigating the chemical species involved in the catalytic processes used to split water. Hydrogen is a useful chemical feedstock[15] and clean fuel,[16,21] and to understanding metal-oxygen intermediates in water oxidation, fuel cell reactions, and enzymes.[148,149] Specifically, in this process of hydrogen and oxygen cycling between water and gases, this dissertation describes research I have conducted on cobalt bis(benzenedithiolate)s as (electro)catalysts for hydrogen production and spectroscopic and density functional theory studies characterizing iron- and nickel-oxygen intermediates with relevance to water oxidation.

Chapter 2 describes a molecular catalyst, [cobalt bis(benzylammoniumdithiolate)]$^+$, covalently attached to graphene oxide as a thin film catalyst for HER. This new member of the acclaimed cobalt dithiolene family of HER catalysts was characterized by UV-Vis and paramagnetic ^{1}H-NMR spectroscopy, cyclic voltammetry, and mass spectrometry, showing similar properties as known cobalt bis(benzenedithiolate) type complexes. The amine-modified complex is then covalently attached to graphene oxide through reaction with epoxide groups, and the resulting GO-Co suspension is drop-cast onto glassy carbon electrodes to give thin films. These films were characterized by atomic force and scanning electron microscopy, which show wrinkled films with a thickness of 330 ± 120 nm. When reduced, the RGO-[cobalt bis(benzylammoniumdithiolate)]$^+$ films (**RGO-1**) show high activity for electrocatalytic hydrogen production in acidic aqueous conditions with turnover frequencies up to 1000 s^{-1} at pH 0, an overpotential of 273 ± 5 mV at pH 3, and a Faradaic efficiency of 97 ± 4 %. With atmospheric

levels of dioxygen, **RGO-1** remains completely stable and delivers 79 ± 3 % Faradaic efficiency for HER. Kinetic and thermodynamic electrocatalysis parameters are further provided, including analysis of the onset potentials, foot-of-the-wave analysis, Tafel slopes, and plateau currents. The latter gives a rate constant of $1.5 \cdot 10^4$ $M^{-1}s^{-1}$ for HER for **RGO-1**. Controlled potential electrolysis for multiple hours shows improved activity and durability over the analogous physisorbed systems. This chapter has been adapted from **Larson, Virginia**; Lehnert, Nicolai*; "Covalent Attachment of Cobalt Bis(Benzylaminedithiolate) to Reduced Graphene Oxide as a Thin Film Electrocatalyst for Hydrogen Production with Remarkable Dioxygen Tolerance", *ACS Catal.* **2024**, *14* (1), 192–210.[2]

Chapter 3 investigates the individual steps in the HER mechanism of cobalt bis(benzenedichlorodithiolate). The first step in HER for this family of catalysts is reduction. Accordingly, the Co^{II} form of the complex is prepared by chemical and electrochemical reduction and characterized. X-ray crystallography shows that this species has square planar geometry, with a Co centered reduction. Further magnetic circular dichroism (MCD), electron paramagnetic resonance (EPR), and UV-Vis spectroscopy on this species support it is a low spin $S_t = ½$ Co^{II} species. The species is reactive towards protons, as expected, but instead of isolating a singly protonated species the reaction proceeds to return the Co^{III} starting complex. These results are being prepared to be published in a paper.

In Chapter 4, the identity and electronic structure of a formally Ni^{IV}-oxo species, prepared with the $TAML^{4-}$ co-ligand ($TAML^{4-}$ = tetraamido macrocyclic ligand), is shown to be best described as an intermediate spin Ni^{III}-oxyl species through in-depth spectroscopic characterization and density functional theory (DFT) calculations. The temperature sensitive and reactive species was characterized by MCD spectroscopy which revealed its spin state as an intermediate spin $S_t = 1$. The DFT studies, with experimental input from extended X-ray absorption fine structure (EXAFS), showed the best agreement with the experimental data to be a 6-coordinate $[Ni(O)(OH)(TAML)]^{3-}$. Due to the low energy of the Ni d-orbitals, the species shows a high degree of bond inversion, giving the SOMO mostly oxygen character. Therefore, the species is best described as a low spin Ni^{III} ferromagnetically coupled with an oxyl radical. This research was performed in collaboration with Professor Wonwoo Nam's group at Ewha Womans University in Seoul, Korea, who synthesized the complex and studied its reactivity, and Professor Jason Shearer's group at Trinity University in Texas, USA, who performed and analyzed the X-ray

absorption spectroscopic data. Adapted from Karmalkar, Deepika[‡]; **Larson, Virginia[‡]**; Malik, Deesha; Lee, Yong-Min; Seo, Mi Sook; Kim, Jin; Vasiliauskas, Dovydas; Shearer, Jason*; Lehnert, Nicolai*; Nam, Wonwoo*; "Preparation and Characterization of a Formally Ni^{IV}–Oxo Complex with a Triplet Ground State and Application in Oxidation Reactions", *J. Am. Chem. Soc.* **2022**, 144, *49*, 22698−22712.[150] The double dagger indicates Deepika Karmalkar and Virginia Larson are co-first authors on this manuscript.

In Chapter 5, a reactive Fe^{II} species with the TMCO (TMCO = 4,8,12-trimethyl-1-oxa-4,8,12-triazacyclotetradecane) co-ligand is investigated and through thorough spectroscopic and theoretical investigations, the species is shown to be a $Fe^{II}(OPh^{\bullet})$ complex. The elusive, reactive blue species was shown through careful synthetic work, by my collaborator Dustin Kass, to include a phenyl group that originated from $NaBPh_4$, and that could be synthesized in an alternative manner by one-electron oxidation of the corresponding Fe^{II}-phenolate complex. Resonance Raman (rRaman) and MCD spectroscopies were able to confirm that the alternative preparation is the same blue species, $Fe^{II}(OPh^{\bullet})$. Additionally, vibrational frequencies calculated by DFT matched the rRaman data well, especially matching the experimental change in the rRaman spectra when $NaB(p\text{-methylphenyl})_4$ is used in place of $NaBPh_4$. MCD spectroscopy and DFT, in agreement with electron paramagnetic resonance (EPR) and Mössbauer, support the identification of the species as a high-spin, $S_t = 2$ Fe^{II} ferromagnetically coupled with a phenoxy radical for an overall $S_t = 5/2$ species. This research was performed in collaboration with Professor Kallol Ray's group at Humboldt University in Berlin, who synthesized the title complex and its variations, and performed the initial spectroscopic characterization and reactivity studies. Ray's collaborators in the Bill group performed the Mössbauer and EPR spectroscopies and related analysis. This chapter is adapted from Kass, Dustin[‡]; **Larson, Virginia[‡]**; Corona, Teresa; Kuhlmann, Uwe; Hildebrandt, Peter; Lohmiller, Thomas; Schnegg, Alexander; Eckhard, Bill; Lehnert, Nicolai*; Ray, Kallol*; "Trapping of a Phenoxyl Radical at a Non-Heme High-Spin Iron(II) Center", *Nat. Chem.* **2024**.[151] This manuscript has been published but has not yet been assigned volume, issue, and page numbers. The double dagger indicates Dustin Kass and Virginia Larson are co-first authors on this manuscript.

In Chapter 6, the electronic structures of a series of Fe^{III}-peroxide complexes with tetra-amine co-ligands of different ring sizes are investigated via spectroscopic characterization and density functional theory calculations, to explain the drastically different reactivities across the

series. DFT analysis shows that the Fe-peroxo bond primarily consists of a δ and pseudo-σ bond. MCD spectra of these complexes show an interesting derivative type signal that is preserved across the series, the lower energy signal of which is shown to correspond to the δ to δ* ligand to metal charge transfer (LMCT) by variable temperature variable field MCD and time dependent-DFT. This δ to δ* electronic transition is also the main electronic transition observed by UV-Vis and gradually increases in energy from 14- to 13- to 12-TMC (TMC = *N*-tetramethylated cyclam). This change in energy reflects a stronger Fe-O_2 bond as the co-ligand ring contracts. Additionally, the complexes show sensitivity of their vibrational properties and electronic transitions to the H-bonding ability of the solvent, which is explained by the δ bond formed between the Fe d_{xy} and the O π*, the latter of which is sensitive to H-bonding. This research was performed in collaboration Professor Wonwoo Nam's group at Ewha Womans University in Seoul, Korea, who synthesized the complexes, studied their reactivity, and performed the rRaman spectroscopy, and Professor Binju Wang's group at Xiamen University, in Xiamen, China who performed the DFT geometry optimizations and DFT reaction coordinate analysis. Adapted from Zhu, Wenjuan;[‡] Wu, Peng;[‡] **Larson, Virginia**;[‡] Kumar, Akhilesh;[‡] Li, Xiao-Xi; Seo, Mi Sook; Lee, Yong-Min; Wang, Binju;* Lehnert, Nicolai;* and Nam, Wonwoo;* "Electronic Structure and Reactivity of Mononuclear Nonheme Iron-Peroxo Complexes as a Biomimetic Model of Rieske Oxygenases: Ring Size Effects of Macrocyclic Ligands", *J. Am. Chem. Soc.* **2024**, *146* (1), 250–262.[152] The double dagger indicates Wenjuan Zhu, Peng Wu, Virginia Larson, and Akhilesh Kumar contributed equally to this manuscript.

Chapter 7 concludes this thesis, discusses preliminary work, especially on photo(electro)catalytic HER with Co bis(benzenedithiolate) type catalysts, and possible future directions.

Chapter 2 Covalent Attachment of Cobalt Bis(Benzylaminedithiolate) to Reduced Graphene Oxide as a Thin Film Electrocatalyst for Hydrogen Production

In this chapter, a new amine functionalized member of the Co bis(benzenedithiolate) family of HER catalysts is synthesized and covalently attached to RGO. The modified RGO-catalyst is drop-cast to make thin films which are shown to be highly active for electrocatalytic hydrogen evolution. The chapter is adapted from: **Larson, Virginia**; Lehnert, Nicolai*; "Covalent Attachment of Cobalt Bis(Benzylaminedithiolate) to Reduced Graphene Oxide as a Thin Film Electrocatalyst for Hydrogen Production with Remarkable Dioxygen Tolerance" *ACS Catal.* **2024**, *14* (1), 192–210.[2]

2.1 Introduction

Hydrogen (H_2) can be produced in the water splitting reaction, specifically on the cathodic side through the hydrogen evolution reaction (HER), where two protons and two electrons are combined to make H_2. This study of a HER molecular catalyst immobilized in thin RGO films continues to develop our understanding of thin film electrocatalysis for the advancement of both clean hydrogen production as well as for other electrocatalytic reactions related to clean energy and chemical syntheses. Please see the Introduction Section 1.1 for further discussion on the benefits of clean hydrogen production from water splitting.

Our group has researched cobalt bis(benzenedithiolate) type catalysts for hydrogen evolution when physisorbed on graphitic electrode surfaces. Please see the Introduction Section 1.2.4 for further discussion on this research. The drawbacks of physisorption as a heterogenization method are that it necessitates a graphitic electrode surface and a catalyst that can π-stack to the surface. Our group has noted that in such systems, catalytic activity is shown to decrease over time; for example, for cobalt bis(benzenedithiolate) complexes adsorbed on HOPG, HER activity decreases to ~10% of the initial current within 8 hrs.[97] As the amount of cobalt on the electrode surface was shown to decrease as well, it was proposed that the catalyst slowly dissociates from the electrode surface, leading to loss of activity. Dissociation is a reasonable deactivation

mechanism, as a physisorbed catalyst is only held to the surface by relatively weak intermolecular forces. Therefore, an analogous system where the catalyst binds more strongly to the electrode surface, by forming a covalent bond between the RGO film on the electrode surface and the cobalt bis(benzenedithiolate) type catalyst was designed.

2.1.1 Scope of This Chapter

In this chapter, a new amine-modified cobalt bis(benzenedithiolate) complex is synthesized and then characterized by UV-Vis and paramagnetic nuclear magnetic resonance spectroscopy, mass spectrometry, and cyclic voltammetry, showing that this complex is similar to other cobalt bis(benzenedithiolate) catalysts reported before. The amine functionality allows the catalyst to form a covalent bond with GO by reacting with epoxide groups on the GO sheets in solution.[153] The modified GO can be drop-cast onto a benign electrode to form a thin film, and can then be reduced in situ to form RGO. The RGO-Co thin films obtained in this way were characterized by scanning electron and atomic force microscopy. The thin film catalyst is shown to be highly active for electrocatalytic hydrogen production in acidic (pH 0-4) aqueous solutions, giving an observed TOF of up to 1000 s^{-1} by cyclic voltammetry. In inert atmosphere, quantitative Faradaic efficiency is observed, while under air, the catalyst maintains 79% Faradaic efficiency for hydrogen evolution. Further, detailed electrochemical discussion is provided in this chapter, including the analysis of catalytic onset potentials, Tafel slopes and plateau currents, and the application of the foot-of-the-wave method. Controlled potential electrolysis reveals a TON of $1.3 * 10^5$ before loss of electrocatalytic activity is observed.

2.2 Results and Analysis

2.2.1 Synthesis and Characterization of the Catalyst

The preparation of the amine-modified catalyst requires the synthesis of the corresponding amine-substituted benzenedithiol ligand. Of the investigated synthetic routes for such a molecule, the one shown in Figure 2.1 was found to be successful. First, the amine group of the 3,4-difluorobenzylamine starting material is protected with a *tert*-butoxycarbonyl (boc) moiety. The aryl-fluorines are then substituted for thiols, forming thioethers, via nucleophilic aromatic substitution. This reaction is the lowest yielding step of the overall synthetic pathway and results

in a mixture of the desired disubstituted product with impurities of the monosubstituted compounds. The mixture is deprotected in one step, removing both the diphenylmethyl and boc protecting groups, to give the protonated amine-modified benzenedithiol ligand. The ligand is then deprotonated and metalated with cobalt, giving the amine-modified cobalt bis(benzenedithiolate) complex **1** (note that complex **1** is the protonated (ammonium) version of the catalyst). While the monosubstituted biproducts of the nucleophilic aromatic substitution are present in the metalation reaction, they are not expected to metalate with Co^{III} since they do not contain the *cis*-dithiolate unit that binds so strongly to trivalent metal ions. Correspondingly, ^{19}F-NMR spectroscopy of the metalated complex does not show ligand fluorine peaks (Figure 2.30), indicating that the monosubstituted biproducts are removed in the metalation process and following workup. Complex **1** is soluble in DMF with a 5% HCl aqueous solution added, such that there are about 10 equivalents of HCl present per catalyst. Complex **1** is more stable in this solution, hereafter referred to as DMF/HCl$_{aq}$, than in its deprotonated form (either as a solid or in solution). Further details on the synthesis of **1** are provided in the Experimental Section (2.4.3).
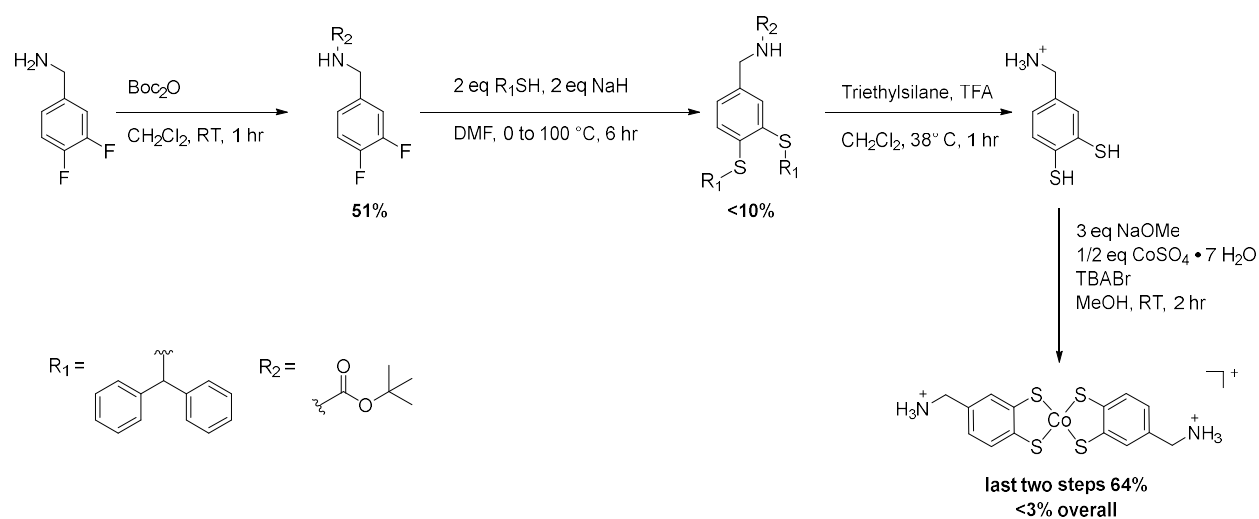
Figure 2.1. Synthetic scheme of the amine-modified catalyst.

25
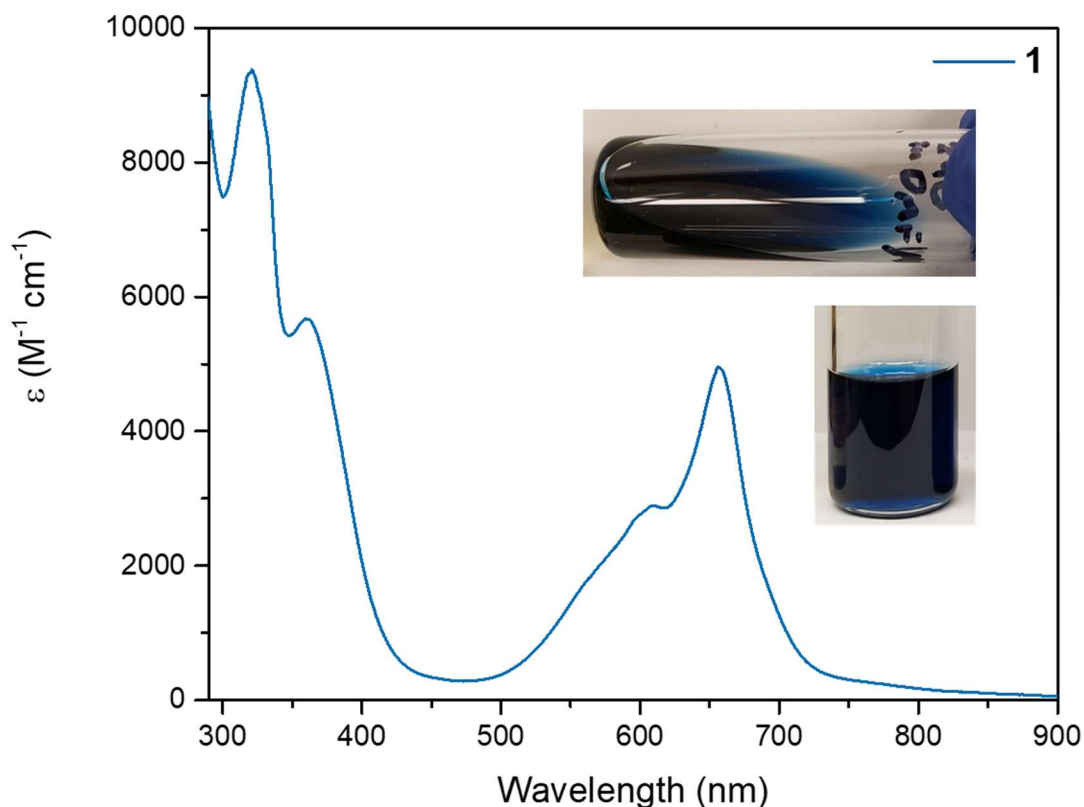
Figure 2.2. UV-Vis spectrum of **1** at 0.12 mM concentration in DMF with trace HCl_{aq}. The inset shows pictures of **1** in DMF/HCl_{aq}.

Complex **1**, a new variation on the class of Co bis(benzenedithiolate) complexes, compares well in terms of spectroscopic properties to other representatives of this group that were previously characterized. Figure 2.2 shows the UV-Vis spectrum of **1**. The data show intense, broad ligand-to-metal charge-transfer (LMCT) bands in the NIR region,[62,97] with a maximum at 657 nm, responsible for the deep blue color of the complex. The higher energy absorption bands are thought to originate from intraligand π-π^* transitions.[154] Both of these features are well conserved across the family of Co bis(benzenedithiolate) complexes,[61,97] implying that **1** is electronically similar to other members of the family, as expected. Complex **1** was also characterized by mass spectrometry, showing a mass of 396.95 m/z which matches well with the calculated 396.94 m/z for [Co(benzylaminedithiolate)$_2$]$^-$, resulting from deprotonation of the amine under the experimental conditions.

As these complexes are paramagnetic, with a four-coordinate (4C), intermediate-spin Co^{III} center ($S_t = 1$), paramagnetic NMR spectroscopy offers a suitable characterization method for these

complexes (Figure 2.3), giving rise to a unique spectral fingerprint. The paramagnetic ^{1}H-NMR spectra of the tetrabutylammonium (TBA[+]) salts of the complexes cobalt bis(benzenedichlorodithiolate) (**2**) and cobalt bis(toluenedithiolate) (**3**) have been previously reported and show the aromatic protons paramagnetically shifted upfield to circa -25 ppm.[155] The tolyl protons of **3** are shifted downfield to 46 ppm. Comparison of the ^{1}H-NMR spectra of **1** to those of these complexes provides further insight into the spectral assignments for **1**. In this case, three paramagnetically shifted proton signals at -20.0, -20.5, -24.1 ppm are observed, which are similar to, but distinct from, the aromatic proton signals of **2** and **3**, and another signal at 30.2 ppm, whose similarity to the tolyl protons of **3** indicates that this peak corresponds to the benzyl protons of **1**. For additional comparison, the acetyl-protected form of the cobalt bis(benzylaminedithiolate) complex, labeled **4**, was prepared as well, by reacting **1** with excess acetic anhydride and triethylamine (TEA). As expected, the paramagnetic ^{1}H-NMR spectrum of **4** is similar to that of **1**, but with shifts in both the upfield and downfield signals.
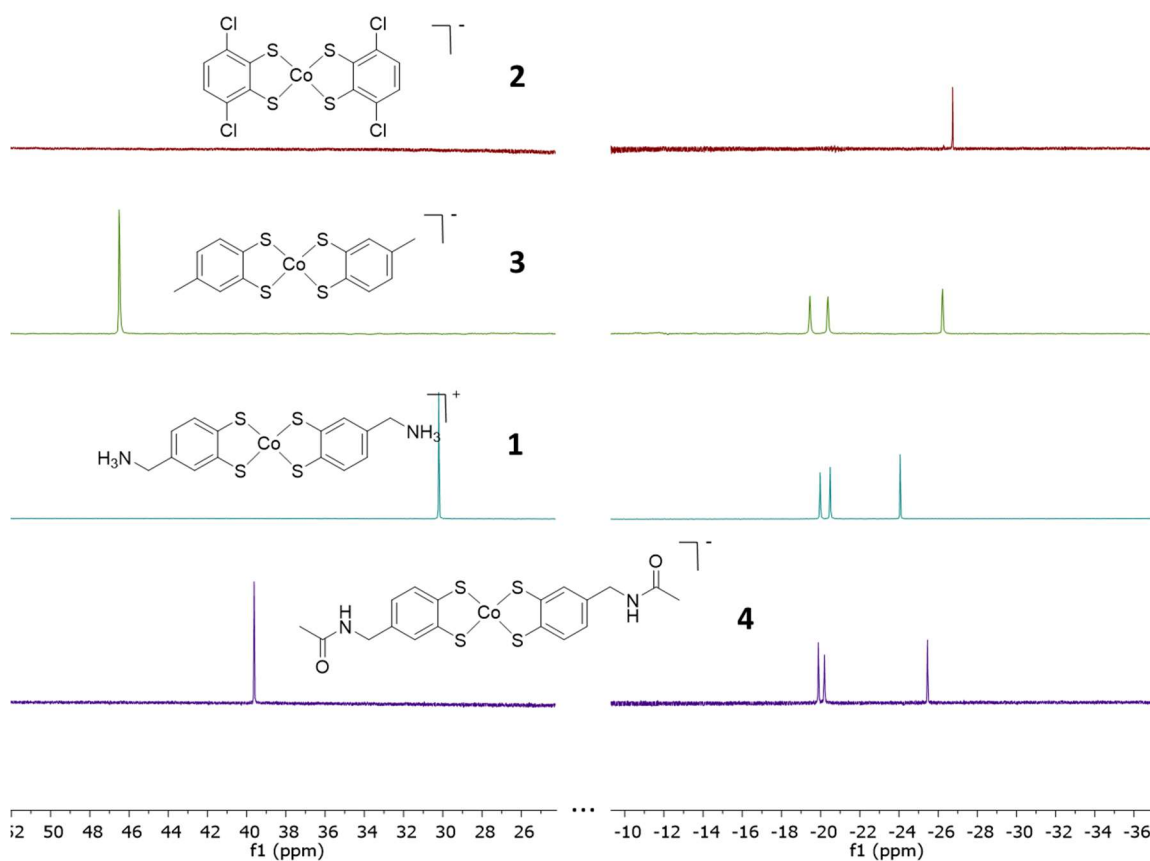
Figure 2.3. Comparison of paramagnetic ^{1}H-NMR spectra of cobalt bis(benzenedithiolate) type complexes, as indicated. From top to bottom: **2**, ^{1}H-NMR (400 MHz, DMF): aromatic: -26.74

ppm; **3**, ^{1}H-NMR (400 MHz, DMF): tolyl: 46.48; aromatic: -19.45, -20.37, -26.23 ppm; **1**, ^{1}H-NMR (500 MHz, DMF/HCl$_{aq}$): benzyl: 30.21; aromatic: -19.98, -20.49, -24.06 ppm; and **4**, ^{1}H-NMR (400 MHz, DMF): benzyl: 39.62; aromatic: -19.89, -20.20, -25.46 ppm. Molecular structures are indicated. See Figure 2.4 for ^{1}H-NMR spectra of **2** and **3** in CDCl$_3$.
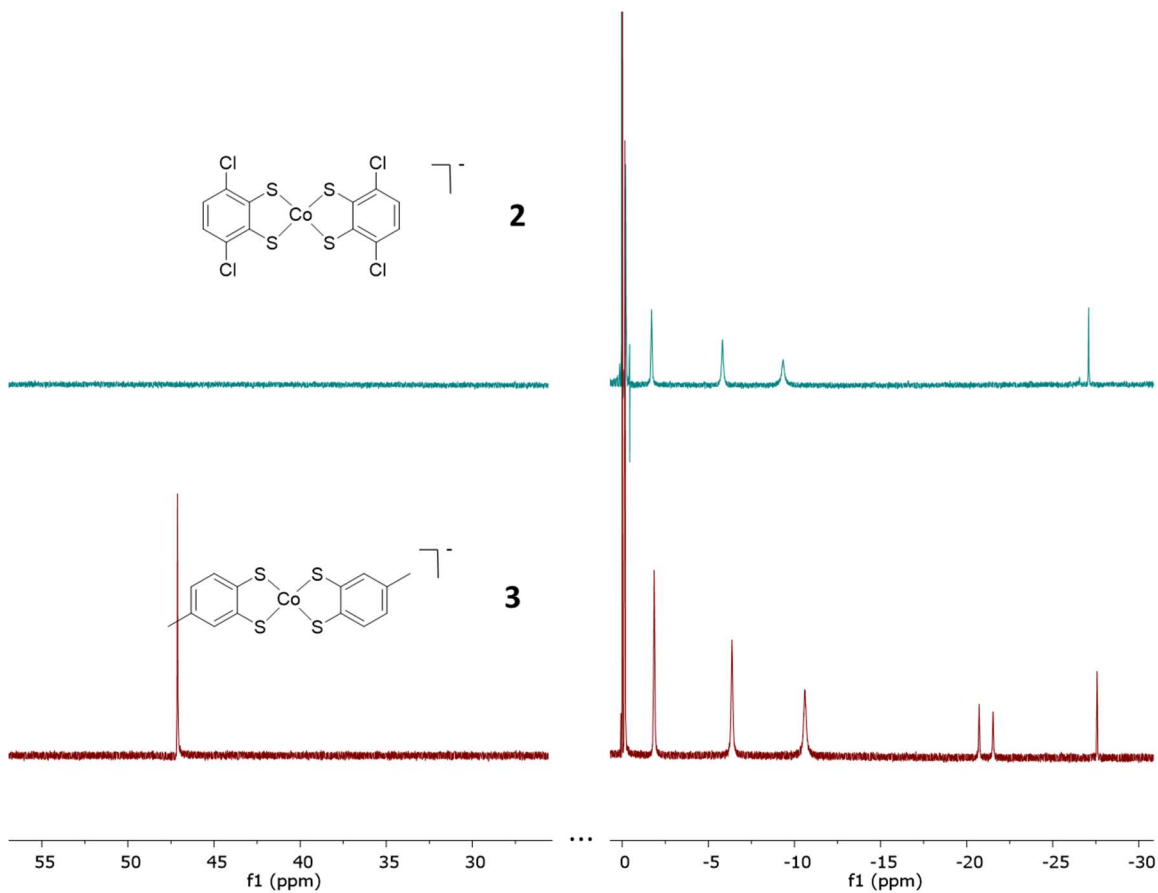
Figure 2.4. Comparison of paramagnetic ^{1}H-NMR spectra of cobalt bis(benzenedithiolate) type complexes in CDCl$_3$. Top: complex **2**, ^{1}H-NMR (400 MHz, CDCl$_3$): TBA$^+$: -0.20, -1.70, -5.82, -9.33; aromatic: -27.08 ppm; Bottom: complex **3**, ^{1}H-NMR (400 MHz, CDCl$_3$): tolyl: 47.13; TBA$^+$: -0.16, -1.85, -6.37, -10.61; aromatic: -20.72, -21.53, -27.57 ppm.

In DMF, none of the complexes show an associated counter ion. However, interestingly, in CDCl$_3$ the tolyl and dichloro complexes have an associated TBA$^+$ counterion that shows paramagnetically shifted signals, see Figure 2.4. Note that paramagnetic N-H (amine or amide) proton signals for **1** nor **4**, nor the acetyl C-H proton signals for **4** are not observed. Likely these are either broad (N-H), or do not show significant paramagnetic shifts (acetyl C-H) and are therefore lost in the solvent suppression region. Without TEA included as a base in the reaction of **1** to **4**, there was no observed reaction. This result shows that complex **1** contains a protonated

amine group, which can be deprotonated by TEA and then participate in classic amine reactivity. TEA is further shown to deprotonate **1** by UV-Vis spectroscopy (see Figure 2.5).
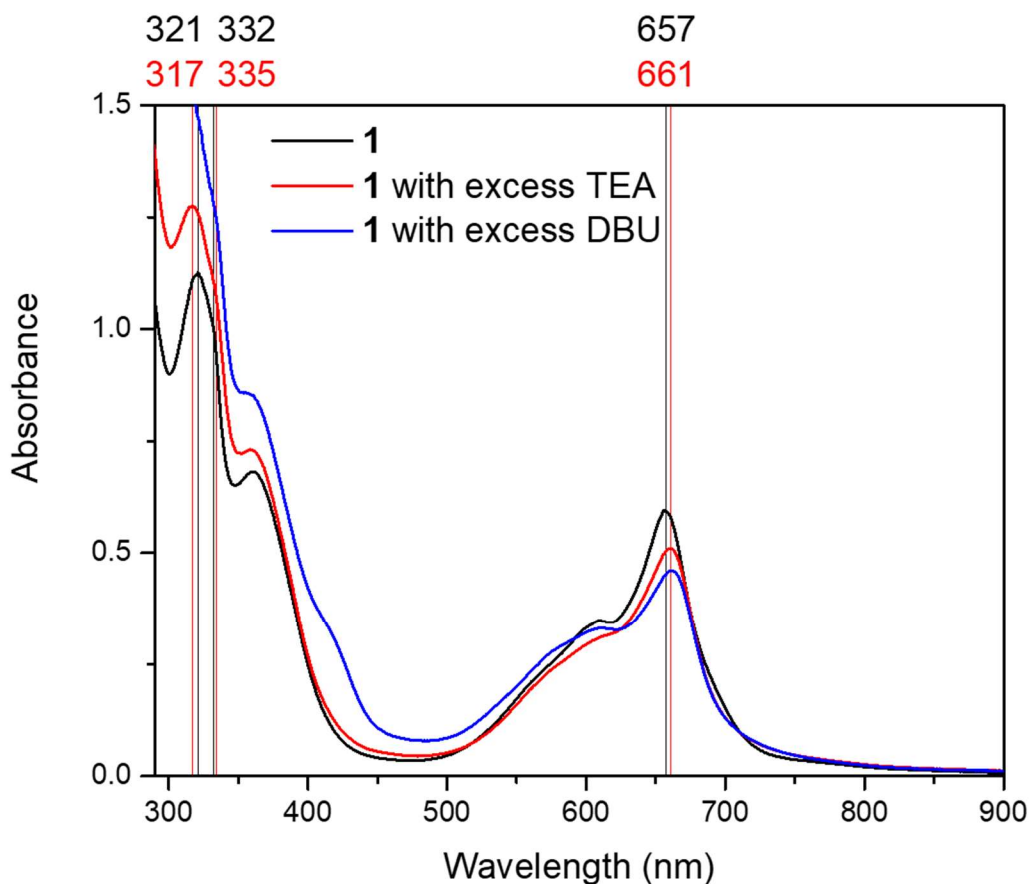
Figure 2.5. Comparison of the UV-Vis spectra of **1**, 0.12 mM in DMF (black), and of **1** after deprotonation by excess organic base, either triethylamine (TEA, red) or 1,8-diazabicyclo[5.4.0]undec-7-ene (DBU, blue). Excess DBU likely destabilizes the complex, with the increase in absorption at 450 nm being attributed to increased light scattering from precipitated particles in solution, caused by decomposition. TEA shows the same band shifts, without the increase in light scattering.

The Co^{III}/Co^{II} couple of **1** was characterized by cyclic voltammetry in DMF. Upon neutralization of the DMF/HCl_{aq} solution with TEA the catalyst shows a largely reversible Co^{III}/Co^{II} redox couple with an $E_{1/2}$ at -1.22 V vs Fc^+/Fc. Varying the scan rate from 0.01 V/s to 5 V/s is accompanied by an increase in the peak current (Figure 2.6a). The peak current increases linearly with respect to the square root of the scan rate, as expected for a molecule dissolved and diffusing in solution (Figure 2.6b).
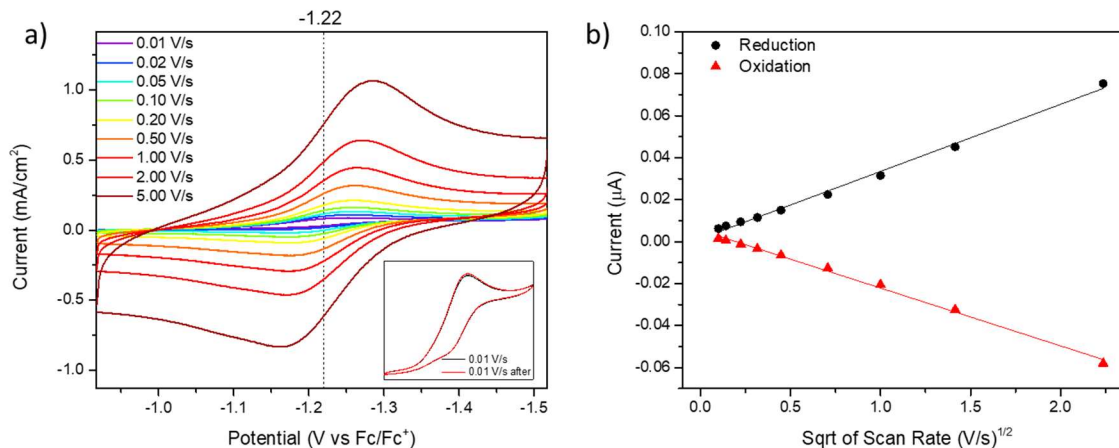
Figure 2.6. Co^{III}/Co^{II} redox couple of deprotonated **1** in DMF at different scan rates, 0.01 V/s through 5 V/s. a) Each scan was conducted twice with the second scan shown, and the inset shows an overlay of the 0.01 V/s first scan and the last scan at 0.01 V/s, after the 5.00 V/s scan. b) Peak current plotted as a function of the square root of the scan rate. The data were fit with a straight line to show the expected scan rate dependence of a redox-active species in solution, with R > 0.99 for both reduction and oxidation data. The acidic (HCl) DMF solvent was neutralized with addition of TEA for these experiments to prevent HER, which would convolute the redox couple. Electrochemical measurements were carried out in a one compartment cell with 0.1 M [TBA](PF$_6$) as the electrolyte. The reference electrode was a silver wire pseudo reference, which was then referenced to Fc$^+$/Fc after the above scans; the counter electrode was Pt wire; and the working electrode was glassy carbon.

2.2.2 Thin Film Preparation and Characterization
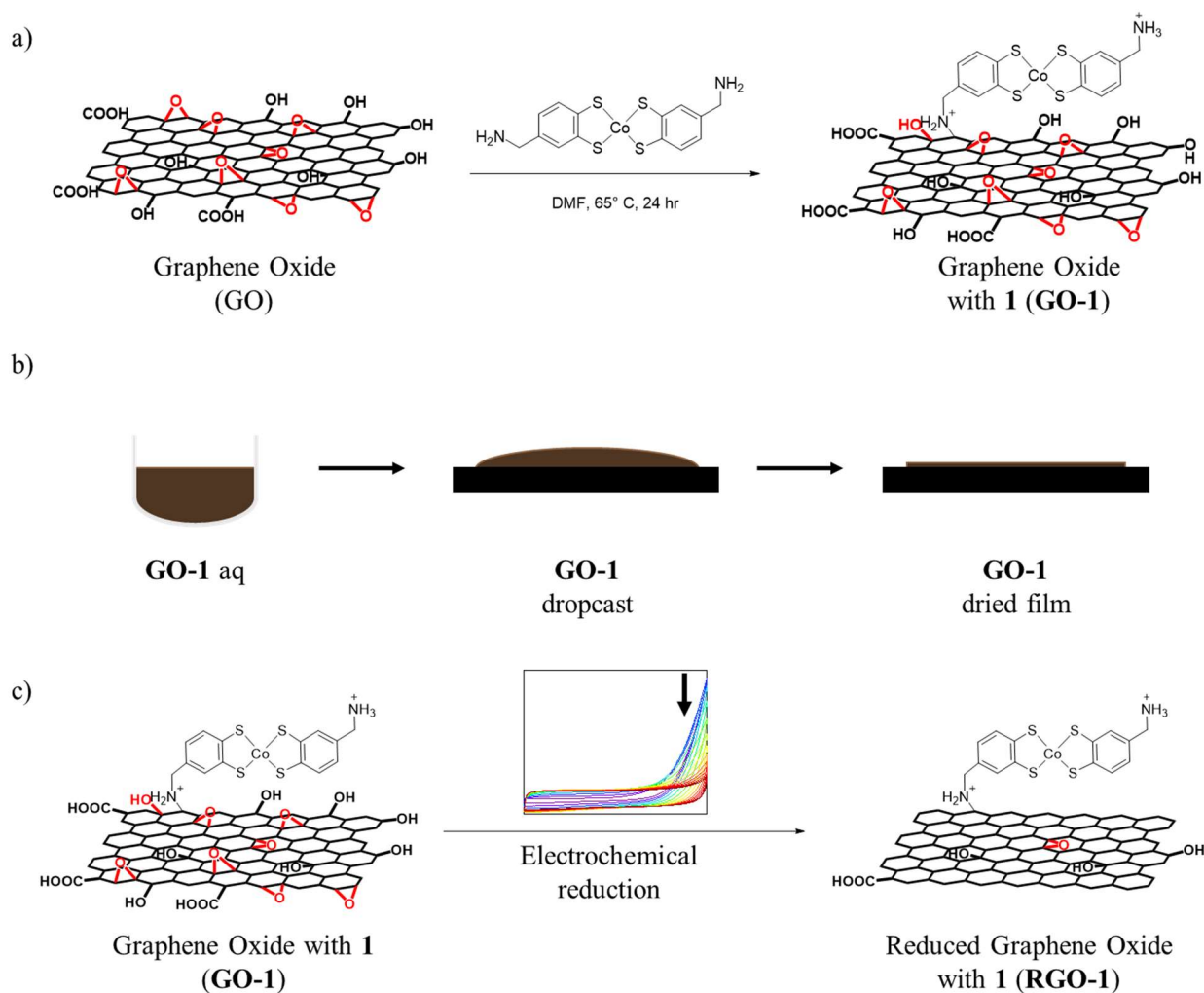
Figure 2.7. a) Covalent attachment of **1** to GO to form **GO-1** by heating in dimethylformamide (DMF) at 65 °C; b) schematic of drop-casting of the aqueous suspension of **GO-1** onto a surface (usually a glassy carbon electrode); c) schematic of electrochemical GO reduction to RGO. Note that the GO sheets shown here are not to scale but serve as a visualization of part of a GO nanosheet.

GO was chosen as the thin film material as it is solution-processable and it provides a direct comparison between physisorption and covalent attachment. GO is an oxidized form of graphite. GO is often made by oxidizing graphite with harsh oxidants, such as H_2SO_4 and $KMnO_4$, in the popular modified Hummers method, and so it has a variety of oxygen functional groups. Here we take advantage of the epoxide functional groups to react with amines.[153] In this study, commercial GO is used for its standardized properties and accessibility. The commercially available GO is

then lyophilized to provide a version of GO that can be precisely weighed out and resuspended in organic solvents.

Lyophilized GO resuspended in DMF was reacted with deprotonated **1** for 24 hours at 65 °C. The product was rinsed with organic solvents and resuspended in water to give GO covalently modified with **1** (**GO-1**, 1 mg GO/mL, Figure 2.7a). Further details on the covalent attachment synthetic procedure are provided in the Experimental Section 2.4.3. The same reaction was performed with **2**, and without the addition of any catalyst. Inductively coupled plasma mass spectrometry (ICP-MS) measurements of ^{59}Co were used to quantify the amount of catalyst in each GO suspension. **GO-1** contains $(2.00 \pm 0.09) \cdot 10^{-10}$ mol Co per 3.5 µL aliquot used to make each 3 mm diameter film, or 2.8 nmol Co/cm^2. This amount of Co is nearly ten times larger than the amount that is retained when **2** is subjected to the same reaction conditions, $(0.23 \pm 0.05) \cdot 10^{-10}$ mol Co per film aliquot. This difference in the amount of Co demonstrates that **1** is able to make a covalent bond with GO, while **2** is not. Instead, minor amounts of **2** are physisorbed to GO, but most of it is removed while rinsing the GO with organic solvents in the workup of this procedure.
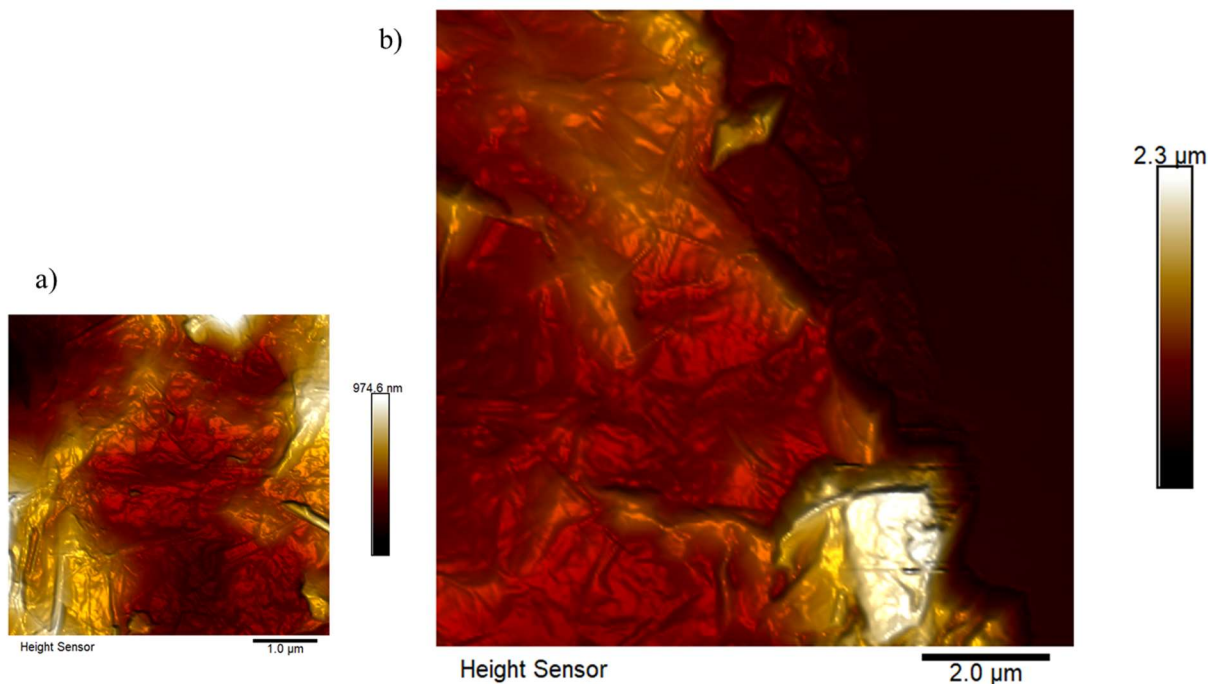
Figure 2.8. Representative AFM images of a **GO-1** film drop-cast on silicon. The images were analyzed using NanoScope Analysis 2.0, and shown here are the 2D data, with a 3D light cast for better visualization. a) A representative AFM image of the middle of a **GO-1** film drop-cast on silicon. b) A representative AFM image of a GO-**1** film drop-cast on silicon where a needle was used to score the film, exposing flat silicon underneath the film (low flat portion shown here on

the right). The height was calculated using the section tool, the resulting lines were fit in Origin with the baseline corrected to the flat silicon background.

Thin films, 3 mm in diameter, of **GO-1** were formed by drop-casting 3.5 μL of the **GO-1** suspension (Figure 2.7b). These films were then characterized using atomic force microscopy (AFM), as shown in Figure 2.8. AFM measurements of **GO-1** thin films drop-cast on silicon show wrinkled films of overlapping GO sheets, mostly flat with some taller ridges distributed throughout. Analysis of these films gives a roughness (R_a) of 146 ± 30 nm of the films (N = 5, 4 AFM images on 2 films, R_a was measured on a 5 x 5 μm area). The film height was found using a needle to score the film, and the difference in height between the silicon and the unharmed film surface gave a film thickness of 330 ± 120 nm (N = 15, three 10 x 10 μm images of two films, with 5 sections per image).
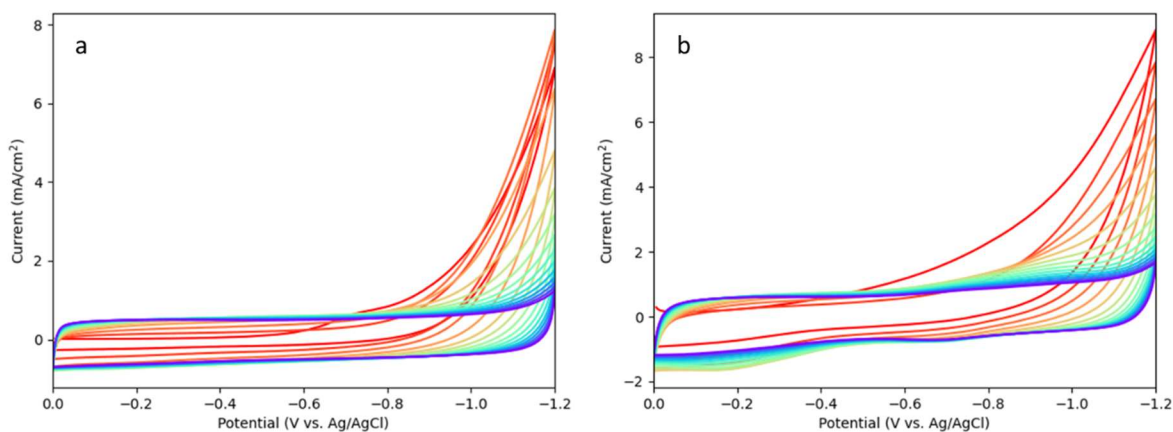
Figure 2.9. Electrochemical reduction by CV of (a) a GO film, (b) a **GO-1** film with 0.1 M KPF_6 as the supporting electrolyte. Scans were carried out with 15 CV loops between 0 and -1.2 V vs Ag|AgCl at 200 mV/s in 0.1 M KPF_6; the working electrode was a GO (a) or **GO-1** (b) film on glassy carbon; carbon felt was used as the counter electrode; Ag|AgCl in saturated KCl was used as the reference. A two compartment cell with half cells separated by a Nafion membrane was used, under N_2. The first CV scan is shown in red and the last in purple. Note that the later CV scans overlay, indicating that GO reduction is complete.

GO, as it is an oxidized form of graphite where the aromatic network is disrupted, must be reduced to RGO to regain conductivity. Electrochemical reduction has been shown to be effective at reducing GO.[156,157] The **GO-1** films are reduced to **RGO-1** films electrochemically, with 15 consecutive reductive cyclic voltammetry (CV) scans from 0 to -1.2 V vs Ag|AgCl at 200 mV/s in 0.1 M KPF_6 as the supporting electrolyte (Figure 2.7c).[78] Examples of the reducing CV scans are shown for a **GO-1** film and a control GO film in Figure 2.9. These control GO films are prepared in the same way as **GO-1** films, with the omission of **1** in the attachment procedure.
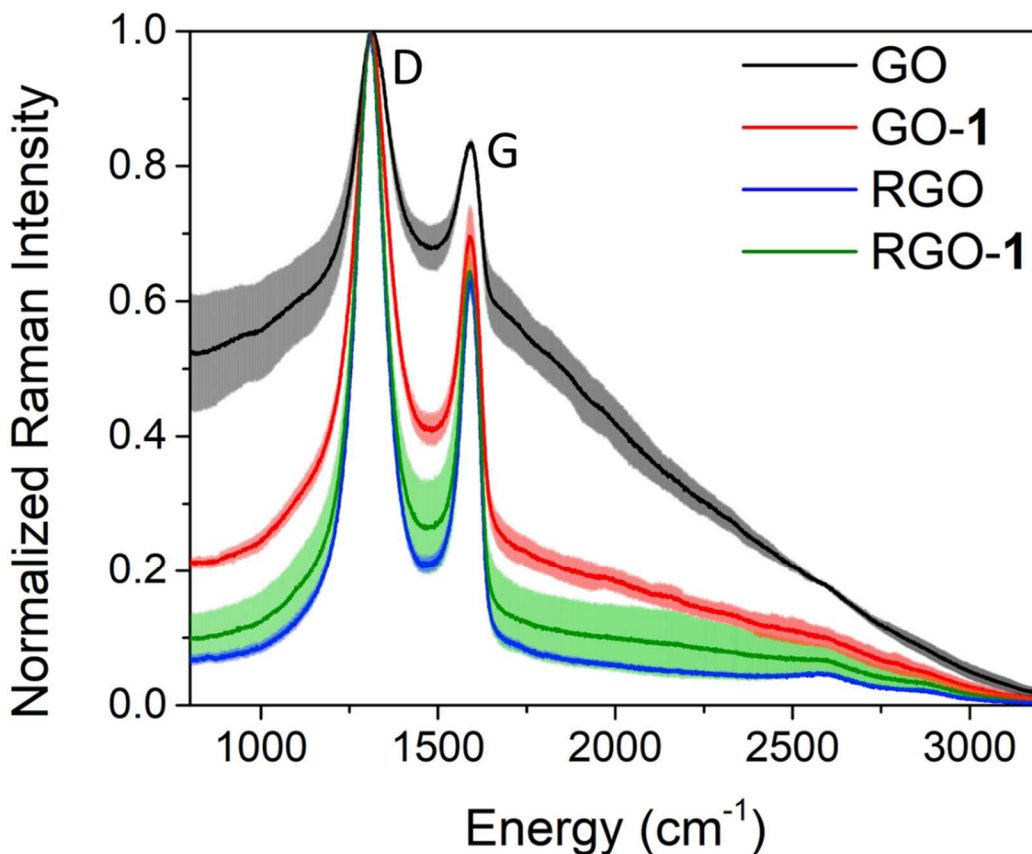
Figure 2.10. Raman spectra of GO films before reduction, and the resulting RGO films after electrochemical reduction with or without catalyst, as indicated. Electrochemical reduction was conducted with 15 CV scans between 0 and -1.2 V vs Ag|AgCl at 200 mV/s in 0.1 M KPF$_6$ solution; the working electrode was a GO or **GO-1** film on glassy carbon; carbon felt was used as the counter electrode; Ag|AgCl in saturated KCl was used as the reference electrode. A two compartment cell with half cells separated by Nafion was used, under N$_2$. The standard deviation is shown for N = 3 sites on each film. For easy comparison between data, the spectra were normalized and then averaged. A 785 nm laser was used for data collection.

Raman spectroscopy shows the reduction of **GO-1** and GO films (Figure 2.10). Raman spectroscopy of graphitic materials is expected to show D and G bands that give information on the crystallinity of the graphitic material. As expected, due to the oxidation and disruption of their graphitic structures, the GO film shows only slight D and G graphitic bands. After reduction of GO to RGO, the D and G bands are much sharper, indicating reestablishment of crystalline graphitic domains.[158] Previous work on RGO prepared in this manner found that these crystalline domains were small.[78] Here as well, RGO was found to give a D/G peak ratio of 1.59 and a G band position of 1591 cm^{-1}, similar to what has been observed for nanocrystalline graphite.[159] The catalyst modified film, **GO-1** shows more reduced character than the GO film, likely reflecting its

modification. Upon electrochemical reduction, **GO-1** undergoes further reduction to **RGO-1**, giving a reduced film with similar characteristics as RGO, but with some higher variability as shown by the increased standard deviation of the Raman signal. This may be due to crosslinking of the GO sheets due to two reactive amine moieties on the catalyst, causing the roughness and ridges observed by AFM, and thereby causing some incomplete reduction in thicker areas of the film.
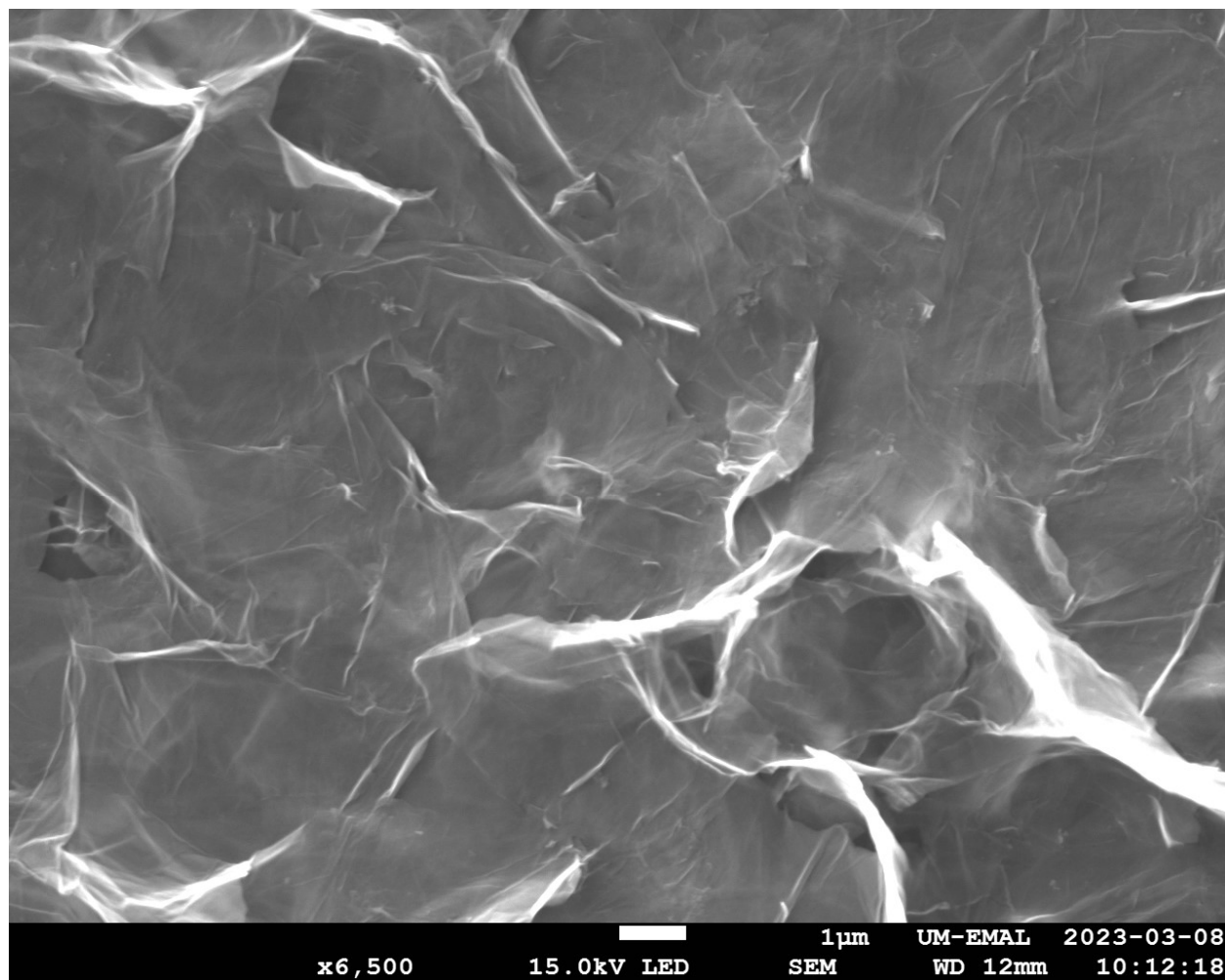
Figure 2.11. SEM image of an **RGO-1** film, prepared by drop-casting a **GO-1** film on a GC electrode, followed by reduction, as described in the Experimental Section 2.4.4 (see also Figure 2.9). The film is shown here at 6500x magnification, with a 1 μm scale bar. The image was taken using a 15.0 kV electron beam and a working distance of 12 mm.

Scanning electron microscopy (SEM) images of the reduced films show a mostly flat, slightly wrinkled film covering the surface, as the RGO sheets overlay each other (see Figure 2.11 for a representative example). These SEM images are similar to RGO films previously

reported.[77,78,160,161] SEM coupled with energy-dispersive X-ray spectroscopy (EDS) shows increased sulfur on the ridges of the films (Figure 2.13). As SEM-EDS measures a deeper cross section of the sample than the thickness of the films, the intensity of the sulfur signal likely varies with film thickness, as the majority of the sulfur signal arises from **1** embedded in the films, leading to the increased signal for the thicker ridge regions. From ICP-MS measurements, the density of Co in the films by mass is ~0.3 %, and by atom it is ~0.07%. Therefore, the amount of cobalt is just below the detection limit for common materials characterization techniques like SEM-EDS and X-ray photoelectron spectroscopy (XPS). No significant signal for Co was observed by SEM-EDS (Figure 2.13). XPS is known to have a sensitivity of roughly 0.1–1 atomic %, and only detects Co on the surface of the films;[162] however, with extensive data collection of the cobalt 2p region were we able to observe a significant Co signal (see Section 2.4.2). The Co spectrum is consistent with a Co^{III} species as expected for **1**, see Figure 2.12. The XPS spectra of the C, N, S regions are shown in Figure 2.12 as well and are consistent with a GO film modified with **1**, with increased N and S signal compared to unmodified **GO**. The presence of Co in the films was further confirmed from ICP-MS data and similar electrochemical activity and reactivity as Co bis(benzenedithiolate) type catalysts physisorbed to graphitic electrode surfaces, as discussed further below.
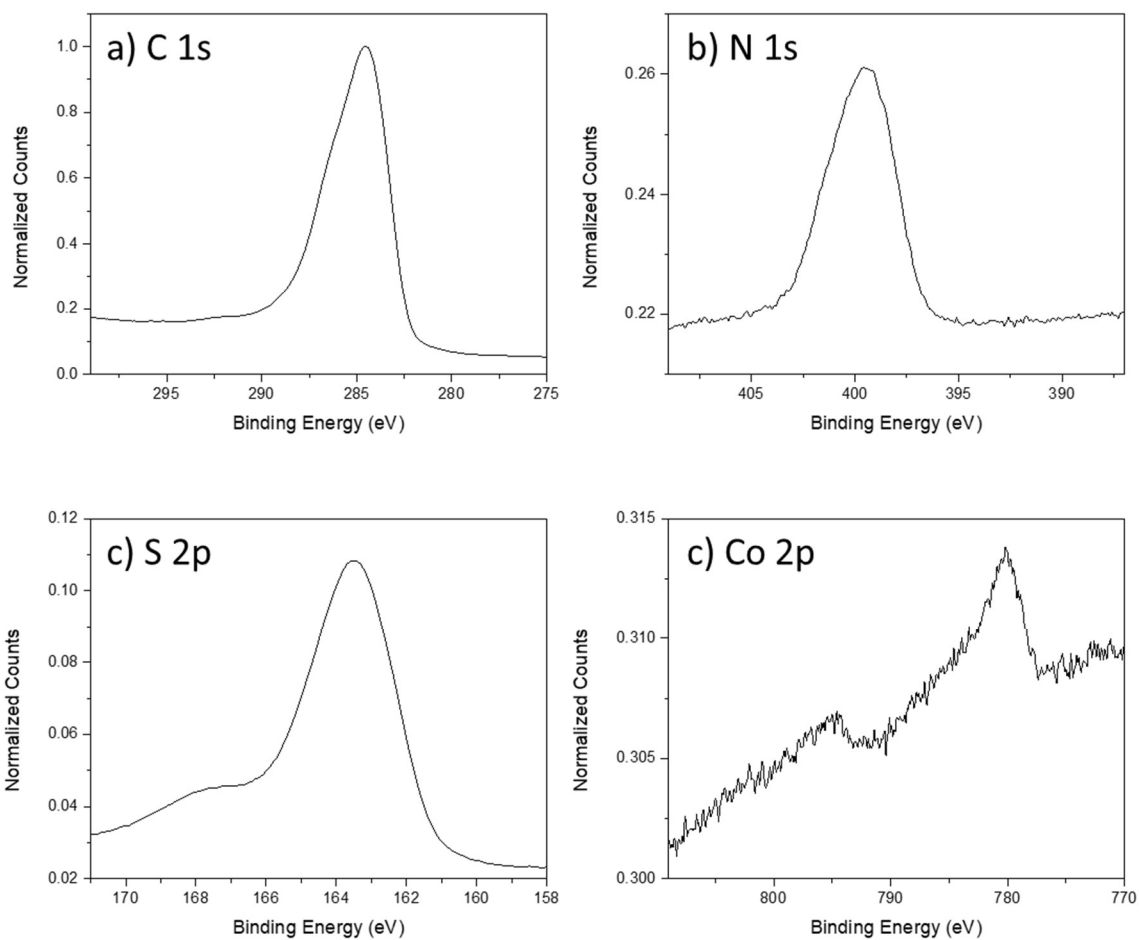
Figure 2.12. XPS spectra of a **GO-1** film, a) Carbon 1s peak, b) N 1s peak, c) S 2p peak, and d) Co 2 p peak. Each spectrum is referenced to C 1s at 284.6 eV and counts are normalized to the C 1s peak.
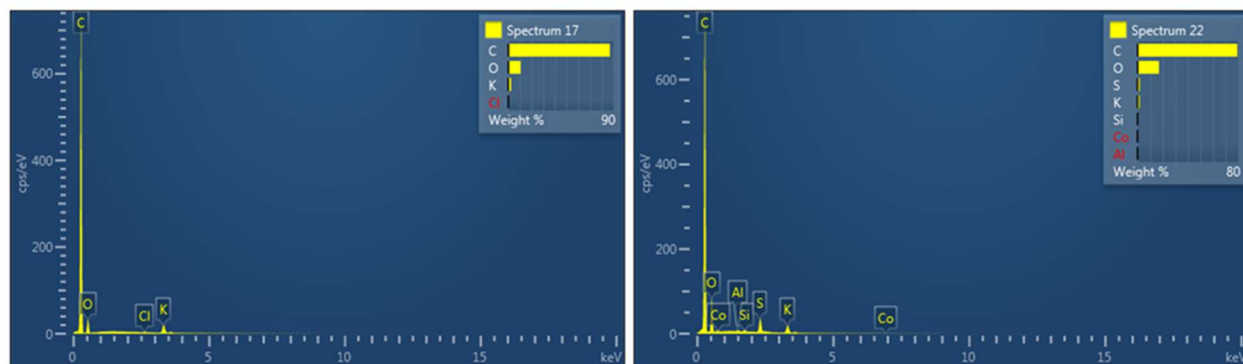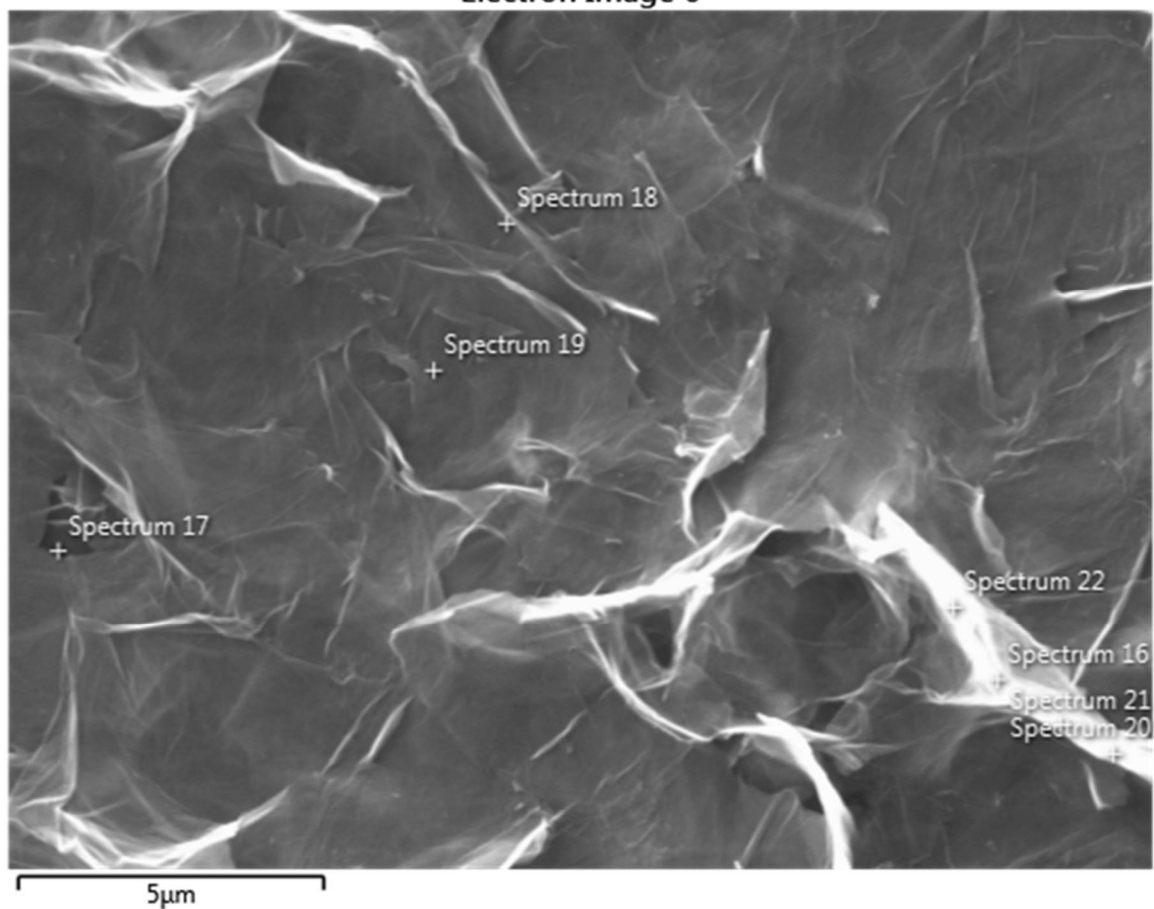
Figure 2.13. Select SEM-EDS data of an **RGO-1** film. Interestingly, sulfur is measured along a thicker ridge of the **RGO-1** film. Note that no significant Co is observed, as Co is likely just below the limit of detection, and is expected to be ¼ the atomic percent of S. The potassium signal is due to minor amounts of potassium remaining after reduction of the film in 0.1 M KPF_6 buffer, see Figure 2.11 for further experimental details.
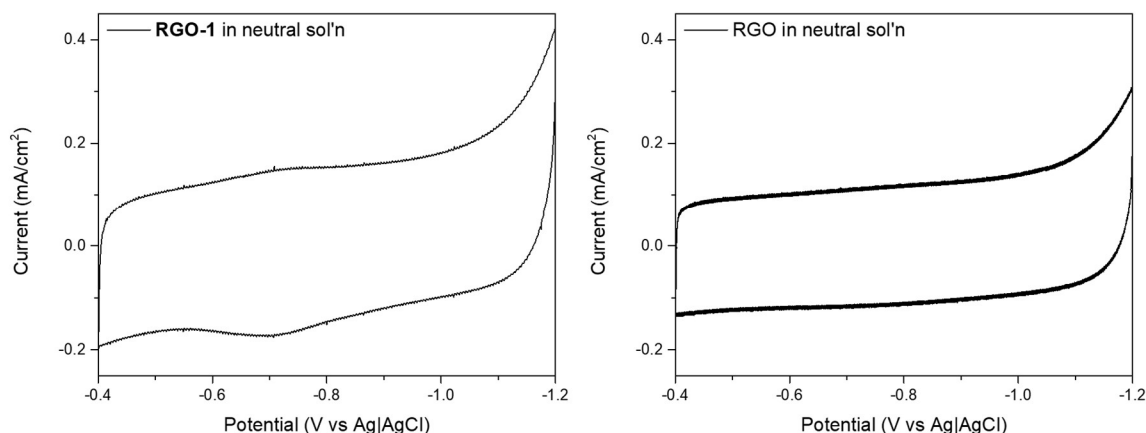
Figure 2.14. CV of **RGO-1** in neutral solution, showing the $Co^{III/II}$ couple of **1** at -0.71 V vs Ag|AgCl, left, compared with the CV of RGO without any catalyst, right. The data were collected with a scan rate of 50 mV/s, using the following electrodes: 3 mm diameter GC working electrode with an **RGO-1** or RGO film, carbon felt counter electrode, and Ag|AgCl in saturated KCl reference electrode. In the experimental setup, half cell compartments are separated by a Nafion membrane, with an aqueous electrolyte solution of 0.1 M KPF_6.

Reduction of the **RGO-1** films allows the Co^{III}/Co^{II} couple of **1** to be visible, see Figure 2.14, at -0.71 V vs. Ag|AgCl. This Co^{III}/Co^{II} couple is similar to other catalysts of this family physisorbed to RGO or HOPG electrodes.[97] It was recently reported that sometimes, due to strong electronic interaction between the catalyst and the electrode band structure, catalyst redox couples are not visible by CV when immobilized on electrode surfaces.[85] This has been observed for a similar system of a cobalt porphyrin on RGO.[77] However, in the majority of cases, catalysts in thin films on electrode surfaces give detectable CV couples, see examples and references in Table 1.1. Integration of the Co^{III}/Co^{II} couple shows $(9.2 \pm 1.2) \cdot 10^{-11}$ mol Co/film or 1.3 ± 0.2 nmol Co/cm^2 (N = 4 films). Because of the small amount of Co in the films and the relatively high charging current of the RGO films, the current and therefore charge passed due to **1** was determined by performing a straight-line background subtraction for each CV measured. Comparing the amount of Co measured by integration of the Co^{III}/Co^{II} couple to the amount of cobalt quantified by ICP-MS shows that about 46% of complex **1** in the films is electrochemically active. This relative amount of active catalyst is comparable to the findings in a recent report of a thin film MOF electrocatalyst,[86] and is higher than observed for other thin film electrocatalysts in the literature.[79,93] It is likely that the remaining, not electrochemically-active complex **1** is located in

39

domains of RGO that are not electronically connected to the electrode, and hence, cannot contribute to electrochemical activity.
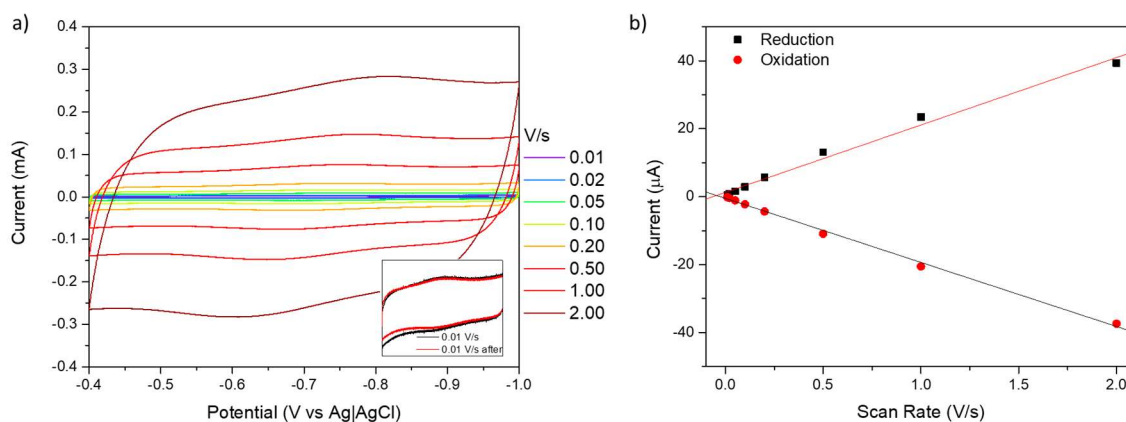
Figure 2.15. Left: scan rate dependence of the Co^{III}/Co^{II} couple of an **RGO-1** film at different scan rates, 0.01 V/s through 2 V/s. This experiment was carried out in a two compartment cell with half cells separated by a Nafion membrane, in 0.1 M KPF_6 solution under N_2, with the working electrode being an **RGO-1** film on glassy carbon; carbon felt was used as the counter electrode; and Ag|AgCl in saturated KCl as the reference electrode. Each scan was conducted twice with the second scan shown. The inset shows an overlay of the 0.01 V/s first scan (black) and the last scan (red) at 0.01 V/s, measured after the fastest scan rate. As the peaks are small with respect to the RGO film charging current, the oxidative and reductive peak currents were determined in Origin using a straight-line background subtraction. Right: the peak heights at different scan rates were fit with a straight line with respect to the scan rate, with R of >0.99 for both the reduction and oxidation signals, indicating a surface-bound, electrochemically active species.

The scan rate dependence of the peak current of the Co^{III}/Co^{II} couple of **1** was also investigated (Figure 2.15a), with straight-line background subtraction as above. The current due to **1** shows a linear increase with increasing scan rate, which is consistent with a surface bound species (Figure 2.15b). In the regime of fast electron transfer, surface adsorption of a redox active species should give rise to two Gaussian-shaped (oxidation and reduction) peaks that are centered at the $E_{1/2}$. Instead, peak to peak separation of ~35 mV is observed, indicating moderately slow ET across our films. The RGO films' residual resistance is also evident from their relatively high charging current. As the peak separation is less than 57 mV at slow scan rates, the film is in between what is predicted for a thick film with slow electron transfer and a thin film with fast electron transfer, as shown by Costentin and Saveant.[163] They termed this in-between type behavior "type AD". This finding of relatively slow electron transfer due to film resistance is also consistent with the fact that only some of the cobalt in **RGO-1** is electrochemically active, as some

areas of the film may be electronically inaccessible, as shown by ICP-MS and Raman spectroscopy.

2.2.3 Electrochemical Analysis of HER Catalysis of RGO-1 Thin Films
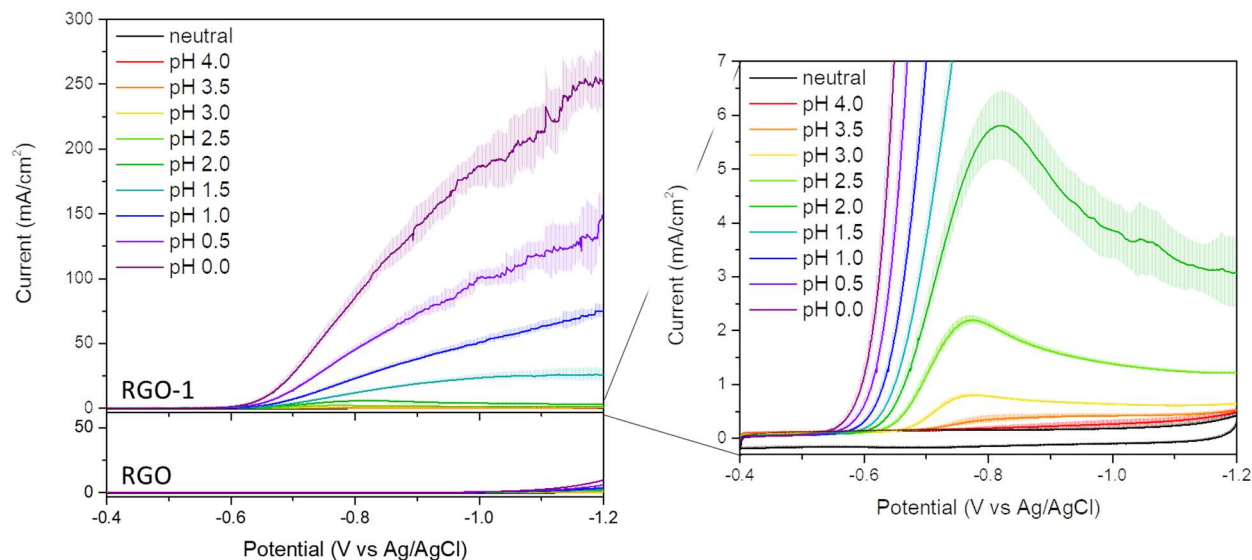
Figure 2.16. CVs monitoring HER activity during an acid titration of **RGO-1** films; here, H_2SO_4 was used to obtain the listed pH values. A comparison to a plain RGO film (without catalyst) is also included. Experimental conditions: 0.1 M PKF_6, working electrode: **RGO-1** or RGO film (as indicated) on glassy carbon, counter electrode: graphitic carbon felt, reference electrode: Ag|AgCl in saturated KCl. Half-cell compartments are separated by a Nafion membrane. For measurements on **RGO-1** films, the standard deviation is shown (N = 3 or 4) as well. The back scans were removed for clarity.

After preparing and characterizing the **RGO-1** films, their electrocatalytic hydrogen evolution was investigated using CV scans by addition of varying amounts of acid, as shown in Figure 2.16. Here, addition of acid and provision of electrons by applying a negative, reducing potential results in an increase in current and the formation of bubbles on the electrode. The reaction produces many H_2 gas bubbles, which also disrupt the smoothness of the CV curves, as the H_2 gas bubbles temporarily block portions of the electrode surface lowering the electrochemically active surface area and hence, the current. This is obvious at high concentrations of acid but is also observed even at lower current densities. Figure 2.16 shows the high HER activity of **RGO-1** in direct comparison to plain RGO films, the latter showing a minimal amount of catalytic current at the different pH values. The reductive catalytic wave of **RGO-1** grows in

with increasing acid concentration. The higher pH region is shown in greater detail in Figure 2.16, right. At pH 4.0 through 2.0, catalysis is substrate diffusion limited, causing a common catalytic wave, which decreases at more reducing potentials as the substrate, here protons, is depleted near and in the film.
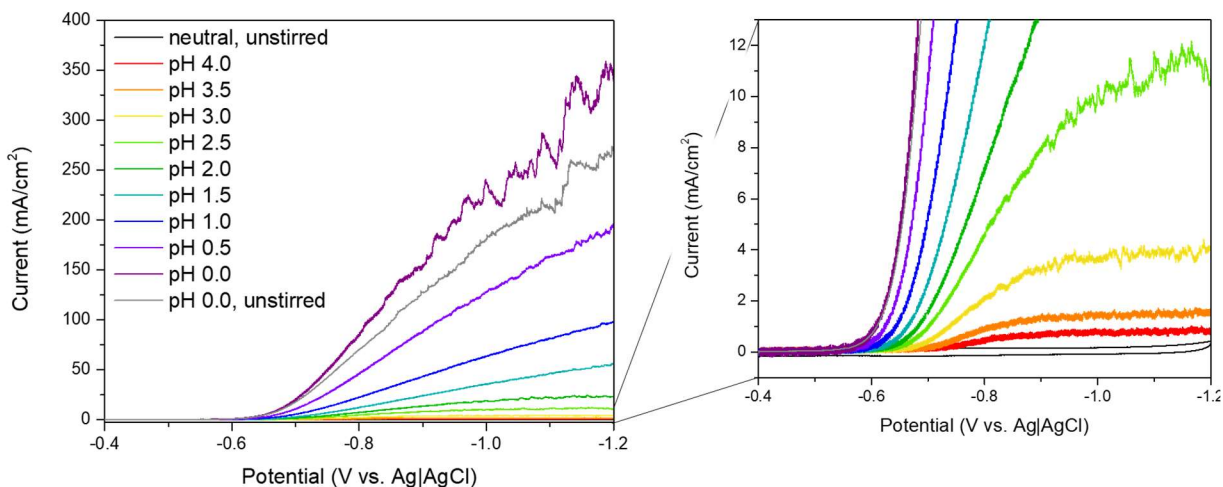
Figure 2.17. CV scans of an **RGO-1** film at the indicated pH values, which were adjusted using H_2SO_4. CV scans were taken with the two compartment cell and the solution stirred (except where indicated otherwise). Left: the full range; right: zoomed in plot to show the data for the higher pH CVs; the legend is the same for both graphs. The setup is the same as the acid titration shown in Figure 2.16, except that the solution was stirred. A CV was taken without stirring after the acid titration (gray), which is within error of those shown in Figure 2.16. The neutral scan (black) is also shown without stirring, as stirring caused the noise to be very large. Experimental conditions: 0.1 M PKF_6 solution; working electrode: **RGO-1** film on glassy carbon; counter electrode: graphitic carbon felt; reference electrode: Ag|AgCl in saturated KCl. The back scans were removed for clarity.

If the solution is stirred, as shown in Figure 2.17, cyclic voltammograms at lower acid concentrations show shapes that are closer to the non-diffusion limited ideal sigmoidal type. At lower pH, with the great increase of H_3O^+ concentration in solution, the CV data are no longer substrate diffusion limited, and electrocatalysis is likely limited by electron transfer in the film and/or removal of product. Here, the current continues to increase as a more negative potential is applied. For the measured acid concentrations and potentials, the maximum current observed in the CVs shown in Figure 2.16 is linear from pH 4 to pH 1 and then falls below the linear line for pHs 0.5 and 0, see Figure 2.18, likely due to built-up of H_2 gas bubbles on the electrode surface.
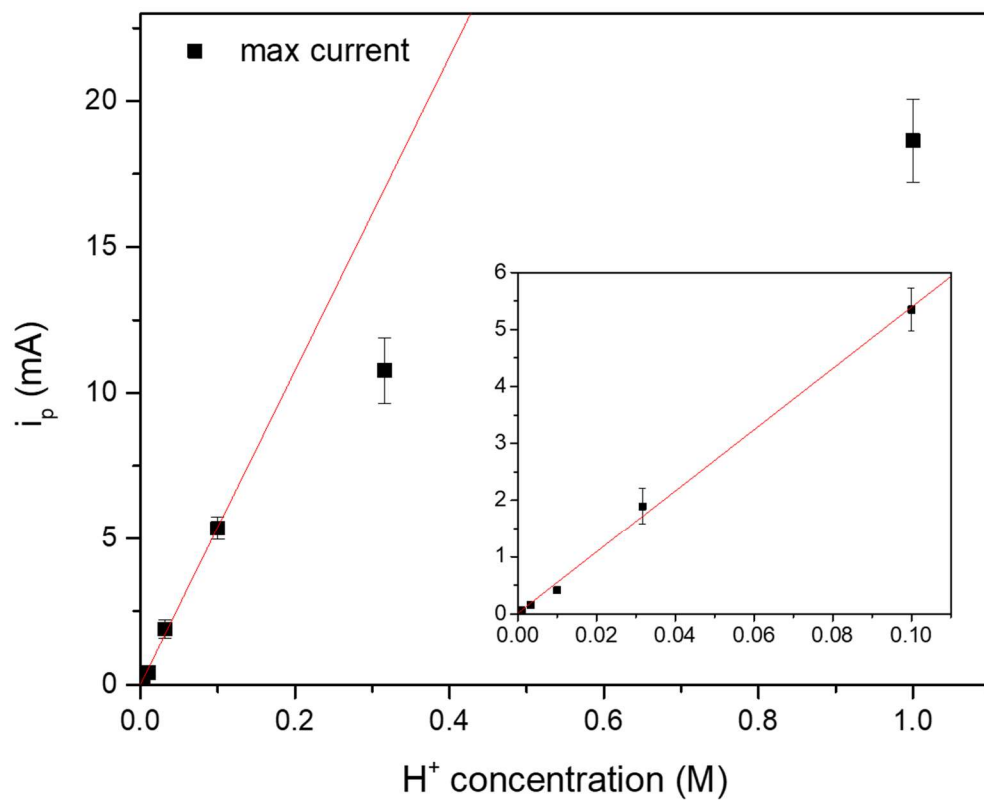
Figure 2.18. Maximum current with respect to the concentration of acid. The data shown here are from the averaged acid titration data of an **RGO-1** film, as shown in Figure 2.16. The inset shows the linear region, pH 4 through pH 1, which is fit with the line: $i_p = (0.01 \pm 0.04) + (54 \pm 1)[H^+]$, with R = 0.997.
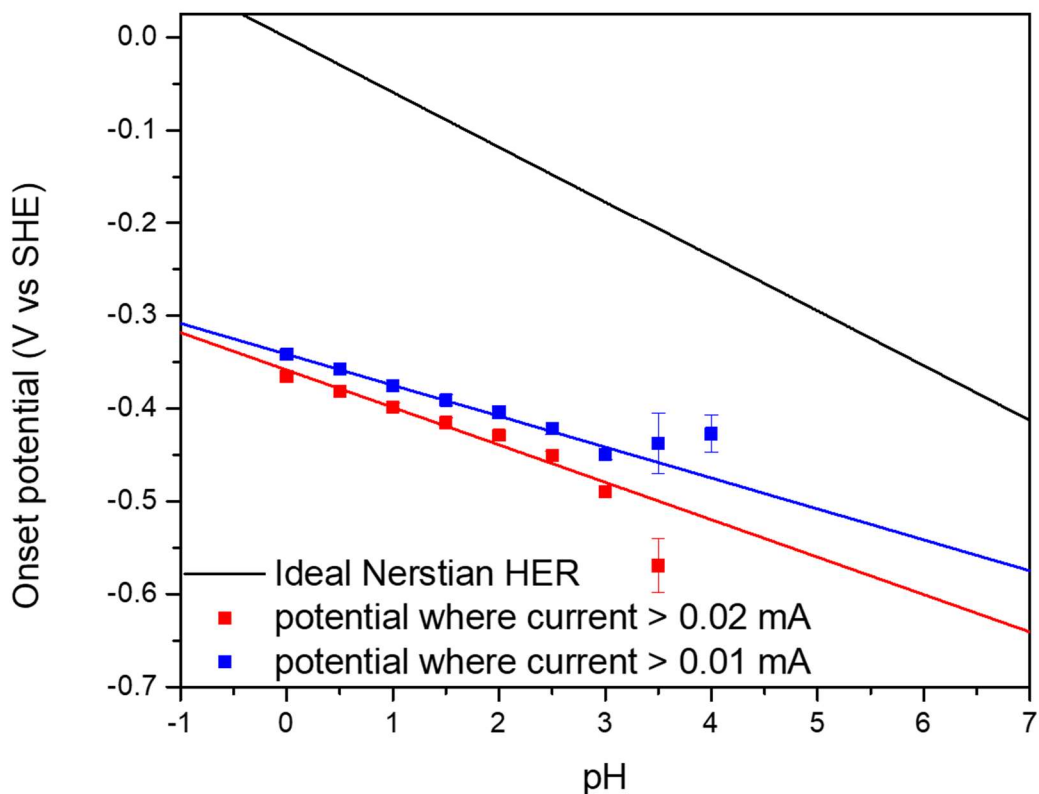
Figure 2.19. The onset potential of the catalytic wave shifts with addition of acid. Here, the standard deviation for three or four trials is shown. The data are taken from the individual acid titrations that were averaged to give the data shown in Figure 2.16. The reference potential is converted from Ag|AgCl in saturated KCl to SHE by the addition of 0.199 V. The slope for the blue line is -0.033 ± 0.002 V/dec, and $R^2 = 0.96$. The slope for the red line is -0.040 ± 0.004 V/dec, and $R^2 = 0.93$.

The onset of catalysis in the **RGO-1** system is nominally the same as the $E_{1/2}$ of **1**. The $E_{cat/2}$ for pH 2-3 is roughly the same as the potential of the $Co^{III/II}$ couple, with $E_{cat/2}$ of -0.702 ± 0.003, -0.697± 0.004, and -0.713 ± 0.002 V vs Ag|AgCl at pH values of 3, 2.5, and 2, respectively. For more acidic and more basic pH values the catalytic waves are less ideal, so $E_{cat/2}$ could not be reliably determined. In addition to analyzing the $E_{cat/2}$, we analyzed the onset potential. Figure 2.19 shows the onset potential for **RGO-1**, defined as the potential at which the current first reaches either 0.01 or 0.02 mA, respectively, upon scanning reductively. Note that the onset potential shifts towards more positive values with increasing acid concentration, as shown in Figure 2.19. This

44

change is reversible; if base is added to the electrolyte solution, the onset potential shifts back to more negative potentials, as shown in Figure 2.20.
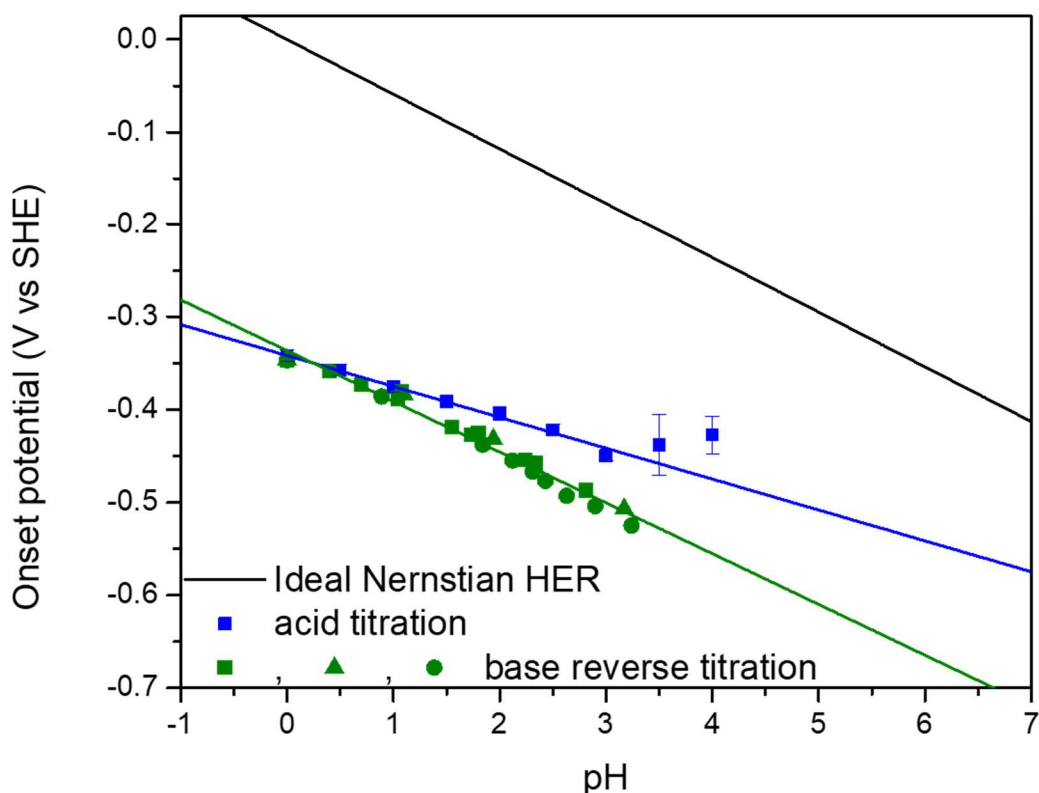
Figure 2.20. Comparison of the onset potentials for the forward (acid) and reverse (adding base) titrations of **RGO-1** films. The blue points show the average (N = 4) and standard deviation for the onset potential, where the current first rises above 0.01 mA, the same as shown in Figure 2.19. The green points show three different trials (square, triangle, circle) for addition of base (KOH), to shift the solution pH back to the marked pH. The data from the trials are fit, together, to give the green line, with a slope of -0.055 ± 0.002 V/dec and an R^2 of 0.98.

There are a few possibilities to explain this shift in onset potential. First, the slope of the onset potential vs pH is not quite Nernstian, implying that this is not due to the fact that the catalyst electronically becomes a part of the electrode, as has been proposed for another system recently.[76] We can also tell this is not the case, as we do observe the $Co^{III/II}$ couple at neutral pH as discussed above. Second, it is possible that the **RGO-1** system is in a unique transition region between behaving like a molecular, redox mediated catalyst and a catalyst embedded in an electrode's electronic structure, which can use inner-sphere electron transfer and shows a Nernstian onset

potential shift. This may occur upon further reduction of RGO under reducing potentials in an acidic solution, making the catalyst sites in the film less electronically distinguished from the electrode and have them behave in a more Nernstian manner, which is supported by the slope upon addition of base, being steeper and closer to Nernstian. Further reduction of RGO under reducing potentials in acidic media is supported by literature precedence.[98] Third, electrocatalytic mechanisms that involve a reduction step coupled to a quick protonation step (so an EC (ET/PT) process) have been observed to show an anodic shift in the onset potential with increasing acid concentration.[164–166] Fourth, it is also possible that the RGO environment changes with acid concentration, for example by protonation of remaining functional groups on the RGO surface, leading to a different rate of proton transport in the films as a function of pH, gradually affecting electrocatalytic activity. We cannot say for sure which one of these reasons (or multiple at the same time) are at work that cause the change of onset potential as a function of pH. What can be said is that the HER mechanism of Co bis(benzenedithiolate) catalysts involves an EC mechanism,[46,47,65,73] which does support the third option discussed above as one contributor.
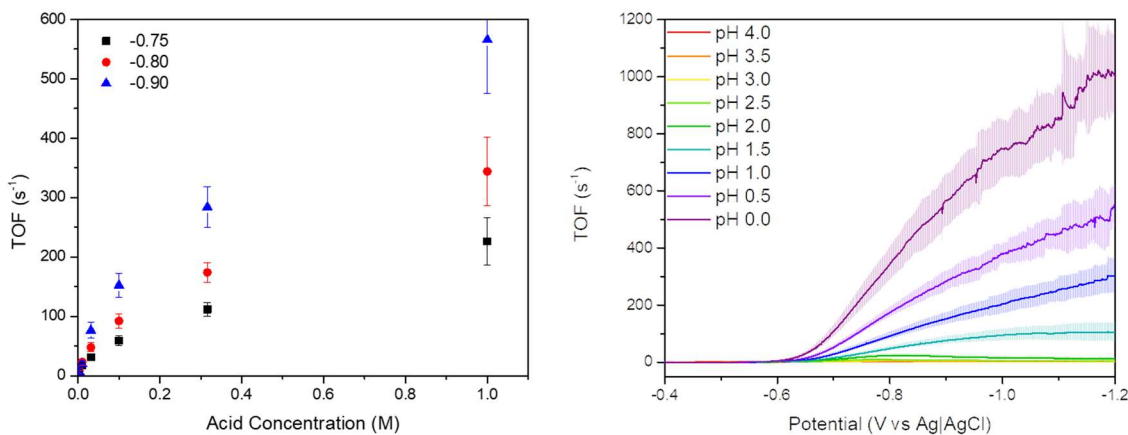
Figure 2.21. TOFs of **RGO-1** at different pHs. Left, selected TOFs at the indicated potentials, plotted vs the acid concentration [M]. Right, further data on TOF [s⁻¹] vs potential at the different pHs tested. The same acid titration data is shown in Figure 2.16, but here the current for each of the individual acid titrations is normalized to the amount of catalyst on the surface of that **RGO-1** film, then the results are averaged, converted to TOF and plotted versus the acid concentration for select potentials (-0.75, -0.80, and -0.90 V vs Ag|AgCl). Standard deviation is shown for N = 3 or 4.

From these CV data, the turnover frequency (TOF) of the catalyst can be calculated, in order to benchmark it against other catalysts reported in the literature. To convert current to TOF,

Faradaic efficiency was measured. After 20 min electrolysis at 1.0 V vs Ag|AgCl in pH 1 solution, 5.6 C of charge were passed and quantitative H_2 was measured in the gas headspace of the cell (Faradaic efficiency of $97 \pm 4\%$, N = 2, see Figure 2.34 and Experimental Section 2.4.4 for further information). This is as expected, as quantitative HER is also observed for the physisorbed analogs of **1**.[73,96,97] The turnover frequency is then calculated as the ratio of current over the amount of electrochemically active catalyst, as determined by integration of the Co^{III}/Co^{II} couple in the CV data (see above). Figure 2.21 left shows the current and TOF at -0.75 V, - 0.80 V, and -0.90 V vs Ag|AgCl. At these potentials, the maximum TOF at pH 0 is observed to be 230 ± 40, 340 ± 60, and 570 ± 90 s^{-1}, respectively, with standard deviations across four films. As expected, the TOF increases with increasing acid concentration. The TOF also increases with applied potential, as a perfectly sigmoidal-shaped CV curve is not observed, as discussed above. Figure 2.21 right shows a version of Figure 2.16, with the y axis transformed into TOF. At pH 0, the TOF is determined to be about 1000 s^{-1} at -1.2 V, demonstrating that **RGO-1** is a highly active catalyst for the HER reaction.
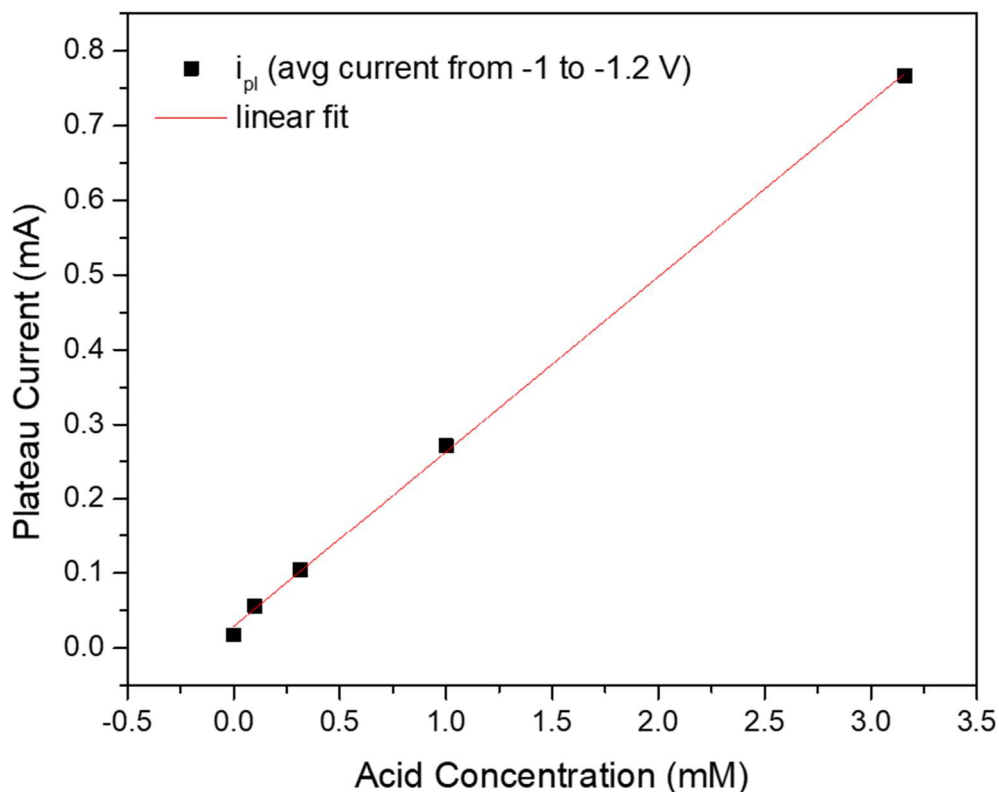
Figure 2.22. Linear increase of plateau current with concentration of acid, see Figure 2.17 for the full data set. The linear fit gives a line with the equation Current [mA] = -0.003 + 0.234*(Acid Concentration [mM]) with R = 0.9997.

Thanks to careful work by chemists in recent decades, we can analyze catalytic CVs by applying a few different equations/models. Each of these methods gives us insight into the mechanism under different limiting conditions. In unstirred solution, as shown in Figure 2.16, we are unable to see sigmoidally-shaped catalytic CVs due to substrate consumption in the vicinity of the electrode surface. However, with stirring to reduce mass transport of protons to the film's surface as a limiting factor of catalysis, as shown in Figure 2.17, near sigmoidally-shaped catalytic waves were observed for low acid concentrations, pH 2.5 and above. At lower pH, the catalytic wave is not sigmoidal, but may be limited by diffusion of protons and H_2 inside the film. Yet for pHs 2.5 and above, a linear increase in plateau current with respect to the acid concentration was observed, see Figure 2.22. This indicates that the film is in the KP_R regime as defined by Costentin

and Saveant where the rate of the catalytic reaction is slow compared to the rate of electron transfer in the film.[163] The plateau current in this regime can be defined as:

$$i_{pl} = nFk\kappa_A C_A^0 mol_{Co}$$

Equation 2. 1

where i_{pl} is the plateau current (in [A]); n is the number of electrons in the reaction studied (here $n = 2$); F is Faraday's constant [C/mol]; k is the rate constant (in [M^{-1}s^{-1}]); mol_{Co} is the moles of the electrochemically active catalyst on the electrode surface (in [mol]); κ_A is the partition coefficient for substrate, in this case protons, between the film and solution (here $\kappa_A = 1$ is assumed); and C_A^0 is the initial concentration of substrate in solution (in [M]). See the Section 2.4.5 for further information on how this equation was obtained. The slope of plateau current with respect to acid concentration thereby gives a rate constant of $k = 1.5 \cdot 10^4$ M^{-1}s^{-1}.

The foot of the wave analysis (FOWA) method analyzes the onset of the catalytic wave, where mass transport effects are limited. Equation 2 shows the standard FOWA equation:

$$\frac{I_c}{I_p} = \frac{\frac{I_{pl}}{I_p}}{1 + \exp\left(\frac{F}{RT}\left(E - E_{\frac{cat}{2}}\right)\right)}$$

Equation 2. 2

where I_c is the catalytic current *density* (in [A/cm^2]) at a certain potential E (in [V]); I_p is the peak current *density* of the catalytic couple when no substrate is present (in [A/cm^2]); I_{pl} is the theoretical plateau current *density*, not limited by mass transport (in [A/cm^2]); F is Faraday's constant; R is the gas constant (in [J K^{-1} mol^{-1}]); T is the absolute temperature (in [K]); and $E_{cat/2}$ is the potential at half of the plateau current (in [V]), not limited by mass transport in solution or in the film.[167,168] As determined above, the **RGO-1** system falls into the KP$_R$ regime.[163] This allows rearrangement of Equation 2.2 such that:

$$i_c = \frac{nFk\kappa_A C_A^0 mol_{Co}}{1 + \exp\left(\frac{F}{RT}(E - E^0\right)}$$

Equation 2. 3

where E^0 is the potential of the Co^{III}/Co^{II} couple (in [V]). See the Section 2.4.5 for further details on how Equation 2.3 was obtained. From Equation 2.3, a rate constant of $3.6 \cdot 10^3$ M^{-1}s^{-1} was calculated for **RGO-1**, see Table 2.1. For more acidic pH values, the rate constant calculated by Equation 2.3 appears to decrease gradually, reaching a value of $3.4 \cdot 10^2$ M^{-1}s^{-1} at pH 0. This

decrease may be a result of the assumption that the partition coefficient (κ_A) is 1 under all conditions. RGO is known to have moderate proton conductivity,[169] so κ_A is likely less than 1 at high concentrations of acid. It may also be that at high acid concentrations the reaction rate and rate of electron transfer are comparable and Equation 2.1 is no longer the best model. Nevertheless, FOWA analysis gives an estimated rate constant of $3.6*10^3$ $M^{-1}s^{-1}$. This value is lower than that obtained from the plateau current analysis above by about a factor of 4, and combined, these rate constants again show that **RGO-1** is a highly active HER catalyst.
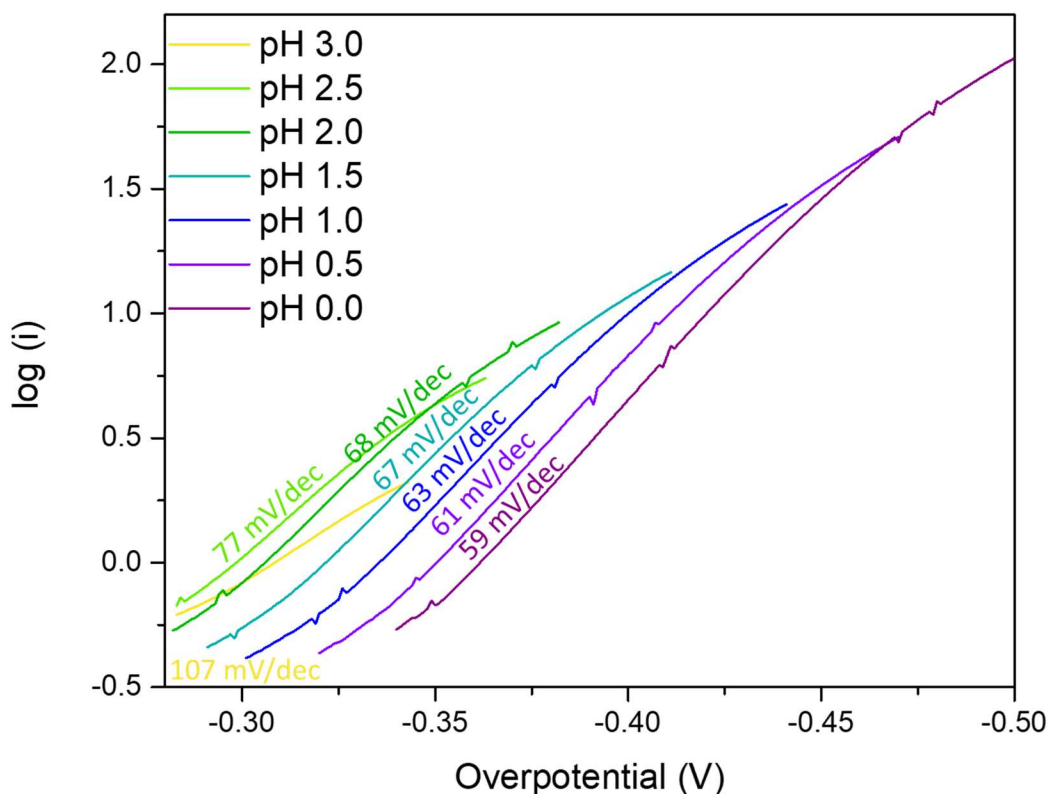
Figure 2.23. Tafel plots of acid titration data for **RGO-1** using electrolyte solutions with different pH, as indicated. The data used to construct the Tafel plots are the same as presented in Figure 2.16, and have been truncated to show the linear parts of the Tafel plots only. Tafel slopes are indicated.

Tafel analysis is known to give insight into the rate limiting step of catalysis. Plotting the log of the current vs overpotential for **RGO-1** gives a linear slope near the onset potential, as shown in Figure 2.23. At large negative overpotentials, the log of the current deviates negatively from the expected linear slope due to mass transport issues, as expected. At small negative potentials, with no or limited catalysis, the log of the current deviates positively from the expected

linear slope, because the HER reaction is not observed to be reversible with **RGO-1** under these conditions. The slope of the Tafel lines is 59 – 77 mV/dec for pH 2.5 and below. In general, Tafel slopes are reliant on α, which must be between 0 and 1. Takanabe and co-workers analyzed the Tafel slopes for steps in the HER reaction,[170] and determined three rate limiting steps that would give different Tafel slopes: the Volmer step (metal hydride formation, slope = 120 mV/dec for α = 0.5), the Heyrovsky step (metal hydride to hydrogen conversion through protonation and electron transfer, slope = 40 mV/dec for α = 0.5), and the Tafel step (two metal hydrides come together to form H_2, 30 mV/dec for α = 0.5). The Tafel step would give too small of a slope, given that α must be between 0 and 1, and here Tafel slopes higher than 60 mV/dec are observed. Hence, our data are not in agreement with this step being rate limiting. This is not surprising, as the surface attachment of our catalysts inhibits such a bimolecular reaction. Both Volmer and Heyrovsky steps are plausible, with a reasonable α for pH 2.5 and less. The Tafel slope for **RGO-1** at pH 3.0 is 107 mV/dec, showing that the metal hydride formation (Volmer step) is likely the rate limiting step at this pH. If the same mechanism is used throughout the pH range tested, α is observed to vary from 0.45 at pH 2.5 to 0.25 at low pH for the Volmer step. Low α, or slow electron transfer, is not unexpected in an RGO film with some resistance.
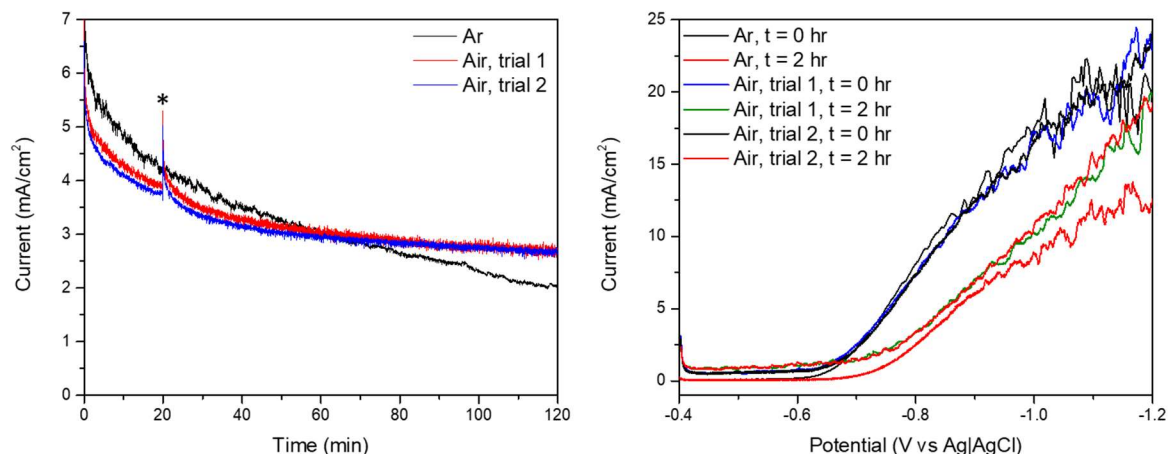
Figure 2.24. Comparison of electrocatalysis under inert (Ar) atmosphere and under ambient air atmosphere, compare to Figure 2.25. Left: 2 hour controlled potential electrolysis at -0.8 V vs Ag|AgCl. Right: comparison of the CVs stirring at 0 and 2 hrs under inert or air atmosphere. Experimental conditions: 0.1 M PKF$_6$, working electrode: **RGO-1** on glassy carbon, counter electrode: graphitic carbon felt, reference electrode: Ag|AgCl in saturated KCl. Half-cell compartments are separated by a Nafion membrane. First, **GO-1** is reduced to **RGO-1** in 0.1 M KPF$_6$ under dinitrogen, with the usual conditions, then the electrolyte is made acidic to pH 2 with

addition of TFA. The system is then sparged with Ar or air, and electrocatalysis is performed. * Indicates where the electrolysis in air was paused to run CVs (not shown), and then CPE was continued.

As there has been interest in recent years in HER catalysts that are dioxygen tolerant,[171] we also investigated the HER ability of **RGO-1** in air. Controlled potential electrolysis measurements were conducted under an ambient air atmosphere and Faradaic efficiency was measured to be 79 ± 3 % (N = 3 films, 2 gas head space aliquots per film), using the same conditions that give quantitative Faradaic efficiency under inert atmosphere. Cyclic voltammetry studies show the same onset potential and current at pH 2, see Figure 2.24, right. Controlled potential electrolysis, see below and Figure 2.24, also shows similar activity between the catalyst under inert atmosphere and in the presence of atmospheric concentrations of O_2. Combined, the 79% maintained Faradaic efficiency, the same onset potential, and similar behavior over 2 hours, show that **RGO-1** is completely stable in the presence of air under electrocatalytic conditions, while maintaining high Faradaic efficiency for HER.

2.2.4 Controlled Potential Electrolysis of RGO-1 Thin Films
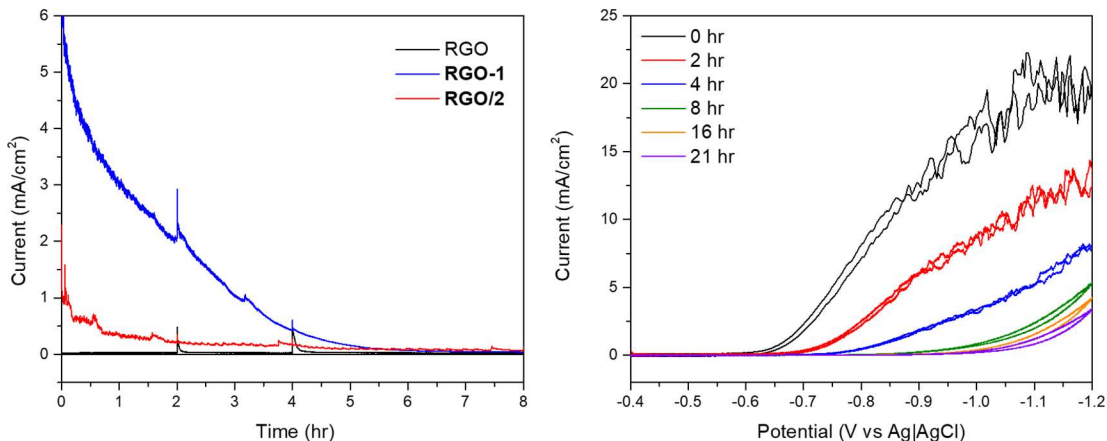
Figure 2.25. Controlled potential electrolysis shows catalytic current over time. Left: current as a function of time when a potential of -0.8 V vs Ag|AgCl is applied to the working electrode. Right: CVs at the marked time points for the **RGO-1** working electrode. For these CVs, stirring of the solution and hydrogen bubbles give slightly noisy data. Experimental conditions: electrolyte: 200 mL of pH 2 (TFA) 0.1 M KPF_6 circulating through the working electrode compartment; working electrode: RGO, **RGO-1** or **RGO/2** films on a 3 mm diameter glassy carbon electrode; counter electrode: graphitic carbon felt; reference electrode: Ag|AgCl in saturated KCl. A three component cell with compartments separated by a Nafion membrane was used. See the Experimental Section (2.4) for further description of the setup. A photo is shown in Figure 2.35.

The catalytic activity of the **RGO-1** films over time was tested with controlled potential electrolysis (CPE). CPE is prone to current errors if even minor impurities are present, and so great efforts were made to keep the electrolyte and cell clean. See the Experimental Section 2.4.4 for further information and for a description of our setup. A photo of the electrochemical flow cell used for these studies is shown in Figure 2.35. In brief, a three-compartment cell was used, with each compartment separated by a Nafion membrane. A 0.1 M KPF_6 solution was added as the electrolyte and made acidic to pH 2 by trifluoroacetic acid (TFA). The solution in each compartment was stirred, and the solution in the working electrode compartment was circulated using a 200 mL reservoir, so the change in acidity from HER would be negligible. The current at -0.8 V vs Ag|AgCl was tracked over time, and intermittent CVs were measured to track activity from -0.4 V to -1.2 V for further information about the film's catalytic status quo throughout the CPE experiments. CVs were taken at t = 0, 2, 4, 8, 16, and 21 hrs. As shown in Figure 2.25, we observed the current decrease to background current within about 8 hrs of CPE. This decrease in catalytic activity over time is further documented by the decrease in catalytic current and negative shift of the onset potential observed in each of the intermittent CVs, showing that the catalyst is somehow degrading in the films. The film was observed to be visually intact after electrolysis. Note that if the film is not dried under vacuum, delamination of the film is sometimes observed during CPE, an example CPE where this occurred is shown in Figure 2.26.
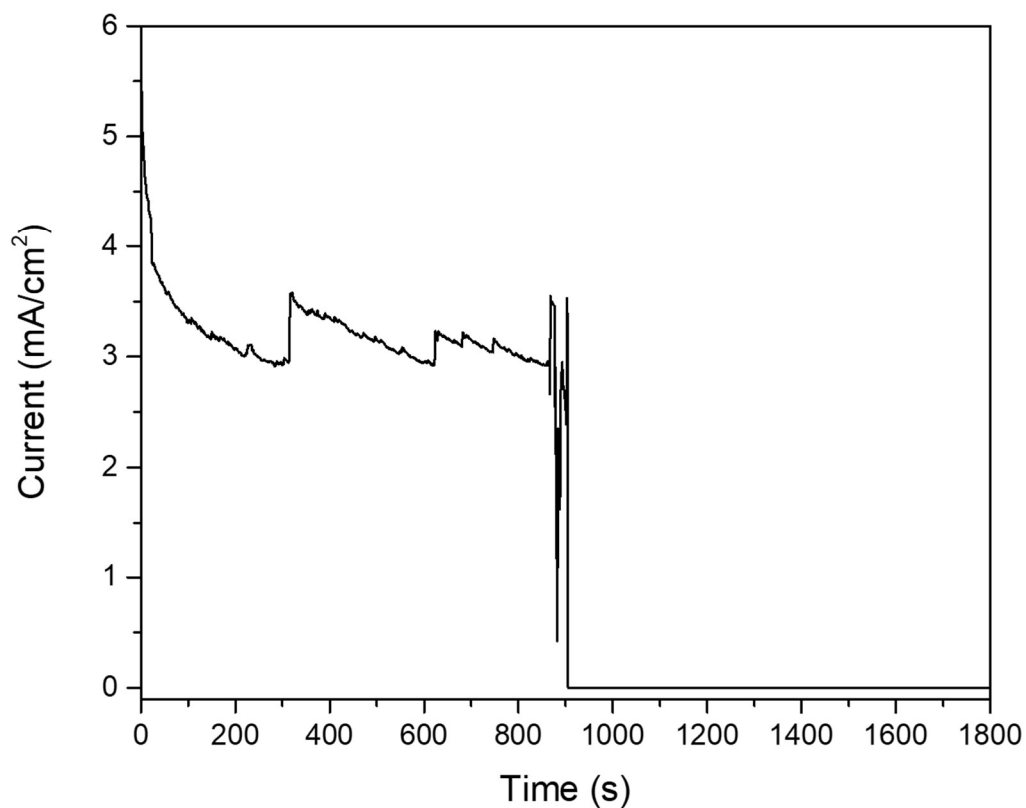
Figure 2.26. Controlled potential electrolysis (-0.9 V vs Ag|AgCl, pH 2) of an **RGO-1** film. This is an example for a data set where the film dissociated off the electrode after about 900 s, which sometimes happens if the film is not dried under vacuum before testing. As a result of the film lifting off the electrode, the current decreased to 0 mA/cm^2.

To determine the reasons for the decreased catalytic activity over time, a **RGO-1** film after electrolysis was analyzed by XPS, SEM, and ICP-MS. XPS, with identical conditions as were used to image **GO-1**, shows no Co present in the film after electrolysis (see Figure 2.27 and compare with Figure 2.12). Additionally, the S 2p and N 1s peaks also show partially reduced intensity with respect to the C 1s peak, which suggests partial ligand degradation or detachment from the RGO film. Taken together, these XPS data and the change in onset potential indicate that demetallation of **1** is a major contributor to the observed decrease in catalytic activity of the film. ICP-MS data of an **RGO-1** film after electrolysis further support demetallation, with decreased amounts of Co measured in the film ($0.8 \cdot 10^{-10}$ mol Co/film, measured for the CPE experiment shown in Figure 2.25 after the conclusion of the 21 hr controlled potential electrolysis, compared with the average

$(2.00 \pm 0.09) \cdot 10^{-10}$ for the starting **GO-1** film). SEM images of the film after electrolysis revealed that while no visual change was observed in the film by the human eye, there were some regions that had been physically damaged by hydrogen bubbles ripping through the RGO film, on the order of 10-100 μm in scale, see Figure 2.28. In other regions, the **RGO-1** film is similar to the film before electrolysis (compare to Figure 2.11). As much of the film is intact, we expect this bubble-induced damage to the structure of the RGO film to be a minor contributor to the loss of catalytic activity.
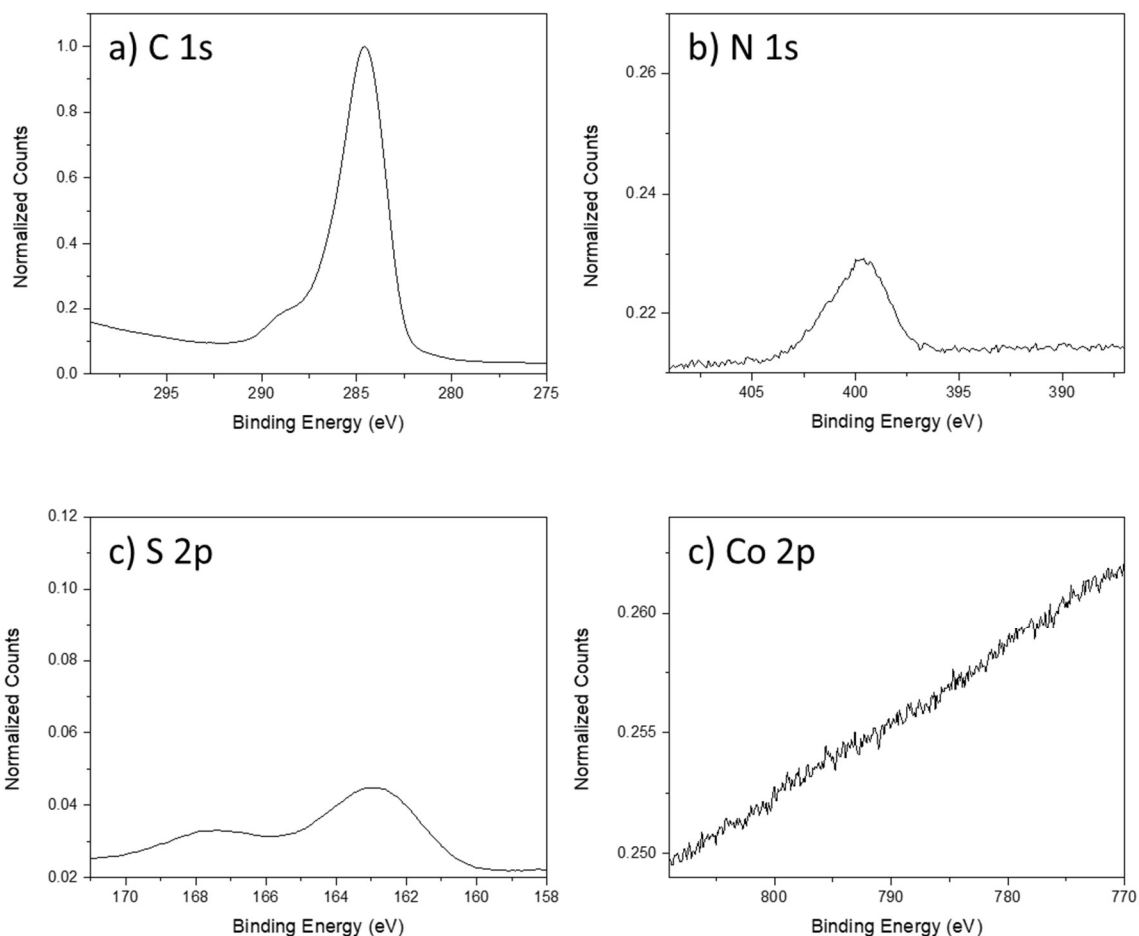
Figure 2.27. XPS spectra of a **RGO-1** film after 16 hrs of electrolysis with the same experimental set up as described in Figure 10, except with a 5 mm diameter glassy carbon disk electrode, a) Carbon 1s peak, b) N 1s peak, c) S 2p peak, and d) Co 2 p peak. Each spectrum is referenced to C 1s at 284.6 eV and counts are normalized to the C 1s peak. Similar scaling is used for easy comparison to Figure 2.12.
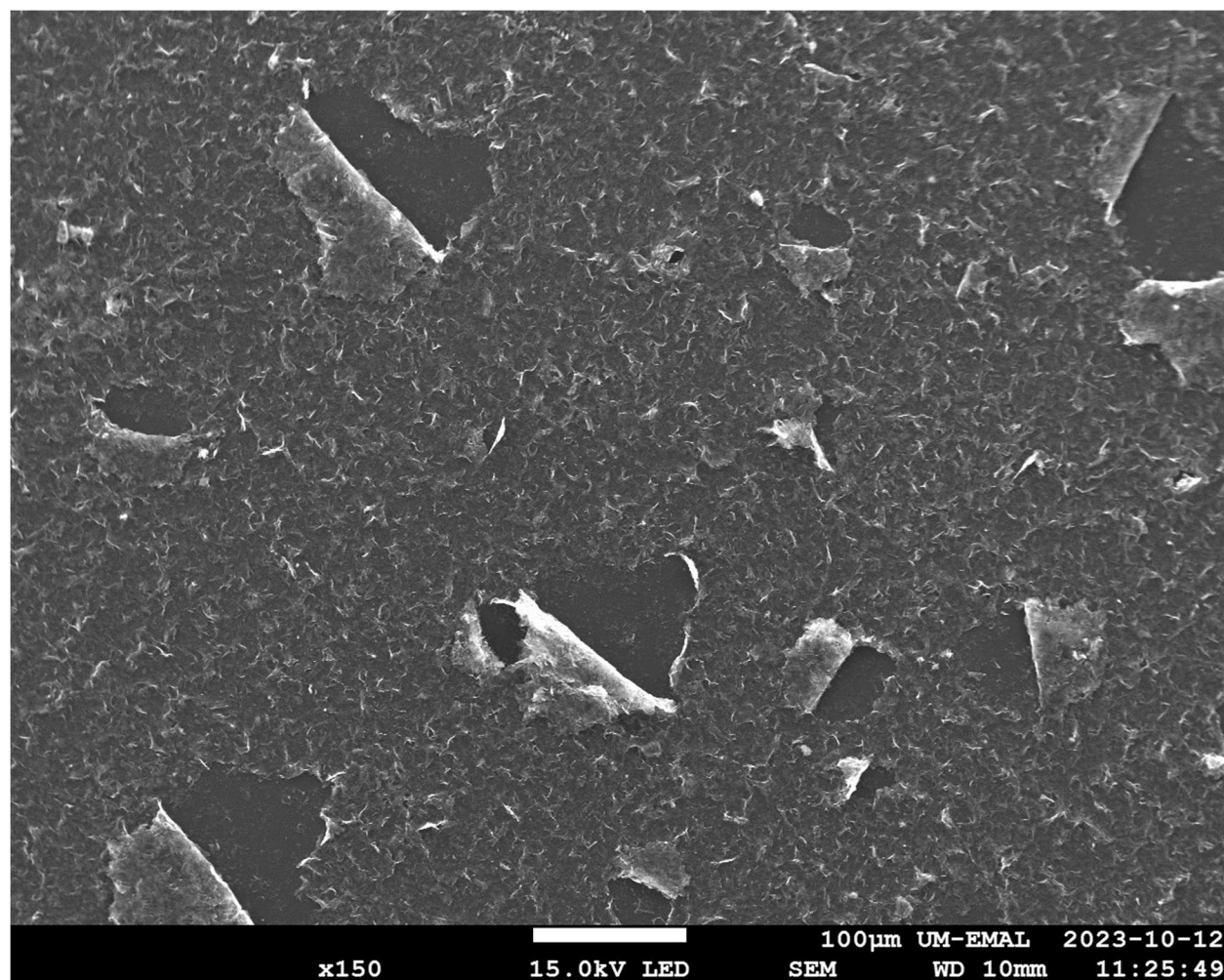
Figure 2.28. SEM image of a **RGO-1** film after 16 hrs of electrolysis with the same experimental set up as described in Figure 2.25, except with a 5 mm diameter glassy carbon disk electrode. The film is shown here at 150x magnification, with a 100 μm scale bar. The image was taken using a 15.0 kV electron beam and a working distance of 10 mm.

To further compare the long-term activity of the **RGO-1** catalytic films to an analogous system where a Co bis(benzenedithiolate) catalyst is embedded in an RGO film without the covalent attachment, **GO/2** was prepared by mixing GO and a solution of **2**, a catalyst without the amine functionality, so that the final film contained $2.0 \cdot 10^{-10}$ mol catalyst, the same amount of Co as measured in **GO-1** by ICP-MS. Here we use "-" to denote covalent attachment and "/" for physisorption. The durability of **RGO/2** was measured in the *exact same way* as described above for **RGO-1.** Integration of the resulting Co^{III}/Co^{II} couple shows $3.2 \cdot 10^{-11}$ mol of electrochemically accessible Co. This is 16% of the total cobalt included in the drop-cast **RGO/2** film, compared to 46% electrochemically accessible Co observed in **RGO-1**, and shows the quick de-physisorption

of **2** from the RGO films. At pH 2, the TOF of **RGO/2** at the maximum of the catalytic wave observed by CV in unstirred solution (at -0.99 V) is 41 s^{-1}; at the same pH **RGO-1** reached a TOF (at -0.82 V, the maximum of the catalytic wave) of 23 s^{-1}. As TOF is calculated with the moles of active catalyst in the denominator, the calculated TOF for **RGO/2** could be falsely low due to the quick de-physisorption observed here. Because of the lower amount of electrochemically active catalyst in **RGO/2**, this control experiment shows lower current overall, as shown in Figure 2.25, left. The CPE shows a decrease in catalytic current in the first few hours of CPE. Taken together, these results demonstrate that covalently attaching **1** to RGO gives improvements in the amount of electrochemically accessible catalyst and in the durability of the system.

2.3 Discussion

This chapter reports the synthesis and characterization of a new member of the cobalt bis(benzenedithiolate) family of catalysts, [cobalt bis(benzylammoniumdithiolate)]$^+$ (**1**). Complex **1** has an amine functionality which gives the catalyst a handle for covalent attachment, taking advantage of typical amine reactivity. Here, **1** is covalently attached to graphene oxide (GO), giving **GO-1**, which is then drop-cast on a glassy carbon electrode, forming thin films with a thickness of 330 ± 120 nm. These **GO-1** thin films can be reduced electrochemically to give **RGO-1** thin films. In **RGO-1**, and the **RGO/2** control, the Co$^{III/II}$ couple is visible in CV scans, which is common in immobilized catalysts, see Table 1.1. Sometimes, due to close electronic interaction between the catalyst and the electrode's band structure, catalyst redox couples are not visible by CV when immobilized on electrode surfaces.[77,85] It should be emphasized that this is not the case for **RGO-1** and **RGO/2**. Especially the latter is notable, as this is a very similar system as the physisorbed CoPC reported recently, where such claims were made.[52] **RGO-1** shows a Co$^{III/II}$ couple that exhibits the expected behavior for an AD type film. Hence, this system represents an experimental example for the predictions of Costentin and Saveant for catalysts in moderately conductive thin films.[163] Integration of the Co$^{III/II}$ couple observed by CV gives 1.3 ± 0.2 nmol Co/cm^2 (N = 4 films), which shows that 46% of the Co measured in the film aliquot by ICPMS is electrochemically active. **RGO-1** shows high HER activity with an E$_{cat/2}$ of -0.7 vs Ag|AgCl at pH 2-3 and quantitative Faradaic efficiency, in line with the expected activity of Co bis(benzenedithiolate) type catalysts. **RGO-1** shows a TOF of 1000 s^{-1} at pH 0. While in non-stirred solution electrocatalysis by **RGO-1** was observed to be limited by mass transport of protons

to the film surface, stirring the solution gave sigmoidal type catalytic waves for pHs 2.5 – 4. The plateau current observed in this acidity range increases linearly with acid concentration, which is characteristic of thin film electrocatalysis in the KP_R regime as defined by Costentin and Saveant. KP_R describes a system where catalysis is relatively slow compared to the electron transfer rate in the film. This confirms that the RGO is indeed reduced and able to conduct electrons effectively to the catalytic centers in the film. Fitting the plateau current gives a rate constant of $1.5 \cdot 10^4$ $M^{-1}s^{-1}$. Foot of the wave analysis (FOWA) was also used to determine the rate constant, this time at the beginning of the catalytic wave in unstirred solution, where mass transport concerns should be limited. Here, assuming KP_R as determined by plateau current analysis, a rate constant of $3.6 \cdot 10^3$ $M^{-1}s^{-1}$ was calculated for pH 3. This is lower than that determined by plateau current analysis, but overall, TOF, plateau current, and FOWA analysis show **RGO-1** is an example of a highly active molecular catalyst for HER in a thin film.

As discussed in the Introduction Section 1.2.2, HER requires two protonation steps and two electron transfer steps. For Co bis(benzenedithiolate) type catalysts, the first step is known to be reduction, followed by protonation. For **1**, the amines allow the catalyst to be protonated, as isolated. The catalyst is readily soluble in DMF/HCl$_{aq}$ and addition of an organic soluble base, like TEA, can deprotonate the catalyst, showing a slight shift in λ_{max} by UV-Vis spectroscopy (see Figure 2.5). The deprotonated form of the catalyst is also reactive towards acetic anhydride, as illustrated in Figure 2. The few nm shifts in electronic absorption energies upon deprotonation are consistent with the acid/base chemistry occurring at the appended amines and not the thiolate moieties, as expected. Therefore, the data for **1** agree with these first two mechanistic steps of reduction and then protonation in the HER catalytic cycle.

Our Tafel analysis provides further mechanistic insight into the rate limiting step. The Tafel slopes suggest that metal hydride formation is rate limiting at low acid concentrations, pH 3.0. At lower pH, with more acid present, it is possible that the mechanism shifts such that protonation and reduction of the metal hydride to yield hydrogen becomes the rate limiting step. Accordingly, the Tafel slopes decrease at lower pH values.

Notably, **RGO-1** is able to maintain a high Faradaic efficiency (79 ± 1 %), the same onset potential, and similar long term catalytic activity when electrocatalysis is performed in the presence of ambient air (Figure 2.24), demonstrating that **RGO-1** is completely air stable under electrocatalytic conditions. The remaining 21% current is attributed to O_2 reduction by the reduced

catalyst, returning it to the Co^{III} form, which can then be re-reduced and active for HER. We also note that the current and onset potential observed by CV is the same under anaerobic and aerobic conditions. This is in contrast to catalysts that are adept at ORR and can show an earlier ORR wave before HER, as is the case for a brominated, fluorinated cobalt corrole.[172] We note that **RGO-1** has two advantages that would give it O_2 tolerance. First, the Co^{III} bis(benzenedithiolate) type catalysts are air stable,[61,97] including **1**. Therefore, even if unwanted oxidation of the reduced Co^{II} catalyst occurs, the catalyst is able to be simply re-reduced, without degradation nor decrease of the amount of active catalyst. Second, embedding the catalyst within an RGO thin film limits the catalyst's access to dioxygen, especially as catalysis proceeds and hydrogen is produced in the film. Hydrogen evolution catalysts with oxygen tolerance are highly desired and currently a hot topic in HER catalyst development.[171] Only a few other, encapsulated catalysts that show high tolerance to dioxygen have been reported.[173–175] The Faradaic efficiency of **RGO-1** under air is similar to that reported for a Ni bis(benzenedithiolate) type catalyst in homogeneous solution,[45] but the same has not yet been reported yet for Co bis(benzenedithiolate) type catalysts.

In order to determine the long-term stability of **RGO-1**, CPE measurements were performed, which show an initial current density of 6 mA/cm^2 at -0.8 V vs Ag|AgCl in pH 2 solution. However, this current decays within 8 hrs. The decrease in catalytic ability of **RGO-1** over time suggests detachment of the catalyst from the film, degradation of the film, demetallation of the catalyst, other degradation of the catalyst, or some combination thereof. In previous studies on Co bis(benzenedithiolate) catalysts physisorbed on graphitic supports, detachment of the catalyst from the film was proposed as the degradation route.[97] We hoped to avoid detachment of the catalyst via covalent attachment, but decline of catalytic activity is still observed, just on a longer time scale when compared with the control system studied here, where catalyst **2** is physisorbed to RGO (**RGO/2**), see Figure 2.25. One possible explanation for this finding is slow degradation of the film. The film is still visually intact after long term CPE, so there is no mechanical damage to the film, even after 21 hrs of continuous electrolysis. Degradation of the active site is supported by the observed shift of the catalytic onset potential by CV over time (see Figure 2.25, right). Additionally, the amount of Co in the film is shown to decrease by XPS and ICP-MS, suggesting that demetallation of the complex is the major contributor to the decline in catalytic activity. XPS shows partial loss of the ligand specific elements (S, N) over the course of electrolysis, suggesting that the degradation of the ligand is a minor contributor to loss of catalytic

activity. SEM images of the film after electrolysis, see Figure 2.28, show that the film is for the most part intact with a similar structure as before electrolysis, with some microscale degradation of the film due to hydrogen bubbles formed near the electrode surface, escaping by ripping the film. Due to the majority of the film being intact, this is a very minor contributor to the observed decrease in catalytic activity.

Interestingly, **RGO-1** thin films have similar catalytic activity for HER in CV experiments as the Co bis(benzenedithiolate) catalysts that are physisorbed on graphitic materials/electrodes, which our group previously reported.[73,97] Please see Table 1.1 for a comparison of these systems. For example, **2** was physisorbed onto a bulk graphite electrode giving a relatively high surface coverage of 14.1 nmol/cm^2, due to the rough surface of this type of electrode.[73] Complex **2** was also shown to be active for HER when physisorbed to HOPG, with lower physisorption, at 0.260 nmol/cm^2 of electrochemically active cobalt.[97] The **RGO-1** film reported here is in between these two systems, with 1.3 ± 0.2 nmol/cm^2 of electrochemically active Co - five times that achieved by physisorption to HOPG, but still less than that achievable for rough graphite electrodes. The physisorbed **RGO/2** film gives 0.45 nmol/cm^2, on par with that of **HOPG/2**. A key consideration in these cases is not only the geometric surface area but the specific surface area and the attachment method. Comparing the TOFs of the catalysts on the surfaces, at pH 1.5 TOFs of 24, 320, and 105 s^{-1} are measured by CV for **graphite/2**, **HOPG/2**, and **RGO-1**. These results show that the electrocatalytic activity for Co bis(benzenedithiolate) catalysts for HER is overall similar in the physisorbed versus chemisorbed systems, but that the covalent attachment leads to a number of distinct advantages. First, the amount of electrocatalytically active Co is much larger, (in our case, about 3 times the amount), contributing to the 6 times higher catalytic currents for **RGO-1** compared to the physisorbed system (**RGO/2**). Second, **RGO-1** has a much better long-term stability (in our case, by a factor of 3-4), and future work is focused to further improve the system in this regard.

RGO-1 thin films discussed herein compare well to other earth abundant transition metal molecular catalysts immobilized on/in carbon-based supports. Please see Table 1.1 and Section 1.2.5 in the Introduction for relevant examples of thin film molecular HER electrocatalysts. Surface densities are often on the order of 1-10 nmol/cm^2 for similar systems, see Table 1.1, which is comparable to the surface density of Co in **RGO-1**, but unfortunately, in many examples from the literature the film thickness is not reported, and so the density of the catalyst in the film is

unknown, and a further, detailed comparison with these systems is not suitable. With regards to current densities, the initial current density for **RGO-1** is fairly good at 6 mA/cm^2, but the instability over time limits it to the lower end of its class with TONs at $1.3 \cdot 10^5$. From this, we conclude that **RGO-1**, while not breaking records in surface coverage, TOF, or TON, is a well-rounded catalyst comparable to top immobilized molecular earth abundant catalysts in each category, with interesting fundamental properties as discussed above that were investigated in great detail in this work, and exceptional stability in air.

In conclusion, the **RGO-1** system reported herein showcases the ability of molecular catalysts in thin films to be highly active for HER, albeit further work is necessary to further improve the durability of the system. The methods and approaches developed for HER electrocatalysts can be applied to other electrocatalytic reactions relevant to renewable energy as well, such as CO_2 capture, nitrate reduction, and the ever-elusive nitrogen fixation.[67,176] Hopefully, this work will guide the development and characterization of other thin film catalysts for HER and other key reactions in renewable energy as we, collectively, develop more sustainable catalytic processes to power our planet.

2.4 Experimental Section

2.4.1 General Synthesis and Chemicals

All chemicals were used as received with the exception of KPF_6 which was recrystallized twice for removal of trace metal ions.[177] In synthetic procedures DI H_2O was used when required; for all electrochemistry milli-Q H_2O with a resistance of ≥ 18 M$\Omega \cdot$cm was used. Cobalt bis(benzenedichlorodithiolate) tetrabutylammonium (TBA) and cobalt bis(toluenedithiolate) TBA were synthesized according to previously published procedures.[61,97] HPLC grade Trifluoroacetic acid with <0.0001 mg/kg Fe was used for electrochemical testing.

2.4.2 Instrumentation

NMR spectra were measured using Varian MR400 (400 MHz), Agilent MR400 (400 MHz), and Bruker Avance Neo 500 MHz instruments in automation mode via Bruker Icon NMR, or a Varian NMR Systems 500 MHz spectrometer. ^{1}H-NMR spectra were referenced to tetramethylsilane (TMS) or residual solvent peaks. Mass spectrometry data were collected on an Agilent 6230 TOF LC-MS system in negative ion mode, with reference ions at m/z 112.9 and

1034. UV-Vis spectra were obtained on an Analytical Jena Specord S600 instrument. All electrochemical measurements were conducted using a BioLogic SP-50 potentiostat with the exception of the controlled potential electrolysis data shown in Figure 2.26, which was obtained using a CH Instruments CHI600E potentiostat. Raman spectroscopy measurements were conducted on a Renishaw RM series Raman microscope with a Leica 50× objective using a 785 nm diode laser. Scanning electron microscopy/EDS images were obtained using a JEOL JSM-7800FLV scanning electron microscope. X-ray photoelectron spectroscopy data were collected on a Kratos Axis Ultra XPS instrument at the Michigan Center for Materials Characterization, using a Monochromatic Al source, with an emission current of 15 mA and voltage of 14 kV. XPS data were recorded with charge neutralization. High resolution spectra were recorded with a pass energy of 20 eV. C 1s spectra were recorded for 5 high resolution scans, N 1s and S 2p data for 15, and Co 2p data for 60. Atomic force microscopy data were collected on a Veeco Dimension Icon Atomic Force Microscope at the Michigan Center for Materials Characterization. Inductively coupled plasma mass spectrometry measurements were performed on a Perkin-Elmer Nexion 2000 ICP-MS. Centrifugation was conducted using an Allegra X-30R centrifuge by Beckman Coulter and a Beckman Coulter FX301.5 rotor. Quantitative H_2 gas headspace analysis was conducted by gas chromatography (GC) using a Thermo Scientific Trace 1310 instrument which utilized Ar carrier gas and a thermal conductivity detector.

2.4.3 Synthetic Procedures

N-boc-3,4-difluorobenzylamine. 3,4-difluorobenzylamine (1.14 g, 8.0 mmol) was added dropwise to di-*tert*-butyl dicarbonate (3.22 mL, 14 mmol), followed by addition of triethylamine (2.9 mL, 21 mmol). To this solution was added 3 mL acetone. The reaction mixture was stirred for 3 hr, and then 10 mL of water was added, followed by product extraction with 10 mL of ethyl acetate. The organic layer was washed with 10 mL of 0.1 M aqueous HCl, saturated aqueous sodium bicarbonate and water before drying over sodium sulfate. The solvent was evaporated to give a crude yellow oil, which was recrystallized from hexanes/chloroform to give clear crystals of N-boc-3,4-difluorobenzylamine (51%, 0.95 g). ^{1}H-NMR (500 MHz, CDCl$_3$): δ 7.09 (m, 2H), 7.00 (m, 1H), 4.87 (s, 1H), 4.26 (d, 2H), 1.46 (s, 9H) ppm; ^{19}F-NMR (400 MHz, CDCl$_3$): δ -137.6 (q, 1F), -140.1 (m, 1F) ppm. See Figure 2.29 and Figure 2.30.
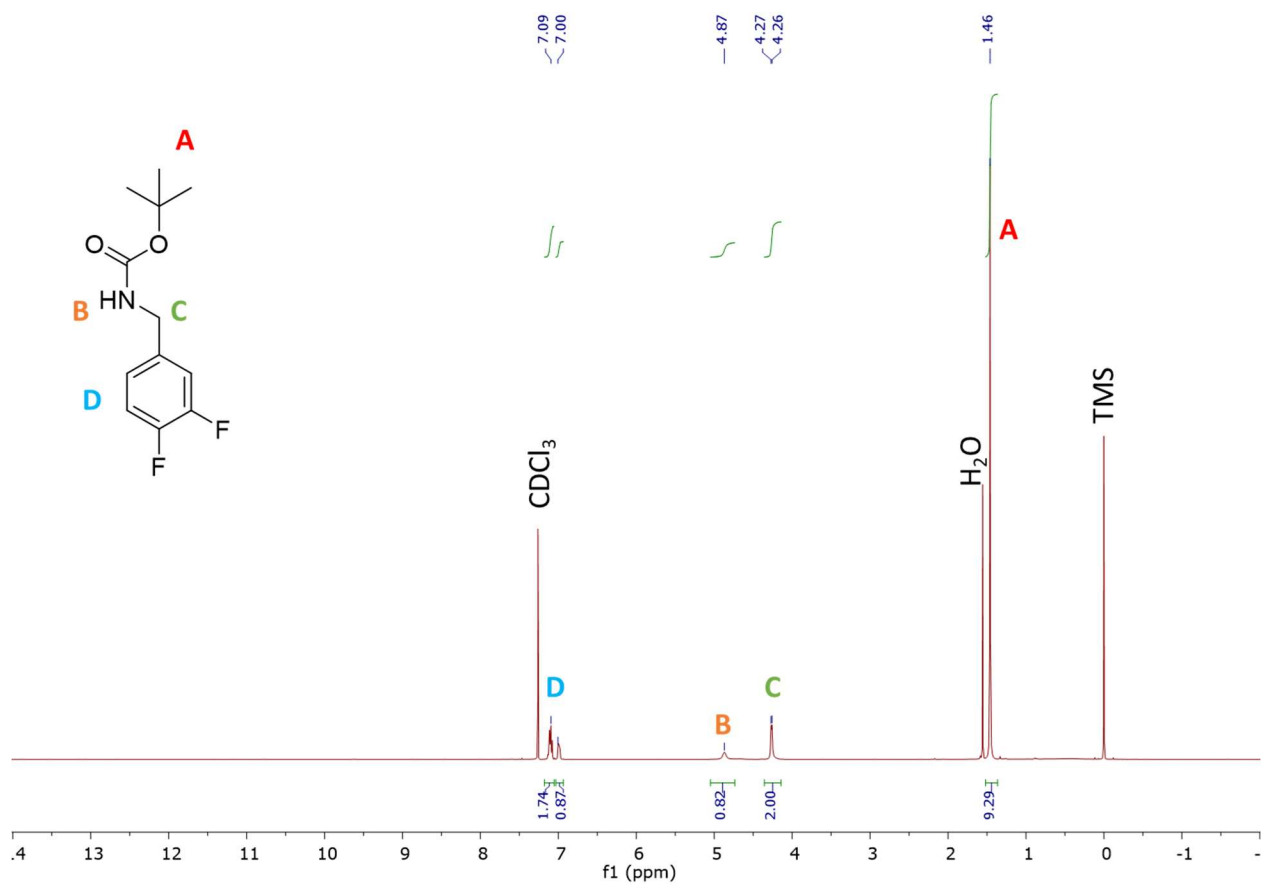
Figure 2.29. ¹H-NMR spectrum of boc-protected 3,4-difluorobenzylamine. ¹H-NMR (500 MHz, CDCl₃): δ 7.09 (m, 2H), 7.00 (m, 1H), 4.87 (s, 1H), 4.26 (d, 2H), 1.46 (s, 9H).
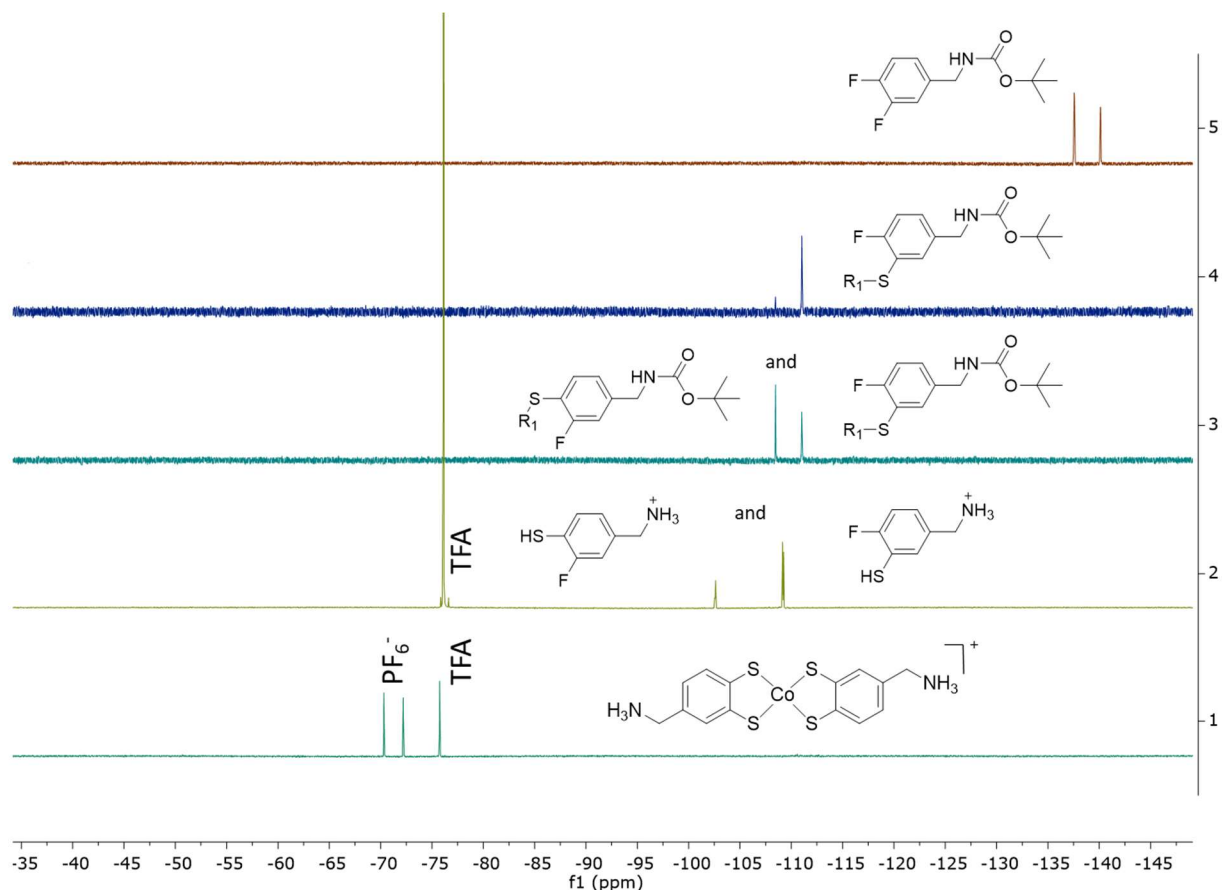
Figure 2.30. ^{19}F-NMR spectra of intermediates and byproducts of the synthetic procedure, and of **1**, as indicated by the structures. R$_1$ is diphenylmethyl, as shown in Figure 2.1. Residual TFA from the deprotection reaction is also observed in the spectra.

Diphenylmethylthiol. Diphenylmethylthiol was prepared following published methods.[178–180] Benzhydrol (2.0 g, 10.9 mmol), Lawesson's reagent (5.0 g, 12.4 mmol), 26.4 mL dry toluene and 0.20 mL H$_2$O were combined in a 50 mL round bottom flask, and the resulting mixture was refluxed for 1/2 hr via a preheated oil bath. The reaction mixture was cooled, concentrated, and the product was purified by column chromatography on silica (eluent 9:1 n-hexanes : ethyl acetate). Yield: 1.45 g, 7.3 mmol, 67%. ^{1}H-NMR (400 MHz, CDCl$_3$): δ 7.20-7.45 (m, 10H), 5.45 (d, 1H), 1.27 (d, 1H) ppm.

N-boc-3,4-bis(diphenylmethylthio)-benzylamine. The reaction was carried out under Ar, using Schlenk line techniques. Diphenylmethylthiol (1.7 mL, 9.0 mmol) was added dropwise to a suspension of NaH (0.22 g, 9.0 mmol) in 15 mL dry dimethylformamide (DMF) at 0 °C in a 50 mL round bottom flask. This mixture was allowed to stir for a few minutes until it turned nearly clear. Then, a solution of N-boc-3,4-difluorobenzylamine (1.00 g, 4.11 mmol) in 5 mL DMF was

added to the reaction mixture. The ice bath was removed, and the reaction heated. Once the reaction reached 50 °C, the Ar inlet needle was removed from the septum, making the reaction a closed system. The reaction was heated to 100 °C and refluxed for 3 hrs. At 3 hrs, the Ar inlet needle was reintroduced and another aliquot of diphenylmethylthiolate was added dropwise, prepared as before with diphenylmethylthiol (0.83 mL, 4.5 mmol) and NaH (108 mg, 4.5 mmol) in 5 mL DMF. The Ar inlet needle was removed again. After stirring and heating to 100 °C for an additional 3 hrs, the solvent was removed to give a crude oil. The desired product was then concentrated by column chromatography, with two consecutive columns (eluent 1:4 acetone : *n*-hexanes). The product could not be isolated in pure form due to similar retention factors of the monosubstituted molecules, causing partial co-elution. Yield: 188 mg, 66% of which was the disubstituted product based on the ^{1}H-NMR spectrum (benzyl proton integration), < 10% total conversion. ^{1}H-NMR (500 MHz, CDCl$_3$): δ 7.20-7.45 (m, 20H), 6.96 (d, 1H), 6.87 (d, 1H), 6.77 (dd, 1H), 5.66 (d, 2H), 4.36 (s, 1H), 4.00 (d, 2H), 1.46 (s, 9H) ppm. See Figure 2.31.

The monosubstituted molecules are also produced in this reaction (see Figure 2.32):

N-Boc-3-diphenylmethylthio-4-fluoro-benzylamine. ^{1}H-NMR (400 MHz, CDCl$_3$): δ 7.20-7.45 (m, 10H), 6.96 (d, 1H), 7.01-7.08 (m, 2H), 6.94 (t, 1H), 5.62 (s, 1H), 4.55 (s, 1H) 4.09 (d, 2H), 1.47 (s, 9H) ^{19}F-NMR (400 MHz, CDCl$_3$): -111 (s, 1 F) ppm.

N-Boc-3-fluoro-4-diphenylmethylthio-benzylamine. ^{1}H-NMR (400 MHz, CDCl$_3$): δ 7.20-7.45 (m, 10H), 7.13 (t, 1H), 6.9 (1H), 6.82 (dd, 1H), 5.62 (s, 1H), 4.79 (s, 1H), 4.22 (d, 2H), 1.45 (s, 9H) ^{19}F-NMR (400 MHz, CDCl$_3$): -108 (s, 1 F) ppm.
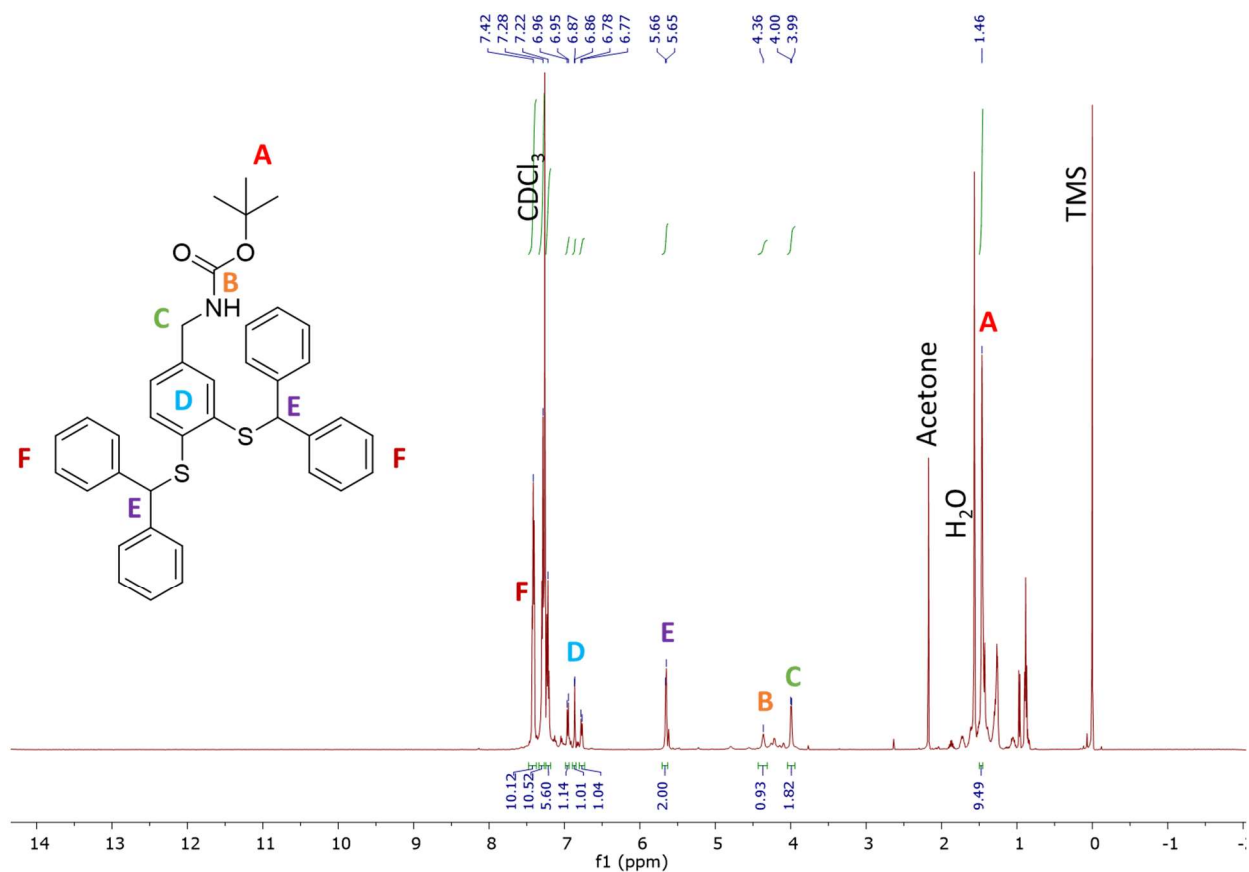
Figure 2.31. ^{1}H-NMR spectrum of N-boc-3,4-bis(diphenylmethylthio)-benzylamine, impure. Both monothioether impurities have been characterized, see Figure 2.32, and contribute to an increase in the integrated area of the phenyl protons "F". ^{1}H-NMR (500 MHz, CDCl$_3$): δ 7.20-7.45 (m, 20H), 6.96 (d, 1H), 6.87 (d, 1H), 6.77 (dd, 1H), 5.66 (d, 2H), 4.36 (s, 1H), 4.00 (d, 2H), 1.46 (s, 9H).
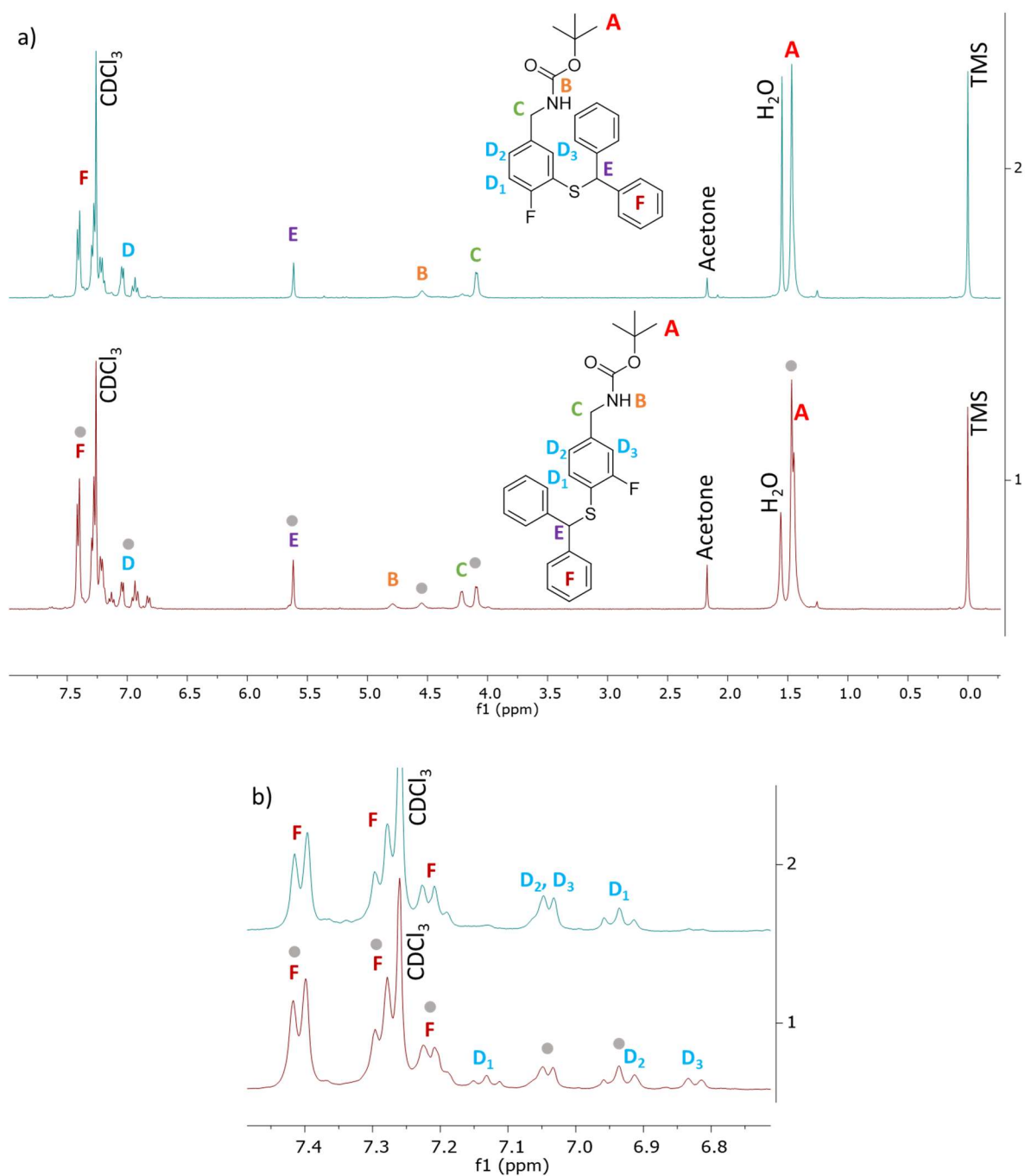
Figure 2.32. ^{1}H-NMR spectral characterization of the monosubstituted byproducts of the nucleophilic aromatic substitution reaction. Panel a: the top spectrum shows the mostly pure N-Boc-3-diphenylmethylthio-4-fluoro-benzylamine, while the lower spectrum shows a ~1:1 mixture of this isomer with N-Boc-3-fluoro-4-diphenylmethylthio-benzylamine. Panel b: a closer look at the aromatic region of the spectra from panel a. Aromatic proton peaks D_1, D_2, and D_3 were assigned with guidance from MestReNova NMR prediction and show the expected integrations. The gray circles mark peaks that originate from N-Boc-3-diphenylmethylthio-4-fluoro-benzylamine.

3,4-dithiolbenzylammonium trifluoroacetate. The deprotection method was adapted from similar diphenylmethyl thioether deprotection reactions published previously.[181] The reaction was carried out under Ar, using Schlenk line techniques. The mixture of products from the above reaction, containing N-boc-3,4-bis(diphenylmethylthio)-benzylamine, was used as the starting point for this reaction. The percent of the disubstituted product (N-boc-3,4-bis(diphenylmethylthio)-benzylamine) and monosubstituted impurities (N-boc-3-diphenylmethylthio-4-fluoro-benzylamine and N-boc-3-fluoro-4-diphenylmethylthio-benzylamine) was first calculated. In a typical reaction, the mixture of products contained 66% disubstituted and 34% monosubstituted product. 110 mg (0.20 mmol total, 0.13 mmol desired disubstituted product) of the mixture was dissolved in 1.4 mL dichloromethane under Ar in a 5 mL round bottom flask. To this solution was added 0.2 mL triethylsilane. Then, after stirring for 3 minutes, 0.6 mL trifluoroacetic acid (TFA) was added dropwise, causing the reaction to change color to slightly yellow. The round bottom flask was sealed, and was heated and stirred at 30 °C for 1 hr. Then the volatiles were evaporated with dinitrogen gas, and the acidic gas was neutralized by bubbling the gas stream through a saturated aqueous sodium bicarbonate solution. Once volatiles were removed, 1 mL hexanes was added to dissolve the diphenylmethane biproduct, and the heterogeneous mixture was stirred at 0 °C for 1/2 hr, and then let sit at 0 °C for 1/2 hr. The hexanes solution was carefully decanted, and the resulting sticky oil product was dried and moved immediately to the following reaction. See Figure 2.33 for representative crude reaction ^{1}H-NMR spectra.
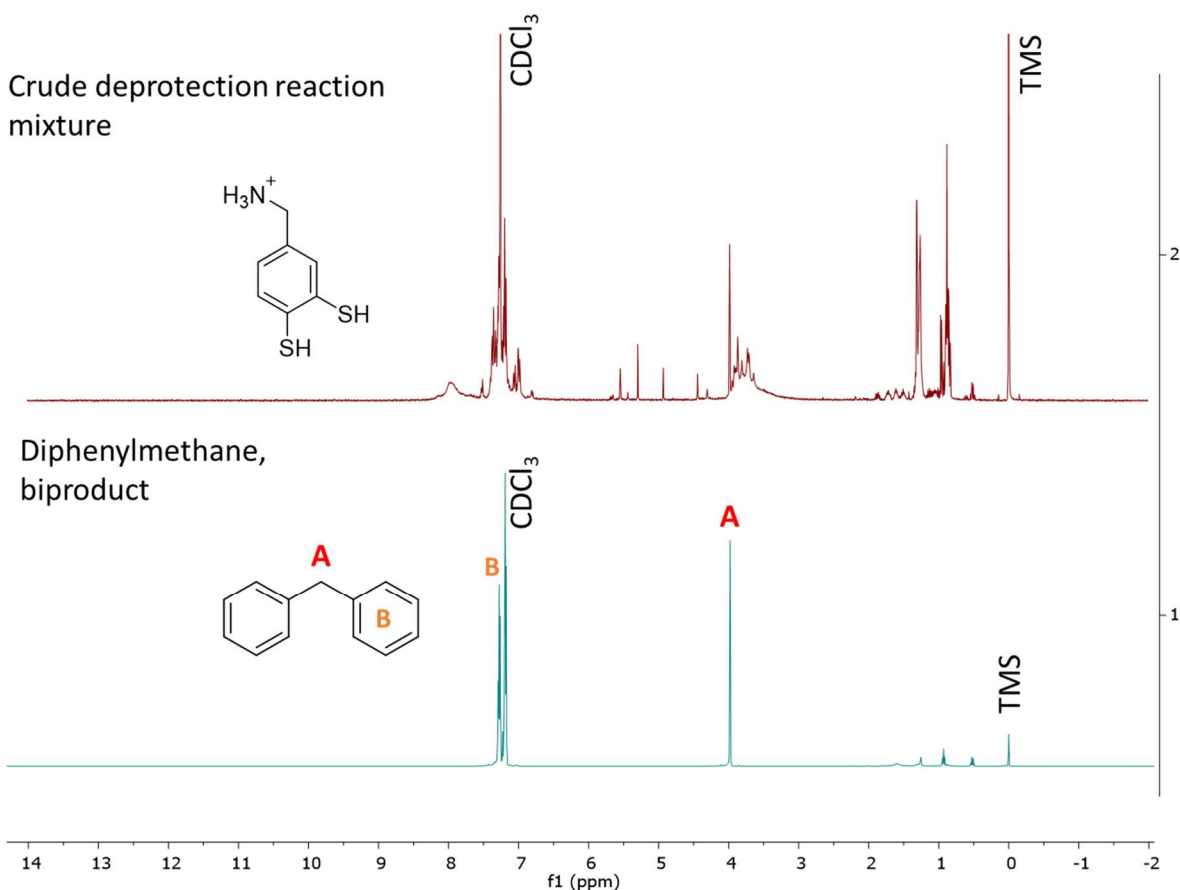
Figure 2.33. ^{1}H-NMR spectra of the crude products from the deprotection reaction. Top: crude deprotection reaction mixture containing 3,4-dithiolbenzylammonium trifluoroacetate. Note that these products are not purified or characterized further, but the solution containing 3,4-dithiolbenzylammonium trifluoroacetate is moved directly forward to metalation. See further discussion in the Experimental Section 2.4.3. Bottom: diphenylmethane is the main product from the deprotection reaction, which is removed in the hexanes wash, showing deprotection of the thiol moieties.

[Cobalt bis(benzylammoniumdithiolate)]Cl (1). The reaction was performed under dinitrogen, using Schlenk line techniques. The product of the above reaction, with assumed 66% 3,4-dithiolbenzylammonium trifluoroacetate and 34% 3,4 or 4,3-thiolfluorobenzylammonium trifluoroacetate, was dissolved in 1.5 mL dry methanol, with 3 equivalents of sodium methoxide for each 3,4-dithiolbenzylammonium trifluoroacetate and 2 equivalents for each thiolfluorobenzylammonium trifluoroacetate (here: 0.54 mmol, 29 mg). A solution of $CoSO_4*7H_2O$ (0.5 eq per 3,4-dithiolbenzylamine; here: 0.066 mmol or 18 mg) in 1.5 mL dry methanol was added to the solution of the deprotonated ligand dropwise. The solution immediately turned dark blue. The solution was stirred for 2 hrs. Then, a solution of 1 eq of [TBA](Br) (0.066

mmol, 21.3 mg) or [TBA](PF$_6$) in 1 mL methanol was added. The reaction was stirred for 2 hrs. Then the volume of the solution was reduced to one fifth. The resulting suspension was filtered and washed with methanol to give [TBA][cobalt bis(benzylaminedithiolate)]. The complex was then dissolved in DMF/HCl (5% aq, 10 eq) for further characterization, to yield the protonated form **1**. Yield: 27.2 mg, 64% of the last two steps. ^{1}H-NMR (500 MHz, DMF, with solvent suppression): δ 30.21, -19.98, -20.49, -24.06 ppm. See Figure 2.3.

Covalent attachment of 1 to GO (GO-1). A 1% GO solution (10 mg/mL) was used as received from gographene.com, lyophilized, and stored in a desiccator until further use. Lyophilized GO (2 mg) was added to a 0.75 mL solution of 2.6 mM **1** in DMF/HCl$_{aq}$. 0.25 mL of triethylamine DMF solution was added (2.4 mg TEA in 1 mL DMF). After mixing well and sonicating for 10 min to resuspend the GO, the solution was sparged with Ar, then the Ar needle was removed from the septum and the reaction was heated to 65 °C. The reaction mixture was stirred for 24 hrs. After cooling, 0.5 mL of DMF was added to the reaction mixture, and the resulting mixture was centrifuged (10 min at 15000 rpm). The supernatant was then decanted and discarded to remove unreacted complex. The resulting dark brown material was resuspended in 1.5 mL DMF with 9 μL of aqueous 5% HCl, let sit for 1 hr to dissolve any free **1**, and then centrifuged. The solid product was rinsed with DMF, then MeOH. Finally, the material was resuspended in 2 mL water to give a 1 mg/mL GO solution, "**GO-1**". The GO control was prepared in the same way as **GO-1**, except that in the procedure, the solution of **1** was substituted with pure DMF.

2.4.4 Experimental Procedures

Film preparation. 3.5 μL of the prepared GO or **GO-1** solution were drop-cast on a polished glassy carbon (GC) electrode (3 mm diameter, unless otherwise specified). The film was allowed to dry in a covered area overnight. Then the film was dried further under vacuum (150 mTorr) for 6 hrs.

GO reduction. GO films were reduced before electrochemical analysis, with 15 reductive cycles of cyclic voltammetry at 200 mV/s from 0 to -1.2 V vs Ag|AgCl in aqueous 0.1 M KPF$_6$ solution. See Figure 2.9.

Faradaic Efficiency. A film was drop-cast on to a GC disk electrode (5 mm diameter), such that the same volume of **GO-1** was used per area. The experiment was performed in a sealed two part cell, with the half cells separated by a Nafion membrane. The reference electrode was SCE in

saturated KCl. The counter electrode was a carbon rod. Experiments were conducted under dinitrogen gas. The film was reduced according to the usual procedure in neutral 0.1 M KPF$_6$, then the electrolyte was switched to 0.1 M KPF$_6$ made acidic to pH 1 with TFA. The cell and solution were then rigorously purged again. A 20 min CPE at -1.04 V vs SCE was performed, and the gas headspace was analyzed by GC, see Figure 2.34. The percent H$_2$ in the gas headspace was determined using a calibration curve. Comparison of this value to the expected percent H$_2$ if all charge passed in the CPE went to H$_2$ production determined the Faradaic efficiency. Our measurements show quantitative Faradaic efficiency for **RGO-1**, with 97 ± 4 % of the expected H$_2$ gas detected (N=2 gas aliquots). Faradaic efficiency in air was measured in the same manner, only the cell was purged with air upon addition of the pH 1 electrolyte. This electrolysis was calculated to have a Faradaic Efficiency of 79 ± 3 %.
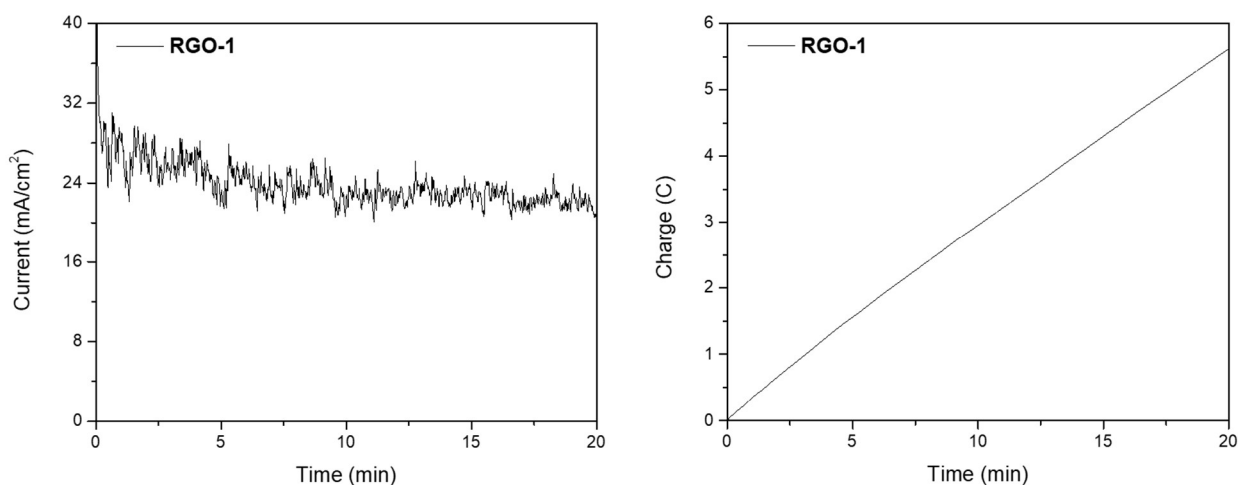
Figure 2.34. Controlled potential electrolysis used for determining Faradaic efficiency. A potential of -1 V vs Ag|AgCl at pH 1 was held for 20 minutes. The working electrode was a 5 mm diameter GC disk with an **RGO-1** film. Gas chromatography of the gas head space after CPE showed a Faradaic efficiency for H$_2$ production of 97± 4 % of the expected H$_2$ gas detected (N=2 gas aliquots). See Experimental Section 2.4.4 for further experimental details.

Controlled Potential Electrolysis. Controlled Potential Electrolysis were conducted in a three part cell, with each electrode separated from the others, see Figure 2.35. Great care was taken to avoid contamination. The glassware used for the cell and for preparation of the electrolyte solution were cleaned with soap and water, rinsed well with water, let sit in an acid bath overnight, rinsed, let sit in a base bath overnight, rinsed well with water, then rinsed well with mille-Q water. A new stir bar was used for the working electrode compartment, while the stir bars for the reference and

counter electrode compartments were cleaned in the acid bath. The rubber o-rings were also cleaned in the acid bath, these were also placed next to the reference electrode and counter electrode cell compartments with fresh Nafion membranes closest to the working electrode cell compartment. The Nafion membranes were rinsed with mille-Q water before use. The counter electrode and reference electrode were also rinsed well with mille-Q water before use. The food grade silicon tubing used for circulating the electrolyte was cleaned by rinsing well with an aqueous 5% H_2SO_4 solution then rinsed well with mille-Q water. The fritted Ar bubbler was rinsed well then soaked an aqueous 5% H_2SO_4 solution at least overnight between uses, and then rinsed well with mille-Q water.

To set up, the main compartment was partially filled with 0.1 M KPF_6 aqueous solution, the tubes were connected and the pump was turned on. The main compartment was sparged well with Ar via a glass pipet carefully inserted through a pre-pierced septum, as was the reservoir. At the same time the reference electrode and working electrode compartments were also sparged with N_2. Then the inlet Ar pipet to the working electrode compartment was removed. It was important that the working electrode compartment was air-tight, or leaks occurred. The glass stopper was wrapped with parafilm and if necessary the septum was further made air-tight with electrical tape. The N_2 sparging pipets were removed from the reference electrode and working electrode compartments and left with a very gentle blanket of N_2 for the course of the experiment. If the solution level dropped significantly in these compartments, they were refilled with mille-Q pure water.

After initial reduction of GO to RGO, the electrolyte was acidified by addition of neat TFA to the reservoir and addition of 1 M aqueous TFA solution to the reference electrode and working electrode compartments. The reservoir solution was allowed to circulate to equilibrate. The reference electrode and working electrode compartments were briefly purged for the same purpose. As noted in Section 2.4.1, high purity TFA was used as an acid source, no metal contamination was allowed in this bottle of TFA.
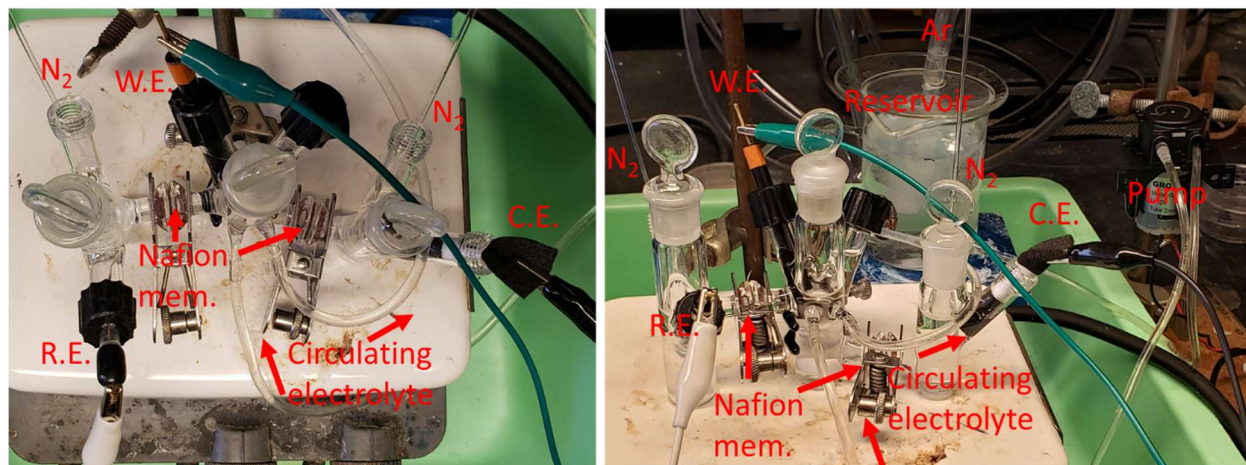
Figure 2.35. Photos of the electrochemical setup used for the CPE experiments. Left: top view. Right: the full setup, including the pump and the reservoir.

2.4.5 Plateau Current and Foot-Of-The-Wave (FOWA) Analysis

Given the standard equation for FOWA analysis,

$$\frac{I_c}{I_p} = \frac{\dfrac{I_{pl}}{I_p}}{1 + \exp\left(\dfrac{F}{RT}\left(E - E_{\frac{cat}{2}}\right)\right)} \qquad \text{Equation 2.4}$$

where I_c is the catalytic current density [A/cm^2] at a certain potential E [V]; I_p is the peak current density of the catalytic couple when no substrate is present [A/cm^2]; I_{pl} is the theoretical plateau current density (not limited by mass transport) [A/cm^2]; F is Faraday's constant [C/mol]; R is the gas constant [J K^{-1} mol^{-1}]; T is the temperature [K]; and $E_{cat/2}$ is the potential where the catalytic current is half of the plateau current [V], if not limited by mass transport in solution or in the film. The plateau current for a KP$_R$ system is described as:[163]

$$I_{pl} = nFkC_p^0 \kappa_A C_A^0 d_f \cdot \left(\frac{1L}{1000 cm^3}\right) \qquad \text{Equation 2.5}$$

$$E_{\frac{pl}{2}} = E^0 = E_{\frac{cat}{2}} \qquad \text{Equation 2.6}$$

Here, n is the number of electrons in the reaction studied (here $n = 2$); k is the rate constant [M^{-1}s^{-1}]; C_p^0 is the concentration of oxidized catalyst in the film before any is reduced [M]; κ_A is the partition coefficient for substrate, here protons, between the film and solution; C_A^0 is the initial concentration of substrate in solution [M]; d_f is the thickness of the film [cm]; and E^0 is the

potential of the Co^{III}/Co^{II} couple [V]. The following definitions were used to simplify the above equation:

$$I_{Pl} = \frac{i_{pl}}{S}$$

Equation 2.7

and

$$C_p^0 = \frac{mol_{Co}}{d_f * S * \frac{10^{-3}L}{cm^3}}$$

Equation 2.8

where i_{pl} is the ideal plateau current [A]; S is the geometric surface area of the film [cm^2]; and mol_{Co} is the moles of electrochemically active Co in the film [mol]. Equation 2.5, Equation 2.6 and Equation 2.7 simplify to give:

$$i_{pl} = nFk\kappa_A C_A^0 mol_{Co}$$

Equation 2.9

Equation 2.9 is used for plateau current analysis, see Section 2.2.3 and Figure 2.22. The peak current (i_p) can be neatly canceled out of Equation 2.4, which is convenient as the Co^{III}/Co^{II} couple is broad and shallow. This, and combining Equation 2.4, Equation 2.6, and Equation 2.9, gives:

$$i_c = \frac{nFk\kappa_A C_A^0 mol_{Co} 10^3}{1 + \exp\left(\frac{F}{RT}(E - E^0)\right)}$$

Equation 2.10

Here, E^0 is taken as the Co^{III}/Co^{II} couple, which is at -0.71 V vs Ag|AgCl (see Eq 3); and κ_A was assumed to be 1. The latter likely overestimates the partition of protons into the film at higher acid concentrations, as it is generally known that RGO without modification is a moderate proton conductor.[169] Still, this assumption allows us to calculate an approximation of the rate constant.

Table 2.1. Table of calculated rate constants k, at different acid concentrations as per Equation 2.10.

[H$^+$] [M]	k [s^{-1}M^{-1}]
0.001	$3.6 \cdot 10^3$
0.00316	$3.6 \cdot 10^3$
0.01	$2.7 \cdot 10^3$
0.0316	$1.4 \cdot 10^3$
0.1	$8.7 \cdot 10^2$
0.316	$5.2 \cdot 10^2$
1	$3.4 \cdot 10^2$

Chapter 3 Spectroscopic Characterization of Intermediates in Hydrogen Evolution Catalysis by Co Bis(benzenedichlorodithiolate)

In this chapter, Co(II) bis(benzenedichlorodithiolate) is prepared and spectroscopically characterized. The reaction of this species with protons is investigated and suggests that Co bis(benzenedithiolate) complexes are capable of homolytic hydrogen evolution. We thank Dr. Jeff Kampf for solving the X-ray crystal structure of $(CoCp_2)_2[Co^{II}(bdt)_2]$. A corresponding manuscript communicating these results regarding the Co(II) species is currently in preparation.

3.1 Introduction

Understanding the mechanisms that catalysts use to conduct their reactions allows for the optimization and troubleshooting of catalytic reactions. In previous work in our group and in the work presented in Chapter 2, we have shown that Co bis(benzenedithiolate) type catalysts, whether physisorbed or covalently attached to the electrode surface, to be highly active catalysts for HER performing well compared to other top heterogenized earth abundant transition metal molecular complexes that have been reported in the literature.[2,26] However, they are shown to decline in activity over time.[2,73,97] Therefore, it is desirable to better understand the molecular mechanism of these catalysts to elucidate the reason(s) for catalyst failure and obtain insight into how the catalyst functions, both homogenously and heterogeneously.

As these catalysts have been studied for roughly 60 years, both as complexes for their inherent geometric and electronic structure,[60,61] and as catalysts for the hydrogen evolution reaction (HER),[2,46,47,73,96,97] there is much known about their electronic and geometric structure, and some information has been obtained about their putative HER mechanism.

First, these complexes are easily synthesized in their Co^{III} state. As discussed in the Introduction, Section 1.2.1, these complexes in their Co^{III} form are square planar and monomeric, though some derivatives not discussed here-in may dimerize.[47,60] The complexes discussed in this chapter are shown in Figure 3.1. The ground state is a mix of $Co^{III}(L)_2$ and $Co^{II}(L^{\bullet})(L)$ character.

However, how the non-innocent benzenedithiolate ligands impact HER catalysis by these complexes is not well understood.
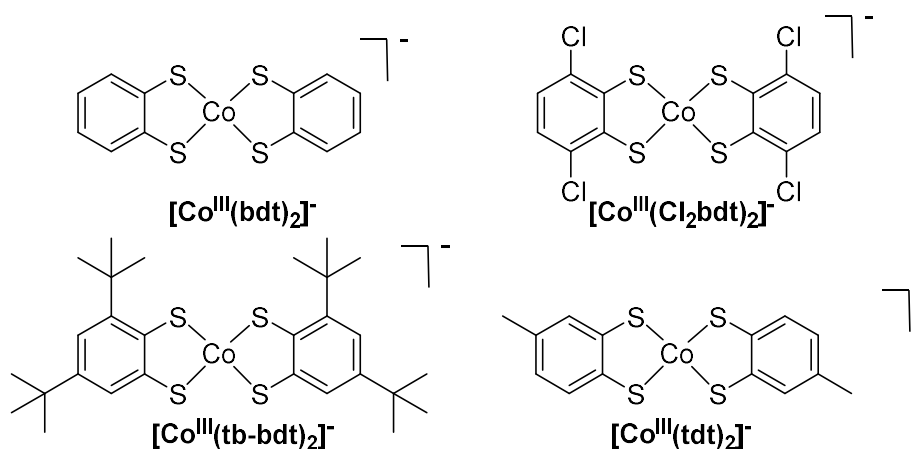
Figure 3.1. Structures of complexes discussed in this chapter. Ligand abbreviations are as follows, bdt = benzene-1,2-dithiolate, Cl_2bdt = 3,6-dichlorobenzene-1,2-dithiolate, tb-bdt = 3,5-di-tert-butylbenzene-1,2-dithiolate, and tdt = toluene-3,4-dithiolate.

As discussed in the Introduction, Section 1.2.2, there are nominally four steps to HER: two electron transfers (E) and two proton transfers (C). Cyclic voltammetry shows that the first step of the HER reaction by Co bis(benzenedithiolate) type complexes is reduction, with catalytic activity taking off at or after the Co(III/II) couple. The second step is protonation, as the Co(II/I) couple is not observed at any accessible potential in the absence of acid. The order of the next two steps has been suggested by density functional theory (DFT) calculations,[65] but has not been determined experimentally. Specifically, Hans and Eisenberg suggest an ECCE mechanism, where protonation initially occurs on the sulfurs of the benzenedithiolate, and after the second reduction, the Co^I center accepts a hydride, and then the resulting Co(III)-H and remaining H-S$_{bdt}$ proton form hydrogen intramolecularly. This mechanism is illustrated in Figure 3.2.
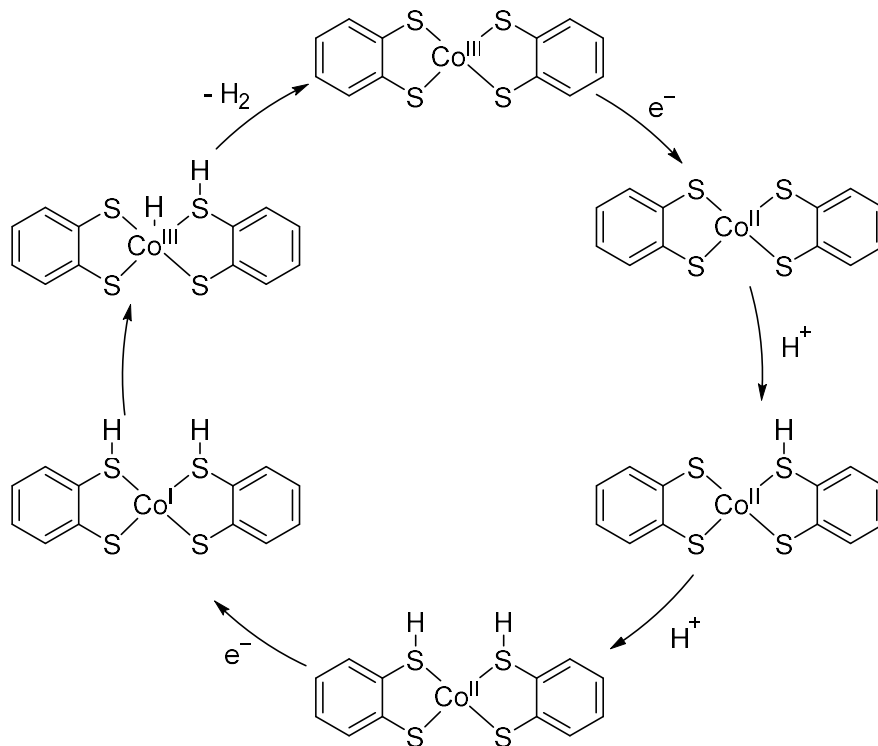
Figure 3.2. Proposed mechanism from Solis and Hammes-Schiffer.[65] This mechanism was calculated to be preferred by [Co(bdt)$_2$]⁻, [Co(Cl$_2$bdt)$_2$]⁻, and [Co(tdt)$_2$]⁻. Here, the parent [Co(bdt)$_2$]⁻ complex is used for illustration. See Figure 3.1 for structures of the other species.

Our group is interested in studying the HER activity of these Co bis(benzenedithiolate) type complexes when immobilized onto electrode surfaces (bdt = benzene-1,2-dithiolate). In particular, we have studied the complexes when physisorbed to graphitic surfaces.[73,96] Therefore, the geometry of the intermediates featured in the mechanism is important. It is possible that during the catalytic cycle, if the catalyst distorts from its square planar structure, its ability to π-stack with the graphitic electrode will be disrupted promoting dissociation of the physisorbed catalyst from the electrode surface. Specifically, the geometric structure of the Co(II) form is unknown. Solis and Hammes-Schiffer calculated that in the quartet state the Co(II) form would be tetrahedral, while the doublet state of Co(II) would be square planar.[65] If the Co(II) form is indeed in the quartet state and tetrahedral, this would give the complex an opportunity to dissociate from the graphitic surface. In their calculations, the tetrahedral quartet structure was indeed slightly energetically favored.[65]

While there have been extensive studies on the Co(III) bdt type complexes and their electronic structure,[60] much less experimental work is available for the reduced Co(II) bdt

complexes, which is likely due to the face that they are very air sensitive. When the early research on these complexes was being performed, preparation of pure samples was challenging.[182] Some research was conducted on $[Co(tdt)_2]^{2-}$ and $[Co(tb\text{-}bdt)_2]^{2-}$ (tdt = toluene-3,4-dithiolate and tb-bdt = 3,5-di-tert-butylbenzene-1,2-dithiolate). In a study by Sawyer et al in 1986, the $[Co(tdt)_2]^-$ complex was electrochemically reduced in MeCN, perhaps incompletely as the 660 nm peak persisted, to obtain a UV-Vis spectrum of the Co(II) form.[182] The reduced $[Co(tb\text{-}bdt)_2]^{2-}$ form was also prepared by electrochemical reduction at reduced temperatures (-25 °C), and the UV-Vis spectrum was published in a thesis in 2005.[154] These data are consistent with our observations, see below, but no further spectroscopic characterization of the $[Co(II)(bdt)_2]^{2-}$ type complexes is known. Additionally, there have been a few studies on Co(II) dithiolene complexes with non-bdt type ligands.[182,183]

Further, none of the intermediates following Co(II) formation in the proposed mechanism illustrated in Figure 3.2 have been experimentally isolated or studied. These catalysts are adept at HER, and these intermediates can be expected to be short-lived under catalytic conditions, which makes their isolation challenging.

For this study, we set out to investigate the above intermediates to further determine the HER mechanism of these complexes and possibly identify points of failure of these Co bis(benzenedithiolate) type catalysts. For this study, we used $[Co(Cl_2bdt)_2]^-$, as it is a highly active catalyst and the required ligand is commercially available (Cl$_2$bdt = 3,6-dichlorobenzene-1,2-dithiolate). In this chapter, I have shown that the Co(III) complex can be reduced by chemical or electrochemical reduction to the Co(II) oxidation state. X-ray crystallography shows that the Co(II) complex retains the same square planar geometry as the starting Co(III) complex. This shows that reduction alone does not promote catalyst dissociation from the electrode surface by twisting the structure to tetrahedral. This Co(II) species has been further characterized by magnetic circular dichroism (MCD), electron paramagnetic resonance (EPR), and UV-Vis spectroscopy. Further reactivity of the Co(II) species is reported and attempts to isolate the other reaction intermediates are discussed.

3.2 Results

3.3 Synthesis and characterization of Co(II) species

The complex [TBA][Co(III)(Cl$_2$bdt)$_2$] was synthesized according to literature procedures.[61,97] The reduced [Co(II)(Cl$_2$bdt)$_2$]$^{2-}$ complex could be prepared chemically, by addition of a stoichiometric reducing agent, cobaltocene, or electrochemically, by controlled potential reductive electrolysis. As expected, given the reported UV-Vis spectra for [Co(II)(tdt)$_2$]$^{2-}$ and [Co(II)(tb-bdt)$_2$]$^{2-}$,[154,182] the Co(II) form gives a light yellow solution, in contrast to the dark blue color of the Co(III) species. The comparison of the UV-Vis spectra may be seen in Figure 3.3. The Co(II) form is highly air sensitive and will oxidize in air to return the Co(III) form, as shown in Figure 3.4.
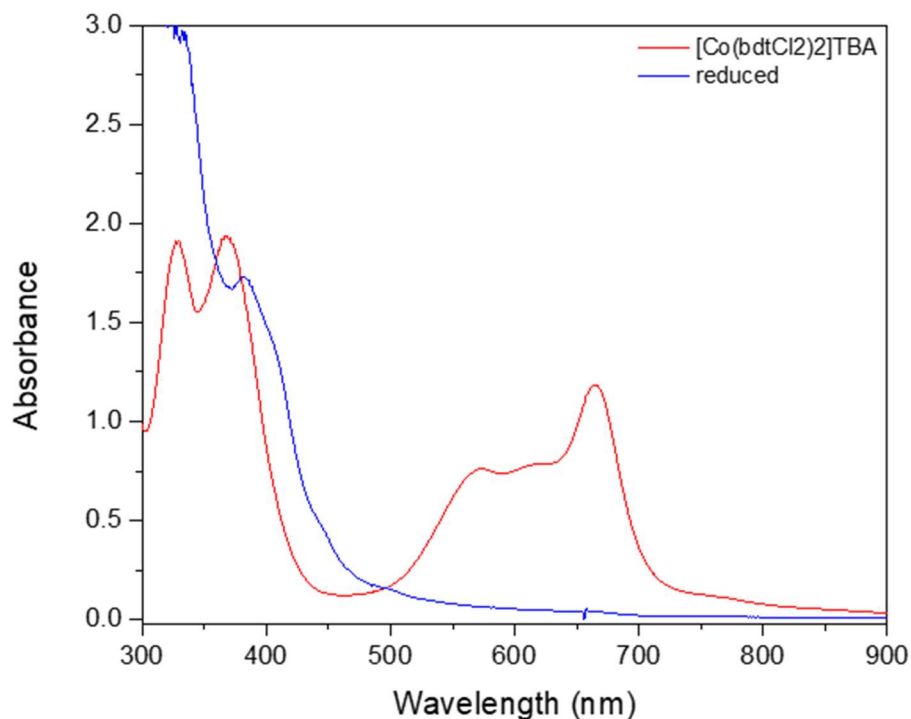
Figure 3.3. Comparison of the UV-Vis spectra of the complexes [Co(III)(Cl$_2$bdt)$_2$]$^-$ and [Co(II)(Cl$_2$bdt)$_2$]$^{2-}$, each one 0.1 mM in THF at room temperature (RT). The data for the Co(II) species were taken under an inert atmosphere, while those for the Co(III) complex were obtained under ambient air.
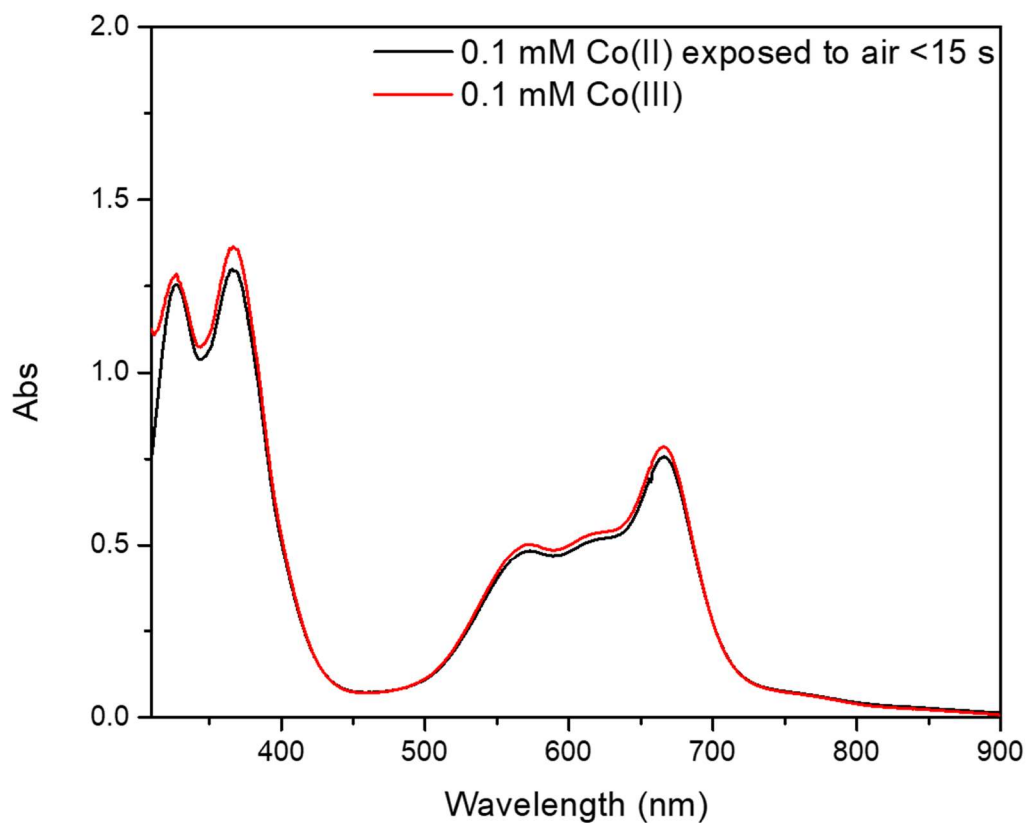
Figure 3.4. Comparison of the UV-Vis spectra of the product of Co(II) oxidation by ambient air and the true $[Co(III)(bdt)_2]^-$ starting complex. Both species are 0.1 mM in acetonitrile in the presence of 0.01 M $[TBA](PF_6)$. The black spectrum, the oxidized Co(II) complex, was taken by mixing 0.1 mL anaerobic 1 mM $[TBA]_2[Co(II)(bdt)_2]$ formed by electrochemical reduction with 0.9 mL acetonitrile under ambient conditions.
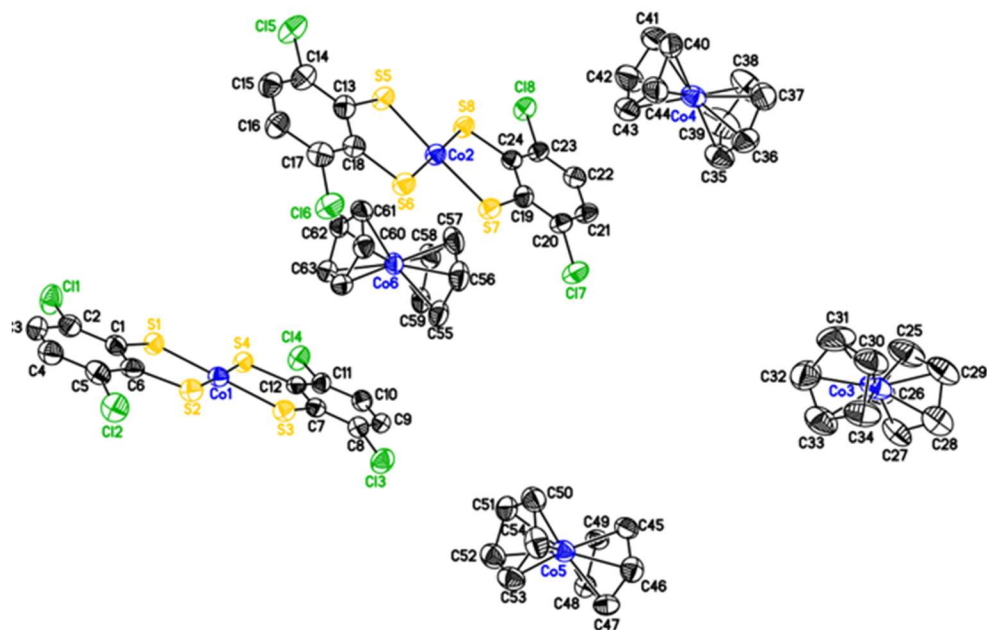
Figure 3.5. X-ray crystal structure of (CoCp$_2$)$_2$[Co(II)(bdt)$_2$] This crystal structure was obtained and solved by Dr. Jeff Kampf, see Experimental Section 3.6.4 for further details and Table 3.1 for select bond lengths. One equivalent of butyronitrile is also present in the crystal but here is omitted for clarity.

High quality crystals of the Co(II) species were obtained by slow evaporation of the chemically reduced species in butyronitrile. X-ray crystallography of this species shows two cobaltocenium cations per each square-planar [Co(II)(Cl$_2$bdt)$_2$]$^{2-}$ dianion. The dianion is strictly planar with the sum of the SCoS angles summing to 360.0°. Comparison to the Co(III) species shows that this is a primarily metal-based reduction, as the aryl ligand bond distances show very little change, see Table 3.1. This suggests that while Solis and Hammes-Schiffer predicted the tetrahedral quartet state of Co(II) would be favored,[65] under these conditions, the complex is experimentally found to be square-planar. This suggests that the species is instead a doublet Co(II) complex.

Table 3.1. Comparison of average bond lengths between the Co(III) and Co(II) state of Co(Cl$_2$bdt)$_2$

Bond	Co(II) catalyst (Å)	Co(III) catalyst (Å)
Co-S	2.182 (4)	2.164 (5)
S-C	1.749 (7)	1.750 (3)
C-C	1.395 (14)	1.393 (11)
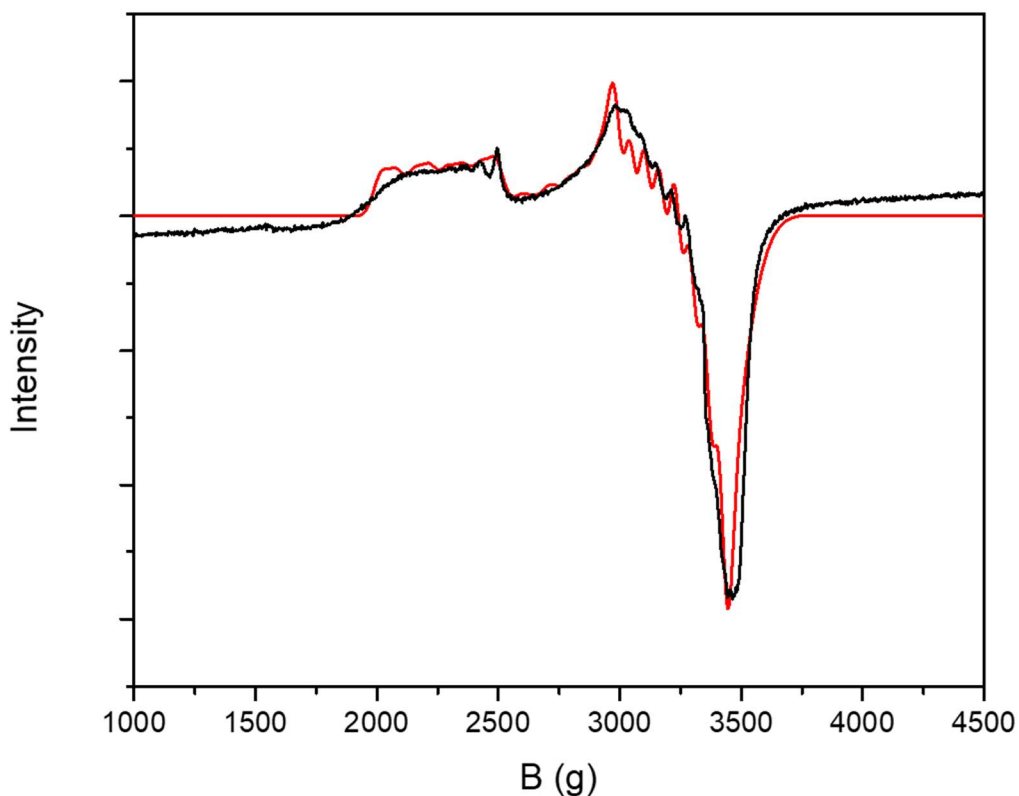
Figure 3.6. EPR spectrum of [TBA][CoCp$_2$][Co(II)(Cl$_2$bdt)$_2$], 1 mM in THF, measured at 10 K. The experimental spectrum is given in black, and the fit is shown in red. The fit parameters are g = (1.95, 2.07, 2.95), g$_{strain}$ = (0.06, 0.014, 0.04), A = (not fit, 180, 280).

The electronic structure of this Co(II) species was further studied by electron paramagnetic resonance (EPR) spectroscopy. Unlike the S_t = 1 Co(III) species, which is EPR silent, the reduced Co(II) complex has a non-integer spin ground state and gives an EPR signal. As expected, due to the I = 7/2 nuclear spin of Co, the EPR spectrum shows Co hyperfine, see Figure 3.6. The EPR spectrum is fit as a Co(II) S_t = 1/2 species, with high A values and g strain as is evident from the relatively smooth nature of this Co(II) spectrum. The g$_z$ value is found to be g$_z$ = 2.95 while g$_x$ and g$_y$ are near g = 2. The exact fitting parameters used are given in the caption of Figure 3.6.
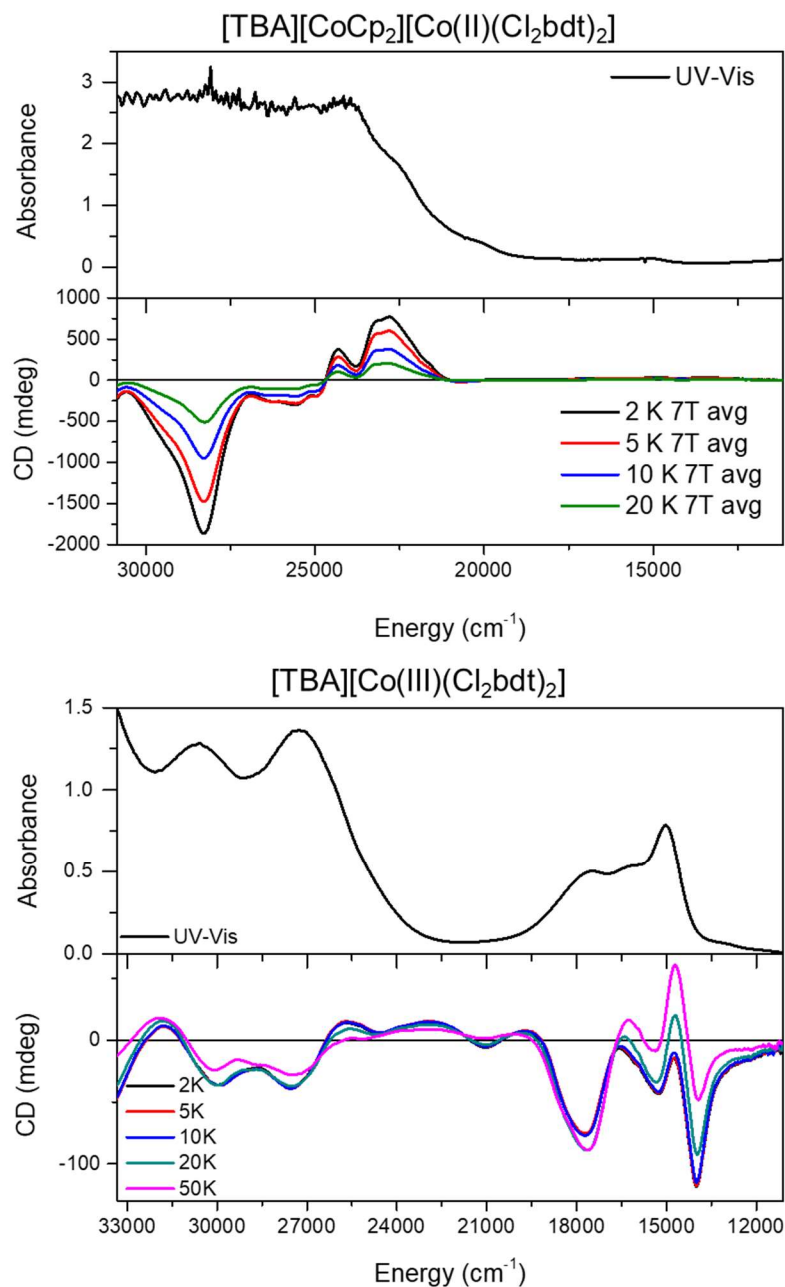
Figure 3.7. Comparison of the MCD standard run data of $[Co(II)(Cl_2bdt)_2]^{2-}$ compared to its UV-Vis absorption spectrum (top) and the MCD standard run data of $[Co(III)(Cl_2bdt)_2]^{-}$ compared to its UV-Vis absorption spectrum (bottom). Co(II) MCD samples were prepared in butyronitrile at 0.5 mM, and a standard run was conducted, at +7, +5, +3, +1, 0, -1, -3, -5, -7 T and 2, 5, 10, and 20 K, shown here are the 7T data for each temperature. The UV-Vis spectrum shown is of $[TBA][CoCp_2][Co(II)(Cl_2bdt)_2]$ at 0.5 mM in butyronitrile and is the same sample as the MCD data. The Co(III) data were measured on a polystyrene film sample, similarly a standard run was conducted, with 50 K data also included, shown here are the 7T data for each temperature. Here, the UV-Vis spectrum is of $[TBA][Co(III)(Cl_2bdt)_2]$, 0.1 mM in acetonitrile. Data for the Co(III) complex were also obtained in butyronitrile at 0.5 mM (not shown). For each, only data with voltage below 750 V are shown.

Further, the Co(III) and Co(II) complexes were studied by magnetic circular dichroism (MCD) spectroscopy. Both species show temperature-sensitive C-term signals, as expected for paramagnetic complexes, as shown in Figure 3.7. Interestingly, the Co(III) species only shows mild temperature dependence until higher temperatures are reached, see the decrease in intensity at 20 and 50 K. This indicates strong axial zero field splitting for the complex, with a negative D value. The shape of the bands for the $[Co(III)(Cl_2bdt)_2]^{2-}$ species align well with previously reported MCD data of the complex $[TBA][Co(III)(tb-bdt)_2]$, see the cited ref.[62] This supports similar electronic structures for the two species, and similar assignments of the optical spectra, featuring several strong LMCT excitations in the visible region, and a few weaker, forbidden d-d transitions.[62] Due to this similarity and the fact that the Co(III) complexes are well studied,[60] the electronic structure of this oxidation state was not further explored.
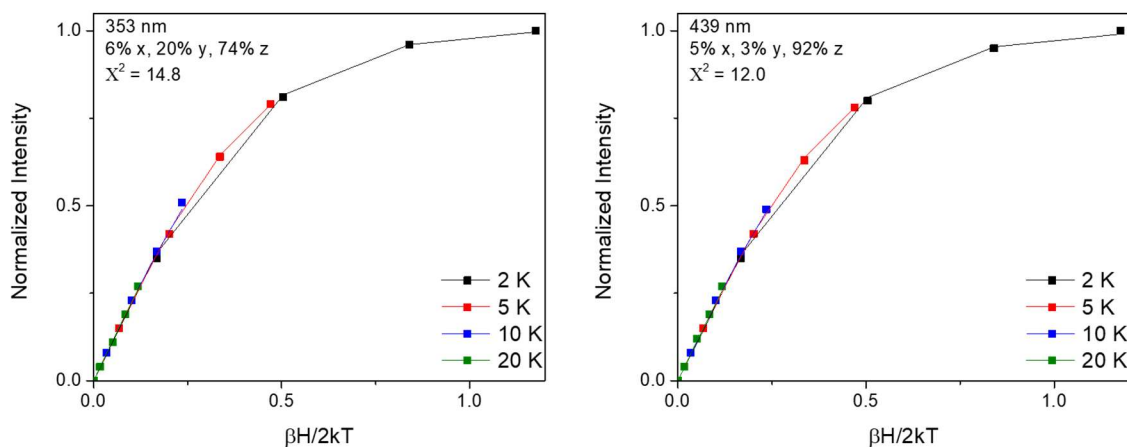
Figure 3.8. Saturation behavior of the two main bands of $[Co(II)(Cl_2bdt)_2]^{2-}$. Left, the saturation behavior of the positive band at 439 nm, or 22779 cm^{-1}. Right, the saturation behavior of the negative band at 353 nm, or 28328 cm^{-1}. Fits of standard run MCD data are shown with color coordinated lines, fit with $S_t = 1/2$ and resulting in the polarizations shown in the panels. Note, standard runs have less data points than full VTVH runs. The lack of nesting of the saturation curves together with the excellent agreement of the fits provides strong evidence that the complex has an $S_t = 1/2$ ground state, as further supported by the EPR data.

The MCD spectra of the Co(II) complex match well with the UV-Vis data of this species, showing features at high energy, but much less intensity in the visible region. The spectra are highly temperature dependent, similarly showing C-term behavior consistent with a paramagnetic complex. The saturation curves of this species were determined for the two most intense bands, at 439 nm (22779 cm^{-1}) and 353 nm (28328 cm^{-1}), as shown in Figure 3.8. These saturation curves

overlay neatly, which is consistent with an $S_t = 1/2$ species, as further suggested by the square-planar geometry and indicated by the EPR fit. These saturation curves can indeed be fit as a $S_t = 1/2$ species, using the g values obtained from the EPR fit.

3.3.1 Reaction of the Co(II) Complex with Protons

According to the proposed mechanism, one equivalent of protons should react with the Co(II) complex to give the singly protonated Co(II) intermediate, with the proton adding to a sulfur of the benzenedithiolate ligand (S_{bdt}). For these studies, the chemical reductant cobaltocene was found to be non-innocent. If the chemical reductant cobaltocene is used, 2 equivalents of protons are needed to return to the starting Co(III) complex quantitatively. This is illustrated by UV-Vis and EPR spectroscopy. First, UV-Vis shows that one equivalent leads to half the expected intensity of the $[Co^{III}(Cl_2bdt)_2]^-$ band, see Figure 3.9. The shoulder at 445 nm due to the $[Co(II)(Cl_2bdt)_2]^{2-}$ is still partially present in the red spectrum in Figure 3.9, suggesting that after 1 equivalent of acid the solution contains 0.5 equivalent $[Co(II)(Cl_2bdt)_2]^{2-}$ and 0.5 equivalent $[Co^{III}(Cl_2bdt)_2]^-$. This is further evident from EPR, as addition of 1 equivalent acid to $[Co(II)(Cl_2bdt)_2]^{2-}$, the $[Co(II)(Cl_2bdt)_2]^{2-}$ is still present, but in reduced intensity, see Figure 3.10.
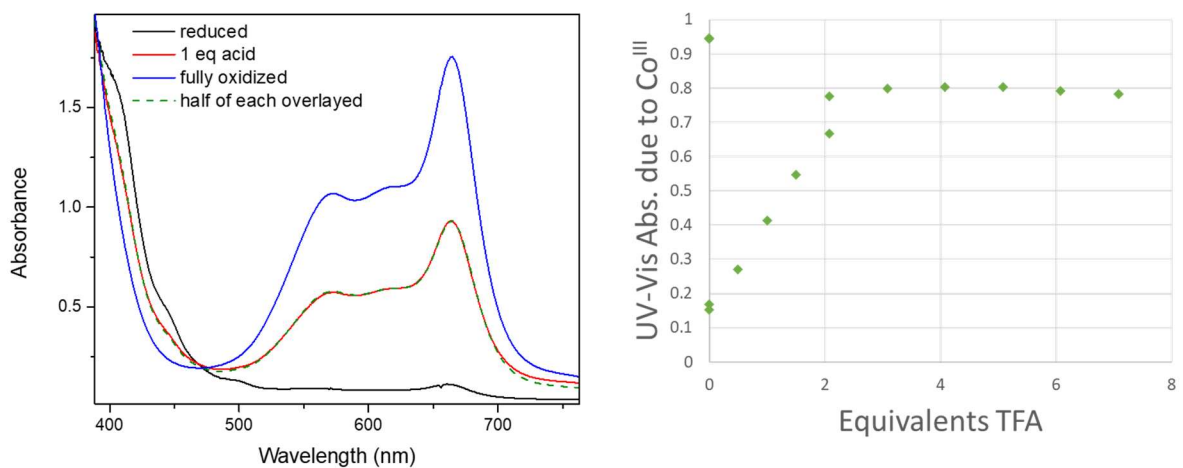
Figure 3.9. UV-Vis data show 2 equivalents of acid are necessary to fully return $[Co^{III}(Cl_2bdt)_2]^-$ when $CoCp_2$ is used as a reductant. Left, UV-Vis spectra of 0.2 mM $[Co(II)(Cl_2bdt)_2]^{2-}$, 0.2 mM $[Co(II)(Cl_2bdt)_2]^{2-}$ with 1 equivalent of TFA added, and then the same fully oxidized by air exposure. These spectra were acquired in THF. The dashed green line shows an overlay of the average of the $[Co(II)(Cl_2bdt)_2]^{2-}$ and the $[Co(II)(Cl_2bdt)_2]^-$ spectra. Right, data from a separate experiment where TFA was titrated to a solution of 0.1 mM $[Co(II)(Cl_2bdt)_2]^{2-}$ in dichloromethane and the $[Co(II)(Cl_2bdt)_2]^-$ fully reappeared after 2 equivalents of TFA. This

titration experiment was performed at room temperature using a dip probe UV-Vis set up in a nitrogen glovebox.
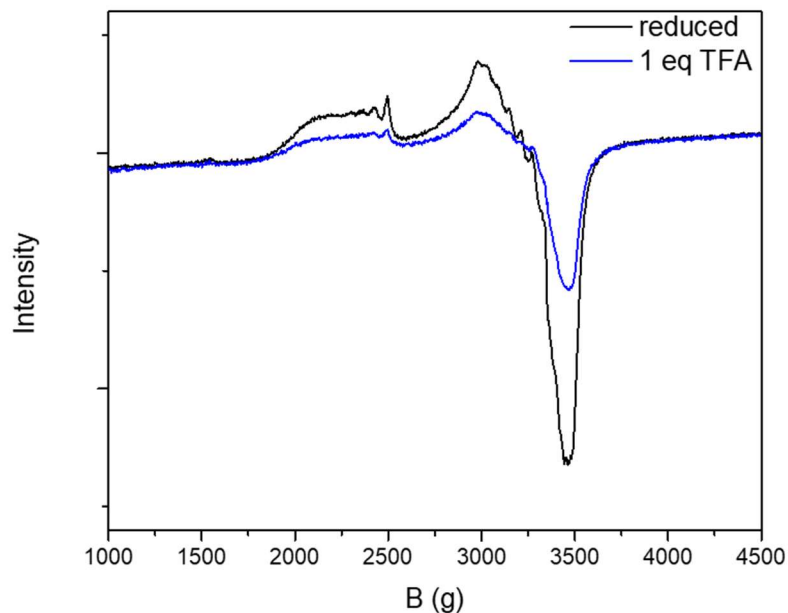
Figure 3.10. EPR spectrum of [TBA][CoCp$_2$][Co(II)(Cl$_2$bdt)$_2$], 1 mM in THF at 10 K compared to the EPR spectrum of the same sample with one equivalent TFA added.

      An additional complication of cobaltocene is that ligand exchange is sometimes observed. Sometimes, formation of a dark purple species is observed upon addition of protons to [TBA][CoCp$_2$][Co^{II}(Cl$_2$bdt)$_2$]. This is more likely if the reducing agent, cobaltocene, was at all oxidized so after addition of what should be one equivalent of cobaltocene, reduction of the [Co(Cl$_2$bdt)$_2$]$^-$ is incomplete. This purple species is characterized by a dark purple color, and a λ_{max} of 559 nm and is proposed to be Co(Cl$_2$bdt)(Cp). Co(Cl$_2$bdt)(Cp) was previously reported by Tsukada et al, who reported a λ_{max} of 555 nm in dichloromethane.[184] It is also similar to the diamagnetic complex Co(S$_2$C$_2$(CF$_3$)$_2$)(Cp) reported previously.[185]

      Due to the two issues discussed above with using cobaltocene as a chemical reductant, we switched to electrochemical reduction of [Co(III)(Cl$_2$bdt)$_2$]$^-$ to prepare [Co(II)(Cl$_2$bdt)$_2$]$^{2-}$. This approach is expected to form high concentration solutions of [Co(II)(Cl$_2$bdt)$_2$]$^{2-}$, as the complex's Co(III/II) couple is well behaved, and this method has been used previously to prepare reduced Co(bdt)$_2$ type species.[154,182] Indeed, the Co(III) complex cleanly converted to Co(II) upon applying a reducing potential in 0.1 M [TBA](PF$_6$) in acetonitrile under Ar, as shown in Figure 3.11. This

formation of the Co(II) complex was confirmed by UV-Vis spectroscopy, see Figure 3.12. The resulting, reduced complex is the same as the one obtained by chemical reduction with cobaltocene. The excess [TBA](PF$_6$) salt is not expected to affect the reaction, especially as it is present in electrocatalytic homogenous HER.
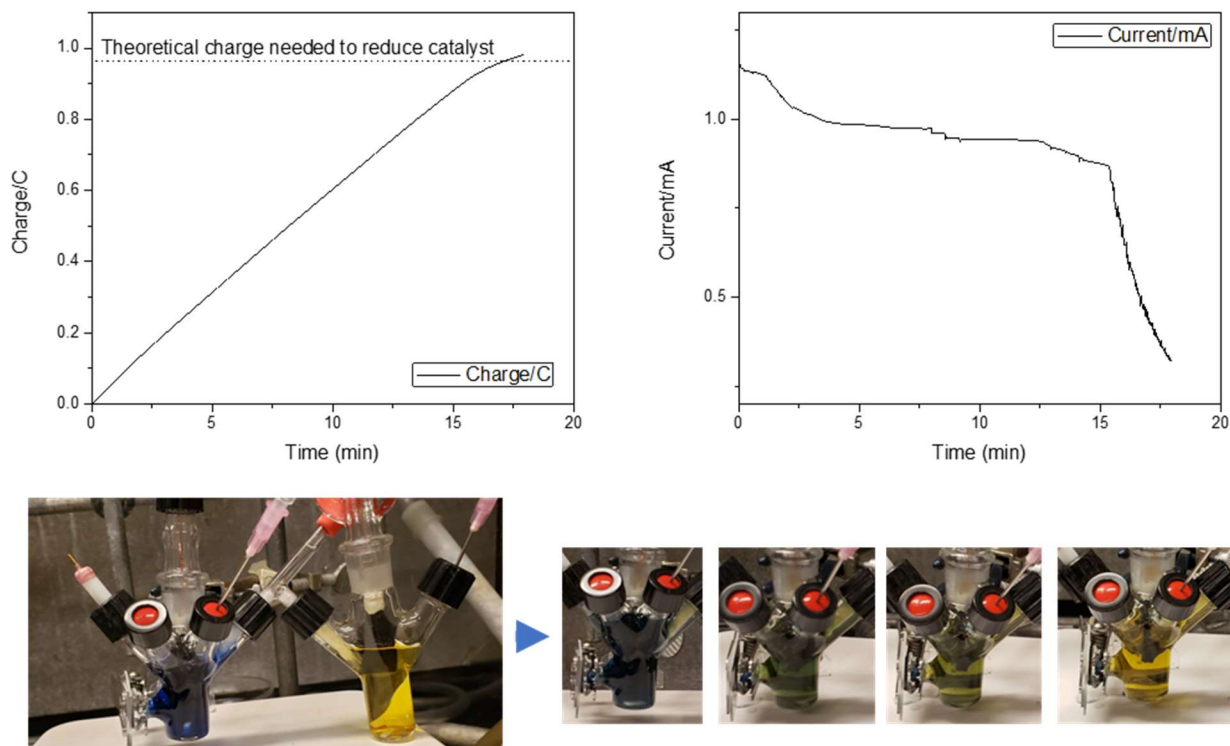
Figure 3.11. Electrochemical reduction of [TBA][Co(III)(Cl$_2$bdt)$_2$] to [TBA]$_2$[Co(II)(Cl$_2$bdt)$_2$]. Here, the experimental conditions are 1 mM [TBA][Co(III)(Cl$_2$bdt)$_2$], 0.1 M [TBA](PF$_6$), MeCN, under Ar on the Schlenk line (working electrode/reference electrode half-cell), 10 mM Fc (counter electrode half-cell), glass wool salt bridge, Ag wire pseudo-reference electrode, graphitic carbon felt for the working and counter electrodes.
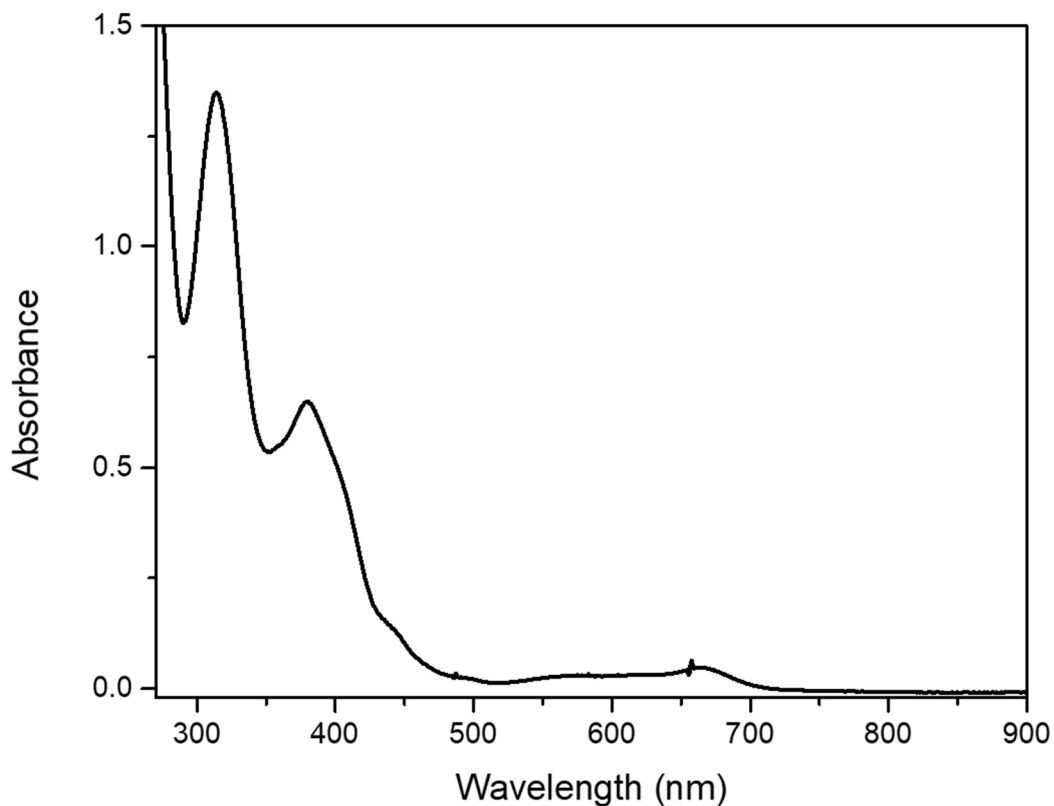
Figure 3.12. UV-Vis spectrum of electrochemically reduced [TBA]$_2$[Co(II)(Cl$_2$bdt)$_2$], 0.1 mM in MeCN.

With a more reliable Co(II) preparation in hand, the reactivity of the reduced complex with protons was again tested. Upon adding one equivalent of protons to the chemically reduced Co(II) complex, we observe quantitative return to the Co(III) starting complex. This was confirmed by multiple UV-Vis trials using varying solvents and temperatures: when stoichiometric trifluoroacetic acid (TFA) was added to the reduced Co(II) complex under anerobic conditions, the Co(III) species was regenerated. An example UV-Vis titration is seen in Figure 3.13. As the Co(II) species is highly air sensitive, minor reoxidation to the Co(III) form is sometimes observed. In these cases, the equivalents of TFA are calculated with respect to the starting amount of Co(II) complex for each trial. The reaction with acid occurs faster than the mixing time scale, and any change in concentration per TFA addition is attributed to mixing of the solutions in the cuvette, not reaction time.
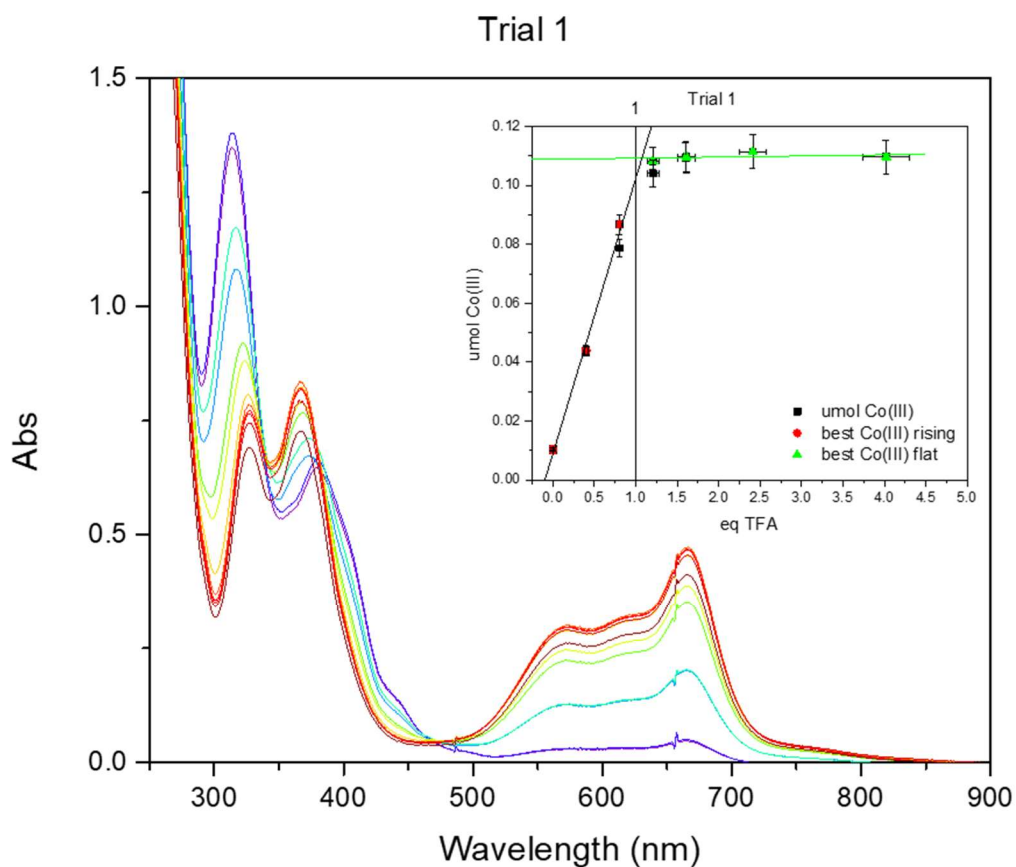
Figure 3.13. UV-Vis monitored titration of the Co(II) complex with acid. The UV-Vis spectrum of the starting solution of the Co(II) complex is shown in purple at 0.1 mM concentration, with additions of 0.1 mL 0.75 mM TFA in acetonitrile. The inset graph shows the absorption at 667 nm, which is attributed to the Co(III) form, with respect to the additions of equivalents of TFA. This UV-Vis titration was performed at RT under Ar.

The inset table within the figure reads:

Equation	y = a + b*x		
Weight	No Weighting		
Residual Sum of Squares	0.04123		
Pearson's r	0.9951		
Adj. R-Square	0.98992		
		Value	Standard Error
all rising	Intercept	0.00276	0.00763
	Slope	1.03481	0.0179
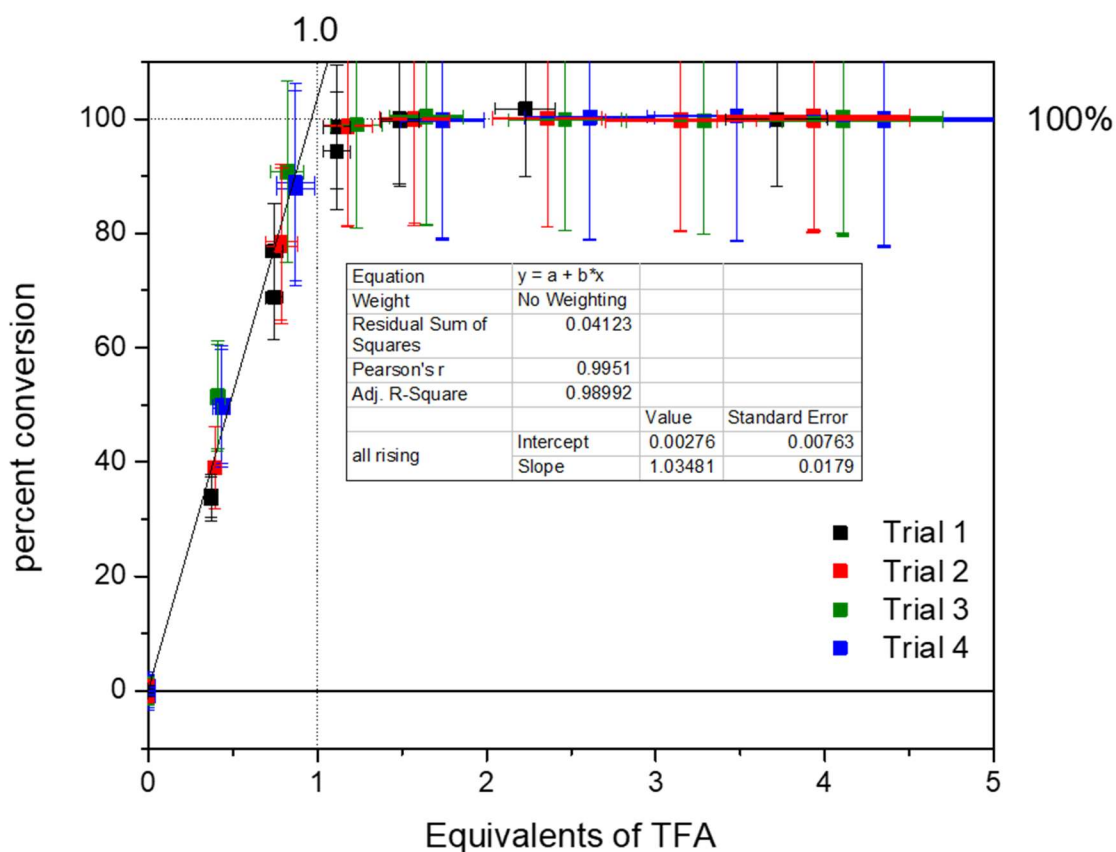
Figure 3.14. Combination of four UV-Vis monitored titration trials of the Co(II) complex with TFA, showing the percent conversion of Co(II) to Co(III) upon addition of acid. Trial 1 is shown in Figure 3.13.

With four UV-Vis titration trials combined, one equivalent of TFA is required to regenerate all of the expected Co(III) complex, see Figure 3.14. While the stoichiometry is as expected, the direct return to the Co(III) complex was unexpected. The DFT-calculated literature mechanism, shown in Figure 3.2, suggests that double protonation followed by reduction is needed before H_2 may be evolved and Co(III) is regenerated, and in this calculated reaction mechanism, only one Co complex participates (unimolecular mechanism with respect to the complex). Here, we observe a reaction where Co(III) is regenerated from only one equivalent of protons. One might propose two Co complexes are coming together to perform HER. If this is the case, there are two possibilities, illustrated in Figure 3.15. First, illustrated in red, is that half of the Co(II) complex could be protonated twice, giving [Co^{II}(H-bdt)$_2$], and then another (remaining) Co(II) complex could reduce this species to close the catalytic cycle without an additional reductive equivalent.

This is unlikely, as the second protonation corresponds to a pKa that is calculated to be ~4 units more acidic,[65] and in the presence of one equivalent of acid, the doubly protonated species is therefore not expected to form. The mechanism in blue could allow a short cut, where two molecules of $[Co(Cl_2bdt)(Cl_2bdt-H)]^-$ could react to produce 0.5 eq of H_2 per the initial concentration of catalyst. Such a bimolecular mechanism of H_2 production has been proposed before for cobaloxime HER catalysts[33,186] and is referred to as the homolytic hydrogen production. This could only be plausible for solution state HER, as reported by the Eisenberg group.[46,47] In contrast, when heterogenized, the catalyst molecules are fixed in space on the electrode surface, unable to come together to homolytically make hydrogen. Therefore, a heterolytic mechanism must also be possible. However, first, is hydrogen being made in this reaction?
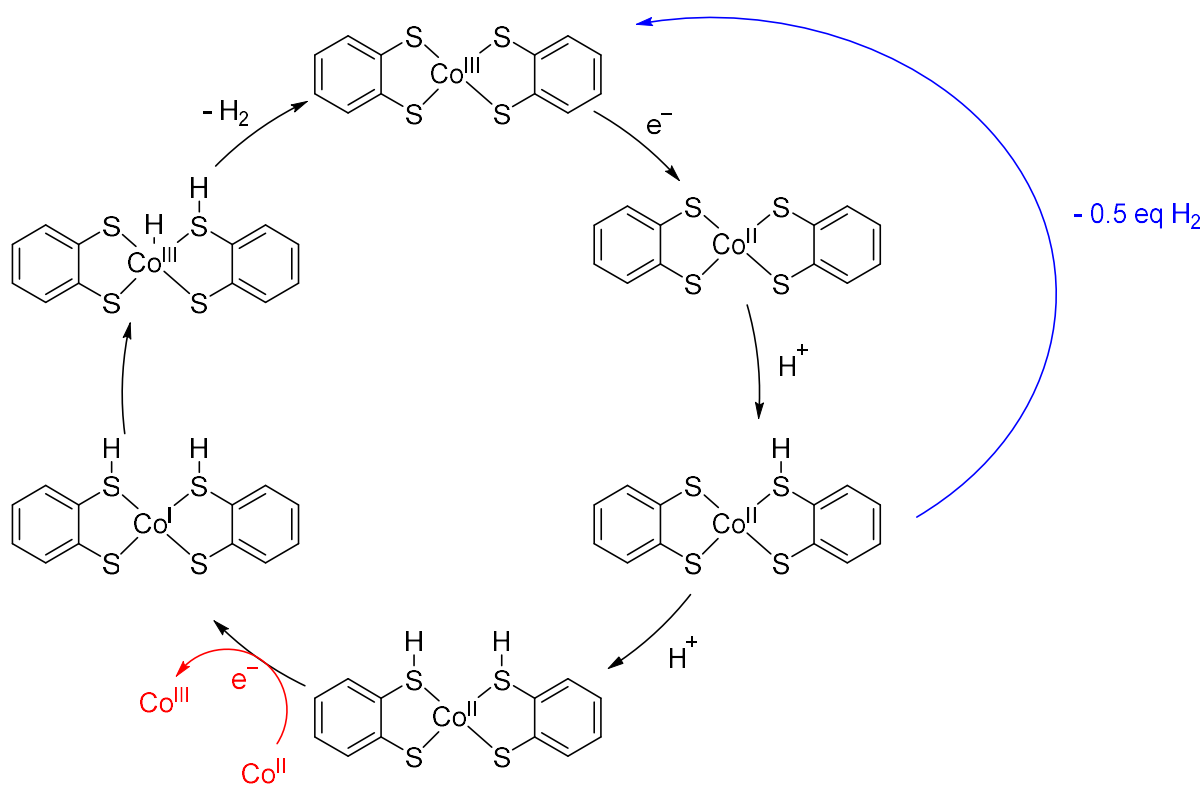
Figure 3.15. Two possible mechanisms to explain the homogenous HER data obtained here. Blue, coupling of two Co(H-S_bdt) protonated species to give H_2 and Red, use of ½ equivalent of the Co(II) to reduce the doubly protonated species.

We measured the hydrogen in the gas headspace upon reacting the electrochemically-generated Co(II) complex with one equivalent of acid (TFA) in a closed vial. Gas chromatography studies showed less than 1 % of the expected hydrogen was produced. This suggests that a different reaction is occurring. Initially we suspected possible hydrogenation of the solvent, acetonitrile.

However, with the already hydrogenated tetrahydrofuran as the solvent, the same addition of one equivalent of acid to the electrochemically reduced Co(II) species also produced negligible hydrogen while returning the blue Co(III) complex. By UV-Vis spectroscopy, no intermediates which could give us an idea of what reaction was occurring were able to be observed at room temperature.

As no intermediates were observed at room temperature, we slowed the reaction down by cooling to low temperatures to see if we could observe the fleeting $[Co(Cl_2bdt)(Cl_2bdt-H)]^-$ species. We repeated the reaction at -40 °C in acetonitrile and at -75 °C in acetone, using a dip probe UV-Vis set up. Unfortunately, these experiments did not show any significant intermediates when TFA was added to a solution of the Co(II) complex. Instead, at -75 °C, with electrochemically reduced Co(II)(Cl_2bdt)_2 in acetone, the same reaction was observed, but slower, see Figure 3.16. Despite the slower reaction, this shows the return of the starting Co(III) complex even at low temperatures. This shows that the reaction occurring has fast kinetics which is consistent with the fast kinetics of electrocatalytic HER that we have observed for this catalyst family.
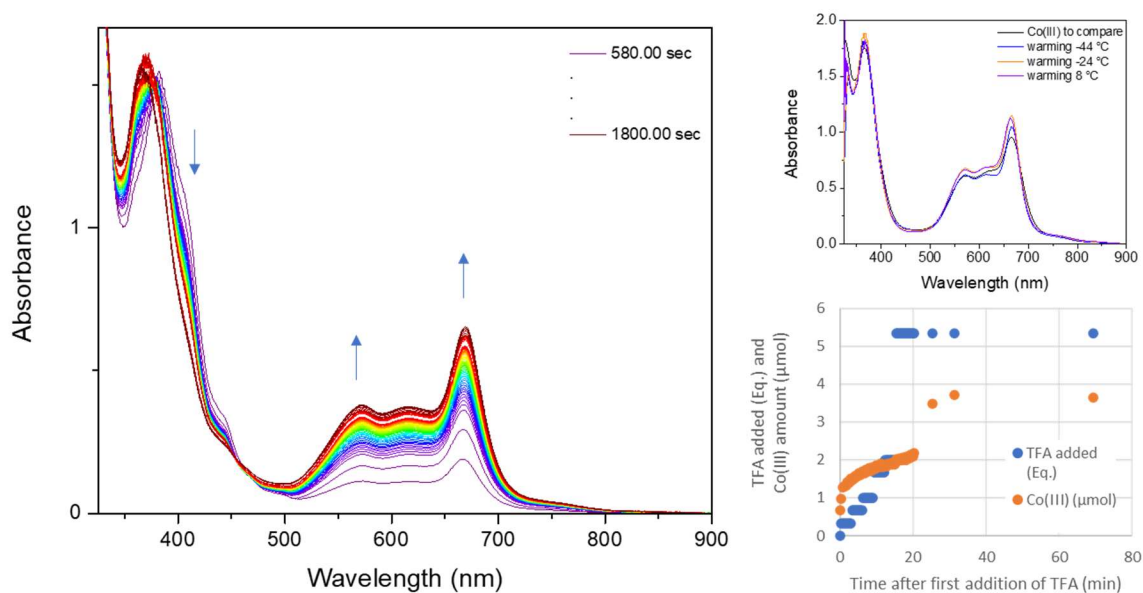
Figure 3.16. Reaction of 0.1 mM [TBA]$_2$[Co(II)(Cl$_2$bdt)$_2$] in acetone with 0.1 M [TBA](PF$_6$) at -75 °C with TFA, 0 through 5.3 equivalents. The left panel shows the changes observed in the UV-Vis spectra at -75 °C. The upper right panel shows the spectra upon warming, which matches well with [TBA][Co(III)(Cl$_2$bdt)$_2$], included for comparison. The lower right panel shows the increase of [TBA][Co(III)(Cl$_2$bdt)$_2$] with time after the first addition of TFA, the number of equivalents of TFA is also plotted.

3.4 Conclusions

In summary, the complex [TBA][Co(III)(Cl$_2$bdt)$_2$] has been reduced to the Co(II) form electrochemically and chemically. This oxygen sensitive species has been characterized by UV-Vis, X-ray crystallography, EPR, and MCD spectroscopy. From these characterization techniques, the Co(II) species has been shown to be square planar at Co, with a metal centered reduction, and an $S_t = 1/2$ ground state. This is in contrast to the DFT predicted, tetrahedral Co(II) geometry.[65] When treated with one equivalent of a proton source, the reaction is very quick and returns the starting Co(III) complex. This reactivity is unexpected, and while this could show that in homogenous solution, the complex is able to do homolytic HER, no hydrogen is produced in this reaction. The reaction that is occurring is still unknown, but has been shown to be consistent across solvents and temperatures. Additional work to isolate intermediate species was therefore unsuccessful.

3.5 Future work

Future work is recommended to include further studies to identify the non-cobalt products in the reaction of [TBA]$_2$[Co(II)(Cl$_2$bdt)$_2$] with one equivalent of acid. Further control reactions, GC-MS analysis of products, and NMR spectroscopy studies should be used to determine what other reaction is occurring.

Future work on this project should also include repeating low temperature studies, going to as low of a temperature as possible. A small portion of the catalyst, reduced in acetonitrile, is recommended to be added to dichloromethane near its freezing point, -96.7 °C. Although it has a similarly low freezing point and can be an acceptable electrolyte solvent, THF is not recommended, because this solvent often contains small amount of peroxides that may react with the [TBA][Co(Cl$_2$bdt)$_2$]. Careful testing and/or purification of THF is required to use this solvent.

Once conditions where protonation of [TBA]$_2$[Co(II)(Cl$_2$bdt)$_2$] occurs, or homogeneous HER is observed, are found, additional studies may be performed using a methyl donor rather than a proton donor to react with Co(II). This approach could be used to identify the location of protonation of the complex. It is expected that the reduced complex would methylate at S rather than at the Co center. Initial studies showed that [TBA][Co(Cl$_2$bdt)$_2$] is unreactive to MeI and [TBA]$_2$[Co(II)(Cl$_2$bdt)$_2$] in acetonitrile with 0.01 M TBAPF$_6$ shows some reactivity towards MeI, causing shifting of the bands resulting from intraligand π-π* transitions.
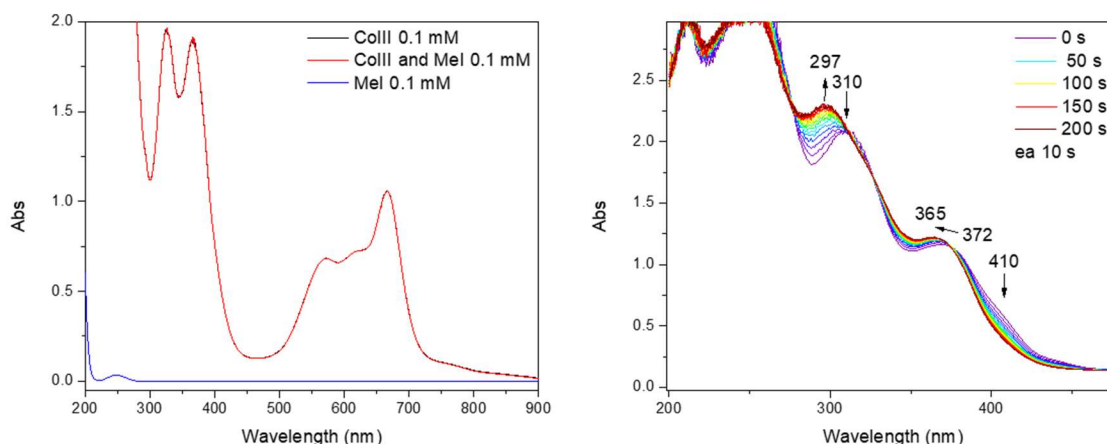
Figure 3.17. Comparison of the reactivity of [TBA][Co(Cl$_2$bdt)$_2$] and [TBA]$_2$[Co(II)(Cl$_2$bdt)$_2$] with MeI. The Co(III) species shows no reactivity, left, as the black and red spectra overlay. The Co(II) species shows formation of a new species with the marked shifts in bands, in 200 s, right.

3.6 Experimental Section

3.6.1 General Synthesis and Chemicals

The chemicals used herein were used as received except for cobaltocene which was sublimed before use for purification. To maintain an air free atmosphere required for these experiments, a nitrogen glovebox, or Schlenk line was employed. Specifically for handling of [Co(Cl$_2$bdt)$_2$]$^{2-}$, Schlenk line techniques with an Ar atmosphere were employed. [TBA][Co(Cl$_2$bdt)$_2$] was synthesized according to past methods.[61,97]

3.6.2 Reduction Procedures

To obtain [TBA][CoCp$_2$][Co(II)(Cl$_2$bdt)$_2$] via chemical reduction, one equivalent of CoCp$_2$ is added to a solution of [TBA][Co(Cl$_2$bdt)$_2$] in the desired solvent.

For electrochemical reduction, a solution of 0.5-3 mM [TBA][Co(Cl$_2$bdt)$_2$] in 0.1 M [TBA](PF$_6$) in acetonitrile or acetone is reduced at -0.2 V more negative than the Co(III/II) redox couple until the current drops and the change in color from blue to yellow is complete, see Figure 3.11 for a representative example. A two-part electrochemical cell with excess Fc as a sacrificial oxidant in the counter electrode half-cell is employed. The charge passed may be slightly more depending on the degree of anaerobicity obtained before reduction occurs. The reference was an

Ag wire pseudo-reference electrode; however, the data were not referenced to Fc^+/Fc after electrolysis to maintain purity of the Co(II) solution.

3.6.3 Instrumentation

NMR spectra were measured using a Varian NMR Systems 500 MHz spectrometer. ^{1}H-NMR spectra were referenced to residual solvent peaks. UV-Vis spectra were obtained on an Analytical Jena Specord S600 instrument. For low temperature experiments a Hellma low temperature immersion probe (dip probe) with a 10 mm path length was used. See Section 4.8.1 for description of the MCD set up. Here, temperatures of 2, 5, 10, 20, and for $[TBA][Co(Cl_2bdt)_2]$, 50 K in series were used for the MCD measurements, and spectra were obtained at +/-7, +/-5, +/-3, +/-1, and 0 T at each temperature. The EPR measurements were conducted on a Bruker X-band EMX spectrometer, which was equipped with an Oxford liquid helium cryostat. The EPR spectrum was fit using SpinCount (Prof. M. P. Hendrich at Carnegie Mellon University). The electrochemistry was conducted using a CH Instruments CHI600E potentiostat.

3.6.4 X-ray crystallography

The X-ray crystallography was performed by Dr. Jeff Kampf, the former crystallographer of the Chemistry department at the University of Michigan, who acquired the data and solved the structure. He provided the following report:

Green plates of $(CoCp_2)_2[Co(II)(bdt)_2]$ were grown from a butyronitrile solution of the compound at -20 deg. C. A crystal of dimensions 0.10 x 0.08 x 0.04 mm was mounted on a Rigaku AFC10K Saturn 944+ CCD-based X-ray diffractometer equipped with a low temperature device and a Micromax-007HF Cu-target micro-focus rotating anode (λ = 1.54187 Å) operated at 1.2 kW power (40 kV, 30 mA). The X-ray intensities were measured at 85(1) K with the detector placed at a distance of 42.00 mm from the crystal. A total of 2028 images were collected with an oscillation width of 1.0° in ω. The exposure times were 1 sec. for the low angle images, 5 sec. for high angle. Rigaku d*trek images were exported to CrysAlisPro for processing and corrected for absorption. The integration of the data yielded a total of 55,226 reflections to a maximum 2θ value of 138.85° of which 12,797 were independent and 11,576 were greater than $2\sigma(I)$. The final cell constants (Table 3.2) were based on the xyz centroids of 15,456 reflections above $10\sigma(I)$. Analysis of the data showed negligible decay during data collection. The structure was solved and refined

with the Bruker SHELXTL (version 2018/3) software package, using the space group P2(1) with Z = 4 for the formula $C_{36}H_{31}NCl_4S_2Co_3$. All non-hydrogen atoms were refined anisotropically with the hydrogen atoms placed in idealized positions. Full matrix least-squares refinement based on F^2 converged at R1 = 0.0642 and wR2 = 0.1634 [based on I > 2sigma(I)], R1 = 0.0708 and wR2 = 0.1712 for all data. Additional details are presented in Table 1 and the CIF file is deposited at CCDC, CCDC number: 2309250.

Table 3.2. Crystal data and structure refinement for $(CoCp_2)_2[Co(II)(bdt)_2]$. One equivalent of butyronitrile is also present but omitted from Figure 3.5 for clarity.

Parameter	Value(s)	
Empirical formula	$C_{36}H_{31}Cl_4Co_3NS_4$	
Formula weight	924.45	
Temperature	85(2) K	
Wavelength	1.54184 Å	
Crystal system, space group	Monoclinic, P2(1)	
Unit cell dimensions	a = 14.3219(2) Å	alpha = 90°
	b = 14.0160(2) Å	beta = 99.4507(17)°
	c = 18.4173(3) Å	gamma = 90°
Volume	3646.82(11) Å^3	
Z, Calculated density	4, 1.684 Mg/m^3	
Absorption coefficient	15.627 mm^{-1}	
F(000)	1868	
Crystal size	0.100 x 0.080 x 0.040 mm	
Theta range for data collection	2.432 to 69.427°	
Limiting indices	-17<=h<=17, -16<=k<=17, -22<=l<=22	
Reflections collected / unique	55226 / 12797 [R(int) = 0.0759]	
Completeness to theta = 67.684	99.8 %	
Absorption correction	Semi-empirical from equivalents	
Max. and min. transmission	1.00000 and 0.64347	

Refinement method	Full-matrix least-squares on F^2
Data / restraints / parameters	12797 / 119 / 924
Goodness-of-fit on F^2	1.069
Final R indices [I>2sigma(I)]	R1 = 0.0642, wR2 = 0.1634
R indices (all data)	R1 = 0.0708, wR2 = 0.1712
Absolute structure parameter	0.139(6)
Extinction coefficient	n/a
Largest diff. peak and hole	0.736 and -0.794 e.A^-3

Chapter 4 Elucidating the Structure of a Reactive Formally Ni^{IV}-Oxo Species with Spectroscopy and Density Functional Theory Calculations

In this chapter, a formal Ni^{IV}-O species is shown to be an S_t = 1 Ni^{III}-oxyl complex by spectroscopic and DFT studies. This research was performed in collaboration Prof. Wonwoo Nam's group at Ewha Womans University in Seoul, Korea, who synthesized the complex, performed the initial characterization, and studied its reactivity, and Prof. Jason Shearer's group at Trinity University in Texas, USA, who performed and analyzed the X-ray absorption studies. Adapted from Karmalkar, Deepika[‡]; **Larson, Virginia**[‡]; Malik, Deesha; Lee, Yong-Min; Seo, Mi Sook; Kim, Jin; Vasiliauskas, Dovydas; Shearer, Jason*; Lehnert, Nicolai*; Nam, Wonwoo*; "Preparation and Characterization of a Formally Ni^{IV}–Oxo Complex with a Triplet Ground State and Application in Oxidation Reactions". *J. Am. Chem. Soc.* **2022**, 144, *49*, 22698−22712.[150] The double dagger indicates Deepika Karmalkar and Virginia Larson are co-first authors on this manuscript. The introduction section is also partially adapted from the cited ref.[1]

4.1 Introduction

High-valent first-row transition metal-oxo species are active intermediates in oxidation reactions that are important in water splitting for the generation of renewable energy, in biology, and in oxidative chemical transformations.[1,148] Renewable energy related reactions which often involve metal-oxo intermediates include the oxidative side of water splitting, referred to as the oxygen evolution reaction (OER), and the reduction of O_2 to water in fuel cells.[104,110,119,187,188] A notable example of the latter is Nocera's artificial leaf, which catalyzes the OER via a high-valent Co-oxo intermediate.[189] Additionally, though more recently developed, there are several molecular Ni OER catalysts that likely also operate through high-valent Ni–O intermeditates.[119] Fe- and Mn-oxo species are active intermediates in enzymes like Cytochrome P450s, methane monooxygenase, mononuclear non-heme iron enzymes, and photosystem II, to name a few examples.[120,190] While Fe, Mn, and Cu are the favored metals for biology – high-valent Cu intermediates have been proposed for some enzymes but are less studied[191–193] – outside of bioinorganic chemistry, similar

species with other transition metals have been used in chemical oxidation reactions, i.e. oxygen atom transfer (OAT) and C-H activation.[106,108,115,116,194,195]

4.1.1 The 'Oxo Wall'
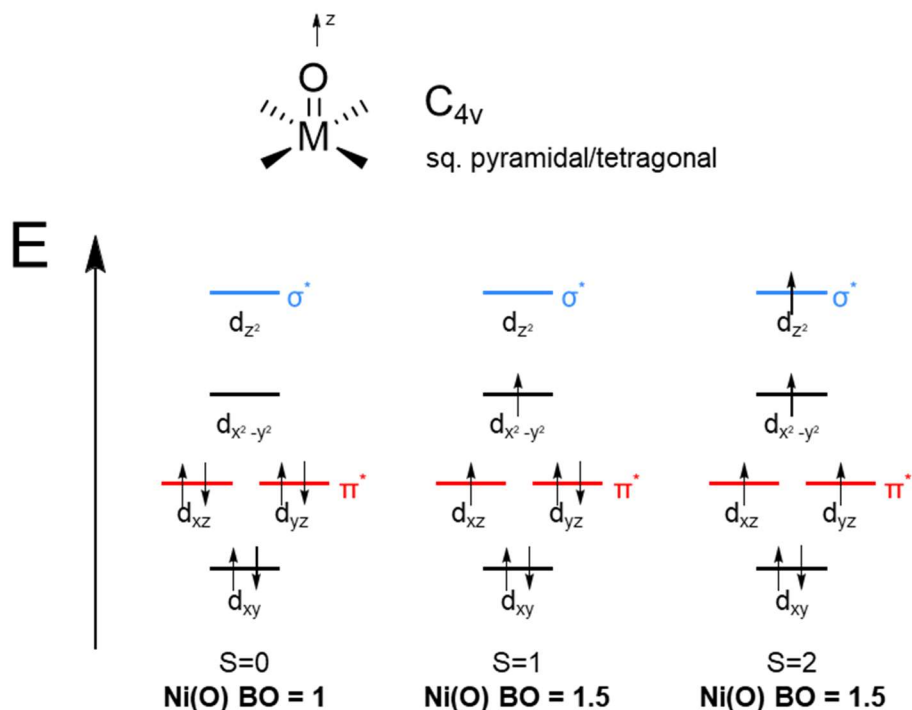
Figure 4.1. Scheme of electronic structure of Ni-oxo complexes in different spin states and the resulting formal Ni–O bond order, illustrating the instability of metal-oxo species past the 'oxo wall'.

Well studied, mononuclear, terminal Ni-oxo complexes are much more rare than their lower atomic number counterparts.[1,196] This is related to the concept of the 'oxo wall',[105,139,197] which is explained in more detail in the Introduction Section 1.3.3 and a number of review articles.[1,139] Nickel is past this 'oxo wall', having two additional metal(d) electrons compared with iron. This makes corresponding Ni^{IV}–O complexes extremely unstable and reactive. A Ni^{IV}=O complex in the low-spin ($S_t = 0$) state has a formal bond order of 1, which would not qualify as a metal=O unit. In addition, a metal-oxyl species may be expected, where bond inversion (valence tautomerization) gives rise to a radical on the oxo ligand. However, with intermediate ($S_t = 1$) or high-spin ($S_t = 2$) ground states, it is theoretically possible to have a formal Ni–O bond order of up to 1.5. This spin-state dependent Ni^{IV}–O bond order is illustrated in Figure 4.1.

4.1.2 Previously Studied Ni-O Complexes

99
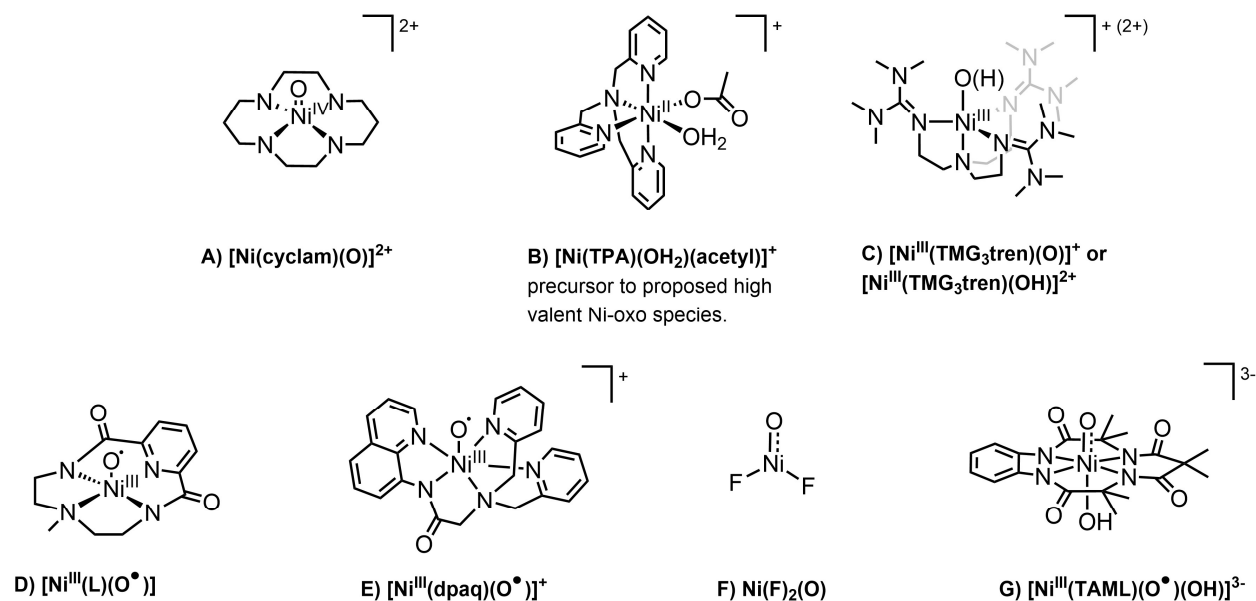
Figure 4.2. Previously reported Ni–O complexes (A – F) and [Ni(TAML)(O)(OH)]$^{3-}$ (G) presented in this chapter. H$_2$L = 6-methyl-3,6,9-triaza-1(2,6)-pyridinacyclodecaphane-2,10-dione.

In line with this predicted instability, high-valent Ni–O species are rare in the literature. Some reports propose these types of species as intermediates for reactions like olefin epoxidation,[198,199] alkane hydroxylation,[200] and for gas phase methane oxidation to methanol (Figure 4.2A, B).[201,202] In 1987, it was known that [Ni(cyclam)]$^{2+}$ and similar complexes could perform olefin epoxidation when activated by PhIO to give a putative Ni^{IV}–O intermediate (Figure 4.2A) as the active species.[198] A further exploration of this reaction indicated that the intermediate had significant Ni^{III}–O$^{\bullet-}$ character.[199] In 2006, a Ni–O complex was suggested as the active species in alkane hydroxylation when activated by meta-chloroperbenzoic acid (m-CPBA), with the precursor [Ni(OH$_2$)(OAc)(TPA)]$^+$ (TPA= tris(2-pyridylmethyl)amine) being shown in Figure 4.2B.[200,203] Additionally, experimental[201,204,205] and theoretical studies[202,205] have suggested that [Ni^{III}–O]$^+$ species may be potent oxidants for the challenging conversion of CH$_4$ into MeOH in the gas phase. However, no direct spectroscopic evidence for a high-valent Ni–oxo species has been reported until very recently, leaving the assignment ambiguous. Even in the above cases, the involvement of a high-valent Ni–O species is debated.[206,207] For example, isotopic labeling and selectivity studies suggest that a m-chlorobenzoyloxy radical is the active species in C-H activation when m-CPBA is reacted with nickel complexes featuring a variety of nitrogen-based co-ligands and appropriate substrates for C-H activation.[206] Nevertheless, high-valent Ni–O species have

great potential as catalysts, and there is great interest in the field in isolating and understanding these reactive intermediates.[1,208]

To date, only a few high valent Ni-O species have been proposed and/or successfully synthesized and characterized, as shown in Figure 4.2. General strategies to obtain these species mirror those used for other types of metal-oxo complexes. This includes, in particular, the reaction of Ni^{II} precursors with O-atom transfer reagents like *m*-CPBA, as first reported in 2012 by Ray and co-workers.[209] Here, reaction of a Ni^{II} precursor, $[Ni^{II}(TMG_3tren)(OTf)]^+$, with *m*-CPBA was thought to yield a trigonal bipyramidal (TBP) terminal Ni^{III}–O or Ni^{III}–OH complex (Figure 4.2C). The reactive species was prepared by oxidizing a Ni^{II} precursor with m-CPBA and analyzed with electron paramagnetic resonance (EPR) spectroscopy, revealing a total yield of only 15% of Ni^{III} species in solution. Of this 15%, two $S_t = 1/2$ species are present in an 85:15 ratio, both being metastable with half-lives of 1 hr at −30 °C. The time course of the corresponding EPR and UV– vis signals of these two intermediates matches, suggesting that they form and decay in similar ways or are somehow related. These intermediates undergo hydrogen atom transfer (HAT) from 9,10-dihydroanthracene with a kinetic isotope effect of 3.9, similar to that seen for alkane hydroxylation catalyzed by $[Ni(OH_2)(OAc)(TPA)]^+$.[200] The mass spectra did not feature ions for Ni–O species but included ions of reasonable degradation products.

In 2015, Company and co-workers reported a $[Ni^{III}(L)(O^•)]$ complex, which was described as a Ni^{III}-oxyl species (Figure 4.2D, H_2L = 6-methyl-3,6,9-triaza-1(2,6)-pyridinacyclodecaphane- 2,10-dione).[210] This species, which features a tetradentate ligand, has a half-life of 4.5h at −30 °C and can be generated by treating the Ni^{II} precursor with m-CPBA (Figure 4.2D).[210] This intermediate appeared to have UV–vis absorption bands at 420 and 580 nm and two rhombic EPR signals consistent with an $S_t = 1/2$ species forming in 16% yield. However, the formation rates for the Ni^{III} species observed by EPR and the species observed by UV–vis spectroscopy are not the same. Instead, density functional theory (DFT) studies suggest that the Ni^{III}–$O^{•−}$ species is EPR- silent, such that the species observed by EPR is, rather, a decay product. X-ray absorption near- edge structure (XANES) spectra suggest that a Ni^{III} complex forms, and extended X-ray absorption fine structure (EXAFS) shows two long Ni–N/O distances (2.12Å) corresponding to the Ni–O and Ni–N(amine) of L^{2-} and three short Ni–N/O distances (1.88Å) corresponding to the Ni– N(pyridine) and Ni–N(amidate) of L^{2-}, which are consistent with a weakly bound oxo or oxyl ligand. The rRaman spectrum features bands at 450 and 477 cm^{-1} that were assigned to Ni–O

species, but this has yet to be confirmed by isotopic labelling. The species [(L)Ni^{III}(O)] reacts with thioanisole, activates weak C–H bonds and converts olefins into epoxides.

A mix of Ni^{IV}(O) and Ni^{III}(O) species was reported by Kim and co-workers in 2016 as intermediates in the catalytic epoxidation of olefins by [Ni^{II}(dpaq)Cl] treated with the oxidant *m*-CPBA (Figure 4.2E).[211] The proposed product [Ni^{III}(O)(dpaq)]$^+$, featuring a N$_5$-donor ligand, is active for catalytic epoxidation of olefins at room temperature (Figure 4.2E).[211] Here, reactivity studies with peroxyphenylacetic acid afforded decay products of the acid characteristic of O–O bond homolysis or heterolysis, suggesting the initial presence of Ni^{IV}–O (74%) and Ni^{III}–O (26%). The EPR and mass spectra are consistent with a Ni^{III} center and a formally Ni^{IV}–O complex, respectively.

Since our 2020 review, there have been a few proposed Ni(O) intermediates,[212–215] but these lack in depth spectroscopic characterization. Recently, O–NiF$_2$ has been prepared in a solid neon matrix by Riedel and co-workers. Here, a $^{16/18}$O-sensitive band was observed in IR spectroscopy at 640 cm^{-1} and assigned to the Ni-F$_2$ symmetric stretch with some influence of the adjacent O. This species was further concluded, based on CASSCF/CASTP2/VTZ-DK calculations, to have a strong degree of oxyl character in the ground state (Figure 4.2F).[216] Despite the interest in mononuclear, terminal Ni–O species and aforementioned in-depth studies of these reactive and unstable intermediates, there is still no direct spectroscopic evidence for a Ni–O bond other than in O–NiF$_2$.

4.1.3 Scope of this Chapter

In this chapter, the synthesis, spectroscopic characterization, and reactivity of a formally Ni^{IV}(O)(TAML) (TAML^{4-} = tetraamido macrocyclic ligand) complex, which has a near tetragonal ligand field symmetry is discussed. UV-Vis by the Nam group, X-ray absorption spectroscopy (XAS) and EXAFS studies by the Shearer group, and magnetic circular dichroism (MCD) spectroscopic by myself show that this species corresponds to a six-coordinate formally Ni^{IV}-O complex with an axially-coordinated hydroxide ligand and an $S_t = 1$ ground state. I further analyze the electronic structure of this complex, using experimentally calibrated DFT calculations, which show a distinct amount of bond inversion for one of the Ni–O π-bonds, giving this complex dominant Ni^{III}-oxyl character. The proposed structure of this species is shown in Figure 4.2G. In agreement with the spectroscopic studies, reactivity studies by the Nam group show that

[Ni(TAML)(O)(OH)]$^{3-}$ is a particularly active catalyst for the OAT reaction and that this species can activate moderately strong C-H bonds.

4.2 Synthesis and Characterization of Complexes 1 – 3 (Nam Group)

4.2.1 Synthesis of [Ni^{II}(TAML)]$^{2-}$ (1) and [Ni^{III}(TAML)]$^-$ (2)

The synthesis and characterization of the Ni^{II} and Ni^{III} complexes was conducted by our collaborators in the Nam group, with primary effort by Deepika Karmalkar. The Ni^{II} complex [Ni^{II}(TAML)]$^{2-}$ (**1**) (TAML^{4-} = tetraamido marcrocyclic ligand, 3,4,8,9-tetrahydro-3,3,6,6,9-hexamethyl-1H-1,4,8,11-benzotetraazocyclotridecane-2,5,7,10-(6H,11H)-tetrone) was characterized by UV-Vis, cold-spray ionization mass spectrometry (CSI-MS), X-band EPR, Evans method, and X-ray crystallography.[150] Of note, this species is a diamagnetic complex with $S_t = 0$ spin state.

The Ni^{III} complex [Ni^{III}(TAML)]$^-$ (**2**) was generated by reacting **1** with a one-electron oxidant such as cerium(IV) ammonium nitrate (CAN). **2** was characterized UV-Vis, CSI-MS, X-band EPR, by Evans method, and X-ray crystallography.[150] EPR and Evan's method agree; **2** is a paramagnetic complex with $S_t = 1/2$ spin state.

4.2.2 Synthesis and Initial Characterization of [Ni(TAML)(O)(OH)]$^{3-}$ (3)

The synthesis and initial characterization of the title formal Ni^{IV}-oxo complex was performed by our collaborators in the Nam group, with primary effort by Deepika Karmalkar. The formally Ni^{IV}-oxo-hydroxo complex [Ni(TAML)(O)(OH)]$^{3-}$ (**3**) was generated by reacting **1** with 2 equivalents of CAN (or by reacting **2** with 1 equivalent of CAN) in the presence of H$_2$O (5.0 µL) in MeCN at -40 $^\circ$C. When **1** was reacted with 2 equivalents of CAN, a distinct color change was observed from yellow (starting) to bright blue within few seconds. **3** shows a prominent electronic absorption band at 728 nm ($\varepsilon = 4000$ M^{-1} cm^{-1}) in MeCN (Figure 4.3a). A titration experiment showed that 1 equivalent of CAN is required for the full conversion of **2** to **3** (Figure 4.3a, inset). Alternatively, **3** can also be generated by reacting **1** with 1.5 equivalents of PhIO (dissolved in

trifluoroethanol (TFE)), followed by addition of 1 equivalent of trifluoromethanesulfonic acid (HOTf) in MeCN at −40 °C.
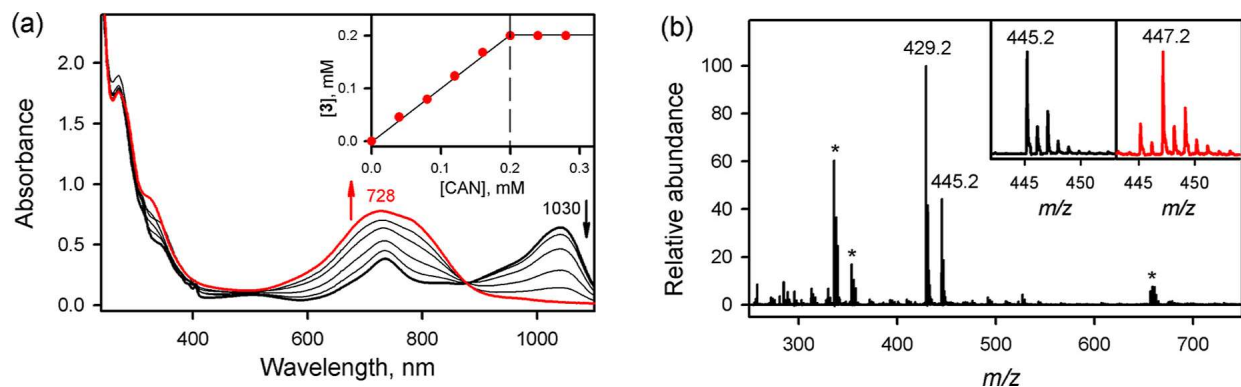
Figure 4.3. UV-Vis and MS of **3**. (a) UV–Vis spectral changes showing the formation of **3** in the reaction of **2** (0.20 mM) with CAN (0–0.20 mM) in MeCN at −40 °C. The inset shows titration data of [Ni^{III}(TAML)]$^-$ (0.20 mM) with CAN (0–0.28 mM). (b) CSI-MS spectra of **3** in positive ion mode. The peaks at m/z = 445.2 correspond to {H$^+$ + [Ni(O)(TAML)]} (calcd. m/z = 445.1). Inset shows the observed isotope distribution pattern for **3**-^{16}O (left panel) and **3**-^{18}O (right panel). The peaks marked with an asterisk (*) originate from zinc triflate, Zn(OTf)^2, {Na$^+$ + [Zn(OTf)(CF$_3$CH$_2$OH)]}, (m/z = 336.0) and {Na$^+$ + [Zn(OTf)(CF$_3$CH$_2$OH)(H$_2$O)]}, m/z = 354.0). This figure was made by Deepika Karmalkar in the Nam group, who also collected and analyzed the data shown in the figure.[150]

Complex **3** is metastable at −40 °C ($t_{1/2}$ ~3 h), which allowed its characterization with various spectroscopic techniques. CSI-MS of **3** shows poor intensity in positive and negative mode under above conditions. In order to trap the intermediate using CSI-MS, 1 equivalent of inactive metal triflates, such as zinc triflate [Zn(OTf)$_2$]$^{2+}$, was added to a solution of **3**, generated using PhIO in the presence of HOTf in MeCN:TFE (v/v = 1:1) at –40 °C. The peak at a mass to charge ratio of m/z = 445.2 in positive mode was assigned to be {H$^+$+[Ni(TAML)(O)]} (calcd. m/z = 445.2), with isotope distribution pattern for Ni-oxygen species. When **3**-^{18}**O** was used, a two-mass unit shift was observed at m/z = 447.2 (Figure 4.3b). The observation of the two-mass unit shift upon ^{18}O-introduction indicates that **3** contains one isotope sensitive oxygen atom.

The X-band EPR spectrum of **3**, measured at 5 K, is silent. In contrast, the EPR spectrum of [Ni^{III}(TAML)]$^-$ shows signals around $g \sim$ 2. This reveals that the oxidation state of **3** is consistent with a formally +4 species, one oxidation state higher than that of the Ni^{III} complex **2**. To confirm the oxidation state of **3,** the reduction of **3** was carried out using ferrocene derivatives. Addition of 1 equivalent of ferrocene (Fc) to **3** led to the formation of the one-electron reduced species, [Ni^{III}(TAML)]$^-$ (**2**), and the addition of 2 equivalents of decamethylferrocene (Me$_{10}$Fc) to

3 gave rise to its two-electron reduced species, $[Ni^{II}(TAML)]^{2-}$ (**1**). The formation of the reduced species from **3** was further confirmed using UV–vis and EPR experiments.[150]

The oxidation state of **3** was also confirmed by cyclic voltammetry (CV). The cyclic voltammogram of $[Ni^{II}(TAML)]^{2-}$ (**1**) in $MeCN/H_2O$ (*v/v* 19:1) displays two reversible oxidation waves at $E_{1/2}$ versus SCE = 0.19 and 0.85 V. The second-electron oxidation potential (E_{ox} = 0.85 V vs SCE) of **1** is the same as the one-electron reduction potential of the Ni–oxyl (**3**) species (E_{red} = 0.85 V vs SCE), which was generated by reacting **1** (2.0 mM) with CAN (2.0 equivalents) in $MeCN/H_2O$ (*v/v* 19:1) at −40 °C. It should be noted that **3** undergoes a comproportionation reaction with **1**, leading to the formation of $[Ni^{III}(TAML)]^-$ in stoichiometric yield.

4.3 X-ray Absorption Spectroscopy and Analysis (Shearer Group)

X-ray absorption spectroscopic studies and analysis were performed by Prof. Jason Shearer and his undergraduate student Dovydas Vasiliauskas. From the XANES region of the Ni K-edge XAS, all three complexes contain nickel in a centrosymmetric ligand environment (i.e., four-coordinate square-planar or six-coordinate quasi-octahedral). Complexes **1** and **2** are shown to be square planar nickel-centers, while **3** is contained in a six-coordinate ligand environment. Further, the edge position of **3** is also not consistent with a Ni^{IV} center; the oxidation state of nickel in **3** is most consistent with a formal Ni^{III} center. Solutions to the EXAFS region are consistent with a six-coordinate nickel center. The data are best modeled with four Ni-N scatterers at 1.96 Å, one Ni-O scatterer at 1.84 Å, and one long Ni-O scatterer at 2.2 Å. The data are therefore most consistent with a Ni^{III} center coordinated by the TAML amidate nitrogen atoms, a short axial O or OH ligand and a longer axially-coordinated ligand.

4.4 Magnetic Circular Dichroism Spectroscopy

MCD spectroscopy was further used to understand the electronic structure of intermediate **3**, to determine the spin state of this species (since MCD **C**-term intensity is obtained for all paramagnetic species, including integer spin species,[217–221] unlike EPR), and with insight from TD-DFT to assign its optical data. Indeed, in the obtained variable-temperature variable-field (VTVH) MCD data, 2-50 K and 0-7 T, **C**-term signals were observed for this species, with signals varying with temperature and magnetic field, as shown in Figure 4.4.
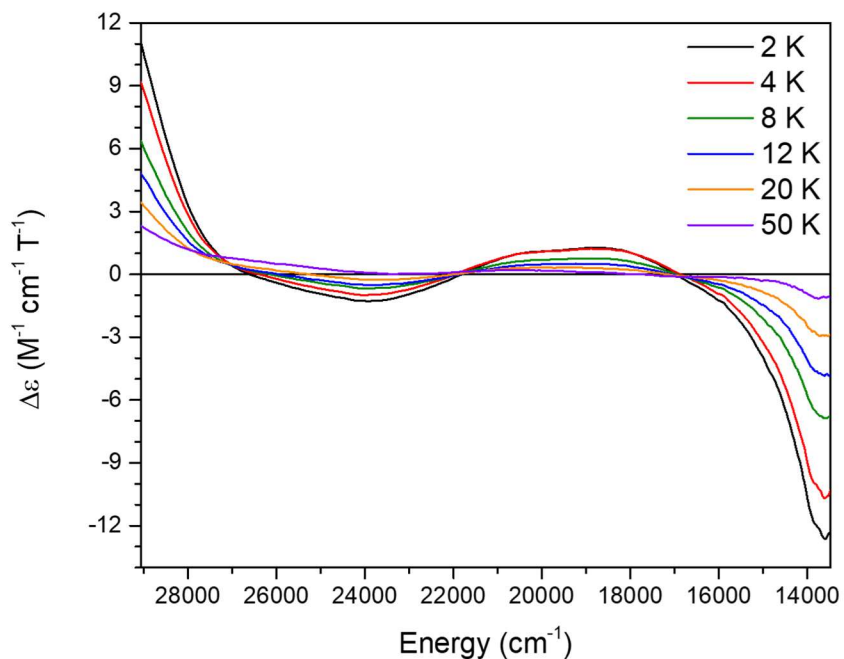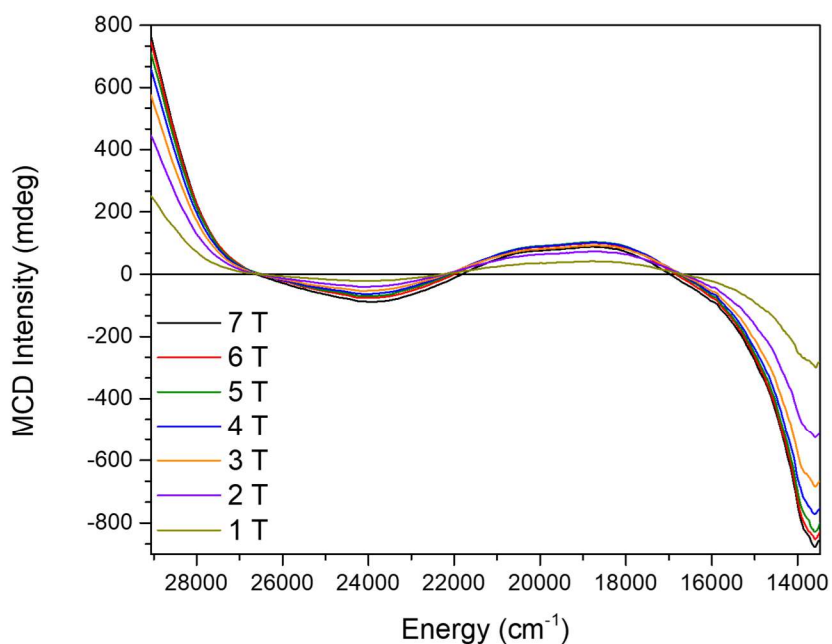
Figure 4.4. MCD data of **3** obtained at 3 mM concentration at 2-50 K, in a frozen glass prepared by reacting $Li_2[Ni^{II}(TAML)]$ (3.0 mM) with CAN (2.0 equivalents) in the presence of H_2O (5 μL) in acetonitrile/butyronitrile (1:2) at –60 °C. (a) Shown is the 7 T averaged baseline corrected data at each temperature. The MCD intensity in mdeg is converted to $\Delta\varepsilon$ as previously described.[222] (b) Shown is the averaged baseline corrected data for each field at 2 K.

Figure 4.5 shows a comparison of the UV-Vis and low-temperature MCD data of **3**. As shown Figure 4.5, the characteristic UV-Vis feature of **3** at 728 nm is also present in the MCD data, and hence, a fit of the VTVH MCD data obtained for this band provides direct insight into the magnetic properties of **3**, especially its spin state (see below).
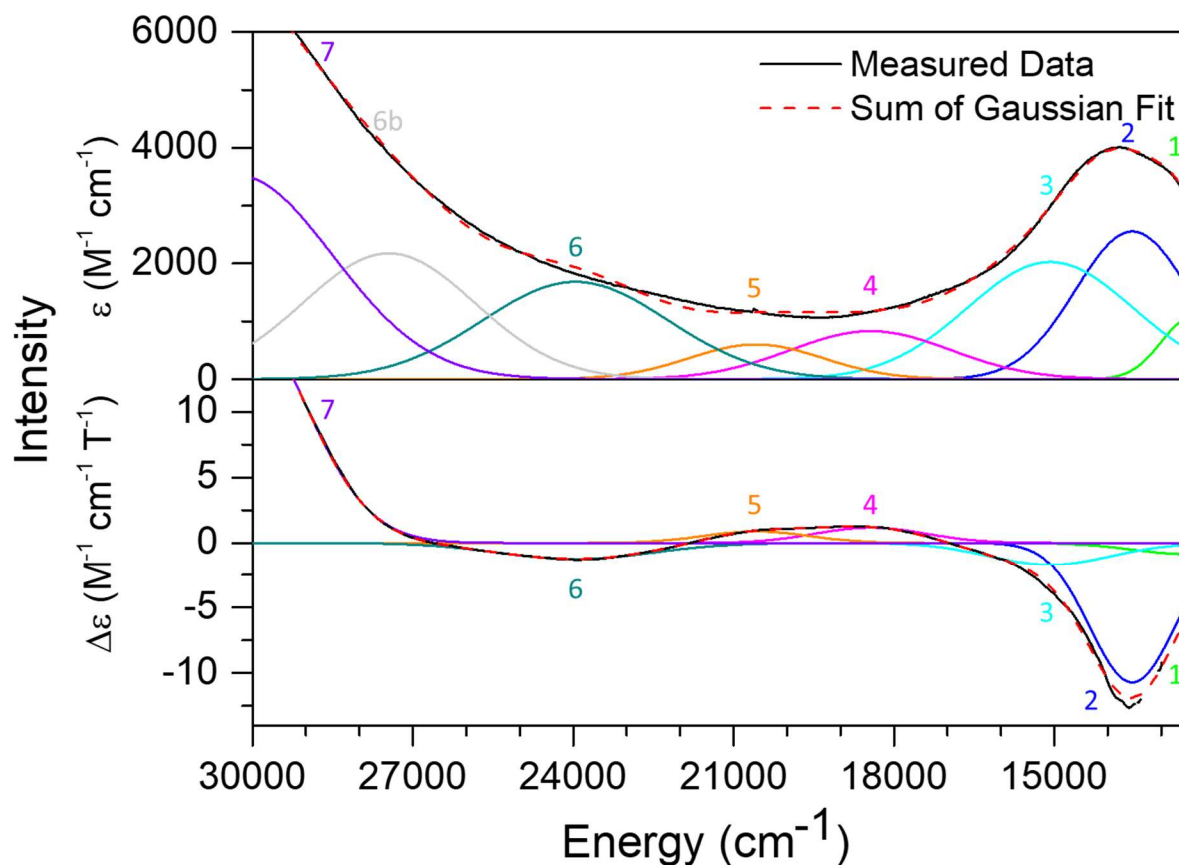
Figure 4.5 UV-Vis and MCD data for intermediate **3**, along with a correlated Gaussian fit of these data (see Table 4.1). Top: UV-Vis spectrum of **3** obtained at 0.20 mM concentration in MeCN at –40 ºC. Bottom: MCD data of **3** obtained at 3 mM concentration at 2 K 7 T, in a frozen glass prepared by reacting $Li_2[Ni^{II}(TAML)]$ (3.0 mM) with CAN (2.0 equivalents) in the presence of H_2O (5 µL) in acetonitrile/butyronitrile (1:2) at –60 ºC. Temperature and field-dependent MCD data are shown in Figure 4.4 a and b, respectively. Further details on the Gaussian fits of these spectra can be found in Figure 4.6.

A correlated Gaussian fit of the UV-Vis and MCD data shown in Figure 4.5, and in detail in Figure 4.6, identifies seven electronic transitions in the optical spectra, as listed in Table 4.1. Our results show that the feature at 728 nm actually corresponds to three different electronic transitions, bands 1 – 3, located at 12440, 13540 and 15080 cm^{-1}. Here, band 2 is the dominant

feature in the MCD data, indicating that this transition involves a significant amount of metal character, and likely corresponds to either a d-d or a charge-transfer (CT) transition. To higher energy, bands 4 – 6 at 18440, 20580 and 23960 cm^{-1} are quite intense in the absorption spectrum but weak in the MCD spectrum, suggesting that these could be ligand-based transitions. Finally, band 7 is again intense both in the UV-Vis and MCD data and could originate from a second CT transition. Further insight into the assignments of bands 2 and 7 can be obtained from the analysis of the VTVH data of these features. Unfortunately, the other optical features are too weak in the MCD spectra to obtain reliable VTVH data for further analysis.
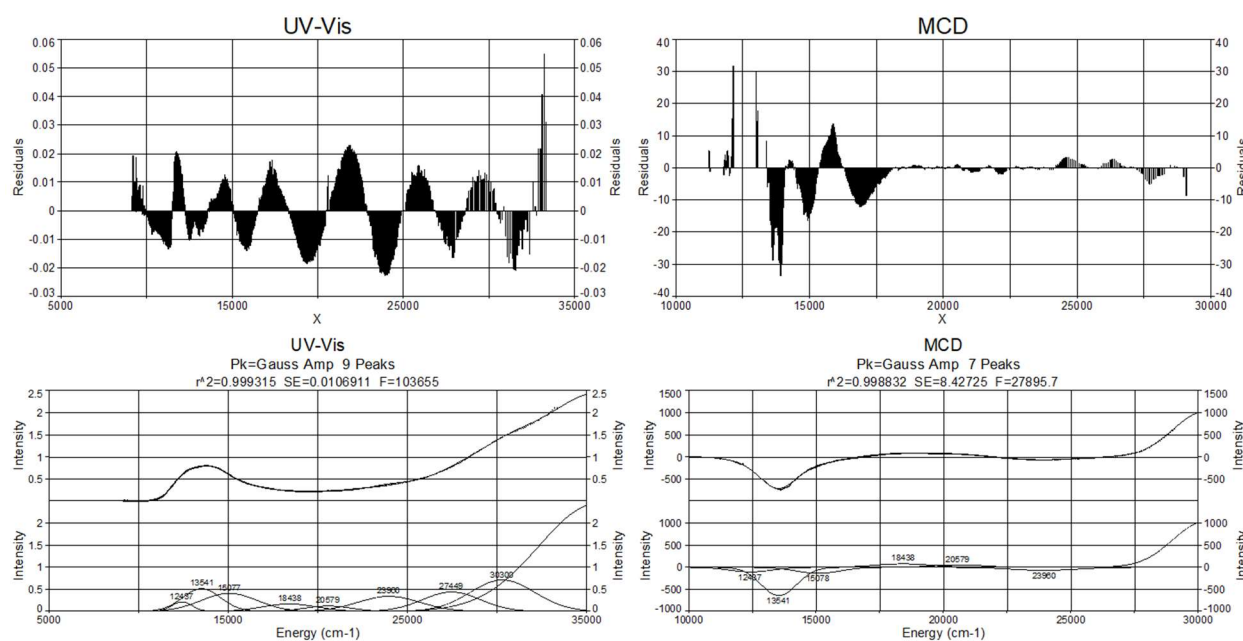
Figure 4.6. Details of the Gaussian fitting of the UV-Vis (left) and MCD 2 K 7 T (right) experimental data shown in Figure 4.5; the resulting Gaussians are listed in Table 4.1. The residuals are shown on the top, and the deconvoluted peaks on the bottom. The X^2 values are 0.9993 for the UV-Vis Gaussian fit, and 0.9988 for the MCD Gaussian fit.
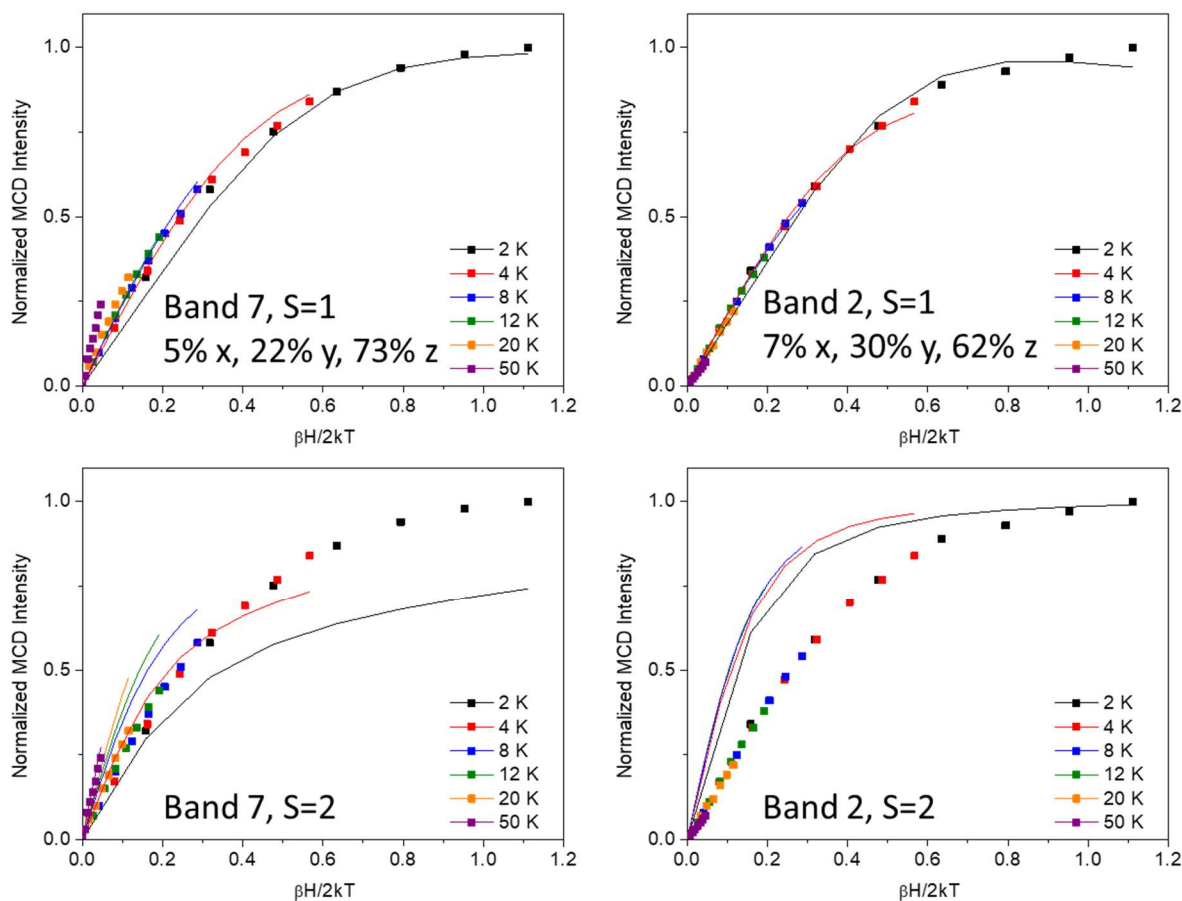
Figure 4.7. MCD VTVH data of 3 obtained at temperatures of 2 - 50 K and magnetic fields of 0 - 7 T, for the two main signals in the MCD spectra, bands 2 (VTVH data obtained at 14265 cm^{-1}, 701 nm, right) and 7 (VTVH data obtained at 28570 cm^{-1}, 350 nm, left). Top panels: the data fit very well with an $S_t = 1$ ground state, using D = 4.0 cm^{-1}, E/D = 0.24, and g = 2.013, 2.070, 2.078. Bottom panels: all attempt to fit the data with $S_t = 2$ failed. The dots are the experimental data while the lines correspond to the fits.

From the temperature- and field-dependent MCD data of bands 2 and 7, obtained at various magnetic fields, 0 - 7 T, and various temperatures, 2 - 50 K, the magnetic saturation data shown in Figure 4.7 were obtained. First, since the MCD features of **3** are temperature-dependent, they correspond to **C**-term signals, which demonstrates that the complex is paramagnetic ($S_t = 1$ or 2). We then attempted to fit the VTVH data for both main MCD features for the $S_t = 1$ and 2 states. However, as shown in Figure 4.7, the data cannot be fit with an $S_t = 2$ ground state, due to the wrong curvature of the saturation curves. As the spin multiplicity increases, the MCD saturation curves become more strongly curved, which is already evident from the simple Brillouin function. The analysis of our VTVH data therefore clearly demonstrates that the formally Ni^{IV}(O) species **3**

has an intermediate spin state, $S_t = 1$ (Figure 4.7, top). The best fit of the VTVH data was obtained using $D = 4.0$ cm^{-1}, $E/D = 0.24$, and $g = 2.013, 2.070, 2.078$, which are based on DFT-predicted zero-field splitting parameters as discussed below.

Fixed E/D = 0.24
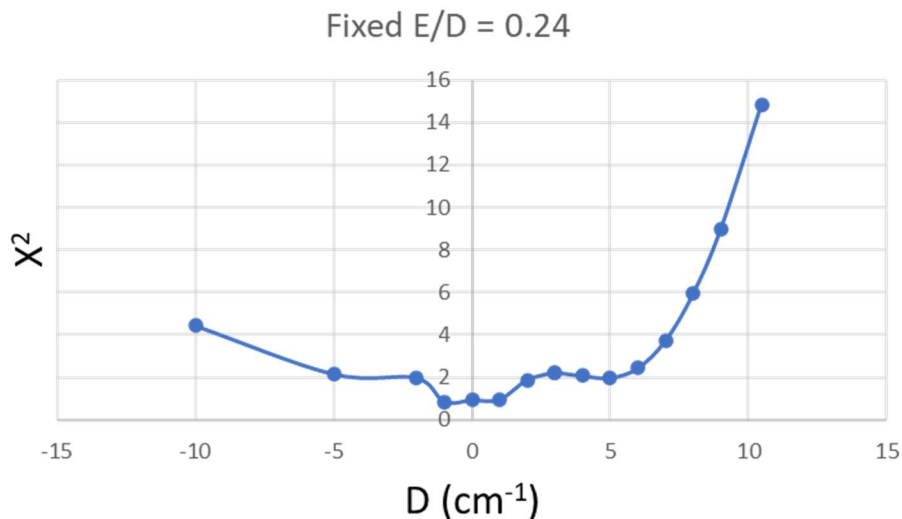
Figure 4.8. X^2 goodness of fit as a function of D. The 701 nm VTVH saturation data are fit with the ZFS parameters obtained for structure B3LYP (3), with the D value varied and the polarizations allowed to optimize. The E/D ratio remains unchanged at 0.24. The X^2 is plotted to illustrate the change in goodness of fit with different D values. The line serves to guide the eye.

Note that the VTVH MCD data could be reasonably fit with a positive D value of up to 6 cm^{-1}, see Figure 4.8. This D value is consistent with the relatively large positive D value calculated for DFT structures B3LYP (2) and B3LYP (3), which are the best models for the structure of the intermediate, see Table 4.2 and section 4.5. The E/D and g values had to be determined by calculation, as the integer spin EPR-silent species **3** prevented experimental determination of these parameters. B3LYP (2) and B3LYP (3) show good agreement for these zero-field splitting (ZFS) parameters, but B3LYP (3) was ultimately chosen as it better models the Ni-OH bond length observed experimentally.

In addition, the fitting of the magnetic saturation curves also provides insight into the polarizations of the corresponding electronic transitions. Based on our fits, both bands 2 and 7 show a large degree of z-polarization, which some additional contribution from y polarization. These polarizations are relative to the orientation of the ZFS-tensor, which is accessible from DFT calculations. As one would expect, the DFT calculations show that the z direction of the ZFS-tensor is associated with the unique Ni–O axis (see Figure 4.13). These results indicate that bands

2 and 7 have charge transfer character between the Ni center and the oxo ligand. Further insight into the assignments of these bands is available from the TD-DFT data, as discussed below.

Table 4.1. Summary of Gaussian fitting and band assignments of the optical spectra for 3. See Table 4.3 for further TD-DFT information.

No.	Energy (cm^{-1})	Intensity		Assignment	Polarization (%x, %y, %z)
		MCD $\Delta\varepsilon$ (M^{-1} T^{-1} cm^{-1})[a]	UV-Vis ε (M^{-1} cm^{-1})		
1	12440	-2.6	1060		-
2	13540	-26.7	2553	Co-ligand (π^*), $O(p_y)\_d_{yz}$ (π^*) $\rightarrow$ $d_{x2-y2}/d_{z2}\_O(p_z)$ (σ^*), Ni-OH/O (π^*) $\rightarrow O(p_x)\_d_{xz}$ (π^*)	7, 30, 62
3	15080	-4.3	2026		-
4	18440	3.5	831		-
5	20580	2.7	600		-
6	23960	-2.2	1682		-
6b	27450	--[b]	2175		-
7	29450	42.9	3528		5, 22, 73

[a] MCD intensity given for the 2 K 1 T spectrum, see Figure 4.9 for fit details.
[b] Band 6b not observed by MCD.

In Table 4.1, the MCD intensity of the features is given according to the intensity of the 2 K 1 T spectra. At 1 T, the signal intensity is still linear with respect to the magnetic field, as opposed to the 7 T data as the intensity of the 2 K 7 T data shows saturation of signal, see Figure 4.7 for saturation behavior, and so the relative intensities between fit bands is less meaningful. The absorptivity of the MCD sample was estimated by comparing the MCD voltage curve to high quality absorption spectra of **3**. The voltage curve of an MCD sample when compared carefully to the background voltage curve can give approximate UV-Vis absorption spectra and allow the estimation of concentration*pathlength which is otherwise ambiguous in a frozen sample.
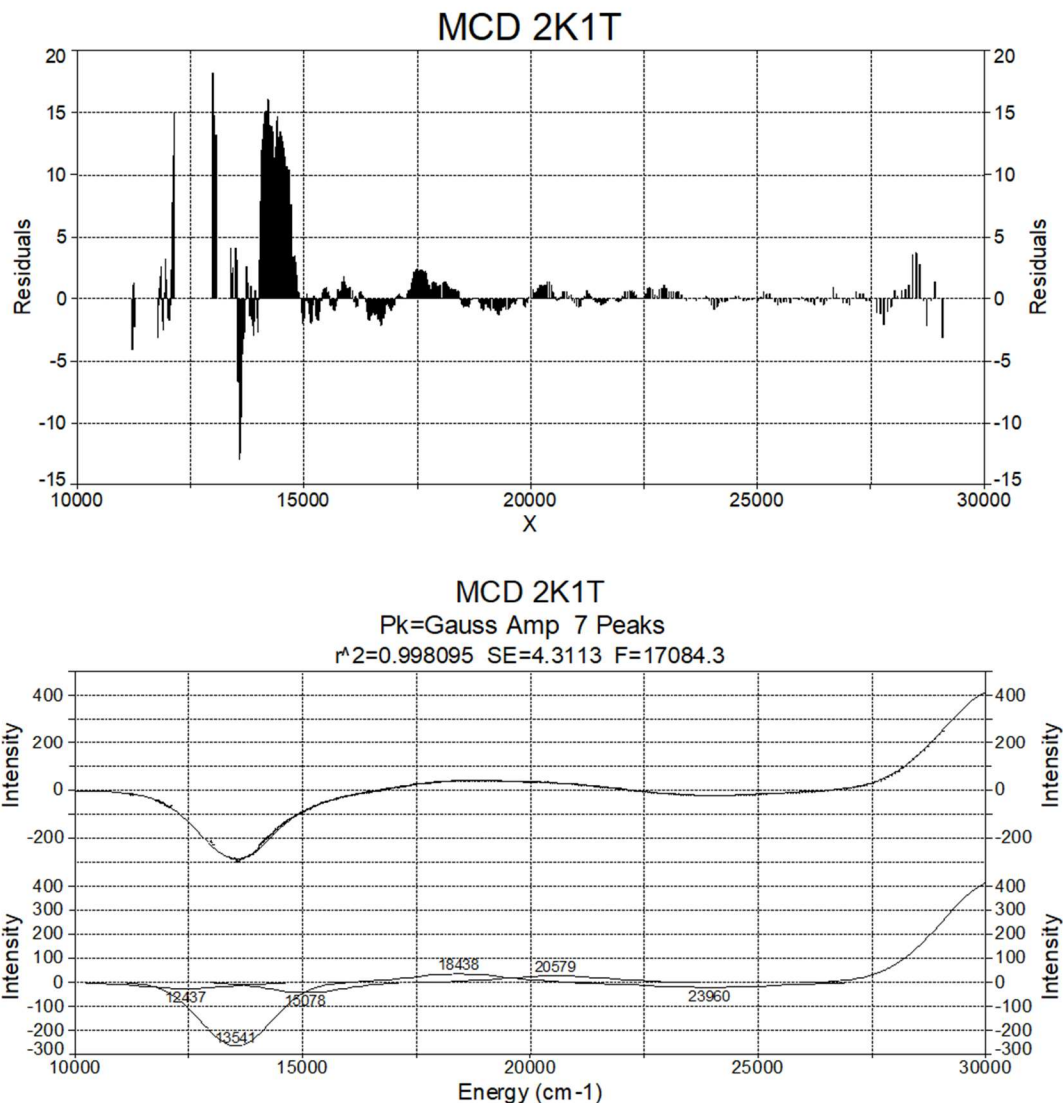
Figure 4.9. Details of the Gaussian fitting of the experimental 2 K 1 T MCD spectrum: residuals, top, and fit, bottom. The X^2 value for this fit is 0.9981. The 2 K 1 T MCD spectrum was used to calculate the band intensities listed in Table 4.1.

4.5 Density Functional Theory (DFT) Calculations.

4.5.1 Coordination Number and Spin State

With these experimental results in hand, we set out to model the putative high-valent Ni(O) intermediate using DFT calculations, in direct comparison to our experimental results. Based on the EXAFS analysis, which shows a short Ni–O vector and indicates that the complex is six-coordinate, we used the DFT calculations to interrogate the nature of the sixth ligand, X, and develop structural models for the intermediate. We also investigated a five-coordinate species, for

comparison. As discussed above, the MCD data indicate that **3** has an $S_t = 1$ ground state, though we also investigated analogous $S_t = 2$ species, to compare structural features and total energies. For this purpose, B3LYP and other functionals were employed, in combination with the TZVP basis set. The results from our DFT calculations are summarized in Table 4.2, and selected structures are shown in Figure 4.10.
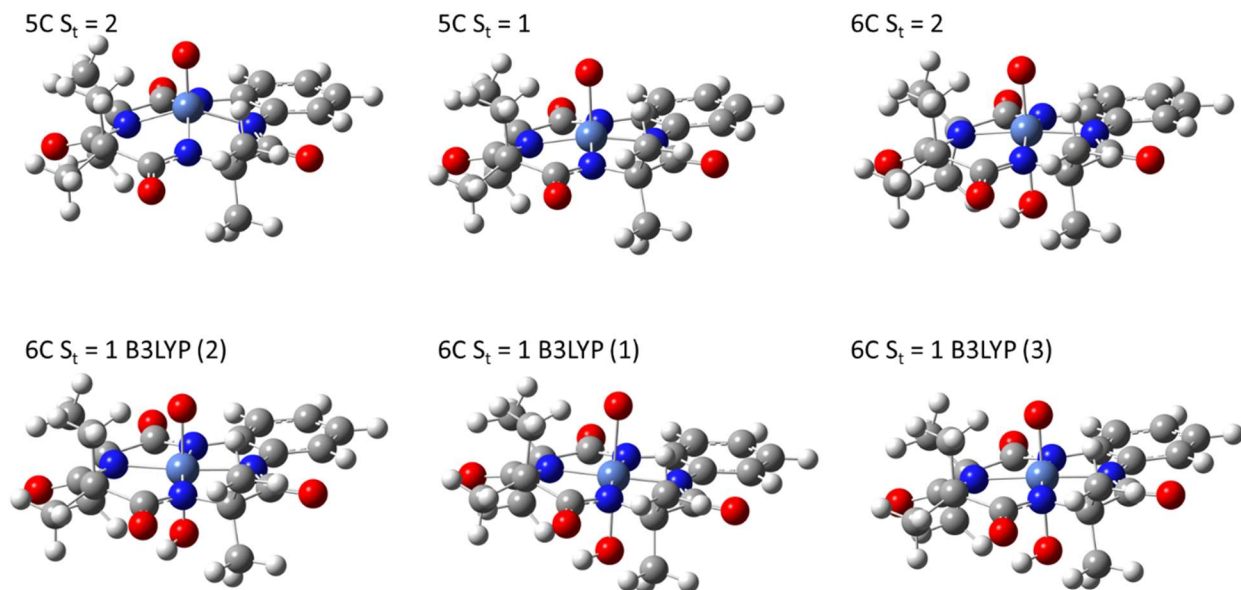
Figure 4.10. Images of select optimized structural models for **3**, optimized in Gaussian with B3LYP/TZVP. See Table 4.2 for details and structural parameters.

Table 4.2. DFT-calculated properties for **3**, compared for different coordination numbers, spin states, and using different functionals. All calculations were performed with the basis set TZVP. Relative energies are only compared across analogous structures, applying the same functional, and are color coded for guidance. See Figure 4.10 for select structures and Section 4.9.1 for Cartesian coordinates.

| | | | $S_t = 1$ | | | | | | $S_t = 2$ | | | |
| | | | 5C[a] | 6C[b] | | | | | 5C | 6C | | |
	Property	Exp. (EXAFS)	B3LYP	B3LYP (1)[c]	B3LYP (2)[d]	B3LYP (3)[e]	TPSSh	BP86	B3LYP	B3LYP	TPSSh	PBE0
	Relative Energy (kcal/mol)		0	0	2	5	0		9	18	17	
Geometry	Ni-O bond (Å)	1.84	1.98	2.15	1.84	1.84[f]	1.81	1.79	1.70	1.84	1.77	1.75
	Ni-OH bond (Å)	2.2	-	2.27	1.94	2.22[f]	1.93	1.97	-	2.26	2.28	2.20
	Avg. Ni-N bond (Å)	1.96	1.88	1.89	1.97	1.93	1.96	1.98	1.99	1.98	1.98	1.97
	Σ<N-Ni-N (°)	-	356	360	360	360	360	360	337	358	355	360
	<O-Ni-OH (°)	-	-	179	179	179	178	178	-	179	178	179
	<Ni-O-H (°)	-	-	97.3	101.1	97.6	100.4	99.1	-	98.4	95.9	98.6
	[C18-Ni-O-H (°)[g]	-	-	-0.1	-20.6	0.4	-8.0	-15.0	-	-8.5	-0.1	-0.1
Vibration	Ni-O (cm^{-1})	-	385 (393)	258, 262, 270	507	N/A	540	585	734	392 (375,363)	585	613, 615
	Ni-OH (cm^{-1})	-	-	202, 213	439	N/A	451, 457	399	-	169, 175, 225, 229	133, 160, 227, 281	184, 242, 292
Spin Density	Ni	-	0.65	0.64	0.75	0.73	0.78	0.83	1.82	1.85	1.82	1.81
	O	-	1.31	1.18	0.95	1.07	0.9	0.74	1.28	1.32	1.30	1.40
	OH	-	-	0.15	-0.06	0.03	-0.05	-0.01	-	0.21	0.23	0.19
	Ns (co-ligand)	-	0.04	0.04	0.34	0.19	0.36	0.39	0.80	0.61	0.64	0.63
	Co-ligand (except Ns)	-	0	-0.02	0.01	-0.02	0.01	0.04	0.10	0.01	0.01	-0.03
EPR	D	-	NC[h]	-4.76	8.93	10.47	NC	NC	-1.03	-113	NC	NC
	E/D	-	NC	0.11	0.30	0.24	NC	NC	0.11	0.10	NC	NC

[a] 5C: five-coordinate structure. [b] 6C: six-coordinate structure. [c] B3LYP (1) is the fully optimized, minimum energy six-coordinate structure for $S_t = 1$, with d_{z2} singly occupied. [d] B3LYP (2) is the fully optimized, six-coordinate structure for $S_t = 1$, with d_{x2-y2} singly occupied (which constitutes a local minimum). [e] B3LYP (3) is a partially optimized structure with the Ni–O and Ni–OH bonds locked at the experimental (EXAFS) distances. [f] These bond distances were fixed during the optimization of structure B3LYP (3). [g] C18 is the dimethylated carbon between the two carbonyls of the amide groups in the $TAML^{4-}$ ligand. [h] NC: not calculated.

To begin, we optimized the structure of a simple, five-coordinate model, with a square-pyramidal structure where the oxo ligand occupies the apical position, in the $S_t = 1$ state. This structure shows a rather long Ni–O bond of 1.98 Å, which does not reproduce the experimental Ni–O distance well, especially when compared to a five-coordinate fit of the EXAFS data, which puts the Ni–O distance at 1.73 Å. Since our XAS data indicate that **3** is a six-coordinate species, we then explored structures with the sixth ligand, X, corresponding to ammonia, water, acetonitrile, and hydroxide, which are all species that are present in solution. However, in our DFT geometry optimizations (B3LYP/TZVP), the neutral ligands ammonia, water and acetonitrile all dissociated from the Ni center, which remained five-coordinate. The only six-coordinate structure that we could optimize has hydroxide coordinated in trans position to the formally oxo group.

4.5.2 Valence Tautomers

This structure, designated as B3LYP (1) in Table 4.2, has a very long Ni–O bond length of 2.15 Å, compared to the experimental Ni-O distance from the EXAFS fit for a six-coordinate complex, 1.84 Å. In this structure, the predicted Ni–OH distance is 2.27 Å. In this case, the Ni center has the (antibonding) d_{z^2} orbital singly occupied, as shown in the MO diagram in Figure 4.11, left, leading to a weakening of the axial Ni–O/OH bonds. The $d_{x^2-y^2}$ orbital constitutes the LUMO in this case, as shown in Figure 4.11, left.
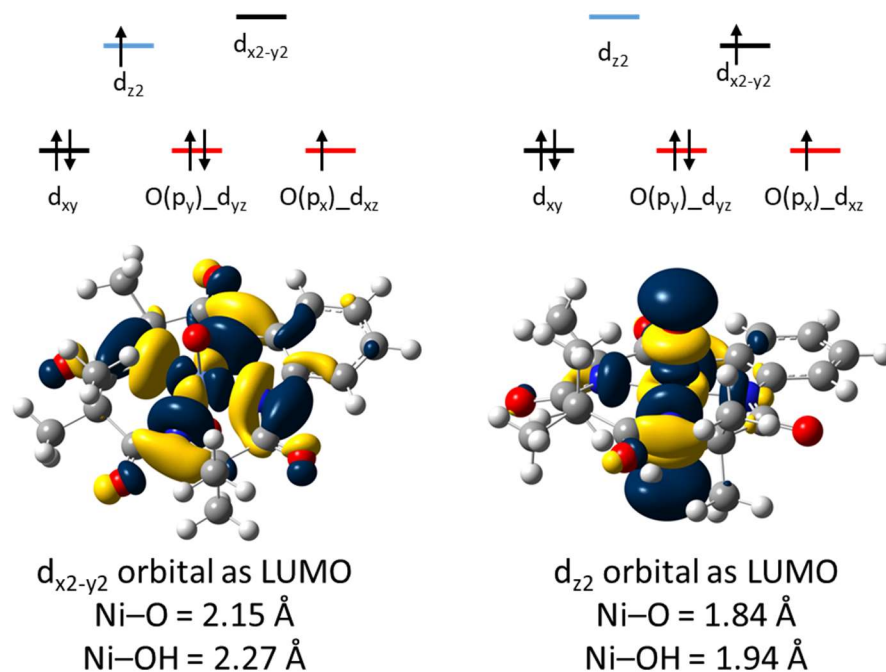
Figure 4.11. Six-coordinate structures for two different valence tautomers of $[\text{Ni(TAML)(O)(OH)}]^{3-}$ were optimized for the $S_t = 1$ ground state, using B3LYP/TZVP. Left: the valence tautomer (1) has the d_{z2} orbital singly occupied, and the LUMO corresponds to the d_{x2-y2} orbital (contour plot shown on the bottom). Right: the valence tautomer (2) has the d_{x2-y2} orbital singly occupied, and the LUMO corresponds to the d_{z2} orbital (contour plot shown on the bottom). The calculated bond lengths are also included. The colors used in the ligand field diagrams on the top correspond to the bonding properties of these d-orbitals with respect to the oxo ligand (as in Figure 4.1): blue is σ-antibonding, black non-bonding, and red π-antibonding.

However, complex **3** can also exist in the alternative valence tautomer where instead, the (antibonding) d_{x2-y2} orbital is singly occupied and d_{z2} is empty (and constitutes the LUMO), which should lead to a strengthening of the axial Ni–O/OH bonds (Figure 4.11, right). Starting our geometry optimization by locking the Ni–O distance at the experimental distance (1.84 Å), letting this structure relax into a local minimum, and then fully optimizing this structure, we are able to obtain a fully optimized structure for the alternative valence tautomer as well. This optimized structure, B3LYP (2), shows a Ni–O bond length of 1.84 Å and is only 2 kcal/mol higher in energy than B3LYP (1). However, the Ni-OH bond length predicted for B3LYP (2) is much shorter, 1.94 Å, than the experimental value of 2.22 Å.

(a)

1.94 Å   2.10 Å   2.20 Å

2.30 Å   2.35 Å   2.40 Å

(b)
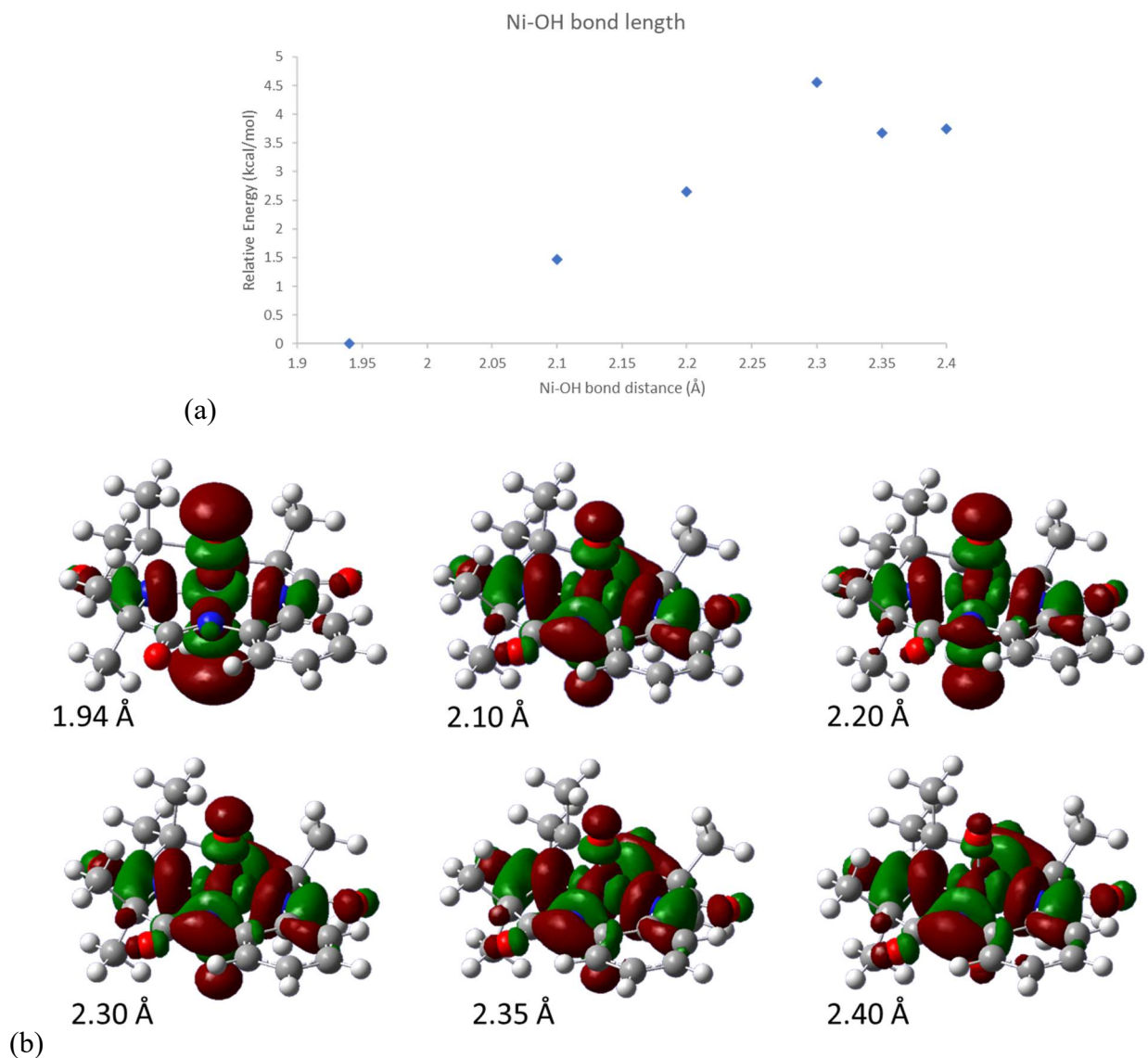
Figure 4.12 (a) To see the effect of stretching the Ni-OH bond, the Ni-OH bond was locked at the distance shown on the x-axis, and the Ni-O bond was locked at 1.84 Å. The rest of the structure was allowed to optimize, using B3LYP/TZVP. The relative energy is plotted versus the Ni-OH bond distance and shows a slight increase in energy. (b) MO plots of the LUMOs of [Ni(TAML)(O)(OH)]$^{3-}$, obtained at different Ni-OH distances, using the structures with energies plotted in (a). As the Ni-OH bond length is increased (value given next to each image) the d_{z2} LUMO gradually mixes with and changes to the d_{x2-y2} orbital.

This Ni–OH bond, however, is a very soft coordinate. When the Ni–OH bond length is increased from 1.94 to 2.22 Å in a relaxed potential energy surface (rPES) scan, the calculated energy increases by only ~3 kcal/mol (Figure 4.12a). Interestingly, as the Ni-OH distance is increased in this rPES scan, the LUMO gradually converts from the d_{x2-y2} to the d_{z2} orbital, via linear combinations of these two orbitals (Figure 4.12b). Due to the flexibility of the Ni-OH bond,

it is likely that hydrogen bonding, via the ammonia or water molecules in solution, could contribute to a longer Ni–OH bond length experimentally. Optimized structures of the relevant valence tautomer (2) with TPSSh and BP86 were also obtained, as shown in Table 4.2.
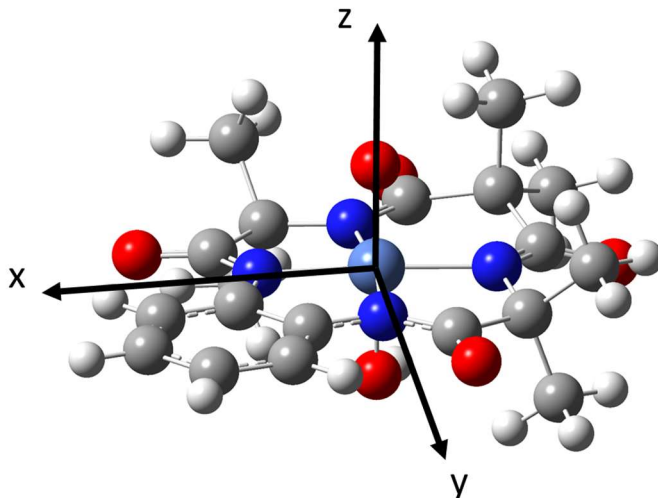
Figure 4.13. Orientation of the *D*-tensor, as calculated for B3LYP (3) using ORCA. Note how the z axis aligns with the Ni-O bond.

Calculated ZFS parameters for both valence tautomers ($S_t = 1$) are also included in Table 4.2. While B3LYP (1) shows a negative *D* value around -5 cm^{-1} and moderate rhombicity, the other valence tautomer, B3LYP (2) and also B3LYP (3), shows a positive *D* value around 8 – 10 cm^{-1} and more pronounced rhombicity. The calculated rhombicity is somewhat surprising, given the general octahedral symmetry of the coordination environment of the Ni center, but note that the benzene ring in the co-ligand restricts two of the nitrogens such that there is a tight <N-Ni-N angle of 85°, while the opposing angle extends to 103°.The experimental VTVH data are best fit with $D = 4.0$ cm^{-1} (with *E*/*D* fixed at the calculated value of 0.24; see Figure 4.7 and discussion above). The calculated orientation of the ZFS-tensor for B3LYP (3) is shown in Figure 4.13, with the z-direction oriented along the Ni–O vector.

For comparison, we further optimized the five- and six-coordinate structures (the latter with bound hydroxide) in the $S_t = 2$ state, and these results are included in Table 4.2. Importantly, both the five- and six-coordinate $S_t = 2$ structures are significantly higher in energy than their $S_t = 1$ counterparts, by 9 and >15 kcal/mol, respectively. Taking further into consideration the results from the analysis of the VTVH MCD data (see above), it is clear that the $S_t = 2$ ground state can be ruled out for **3**.

In summary, while the [Ni(TAML)(O)(OH)]$^{3-}$ intermediate (**3**) could exist in two possible electronic ground states, based on the EXAFS data, the valence tautomer with the shorter Ni-O bond length, (2), is favored (with d_{x2-y2} singly occupied). The sixth ligand is modeled with hydroxide, which forms a flexible Ni–OH bond, likely modulated by hydrogen bonding. For further analysis of the electronic structure of this intermediate, we generated a third structure, B3LYP (3), where the Ni-O and Ni-OH bond distances were fixed based on the experimental (EXAFS) distances, and the rest of the structure was reoptimized (see Table 4.2). This model is only slightly higher in energy than both of the minimum structures, B3LYP (1) and B3LYP (2).

4.5.3 Molecular Orbital Diagram
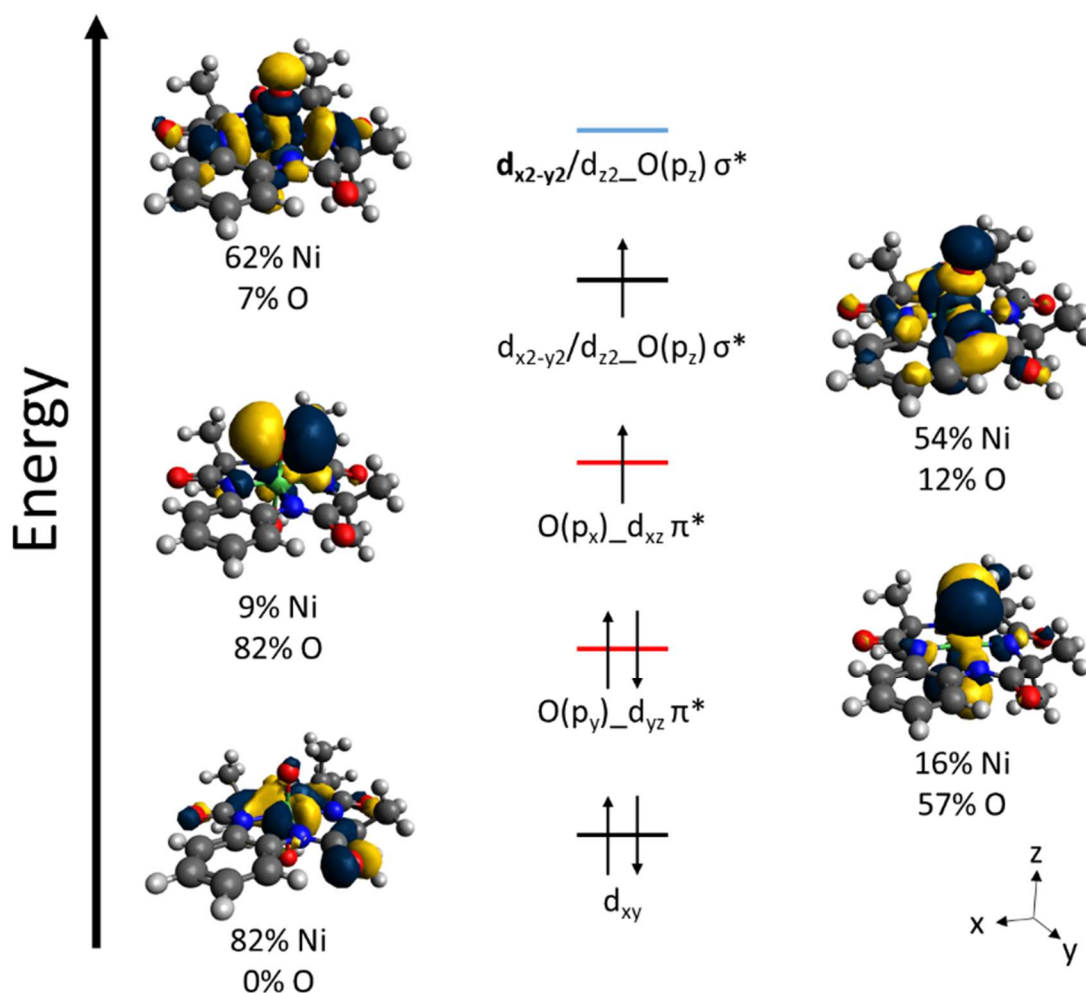
Figure 4.14. Scheme of MO diagram of [Ni(O)(OH)(TAML)]$^{3-}$. These molecular orbitals were calculated using TPSSh/TZVP for the B3LYP (3) optimized structure and visualized in Avogadro. Shown are the corresponding β-spin MOs.

To further interrogate the electronic structure of the $[Ni(TAML)(O)(OH)]^{3-}$ intermediate (**3**), we then analyzed the MO diagram for the B3LYP (3)-optimized structure, using TPSSh/TZVP calculations. As shown in Figure 4.14, with the Ni-OH bond set to 2.22 Å, the d_{x2-y2} and d_{z2} orbitals become somewhat mixed, making it difficult to assess the strength of the Ni–O σ bond. This information is more readily available from the MO diagram of the B3LYP (2) structure with the shorter Ni–OH bond. In this case, the LUMO of the complex is the antibonding combination of d_{z2} and the $O(p_z)$ orbital, $d_{z2}\_O(p_z)$, which has 54% Ni(d) and 16% O character, as shown in Figure 4.15. The corresponding bonding MO at lower energy is fully occupied, giving rise to a Ni–O σ bond with a formal bond order of 1.
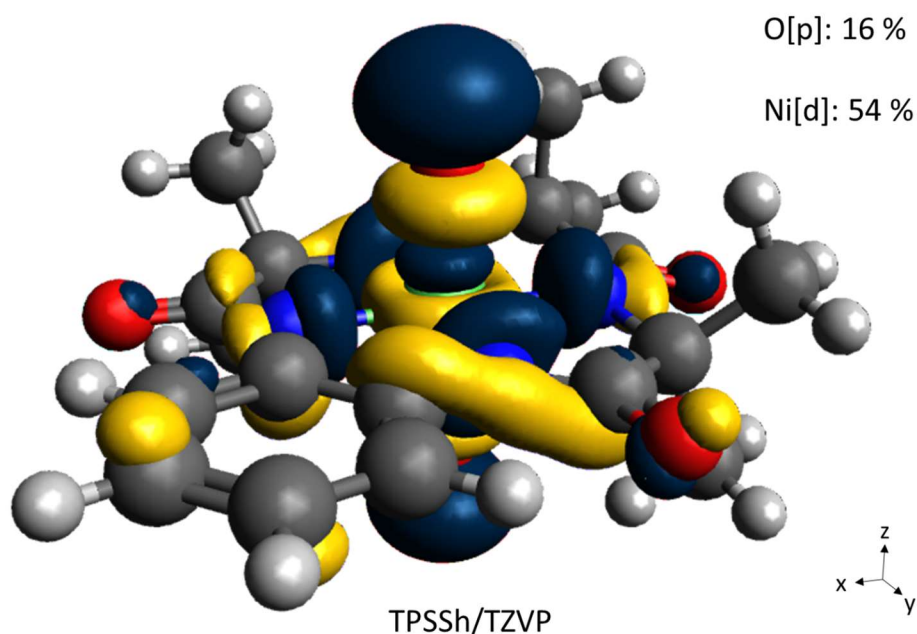
Figure 4.15. Molecular orbital image of the $d_{z2}\_O(p_z)$ σ-antibonding LUMO, obtained with TPSSh/TZVP for the structure B3LYP (2) (shown is the corresponding β-MO). This orbital has 16% $O(p_z)$ and 54% Ni(d) character.

At lower energy, the first SOMO is the d_{x2-y2} orbital, which is non-bonding to the oxo ligand. As shown in Figure 4.14, the two dπ orbitals of Ni, d_{xz} and d_{yz}, undergo π-bonding interactions with the $O(p_x)$ and $O(p_y)$ orbitals. Here, both π-bonding interactions are inverted, with the antibonding combinations shown in Figure 4.14 having dominant O(p) character. However, in the case of d_{yz}, both the bonding combination with $O(p_y)$ at lower energy and the antibonding combination at higher energy, shown in Figure 4.14, are fully occupied, which means that this orbital interaction does not contribute to the Ni–O bond. In the case of d_{xz}, the bonding

combination with $O(p_x)$ at lower energy is doubly occupied, but the corresponding antibonding MO is only singly occupied, as shown in Figure 4.14, which means that this orbital interaction could contribute 1/2 bond order to the Ni–O bond. However, as shown in Figure 4.14, the orbital $O(p_x)\_d_{xz}$ shows very strong bond inversion, with 82% O(p) and only 9% Ni(d) contribution. Hence, this interaction constitutes a very weak Ni–O π-bond, which means that the Ni–O bond in **3** is de facto a Ni–O single (σ) bond. In addition, the oxo ligand in **3** is oxidized and has very clear oxyl character, as reflected by its large amount of spin density of about +1.0, creating a "hole" in the $O(p_x)$ orbital (see Figure 4.16 for a larger image of the electron hole). Therefore, the electronic structure of **3** is best described as a Ni^{III}-$O^{\bullet-}$ complex, where the spins of the Ni^{III} ($S_t = 1/2$) and the oxyl ligand ($S_t = 1/2$) are ferromagnetically coupled (see spin densities listed in Table 4.2), giving the experimentally observed $S_t = 1$ ground state. In other words, the oxo ligand serves as a non-innocent ligand in **3**. In contrast, and surprisingly, the $TAML^{4-}$ ligand is not redox-active in complex **3** and does not accumulate any notable spin density. This is surprising, considering that large number of M^{IV}-$TAML^{4-}$ complexes have been reported where the TAML ligand is bound in the one-electron oxidized, $TAML^{\bullet3-}$, form.[1,223–225] The Ni^{III}-$O^{\bullet-}$ electronic structure description of **3** as outlined above implies that the Ni–O bond is actually quite weak. In agreement with this finding, the calculated Ni–O stretching frequency is located around 500 cm^{-1}, as shown in Table 4.2, which reflects the single bond character of the Ni–O interaction. Finally, as expected, the nonbonding d_{xy} orbital is lowest in energy and has no contribution from the oxyl ligand.

O[p]: 82 %

Ni[d]: 9 %
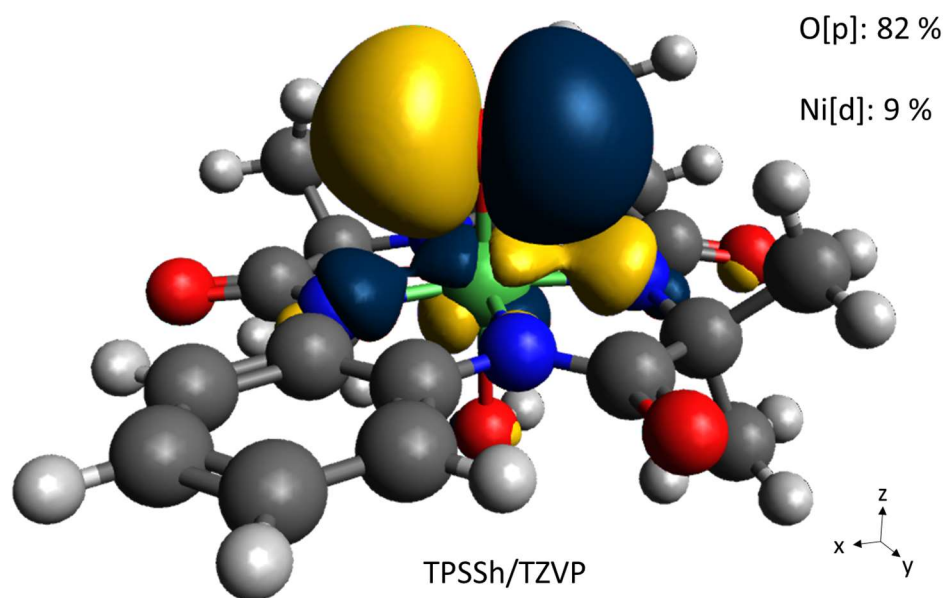
TPSSh/TZVP

Figure 4.16. Molecular orbital image of the SOMO for a TPSSh/TZVP calculation on structure B3LYP (3) (shown is the unoccupied β-MO). The electron hole is located in the oxygen (p_x) orbital, with 82% O(p_x) and only 9% Ni(d) character.

4.5.4 Time Dependent DFT

To further assign the optical spectra of **3**, we performed TD-DFT calculations, using the B3LYP (3) structure and the functionals B3LYP, TPSSh, BP86, and PBE0, which contain varying amounts of Hartree-Fock exchange. Figure 4.17 compares the absorption spectra calculated with these functionals to the experimental data. As evident from the figure, TPSSh matches the experimental absorption spectrum the best, so this functional was used for electronic structure analysis. TD-DFT predicts a broad absorption band around 550 nm (18000 cm^{-1}), which corresponds to the calculated transitions 6 – 13, see Table 4.3, and which we assign to the experimental absorption band at 728 nm (13740 cm^{-1}) that is indicative of the formation of **3**. By analyzing the electronic transitions predicted by TD-DFT, we found that this spectral region is mostly dominated by mixed ligand-to-metal charge transfer (CT) transitions, mostly into $d_{x^2-y^2}$/d_{z^2}_O(p_z) (σ^*) as the acceptor MO, in agreement with the mixed polarizations observed for band 2 (see Figure 4.7, Table 4.1, and Table 4.3). Interestingly, we do not see much CT into the O(p_x)_d_{xz} hole in the low-energy region of the absorption spectrum. Of the low-energy TD-DFT predicted excitations, transition 10 is the only one with significant z polarization (88%),

122

corresponding to a co-ligand (π) $\rightarrow$ $d_{x2-y2}/d_{z2}\_O(p_z)$ (σ*) and Ni-OH/O (π*) $\rightarrow$ $O(p_x)\_d_{xz}$ (π*) transition.
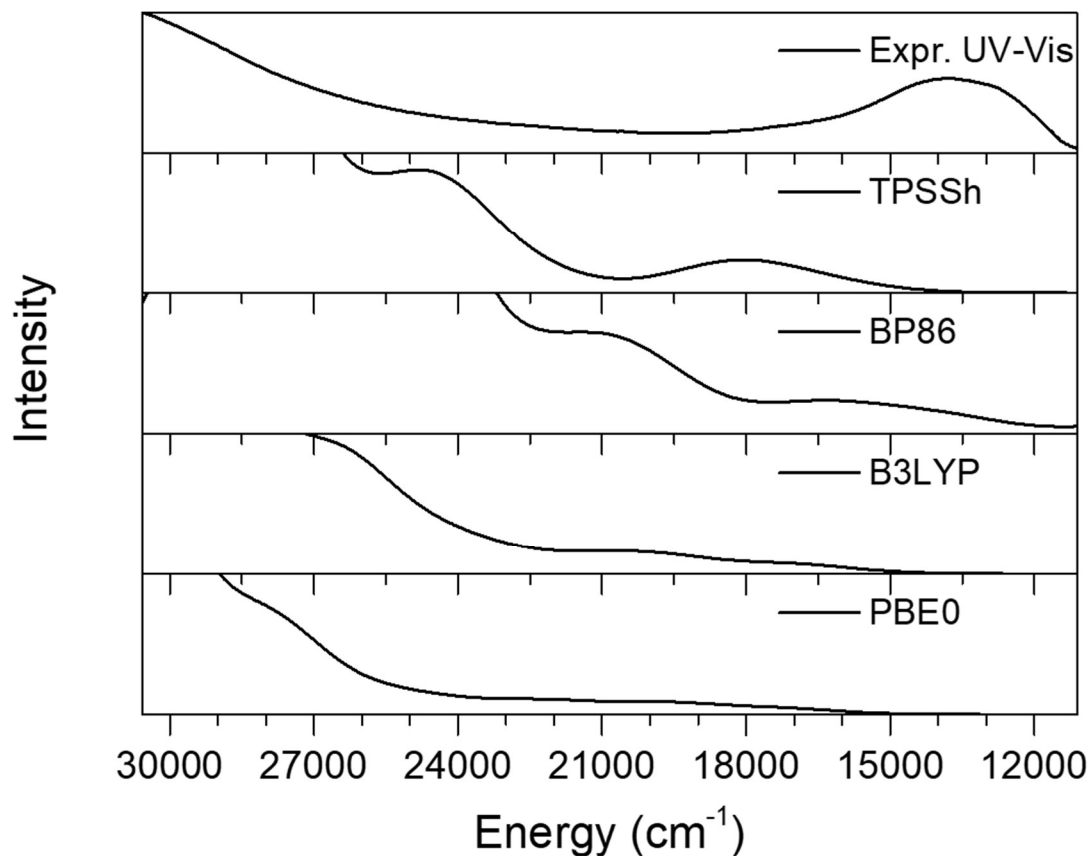
Figure 4.17. TD-DFT calculations on structure B3LYP (3), where the Ni–O and Ni–OH bond lengths were fixed at the experimental values (from EXAFS; see Table 4.2 and text). All TD-DFT calculations were performed with the program ORCA, using the indicated functionals and the TZVP basis set.

Table 4.3. Select TD-DFT excitations, their energy/wavelength, oscillator strength, description of the molecular orbitals that contribute to the transition, and their tentative assignment referencing the bands in Figure 4.5

TD-DFT excitation #	Energy (cm^{-1})	Wavelength (nm)	Oscillator Strength	Molecular Orbital Transitions, in Order of Decreasing Contribution [a]	Band
6	16007	625	0.0011	aryl/amide (π^*), OH(p_y), d_{yz}_OH/O(p_y) (π/π^*) $\rightarrow$ d_{x2-y2}/d_{z2}_O(p_z) (σ^*)	1
8	17046	587	0.0007	O(p_y)_d_{yz} (π^*), aryl/amide (π^*) $\rightarrow$ d_{x2-y2}/d_{z2}_O(p_z) (σ^*)	$\downarrow$
10	17793	562	0.0026	aryl/amide (π^*), OH/O(p_y)_d_{yz} (π^*), OH/O(p_x)_d_{xz} (π^*) $\rightarrow$ d_{x2-y2}/d_{z2}_O(p_z) (σ^*), O(p_x)_d_{xz} (π^*)	2
13	18828	531	0.0024	O(p_y)_d_{yz} (π^*), amide (π^*) $\rightarrow$ d_{x2-y2}/d_{z2}_O(p_z) (σ^*)	$\uparrow$
18	22319	448	0.0022	amide/aryl (π^*), OH/O(p_z), OH(p_y), d_{yz}_OH/O(p_y) (π/π^*) $\rightarrow$ d_{x2-y2}/d_{z2}_O(p_z) (σ^*)	
20	23255	430	0.0017	aryl/amide (π^*), d_{yz}_OH/O(p_y) (π), OH/O(p_z), O(p_y)_d_{yz} (π^*) $\rightarrow$ d_{x2-y2}/d_{z2}_O(p_z) (σ^*)	3, 4, 5
22	24119	415	0.0028	amide O lone pairs, O(p_y)_d_{yz} (π^*) $\rightarrow$ d_{x2-y2}/d_{z2}_O(p_z) (σ^*), aryl/amides (π^*)	$\downarrow$
26	24515	408	0.0048	amide O lone pairs, amide (π^*), OH/O(p_z) $\rightarrow$ O(p_x)_d_{xz} (π^*), d_{x2-y2}/d_{z2}_O(p_z) (σ^*)	$\blacktriangledown$
27	24695	405	0.0062	amide O lone pairs, amide (π^*), OH/O(p_z) $\rightarrow$ O(p_x)_d_{xz} (π^*), d_{x2-y2}/d_{z2}_O(p_z) (σ^*)	$\blacktriangle$
39	27542	363	0.0031	aryl/amide (π), OH/O(p_z) $\rightarrow$ O(p_x)_d_{xz} (π^*), aryl/amide (π^*)	6
40	27697	361	0.0072	OH/O(p_z), aryl/amide (π) $\rightarrow$ aryl/amide (π^*), O(p_x)_d_{xz} (π^*)	$\downarrow$
44	28604	350	0.0161	aryl/amide (π), OH/O(p_z) $\rightarrow$ aryl/amide (π^*)	$\blacktriangledown$
45	28900	346	0.0222	O(p_y)_d_{yz} (π^*), aryl/amide (π^*) $\rightarrow$ aryl/amide (π^*)	$\blacktriangle$
51	29930	334	0.0276	O(p_y)_d_{yz} (π^*), aryl/amide (π^*) $\rightarrow$ aryl/amide (π^*)	
52	30012	333	0.0171	amide (π^*), d_{yz}_OH/O(p_y) (π), O(p_y)_d_{yz} (π^*) $\rightarrow$ aryl/amide (π^*)	
53	30136	332	0.0089	O(p_y)_d_{yz} (π^*) $\rightarrow$ aryl/amide (π^*)	
54	30206	331	0.0072	amide O lone pairs $\rightarrow$ d_{x2-y2}/d_{z2}_O(p_z) (σ^*)	7
55	30351	330	0.0108	amide (π^*), OH/O(p_z), d_{yz}_OH/O(p_y) (π) $\rightarrow$ aryl/amide (π^*)	
56	30456	328	0.0085	d_{x2-y2}/d_{z2}_O(p_z) (σ^*) $\rightarrow$ aryl/co-ligand (σ^*)	
57	30531	328	0.0299	amide O lone pairs $\rightarrow$ O(p_x)_d_{xz} (π^*), d_{x2-y2}/d_{z2}_O(p_z) (σ^*)	
58	30592	327	0.0276	amide O lone pairs, amide (π^*), OH/O(p_z) $\rightarrow$ d_{x2-y2}/d_{z2}_O(p_z) (σ^*), aryl/amide (π^*)	
59	30709	326	0.0302	amide O lone pairs, Ni(d_{xy}), amide (π^*), d_{yz}_OH/O(p_y) (π^*) $\rightarrow$ O(p_x)_d_{xz} (π^*), d_{x2-y2}/d_{z2}_O(p_z) (σ^*), aryl/amide (π^*)	
60	30918	323	0.0173	amide O lone pairs $\rightarrow$ d_{x2-y2}/d_{z2}_O(p_z) (σ^*)	
62	31270	320	0.0091	amide O lone pairs, O(p_y)_d_{yz} (π^*) $\rightarrow$ d_{x2-y2}/d_{z2}_O(p_z) (σ^*), aryl C-H (σ^*)	
63	31291	320	0.0045	O(p_y)_d_{yz} (π^*) $\rightarrow$ aryl C-H (σ^*)	
64	31540	317	0.0015	amide O lone pairs $\rightarrow$ O(p_x)_d_{xz} (π^*)	$\blacktriangledown$

				amide (π^*), d_{yz}_OH/O(p_y) (π^*) → aryl/amide (π^*)	7
65	31598	317	0.0380		
66	31744	315	0.0103	d_{x2-y2}/d_{z2}_O(p_z) (σ^*) → aryl/co-ligand (σ^*)	
73	32675	306	0.0024	aryl (π), d_{xz}_O/OH(p_x) (π), N/O/OH_Ni (σ), O(p_z)_d_{z2} (σ)→ O(p_x)_d_{xz} (π^*), d_{x2-y2}/d_{z2}_O(p_z) (σ^*)	
86	34276	292	0.0249	Ni(d_{xy}) → d_{x2-y2}/d_{z2}_O(p_z) (σ^*)	
96	35599	281	0.0059	N/OH/O_Ni (σ), amide O lone pair → O(p_x)_d_{xz} (π^*), d_{x2-y2}/d_{z2}_O(p_z) (σ^*)	

[a] TAML^{4-} co-ligand MOs involved in electronic transitions are classified by their location on the TAML^{4-} ring. Here, "co-ligand" refers to the whole TAML^{4-} ligand, "amide O lone pairs" refers to the occupied p orbitals on the O atoms of TAML^{4-}, "co-ligand π" refers generally to amide and aryl π MOs, which can also be referred to separately.

In the visible range of the spectrum (experimental bands 4 - 6), TD-DFT predicts mostly CT transitions originating from aryl/amide(π) and amide-O lone pairs into the d_{x2-y2}/d_{z2}_O(p_z) (σ^*) and O(p_x)_d_{xz} orbitals of the Ni–O unit, none of which have much oscillator strength (calculated bands 18 to 39; see Table 4.3). Finally, a number of calculated bands (44 – 58) with larger oscillator strengths are found in the energy region of band 7. However, these features are mostly intra-co-ligand $\pi \rightarrow \pi^*$ transitions, with some admixture of Ni-O (π^*) → aryl/amide (π^*) and amide-O lone pair → d_{x2-y2}/d_{z2}_O(p_z) (σ^*) and O(p_x)_d_{xz} CT character, with anywhere between 5 – 25% z polarization. Further information on the TD-DFT results and assignments can be found in Table 4.3.

We also performed TD-DFT calculations for the other structures, B3LYP (1) and B3LYP (2), and these results are shown in Figure 4.18. It is notable here that the TD-DFT calculations for valence tautomer B3LYP (1) with the long Ni–O bond (d_{z2} orbital singly occupied) show by far the worst agreement with the experimental absorption spectrum, further indicating that this is not the experimentally observed valence tautomer. Comparing the TD-DFT results for structures B3LYP (2) with the short Ni–O bond (d_{x2-y2} orbital singly occupied) and the analogous B3LYP (3) with the longer Ni–OH bond, it is notable that B3LYP (3) with the weakly coordinated sixth ligand does in fact reproduce the experimental absorption spectrum the best, in support of the EXAFS results.
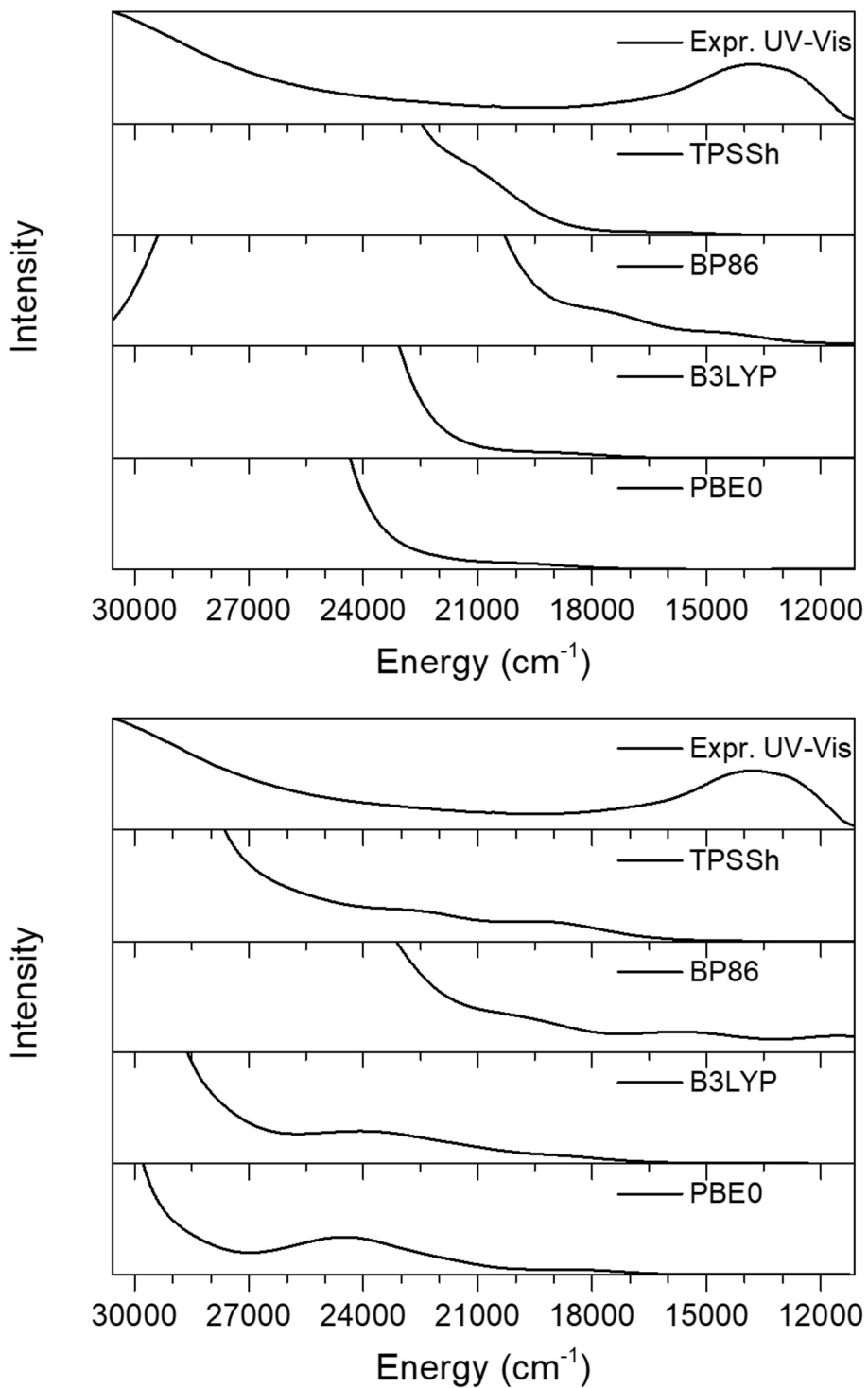
Figure 4.18. TD-DFT calculations using fully optimized structures of the two valence tautomers of 3, performed with the indicated functionals and the basis set TZVP. Top: for structure B3LYP (1), and bottom: for structure B3LYP (2). Compare to Figure 4.17 for the TD-DFT results for structure B3LYP (3). All TD-DFT calculations were performed using ORCA.

4.6 Reactivity Studies of 3 (Nam Group)

The reactivity of **3** in oxygen atom transfer (OAT) and hydrogen atom transfer (HAT) reactions was investigated by our collaborators in the Nam group. **3** was shown to be reactive for OAT, converting thioanisoles to their methyl phenyl sulfoxide, with a quick second-order rate constant (k_2) of 4.3×10^3 M^{-1} s^{-1} at -40 °C. Detailed studies show that the OAT reaction occurs via an electron-transfer mechanism and the Hammet plot indicates an electrophilic nature of **3**. Similarly, **3** was able to oxidize styrene with a second order rate constant (k_2) of 2.5 M^{-1} s^{-1} again in MeCN at -40 °C, with reactivity with substituted styrenes showing OAT occurs with an electron transfer mechanism and the Hammett plot indicating **3** is electrophilic.

3 is also able to activate weak C-H bond activation of hydrocarbons with the bond dissociation energies (BDEs) of $75 - 82$ kcal mol^{-1}. Additionally, **3** reacts with xanthene affording a second-order rate constant (k_2) of 1.2 M^{-1} s^{-1} at 0 °C. These studies support that **3** contains a reactive Ni^{III}-oxyl moiety, as expected from its electronic structure. Additionally, though this is not a catalyst, as it shows similar reactivity, the studies shown herein can provide insight into the electronic structure of intermediates in catalytic cycles of OAT and C-H activation reactions.

4.7 Discussion

In this chapter, the rigorous spectroscopic and theoretical characterization of a terminal Ni-oxyl complex, [Ni(TAML)(O)(OH)]$^{3-}$ (**3**) is presented. This reactive intermediate, formally a Ni^{IV}-oxo complex, is generated by the oxidation of the corresponding four-coordinate Ni^{II}- and Ni^{III}-TAML^{4-} precursors, using either CAN or an O-atom transfer agent like PhIO, at low temperature. Generation of **3** is accompanied by the rise of a new absorption feature at 728 nm in the UV-Vis spectrum. The presence of an oxo-type ligand in **3** is supported by CSI-MS spectroscopy in conjecture with ^{18}O isotope labeling. In agreement with the formal Ni^{IV} state, the complex is EPR silent. For example, upon addition of 1 equivalent of CAN to a solution of the EPR-active Ni^{III} precursor ($S_t = 1/2$), the EPR signal of this species disappears, but can be regenerated when 1 equivalent of reductant is subsequently added. These results demonstrate that complex **3** is a one-electron oxidized species compared to the Ni^{III} precursor. But what is the actual nature of this species? Based on these data, it is tempting to assign **3** as a Ni^{IV} complex. However, there is a reason that Ni^{IV} complexes are sparse, and reports of well-characterized Ni^{IV} complexes in the literature are lacking. Considering the presence of the non-innocent TAML^{4-} ligand in **3**, it is clear

that a thorough spectroscopic characterization is needed to order to make any claims about a high oxidation state of the Ni center in **3**.

From XAS, complex **3** shows a Ni K-edge that has an edge-energy that is essentially identical with that of the Ni^{III} precursor complex, indicating that the oxidation state of the Ni center in **3** is better described as Ni^{III}. EXAFS shows a Ni–O vector at 1.84 Å, again confirming the presence of an oxo-type ligand, but also the presence of a sixth scatterer at about 2.2 Å from the Ni center although the nature of which cannot be identified from those data. Since **3** is EPR silent, we used low-temperature MCD spectroscopy to further delineate the optical and magnetic properties of **3**. Analysis of the VTVH MCD data of the 728 nm feature clearly shows that the intermediate has an $S_t = 1$ ground state with a $[d_{xy},O(p_y)\_d_{yz},O(p_x)\_d_{xz}]^5[d_{x2-y2},d_{z2}]^1$ electron configuration. The 728 nm absorption feature is deconvoluted into three transitions, which, based on the TD-DFT results, corresponds to mixed ligand-to-metal charge transfer (CT) transitions, mostly into $d_{x2-y2}/d_{z2}\_O(p_z)$ (σ^*) as the acceptor MO, in agreement with the mixed polarizations observed for band 2. This indicates the co-ligand oxidation and reduction of the Ni-O unit in the excited state. It is notable that this absorption feature has a quite substantial intensity in the absorption spectrum ($\varepsilon = 2500$ $M^{-1}cm^{-1}$), but that laser excitation of this band does not lead to the resonance enhancement of the Ni-O stretch. The complex shows a relatively small D value of about 4 cm^{-1} and a moderate rhombicity arising from the lack of the four-fold symmetry of the $TAML^{4-}$ ligand.

In order to obtain further insight into the nature of **3**, we then turned to DFT calculations. Structure optimizations with neutral molecules like water, solvent (CH_3CN), ammonia, etc. as the sixth ligand led to five-coordinate structural models for **3**, where the sixth ligand is expelled. However, an anionic ligand like hydroxide is able to stably coordinate to the Ni center, generating a six-coordinate structure in agreement with the EXAFS results. We therefore propose that **3** corresponds to the complex $[Ni(TAML)(O)(OH)]^{3-}$. This complex could in theory exist in either the $S_t = 1$ or 2 state, but the DFT calculations show that the $S_t = 2$ state is >15 kcal/mol higher in energy, in agreement with the MCD result that shows an $S_t = 1$ ground state for **3**. DFT calculations further show that in the $S_t = 1$ state with a $[d_{xy},O(p_y)\_d_{yz},O(p_x)\_d_{xz}]^5[d_{x2-y2},d_{z2}]^1$ electron configuration, the d_{z2} and d_{x2-y2} orbitals are quasi degenerate, which means that the complex can exist in two valence tautomers where either the d_{z2} or the d_{x2-y2} orbital is singly occupied. We were able to generate optimized structures for both valence tautomers and show that they are within 2

kcal/mol (B3LYP). However, the two valence tautomers lead to very different geometric structures for **3**, where single occupation of d_{z^2} (isomer B3LYP (1) in Table 4.2, with the z axis along the Ni–O vector) causes a substantial increase in the Ni–O bond to 2.15 Å, in stark contrast to the experimental data. On the other hand, the valence tautomer, in which $d_{x^2-y^2}$ is singly occupied (isomer B3LYP (2) in Table 4.2), reproduces the experimental Ni–O distance of 1.84 Å exactly. Based on these results, complex **3** has the electron configuration $[d_{xy}^2, d_{yz}^2, d_{xz}^1, d_{x^2-y^2}^1]$ (in the coordinate system applied here), which should give rise to a strong Ni–O bond with a formal bond order of 1.5 (see Figure 4.1), which is somewhat at odds with the experimental Ni–O distance of 1.84 Å.

Further analysis of the electronic structure of $[Ni(TAML)(O)(OH)]^{3-}$ shows that the Ni–O π-bond shows an unprecedented amount of bond inversion, where the antibonding combination of $O(p_x)$ and d_{xz} is largely located on the oxo ligand (82% O(p) character according to the TPSSh calculation). Therefore, the electronic structure of **3** is best described as a low-spin Ni^{III} complex ($S = 1/2$) with a bound oxyl ($O^{\bullet-}$) ligand ($S = 1/2$) where the spins of the Ni and the oxyl are ferromagnetically coupled, giving rise to the observed $S_t = 1$ ground state for **3**. In other words, the oxo group serves as a non-innocent ligand in **3**, in agreement with the XAS results that show that the Ni center in **3** is best described as Ni^{III}. With this large degree of bond inversion, the Ni–O interaction is best described as a single σ-bond, in line with the observed Ni–O distance of 1.84 Å. In contrast, and surprisingly, the $TAML^{4-}$ ligand is innocent, and simply serves as a strongly donating ligand, further stabilizing the Ni–O unit in **3**. These results were further corroborated using post HF computations which were computed by Prof. Jason Shearer. NEVPT2 calculations of **3** show the compound possesses little multiconfigurational character with the leading Ni^{III}-$O^{\bullet-}$ configuration comprising over 99% of the CASSCF wavefunction. Thus, the compound is best described as possessing a Ni^{III}-oxyl moiety coordinated by a redox innocent $TAML^{4-}$ ligand framework.

The fact that **3** contains a Ni^{III}-$O^{\bullet-}$ unit, and not a Ni^{IV} center, is again in agreement with the notion that the Ni^{IV} oxidation state is difficult to stabilize in complexes with organic co-ligands that contain N- and O-donor groups, due to the strongly oxidizing nature of Ni^{IV}. Correspondingly, claims of Ni^{IV} complexes in the literature have to be taken with some skepticism. For example, in a recent study, the preparation of a Ni^{IV}-nitrato complex was claimed.[226] Although the authors note an ~0.7 eV blue-shift of Ni K-edge XAS features of this complex relative to the Ni^{III} starting

material, they also acknowledge the difficulties of making oxidation state assignments on the basis of XANES edge-shifts alone. Furthermore, the authors highlight that both formal Ni[III] and Ni[IV] complexes possess significant ligand non-innocence. Therefore, the authors note that the putative Ni[IV]-nitrato complex can actually be described as a physical d^8 Ni[II] species. In other cases, the difficulty of stabilizing Ni[IV] has also been acknowledged in the literature, for example for complexes [Ni[III](L)(O•)] and [Ni[III](dpaq)(O•)]$^+$ (see Figure 4.2),[210,211] which the authors cautiously describe as Ni[III]-oxyl species (despite the fact that insufficient characterization of these complexes is available to fully support this claim, see discussion in Section 4.1). In addition, bond inversion is a known problem for Ni complexes, and has even been invoked for explaining the photochemistry of Ni[II]-aryl complexes, where a photochemically accessible ligand-field excited state induces inversion of the Ni[II]-C bond, leading to C-H activation of a THF solvent molecule.[227] Based on these considerations, [Ni(TAML)(O)(OH)]$^{3-}$ is, in fact, the first well-characterized, terminal Ni–O complex reported to this date. The quest for a true Ni[IV]-oxo complex continues.

4.8 Experimental

4.8.1 Magnetic Circular Dichroism

The MCD spectroscopy setup uses an Oxford SM4000 cryostat and a JASCO J-815 CD spectrometer. The SM4000 cryostat uses a liquid helium-cooled super conducting magnet, providing magnetic fields of 0-7 T. A gaseous nitrogen-cooled xenon lamp is the light source for the JASCO J-815 CD spectrometer, and the detector is a photomultiplier in the UV-Vis range. The samples are loaded into the Oxford Cryostat variable temperature insert (VTI) chamber, which can reach temperatures 1.5 K – 300 K and has four optical windows made of Suprasil B quartz for optical access to the sample. The temperature was set to 2, 4, 8, 12, 20, and 50 K in sequence and spectra were recorded between 300 and 900 nm at varying fields (-7 to +7 T) for each temperature. The UV-Vis and MCD data were fit using the program PeakFit (v. 4.12) using the fewest Gaussians required, with the quality of fit evaluated by X^2.

4.8.2 Electronic Structure Calculations

Geometry optimization and frequency calculations were performed using Gaussian 09.[228] The functionals B3LYP,[229–231] BP86,[229,232] PBE0,[233] and TPSSh[234–236] were used with the basis set

TZVP for all of these calculations. ORCA (version 4.0)[237] was used to perform the EPR and time-dependent DFT calculations on the corresponding, optimized structures.

4.8.3 Synthesis of Complexes (Nam Group)

Complexes **1**, **2** and **3** were prepared by the Nam group, but the synthesis is provided here for the reader.

Synthesis of [Ni^{II}(TAML)]^{2−} (1). The Li_2[Ni^{II}(TAML)] was synthesized by deprotonating H_4-TAML (200 mg) ligand with lithium bis(trimethylsilyl)amide (3.0 mL of 1.0 M THF solution) under argon atmosphere in dry and deoxygenated tetrahydrofuran (THF) (30 mL) at 25 °C, followed by slow addition of Ni(acac)_2 (210 mg) dissolved in 2 mL CH_3CN. The reaction mixture was stirred overnight and then the solvent was removed on the rotary evaporator, giving dark yellow solid. The solid was dissolved in minimum amount of H_2O and filtered, and the filtrate was evaporated to dryness under reduced pressure, leaving yellow solid of Li_2[Ni^{II}(TAML)]. The complex was further purified using water-acetonitrile mixture. Li_2[Ni^{II}(TAML)] is highly soluble in water but has poor solubility in organic solvents. Hence for all reactions, 5.0 μL of H_2O was used to dissolve **1** which was then added to 2 mL of acetonitrile. To improve solubility of **1** for crystallization, counter-ion Li^+ was exchanged with (K(2.2.2-cryptand))^+. (K(2.2.2-cryptand))_2[Ni^{II}(TAML)] complex was synthesized by stirring the solution of Li_2[Ni^{II}(TAML)] with KCl (excess) and 2,2,2-cryptand (5 eq) in water. The obtained solid was filtered, washed with water, dried and recrystallized in acetonitrile/Et_2O solution. Yellow crystals suitable were successfully grown by storing a solution of [Ni^{II}(TAML)]^{2−} in acetonitrile/diethyl ether (1:10) at 25 °C.

Generation and isolation of [Ni^{III}(TAML)]^− (2). Li[Ni^{III}(TAML)] was generated by oxidizing Li_2[Ni^{II}(TAML)] with 1 eq of CAN in MeCN at 25 °C. **2** is highly stable at room temperature and it does not show reactivity with substrates such as thioanisole, styrene or xanthene. Solid powder was isolated by adding diethyl ether directly into an MeCN solution of Li[Ni^{III}(TAML)]. For crystallization of **2**, cation exchange from Li^+ ion to PPh_4^+ ion was performed by adding 10 eq of PPh_4Cl to a solution of Li[Ni^{III}(TAML)] in MeCN. Single crystals of PPh_4[Ni^{III}(TAML)] were obtained by slow diffusion of Et_2O into a saturated MeCN solution of PPh_4[Ni^{III}(TAML)] at −20 °C.

Generation of [Ni^{IV}(O)(OH)(TAML)]³⁻ (3). 3 was generated by reacting **1** (0.20 mM) with CAN (0.40 mM) in the presence of H_2O (5.0 µL) in MeCN at −40 °C. Alternatively, **3** can also be generated by reacting **1** (0.20 mM) with PhIO (1.5 eq dissolved in trifluoroethanol (TFE)) followed by addition of HOTf (1 eq) in MeCN at −40 °C. For all reactivity studies, **3** was generated by reacting **1** with 1.5 eq PhIO (in TFE) followed by addition of 1 eq of HOTf in MeCN at −40 °C or at 0 °C. **3-¹⁸O** was prepared using PhI¹⁸O instead of PhI¹⁶O. **3** can be generated in more than 95 % yield using other solvents such as acetone, TFE and also mixture of solvents such as acetonitrile:acetone (v/v = 1:9) and acetonitrile:butyronitrile (v/v = 1:2). For characterization techniques (such as EXAFS, MCD, EPR, and ¹H-NMR), higher concentration of **3** was prepared (up to 8.0 mM) in MeCN or mixture solvent depending on the requirement of technique used.

4.9 Appendix for Chapter 4

4.9.1 Tables of Coordinates of DFT Structures

Table 4.4. Coordinates of the fully optimized structure of five-coordinate [Ni(TAML)(O)]$^{2-}$ with $S_t = 1$. Calculated using B3LYP/TZVP.

N	-1.14520500	1.44076900	-0.15831800
N	1.41706000	-1.26376600	-0.02729900
N	1.41704200	1.26379600	-0.02710500
N	-1.14519800	-1.44079600	-0.15822500
O	-3.23317700	-2.32757500	-0.42371600
O	1.83798000	-3.51812400	-0.28895700
O	0.01358400	-0.00012900	2.13695600
O	1.83794800	3.51813600	-0.28894600
C	2.69856400	-0.71309500	0.02130600
C	-0.47041700	-2.75461100	-0.28497900
C	1.06883600	-2.55077900	-0.19246300
C	3.91209000	1.40472900	0.04217400
C	-2.47757000	1.35849800	-0.19484100
C	1.06880600	2.55080300	-0.19233700
C	2.69855900	0.71312900	0.02139600
C	-3.28650100	0.00008900	1.72241200
C	-3.16129100	0.00000100	0.17393900
C	5.11561700	0.69545400	0.06902800
C	3.91210800	-1.40467900	0.04201100
C	-2.47757000	-1.35852800	-0.19468900
C	-4.57419100	-0.00005100	-0.43479400
C	-0.47044000	2.75459500	-0.28501000
C	5.11562500	-0.69539100	0.06894600
C	-0.87154800	-3.70118500	0.86353200
C	-0.87172000	3.70116700	0.86345200
C	-0.74609200	-3.41392800	-1.65211800
C	-0.74598400	3.41390300	-1.65218200
H	3.88949000	-2.48414200	0.03095400
H	6.05427900	-1.24115100	0.09130800
H	6.05426500	1.24122300	0.09144700
H	3.88945700	2.48419200	0.03124500
H	-2.29792900	0.00007700	2.18656200
H	-3.83881200	0.88855300	2.04379000
H	-3.83888400	-0.88829300	2.04388900
H	-5.10689700	0.89640600	-0.12190600
H	-4.53130100	-0.00012500	-1.52702200
H	-5.10688200	-0.89647900	-0.12179200
H	-0.67104800	-3.21901100	1.82302200
H	-1.93389800	-3.93133200	0.79725800
H	-0.28196400	-4.61860000	0.80249800
H	-1.93407400	3.93127300	0.79707000
H	-0.67130500	3.21900400	1.82296500
H	-0.28216900	4.61860500	0.80246500
H	-1.80400800	-3.65297600	-1.73938000
H	-0.47333800	-2.72614500	-2.45713300
H	-0.13789700	-4.31604400	-1.74676000
H	-0.47314100	2.72612000	-2.45716600
H	-1.80389500	3.65293300	-1.73954800
H	-0.13779100	4.31602500	-1.74676900
Ni	0.04375600	-0.00000500	0.15598600

Table 4.5. Coordinates of the fully optimized structure of six-coordinate [Ni(TAML)(O)(OH)]$^{3-}$ with $S_t = 1$, with an optimized Ni-O bond length of 2.15 Å, referred to as **B3LYP (1)**. Calculated using B3LYP/TZVP.

N	-1.17275600	-1.46223800	0.03508400
N	1.42314700	1.27443900	-0.07944500
N	1.42324700	-1.27427600	-0.07975400
N	-1.17308200	1.46187500	0.03493500
O	-3.28413700	2.32264100	0.29801600
O	1.82716400	3.54292300	0.09205200
O	-0.03564700	0.00046800	-2.20183700
O	1.82784000	-3.54263100	0.09227400
O	-3.28358900	-2.32311900	0.29962600
C	2.68991000	0.71863400	-0.14671500
C	-0.47412300	2.75047900	0.24041800
C	1.06671700	2.55293300	0.06392500
C	3.90943300	-1.40315300	-0.20983900
C	-2.49042100	-1.37086800	0.06027200
C	1.06713500	-2.55283600	0.06401800
C	2.69008100	-0.71819400	-0.14490800
C	-3.13143700	-0.00079000	-1.92136900
C	-3.14141500	-0.00045100	-0.36940900
C	5.11683500	-0.69581800	-0.25208800
C	3.91036500	1.40334600	-0.19030300
C	-0.68154500	-3.25865600	1.68529500
H	3.88418000	2.48364700	-0.17959200
H	6.05649100	1.24392200	-0.28687400
H	6.05543800	-1.24370400	-0.30990200
H	3.88314200	-2.48345900	-0.19831700
H	-2.10664800	-0.00079300	-2.30236700
H	-3.65162300	-0.89129000	-2.29384500
H	-3.65180300	0.88943400	-2.29425400
H	-5.10471700	-0.90033100	-0.24930600
H	-4.65861800	-0.00030100	1.20038300
H	-5.10487400	0.89910300	-0.24968200
H	-0.77666300	3.39548200	-1.80198500
H	-1.97525200	4.03226000	-0.65336700
H	-0.30672800	4.69829200	-0.68689800
H	-1.97509600	-4.03425800	-0.64837900
H	-0.77811500	-3.39883700	-1.79935300
H	-0.30625000	-4.69954300	-0.68268500
H	-1.74251200	3.47395600	1.83936100
H	-0.35710700	2.47223800	2.36601600
H	-0.08788000	4.16551900	1.84647000

C	-2.49074800	1.37033900	0.05963800
C	-4.60391100	-0.00049500	0.10856200
C	-0.47352900	-2.75048800	0.24171400
C	5.11648200	0.69602500	-0.26034500
C	-0.92033200	3.79998100	-0.79669000
C	-0.92044600	-3.80172800	-0.79320700
C	-0.68355300	3.26130100	1.68277300

H	-0.35393700	-2.46808500	2.36628300
H	-1.74043200	-3.47052700	1.84346700
H	-0.08611300	-4.16283400	1.85011700
Ni	0.04218100	-0.00000100	-0.05405400
O	0.15594500	0.00009600	2.21338700
H	-0.79343000	0.00115600	2.38388000

Table 4.6. Coordinates of the fully optimized local minimum structure of six-coordinate [Ni(TAML)(O)(OH)]$^{3-}$ with $S_t = 1$, with an optimized Ni-O bond length of 1.84 Å, referred to as **B3LYP (2)**. Calculated using B3LYP/TZVP.

N	-1.21945200	-1.55923700	-0.05975500		C	-0.67152600	-3.31720600	1.62136000
N	1.49742500	1.33824800	-0.06083600		H	3.95669600	2.46813200	-0.10476700
N	1.46590500	-1.31550200	-0.04668600		H	6.11746500	1.20823300	-0.18999200
N	-1.19205000	1.52055300	0.05324200		H	6.08540700	-1.28199100	-0.23866800
O	-3.32051200	2.36634400	0.23990400		H	3.89922700	-2.49266500	-0.16500300
O	1.83958900	3.62358700	0.14505100		H	-2.21072800	0.01730600	-2.25718800
O	0.01490200	0.02112700	-1.87851900		H	-3.74012100	-0.90964200	-2.20414100
O	1.82707400	-3.60412200	-0.01699900		H	-3.77845500	0.87113800	-2.20472700
O	-3.33623300	-2.33043500	0.42331900		H	-5.13254800	-0.88345700	-0.10134000
C	2.72986000	0.73025000	-0.10058600		H	-4.61300300	-0.00632500	1.33380700
C	-0.46246100	2.79914900	0.17535700		H	-5.10996000	0.91586200	-0.08800100
C	1.11905700	2.59783800	0.07554000		H	-0.67958500	3.27108200	-1.92667200
C	3.93556700	-1.41140400	-0.16325700		H	-1.92415900	3.99516200	-0.88674000
C	-2.51942800	-1.42246100	0.09498900		H	-0.25891000	4.66899300	-0.91067000
C	1.09155100	-2.58831300	0.00636600		H	-1.97191200	-4.11035100	-0.68522300
C	2.71113600	-0.72867500	-0.10327600		H	-0.77390500	-3.51550400	-1.85532400
C	-3.22437300	-0.00766400	-1.85211000		H	-0.30756000	-4.78783400	-0.70817300
C	-3.16324900	-0.00509900	-0.30190400		H	-1.79362400	3.67612000	1.64181000
C	5.15337000	-0.72146500	-0.18515700		H	-0.42633500	2.76828300	2.33551800
C	3.96937000	1.38596500	-0.12108300		H	-0.13932000	4.37736700	1.63653200
C	-2.50741600	1.41413600	0.06482000		H	-0.37580900	-2.51744500	2.30324100
C	-4.60500700	0.00744800	0.23997100		H	-1.72374400	-3.55980600	1.78111000
C	-0.47844800	-2.80703600	0.17304900		H	-0.04621100	-4.19971700	1.79249800
C	5.17084600	0.67011900	-0.18136200		Ni	0.02297000	0.00048700	-0.04210100
C	-0.86191300	3.75855400	-0.96556000		O	0.07280400	-0.04139100	1.89362300
C	-0.91399800	-3.88744100	-0.83649800		H	-0.80835300	0.28346200	2.10820500
C	-0.72818900	3.46007800	1.54600300					

Table 4.7. Coordinates of the partially optimized structure of six-coordinate [Ni(TAML)(O)(OH)]$^{3-}$ with $S_t = 1$, with frozen Ni-O and Ni-OH bond lengths of 1.84 and 2.22 Å, respectively, referred to as **B3LYP (3)**. Calculated using B3LYP/TZVP.

N	-1.25685900	-1.50311400	-0.02358300		C	-0.75027400	-3.23676400	1.68693100
N	1.51910500	1.30491600	-0.06915700		H	4.02462100	2.37825500	-0.11741000
N	1.38430000	-1.29551000	-0.08953900		H	6.13816100	1.03653300	-0.21801500
N	-1.12371500	1.50059900	-0.00960200		H	6.01120800	-1.44871900	-0.28264900
O	-3.21149400	2.38571000	0.30380400		H	3.78342300	-2.57857700	-0.21154000
O	1.91637800	3.58174200	0.11129400		H	-2.15701700	0.05084900	-2.29472100
O	0.01970800	0.01777200	-1.96204700		H	-3.71837200	-0.82952100	-2.27400100
O	1.74257800	-3.57253200	0.07002700		H	-3.69968000	0.95071800	-2.27296600
O	-3.39940300	-2.26415000	0.35416300		H	-5.14826900	-0.76513100	-0.19065400
C	2.74091700	0.67913700	-0.12622000		H	-4.63977100	0.12588100	1.24245800
C	-0.39036100	2.77585800	0.21866200		H	-5.08149600	1.03267000	-0.20506100
C	1.17074400	2.57606700	0.06498000		H	-0.67557500	3.46151100	-1.81796400
C	3.85892000	-1.50054400	-0.20815700		H	-1.87548900	4.08276300	-0.66487500
C	-2.56116200	-1.36292800	0.06225900		H	-0.20136700	4.73637400	-0.67533500
C	0.99754400	-2.56883500	0.04343100		H	-2.06683700	-4.06994800	-0.60019900
C	2.66815200	-0.76578600	-0.14346200		H	-0.86795600	-3.51321200	-1.78693100

C	-3.18014600	0.05453600	-1.91058700	H	-0.40896500	-4.76498700	-0.61385200
C	-3.15537500	0.05286600	-0.35945600	H	-1.66683800	3.49889600	1.81556800
C	5.10129600	-0.85411100	-0.22556100	H	-0.30243700	2.47121000	2.34136900
C	3.99946400	1.29687500	-0.14375400	H	-0.00141200	4.16481800	1.84349000
C	-2.44569800	1.41715700	0.04669900	H	-0.41396500	-2.43114900	2.34464100
C	-4.60661400	0.11770700	0.14973400	H	-1.80982900	-3.43656900	1.85831700
C	-0.55399000	-2.76702400	0.22630700	H	-0.15935000	-4.13965900	1.87389200
C	5.17144800	0.53572900	-0.21184000	Ni	0.03652500	0.01766000	-0.12212400
C	-0.82086500	3.84495600	-0.80421400	O	0.10094600	0.00247700	2.09688900
C	-1.00806000	-3.86208400	-0.75979800	H	-0.85065100	0.00454800	2.25202600
C	-0.60999500	3.27245200	1.66471600				

Table 4.8. Coordinates of the fully optimized structure of six-coordinate [Ni(TAML)(O)(OH)]$^{3-}$ with $S_t = 1$. Calculated using TPSSh/TZVP.

N	1.20762000	1.54323200	-0.07089200	C	0.67573800	3.25854900	1.65894900
N	-1.47366900	-1.32690500	-0.06194300	H	-3.92281600	-2.48491600	-0.11742100
N	-1.46711800	1.31699000	-0.05301600	H	-6.09952200	-1.24187200	-0.18223600
N	1.20322100	-1.52613400	-0.03698100	H	-6.09176500	1.25244300	-0.21085600
O	3.33098000	-2.31200000	0.40145900	H	-3.90974800	2.48460900	-0.14285500
O	-1.81724800	-3.62306700	0.08975400	H	2.04278500	-0.01234300	-2.22508800
O	-0.08048900	-0.00434100	-1.90247800	H	3.59029700	0.89906600	-2.29403700
O	-1.82326800	3.61298100	0.04894500	H	3.61097500	-0.88499900	-2.29012300
O	3.32682100	2.30583200	0.45088300	H	5.10745900	0.90355200	-0.30212700
C	-2.71314600	-0.73193100	-0.10799900	H	4.70639700	0.01462800	1.17137500
C	0.47625100	-2.78527500	0.19903900	H	5.10375600	-0.89943500	-0.29005200
C	-1.09368500	-2.59392900	0.04983200	H	0.77710400	-3.48151800	-1.83182400
C	-3.93970600	1.40109000	-0.15092200	H	1.98114200	-4.07313700	-0.66033800
C	2.51275700	1.40478500	0.08757700	H	0.31546100	-4.76074600	-0.68154800
C	-1.09190100	2.58915300	0.03478300	H	1.97996100	4.10716300	-0.60701700
C	-2.70886800	0.72590700	-0.10485300	H	0.78678300	3.55134900	-1.80726000
C	3.08932600	0.00207900	-1.90242600	H	0.31309900	4.79203300	-0.62162700
C	3.14254600	0.00509600	-0.35369900	H	1.75945800	-3.50138000	1.78871700
C	-5.15231700	0.70001300	-0.16855900	H	0.36684600	-2.51881200	2.33253700
C	-3.94757100	-1.40116100	-0.12700700	H	0.10135500	-4.20574700	1.80266600
C	2.51452100	-1.39693700	0.08109700	H	0.36330500	2.44391400	2.31750400
C	4.61662900	0.00550100	0.08096200	H	1.73446300	3.47915000	1.82003100
C	0.47424500	2.78956800	0.19928900	H	0.06221900	4.14788100	1.84838300
C	-5.15619200	-0.69451900	-0.17584100	Ni	-0.02097100	0.00090100	-0.09729100
C	0.92030200	-3.85748400	-0.81392100	O	-0.02549800	0.01219900	1.83103500
C	0.92081000	3.89429200	-0.77629500	H	0.91665700	-0.11704500	2.00803100
C	0.69539000	-3.29849400	1.64038800				

Table 4.9. Coordinates of the fully optimized structure of six-coordinate [Ni(TAML)(O)(OH)]$^{3-}$ with $S_t = 1$. Calculated using BP86/TZVP.

N	-1.22651000	-1.55647300	-0.05522900	C	-0.67419700	-3.27122900	1.67539200
N	1.49914600	1.33768900	-0.04419100	H	3.96328700	2.48681900	-0.09176600
N	1.46802600	-1.31873500	-0.06597100	H	6.14474300	1.21805100	-0.17419600
N	-1.20239700	1.52528000	0.00018900	H	6.11442100	-1.29039100	-0.23546900
O	-3.34148200	2.34150500	0.37343700	H	3.90743000	-2.51227500	-0.17648700
O	1.83902300	3.64449400	0.11847300	H	-2.04512700	0.02734800	-2.22708100
O	0.05340400	0.02290400	-1.90027600	H	-3.59523200	-0.90942300	-2.30534800
O	1.82961300	-3.62374500	0.03816800	H	-3.63494300	0.88609800	-2.30240400
O	-3.35831000	-2.31744800	0.46964300	H	-5.14402600	-0.89532900	-0.30333000
C	2.73462100	0.73296100	-0.09987600	H	-4.73303400	-0.01161400	1.18201900
C	-0.47234700	2.79674400	0.20332200	H	-5.12742300	0.92168600	-0.28198800
C	1.11259700	2.60904200	0.06924400	H	-0.75793000	3.41699800	-1.86140200
C	3.94984900	-1.42110000	-0.17259900	H	-1.97564300	4.06572300	-0.71657600
C	-2.53768100	-1.41317700	0.10066500	H	-0.29347100	4.74758100	-0.75129500

C	1.08801500	-2.59928400	0.02642200
C	2.71711800	-0.73355400	-0.11491900
C	-3.10355800	-0.00129000	-1.90664400
C	-3.16422900	-0.00354900	-0.35317300
C	5.17312900	-0.72671000	-0.18274100
C	3.98229300	1.39490900	-0.11438800
C	-2.52664100	1.40489100	0.08334600
C	-4.64266700	0.00437100	0.08384000
C	-0.48710500	-2.80320500	0.20717900
C	5.18953600	0.67559900	-0.17526200
C	-0.90731500	3.83722700	-0.85399100
C	-0.93913400	-3.91070200	-0.77130900
C	-0.70621900	3.35294100	1.63174800

H	-2.00316200	-4.13101400	-0.59217100
H	-0.81639700	-3.55898800	-1.80862200
H	-0.32022100	-4.81205000	-0.62757700
H	-1.78007800	3.55491200	1.76751400
H	-0.37694400	2.59196200	2.35670500
H	-0.11236800	4.27216100	1.77566100
H	-0.36501500	-2.44124600	2.33044600
H	-1.73807800	-3.49984200	1.84535200
H	-0.04792500	-4.15986200	1.86976500
Ni	0.02116600	0.00196200	-0.11441300
O	0.04567600	-0.03007600	1.85613600
H	-0.88315000	0.21304100	2.02605100

Table 4.10. Coordinates of the fully optimized structure of five-coordinate $[Ni(TAML)(O)]^{2-}$ with $S_t = 2$. Calculated using B3LYP/TZVP.

N	1.15057000	-1.45468300	-0.11276900
N	-1.44516500	1.27240600	0.05519300
N	-1.44594600	-1.27257600	0.05793100
N	1.15139000	1.45430200	-0.11318900
O	3.22423800	2.30612000	-0.58286000
O	-1.84564900	3.50385500	-0.38978100
O	0.08607600	0.00138300	2.29961500
O	-1.84713900	-3.50320900	-0.39037700
O	3.22275900	-2.30695800	-0.58437400
C	-2.71595800	0.71725400	0.03152800
C	0.45669000	2.73735800	-0.33148200
C	-1.08832800	2.53699400	-0.20761100
C	-3.93445400	-1.40265700	-0.02393400
C	2.47497500	-1.36175800	-0.25131600
C	-1.08951700	-2.53683700	-0.20698200
C	-2.71640600	-0.71668600	0.03273100
C	3.38758300	-0.00102800	1.64663300
C	3.17634200	-0.00068900	0.10979900
C	-5.13694500	-0.69485800	-0.07585800
C	-3.93366100	1.40382300	-0.02603000
C	2.47575900	1.36108000	-0.25085400
C	4.56461000	-0.00096800	-0.55590400
C	0.45547900	-2.73747900	-0.33143700
C	-5.13654400	0.69661600	-0.07676400
C	0.87720800	3.78529600	0.71818700
C	0.87601000	-3.78592500	0.71775100

C	0.69288600	3.27985100	-1.75879500
C	0.69102200	-3.27952800	-1.75901600
H	-3.91061800	2.48357600	-0.04339800
H	-6.07453500	1.24275900	-0.11867400
H	-6.07524200	-1.24053200	-0.11689000
H	-3.91201300	-2.48244400	-0.03985900
H	2.43913100	-0.00097900	2.18324100
H	3.95617900	-0.88916600	1.93882900
H	3.95656100	0.88674500	1.93914900
H	5.11033800	-0.89732100	-0.26554400
H	4.47713100	-0.00109200	-1.64441400
H	5.11050300	0.89532600	-0.26573300
H	0.71176800	3.38907200	1.72321200
H	1.93538700	4.01705700	0.59995000
H	0.27727300	4.68990100	0.59691300
H	1.93430500	-4.01728600	0.59966600
H	0.71006300	-3.39045100	1.72299000
H	0.27646300	-4.69068800	0.59571400
H	1.74586400	3.51806400	-1.89337100
H	0.40752600	2.52148000	-2.49268900
H	0.07269500	4.16417500	-1.91631900
H	0.40629100	-2.52053000	-2.49251800
H	1.74375400	-3.51859100	-1.89392000
H	0.06997100	-4.16318600	-1.91679100
Ni	-0.00812600	-0.00002500	0.59887900

Table 4.11. Coordinates of the fully optimized structure of six-coordinate $[Ni(TAML)(O)(OH)]^{3-}$ with $S_t = 2$. Calculated using B3LYP/TZVP.

N	1.22270800	1.55799000	-0.10036000
N	-1.48852400	-1.32648900	-0.19212700
N	-1.46999400	1.31400600	-0.10444600
N	1.19390200	-1.53149200	-0.01088300
O	3.30349200	-2.33650900	0.42533300
O	-1.85448400	-3.58631600	0.17049300
O	0.06053700	0.01208800	-2.14838000
O	-1.82958400	3.59403100	0.08070700
O	3.31754700	2.30299000	0.50110400
C	-2.72921300	-0.72665300	-0.15852300

C	0.65452600	3.19699200	1.69539200
H	-3.94801400	-2.47089500	-0.13350200
H	-6.11288800	-1.22101600	-0.06839600
H	-6.09538800	1.26936500	-0.04400800
H	-3.91256800	2.48973500	-0.04975800
H	2.28223000	-0.03718600	-2.28167100
H	3.81140300	0.87124400	-2.17720400
H	3.83041500	-0.90807200	-2.15796100
H	5.13480000	0.88172500	-0.05627900
H	4.59746900	0.00447900	1.37295800

C	0.45118800	-2.78542900	0.22370500	H	5.12108800	-0.91654800	-0.03798700
C	-1.11779000	-2.58119300	0.04522300	H	0.76971400	-3.50764400	-1.79912100
C	-3.94531500	1.40904900	-0.08549100	H	1.95042600	-4.10370300	-0.61398400
C	2.51669900	1.40954000	0.10760300	H	0.28185700	-4.76781800	-0.64497500
C	-1.09159800	2.58406200	0.03543700	H	1.97333400	4.14851200	-0.54384600
C	-2.71875200	0.72933600	-0.11783200	H	0.78630700	3.63730600	-1.76320600
C	3.27476000	-0.02050200	-1.83018700	H	0.30988300	4.82640900	-0.53348400
C	3.17288600	-0.00511200	-0.28381800	H	1.69709200	-3.48853800	1.85122900
C	-5.15938300	0.71350900	-0.06192400	H	0.30797100	-2.48011400	2.34585500
C	-3.96490900	-1.38914700	-0.12717500	H	0.03812700	-4.17403500	1.84669700
C	2.50409600	-1.41075100	0.11452300	H	0.34121600	2.34752400	2.30838100
C	4.60565800	-0.01019600	0.28055000	H	1.70514500	3.42244100	1.88546300
C	0.47534800	2.79075400	0.21282300	H	0.03206700	4.07012100	1.91741100
C	-5.16970500	-0.67784100	-0.09729800	Ni	-0.01069500	0.00331800	-0.30580700
C	0.89626900	-3.87284200	-0.77572600	O	-0.11102500	0.01002400	1.95187300
C	0.91698000	3.93629100	-0.71878400	H	0.82444600	-0.13274800	2.13515400
C	0.64072900	-3.27686900	1.67658800				

Table 4.12. Coordinates of the fully optimized structure of six-coordinate $[\text{Ni(TAML)(O)(OH)}]^{3-}$ with $S_t = 2$. Calculated using TPSSh/TZVP.

N	-1.20836300	-1.53173300	-0.07024800	C	-0.63894600	3.15860600	1.72903200
N	1.46843600	1.31495100	-0.17809300	C	-0.63650000	-3.15645900	1.73132000
N	1.46860300	-1.31400700	-0.17581700	H	3.91694400	2.48501200	-0.07089600
N	-1.20886500	1.53109600	-0.07073400	H	6.09546200	1.24748000	0.00195500
O	-3.30394600	2.28798000	0.54007000	H	6.09632900	-1.24672200	-0.01873400
O	1.83112200	3.58207700	0.17399400	H	3.91717400	-2.48425200	-0.08591700
O	-0.03336500	-0.00177400	-2.17420200	H	-2.18862700	-0.00128600	-2.25272600
O	1.83234500	-3.58162400	0.17197400	H	-3.73465500	-0.89361800	-2.20115300
O	-3.30273800	-2.28802200	0.54385400	H	-3.73529600	0.89005300	-2.20197000
C	2.71491600	0.72782800	-0.15343300	H	-5.11959800	-0.90233700	-0.14627800
C	-0.46596000	2.76462000	0.24446100	H	-4.64969600	-0.00050900	1.29971500
C	1.09265100	2.57309100	0.05390100	H	-5.11985800	0.90041300	-0.14685000
C	3.94584600	-1.40114100	-0.10598600	H	-0.81648100	3.62139300	-1.72085900
C	-2.50833600	-1.39199400	0.13214900	H	-1.98012900	4.12672400	-0.47044600
C	1.09337700	-2.57272800	0.05322700	H	-0.30975500	4.80061700	-0.48565300
C	2.71488400	-0.72658800	-0.15090700	H	-1.97942400	-4.12805700	-0.46563300
C	-3.20160100	-0.00142900	-1.84389400	H	-0.81708700	-3.62418400	-1.71787000
C	-3.16064500	-0.00070200	-0.29685500	H	-0.30889200	-4.80156800	-0.48154500
C	5.15492200	-0.69688000	-0.04481200	H	-1.69402300	3.36804800	1.92352100
C	3.94521100	1.40188000	-0.08869500	H	-0.30513900	2.30701800	2.33082700
C	-2.50905700	1.39141500	0.13058900	H	-0.02337900	4.03954500	1.94657200
C	-4.61314400	-0.00077400	0.20733700	H	-0.30327500	-2.30324000	2.33118000
C	-0.46498100	-2.76464400	0.24591200	H	-1.69122900	-3.36665200	1.92689600
C	5.15536100	0.69764000	-0.05390800	H	-0.01986500	-4.03639900	1.94993400
C	-0.92655000	3.91468000	-0.67122900	Ni	0.00654500	0.00004400	-0.40856000
C	-0.92609000	-3.91604400	-0.66772800	O	0.12500400	0.00064700	1.86299000
				H	-0.83098700	0.00258400	2.01237700

Table 4.13. Coordinates of the fully optimized structure of six-coordinate $[\text{Ni(TAML)(O)(OH)}]^{3-}$ with $S_t = 2$. Calculated using PBE0/TZVP.

N	-1.20774700	-1.53366300	-0.07487400	C	-0.63411300	-3.15827300	1.70291600
N	1.46898400	1.31446400	-0.16985700	H	3.90402600	2.47912800	-0.07606800
N	1.46913200	-1.31416200	-0.16901900	H	6.08091600	1.24418500	-0.01505600
N	-1.20795100	1.53324300	-0.07484100	H	6.08162400	-1.24404900	-0.03531100
O	-3.29573300	2.28677100	0.51003200	H	3.90418600	-2.47891600	-0.09126300

O	1.82107900	3.57456600	0.14430400	H	-2.20620700	-0.00047600	-2.25956700
O	-0.03282700	-0.00079600	-2.09955300	H	-3.74623100	-0.89197000	-2.18427900
O	1.82175600	-3.57398900	0.14644000	H	-3.74652100	0.89059700	-2.18457000
O	-3.29526500	-2.28685100	0.51135000	H	-5.10047200	-0.90193000	-0.12136400
C	2.70755100	0.72613800	-0.14798100	H	-4.61302600	-0.00021000	1.31511100
C	-0.46569100	2.75778800	0.22722900	H	-5.10053100	0.90119800	-0.12157600
C	1.09141000	2.56780900	0.03981200	H	-0.80465500	3.59507300	-1.73913100
C	3.93488000	-1.39570900	-0.11015800	H	-1.97296100	4.10935900	-0.49925800
C	-2.50076400	-1.39417800	0.11944200	H	-0.30282000	4.78327400	-0.51322700
C	1.09180600	-2.56751400	0.04123100	H	-1.97206100	-4.10994800	-0.49828700
C	2.70752100	-0.72551400	-0.14578800	H	-0.80337300	-3.59599200	-1.73794900
C	-3.21050900	-0.00054000	-1.83223000	H	-0.30186900	-4.78367100	-0.51135600
C	-3.15044900	-0.00028900	-0.29464200	H	-1.68885500	3.36424000	1.89952700
C	5.14107300	-0.69415800	-0.05665600	H	-0.29684700	2.31093100	2.30728400
C	3.93438400	1.39590400	-0.09292800	H	-0.02169400	4.04161700	1.91582400
C	-2.50105500	1.39392800	0.11889800	H	-0.29836300	-2.30954000	2.30793800
C	-4.58982300	-0.00030900	0.22271000	H	-1.68890600	-3.36461800	1.90007800
C	-0.46531000	-2.75782200	0.22818600	H	-0.02096500	-4.04017700	1.91777500
C	5.14144500	0.69433400	-0.06524800	Ni	0.01012000	-0.00004200	-0.34766700
C	-0.91853600	3.89659500	-0.69248300	O	0.11025400	0.00054600	1.85044900
C	-0.91758800	-3.89711200	-0.69122500	H	-0.83246900	0.00225300	2.03767300
C	-0.63395400	3.15886600	1.70186100				

Chapter 5 Spectroscopic and Theoretical Characterization of a Phenoxyl Radical Trapped by a Non-Heme High-Spin Iron(II) Center

In this chapter, a reactive Fe^{II} species is shown to be the first $Fe^{II}(OPh^\bullet)$ complex through spectroscopic and theoretical investigations. This research was performed in collaboration with Prof. Kallol Ray's group, who synthesized the complexes, performed the initial characterization, and reactivity studies. Dr. Eckhard Bill and Alexander Schnegg performed the Mössbauer and EPR spectroscopies. This chapter is adapted from Kass, Dustin[‡]; **Larson, Virginia**[‡]; Corona, Teresa; Kuhlmann, Uwe; Hildebrandt, Peter; Lohmiller, Thomas; Schnegg, Alexander; Eckhard, Bill; Lehnert, Nicolai*; Ray, Kallol*; "Trapping of a Phenoxyl Radical at a Non-Heme High-Spin Iron(II) Center", *Nat. Chem.* **2024**, which has been published, but not yet assigned volume, issue, and page numbers.[151] The double dagger indicates Dustin Kass and Virginia Larson are co-first authors on this manuscript.

5.1 Introduction

Reaction of Fe^{II} molecular complexes with oxidants such as oxygen gas usually causes oxidation of the Fe^{II}. This could yield an Fe-superoxide, Fe-(hydro)peroxide or $Fe^{IV}=O$ type species, or a similar moiety bridged between two Fe centers, see the Introduction Section 1.3 for further discussion. These have been well studied and have characteristic spectroscopic markers: superoxide ($O_2^{\bullet-}$) moieties show O-O stretches near 1100 cm^{-1} and (hydro)peroxide (O_2^{2-}) near 800 cm^{-1}. The reaction of Fe(TMC) with oxygen follows this chemistry, producing a mild oxidant $Fe^{IV}(O)$ (TMC = 1,4,8,11 tetramethyl–1,4,8,11–tetraazacyclotetradecane). Specifically, the reaction of $[Fe^{II}(TMC)(CH_3CN)]^{2+}$ with O_2 in CH_3CN in the presence of scandium triflate ($Sc(OTf)_3$) and BPh_4^- at 25 °C leads to the formation of the complex $[Fe^{IV}(O)(TMC)(CH_3CN)]^{2+}$.[238] This same reaction can occur with $HClO_4$ as a replacement for the Lewis acid $Sc(OTf)_3$, see Figure 5.1. Interestingly, this is more than a simple oxidation reaction, as the reductant $NaBPH_4$ is unstable under these conditions and decays via an autocatalytic radical

chain mechanism forming phenol (PhOH, 28%), biphenyl (Ph−Ph, 31%), and diphenylborinic acid (Ph$_2$B(OH), 41%) as BPh$_4^-$-derived products, see Figure 5.3.

5.1.1 Ligand Effects: TMC versus TMCO
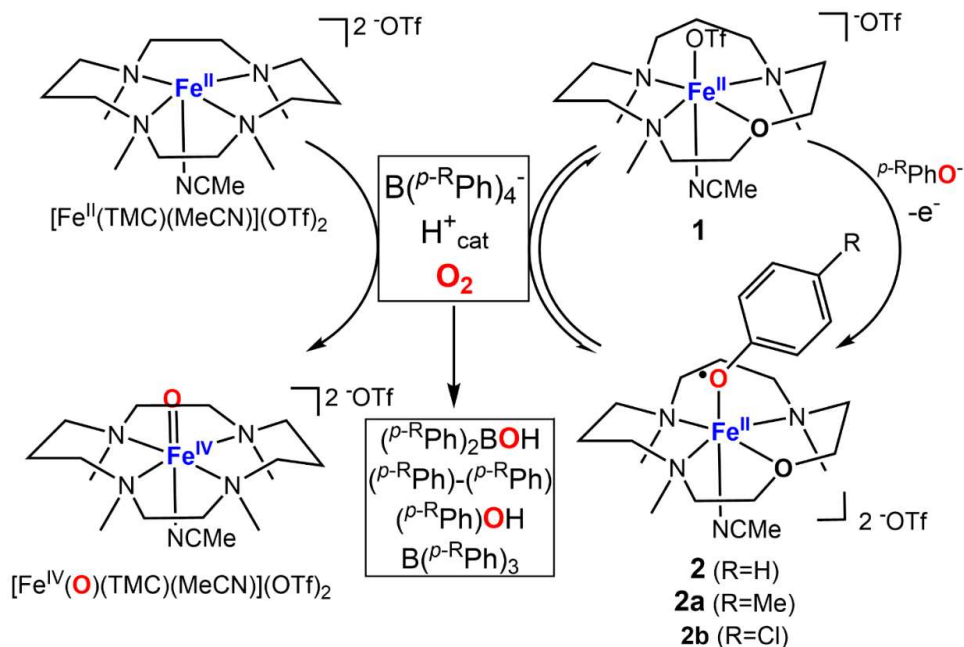
Figure 5.1. O$_2$ activation at [Fe^{II}(TMC)(CH$_3$CN)](OTf)$_2$ and [Fe^{II}(TMCO)(CH$_3$CN)(OTf)](OTf) (**1**) centers in the presence of NaB($^{p\text{-}R}$Ph)$_4$ and H$^+$ ions yielding [Fe^{IV}(O)(TMC)(CH$_3$CN)]](OTf)$_2$ and **2**, respectively, as well as the alternative synthesis of **2** by (electro)chemical oxidation of **1** in presence of $^{p\text{-}R}$PhO$^-$ anions. This figure was made by Dustin Kass in the Ray group.[151]

When one nitrogen donor in the TMC co-ligand is swapped for oxygen, the reactivity is modified. The Ray group has previously shown that the sluggish oxidant [Fe^{IV}(O)(TMC)(CH$_3$CN)]$^{2+}$ is transformed into a highly reactive oxidant [Fe^{IV}(O)(TMCO)(OTf)]$^+$ (TMCO = 4,8,12-trimethyl-1-oxa-4,8,12-triazacyclotetradecane) upon replacement of an NMe donor in TMC by an oxygen atom.[239] The higher reactivity of [Fe^{IV}(O)(TMCO)(OTf)]$^+$ relative to [Fe^{IV}(O)(TMC)(CH$_3$CN)]$^{2+}$ can be explained by a large positive shift of the measured Fe^{IV}/Fe^{III} potential comparing [Fe^{IV}(O)(TMC)(CH$_3$CN)]$^{2+}$ (0.37 V *vs* SCE) and [Fe^{IV}(O)(TMCO)(OTf)]$^+$ (+0.90 V *vs* SCE).[239]

This also affects the reactivity of the Fe^{II}(TMCO) complex with NaBPh$_4$, O$_2$ and H$^+$ (Figure 5.1). Although the radical chain mechanism is valid for the reactions of both **1** and [Fe^{II}(TMC)(CH$_3$CN)$_2$]$^{2+}$ with BPh$_4^-$ and H$^+$ in O$_2$-saturated CH$_3$CN solutions, the nature of the products formed in the two cases is different. With TMCO as a co-ligand, this reaction produced

a species distinct from the known $Fe^{IV}(O)(TMCO)$, and though initially thought to be a superoxide or peroxide type species, did not fit the spectroscopic markers for such a species.

This unknown species, complex (**2**), was identified as an Fe^{II}–$OPh^•$ through careful synthetic and spectroscopic investigations by Dustin Kass and spectroscopic investigation and density functional theory calculations by me. The $PhO^•$ radical is generated via an autocatalytic radical chain mechanism in the reaction of sodium tetraphenylborate ($NaBPh_4$), dioxygen (O_2) and catalytic amounts of H^+. Complex **2** represents an extremely rare example of a spectroscopically characterized O_2-derived iron(II)-radical intermediate in biological and chemical oxidation reactions, considering both heme[240–242] and non-heme[243] iron active sites. The redox potential (0.94 V vs. NHE)[244] necessary for the generation of phenoxyl radicals is relatively high as compared to metal-centered oxidation potentials such as those for Fe^{II}/Fe^{III} and Co^{II}/Co^{III} couples, and so a phenoxy radical is usually able to oxidize Fe^{II} or Co^{II} species.

5.1.2 Iron(II) Coupled Radical Species in Biology

Iron(II)-radical interactions, such as proposed in isopenicillin N synthase (IPNS)[245] and pterin-dependent hydroxylases, are thought to play a vital role in the functioning of non-heme iron enzymes, yet there is no direct spectroscopic evidence that would provide unambiguous proof for these proposed intermediates. Even in heme chemistry, a controversy remains concerning the exact electronic structure of the oxy intermediate in hemoglobin, either iron(II)-dioxygen or iron(III)-superoxide, dating back to pioneering work of Pauling, Monod, and Perutz starting in the 1930s.[240,241] Metal-phenoxyl radical interactions,[246–250] especially using tyrosyl radicals, have been implicated in various enzymatic reactions such as the R2 subunit of the non-heme diiron enzyme ribonucleotide reductase (RNR)[251–253] and the active sites of galactose oxidase (GO)[247,254–256] and glyoxal oxidase (GLO).[257–260] A related Fe^{II} radical in biology is the Fe^{II}-(semiquinonate) intermediate formed after O_2 binding in non-heme iron ring cleaving dioxygenases.[243,261–266] Nevertheless, the involvement of iron(II)-reactive intermediates in oxygenase chemistry is controversial.[265] The strongest evidence comes from the X-ray structure of the Fe/O_2 adduct of an extradiol dioxygenase,[243] in which the radical character of the bound aromatic substrate is inferred from its non-planar geometry.

5.1.3 Reactivity of Phenoxy Radicals in Synthetic Inorganic Chemistry

The high reactivity of a bare phenoxyl radical has also eluded the isolation of metal-($^{\bullet}$OPh) cores in synthetic chemistry. A limited number of metal-phenoxyl radical complexes known in the literature have been synthesized by chemical or electrochemical oxidation of the respective metal-phenolate precursors.[267–269] These complexes involve metal centers that are difficult to oxidize (for example Fe^{III},[269–271] Cu^{II} and Ni^{III}[272]) and include electronically and sterically modified phenolates, such as bidentate catecholate,[273] *o*-aminophenolate,[274] or ortho and para substituted monodentate phenolates that are appended to macrocyclic ligands.[269,275]

5.1.4 Scope of this Chapter

In this chapter, we show that by tuning the electronic properties of the auxiliary ligand, it is possible to bind a phenoxyl radical at an Fe^{II} center to form a Fe^{II}–OPh$^{\bullet}$ complex (**2**). Complex **2** is shown to be a high spin Fe^{II} center ferromagnetically coupled to a phenoxy radical ligand, $[Fe^{II}(TMCO)(OPh^{\bullet})(CH_3CN)]^{2+}$, where the in-situ formed phenoxyl radical (PhO$^{\bullet}$), generated by the radical chain reaction in Figure 5.3, is trapped at the (TMCO)Fe^{II} center to form **2**. This assignment is supported by Mössbauer and electron paramagnetic resonance (EPR) spectroscopies by the Bill group; UV-Vis absorption spectroscopy by the Ray group; and magnetic circular dichroism (MCD), resonance Raman (rRaman), and density functional theory calculations by me. This research, therefore, establishes a strategy for stabilizing an oxidation-prone ferrous center in the presence of highly oxidizing O_2 and PhO$^{\bullet}$. This opens up the possibility for the PhO$^{\bullet}$ cofactor, with its full oxidizing capabilities, to act as an independent redox center next to a Fe^{II} site during substrate oxidation reactions, analogous to the Cu^{II}-(Tyr-Cys$^{\bullet}$) cofactor in GO and GLO. It also stresses the importance of a combined study involving theoretical and advanced spectroscopic methods to unravel the complicated electronic structures of biologically relevant coordination motifs.

5.2 Synthesis of the Intermediate (Ray Group)
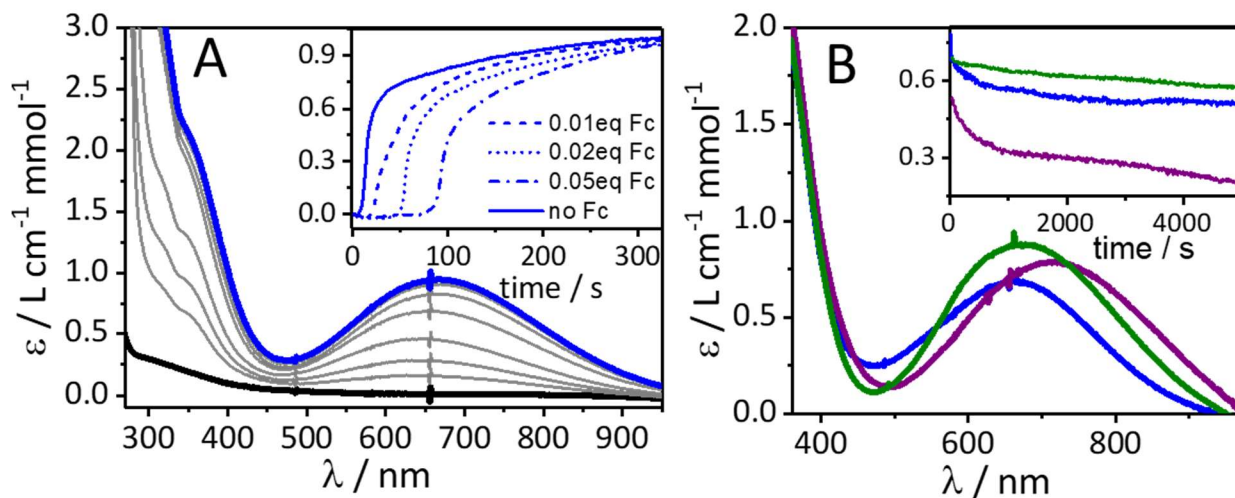
Figure 5.2. A) UV-Vis spectral changes associated with the formation of **2** (blue) starting from **1** (black) by addition of excess O_2, NaBPh$_4$ (1.3 eq) and HClO$_4$ (0.5 eq) in CH$_3$CN at 0 °C. Inset: Time traces for the formation of **2** with different amounts of Fc showing a sigmoidal feature with an increase of the induction time with increasing amount of Fc (straight no Fc, dashed 0.01 eq Fc, dotted 0.02 eq Fc, dashed and dotted 0.05 eq Fc). B) Comparison of the UV-Vis spectra of **2**, **2a** and **2b** Inset: time traces of the decay of the characteristic ~700 nm band associated with **2**, **2a** and **2b** at 10 °C. This figure was made by Dustin Kass in the Ray group, who also collected and analyzed the data shown in the figure.[151]

The title intermediate was synthesized by the Ray group. The corresponding complex [Fe^{II}(TMCO)(CH$_3$CN)(OTf)]$^+$ (**1**)[239] reacts with BPh$_4^-$ and HClO$_4$ in CH$_3$CN at 0 °C to form a deep blue species **2**. Its intense absorption bands at 360 and 665 nm ($\varepsilon \sim$ 4400 and 2800 M^{-1} cm^{-1}; Figure 5.2A) are clearly distinct from the absorption spectrum of the previously reported complex [Fe^{IV}(O)(TMCO)(OTf)]$^+$ and similar to that of the spectrum reported for a rare example of an iron(II) center bound to an iminobenzosemiquinonate (ISQ) radical.[239,276] The related deep blue species **2a** and **2b** were observed in reactions of **1** with O$_2$ and H$^+$ in the presence of B($^{p\text{-}Me}$Ph)$_4^-$ or B($^{p\text{-}Cl}$Ph)$_4^-$, respectively, containing methyl or chloride substitutions in the *para* position of the phenyl groups. Notably **2**, **2a** and **2b** differ slightly with respect to the energy of their characteristic absorption at ~660 nm (Figure 5.2B) and also in their self-decay rates (Figure 5.2B, inset), which suggest incorporation of the $^{p\text{-}R}$Ph group from B($^{p\text{-}R}$Ph)$_4^-$ (R = -H, -Me or -Cl) into complexes **2**, **2a** and **2b**. The formation of **2** is reversible, only requires catalytic acid, inhibits the autocatalytic degradation of BPh$_4$, and shows an induction period when ferrocene (Fc) is added all of which supports the formation mechanism shown in Figure 5.3.
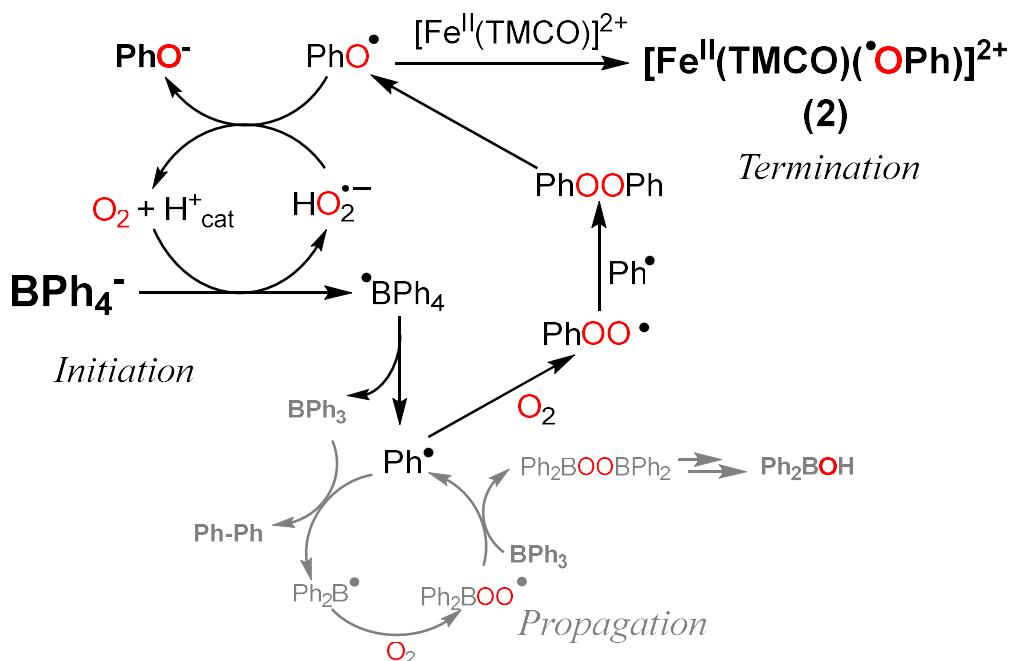
Figure 5.3. H^+ and O_2 promoted electron-transfer chain reactions for formation of **2** in reaction of **1** with O_2 and BPh_4^-. The proposed mechanism is based on previous proposals[238,277] for the decomposition mechanism of BPh_4^- and the Sc^{3+}-promoted electron-transfer chain reactions for formation of $[Fe^{IV}(O)(TMC)(CH_3CN)]^{2+}$. This figure was made by Dustin Kass in the Ray group.[151]

5.3 Alternative Synthesis of 2 (Ray Group)

Consistent with its $[Fe^{II}(TMCO)(OPh^\bullet)(CH_3CN)]^{2+}$ assignment, the Ray group was able to synthesize complex **2** by the (electro)chemical oxidation of **1** in presence of phenol (PhOH) or phenolate (PhO⁻), showing the same characteristic absorption band at 665 nm, albeit in lower yields. The use of different para-substituted phenols ($^{p\text{-}X}$Ph-OH; X=CH$_3$ or Cl) in the reaction can reproduce the absorption bands of **2a** and **2b** obtained by **1**/O_2/BPh_4^-/H^+ reaction. The spectroscopic properties (MCD, Mössbauer, rRaman, UV-Vis absorption) of **2** obtained from both synthesis methods are comparable (see below), further supporting our assignment.

5.4 First Set of Characterization of 2 (Bill and Ray Groups)

Dustin Kass in the Ray group performed and analyzed the initial characterization of the complex. Mass spectrometry showed incorporation of a OPh moiety into **2**, with sensitivity to ^{18}O labeling and modification of the phenyl ring, as in **2a**. Paramagnetic ^{1}H-NMR spectroscopy

confirms the paramagnetic and symmetric nature of **2** with identification of six peaks over a broad range of more than 400 ppm.

5.4.1 Electron Paramagnetic Resonance (Bill Group)

The EPR spectroscopy was performed and data were analyzed by Ray's collaborators, Eckhard Bill and Alexander Schnegg. The X-band EPR spectrum of **2** shows a narrow signal at the spectral position of an effective g value $g_{eff} = 4.3$ from unidentified iron(III) impurities, but in fact the major part of the absorption belongs to another $S_t = 5/2$ species. This contribution could be simulated with nearly axial zero-field splitting parameters, $D = +3$ cm^{-1} and $E/D = 0.07$ (ca. 85%). Note that a reasonable fit to the X-band EPR spectrum can also be obtained by a $S_t = 3/2$, however, because of the large g-values required to match the intensity maximum of the EPR spectrum we discard the possibility of $S_t = 3/2$. The aryl substituted compounds **2a** and **2b** also show near identical $S_t = 5/2$ signals with highly similar turning points as that assigned to **2** emphasizing the electronic similarity of the compounds.

5.4.2 Mössbauer (Bill Group)

The Mössbauer spectroscopy and analysis was performed by Ray's collaborators, Eckhard Bill and Alexander Schnegg. The zero-field Mössbauer parameters of **2** (quadrupole splitting ΔE_Q = 3.28 mm s^{-1} and isomer shift $\delta = 1.32$ mm s^{-1}) are similar to those of **1** ($\Delta E_Q = 2.91$ mm s^{-1}, $\delta =$ 1.15 mm s^{-1}), and both sets are unique for Fe^{II} with a local high-spin state $S_{Fe} = 2$. The increased δ and ΔE_Q in **2** presumably reflect the different bonding situation at iron with lower s-electron density and higher asymmetry in the distribution of the valence charge.[278] Nevertheless, the Mössbauer spectrum of **2** reveals unambiguously that the Fe^{II} oxidation state of **1** remains unchanged upon reaction with O$_2$ in the presence of NaBPh$_4$ and HClO$_4$ forming **2**.

The different total spin states of $S_t = 2$ for **1** and $S_t = 5/2$ for **2**, as evident from EPR and magnetic susceptibility measurements, are corroborated by magnetic Mössbauer spectra. The hyperfine structure and specifically the field dependence could be reasonably well simulated with $S_t = 5/2$ and the spin Hamiltonian parameters D, E/D, and g, as obtained from the EPR fit above. Reasonable fits of the magnetic Mössbauer spectra of **2** can also be obtained with $S_t = 3/2$; however, the extreme A values and the systematic misfit at 160 K, 7 Tesla led them to discard this solution.

5.5 Resonance Raman Studies
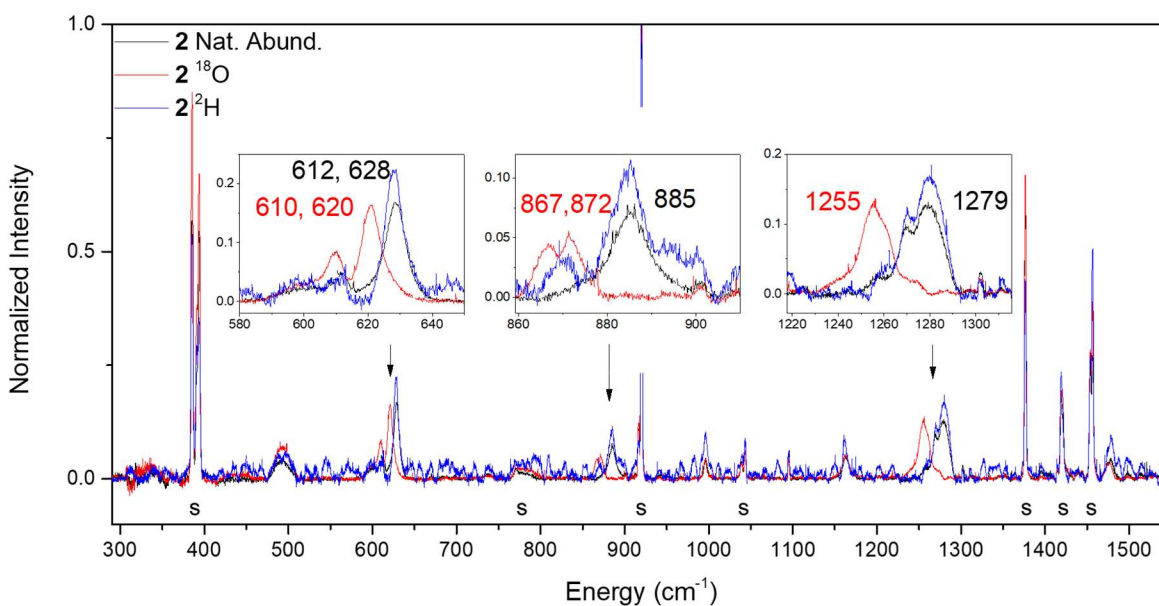
Figure 5.4 Resonance Raman spectra (90 K, λ_{exc} = 647 nm) of **2** prepared at -10 °C in CH$_3$CN, generated by using $^{16}O_2$ (black) and $^{18}O_2$ (red). The blue traces refer to **2** prepared using ^{2}HClO$_4$. **A**, overview spectra; peaks due to non-lasing plasma lines or solvent are marked by "s". The insets show a zoomed in portion of the spectra. The spectra are referenced and normalized to the acetonitrile peak at 920 cm^{-1}.

The rRaman spectrum (Figure 5.4) of **2** (generated in the reaction of **1** with NaBPh$_4$/O$_2$/H$^+$) in frozen CH$_3$CN solution upon 647 nm excitation reveals three main peaks at 628, 885, and 1279 cm^{-1}, which are sensitive to ^{18}O labelling, but do not respond to deuterium labelling. Some of the peaks exhibit broad and asymmetric bandshapes or even allow resolving two adjacent maxima, separated by ca. 10 cm^{-1} or less. These findings could be the results of mode mixing or potentially the coexistence of conformational sub-states.
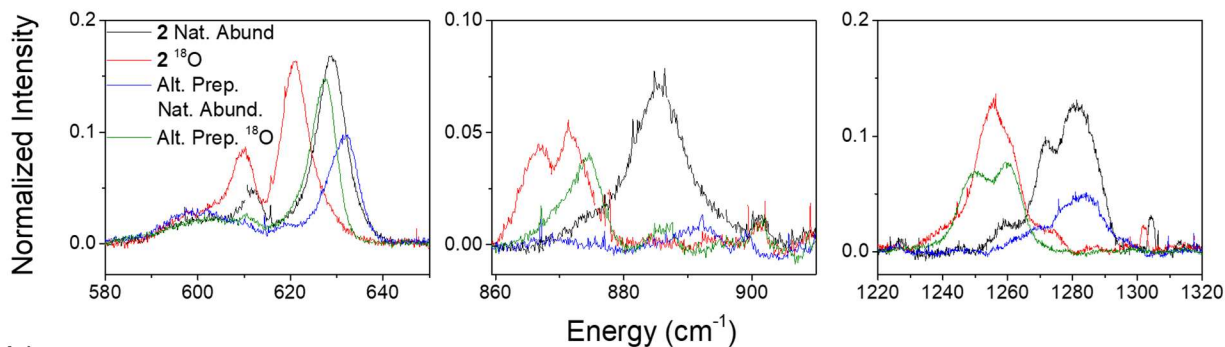
Figure 5.5. rRaman spectra of **2** generated by the alternative preparation (oxidation of the Fe^{II}-phenolate precursor with NO^+, $^{16}O_2$ (blue) and $^{18}O_2$ (green)) compared with the usual preparation of **2** ($^{16}O_2$ (black) and $^{18}O_2$ (red)).

A comparable rRaman spectrum (with the ^{18}O-sensitive bands at 634, 893 and 1285 cm^{-1}) was also obtained from the frozen sample of **2** generated by an alternative synthetic procedure involving the oxidation of **1** by the nitrosonium cation in the presence of an excess of phenol (Figure 5.5). Thus, both synthetic routes yield essentially the same species, although the spectra display minor differences in frequencies and relative intensities of the ^{18}O-sensitive bands at 628 and 1279 cm^{-1}, presumably due to slight alterations in the coordination environment. In contrast, larger differences are observed for the 885 cm^{-1} band (Figure 5.5), which, in the alternate preparation, is shifted to 893 cm^{-1} and shows only very weak intensity. Thus, on the one hand, we cannot rule out that the intense band at 885 cm^{-1} observed for **2** in the original preparation (see data in Figure 5.4) originates from some sort of side-product (for example, an Fe^{III}-phenylperoxo complex formed from the PhOO$^{•}$ radical; see mechanistic scheme in Figure 5.3) of the reaction of **1** with NaBPh$_4$, O_2 and H^+, in line with the ~15% Fe^{III} impurity observed in the EPR and Mössbauer measurements. On the other hand, our density functional theory (DFT) calculations (see below) do indicate that the Fe^{II}-phenoxy radical complex does show an ^{18}O-sensitive feature in the $850 - 900$ cm^{-1} region, which would support the assignment of the 885 cm^{-1} band to **2**. Based on the available data, this issue cannot be further resolved.
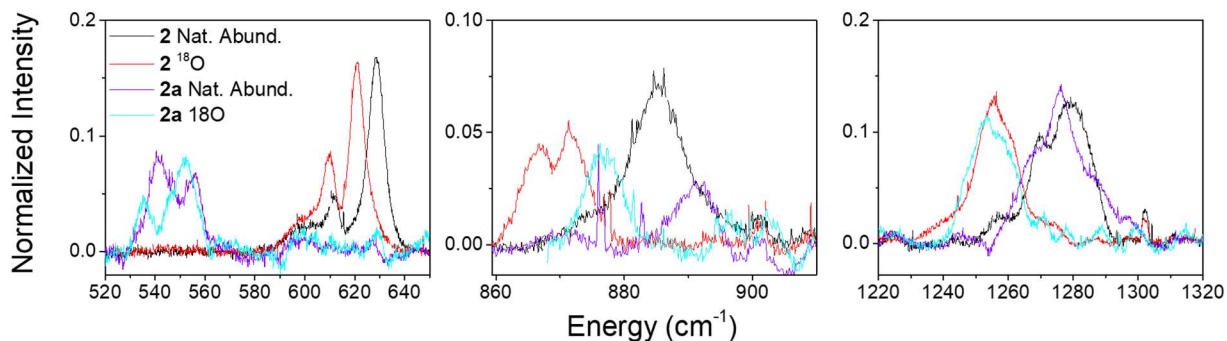
Figure 5.6. rRaman spectra of **2a** ($^{16}O_2$ (purple) and $^{18}O_2$ (cyan)) compared with **2** ($^{16}O_2$ (black) and $^{18}O_2$ (red)), both generated by the regular preparation.

Note that the energy of the vibration at 628 cm^{-1} is strongly dependent on the nature of the para-substituent in the phenyl ring (Figure 5.6); this feature is shifted to 541/556 cm^{-1} in **2a** containing a methyl substituent, whereas the position of the higher energy vibration at ~1280 cm^{-1} remains essentially unaltered. This is consistent with the iron(II)-phenoxyl radical assignment of **2/2a**, as DFT studies show that the vibrational frequency of the band at ~630 cm^{-1} with predominant Fe-OPh stretching character should be strongly affected by changing the para-phenyl position to a methyl group, while the band at ~1280 cm^{-1} should not be. The alternate assignment of **2** as a Fe^{II}(O$_2$·$^{-}$) species with the Fe-O vibration at 628 cm^{-1} and the O-O vibration at 1280 cm^{-1} is not consistent with DFT calculations (see below).

5.6 Magnetic Circular Dichroism
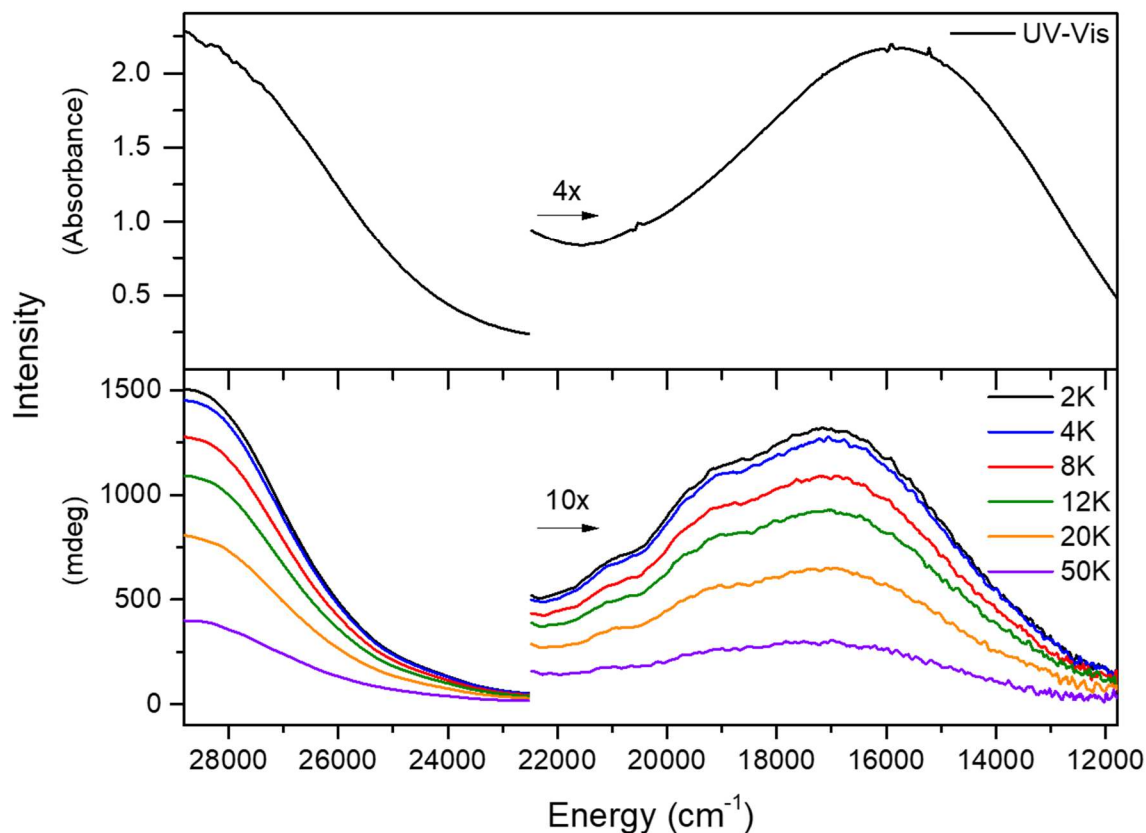
Figure 5.7. Comparison of the UV-Vis (top) and MCD (bottom) spectra of **2**. UV-Vis and MCD samples were prepared at 8 mM in butyronitrile with O_2, 2 eq NaBPh$_4$, and 0.25 eq HClO$_4$ at -5 °C. The UV-Vis spectrum was measured at -5 °C with 8 mM concentration. The MCD spectra were measured at temperatures of 2-50 K and magnetic fields of 0-7 T; here we show the 7 T data for each temperature.

The magnetic circular dichroism variable-temperature variable-field (MCD VTVH) measurements inform on the optical properties and the electronic structure of **2**. The MCD signals align well with the UV-Vis data as shown in Figure 5.7. The MCD signal shows a temperature dependence, characteristic of **C**-term signals, confirming that **2** is a paramagnetic complex. The field dependent data is shown in Figure 5.8; this figure also shows the relative intensities of the bands, without the scaling in Figure 5.7.
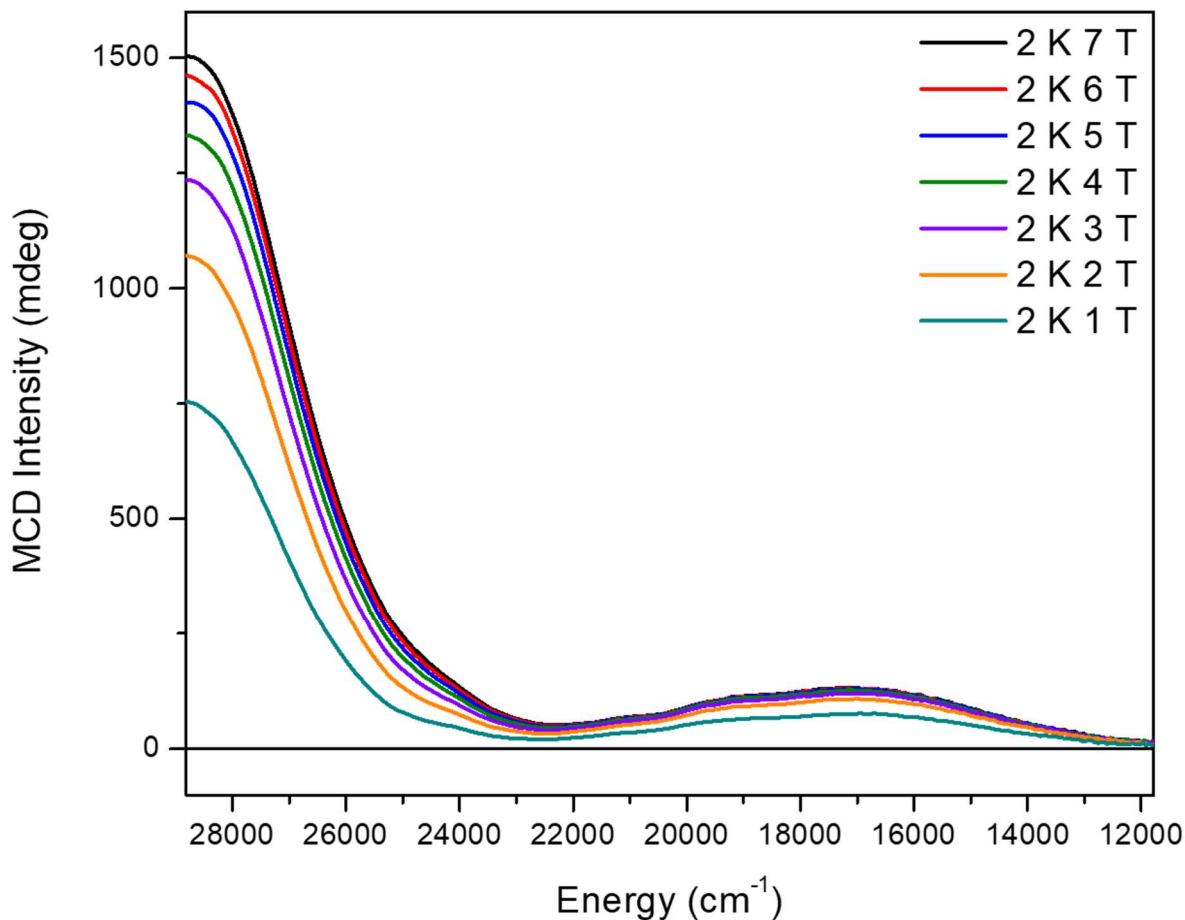
Figure 5.8. Magnetic field-dependent MCD data of **2**, at 2 K and 0-7 T. The MCD samples were prepared at 8 mM concentration in butyronitrile with O_2, 2 eq $NaBPh_4$, and 0.25 eq $HClO_4$ at -5 °C.
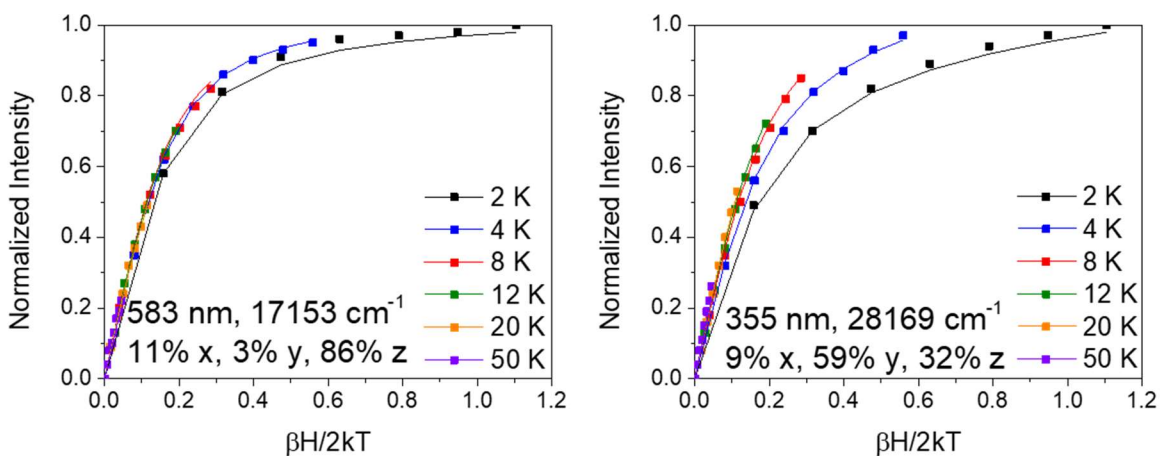
Figure 5.9. VTVH saturation curves for the two main features at 583 nm (17153 cm^{-1}, left) and 355 nm (28169 cm^{-1}, right), with data obtained at 2-50 K, 0-7 T. The data are fit for an $S_t = 5/2$

ground state with ZFS parameters from the EPR fit: $D = +3$ cm^{-1}, $E/D = 0.07$, g = (1.90, 1.95, 2.10). The colored symbols represent the experimental data while the lines correspond to the fits.

Further, the VTVH saturation data derived for the two major bands at 583 and 355 nm both fit well with the zero-field splitting (ZFS) parameters derived from the EPR $S_t = 5/2$ simulation, Figure 5.9.
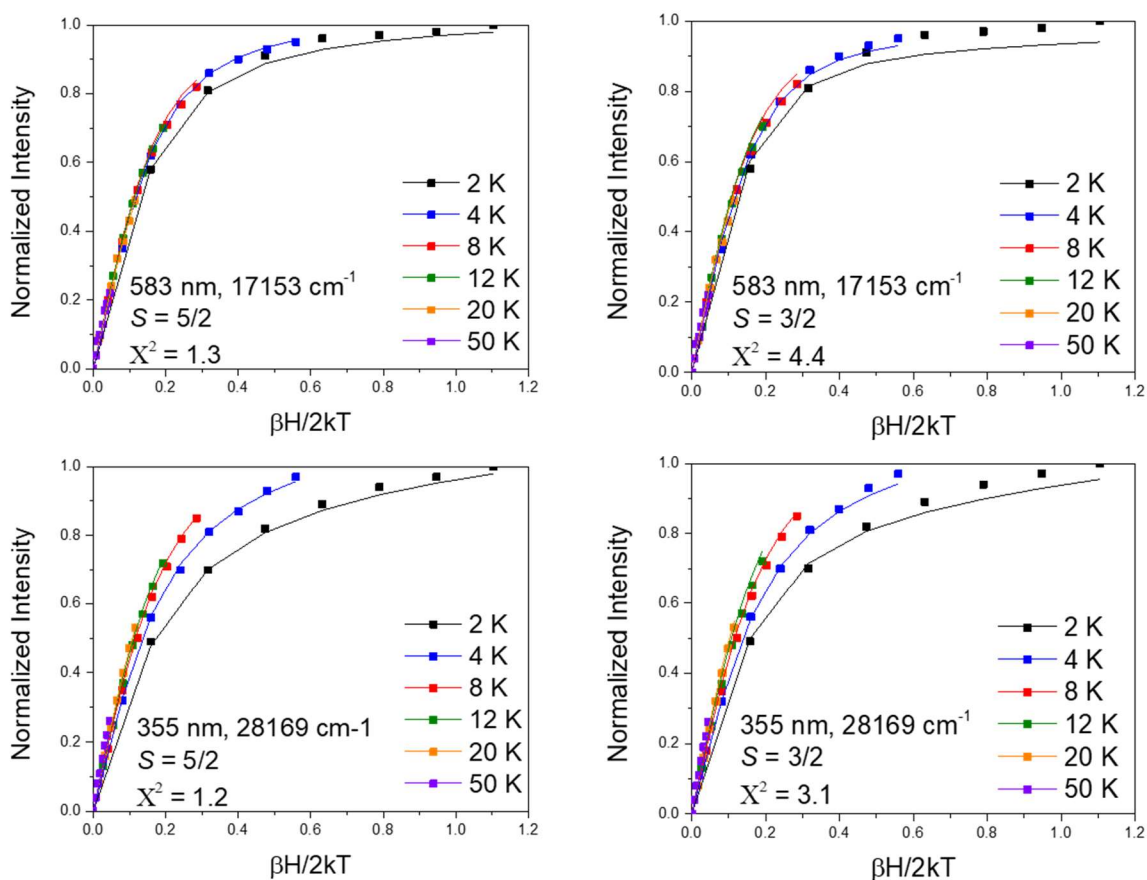
Figure 5.10. Comparison of VTVH saturation curves obtained at 583 and 335 nm, fit with EPR parameters derived from using an $S_t = 5/2$ or 3/2 spin state. Note how the X^2 is better using the $S_t = 5/2$ state and corresponding fit parameters. The MCD samples of 2 were prepared at 8 mM concentration in butyronitrile with O_2, 2 eq NaBPh$_4$, and 0.25 eq HClO$_4$ at -5 °C, as in Figure 5.7 and Figure 5.8. Data were obtained at 2-50 K, 0-7 T.

In contrast, the $S_t = 3/2$ spin state does not only result in a poor fit for the EPR spectrum, but also does not fit the VTVH MCD data as well, as shown in Figure 5.10. In agreement with the EPR and Mössbauer results, this further supports the $S_t = 5/2$ spin state for **2**. In addition, the VTVH fit provides polarization data for the corresponding electronic transitions. We calculated the ZFS tensor for the six-coordinate structure with CH$_3$CN bound trans to the phenoxy radical ($S_t = 5/2$).

The calculation shows that the z-axis of the ZFS tensor is aligned with the Fe-OPh• vector. The calculated parameters are $D = -1.19$ cm^{-1} and $E/D = 0.05$. As shown in Figure 5.9, the less intense band at low energy is mostly z polarized, which could be a charge transfer (CT) transition between the Fe^{II} center and the bound phenoxy ligand, consistent with the observed shift of this transition upon changing the para-substituent of the phenoxy ligand in **2/2a/2b**. The intense band at higher energy is largely y-polarized and likely related to a CT transition between the Fe^{II} center and the TMCO co-ligand.
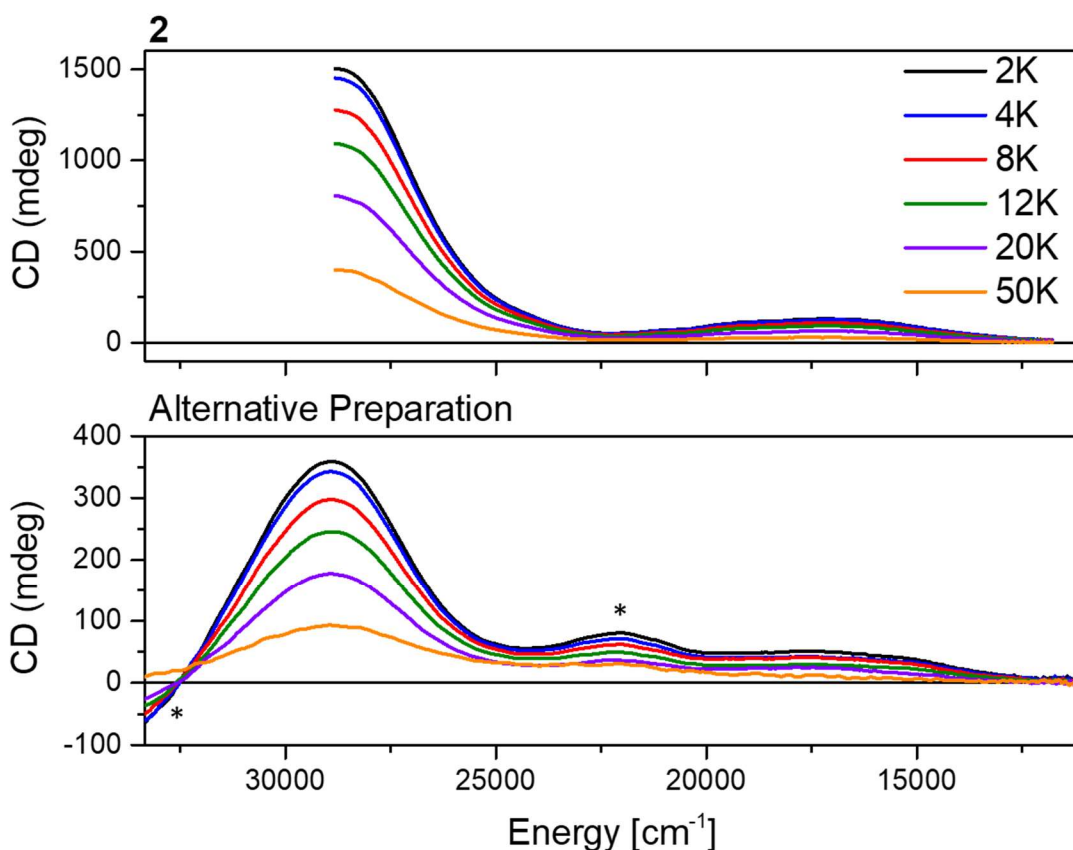
Figure 5.11. Comparison of the MCD data of **2** and of the same complex but prepared through an alternative method using NO$^+$ oxidation of the Fe^{II}-phenolate precursor. Data were obtained at 2-50 K, 0-7 T; shown here are the 7 T spectra for each temperature. The MCD sample of **2** was prepared at 8 mM concentration in butyronitrile with O$_2$, 2 eq NaBPh$_4$, and 0.25 eq HClO$_4$ at -5 °C, as shown in Figure 5.7 and Figure 5.8. The MCD sample from the alternative preparation of **2** was prepared at 2.5 mM, with 5 eq of phenol and 1 eq of NOSbF$_6$ in MeCN : butyronitrile 1:3 at -25 °C. * marks probable impurities that are only present in the sample from the alternative preparation method.
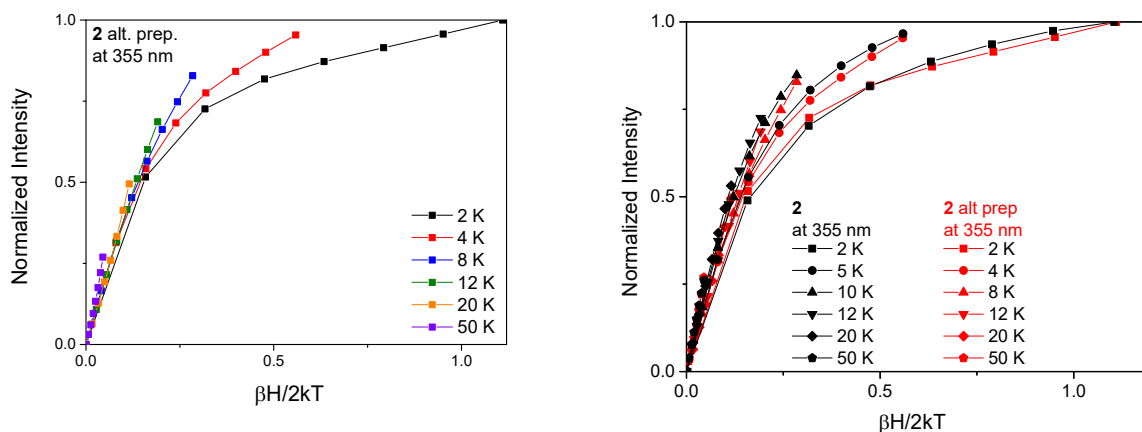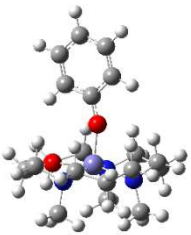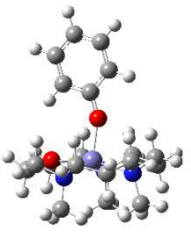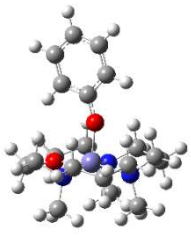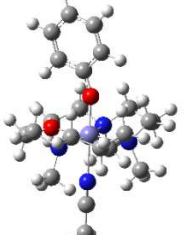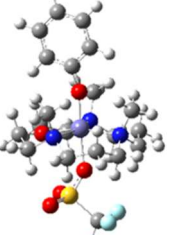
Figure 5.12. Comparison of VTVH Saturation Curves for **2** and for the alternative preparation of **2**, obtained at 355 nm for each. Left, saturation curves of the alternate preparation of **2**. Right, comparison of these data (alternate preparation) to saturation data of **2** prepared in the regular way (with 2 eq NaBPh$_4$, and 0.25 eq HClO$_4$ at -5 °C in the presence of O$_2$). See Figure 5.11 for further details on MCD samples.

In addition, MCD measurements were conducted on a sample resulting from the alternative preparation method of **2** (Figure 5.11), and the resulting VTVH MCD saturation curves (Figure 5.12) agree well with those in Figure 5.9, prepared from autocatalytic degradation of NaBPh$_4$. These results further confirm the nature of **2** as a Fe^{II}-phenoxy radical species.

5.7 Towards a Theoretical Description of 2
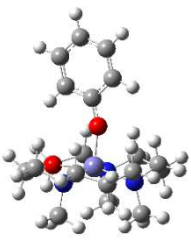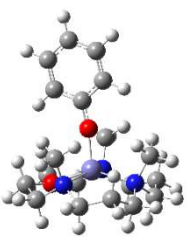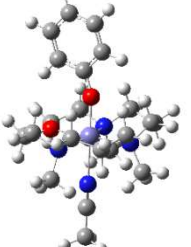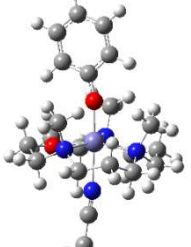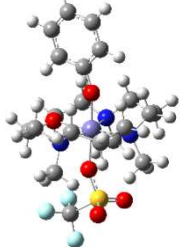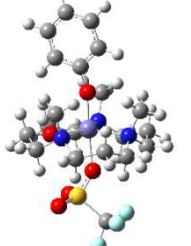
We have analyzed a variety of possible structures of the Fe^{II}(OPh$^\bullet$) intermediate, differing with respect to spin state, magnetic coupling between Fe and the phenoxy radical, coordination states, and details of the co-ligand conformation. The calculated relative energies, spin densities, vibrational frequencies, and Mössbauer parameters are listed in Table 5.1 and Table 5.2.

Table 5.1. Comparison of DFT-calculated parameters for different ground states of the Fe(TMCO)(OPh$^\bullet$) intermediate with different axial ligands, using both ferro- and antiferromagnetic coupling (FC/AFC) between the Fe^{II} center and the phenoxy radical ligand.[a]

Spin Coordination Co-ligand orientation [b]	Exp.	hs-Fe^{II}, FC 5C N-Me trans	hs-Fe^{II}, AFC 5C N-Me trans	is-Fe^{II}, FC 5C N-Me trans	hs-Fe^{II}, FC 6C, MeCN N-Me trans	hs-Fe^{II}, FC 6C, OTf N-Me cis
Image						
Relative Energy [kcal/mol]	-	0.0	3.3	11.9	-	-
Geometry						
Fe-O distance [Å]	-	1.88	2.02	1.88	1.97	1.86
C(Ph)-O [Å]	-	1.31	1.28	1.32	1.30	1.33
<Fe-O-C1(Ph) [°]	-	161	153	157	161	165
Spin Density						
Fe	-	3.95	3.76	2.46	3.97	4.11
OPh total	-	0.76	-0.93	0.66	0.77	0.48
O	-	0.35	-0.23	0.35	0.04	0.31
Ph	-	0.41	-0.70	0.31	0.21	0.17
Co-ligand total	-	0.29	0.17	-0.12	0.25	0.35
Co-ligand backbone	-	0.05	0.04	-0.01	0.33	0.05
Co-ligand Ns, O	-	0.24	0.13	-0.11	0.44	0.30
Sum in total:	-	5.00	3.00	3.00	5.00	5.00
Vibrations [cm^{-1}] (^{18}O)						
Fe-O	628 (610, 621)	560 (550)	570	555	539 (528)	605
δ_{ip}(Ph)/C-O	885 (867, 872)	865 (851)	836	863	852 (840)	883
O-Ph	1279, 1270 (1255)	1160, 1168, 1262 (1157, 1254)	1416, 1511	1149,1243,	1173, 1286 (1171, 1275)	1180, 1257
Mössbauer [mm s^{-1}]						
δ	1.32	0.68	0.91	0.56	0.81	0.61
ΔE_q	3.28	1.96	4.37	-1.48	1.95	1.02
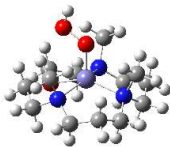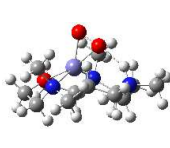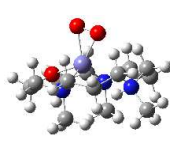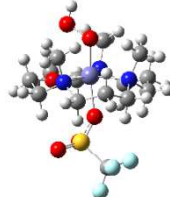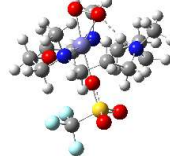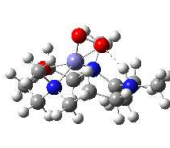
[a] All structures shown here were calculated using B3LYP/TZVP. See Experimental Section 5.10.3 for further information. [b] TMCO N-Me groups orientation with respect to the phenoxy radical moiety.

Table 5.2 DFT-calculated properties for additional structures to the ones listed in Table 5.1. Each structure has a hs-Fe^{II} center with a ferromagnetically coupled phenoxy radical. Relative energies are compared between structures with the same number of atoms. All calculations were performed with B3LYP/TZVP.

Coordination Co-ligand orientation [a]	Exp.	5C N-Me down	5C N-Me up	6C, MeCN N-Me down	6C, MeCN [b] N-Me up	6C, OTf⁻ N-Me down	6C, OTf⁻ N-Me up
Image							
Relative Energy [kcal/mol]	-	0.0	0.2	1.5	0.0	4.8	0.0
Geometry							
Fe-O distance [Å]	-	1.88	1.89	1.97	1.91	1.89	1.86
C(Ph)-O [Å]	-	1.31	1.30	1.30	1.31	1.33	1.33
<Fe-O-C1(Ph) [°]	-	161	171	161	169	161	165
Spin Density							
Fe	-	3.95	3.93	3.97	3.97	4.11	4.11
OPh	-	0.76	0.83	0.77	0.75	0.46	0.48
Co-ligand	-	0.29	0.24	0.25	0.27	0.35	0.35
Vibrational modes [cm^{-1}]							
Fe-O stretch	628	560	562	539	553	594	605
O-Ph stretch	1279	1160, 1168, 1262	1175, 1294	1173, 1286	1172, 1279	1256	1180, 1257
Mössbauer [mm s^{-1}]							
δ	1.32	0.68	0.79	0.81	0.79	0.61	0.61
ΔEq	3.28	1.96	2.13	1.95	1.94	1.15	1.02

[a] "N-Me down" – the TMCO N-methyl groups are trans to the phenoxy ligand, "N-Me up" – the TMCO N-methyl groups are cis to the phenoxy ligand. [b] MeCN dissociates during the optimization; therefore, in this structure the Fe-N(CCH3) bond was fixed at 2.3 Å during the geometry optimization (the rest of the structure was allowed to optimize).

Table 5.3 DFT-calculated properties for Fe-hydroperoxide and -superoxide adducts. Compare to Table 5.1 and Table 5.2. Relative energies are compared between structures with the same number of atoms. All calculations were performed with B3LYP/TZVP. Here, L = TMCO.

Structure	Exp.	$[Fe(OOH)(L)]^{2+}$	$[Fe(OOH)(L)]^{2+}$	$[Fe(OO)(LH)]^{2+}$	$[Fe(OO)(LH)]^{2+}$	$[Fe(OOH)(L)(OTf)]^{+}$	$[Fe(OO)(LH)(OTf)]^{+}$	$[Fe(OO)(LH)]^{2+}$
Spin State		5/2	5/2	5/2	5/2	5/2	5/2	3/2
Co-ligand orientation [a]		N-Me down	N-Me up	N-Me up	N-Me down	N-Me up	N-Me up	N-Me up
Image								
Relative Energy [kcal/mol]	-	0.0	2.2	16.4	28.6	0	28.4	18.8
Geometry Fe-O distances [Å]	-	1.86, 2.83	1.86, 2.80	1.98, 1.99	1.97, 2.00	1.91, 2.85	2.04, 2.04	1.85, 1.87
O-O distance [Å]	-	1.42	1.41	1.35	1.35	1.43	1.35	1.39
O-H [Å]	-	0.97	0.97	2.01	3.31	0.97	1.77	1.93
<Fe-O-O [°]	-	119	117	70	71	116	71	69
Spin Density Fe	-	4.07	4.06	3.71	3.66	4.14	3.76	3.18
O_2	-	0.50	0.53	1.16	1.21	0.39	1.08	-0.28
Vibrational modes [cm^{-1}] Fe-O stretch	628	530	526, 528	332[s], 354, 398[as], 399	369[as], 385, 408,	468, 479, 497	236,257[s], 317, 326[as], 335[as]	329, 424[as], 434[as], 440[s], 441, 478[s], 491[s]
O-O stretch	1279	929	918, 924	1100	1116	905, 922	1074	1032
Mössbauer [mm s^{-1}] δ	1.32	0.45	0.50	0.94	0.94	0.52	0.95	0.67
ΔEq	3.28	0.96	0.98	2.31	2.44	0.96	2.56	3.11

[a] "N-Me down" – the TMCO N-methyl groups are trans to the hydroperoxide or superoxide ligand. "N-Me up" – the TMCO N-methyl groups are cis to the hydroperoxide or superoxide ligand. [s] = symmetric and [as] = antisymmetric.

5.7.1 Spin State

Among the structures listed in Table 5.1, complexes with an intermediate spin (is) state of the iron(II) center ($S = 1$) can readily be discarded due to their high relative energy. For example, in the corresponding five-coordinate structures with no axial ligand bound trans to the phenoxy radical, the high-spin (hs) Fe^{II} state ($S = 2$) is favored energetically by 12 kcal/mol when compared with an intermediate spin state of the iron center. Comparing ferromagnetic (FC, $S_t = 5/2$) and antiferromagnetic coupling (AFC, $S_t = 3/2$) of the phenoxy radical with a hs-Fe^{II} center, the ferromagnetically coupled species is favored by 3.3 kcal/mol. Note that AFC states were not further considered, as our experimental data show that **2** is an $S_t = 5/2$ species.

5.7.2 Structural Variations

Ferromagnetically coupled, six-coordinate hs-Fe^{II}-phenoxy radical species in which either solvent (CH_3CN) or the counter ion (triflate, OTf^-) occupies the 6th coordination site were further evaluated, as shown in Table 5.1. Another structural variation concerns the position of the N-methyl groups of the TMCO co-ligand, which can point to either side of the Fe(TMCO) plane. Different structures of **2** with $S_t = 5/2$ that incorporate these structural variations were optimized as well (Table 5.2). The energies of the different structures obtained in this way are close (within the typical DFT error of $\pm 4 - 5$ kcal/mol) but show a slight preference for the N-methyl groups on the opposite site as the CH_3CN or triflate ligands. It is possible that a mixture of these species exists in solution as well, which would explain the somewhat broad rRaman signals observed for **2**.

Based on these results, either 5C or 6C ferromagnetically coupled species are possible candidates for **2**, in line with the experimental data from EPR, MCD, and Mössbauer spectroscopy that uniformly indicate $S_t = 5/2$ for **2**. For a representative selection of these complexes (Table 5.1), a careful comparison of the calculated parameters, however, reveals that there is no single species providing an equally good description of both the rRaman and the Mössbauer parameters.

We thus also checked alternative interpretations of **2** as a $Fe^{II}(O_2^{-\bullet})$ species. However, for all of the Fe-superoxide and -peroxide complexes that were considered, none is able to reproduce the experimental parameters, especially the vibrational properties, of **2** (Table 5.3).

5.7.3 Discrepancies Between DFT and Experiment

We investigated the possible intrinsic deficiencies of our theoretical approach. For the precursor complex $[Fe^{II}(TMCO)(OTf)(CH_3CN)]^+$ (**1**), the calculated Mössbauer data ($\delta = 1.01$; $\Delta E_Q = 3.23$ mm s^{-1}) agree very well with the experimental values ($\delta = 1.15$ mm s^{-1}, $\Delta E_Q = 2.91$ mm s^{-1}). However, **1** also has a relatively simple electronic structure in contrast to **2**. Upon formation of **2**, the experimental data show that both the quadrupole splitting and the isomer shift increase, which is not reproduced by the calculations. Over the variety of hs-Fe^{II}-OPh$^\bullet$ structures with $S_t = 5/2$ (ferromagnetically coupled) that we investigated, we found $\delta = 0.6 – 0.8$ mm s^{-1} and $\Delta E_Q = 0.8 – 2.1$ mm s^{-1} (Table 5.1 and Table 5.2). These results indicate a systematic error in the DFT calculations, which overestimate the amount of electron donation from the hs-Fe^{II} center to the phenoxy radical, giving the iron center too much ferric character, and hence, too low of an isomer shift. Thus, even for the complex showing the closest match with the experimental Mössbauer parameters, i.e. the 6C structure where the 6th coordination site is occupied by acetonitrile, on the same side as the N-methyl groups of the co-ligand, the isomer shift and quadrupole splitting are calculated too low ($\delta = 0.81$ mm s^{-1} and $\Delta E_Q = 1.95$ mm s^{-1}; see Table 5.1). Note that this model was used for the electronic structure analysis below.

Additionally, calculations of the normal modes reveal an underestimation specifically of the Fe-O stretching frequency, which appears to be an intrinsic deficiency of the present DFT approach.

5.7.4 Vibrational Assignments

The DFT results allow us to assign the rRaman spectra of **2**. The band at 628 cm^{-1} corresponds to a primary Fe-O stretching vibration, which is predicted between 530 and 570 cm^{-1}. Only for the 6C complex with triflate coordinated to the Fe^{II} center, this mode is predicted at somewhat higher frequency (605 cm^{-1}), but this species shows quite low values for the predicted Mössbauer isomer shift and the quadrupole coupling.

Based on the DFT results, the mode at 1279 cm^{-1} is a mixed C-O stretch/phenyl ring vibration (referred to as "O-Ph" in the following). Importantly, the nature of the exchange coupling affects the O-Ph vibration: whereas a ferromagnetically-coupled hs-Fe^{II}-phenoxy radical unit reproduces the vibrational frequency of this mode well, antiferromagnetic coupling leads to an

overestimate of the energy of this vibration by 200 cm^{-1}. This agrees well with the conclusions from the EPR, Mössbauer, and MCD analysis, which all favor the $S_t = 5/2$ ground state.
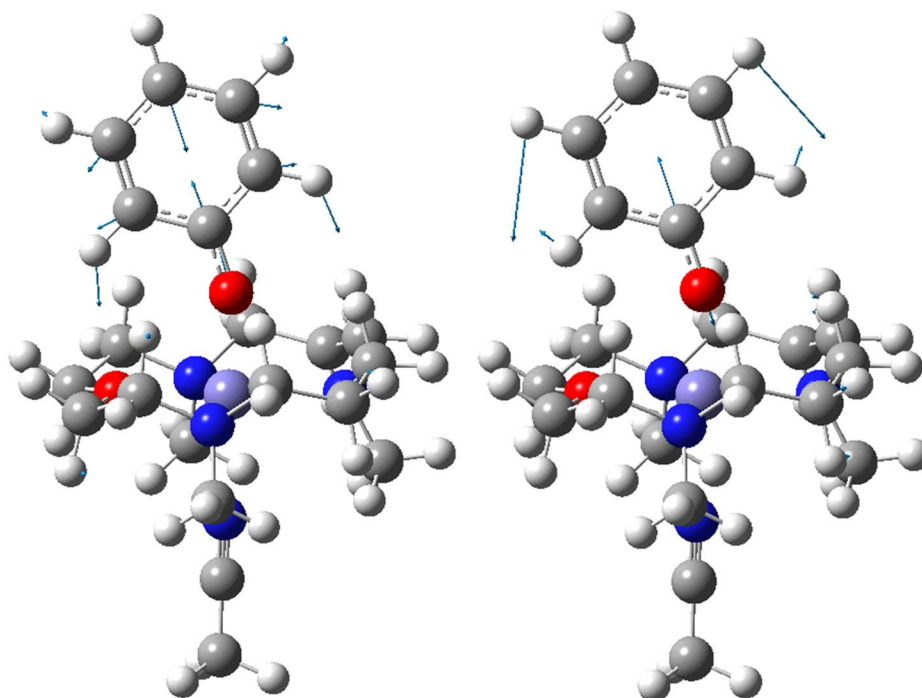
Figure 5.13. Left: arrow diagram of the Fe-O stretch, calculated at 539 cm^{-1}. Right: arrow diagram of the O-Ph vibration, calculated at 1286 cm^{-1}.

In addition, the hs-Fe^{II}-phenoxy radical model replicates the experimental vibrational trends observed for the derivatives of **2** that carry a para-substituent on the phenoxy moiety (such as in **2/2a**; see Figure 5.6). The Fe-O stretch at 628 cm^{-1} involves movement of the para-substituent of the phenyl ring (H in **2** and Me in **2a**), while the O-Ph mode at 1279 cm^{-1} does not, as shown in Figure 5.13. Correspondingly, in the rRaman spectrum of **2a**, the Fe-O stretch shifts to lower energy by 87 cm^{-1} compared to **2** (see Figure 5.6), whereas O-Ph mode at 1279 cm^{-1} is essentially unaffected by this substitution. Interestingly, DFT also predicts a mixed in-plane phenyl ring bending vibration with some C-O stretching character (referred to as δ_{ip}(Ph)/C-O in the following) at 865 cm^{-1} for **2**. However, as discussed above, since the rRaman feature observed experimentally in this energy region in the alternate synthesis (oxidation of **1** in presence of phenol and NO$^+$) shows a much lower intensity, it is unclear whether this band originates from **2**. In any case, the DFT-predicted mode in this energy region is included in Table 5.1 as well.

In addition to the absolute frequencies, we also considered the $^{18}O/^{16}O$ isotopic shifts in which the systematic errors of DFT-calculated frequencies should be largely cancelled. The $^{18}O/^{16}O$ isotopic shifts were calculated for the 5C hs-Fe^{II} ferromagnetically coupled species and the analogous 6C complex with CH$_3$CN as the 6th ligand (see Table 5.1). The vibrations are ^{18}O sensitive, as expected, and the predicted isotopic shifts for the Fe-O and δ_{ip}(Ph)/C-O vibrations at ~600 and ~850 cm^{-1}, respectively, show good agreement with the experimentally observed shifts. The underestimation of the $^{18}O/^{16}O$ isotopic shift of the O-Ph vibration at higher energy, observed to shift ~20 cm^{-1} and calculated as ~10 cm^{-1}, is likely due to variations in the exact composition of this mode with respect to phenyl ring, C-O stretch and TMCO co-ligand contributions, where an underestimate of the C-O stretching contribution in the DFT calculations would decrease the magnitude of the $^{18}O/^{16}O$ isotopic shift.

5.7.5 Electronic Structure Analysis
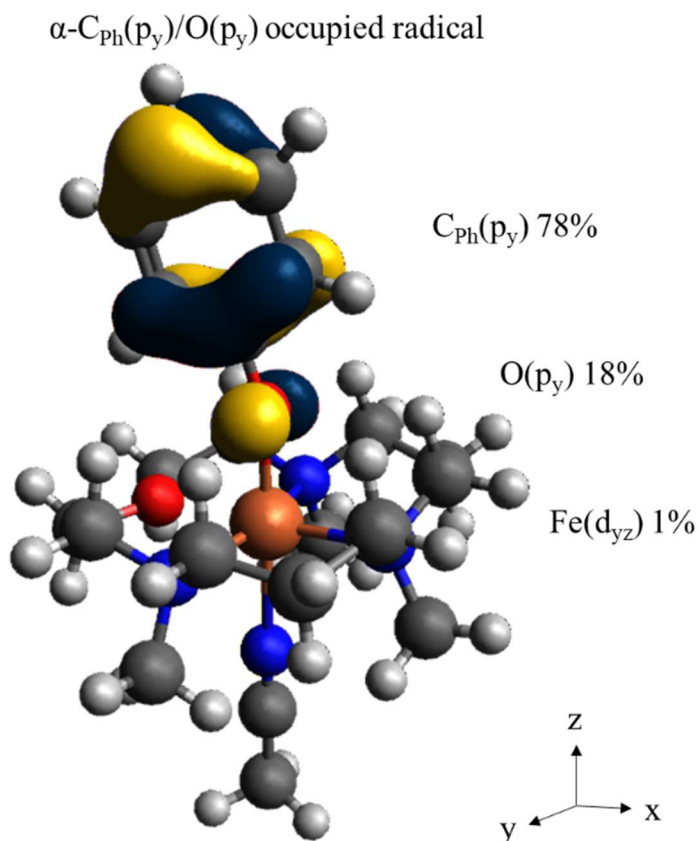
Figure 5.14. Occupied α-spin orbital, showing the unpaired electron of the phenoxy radical, coordinated to the hs-Fe^{II} center. Calculated for the 6C structure with MeCN bound in trans position to the phenoxy radical group, with $S_t = 5/2$ spin. Calculated with B3LYP/TZVP.

For an overall $S_t = 5/2$ species with a hs-Fe^{II} center, all five majority spin (α-) d-orbitals are singly occupied, plus one of the minority spin (β-) d-orbitals is occupied as well, giving rise to a hs-Fe^{II} center with $S = 2$. In addition, the O-Ph(π^*) orbital of phenolate, labeled $C_{Ph}(p_y)/O(p_y)$ in the following, is oxidized by one electron, forming a phenoxy radical ligand ($S = 1/2$). In the ferromagnetically coupled ground state, it is the β-$C_{Ph}(p_y)/O(p_y)$ orbital that is oxidized, creating one additional α-spin on the phenoxy ligand, which leads to the observed $S_t = 5/2$ ground state of **2**. The singly-occupied phenoxy based MO shows delocalization of the hole throughout the phenyl ring $C(p_y)$ orbitals but has dominant $O(p_y)$ character, as shown in Figure 5.14. According to this electronic structure description, calculated spin densities of Fe and OPh$^\bullet$ are +3.97 and +0.77 (Table 5.1), respectively. The σ-bonds between the singly-occupied d_{x2-y2} orbital of iron and the TMCO co-ligand further causes the transfer of some α-electron density to the co-ligand (in a coordinate system where the Fe-OPh vector corresponds to the z axis).

A) DFT MOs

β-d_{yz}_$C_{Ph}(p_y)$/$O(p_y)$ HOMO

$C_{Ph}(p_y)$ 34%

$O(p_y)$ 3%

$Fe(d_{yz})$ 60%

β-$C_{Ph}(p_y)$/$O(p_y)$_d_{yz} LUMO

$C_{Ph}(p_y)$ 45%

$O(p_y)$ 23%

$Fe(d_{yz})$ 30%
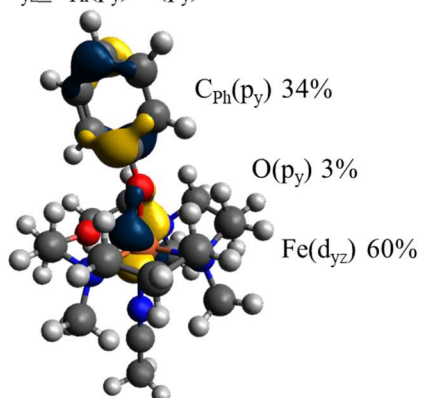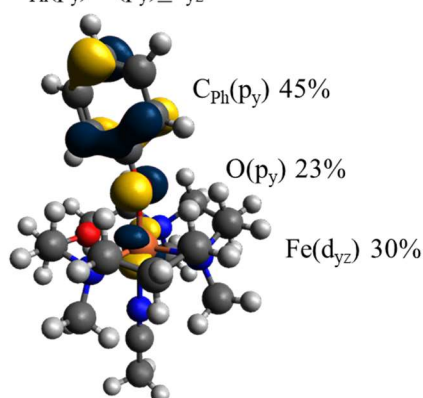
B) CASSCF MOs

d_{yz} HOMO

$C_{Ph}(p_y)$ 1%

$O(p_y)$ 1%

$Fe(d_{yz})$ 97%

$C_{Ph}(p_y)$/$O(p_y)$ radical

$C_{Ph}(p_y)$ 70%

$O(p_y)$ 27%

$Fe(d_{yz})$ 2%
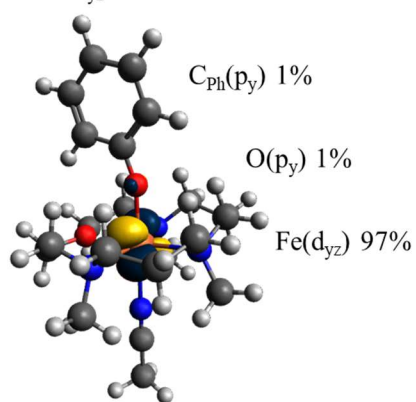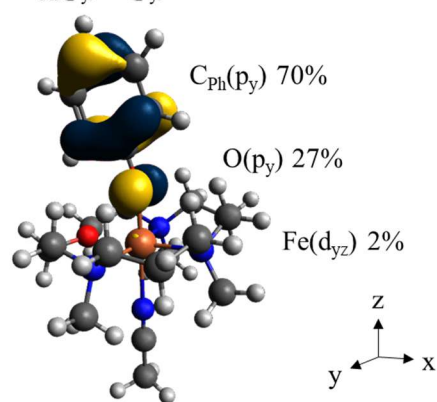
Figure 5.15. Images of the HOMO and LUMO, showing bonding and antibonding combinations between the iron d_{yz} and the phenoxyl radical O-Ph(π^*) orbitals, respectively. A) the molecular orbitals as calculated by DFT, left: the occupied β-d_{yz}_$C_{Ph}(p_y)$/$O(p_y)$ MO, which corresponds to the single β-d orbital of a hs-Fe^{II} center. Note that this MO has ~40% phenoxyl radical character. Right: the unoccupied, antibonding β-$C_{Ph}(p_y)$/$O(p_y)$_d_{yz} MO, which corresponds to the "hole" on the phenoxyl radical ligand. B) the molecular orbitals as calculated by CASSCF(25,17), here, the predominately $Fe(d_{yz})$ orbital (left) is mostly doubly occupied and the $C_{Ph}(p_y)$/$O(p_y)$ (right) is mostly singly occupied illustrating the phenoxy radical, see discussion in text. The percent contribution of each component is listed. Calculated for the 6C hs-Fe^{II}-OPh$^\bullet$ structure with MeCN bound trans to the phenoxyl radical (see Table 5.1).

Importantly, the empty β-$C_{Ph}(p_y)$/$O(p_y)$ orbital of the phenoxy ligand further interacts with the occupied β-d_{yz} orbital of the iron center, as shown in Figure 5.15A. According to the DFT calculations, the resulting bonding (occupied) MO, d_{yz}_$C_{Ph}(p_y)$/$O(p_y)$ (Figure 5.15A, left), has 60% iron and ~40% phenoxy character. The exact amount of Fe/phenoxy character of this MO therefore determines the oxidation state of the iron center, which then impacts the calculated Mössbauer

parameters. With ~40% phenoxy character, the DFT calculations predict the iron center to be too ferric, causing the calculated Mössbauer isomer shift to be too small. In the real system, this MO must therefore have much more predominant β-d_{yz} character (less phenoxy character), in agreement with the iron center being ferrous in **2**, and the experimental isomer shift of 1.32 mm/s.
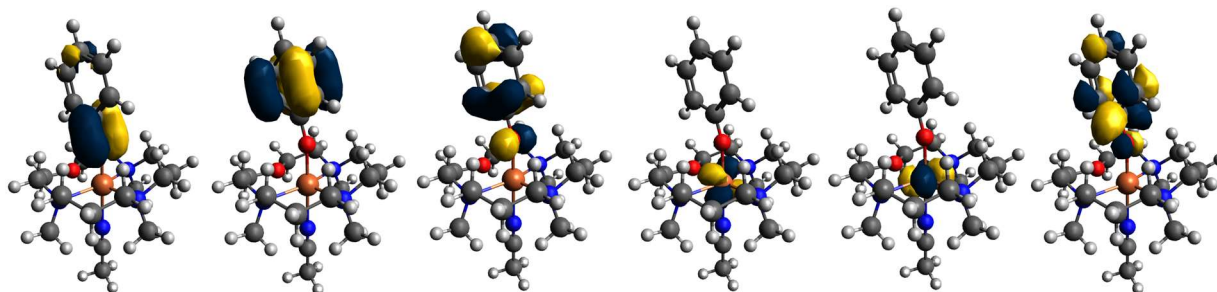
Figure 5.16. OC$_{Ph}$, Ph, OPh, d_{yz}, d_{xy}, and OC$_{Ph}$* MO from CASSCF(25,17). Energies (hartrees) are as follows: OC$_{Ph}$, -0.75; Ph, -0.54; OPh, -0.47; d_{yz}, -0.45; d_{xy}, -0.41; and OC$_{Ph}$*, +0.13. See Table 5.4 for electron configuration contributions to the ground state and further description of orbital abbreviations used here.
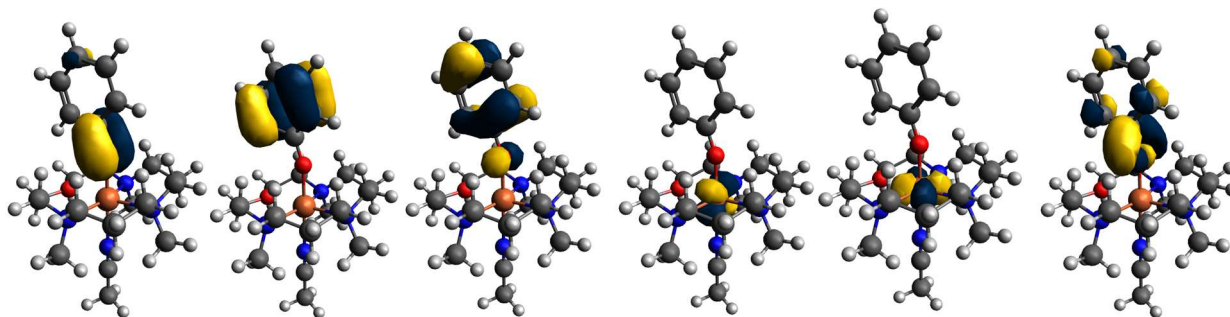
Figure 5.17. OC$_{Ph}$, Ph, OPh, d_{yz}, d_{xy}, and OC$_{Ph}$* MO from CASSCF(17,13). Energies (hartrees) are as follows: OC$_{Ph}$, -0.73; Ph, -0.52; OPh, -0.47; d_{yz}, -0.39; d_{xy}, -0.40; and OC$_{Ph}$*, -0.31. See Table 5.4 for electron configuration contributions to the ground state and further description of orbital abbreviations used here.
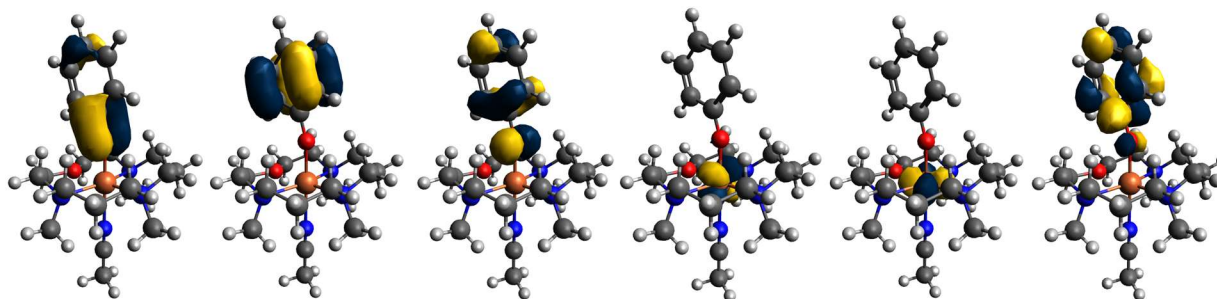
Figure 5.18. OC$_{Ph}$, Ph, OPh, d_{yz}, d_{xy}, and OC$_{Ph}$* MO from CASSCF(13,11). Energies (hartrees) are as follows: OC$_{Ph}$, -0.76; Ph, -0.56; OPh, -0.51; d_{yz}, -0.43; d_{xy}, -0.43; and OC$_{Ph}$*, -0.00. See Table 5.4 for electron configuration contributions to the ground state and further description of orbital abbreviations used here.
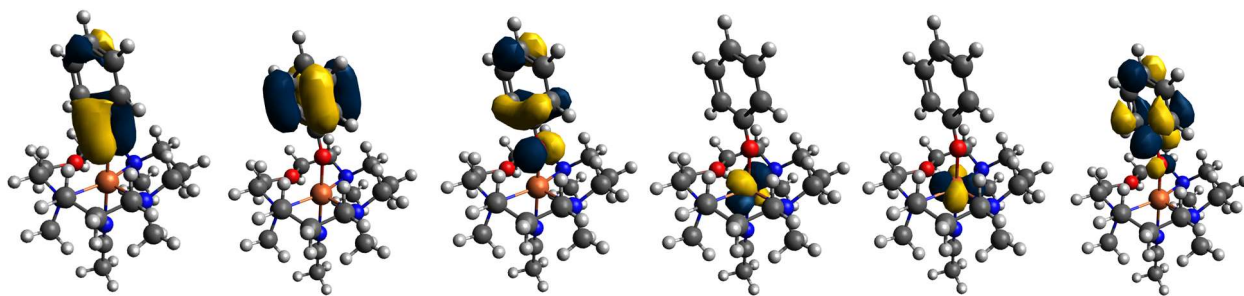
Figure 5.19. OC_{Ph}, Ph, OPh, d_{yz}, d_{xy}, and OC_{Ph}* MO from CASSCF(13,10). Energies (hartrees) are as follows: OC_{Ph}, -0.75; Ph, -0.56; OPh, -0.51; d_{yz}, -0.43; d_{xy}, -0.43; and OC_{Ph}*, -0.01. See Table 5.4 for electron configuration contributions to the ground state and further description of orbital abbreviations used here.
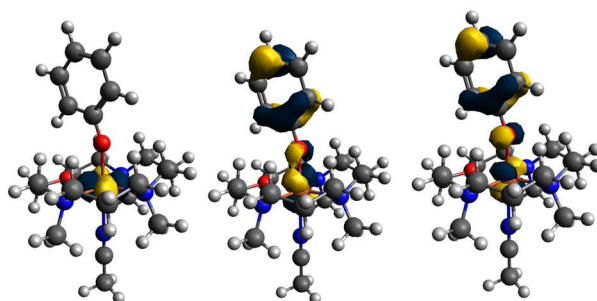
Figure 5.20. Relevant orbitals of the CASSCF(7,7): d_{xy}, OPh_d_{yz}, and d_{yz}_OPh. Note Fe/OPh mix is nearly 50/50. Energies (hartrees) are as follows: d_{xy}, -0.54; OPh_d_{yz}, -0.48; and d_{yz}_OPh, -0.44. This calculation predicted 77% $(d_{xy})^1$(OPh_$d_{yz})^2$(d_{yz}_OPh$)^1$, 20% $(d_{xy})^1$(OPh_$d_{yz})^1$(d_{yz}_OPh$)^2$, and 3% $(d_{xy})^2$(OPh_$d_{yz})^1$(d_{yz}_OPh$)^1$.

We further interrogated this issue using complete active space self-consistent field (CASSCF) calculations. A CASSCF(25,17) calculation with 25 electrons in 17 orbitals including Fe-TMCO bonding MOs, Fe-OPh bonding MOs, the HOMO, SOMOs, and a few unoccupied OPh MOs was performed (See Figure 5.16 and Table 5.4). Interestingly, this calculation gave an electronic structure with mostly Fe^{II}(OPh$^\bullet$) character, which is the dominant contribution to the ground state (86%), and which has the electronic configuration $(d_{yz})^2$($C_{Ph}(p_y)$/O(p_y))^1($d_{xy})^1$ (Table 5.4). Importantly, in the CASSCF calculations the covalency of the Fe-OPh bond is greatly reduced. Here, the HOMO is Fe based (d_{yz}, 97%) and the phenoxyl radical SOMO only has 2% Fe character, as shown in Figure 5.15B. In addition to this dominant electron configuration, there is a 6% Fe^{III}(OPh$^-$) contribution, $(d_{yz})^1$($C_{Ph}(p_y)$/O(p_y))^2($d_{xy})^1$, and a 3% contribution of ligand-field excited states, where the β electron in the d_{yz} orbital is excited into the d_{xy} orbital, $(d_{yz})^1$($C_{Ph}(p_y)$/O(p_y))^1($d_{xy})^2$. Smaller CASSCF calculations, CASSCF(17,13), CASSCF(13,11), and CASSCF(13,10) are also consistent with this result, giving 82% - 90% Fe^{II}(OPh$^\bullet$) and 3-8% Fe^{III}(OPh$^-$) character in the ground state, again with minimal covalency of the Fe-OPh bond (Table

164

5.4 ; Figure 5.17 - Figure 5.19). With an inadequately small active space, CASSCF(7,7), a similar electronic structure as is predicted by DFT is calculated (see Figure 5.20). With CASSCF(7,7) a covalent $d_{yz}\_C_{Ph}(p_y)/O(p_y)$ bond is calculated which highlights the necessity of a sufficiently large active space to obtain useful CASSCF calculation results. Hence, with a large enough active space, CASSCF corrects the error in the DFT electronic structure description, which gives mixed $Fe(d_{yz})$ and phenoxyl radical MOs as described above and shows that the intermediate is in fact an $Fe^{II}(OPh^\bullet)$ complex, in agreement with the experimental Mössbauer data.

Table 5.4. Contributions of electron configurations to the ground state as calculated for the CASSCF active spaces listed. See Figure 5.16 - Figure 5.19 for visualizations and energies of the orbitals here. Here, some orbital abbreviations are simplified for easy comparison of configurations. "OC_{Ph}" refers to the π bonding MO $O(p_y)/C_{CO}(p_y)$ where C is primarily the C directly connected to the O of phenoxy moiety, "OC_{Ph}^*" is the corresponding antibonding orbital. "Ph" is the π bonding orbital in the phenyl ring $C(p_y)$. "OPh" refers to $C_{Ph}(p_y)/O(p_y)$.

Configuration	CASSCF (25,17)	CASSCF (17,13)	CASSCF (13,11)	CASSCF (13,10)
$(OC_{Ph})^2(Ph)^2(OPh)^1(d_{yz})^2(d_{xy})^1(OC_{Ph}^*)^0$	86%	80%	79%	81%
$(OC_{Ph})^2(Ph)^2(OPh)^2(d_{yz})^1(d_{xy})^1(OC_{Ph}^*)^0$	6%	3%	8%	7%
$(OC_{Ph})^2(Ph)^2(OPh)^1(d_{yz})^1(d_{xy})^2(OC_{Ph}^*)^0$	3%	10%	3%	4%
$(OC_{Ph})^1(Ph)^2(OPh)^1(d_{yz})^2(d_{xy})^1(OC_{Ph}^*)^1$	1%		3%	3%
$(OC_{Ph})^2(Ph)^1(OPh)^2(d_{yz})^2(d_{xy})^1(OC_{Ph}^*)^0$		2%		
$(OC_{Ph})^2(Ph)^2(OPh)^0(d_{yz})^2(d_{xy})^1(OC_{Ph}^*)^1$			1%	2%

5.8 Reactivity Studies of 2 (Ray Group)

Reactivity studies were performed by our collaborators in the Ray Group. Complex **2** shows the typical hydrogen atom abstraction (HAA) reactivity expected for a metal bound radical. For example, **2** performs HAA from xanthene to form xanthone and major iron(II) products with a KIE of 4.0. HAA is also observed in the reactions of **2** with fluorene, indene, dihydroanthracene (DHA) and 2,4,6-tri-*tert*-butylphenol to form oxidized products of varying yields in presence of excess O_2. Notably, for DHA exceptional high yields up to 200% (based on iron) of oxidized products (anthracene 48%, anthrone 145%, antharachinone 4%) are detected. Different reaction conditions for the reaction of **2** with substrates were employed, which revealed that significant amounts of oxidized products are only obtained in the presence of excess O_2. No products were obtained in blank reactions in the absence of **2**. Thus, **2** performs HAA from different substrates to form radical species, which in the presence of O_2 yields the products. Furthermore, Hammett analysis of the reaction rates of **2** with different *para*-substituted 2,6-di-*tert*-butylphenols afforded

a negative reaction constant (ρ) of -0.49, which reflects the electrophilic character of **2** in reactions with phenols. In all these reactions, which were performed in the presence of excess O_2, the iron(II) oxidation state stays unaltered. Remarkably, the HAA reactions rates of **2** are found to be comparable to the rates observed for some high-valent oxoiron(IV) complexes known in the literature, for example $[Fe^{IV}(O)(cyclam)(MeCN)]^{2+}$ [279] and $[Fe^{IV}(O)(TMC)(OTf)]^{+}$;[280] **2** is, however, a sluggish oxidant relative to $[Fe^{IV}(O)(TMCO)(OTf)]^{+}$.[239]

5.9 Conclusions

Intermediates in the reaction cycle of an oxygenase are usually very informative with respect to the chemical mechanism of O_2 activation and insertion. However, detection of these intermediates is often complicated by their short lifetimes and the regulatory mechanism of the enzyme optimized to ensure specificity. The present study demonstrates that model compounds may provide important insights into the mechanism of such enzymatic reactions. For example, based on this study an elusive iron(II)-phenoxyl radical has now been included to the list of commonly known metal-radical species that can be utilized in biology or chemistry for HAA reactions. The spectroscopic markers of the hs-Fe^{II}-OPh$^{\bullet}$ core in **2** include: a) a broad absorption band of moderate intensity at 695 nm and b) Fe-O and O-Ph vibrational modes at 628 cm^{-1} and 1279 cm^{-1}, respectively. To the best of our knowledge, **2** is the only example of a well characterized oxygen-derived iron(II)-reactive intermediate; no precedents for a phenoxyl radical bound to a ferrous center in chemistry or biology exist. We therefore hope that the unique spectroscopic properties of **2** will form a basis for all future investigations targeted towards the identification of novel reactive intermediates in various heme and non-heme oxygenases. The stabilization of the ferrous center in the presence of PhO$^{\bullet}$ and O_2 can be attributed to the weak ligand field associated with the N_3O macrocycle of the TMCO ligand, which makes the iron(III) and iron(IV) oxidation states unstable. Accordingly, using the stronger donating N_4 macrocycle of the TMC ligand in the same reaction[239] led to the generation of the Fe^{IV}=O core. Thus, the present study not only provides an opportunity to elucidate elementary steps in the biological dioxygen activation, but it also underlines the importance of subtle electronic changes for the nature, stability, and reactivity of the biologically relevant metal-dioxygen intermediates.

5.10 Experimental Section

5.10.1 Resonance Raman Spectroscopy.

All rRaman spectra reported in this chapter were measured with 3-8 mM samples in 3 mm EPR tubes. The 647 nm excitation line from a Kr gas ion Coherent Innova laser was used for excitation, with a power of 20 - 40 mW. Samples were measured at liquid nitrogen temperature by using an EPR coldfinger dewar with liquid nitrogen. The scattered light was focused onto an Acton two-stage TriVista 555 monochromator and detected by a liquid nitrogen-cooled Princeton Instruments Spec-10:400B/LN CCD camera. The spectral resolution was ca. 2 cm^{-1}. Single-pixel spikes due to cosmic rays were manually removed. Spectra reported here were baseline corrected and then referenced and normalized to the known acetonitrile peak[281] at 920 cm^{-1}, for best comparison between different samples.

5.10.2 Magnetic Circular Dichroism Spectroscopy.

See Section 4.8.1 for description of Magnetic Circular Dichroism spectroscopy.

5.10.3 Computational Details

Geometry optimizations and frequency calculations were performed using the program package Gaussian 09.[282] All the calculations included here were performed with Becke's three-parameter hybrid functional, B3LYP,[229–231] and TZVP[283,284] as the basis set. Orca (version 4.0)[237] was used to perform Mössbauer and EPR calculations on the Gaussian-optimized structures. For the Mössbauer calculations all non-iron atoms were described with the TZVP basis set, while for iron the larger CP(PPP) basis set[285,286] was used. Mössbauer isomer shifts were obtained from these calculations using empirical correlations as established by Neese and co-workers.[287] MO images were visualized in Avogadro (Avogadro: an open-source molecular builder and visualization tool. Version 1.2.0. http://avogadro.cc/).[288] CASSCF calculations were performed in Orca with TZVP as the basis set on the preferred structural model: hs-Fe^{II} [Fe(TMCO)(OPh)(MeCN)]$^{2+}$, with overall $S_t = 5/2$ (ferromagnetically coupled) and N-Me trans to the phenoxy moiety.

5.10.4 Synthetic Procedures (Ray Group)

Complexes **1**, **2**, and variations on **2** were prepared by the Ray Group. The synthetic procedures are provided for the reader.

Synthesis and characterization of 1. TMCO ligand, **1** and [57]Fe-enriched **1** were synthesized as previously reported.[239]

Generation and characterization of compound 2. The reaction of **1** with O_2, $NaBPh_4$ and $HClO_4$ to form compound **2** was monitored by UV-Vis. In a typical experiment, 1 mL of a 1 mM solution of **1** in acetonitrile was placed in a 0.5 cm path-length cuvette. The quartz cell was placed in the Unisoku cryostat of the UV-Vis spectrophotometer and cooled down to 0 °C. After reaching thermal equilibrium a UV-Vis absorption spectrum of the starting **1** was recorded. Then, 100 µL of a solution of $NaBPh_4$ (1.5 eq) and 100 µL of a solution of $HClO_4$ (0.1 to 1 eq) in acetonitrile were added in presence of O_2. The formation of a band at λ_{max} [ε, $M^{-1}cm^{-1}$] = 360 nm [4400] and 665 nm [2800] was observed. **2** was fully formed within 150 s and the half-life time ($t_{1/2}$) is 0.75 h.

Chemical generation of 2. In a typical experiment 1 mL of a 1 mM solution of **1** in acetonitrile was placed in a 0.5 cm path length cuvette in the aforementioned cryostat of the UV-Vis instrument. Either 5 eq of phenol or 1.5 eq of KOPh dissolved in 100 µL of acetonitrile were added under inert conditions. 1.1 eq of $NO^+SbF_6^-$ were added and the formation of the typical absorption feature of **2** at 665 nm was observed (though in lower yield for phenol).

5.11 Appendix for Chapter 5

5.11.1 Tables of Coordinates of DFT Structures

Table 5.5. Coordinates of the fully optimized structure of hs-Fe^{II} [Fe(TMCO)(OPh)]$^{2+}$, with overall S_t = 5/2 (ferromagnetically coupled) and N-Me trans to the phenoxy moiety. Calculated using B3LYP/TZVP.

C	-0.24786400	-1.25312100	2.91834700	C	-2.42126700	-2.37208500	1.11840000
H	-1.17517700	-1.33836800	3.48876500	H	-2.50893400	-3.41047900	1.45162400
H	0.59328100	-1.29811400	3.61292800	H	-3.11188000	-2.21905600	0.29545600
C	-0.09914700	-2.32578100	1.84344300	H	-2.71966600	-1.71837000	1.93583900
H	0.91939500	-2.30695100	1.45684100	C	-3.09315700	-0.00243700	-1.79376700
H	-0.27589700	-3.31402000	2.28022000	H	-3.43593400	-0.00339000	-2.83234400
C	-0.63912600	-2.91401300	-0.48718300	H	-3.49520100	0.87739200	-1.30106100
H	-0.81331500	-3.96794500	-0.24509300	H	-3.49494800	-0.88145600	-1.29944800
H	0.43446700	-2.78665800	-0.63190300	C	-2.42213400	2.37380700	1.11377100
C	-1.37532100	-2.58097800	-1.79140700	H	-2.51013100	3.41290100	1.44472000
H	-2.44825900	-2.74853000	-1.69221800	H	-2.72012200	1.72185300	1.93277700
H	-1.04934600	-3.33615500	-2.51182000	H	-3.11289300	2.21875200	0.29130300
C	-1.08234400	-1.23004200	-2.45925700	Fe	-0.62415000	0.00002500	0.13729800
H	-0.00572600	-1.10017300	-2.56366900	N	-1.02564200	-2.07696900	0.69662900
H	-1.51057200	-1.23852300	-3.46659000	N	-1.60493100	-0.00215000	-1.74977100

C	-1.08281000	1.22443200	-2.46180800	N	-1.02645900	2.07830500	0.69240000
H	-1.51089700	1.23062800	-3.46924600	O	-0.23359400	0.00249800	2.20809900
H	-0.00610100	1.09488900	-2.56585800	O	1.15437500	-0.00033300	-0.46769200
C	-1.37662700	2.57662900	-1.79687200	C	3.19054100	0.00061800	0.76238100
H	-2.44969100	2.74362800	-1.69792500	C	4.56933000	0.00067800	0.74729700
H	-1.05126000	3.33056700	-2.51885600	C	5.26170300	-0.00000100	-0.47167400
C	-0.64055100	2.91294900	-0.49336000	C	4.55939100	-0.00075100	-1.68307500
H	0.43308400	2.78590500	-0.63789000	C	3.18008500	-0.00091700	-1.68627500
H	-0.81530000	3.96731900	-0.25361300	C	2.46808600	-0.00019700	-0.45878100
C	-0.09984500	2.33003400	1.83846800	H	2.64235600	0.00121000	1.69551000
H	-0.27693000	3.31915300	2.27310300	H	5.12223700	0.00121400	1.67783900
H	0.91864400	2.31077800	1.45175300	H	6.34389500	0.00007200	-0.47586100
C	-0.24798500	1.25959900	2.91570500	H	5.10201900	-0.00125200	-2.61948000
H	0.59332700	1.30617300	3.60997800	H	2.62577600	-0.00166600	-2.61589500
H	-1.17518200	1.34586400	3.48617200				

Table 5.6. Coordinates of the fully optimized structure of hs-Fe^{II} [Fe(TMCO)(OPh)]$^{2+}$, with overall $S_t = 3/2$ (antiferromagnetically coupled) and N-Me trans to the phenoxy moiety. Calculated using B3LYP/TZVP.

C	0.37637300	3.01809900	-1.01386400	C	2.51927300	1.21269400	-2.25858400
H	1.35734100	3.49729000	-0.96766800	H	2.63822600	1.58479000	-3.28114400
H	-0.38444600	3.79886500	-1.08037900	H	3.17031200	0.35458700	-2.12925700
C	0.24364300	2.05299200	-2.18449800	H	2.84625800	1.98816600	-1.56809100
H	-0.79176800	1.71809000	-2.25314500	C	3.03029100	-1.89583400	-0.15895400
H	0.48619800	2.57164000	-3.11823900	H	3.34748600	-2.94140300	-0.22637800
C	0.66394300	-0.25644000	-2.91650300	H	3.45469900	-1.46807400	0.74327900
H	0.84007200	0.05779700	-3.95141200	H	3.44141500	-1.36016100	-1.00801100
H	-0.41593600	-0.36182800	-2.79478400	C	2.55268900	0.85607100	2.38212300
C	1.33546900	-1.62065400	-2.70101500	H	2.69695400	1.04620600	3.45036500
H	2.41227900	-1.55295000	-2.85792400	H	2.86242700	1.74057600	1.82855200
H	0.98180700	-2.24980200	-3.52251200	H	3.19900100	0.03590100	2.08892800
C	1.01078200	-2.39919700	-1.41693900	Fe	0.59108900	0.13154400	0.00896000
H	-0.07063600	-2.47879000	-1.30305400	N	1.10317700	0.84633600	-1.99678000
H	1.40066300	-3.41812400	-1.52163200	N	1.54713900	-1.80934200	-0.14337800
C	1.02541400	-2.58540700	1.03208400	N	1.13117600	0.53598800	2.09378300
H	1.41488400	-3.60833200	0.97625100	O	0.17288400	2.22602900	0.17378100
H	-0.05737200	-2.64692000	0.92084800	O	-1.29289800	-0.60369300	-0.03904900
C	1.36764700	-2.00997000	2.41449500	C	-3.20539500	0.80678400	0.05422600
H	2.44645400	-1.96803700	2.56684500	C	-4.57114200	0.89508500	0.06309600
H	1.02204100	-2.75526900	3.13622700	C	-5.35981600	-0.27507100	-0.00648500
C	0.70242200	-0.69342000	2.84173300	C	-4.75829400	-1.54748000	-0.08582300
H	-0.37935600	-0.77860200	2.72051800	C	-3.39378100	-1.66083800	-0.09629100
H	0.89348100	-0.53899300	3.90980200	C	-2.56567500	-0.48179000	-0.02667600
C	0.27994400	1.70062300	2.47903700	H	-2.57934200	1.68753600	0.10671200
H	0.54414800	2.07268400	3.47467800	H	-5.05808400	1.85992800	0.12359000
H	-0.75501100	1.35982400	2.51880800	H	-6.43936100	-0.19242000	0.00118100
C	0.39276400	2.83132900	1.46416600	H	-5.38140000	-2.43087300	-0.13821100
H	-0.36812700	3.59051400	1.65806400	H	-2.90551200	-2.62468800	-0.15658400
H	1.37227000	3.31571300	1.47562200				

Table 5.7. Coordinates of the fully optimized structure of is-Fe^{II} [Fe(TMCO)(OPh)]$^{2+}$, with overall $S_t = 3/2$ (ferromagnetically coupled) and N-Me trans to the phenoxy moiety. Calculated using B3LYP/TZVP.

C	0.08642900	1.26507200	2.85070900	C	2.31542500	2.33923700	1.15622400
H	0.94644400	1.43004900	3.50133100	H	2.35648700	3.36423900	1.53385900
H	-0.81730100	1.23607400	3.46108600	H	3.04882800	2.23922400	0.36419000
C	-0.05050400	2.29211700	1.73888200	H	2.58563100	1.65891400	1.96153200
H	-1.04296100	2.22216100	1.29778900	C	3.11677200	0.00026600	-1.59055700

H	0.07665200	3.30227900	2.13925300
C	0.62234900	2.90419500	-0.52875600
H	0.78955700	3.94839400	-0.24568400
H	-0.44124400	2.78025400	-0.73137900
C	1.42314000	2.57596600	-1.78314000
H	2.48993300	2.75171000	-1.63933000
H	1.12341500	3.30713100	-2.53857400
C	1.14893100	1.20591500	-2.39468300
H	0.07722000	1.07934900	-2.53384300
H	1.62184000	1.15714300	-3.37962100
C	1.14911000	-1.20572500	-2.39477900
H	1.62211200	-1.15687400	-3.37966800
H	0.07740500	-1.07923900	-2.53404400
C	1.42334300	-2.57580000	-1.78328800
H	2.49013100	-2.75150200	-1.63938700
H	1.12371500	-3.30694500	-2.53877900
C	0.62246400	-2.90413800	-0.52899500
H	-0.44112000	-2.78018000	-0.73165700
H	0.78967100	-3.94835500	-0.24599300
C	-0.05037100	-2.29230000	1.73871900
H	0.07685300	-3.30248200	2.13902100
H	-1.04284400	-2.22237800	1.29766000
C	0.08648700	-1.26532000	2.85061700
H	-0.81725300	-1.23641400	3.46098300
H	0.94649700	-1.43029600	3.50124400
H	3.50272900	0.00031200	-2.61317000
H	3.49786100	-0.87953500	-1.08307600
H	3.49767500	0.88015000	-1.08306700
C	2.31556700	-2.33927600	1.15591700
H	2.35668200	-3.36429900	1.53348900
H	2.58582800	-1.65899300	1.96123800
H	3.04890700	-2.23920900	0.36382600
Fe	0.68571300	-0.00000700	0.24060500
N	0.94609000	2.03497600	0.64611500
N	1.62461300	0.00010700	-1.61567200
N	0.94618300	-2.03501700	0.64593900
O	0.24804700	-0.00009500	2.16073800
O	-1.04947100	-0.00002500	-0.49197300
C	-3.11909100	-0.00006200	0.70197800
C	-4.50118900	-0.00006000	0.66294000
C	-5.17161600	-0.00003000	-0.56411800
C	-4.44519200	0.00000000	-1.75786800
C	-3.06301500	0.00000000	-1.73423600
C	-2.37323800	-0.00003200	-0.49965000
H	-2.59624900	-0.00008100	1.64988800
H	-5.06830500	-0.00007900	1.58506500
H	-6.25335700	-0.00002700	-0.58866400
H	-4.96716100	0.00002400	-2.70607700
H	-2.49443200	0.00002500	-2.65545400

Table 5.8. Coordinates of the fully optimized structure of hs-Fe^{II} [Fe(TMCO)(OPh)]$^{2+}$, with overall S_t = 5/2 (ferromagnetically coupled) and N-Me cis to the phenoxy moiety. Calculated using B3LYP/TZVP.

C	0.32036100	-1.24012700	2.91429600
H	-0.76496100	-1.36713100	2.89809300
H	0.65643000	-1.21028200	3.95208400
C	1.06624100	-2.31230400	2.14987700
H	2.13330900	-2.16436500	2.31288700
H	0.80456600	-3.30288200	2.53456300
C	1.91987400	-2.90845500	-0.04943200
H	1.80407100	-3.98990600	0.07595500
H	2.85471200	-2.63101200	0.44033800
C	2.02911400	-2.56979300	-1.53280000
H	1.08066200	-2.71179700	-2.05398200
H	2.70142500	-3.31166100	-1.97112200
C	2.65181200	-1.20755600	-1.83063500
H	3.50436100	-1.05659900	-1.16622800
H	3.04133000	-1.19962100	-2.85326200
C	2.65159800	1.20724500	-1.83103900
H	3.04113800	1.19901100	-2.85365500
H	3.50416500	1.05668600	-1.16656200
C	2.02863300	2.56947700	-1.53373400
H	1.08014600	2.71107300	-2.05496000
H	2.70078800	3.31130800	-1.97235500
C	1.91935000	2.90870300	-0.05050100
H	2.85424600	2.63162900	0.43936500
H	1.80334200	3.99018000	0.07445800
C	1.06584300	2.31322600	2.14903600
H	0.80398500	3.30389500	2.53336700
H	2.13294000	2.16556000	2.31210300
C	0.32017900	1.24119400	2.91386900
H	0.65631000	1.21178000	3.95164900
H	-0.76516500	1.36800300	2.89767600
C	-0.47883200	-2.91225000	0.36656700
H	-0.41591900	-3.97123600	0.63341100
H	-0.70235500	-2.83020900	-0.69393600
H	-1.29836800	-2.45812200	0.91748200
C	0.77636100	-0.00048800	-2.81477900
H	1.30864500	-0.00054200	-3.76975500
H	0.14198500	0.87979900	-2.76336700
H	0.14223500	-0.88094000	-2.76313100
C	-0.47935300	2.91221500	0.36550700
H	-0.41664900	3.97131000	0.63198000
H	-1.29879300	2.45812400	0.91659200
H	-0.70284700	2.82974700	-0.69496600
Fe	0.61812800	0.00005200	0.15702800
N	0.80408800	-2.22444100	0.68036100
N	1.75845300	-0.00021000	-1.68772600
N	0.80369800	2.22476800	0.67956300
O	0.66987100	0.00044600	2.26001900
O	-1.20756500	-0.00014200	-0.32919600
C	-3.35158500	0.00032000	0.68212300
C	-4.71931600	0.00024100	0.52825400
C	-5.28426600	-0.00039400	-0.75695000
C	-4.46262500	-0.00094600	-1.89353500
C	-3.09217200	-0.00086400	-1.75876500
C	-2.50369700	-0.00022700	-0.46197800
H	-2.90274000	0.00079600	1.66744400
H	-5.36431800	0.00066400	1.39743100
H	-6.36057500	-0.00045300	-0.87073100
H	-4.91000600	-0.00143700	-2.87901100
H	-2.44665600	-0.00127600	-2.62683400

Table 5.9. Coordinates of the fully optimized structure of hs-Fe^{II} [Fe(TMCO)(OPh)(MeCN)]$^{2+}$, with overall S_t = 5/2 (ferromagnetically coupled) and N-Me trans to the phenoxy moiety. Calculated using B3LYP/TZVP.

C	-0.18883400	1.24404200	-2.77118000	H	-2.38820300	2.41772200	-1.57798900
H	-1.18711600	1.41244300	-3.18209000	C	-2.22276300	0.01920700	2.61497200
H	0.52596700	1.22794800	-3.59712800	H	-2.25444600	0.02565200	3.70825100
C	0.22758900	2.29832500	-1.74702600	H	-2.74429500	-0.86320800	2.25518000
H	1.27283700	2.14073100	-1.48894500	H	-2.74318400	0.89812500	2.24500900
H	0.14048700	3.29435300	-2.19398400	C	-1.89292500	-2.86638400	-0.68238800
C	0.11890400	2.88544600	0.64790300	H	-1.75368000	-3.93804500	-0.85547600
H	0.09112000	3.96732000	0.47868400	H	-2.39054200	-2.43534000	-1.54643400
H	1.16406000	2.58044300	0.62716700	H	-2.53852100	-2.73357500	0.18075300
C	-0.47102600	2.58654700	2.03444100	Fe	-0.52110200	0.00047700	0.00324400
H	-1.54752500	2.76462100	2.05248300	N	-0.57755400	2.20509800	-0.49136800
H	-0.05736200	3.34528800	2.70404700	N	-0.81253800	0.01557200	2.14537200
C	-0.11387000	1.24103400	2.68139800	N	-0.57983100	-2.21041500	-0.46237300
H	0.95409000	1.07064900	2.57004200	O	-0.15980000	-0.01326700	-2.07168800
H	-0.32715200	1.29989400	3.75345600	O	1.42086500	0.00158600	0.31804500
C	-0.11507600	-1.20353300	2.69726100	C	3.24200100	-0.00938600	-1.22110200
H	-0.32765300	-1.24768100	3.77015800	C	4.60558600	-0.01169600	-1.42093500
H	0.95302400	-1.03611700	2.58277800	C	5.48160200	-0.00515100	-0.32625800
C	-0.47439700	-2.55711300	2.06869700	C	4.97599900	0.00390200	0.97994800
H	-1.55120100	-2.73315800	2.08913500	C	3.61509700	0.00632700	1.19787300
H	-0.06207500	-3.30732500	2.74866800	C	2.70680400	-0.00035900	0.09957900
C	0.11530400	-2.87617000	0.68637900	H	2.56125200	-0.01440300	-2.06092900
H	1.16100000	-2.57329400	0.66155400	H	5.00594000	-0.01862400	-2.42671000
H	0.08570600	-3.96023300	0.53216500	H	6.55112600	-0.00707600	-0.49143800
C	0.22595000	-2.32053600	-1.71621400	H	5.65842400	0.00894800	1.82007900
H	0.13881000	-3.32236000	-2.14999600	H	3.21821600	0.01320800	2.20469800
H	1.27109500	-2.15994900	-1.45964800	N	-2.83171800	-0.00172800	-0.42293000
C	-0.18957000	-1.27974600	-2.75442400	C	-3.96293000	-0.00484900	-0.63191900
H	0.52542500	-1.27517600	-3.58035500	C	-5.39049700	-0.00928600	-0.88847400
H	-1.18789900	-1.45297400	-3.16322600	H	-5.71083500	-1.00291600	-1.20660900
C	-1.89029200	2.85904700	-0.71931800	H	-5.93222300	0.26306200	0.01912000
H	-1.75038300	3.92841800	-0.90542100	H	-5.63248300	0.70910900	-1.67358100
H	-2.53611400	2.73687000	0.14515500				

Table 5.10. Coordinates of the partially optimized structure of hs-Fe^{II} [Fe(TMCO)(OPh)(MeCN)]$^{2+}$, with overall S_t = 5/2 (ferromagnetically coupled) and N-Me cis to the phenoxy moiety. Calculated using B3LYP/TZVP. MeCN dissociates during the optimization; therefore, in this structure the Fe-N(CCH$_3$) bond was fixed at 2.3 Å during the geometry optimization (the rest of the structure was allowed to optimize).

C	-0.19911200	-1.25226800	-2.77355100	H	1.62968600	-2.41253200	-0.99575500
H	0.87937300	-1.39101800	-2.88303500	C	0.19477300	-0.00105800	3.00841900
H	-0.65241300	-1.25654200	-3.76727200	H	-0.13626200	-0.00147400	4.05083000
C	-0.85011200	-2.32054500	-1.90205600	H	0.80586200	0.87824000	2.83056300
H	-1.92937200	-2.18712600	-1.94242300	H	0.80632900	-0.87993000	2.83002600
H	-0.62221300	-3.31225600	-2.30648900	C	0.90473900	2.86708500	-0.31968900
C	-1.40561000	-2.89806900	0.42593400	H	0.83016200	3.93554200	-0.54354200
H	-1.31103300	-3.98093100	0.29091700	H	1.62742000	2.41584600	-0.99337300
H	-2.40620800	-2.62195800	0.09548900	H	1.27500800	2.74450400	0.69380300
C	-1.25987400	-2.57079300	1.91865300	Fe	-0.40040600	0.00029000	0.00667600
H	-0.23321600	-2.72068000	2.25592900	N	-0.42198600	-2.21733100	-0.47426600
H	-1.83764700	-3.33156700	2.45006600	N	-0.98769000	-0.00113700	2.10220800
C	-1.81688600	-1.22383900	2.39872700	N	-0.42409400	2.21807500	-0.47220300
H	-2.79882300	-1.06643900	1.95634800	O	-0.46741000	0.00110500	-2.11973700
H	-1.95991100	-1.26951200	3.48313000	O	1.49770800	0.00117300	0.24698300
C	-1.81802700	1.22051000	2.39987300	C	3.43982700	0.00152000	-1.12039600

H	-1.96113000	1.26504100	3.48431400	C	4.81561900	0.00109300	-1.20847000
H	-2.79979900	1.06262400	1.95731100	C	5.59688300	-0.00001600	-0.04507900
C	-1.26229200	2.56846500	1.92104900	C	4.98425600	-0.00069700	1.21385400
H	-0.23577900	2.71904400	2.25845400	C	3.60912400	-0.00027400	1.31925800
H	-1.84080600	3.32820100	2.45313700	C	2.80044100	0.00081600	0.14982000
C	-1.40839400	2.89700500	0.42864000	H	2.83017500	0.00242400	-2.01483600
H	-2.40872400	2.62022800	0.09794000	H	5.29689600	0.00163900	-2.17807300
H	-1.31484800	3.98008000	0.29463000	H	6.67641000	-0.00034700	-0.12060500
C	-0.85229400	2.32226200	-1.89990700	H	5.59433900	-0.00152900	2.10792600
H	-0.62520400	3.31453400	-2.30342000	H	3.12895100	-0.00076200	2.28803700
H	-1.93144600	2.18801200	-1.94039100	N	-2.66525800	-0.00065900	-0.39387700
C	-0.20041100	1.25533800	-2.77242800	C	-3.76828100	-0.00123500	-0.72294600
H	-0.65389900	1.26010000	-3.76606500	C	-5.16054300	-0.00207300	-1.13094000
H	0.87791700	1.39523200	-2.88199500	H	-5.37599100	-0.89216900	-1.72474400
C	0.90750800	-2.86514500	-0.32245500	H	-5.80705700	0.00155200	-0.25153600
H	0.83401400	-3.93346500	-0.54732400	H	-5.37511600	0.88364100	-1.73154300
H	1.27771900	-2.74315600	0.69112900				

Table 5.11. Coordinates of the fully optimized structure of hs-Fe^{II} [Fe(TMCO)(OPh)(OTf)]$^+$, with overall S_t = 5/2 (ferromagnetically coupled) and N-Me trans to the phenoxy moiety. Calculated using B3LYP/TZVP.

C	0.13670600	-2.61769000	-1.24005800	C	-0.89467700	3.06591000	-0.01862500
H	-0.93856100	-2.76622000	-1.36172300	H	-0.71099300	4.14451400	-0.02316000
H	0.63373600	-3.59085200	-1.26611200	H	-1.48119000	2.81248000	0.85929900
C	0.73890300	-1.69946100	-2.30050500	H	-1.47799000	2.80454500	-0.89633000
H	1.81627900	-1.65264500	-2.15133100	C	-1.15107000	-0.26122400	2.86134800
H	0.55258800	-2.11674800	-3.29574400	H	-1.03570200	-0.44085700	3.93531000
C	1.08577100	0.67918500	-2.86704500	H	-1.79262900	-1.02634800	2.43854200
H	1.04386400	0.51548500	-3.94987200	H	-1.64816300	0.68909900	2.70540000
H	2.10595700	0.47900100	-2.54293800	Fe	0.29011500	0.16202800	0.00071600
C	0.73222000	2.14738300	-2.57752600	N	0.18864700	-0.31564100	-2.20366400
H	-0.32825600	2.33549600	-2.74963700	N	0.40302000	2.33799400	-0.01271400
H	1.24912800	2.73662600	-3.33963200	N	0.18526000	-0.29072600	2.21038200
C	1.19150000	2.73109800	-1.23408200	O	0.40183000	-1.96993900	0.01323500
H	2.22279600	2.43685800	-1.05855600	O	2.17841300	0.17120800	0.00359500
H	1.16481700	3.82385600	-1.30134500	C	3.75012600	-1.63757400	0.00611600
C	1.18781100	2.74526800	1.20645100	C	5.07273500	-2.05567700	0.00495400
H	1.16111100	3.83874800	1.26077500	C	6.11100400	-1.12609300	0.00093800
H	2.21954900	2.44882700	1.03765800	C	5.81364100	0.23565800	-0.00176800
C	0.72402800	2.17768400	2.55523700	C	4.49662800	0.66756400	-0.00070800
H	-0.33737400	2.36649800	2.72087800	C	3.43806600	-0.26298400	0.00300600
H	1.23712700	2.77706400	3.31199700	H	2.94670200	-2.36029400	0.00943600
C	1.07846400	0.71366300	2.86461100	H	5.29789600	-3.11506700	0.00723800
H	2.10013900	0.51088600	2.54688500	H	7.14048700	-1.45910900	0.00001000
H	1.03273800	0.56351800	3.94923700	H	6.61480600	0.96407000	-0.00469500
C	0.73928800	-1.67177200	2.32337200	H	4.27075100	1.72608600	-0.00268700
H	0.55463900	-2.07778900	3.32356300	C	-4.19142700	-1.04507100	0.00173400
H	1.81639500	-1.62352500	2.17266000	F	-3.88718200	-1.76415700	1.09199300
C	0.13919200	-2.60398300	1.27400800	F	-3.88362100	-1.77461900	-1.08056300
H	0.63917600	-3.57529100	1.31090900	F	-5.48602800	-0.77814800	-0.00168600
H	-0.93550900	-2.75453000	1.39805300	S	-3.19199300	0.57155100	-0.00447300
C	-1.14648500	-0.28964700	-2.85722400	O	-1.75965600	-0.00571300	-0.00025800
H	-1.02964000	-0.47867800	-3.92942100	O	-3.51074000	1.24999600	1.26019000
H	-1.64256600	0.66260900	-2.71018700	O	-3.50796700	1.23843100	-1.27597500
H	-1.78979300	-1.05022100	-2.42896000				

Table 5.12. Coordinates of the fully optimized structure of hs-Fe^{II} [Fe(TMCO)(OPh)(OTf)]$^+$, with overall $S_t = 5/2$ (ferromagnetically coupled) and N-Me cis to the phenoxy moiety. Calculated using B3LYP/TZVP.

C	-0.49515500	-1.13843800	-2.73715100		C	-1.14337900	2.22848200	2.11118100
H	-1.56512000	-1.16652100	-2.96249100		H	-0.85935400	2.99200900	2.84181900
H	0.02360500	-1.84768400	-3.38537700		H	-1.75910300	1.47825400	2.59760000
C	0.12077600	0.24447700	-2.90499500		H	-1.73478700	2.68718500	1.32503500
H	1.19878300	0.14637800	-2.81221400		C	-1.78753900	-2.10657500	1.90342400
H	-0.10783000	0.62441100	-3.90634400		H	-1.73465400	-2.98439000	2.55533900
C	0.60523800	2.33440000	-1.70652500		H	-2.48263700	-2.30898900	1.09382600
H	0.53740200	2.96610500	-2.59948800		H	-2.17941900	-1.26802500	2.47072400
H	1.60658300	1.91218800	-1.67954000		Fe	-0.41421900	0.05096500	0.07577400
C	0.38864700	3.21145100	-0.46452700		N	-0.36136000	1.20233000	-1.86280500
H	-0.64922000	3.54133500	-0.38849800		N	0.07485500	1.60192600	1.53769100
H	0.95923600	4.12646400	-0.64447500		N	-0.43965300	-1.79802200	1.36473800
C	0.90566900	2.66816300	0.87420000		O	-0.28576000	-1.50327800	-1.36151200
H	1.89979000	2.25749900	0.72736000		O	-2.25901100	0.24050000	0.20323400
H	0.99140100	3.50058800	1.58095300		C	-4.12298100	-0.83713800	-0.82157700
C	0.88503600	0.99610000	2.65395400		C	-5.49715000	-0.94585700	-0.97237600
H	0.98147100	1.75755600	3.43559300		C	-6.35339500	-0.10251200	-0.26656100
H	1.87796100	0.79980800	2.26068200		C	-5.82044600	0.85479700	0.59536400
C	0.33276800	-0.28846400	3.28414200		C	-4.44862800	0.97316000	0.75643500
H	-0.70313300	-0.16245000	3.60460600		C	-3.57597300	0.12564700	0.04813600
H	0.89637000	-0.41969600	4.21178400		H	-3.45901400	-1.49121800	-1.37206800
C	0.52063500	-1.59301600	2.49728000		H	-5.90484300	-1.69115000	-1.64391800
H	1.52796000	-1.63376800	2.08896300		H	-7.42504700	-0.19023000	-0.38716300
H	0.41368700	-2.43681700	3.18847600		H	-6.48103800	1.51286500	1.14586400
C	0.01139700	-2.93234400	0.49917500		H	-4.03676800	1.71574700	1.42627800
H	-0.27710700	-3.88897500	0.94716800		O	1.72063400	-0.03476000	-0.00840800
H	1.09593700	-2.90307300	0.43495500		S	2.92015000	-0.83062600	-0.55690400
C	-0.56653500	-2.83818700	-0.90682200		O	3.10313700	-2.10869500	0.15255600
H	-0.06604100	-3.55869200	-1.55730400		O	2.97940200	-0.81901400	-2.02784000
H	-1.64484400	-3.01874200	-0.94349400		C	4.35209900	0.27799700	0.01647500
C	-1.68896300	1.73128900	-2.26066800		F	4.20722500	1.50471000	-0.50587600
H	-1.59565800	2.31808700	-3.18013300		F	4.33863700	0.38428900	1.35158400
H	-2.10423800	2.35944700	-1.47840600		F	5.50705100	-0.23332300	-0.37425800
H	-2.38607000	0.91608500	-2.43180300					

Table 5.13. Coordinates of the fully optimized structure of [Fe(TMCO)(OOH)]$^{2+}$, with overall $S_t = 5/2$ and N-Me trans to the hydroperoxide moiety. Calculated using B3LYP/TZVP.

C	1.26051600	-2.79714900	-0.43080700		H	-3.31182300	-2.17211900	-0.20083800
H	1.39709800	-3.07460900	-1.47735700		H	-2.26663600	-1.79871300	1.17620500
H	1.24927000	-3.70140100	0.17920200		C	-1.25863500	-2.79806700	-0.43087400
C	2.31516100	-1.82746100	0.08815500		H	-1.24671400	-3.70239600	0.17900900
H	2.26794700	-1.79685400	1.17605000		H	-1.39506800	-3.07547600	-1.47745600
H	3.31323600	-2.16969900	-0.20106200		C	2.36295700	-0.37401000	-1.87789400
C	2.92141500	0.54327200	0.34145900		H	3.39570200	-0.67751400	-2.06982500
H	3.96801000	0.37433500	0.06938000		H	2.22883300	0.63657000	-2.25000400
H	2.81499700	0.30195500	1.39937300		H	1.69680300	-1.03422800	-2.43009300
C	2.57775600	2.01818400	0.11545400		C	-0.00118500	2.58997800	-1.48388500
H	2.73290500	2.30925400	-0.92407900		H	-0.00104700	3.68213600	-1.43680900
H	3.33106600	2.58368700	0.67064100		H	-0.88131100	2.26921000	-2.03192900
C	1.22623500	2.51319300	0.64083500		H	0.87853700	2.26897900	-2.03245000
H	1.10344900	2.21956700	1.68363500		C	-2.36314900	-0.37553600	-1.87750100
H	1.21364200	3.60674800	0.60689700		H	-3.39591200	-0.67916400	-2.06917200
C	-1.22819800	2.51235800	0.64103500		H	-1.69706300	-1.03568700	-2.42985700
H	-1.21646200	3.60592000	0.60698500		H	-2.22920700	0.63505100	-2.24965500
H	-1.10495600	2.21895100	1.68384900		Fe	0.00001400	-0.07882300	0.12545400
C	-2.57946100	2.01623400	0.11605800		N	2.07100900	-0.43663900	-0.41897600

H	-2.73520700	2.30719600	-0.92341400	N	-0.00089900	2.02723900	-0.10319100
H	-3.33306900	2.58107800	0.67151000	N	-2.07084400	-0.43816000	-0.41866100
C	-2.92176500	0.54102700	0.34212800	O	0.00066800	-2.09912900	-0.28796600
H	-2.81475000	0.29976000	1.40000300	O	0.00087500	-0.11800600	1.98168900
H	-3.96833400	0.37121400	0.07047800	O	0.00140100	-1.36689400	2.64833600
C	-2.31395900	-1.82921300	0.08830500	H	0.00115100	-1.09604600	3.58348600

Table 5.14. Coordinates of the fully optimized structure of [Fe(TMCO)(OOH)]$^{2+}$, with overall S_t = 5/2 and N-Me cis to the hydroperoxide moiety. Calculated using B3LYP/TZVP.

C	-1.24525500	-2.67106000	-0.79225400	H	3.29983800	-2.09275500	-1.07172800
H	-1.37957900	-3.13541800	0.18621000	H	2.15024800	-1.32712600	-2.17050500
H	-1.19712900	-3.44838200	-1.55577900	C	1.24474500	-2.67115700	-0.79302100
C	-2.30300300	-1.64887700	-1.13992400	H	1.19629900	-3.44811700	-1.55689800
H	-2.15109700	-1.32760500	-2.17006500	H	1.37937300	-3.13599200	0.18517300
H	-3.30038000	-2.09256400	-1.07052500	C	-2.87272200	-0.73912700	1.04850000
C	-2.88919300	0.70770700	-0.92039700	H	-3.93050600	-0.95227200	0.87507400
H	-3.96751200	0.52646700	-0.87978600	H	-2.78800400	0.11124100	1.71898700
H	-2.60407400	0.70000400	-1.97385600	H	-2.40965700	-1.59608300	1.53010900
C	-2.57090100	2.07686500	-0.33126700	C	0.00004700	2.56803700	1.40584200
H	-2.73433200	2.10731400	0.74706200	H	0.00022400	3.66063500	1.40511500
H	-3.30780500	2.77081900	-0.74367500	H	0.87988900	2.21403800	1.93552500
C	-1.20693300	2.63236300	-0.72504900	H	-0.88014300	2.21433800	1.93514000
H	-1.05090100	2.46900100	-1.79271900	C	2.87242200	-0.74047400	1.04835400
H	-1.19059100	3.71381900	-0.56313600	H	3.93005300	-0.95433800	0.87487900
C	1.20784000	2.63216800	-0.72453700	H	2.40873600	-1.59720800	1.52975000
H	1.19166500	3.71360800	-0.56251300	H	2.78832500	0.10978500	1.71906200
H	1.05216700	2.46896400	-1.79228300	Fe	-0.00006100	-0.07276300	0.13953600
C	2.57152200	2.07628200	-0.33030700	N	-2.19938600	-0.44607200	-0.25418300
H	2.73442100	2.10626400	0.74811900	N	0.00026900	2.06791300	-0.00946400
H	3.30877500	2.77023800	-0.74208300	N	2.19932000	-0.44652300	-0.25424200
C	2.88975400	0.70726500	-0.91979300	O	-0.00021800	-1.92407900	-0.79413300
H	2.60510200	0.69997800	-1.97337700	O	-0.00006300	-0.37598000	1.97261100
H	3.96799700	0.52569600	-0.87875100	O	-0.00043200	-1.72074600	2.39929400
C	2.30248300	-1.64892400	-1.14057400	H	-0.00037100	-1.62970600	3.36914400

Table 5.15. Coordinates of the fully optimized structure of [Fe(TMCO(H))(OO)]$^{2+}$, with overall S_t = 5/2 and N-Me cis to the superoxide moiety. Calculated using B3LYP/TZVP.

C	3.30085700	-0.82042000	-0.47302500	H	1.62814100	3.27418000	-1.51684900
H	3.79650900	-1.15113600	0.43956000	H	1.19869500	1.67604100	-2.13013700
H	4.06616200	-0.58578500	-1.21289800	C	2.82098400	1.65843400	-0.73324300
C	2.32450600	-1.84600200	-1.03437400	H	3.51551400	1.54960600	-1.56681100
H	2.00862200	-1.51821200	-2.02535800	H	3.29283200	2.27758600	0.02961800
H	2.82354600	-2.81398600	-1.14799700	C	1.39236900	-2.79013900	1.03197300
C	0.00772000	-2.64950600	-0.97619300	H	1.73139100	-3.79128800	0.75130600
H	0.17803200	-3.72900500	-0.95968700	H	0.50112100	-2.87860400	1.64983300
H	0.10222100	-2.33667900	-2.01755700	H	2.16577200	-2.31156400	1.62989300
C	-1.41940800	-2.35505900	-0.48323700	C	-4.28118000	-1.12223300	-0.17818800
H	-1.45179700	-2.38292500	0.60744400	H	-4.69161800	-1.09555900	-1.18551000
H	-2.06578000	-3.15867800	-0.83711800	H	-4.97439600	-0.66139900	0.52126500
C	-1.92433100	-1.00513100	-1.00966100	H	-4.08893800	-2.14813500	0.12381000
H	-1.10975400	-0.28402100	-1.06925400	C	0.59634900	3.06381900	0.87792200
H	-2.34017500	-1.09797500	-2.01366000	H	0.57427900	4.08659800	0.48972100
C	-3.22576100	1.11406400	-0.55140700	H	1.55307900	2.89170200	1.36644900
H	-4.18606300	1.37072900	-0.10817900	H	-0.17998000	2.95243100	1.63053500
H	-3.34611800	1.13137500	-1.63517500	Fe	0.63594200	0.04590100	0.61951600
C	-2.17415100	2.11648800	-0.05173900	N	1.09432400	-1.97655700	-0.18721900

H	-1.90968500	1.87081000	0.97732000	N	-2.98948400	-0.34657500	-0.16145400
H	-2.70969200	3.06453800	0.01872800	N	0.39680800	2.07960300	-0.22853300
C	-0.90971900	2.34684900	-0.91685500	O	2.53416800	0.36547000	-0.15048100
H	-0.93577200	1.72880200	-1.81554300	H	-2.64414000	-0.34137700	0.80544600
H	-0.90136500	3.38379600	-1.26684700	O	0.16985000	0.12519300	2.54473800
C	1.49776000	2.22398000	-1.23475200	O	-0.91435000	-0.24959700	1.83041200

Table 5.16. Coordinates of the fully optimized structure of [Fe(TMCO(H))(OO)]$^{2+}$, with overall S_t = 5/2 and N-Me trans to the superoxide moiety. Calculated using B3LYP/TZVP.

C	-2.98510500	-1.25802900	-0.53600200	H	-2.17067600	3.25054700	-0.65172900
H	-3.10724000	-1.16634000	-1.61765700	H	-1.99468600	2.48797900	0.92975100
H	-3.95038200	-1.52386400	-0.10184100	C	-2.98518800	1.25798500	-0.53594600
C	-1.94090900	-2.30720300	-0.14485200	H	-3.95045500	1.52375700	-0.10172400
H	-1.99453700	-2.48790700	0.92973200	H	-3.10737900	1.16632800	-1.61759600
H	-2.17055300	-3.25052900	-0.65172000	C	-0.35104200	-1.86074300	-1.93566700
C	0.45336900	-2.79559600	0.18381800	H	-0.44182300	-2.87393800	-2.33925500
H	0.25214500	-3.81321100	-0.16833600	H	0.62945600	-1.47628900	-2.21018800
H	0.25678500	-2.78520900	1.25731000	H	-1.09903100	-1.23346300	-2.41245500
C	1.95077900	-2.52239900	-0.06797000	C	3.53383500	0.00000700	-1.39682200
H	2.19595200	-2.60843800	-1.12839200	H	4.52551100	-0.00022000	-0.95056900
H	2.46053400	-3.37398800	0.39084000	H	3.40490800	0.88962400	-2.00769200
C	2.61591600	-1.28595300	0.55766800	H	3.40465500	-0.88933600	-2.00804200
H	2.19219000	-1.06354900	1.53272300	C	-0.35092000	1.86090800	-1.93555700
H	3.68285800	-1.46004400	0.68620700	H	-0.44152000	2.87414100	-2.33909000
C	2.61603500	1.28589000	0.55767100	H	-1.09894500	1.23376300	-2.41247000
H	3.68299400	1.45993600	0.68611600	H	0.62954900	1.47631300	-2.20997100
H	2.19238000	1.06353300	1.53277100	Fe	-0.57259200	0.00009100	0.66890900
C	1.95080000	2.52236700	-0.06789600	N	-0.53421300	-1.86417100	-0.46209400
H	2.19593400	2.60847500	-1.12832000	N	2.51832800	-0.00005500	-0.28318200
H	2.46058000	3.37392500	0.39094900	N	-0.53427700	1.86427700	-0.46200700
C	0.45335400	2.79559500	0.18401000	O	-2.52738400	-0.00003600	0.00302200
H	0.25681400	2.78506000	1.25751000	O	-0.90438900	-0.00046300	2.63899500
H	0.25215900	3.81326900	-0.16799000	O	0.41581700	0.00006200	2.37164800
C	-1.94101500	2.30724300	-0.14482700	H	1.59852800	0.00001100	-0.72463600

Table 5.17. Coordinates of the fully optimized structure of [Fe(TMCO)(OOH)(OTf)]$^+$, with overall S_t = 5/2 and N-Me cis to the hydroperoxide moiety. Calculated using B3LYP/TZVP.

C	-1.37253400	1.25050900	-2.64594700	H	-2.45561200	-1.36241300	-2.73861300
H	-2.45494500	1.36307200	-2.73890500	C	3.67266200	0.00005800	0.17913600
H	-0.92181300	1.24612200	-3.64036700	C	-2.45815000	2.81504700	-0.16986500
C	-0.71809100	2.32769800	-1.79133700	H	-2.40116100	3.88906300	-0.37285000
H	0.36153000	2.21984800	-1.85918900	H	-2.81372600	2.65991200	0.84377100
H	-0.99077000	3.31573800	-2.17647600	H	-3.17603400	2.35720600	-0.84324300
C	-0.12567600	2.87377400	0.54008500	C	-1.81466500	0.00008000	3.08627100
H	-0.21322300	3.95597500	0.39222600	H	-1.52241100	0.00014100	4.14046800
H	0.86903600	2.57882000	0.21327100	H	-2.42210500	-0.87608400	2.88161400
C	-0.29386400	2.56875800	2.03645200	H	-2.42203900	0.87625700	2.88148400
H	-1.31953800	2.74668600	2.36393800	C	-2.45898900	-2.81441300	-0.16963100
H	0.30038200	3.32211000	2.56047300	H	-2.40233800	-3.88849200	-0.37238400
C	0.23129200	1.22006800	2.54498000	H	-3.17675500	-2.35650900	-0.84309600
H	1.22108100	1.04950100	2.13238700	H	-2.81449400	-2.65892600	0.84397400
H	0.32871700	1.27040900	3.63452700	F	3.60552900	1.08695200	0.95905200
C	0.23101300	-1.22034800	2.54497100	F	3.60577200	-1.08624400	0.95987400
H	0.32837400	-1.27074500	3.63452100	F	4.81650800	-0.00006000	-0.48264900
H	1.22085900	-1.04998600	2.13242700	Fe	-1.05688100	0.00017600	0.10783500
C	-0.29440800	-2.56891200	2.03639600	N	-1.11856800	2.20128100	-0.35585600
H	-1.32006600	-2.74672100	2.36399100	N	-0.59775100	-0.00004700	2.22921000
H	0.29979800	-3.32238200	2.56030300	N	-1.11924300	-2.20108600	-0.35581300

C	-0.12643100	-2.87386300	0.54000200
H	0.86831900	-2.57913700	0.21310200
H	-0.21425800	-3.95603700	0.39209600
C	-0.71898500	-2.32768600	-1.79133200
H	-0.99208400	-3.31562800	-2.17642700
H	0.36067600	-2.22029100	-1.85929700
C	-1.37314000	-1.25027100	-2.64586900
H	-0.92261800	-1.24608000	-3.64037900

O	-1.08641700	0.00006800	-1.98696000
O	1.03185000	-0.00017000	-0.05078800
O	2.31634400	-1.27079700	-1.77819700
O	2.31628200	1.26903700	-1.77934900
S	2.21792900	-0.00054900	-1.04273500
O	-2.92904600	0.00036400	0.48327300
O	-3.80167500	0.00054400	-0.65461900
H	-4.67098800	0.00057800	-0.22533300

Table 5.18. Coordinates of the fully optimized structure of [Fe(TMCO(H))(OO)(OTf)]$^+$, with overall S_t = 5/2 and N-Me cis to the superoxide moiety. Calculated using B3LYP/TZVP.

C	-0.56549800	-2.89726100	1.28663300		H	0.25131800	-3.62021500	-1.35259100
H	0.25530900	-3.61559000	1.36694200		C	1.88534800	-1.60508700	2.84017700
H	-1.51394300	-3.42662200	1.40226800		H	1.69986800	-1.71536600	3.91398800
C	-0.48495500	-1.77237400	2.33053700		H	2.80451600	-1.04470200	2.69237800
H	-1.35594400	-1.13461800	2.20464800		H	2.03659900	-2.58694700	2.39913800
H	-0.53231000	-2.21565000	3.33113700		C	3.47791000	2.68967500	-0.01268300
C	0.54409500	0.43224800	2.81329900		H	3.40719600	3.77514000	-0.01403400
H	0.53810200	0.30730600	3.90188300		H	4.00301900	2.34575800	-0.90032400
H	-0.43666300	0.80216400	2.52520400		H	4.00757500	2.34827400	0.87322400
C	1.61439600	1.50678900	2.47454600		C	1.87230500	-1.61300000	-2.84227800
H	2.60777600	1.05952000	2.39568200		H	1.68145500	-1.72725100	-3.91473100
H	1.66860400	2.14793500	3.35629200		H	2.02711000	-2.59309600	-2.39857700
C	1.35445800	2.47249600	1.29061400		H	2.79148200	-1.05093400	-2.70107700
H	0.29591800	2.53194700	1.07047900		Fe	0.91528900	-0.77216700	0.00028500
H	1.69444500	3.47385200	1.54847700		N	0.74192400	-0.91788000	2.19063300
C	1.34746900	2.46883500	-1.30442700		N	2.09109500	2.11837500	-0.00832900
H	1.68706800	3.46896600	-1.56757000		N	0.73135600	-0.92512200	-2.18915400
H	0.29012500	2.52998600	-1.07865300		O	-0.51989800	-2.24280000	0.00609600
C	1.60035900	1.49926300	-2.48669600		H	2.23783300	1.10179000	-0.00712700
H	2.59453800	1.05289100	-2.41292700		O	2.64424500	-1.84977200	-0.00277200
H	1.64831200	2.13761300	-3.37083800		O	2.94068100	-0.52795300	-0.00616000
C	0.52892400	0.42271600	-2.81517500		C	-3.46644000	0.25903700	-0.00344200
H	-0.45023100	0.79273700	-2.52230300		F	-3.43188500	-0.50751200	-1.10263200
H	0.51651700	0.29414200	-3.90328900		F	-4.59230900	0.95139700	0.01245000
C	-0.49512900	-1.78151400	-2.32020400		F	-3.42287400	-0.54257500	1.07027800
H	-0.54657800	-2.22863500	-3.31890500		O	-2.07555200	2.20390300	-1.25263700
H	-1.36623400	-1.14427600	-2.19269200		O	-0.77421400	0.50749100	-0.00122400
C	-0.56996800	-2.90248700	-1.27164400		O	-2.07609300	2.17626900	1.28768000
H	-1.51823100	-3.43345800	-1.38132000		S	-1.98263000	1.44944600	0.00946700

Table 5.19. Coordinates of the fully optimized structure of [Fe(TMCO(H))(OO)]$^{2+}$, with overall S_t = 3/2 and N-Me cis to the superoxide moiety. Calculated using B3LYP/TZVP.

C	3.27103400	-0.91713800	-0.29508900		H	1.71582400	3.06205400	-1.69307100
H	3.66123800	-1.31524000	0.64030600		H	1.27968800	1.41331000	-2.14752600
H	4.11555500	-0.70324700	-0.94897900		C	2.86603400	1.53868600	-0.70096900
C	2.28055200	-1.84367900	-0.97850900		H	3.59156800	1.32724400	-1.48569100
H	2.04246300	-1.44867300	-1.96692000		H	3.31421500	2.23855600	0.00178800
H	2.72262500	-2.83563100	-1.11488900		C	1.20498700	-2.80091800	1.00798500
C	-0.06054000	-2.56137700	-1.07000000		H	1.54711100	-3.79491000	0.70892600
H	0.12763400	-3.63687600	-1.11743800		H	0.27659300	-2.88738800	1.56516400
H	0.06823500	-2.17726100	-2.08345400		H	1.94818300	-2.35949900	1.67058200
C	-1.50392000	-2.31485500	-0.60654200		C	-4.26025700	-1.00050600	0.03952200
H	-1.56904500	-2.40587900	0.47876600		H	-4.80515900	-0.95884800	-0.90163200
H	-2.12526400	-3.11084700	-1.01758600		H	-4.83982900	-0.52677800	0.82817300
C	-2.02358600	-0.94807400	-1.07885200		H	-4.05713000	-2.03335400	0.30926200
H	-1.19376400	-0.26038400	-1.22398200		C	0.70887600	3.04239100	0.74942700
H	-2.54813900	-1.02415800	-2.03168600		H	0.78033700	4.03463200	0.29401700
C	-3.19787000	1.19979900	-0.49313800		H	1.63150300	2.82903200	1.28370100
H	-4.11337900	1.48496200	0.02173200		H	-0.09357600	3.03512900	1.47934200

H	-3.39889200	1.22517800	-1.56467000	Fe	0.66144300	-0.00221000	0.67920300
C	-2.08097500	2.16061100	-0.06670900	N	0.99977600	-1.93931300	-0.20258700
H	-1.77774000	1.91591000	0.95279900	N	-2.96108700	-0.25976600	-0.11717500
H	-2.56265000	3.13636400	0.01105600	N	0.46032500	2.01130300	-0.30553700
C	-0.84107300	2.30620200	-0.98467600	O	2.57040600	0.31533200	0.03308800
H	-0.91305100	1.65909500	-1.85967300	H	-2.47019900	-0.25215200	0.79395200
H	-0.79802300	3.32862000	-1.37305300	O	0.00389900	0.50746300	2.33543600
C	1.56564000	2.04804000	-1.30575300	O	-0.80192400	-0.45306800	1.74501700

Chapter 6 Electronic Structure of Mononuclear Nonheme Iron-Peroxo Complexes: Ring Size Effects of Macrocyclic Ligands

In this chapter, a series of Fe^{III}(*n*-TMC)(peroxide) complexes with different ring sizes and reactivities are investigated via MCD spectroscopy and DFT calculations. Our collaborators in Prof. Wonwoo Nam's group synthesized and performed the initial characterization of the complexes. Prof. Binju Wang's group optimized the DFT structures and performed the reaction coordinate DFT calculations. Adapted from Zhu, Wenjuan;[‡] Wu, Peng;[‡] **Larson, Virginia**;[‡] Kumar, Akhilesh;[‡] Li, Xiao-Xi; Seo, Mi Sook; Lee, Yong-Min; Wang, Binju;* Lehnert, Nicolai;* and Nam, Wonwoo;* "Electronic Structure and Reactivity of Mononuclear Nonheme Iron-Peroxo Complexes as a Biomimetic Model of Rieske Oxygenases: Ring Size Effects of Macrocyclic Ligands", *J. Am. Chem. Soc.* **2024**, *146* (1), 250–262.[152] The double dagger indicates Wenjuan Zhu, Peng Wu, Virginia Larson, and Akhilesh Kumar contributed equally to this manuscript.

6.1 Introduction

Mononuclear nonheme metal-oxygen species, such as high-valent metal-oxo, -hydroperoxo, -peroxo, and –superoxo complexes, have been invoked as reactive intermediates in biological and biomimetic oxidation reactions.[111,115,136,208,289–293] As discussed in the Introduction, such complexes are intermediates in renewable energy related reactions such as the oxygen evolution reaction and the oxygen reduction reaction, see Section 1.3.1.[117,118] In biology, mononuclear nonheme iron enzymes are highly versatile in nature and are involved in metabolically vital oxidative transformations.[111,262,289–292,294–296] These enzymes activate dioxygen to carry out a broad range of oxidative reactions, including hydroxylation, halogenation, desaturation, epoxidation and *cis*-dihydroxylation, and aromatic ring cleavage reactions.[111,262,289–292,294–296]

6.1.1 Relevance to Rieske Oxygenases

One category of the nonheme iron enzymes that has received renewed attention recently is Rieske oxygenases.[297,298] These O_2-activating enzymes catalyze the *cis*-dihydroxylation of aromatic compounds.[299–301] More recently, Rieske oxygenases have been shown to be involved in monooxygenation(s), demethylations, desaturation, C–H activation, and cyclization reactions.[302–309] The Rieske oxygenase family has a Rieske-type [2Fe2S] iron−sulfur cluster as an electron transfer site and a mononuclear Fe^{II} site for O_2 activation.[310] All of the reactions catalyzed by Rieske oxygenases are presumed to follow the same mechanism of O_2 activation, where O_2 binding to an Fe^{II} center leads to an Fe^{III}-superoxo intermediate, which may further undergo one-electron reduction from the Rieske center to afford an Fe^{III}-peroxo or Fe^{III}-hydroperoxo species.[309,311] In aromatic *cis*-dihydroxylation, the Fe^{III}-(hydro)peroxo or a corresponding $Fe^{V}(O)(OH)$ intermediate, which is formed via the (hydro)peroxo O–O bond cleavage, have been proposed as reactive intermediates in enzymatic and biomimetic reactions.[312–315] However, despite the recent discovery of the diverse oxidation reactions by Rieske oxygenases, the nature of the reactive oxygenating intermediate(s) still remains elusive.

6.1.2 (n-TMC) Metal-Peroxo and Metal-Superoxo Complexes

Our understanding of such mononuclear nonheme metal-oxygen intermediates has been advanced greatly by synthesizing their model compounds, characterizing them structurally and spectroscopically, and investigating their reactivities and mechanisms in various oxidation reactions.[1,108,115,116,134,136,208,293,316] The oxidation state of the O_2 ligand affects reactivity; for example, it has been shown that side-on metal-peroxo species are nucleophiles in aldehyde deformylation reactions,[317] whereas end-on metal-superoxo species are electrophiles in the oxidation of organic substrates.[318–323]

In particular, mononuclear nonheme metal-dioxygen species (M-O_2) with macrocyclic ligands, such as *N*-tetramethylated cyclam (*n*-TMC), have been extensively investigated;[324,325] the *n*-TMC ligands frequently used are 1,4,7,10-tetramethyl-1,4,7,10-tetraazacyclododecane (12-TMC), 1,4,7,10-tetramethyl-1,4,7,10-tetraazacyclotridecane (13-TMC), and 1,4,8,11-tetramethyl-1,4,8,11-tetraazacyclotetradecane (14-TMC) (see Figure 6.1a). With these macrocyclic *n*-TMC ligands, metal-O_2 complexes, such as side-on $M^{(n+1)+}$-peroxo and end-on M^{n+}-superoxo (Figure 6.1b), have been successfully synthesized and characterized spectroscopically and/or

structurally.[326,327,336–338,328–335] For example, an end-on Ni^{II}-superoxo complex was synthesized with the 14-TMC ligand,[326] whereas a side-on Ni^{III}-peroxo complex was obtained with the 12-TMC ligand.[327] Interestingly, in the case of the 13-TMC ligand, both end-on Ni^{II}-superoxo and side-on Ni^{III}-peroxo complexes were synthesized depending on the bases present in reaction solutions, such as an end-on Ni^{II}-superoxo 13-TMC complex in the presence of tetramethylammonium hydroxide (TMAH) and a side-on Ni^{III}-peroxo 13-TMC complex in the presence of triethylamine (TEA).[328] The ring size effect of the TMC ligands on the formation of the side-on $M^{(n+1)+}$-peroxo and end-on M^{n+}-superoxo complexes was also observed in Cr-O_2 species, such as an end-on Cr^{III}-superoxo complex with 14-TMC and a side-on Cr^{IV}-peroxo complex with 12-TMC.[329,330] In contrast, in the cases of Mn-O_2, Fe-O_2, and Co-O_2 complexes, only side-on M-O_2 complexes were synthesized irrespective of the ring size of the n-TMC ligands.[315,331–338]
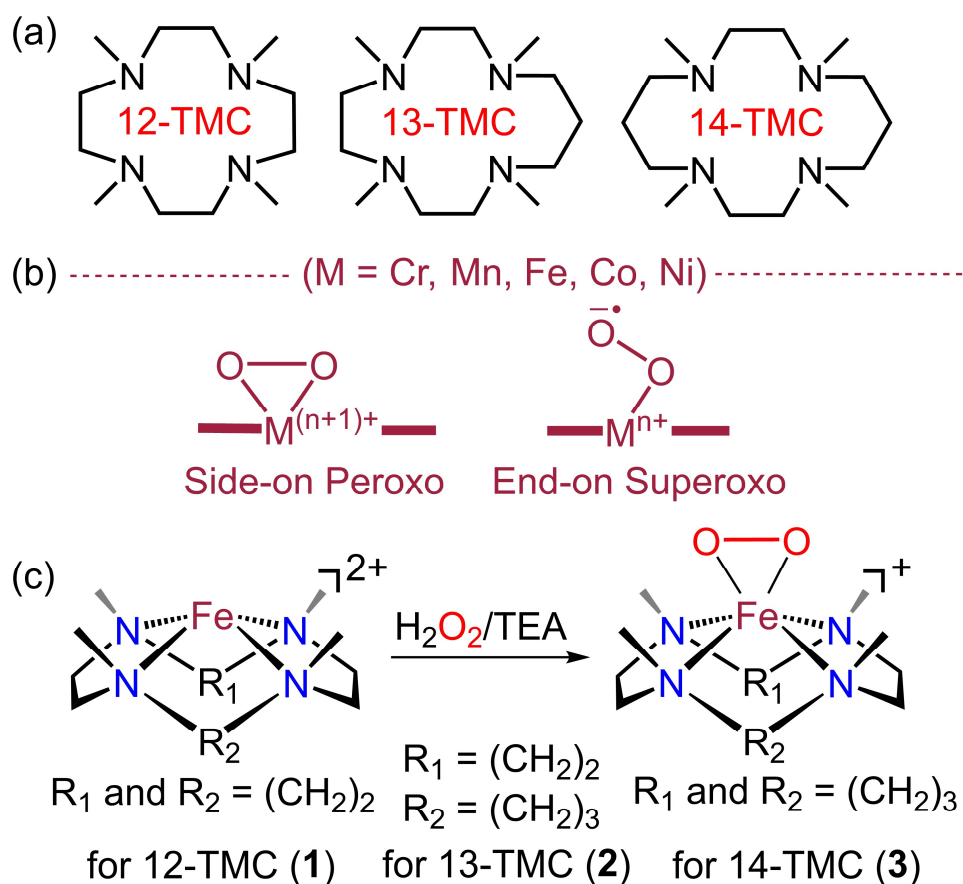
Figure 6.1. (a) n-TMC Ligands, (b) Side-on vs End-on Metal-O_2 Complexes, and (c) Synthetic Procedure for Iron(III)-Peroxo n-TMC Complexes. Figure made by Wenjuan Zhu in the Nam group.[152]

6.1.3 Previous Ferric-Peroxide Complexes

An early well characterized example of a ferric-peroxide species, $[Fe(O_2)(EDTA)]^{3-}$, shows a high spin Fe^{III} center by electron paramagnetic resonance (EPR) and an O-O stretch at 816 cm^{-1}, and an Fe-O2 stretch at 459 cm^{-1}, by resonance Raman (rRaman).[339] Other early examples – $[Fe(O_2)(TPEN)]^+$ and $[Fe(O_2)(trispicMeen)]^+$– reported very similar properties.[340,341] The ligands abbreviations for these complexes are ethylenediaminetetraacetate (EDTA), N-methyl-N,N',N'-tris(pyridylmethyl)ethane-1,2-diamine (trispicMeen), and N,N,N',N'-tetrakis(2-pyridylmethyl)ethane-1,2-diamine (TPEN). These research efforts near the turn of the millennium focused on spectroscopically characterizing the side-on bound Fe-peroxide species, especially in comparison to the end-on bound Fe-hydroperoxide.[342] Upon protonation of $[Fe(O_2)(TPEN)]^+$ and $[Fe(O_2)(trispicMeen)]^+$, the end-on bound Fe-hydroperoxide shows a stronger Fe-O stretch (by ~150 cm^{-1}) and a minor (~20 cm^{-1}) reduction in the O-O stretch energy.[340] Roughly a decade later ferric-peroxides with n-TMC co-ligands began to be investigated.

The Nam group has previously reported each of the $Fe^{III}(O_2)(n$-TMC) complexes discussed herein. Recently, a side-on iron(III)-peroxo complex bearing the 14-TMC ligand, $[Fe^{III}(O_2)(14$-TMC)$]^+$, was characterized structurally and spectroscopically with X-ray crystallography and various spectroscopic methods.[335] This species was also used to further understand the differences in the nuclear resonance vibrational spectra between Fe-O$_2$ and Fe-OOH.[343] More recently, a side-on iron(III)-peroxo complex bearing the 13-TMC ligand, $[Fe^{III}(O_2)(13$-TMC)$]^+$, was successfully synthesized and characterized. This complex shows unprecedented electrophilic reactivity in the C–H bond activation and oxygen atom transfer (OAT) reactions.[336] The observation of the electrophilic reactivity of $[Fe^{III}(O_2)(13$-TMC)$]^+$ provided a new mechanistic insight into the unexpected reactivity of nonheme iron-peroxo species in biomimetic oxidation reactions. More interestingly, by reducing the ring size of the n-TMC macrocyclic ligand, such as from 13-TMC to 12-TMC, a side-on iron(III)-peroxo complex, $[Fe^{III}(O_2)(12$-TMC)$]^+$, was obtained, which shows an interesting reactivity in the cis-dihydroxylation of olefins and naphthalene derivatives to yield the corresponding cis-diol products.[315]

As alluded above, the ring size of the macrocyclic n-TMC ligands, as well as the nature of the metal ions, plays a vital role in determining the geometric and electronic structures of metal-O$_2$ intermediates as well as their reactivities in oxidation reactions. It has also been shown that iron(III)-peroxo n-TMC complexes exhibit diverse reactions depending on the ring size of the

TMC ligands, such as nucleophilic versus electrophilic reactivity and olefin epoxidation versus *cis*-dihydroxylation.[315,334–336] Thus, the structurally and spectroscopically well characterized synthetic $[Fe^{III}(O_2)(n\text{-}TMC)]^+$ complexes provide us with a unique opportunity to systematically investigate the ring size effect of the macrocyclic TMC ligands on the physicochemical properties of iron-peroxo complexes. As part of our ongoing efforts to elucidate the physicochemical properties of metal-O_2 complexes, we decided to investigate the ring size-electronic structure-electrophilic reactivity correlation in oxidation reactions by using the structurally and spectroscopically well characterized mononuclear nonheme iron(III)-peroxo complexes bearing different *n*-TMC ligands, $[Fe^{III}(O_2)(n\text{-}TMC)]^+$.

6.1.4 Scope of Chapter

Herein, the series of iron(III)-peroxo complexes, $[Fe^{III}(O_2)(12\text{-}TMC)]^+$ (**1**), $[Fe^{III}(O_2)(13\text{-}TMC)]^+$ (**2**), and $[Fe^{III}(O_2)(14\text{-}TMC)]^+$ (**3**), prepared by the Nam group under identical reaction conditions (Figure 6.1c),[315,334–336] are studied. Specifically, they are spectroscopically characterized with UV-Vis and rRaman by the Nam group, and magnetic circular dichroism (MCD) spectroscopy by me. I also performed density functional theory (DFT) calculations to elucidate the electronic structures of the iron(III)-peroxo complexes, **1 – 3**, in conversation with the experimental spectroscopic data. The complexes were carefully analyzed to understand the origin of the drastic reactivity difference in HAT reactions of **1 – 3**; that is, the ring size effect of the *n*-TMC ligands on the reactivity of iron(III)-peroxo *n*-TMC complexes in C–H bond activation reactions.

6.2 Synthesis and Characterization of 1 – 3 (Nam Group)
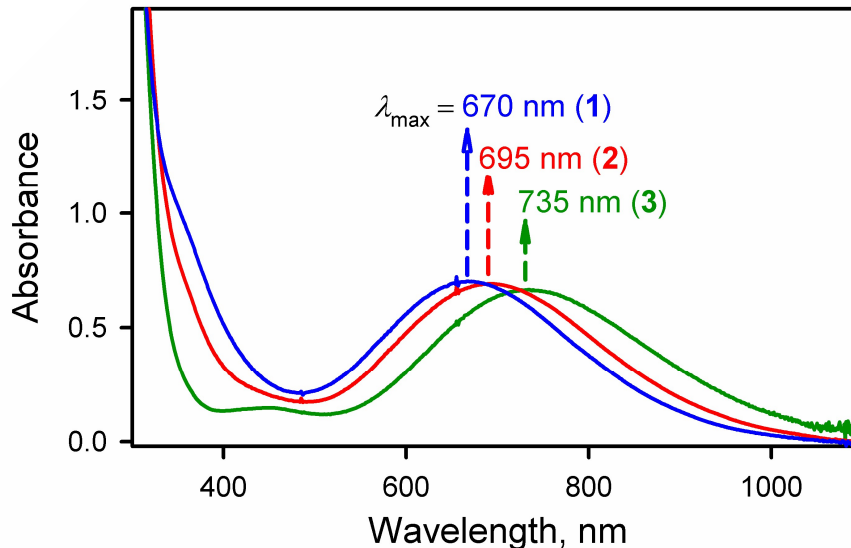
Figure 6.2. UV–Vis spectra of **1** – **3** obtained in the reaction of $[Fe^{II}(n\text{-TMC})]^{2+}$ (1.0 mM) and H_2O_2 (5.0 mM) in the presence of TEA (5.0 mM) in $CF_3CH_2OH:CH_3OH$ (1:1 v/v) at –60 °C; λ_{max} = 670 nm for **1** (blue), λ_{max} = 695 nm for **2** (red), and λ_{max} = 735 nm for **3** (green). Figure by Wenjuan Zhu in the Nam group, who also collected and analyzed the data shown in the figure.[152]

The iron(III)-peroxo complexes were synthesized by the Nam group. The iron(III)-peroxo complex $[Fe^{III}(12\text{-TMC})(O_2)]^+$ (**1**) (see Figure 6.1 for structure), was synthesized by reacting $[Fe^{II}(12\text{-TMC})(CH_3CN)_2]^{2+}$ (1.0 mM) with H_2O_2 (5.0 mM) in the presence of TEA (5.0 mM) in $CF_3CH_2OH:CH_3OH$ (1:1 v/v) at –60 °C.[315] **1**, with an electronic absorption band (λ_{max}) at 670 nm at –60 °C (Figure 6.2), was fully generated in the solvent mixture of CF_3CH_2OH and CH_3OH (1:1 v/v), similar to the previous report,[315] and this solvent mixture was used for the generation of other iron(III)-peroxo species. Intermediate **2** bearing 13-TMC, $[Fe^{III}(O_2)(13\text{-TMC})]^+$, was generated by adding H_2O_2 (10 mM) to a solution containing $[Fe^{II}(13\text{-TMC})(CH_3CN)]^{2+}$ and TEA (5.0 mM) in a solvent mixture of CF_3CH_2OH and CH_3OH (1:1 v/v) at –20 °C.[336] Interestingly, the maximum absorption band (λ_{max}) of the iron(III)-peroxo complexes was found to vary depending on reaction temperatures, and complex **2** exhibits λ_{max} at 695 nm at –60 °C (Figure 6.1). Intermediate **3** bearing 14-TMC, $[Fe^{III}(O_2)(14\text{-TMC})]^+$, was prepared and isolated as a solid for further reactions.[335] Complex **3** was highly stable in $CF_3CH_2OH:CH_3OH$ (1:1 v/v) at 10 °C with λ_{max} at 770 nm, but the absorption band shifts to 735 nm at –60 °C (Figure 6.1).
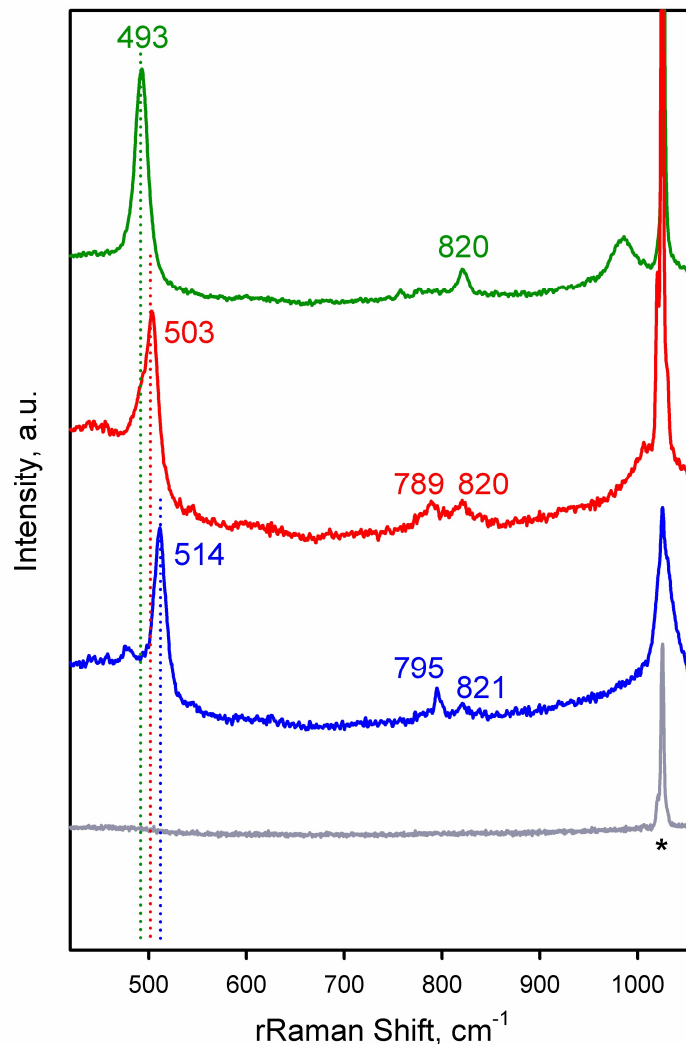
Figure 6.3. rRaman spectra of **1** (green line), **2** (red line), and **3** (blue line) in MeOH at 77 K (λ_{ex} = 785 nm). Gray line shows the spectrum for solvent only. The peak marked with asterisk (*) is from solvent. Data acquired and figure made by the Nam group.[152]

The iron(III)-peroxo complexes were then characterized with various spectroscopic techniques.[315,334–336] Although the rRaman spectra of the intermediates **1** – **3** were reported previously,[315,335,336] the rRaman spectra of **1** – **3** were remeasured to compare the Fe-O stretches of **1** – **3** under identical reaction conditions (Figure 6.3). In the rRaman experiments, we observed an interesting trend, such as the increase of the Fe-O stretching frequency as the ring size of the n-TMC ligands decreases (e.g. at 493 cm^{-1} for **3** and at 514 cm^{-1} for **1**) (Figure 6.3). We also observed that there is a linear correlation between the Fe-O stretching frequencies and the electronic absorption bands in the UV-Vis spectra (Figure 6.2 and Figure 6.3), such as complex **1** with the highest Fe-O stretching frequency shows the most blue-shifted absorption band in the UV-Vis

spectrum (Figure 6.2). This trend is further analyzed in the electronic structure section below. EPR measurements show that complexes **1** – **3** are all in the high-spin ferric state with EPR signals centered at g = 4.3, as reported previously.[315,335,336]

6.3 Magnetic Circular Dichroism
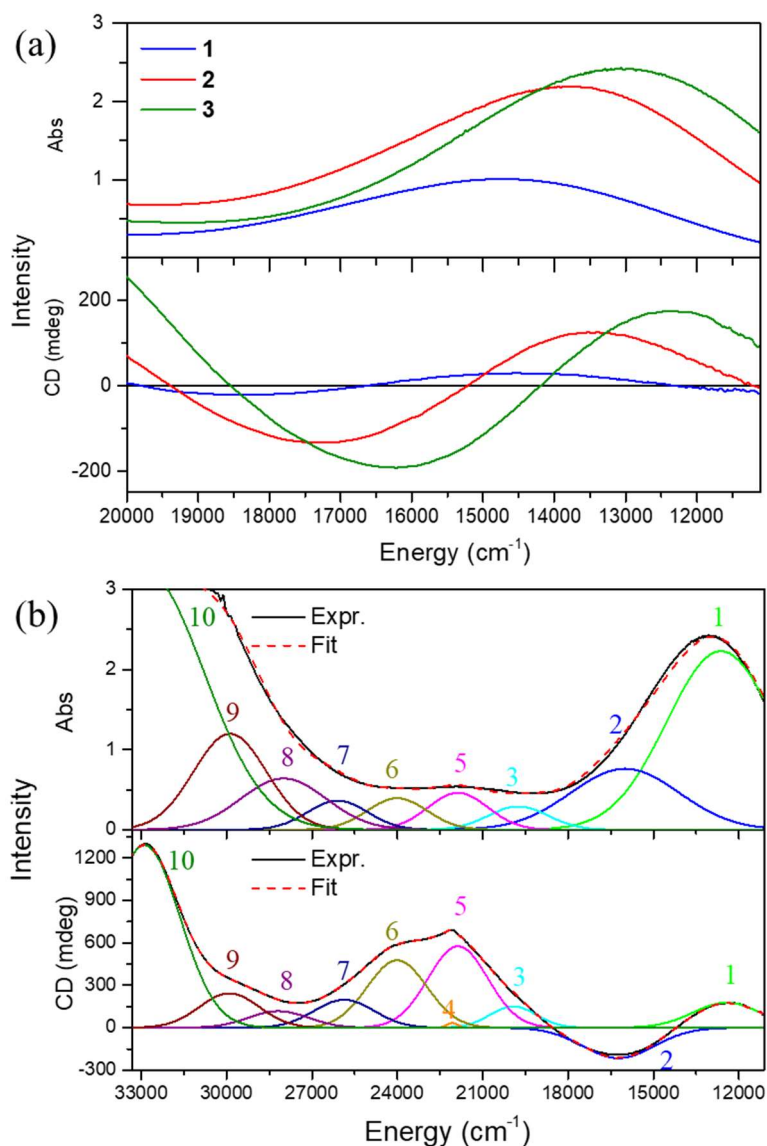
Figure 6.4. Comparison of MCD and UV−Vis spectra for intermediates **1** – **3**. UV−Vis data were acquired in $CH_3OH:CH_3CH_2OH$ (4:1 v/v). MCD VTVH data were acquired for 2 − 50 K, 0 − 7 T on frozen glass samples of intermediates **1** – **3** in $CH_3OH:CH_3CH_2OH$ (4:1 v/v). (a) 2 K 7 T MCD data are shown here for intermediates **1** – **3**, see Figure 6.6 for further temperatures and higher energy data. Each of the samples shows MCD bands at higher energy, >25,000 cm^{-1}, as well, some

of which are also present in decay samples as shown in Figure 6.7. Intermediates **2** and **3** were 4.0 mM and intermediate **1** was 2.0 mM, for both UV–Vis and MCD measurements. (b) Correlated fit of the UV–Vis absorption and 2 K 7 T MCD spectra for complex **3**, which is by far the most stable complex in the series. See Figure 6.5 for further details on this Gaussian fit. Note that band 9 may be due to the decay product; see Figure 6.7.

MCD spectroscopy was used to gain further insight into the electronic structure of the intermediates. For **1 – 3**, variable temperature variable field (VTVH) MCD data were collected from 2 – 50 K and 0 – 7 T. The 2 K 7 T MCD spectra are compared with the UV–Vis spectra for each species in Figure 6.4a. The UV–Vis spectra of **1 – 3** show a major absorption feature in the 13,000 – 15,000 cm^{-1} range, which appears upon formation of the iron-peroxo intermediates. Interestingly, the energy of this band is solvent sensitive, shifting to higher energy in hydrogen-bond donating solvents. For example, the λ_{max} of **3** shifts from 11,500 cm^{-1} in MeCN to 13,300 cm^{-1} in trifluoroethanol (TFE) (Table 6.1), suggesting that this band corresponds to an electronic transition that involves the peroxo moiety. There is also a less intense absorption band at 21,980 cm^{-1}, which is visible for the most stable complex **3**.
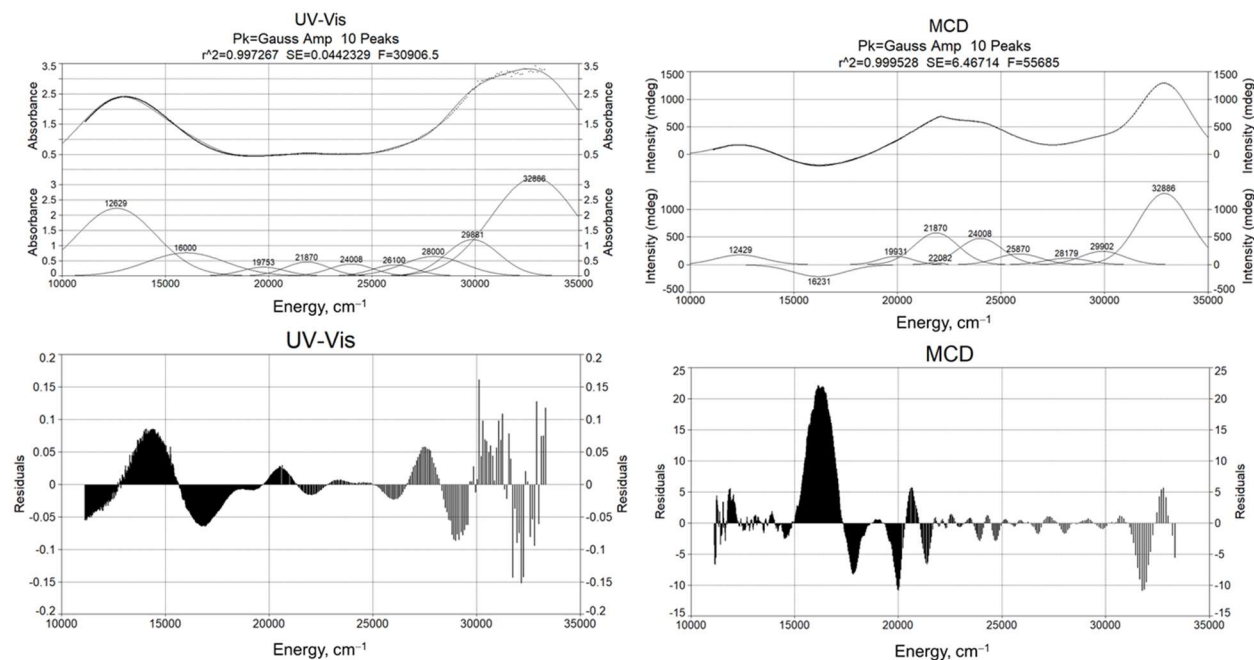
Figure 6.5. Further details of the Gaussian fit of the UV-Vis absorption spectrum and 2 K 7 T MCD spectrum for **3**, left and right, respectively. Top left: the individual Gaussians sum up to give a fit of the UV-Vis spectrum with R^2=0.997. Bottom left: the residuals of the fit of the UV-Vis spectrum. Top right: the individual Gaussians sum up to give a fit of the 2 K 7 T MCD data with R^2=0.9995. Bottom right: the residuals of the fit of the MCD spectrum.

Full MCD and UV-Vis spectra
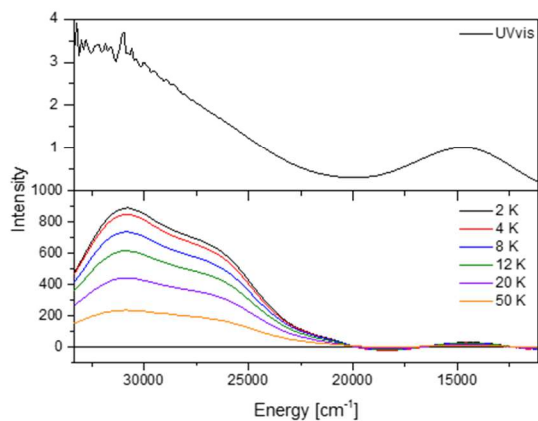
MCD and UV-Vis spectra, low energy region
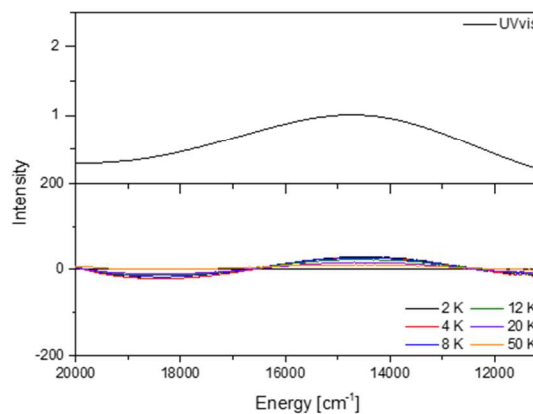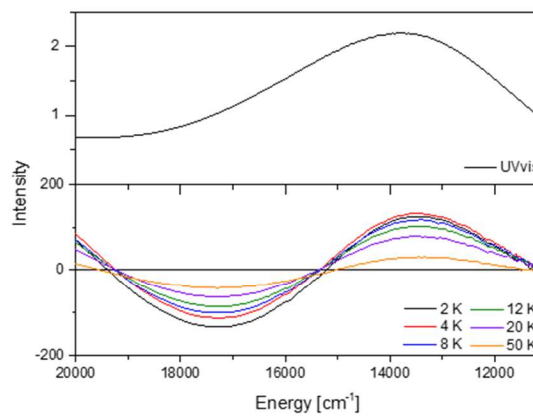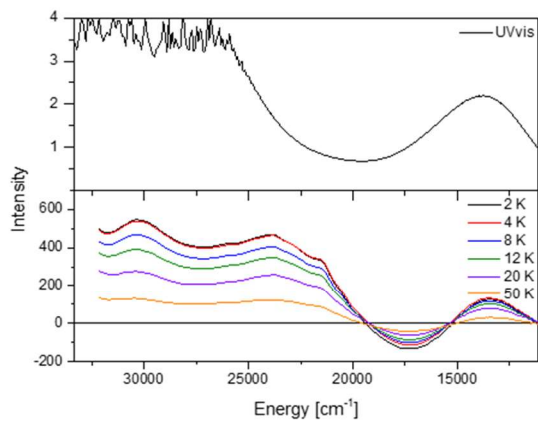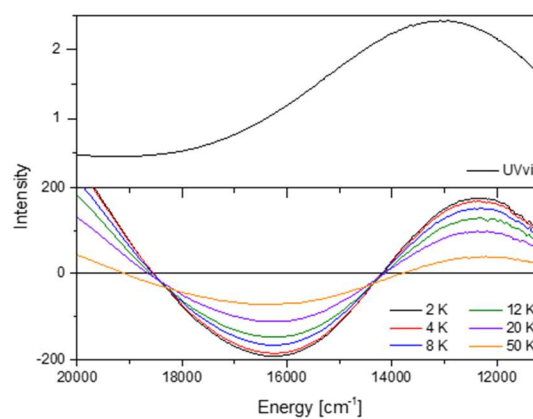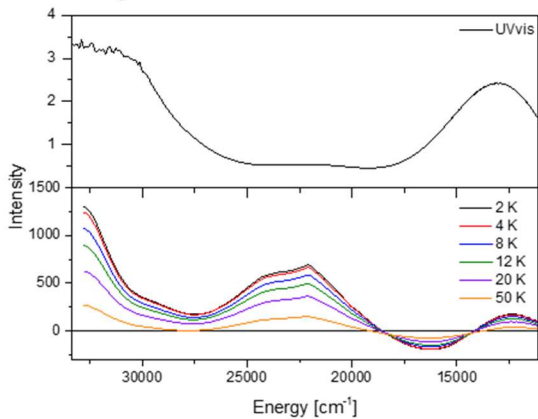
Figure 6.6. VTVH MCD data for complexes **1 – 3**. Shown here are the 7 T data for each temperature 2 – 50 K. The full spectra are shown on the left, and the low energy region is shown on the right. For each data set, MCD spectra are cut when the voltage curve raises above 750 V.
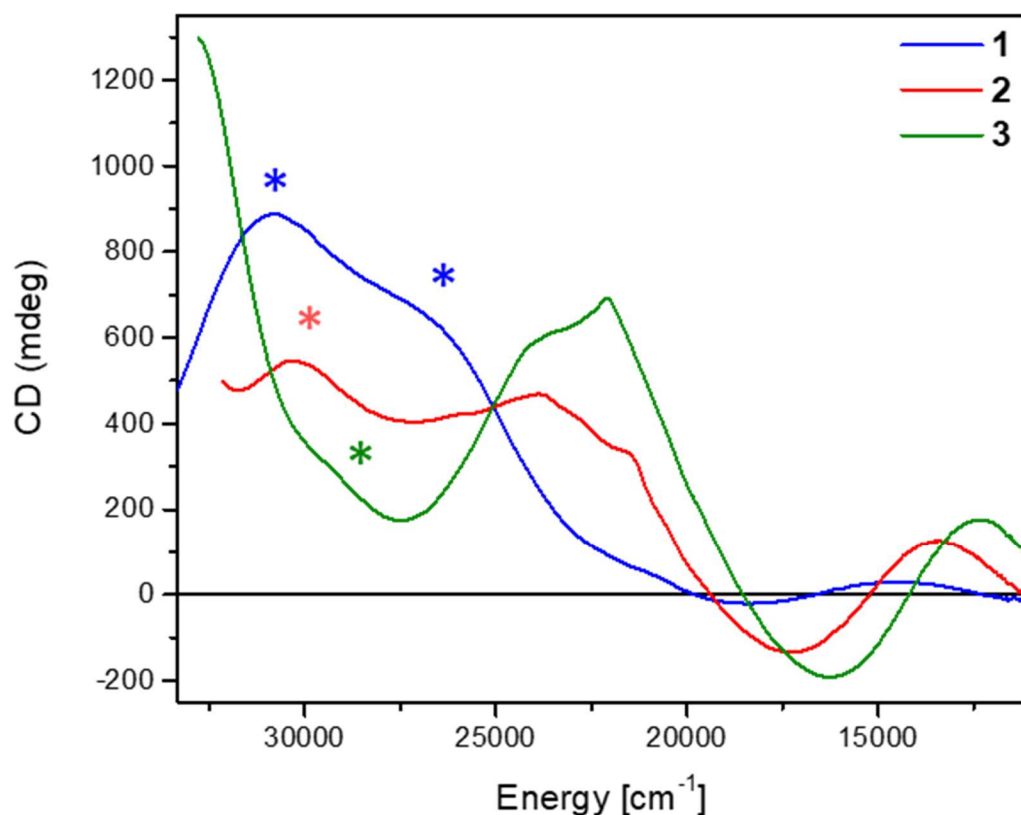
Figure 6.7. Comparison of the full range 2 K 7 T MCD data for intermediates **1 − 3**. Asterisks mark bands that also appear in the decay samples, and therefore indicate the presence of decay products. Each MCD spectrum is shown for the range where the corresponding voltage curve is below 750 V.

The MCD spectra show features that match well with those observed in the absorption spectra, as shown in Figure 6.4. As **3** is the most stable compound, the 2 K 7 T MCD and UV−Vis spectra of **3** were fitted with Gaussians to deconvolute the spectra and identify the major contributing bands. As shown in Figure 6.4b, a very good agreement between the fits of the MCD and UV−Vis spectra was obtained. Interestingly, MCD resolves the bands in the $13{,}000 - 15{,}000$ cm^{-1} range into two features with opposite intensity (see bands 1 and 2 in Figure 6.4b), with the shape of a pseudo-**A** type signal.[220] This is not an **A**-term signal, which would be temperature independent (see Figure 6.6 for temperature dependence of this signal), but instead results from two **C**-term signals with opposite signs, close in energy. In the case of a pseudo-**A** type signal, the two corresponding excited states would be coupled by spin-orbit coupling, in orthogonal direction

188

to the two transition-dipole vectors of the two underlying electronic transitions. This putative pseudo-**A** term signal is conserved across the series of complexes, shifting to lower energy upon increasing the size of the co-ligand ring. It should be further noted that the maximum of the broad absorption band in the $13,000 - 15,000$ cm^{-1} range for each compound lines up with the lower energy component of the putative pseudo-**A** term signal in the MCD (band 1 in the fit). The MCD signals for **2** and, especially, **1** are less intense than those for **3** due to the increased decomposition of the intermediates **2** and **1** resulting from their decreased stability, which is reflected in an increase in the signals of decay species in their MCD spectra (Figure 6.7). Therefore, we only obtained reliable MCD VTVH saturation curves for **2** and **3**, which are shown in Figure 6.8–Figure 6.10. These show nominally the same behavior. The fitting of the MCD VTVH saturation curves is further discussed below, with input from time-dependent density functional theory (TD-DFT) calculations, to ultimately assign the underlying electronic transitions.
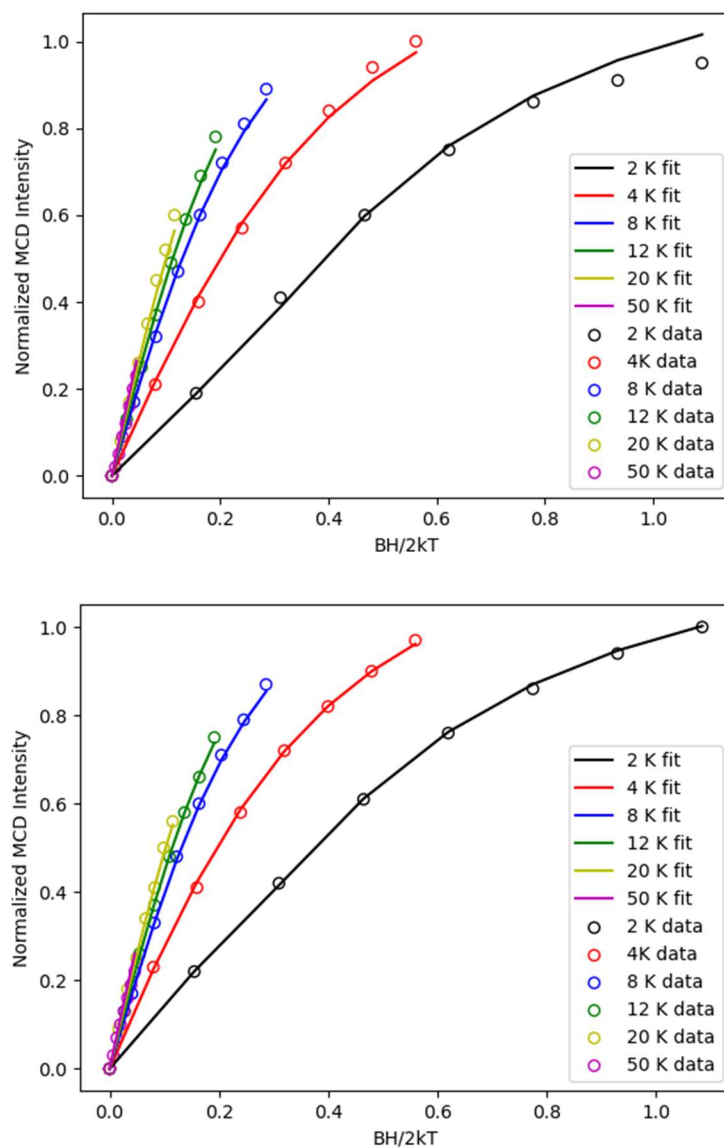
Figure 6.8. VTVH MCD saturation curves and fits for (top) **2** at 742 nm (13477 cm^{-1}) and (bottom) **3** at 811 nm (12330 cm^{-1}). Spectra were obtained with temperatures of 2 – 50 K and magnetic fields of 0 – 7 T. The data were fit with $S_t = 5/2$, $E/D = 0.3$, and $g = 2, 2, 2$. For **2**, $D = -0.25$ cm^{-1} and for **3**, $D = -0.28$ cm^{-1}. For **2**, top, this fit gave a X^2 of 3.23, and polarizations of 7% x, 10% y, and 83% z. For **3**, bottom, this fit gave a X^2 of 0.93, and polarizations of 7% x, 9% y, and 84% z.
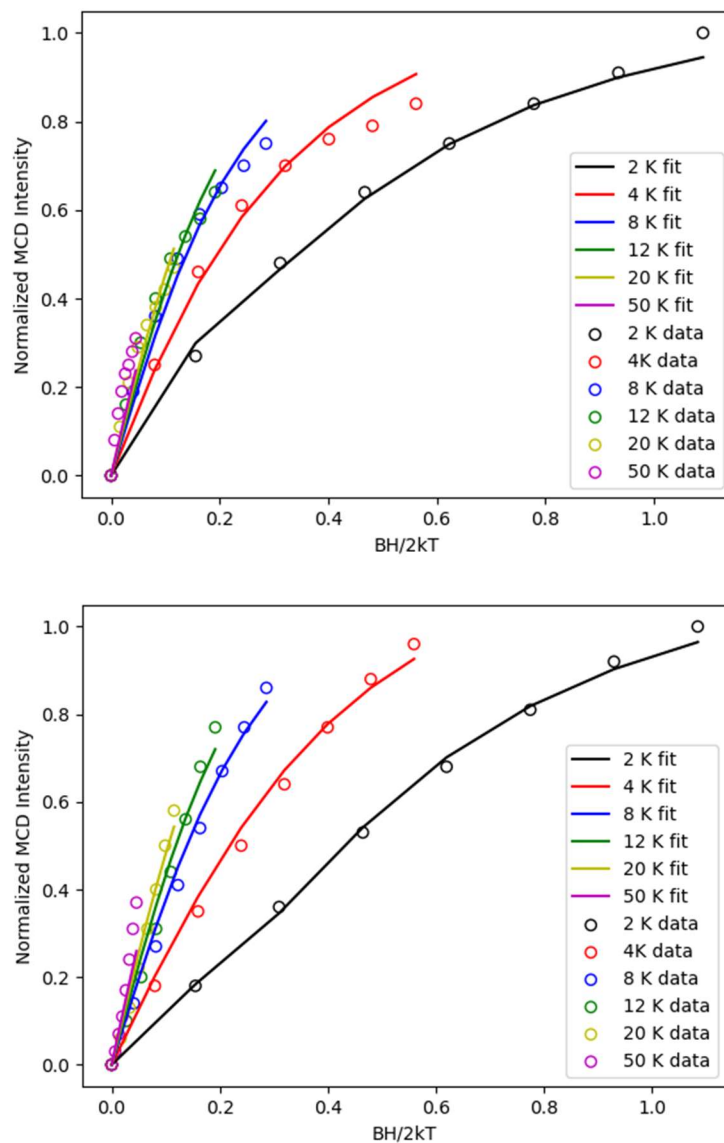
Figure 6.9. VTVH MCD saturation curves and fits for (top) **2** at 580 nm (17241 cm^{-1}) and (bottom) **3** at 615 nm (16260 cm^{-1}). Spectra were obtained with temperatures of 2 – 50 K and magnetic fields of 0 – 7 T. The data were fit with $S_t = 5/2$, $E/D = 0.3$, and $g = 2, 2, 2$. For **2**, $D = -0.25$ cm^{-1} and for **3**, $D = -0.28$ cm^{-1}. For **2**, top, this fit gave a X^2 of 13.5, and polarizations of 8% x, 14% y, and 78% z. For **3**, bottom, this fit gave a X^2 of 8.37, and polarizations of 7% x, 11% y, and 82% z.
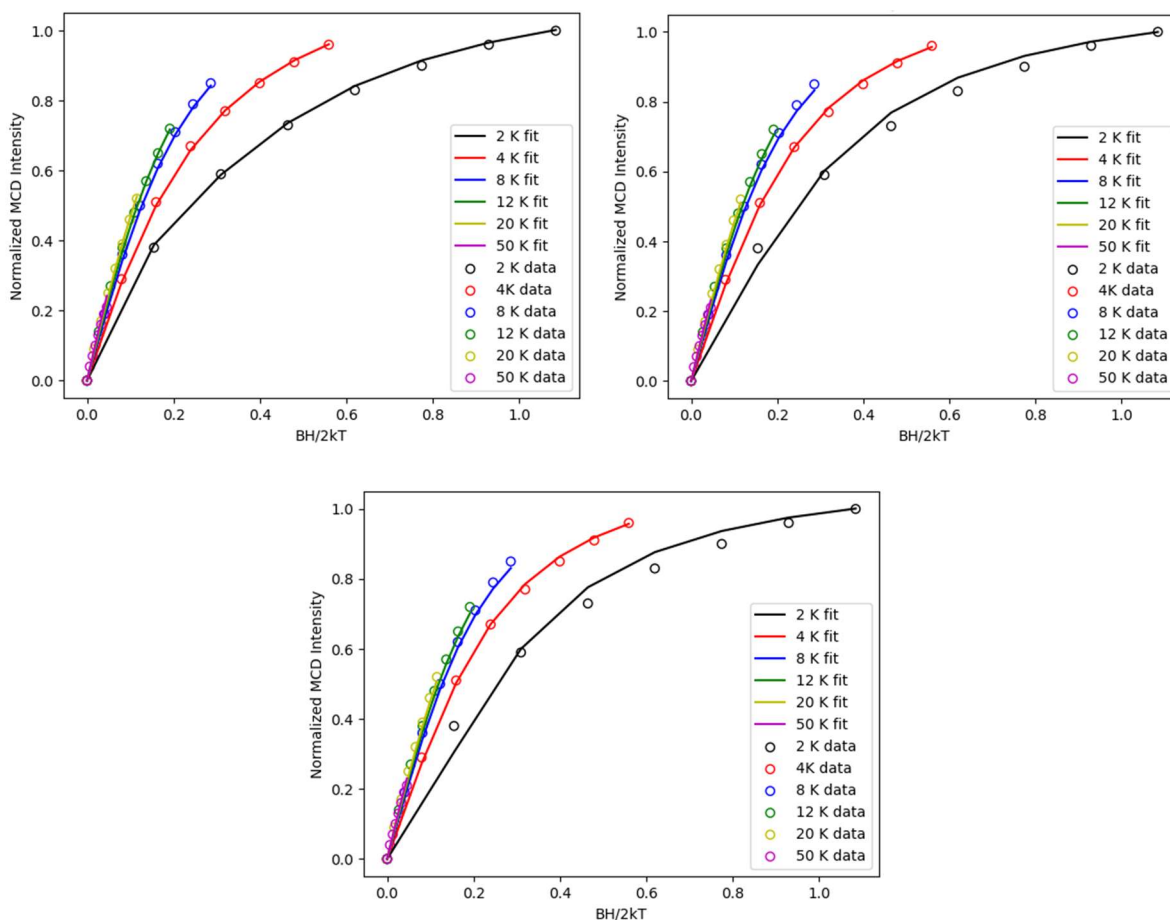
Figure 6.10. VTVH MCD saturation curves and fitting for **3** at 469 nm (21322 cm^{-1}). Spectra were obtained with temperatures of 2 – 50 K and magnetic fields of 0 – 7 T. The data were fit with $S_t =$ 5/2, D = –0.28 cm^{-1}, E/D = 0.3, and g = 2, 2, 2. Top left, this fit gave a X^2 of 0.64, and polarizations of 9% x, 12% y, and 79% z. Top right, this fit gave a X^2 of 1.77, and polarizations of 83% x, 1% y, and 16% z. Finally, bottom, the fit gave a X^2 of 2.69, and polarizations of 1% x, 95% y, and 4% z.

6.4 Density Functional Theory Calculations

6.4.1 Structure Optimization (Wang Group)

$[Fe(O_2)(12\text{-TMC})]^+$ $[Fe(O_2)(13\text{-TMC})]^+$ $[Fe(O_2)(14\text{-TMC})]^+$

$[Fe(O_2)(12\text{-TMC})]^+$, 3 TFE $[Fe(O_2)(13\text{-TMC})]^+$, 3 TFE $[Fe(O_2)(14\text{-TMC})]^+$, 3 TFE
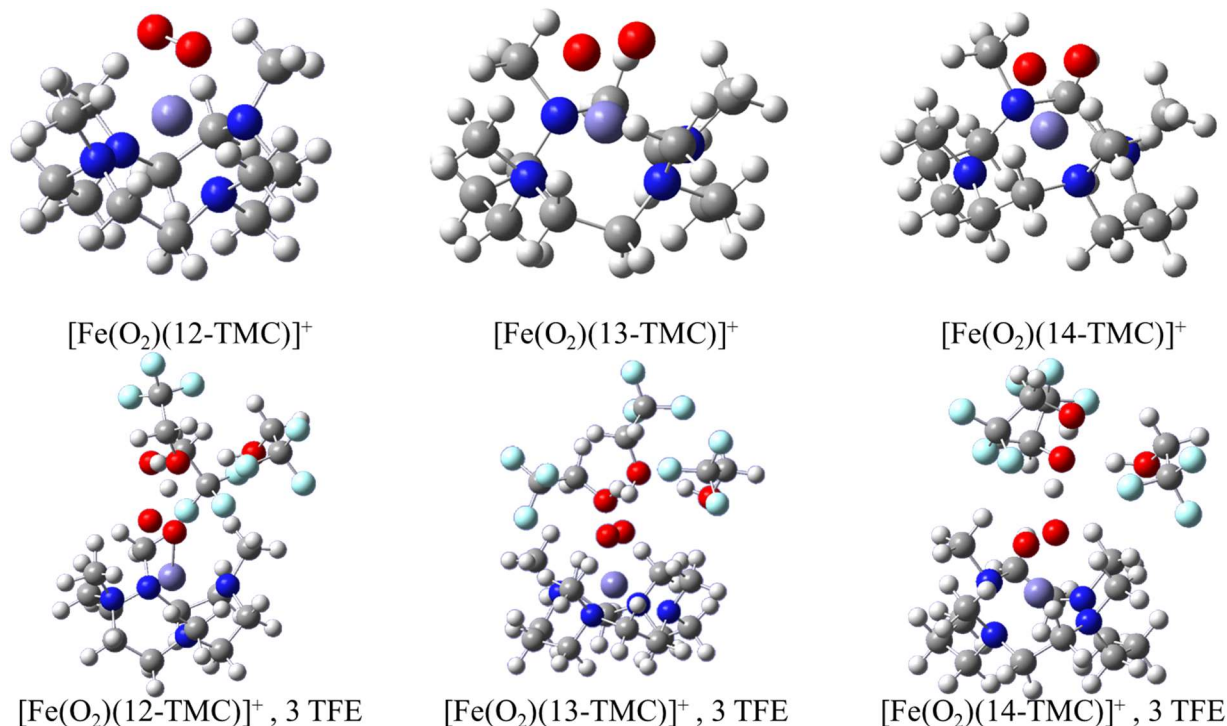
Figure 6.11. Structures of **1**, **2**, and **3** optimized alone (top) or in the presence of 3 TFE molecules (bottom). The structures were optimized by the Wang Group with B3LYP/def2-SVP, an SMD solvent field with TFE, and the gd3 dispersion correction. Figure was prepared by myself.

      With two groups working on DFT calculations on this project, it was important that we use the same structures, functionals, and basis sets: the Wang group optimized structures for their calculations (see Section 6.7) and we used the same structures for our analysis. DFT calculations were used to obtain fully optimized structures of intermediates **1** – **3** to better understand their geometric and electronic structural differences. The $[Fe^{III}(O_2)(n\text{-TMC})]^+$ structures were optimized alone and in the presence of 3 TFE molecules, as the intermediates are known to show slight differences in properties with different solvents (Table 6.1 and Table 6.2). The optimized structures (B3LYP/def2-SVP, with TFE solvent field and dispersion correction) are shown in Figure 6.11.

6.4.2 Analysis of DFT Structures

The optimized structure of **3** matches well with the experimental structure of this species, obtained with X-ray crystallography.[335] Extended X-ray absorption fine structure (EXAFS) measurements are also available for **3** (see Table 6.3). Calculated bond distances are within 0.05 Å for Fe-O and Fe-N$_{TMC}$ bond lengths compared to the experimental data. Similarly, complex **2** gives a good agreement between structural data from EXAFS and DFT. The EXAFS measurement for **1** was previously reported and suggests two distinct Fe-N$_{TMC}$ bond distances,[336] which was not replicated in the DFT calculations. According to DFT, the rhombicity of the structure of **1** is largely due to the two nitrogens in the co-ligand that are located on the y axis (in the coordinate system used here) bending away from the peroxo unit, but not due to a difference in the Fe-N$_{TMC}$ bond lengths. However, our results also show that **1** is particularly susceptible to structural distortions induced by strong H-bonding from solvent molecules (here by including 3 TFE molecules in the calculations; see Figure 6.11 and Table 6.3), causing a distortion of the Fe-peroxo unit with two significantly different Fe-O bond lengths. Hence, since the solvent mixture used for EXAFS measurements on **1** contained TFE, the two different Fe-ligand bond lengths observed by EXAFS could also result from a distorted Fe-peroxo unit. Within this interpretation, the EXAFS data match the DFT-predicted structure within 0.05 Å for Fe-O and Fe-N$_{TMC}$ bond lengths (see Table 6.3).

Table 6.1. The UV-Vis λ_{max} of the low-energy absorption band of **3** shifts with the hydrogen bonding ability of the solvent. Data in table acquired by the Nam group.[152]

Solvent	T (°C)	λ_{max}, nm (cm^{-1})
TFE	0	750[a] (13,333)
TFE:MeOH (1:1 v/v)	0	765 (13,071)
MeOH	0	780 (12,820)
MeCN	0	870 (11,494)
acetone:TFE (3:1 v/v)	−40	782[b] (12,787)

[a] Taken from the cited reference.[335] [b] Taken from the cited reference.[334]

Table 6.2. rRaman vibrational frequencies (cm^{-1}) of **2** and **3** in different solvents. Data in table acquired by the Nam group.[152]

Solvent	2		3	
	ν_s(Fe-O)	ν(O-O)	ν_s(Fe-O)	ν(O-O)
acetone	502	822	487[a]	825[a]
MeCN	504	822		
MeOH	503	820, 789	493	820
acetone:TFE	506	n.d.[b,c]		
TFE	512	790	501	n.d.[b,c]

[a] Taken from the cited reference.[335] [b] n.d.: not detected. [c] Vibrational frequencies of O–O could not be detected because they probably overlapped with the solvent peaks.

Table 6.3. Summary of DFT-calculated geometric parameters and comparison to experimental values obtained by X-ray crystallography and/or EXAFS. See Experimental Section (6.9) for further details. Each structure was fully optimized using B3LYP/def2-SVP by the Wang group. I tabulated the calculated geometric parameters. X-ray crystal structure by the Nam group.[152]

Ligand	14-TMC				13-TMC			12-TMC		
	X-ray crystal	EXAFS[a]	w/o TFE	explicit TFE	EXAFS[a]	w/o TFE	explicit TFE	EXAFS[a]	w/o TFE	explicit TFE
Geometry: bond distances (Å) and angles (°)										
O-O	1.46		1.42	1.43		1.43	1.44		1.40	1.44
Fe-O1	1.91	1.92	1.96	1.95	1.92	1.94	1.94	1.91	1.97	1.89
Fe-O2	1.91	1.92	1.95	1.95	1.92	1.95	1.96	1.91	1.97	2.07
Fe-N	2.23	2.22	2.27	2.26	2.20	2.26	2.25	2.12, 2.25	2.27	2.23
O-H			N/A	1.52		N/A	1.53		N/A	1.46
<O-Fe-O	45.0		42.7	43.0		43.1	43.4		41.4	42.4

[a] EXAFS data were collected on **1**[b], **2**[c], and **3**[d] in CF$_3$CH$_2$OH:CH$_3$OH (1:1 v/v), CF$_3$CH$_2$OH, and acetone, respectively. [b] Taken from the cited reference.[315] [c] Taken from the cited reference.[336] [d] Taken from the cited reference.[335]

Table 6.4. Summary of DFT-calculated vibrational parameters and comparison to experimental values obtained by rRaman. Each structure was fully optimized using B3LYP/def2-SVP by the Wang group. I calculated the vibrational frequencies. See Experimental Section (6.9) for further details. The rRaman data were obtained in CH_3OH solution, see Table 6.2 for further solvents, by the Nam group. Values are given in cm^{-1}.

ligand	14-TMC			13-TMC			12-TMC		
	rRaman	w/o TFE	explicit TFE	rRaman	w/o TFE	explicit TFE	rRaman	w/o TFE[a,b]	explicit TFE
ν(O-O) (calcd. rel. intensity)	820	857	917 (1)	820, 789	866	900 (1)	808	928	905 (1)
ν_s(Fe-O) (calcd. rel. intensity)	493	440	488 (0.23)	503	467	519 (0.16)	514	238	551 (0.34)
ν_{as}(Fe-O) (calcd. rel. intensity)		330	392 (0.01)		360	406 (0.03)		356	326, 394 (0.07)

[a] The vibrations reported for this complex were calculated using ORCA.
[b] Note that if the structures without explicit TFE are allowed to reoptimize in Gaussian with TPSSh instead of B3LYP, the ν_s(Fe-O) frequencies are calculated to be 444, 467/(456, 481), and 463/(487) cm^{-1} for $[Fe(O_2)(14\text{-TMC})]^+$, $[Fe(O_2)(13\text{-TMC})]^+$, and $[Fe(O_2)(12\text{-TMC})]^+$, respectively.

Table 6.5. Summary of DFT-calculated spin densities. Each structure was fully optimized using B3LYP/def2-SVP by the Wang group. I tabulated the calculated spin densities. See Experimental Section (6.9) for further details.

ligand	14-TMC		13-TMC		12-TMC	
	w/o TFE	explicit TFE	w/o TFE	explicit TFE	w/o TFE	explicit TFE
Fe	4.01	4.07	4.02	4.07	3.93	4.09
Sum O_2	0.75	0.63	0.73	0.60	0.87	0.56
O1	0.37	0.35	0.37	0.33	0.43	0.34
O2	0.38	0.28	0.36	0.28	0.43	0.22

The DFT calculations are further able to reproduce key trends in the rRaman data. For complexes **1 – 3**, the O–O stretching modes are somewhat difficult to assign and are observed as very weak features in the $790 – 860$ cm^{-1} range in the rRaman spectra, with no clear trend among the complexes (see Table 6.2 and Table 6.4). Our DFT calculations generally overestimate the frequencies of the O–O stretching modes, predicted around 860 cm^{-1} for **2** and **3** (without hydrogen bonding), which is, however, not unusual for the B3LYP functional.[344–347] For **1**, despite the good agreement between the optimized structure and the EXAFS data, there are significant deviations in the calculated spectroscopic properties for the structure without explicit TFE compared to experiment, indicating that DFT is less accurate in predicting the properties of **1**. The O–O stretch, for example, is clearly overestimated at 928 cm^{-1}. In the side-on Fe-peroxo structures of **1 – 3**,

196

both symmetric (ν_s) and antisymmetric (ν_{as}) Fe-O stretches exist. Experimentally, the Fe-O stretch is easily identified as an intense mode in the rRaman data, but the exact Fe-O mode to which this feature corresponds has not previously been determined. DFT predicts ν_s(Fe-O) at higher energy and with distinctively larger Raman intensity, and based on these results, we assign the experimentally observed Fe-O mode to the symmetric stretch. The calculated vibrational frequencies of ν_s(Fe-O) for **1** – **3** match the experimentally observed trend of decreasing Fe-O stretching energies with increasing ligand ring size. The exception to this is again **1** modeled without explicit TFE, which predicts ν_s(Fe-O) at unreasonably low energy, when using B3LYP. This can be mostly corrected if the structures are allowed to reoptimize in Gaussian, using TPSSh as the functional instead, and the frequencies recalculated (see Table 6.4 footnote b).

Like the optical band 1 (see Figure 6.4), ν_s(Fe-O) is sensitive to the H-bonding ability of the solvent. The energy of this mode increases by 10 and 14 cm^{-1} for **2** and **3**, respectively, upon switching the solvent from acetone to TFE (see Table 6.1). A mixture of acetone:TFE (3:1 v/v) produces shifts in between these two extremes. Unfortunately, due to the instability of **1**, rRaman data for this species were only acquired in methanol, so no further trends could be derived in this case. Nevertheless, these results again show that the peroxo ligand in **1** – **3** is susceptible to H-bonding interactions, in agreement with the DFT results. Here, H-bonding causes a stabilization of the $O_2(\pi^*)$ orbitals in energy, as further discussed below, and desymmetrizes the Fe-O stretching vibrations.

6.5 Electronic Structure and Assignment of Optical Spectra

1

74 % Fe
17 % O_2

32 % Fe
67 % O_2

$d_{yz}\_O_2(\pi_{yz}*)$ ps. $\sigma*$ $O_2(\pi_{xy}*)\_d_{xy}$ $\delta*$

2

55 % Fe
37 % O_2

79 % Fe
18 % O_2

$d_{yz}\_O_2(\pi_{yz}*)$ ps. $\sigma*$ $d_{xy}\_O_2(\pi_{xy}*)$ $\delta*$

3

58 % Fe
33 % O_2

79 % Fe
18 % O_2
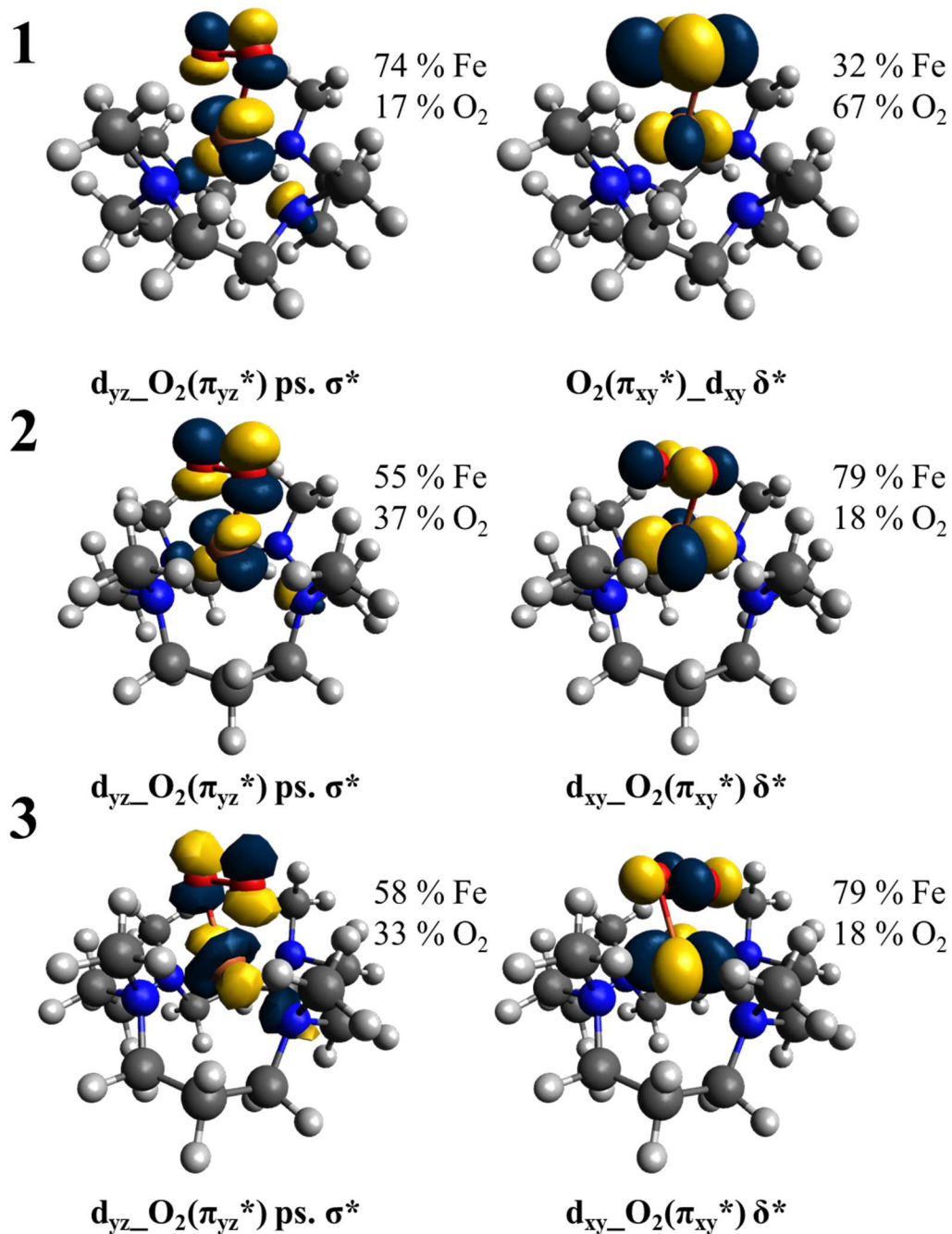
$d_{yz}\_O_2(\pi_{yz}*)$ ps. $\sigma*$ $d_{xy}\_O_2(\pi_{xy}*)$ $\delta*$

Figure 6.12. Fe-O_2 bonding interactions in complexes **1** – **3**. Shown are the corresponding, antibonding combinations, which generally correspond to the d-orbitals of the iron center and which are singly occupied. Left: $d_{yz}\_O_2(\pi_{yz}*)$ pseudo-$\sigma*$; right: $d_{xy}\_O_2(\pi_{xy}*)$ $\delta*$ (note that for **1**, this orbital interaction is inverted, so the singly-occupied orbital is labeled $O_2(\pi_{xy}*)\_d_{xy}$). Depicted here are the unoccupied β-MOs, calculated with PBE0/def2-SVP.
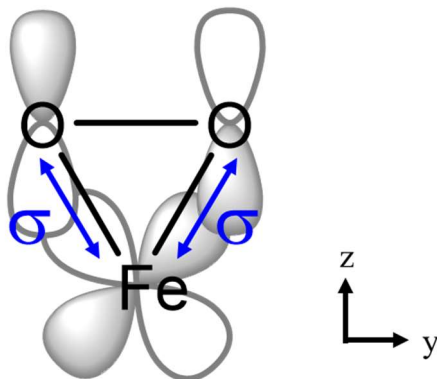
Figure 6.13. A scheme showing the pseudo-σ bond between the d_{yz} orbital and the π^* orbital of the peroxo ligand in the yz plane.

The Fe-peroxo complexes **1** – **3** contain high-spin Fe^{III} centers ($S_t = 5/2$), as evident from EPR spectroscopy. This means that in each case, five d-orbitals of iron are singly occupied with all electrons having parallel spin, and the O_2-derived ligand corresponds to a closed shell peroxo unit. The calculated molecular orbital (MO) diagrams of these complexes generally match this electronic structure description. Full MO diagrams can be found in Figure 6.14 – Figure 6.16. These were derived using PBE0/def2-SVP calculations, which show the closest match between the TD-DFT calculated and experimental absorption spectra of the complexes (vide infra). For the following discussion, we use a coordinate system where the z axis is located within the Fe-O_2 plane, between the two Fe-O bonds, and the y axis is parallel to the O–O bond. The MO diagram of complex **3** is shown in Figure 6.16. Here, the lowest lying d-orbital corresponds to the antibonding combination of the d_{xy} orbital of iron and the π^* orbital of the peroxo ligand in the xy plane, forming an unusual δ bond. The antibonding MO, $d_{xy}\_O_2(\pi_{xy}^*)$, is singly occupied and has 79% iron and 18% peroxo character (see Figure 6.12). The corresponding, bonding combination $O_2(\pi_{xy}^*)\_d_{xy}$ constitutes the HOMO of the complex. Although this is a quite covalent Fe-O_2 bond, this interaction makes a smaller contribution to the overall Fe-O_2 bond strength, due to the limited orbital overlap between the d_{xy} and the $O_2(\pi_{xy}^*)$ orbitals. To higher energy are the d_{xz} and d_{z^2} orbitals, which show minimal interaction with the peroxo ligand. Next in energy is the $d_{x^2-y^2}$ orbital, which binds to the nitrogen donors of the 14-TMC ligand in the xy plane. The highest energy d-orbital, $d_{yz}\_O_2(\pi_{yz}^*)$, corresponds to a strong pseudo-σ bond between the d_{yz} orbital and the π^* orbital of the peroxo ligand in the yz plane. This bond is called a pseudo-σ bond as the orbital overlap between the iron and each O is as a sigma bond, see Figure 6.13. Due to the excellent

orbital overlap, this is a strong Fe-O_2 bond, causing the antibonding MO, $d_{yz}\_O_2(\pi_{yz}{}^*)$, to be the highest energy d-orbital of iron (see Figure 6.12). This MO is singly occupied and has 58% iron and 33% peroxo character. Figure 6.12 shows the main Fe-O_2 antibonding d-orbitals, $d_{xy}\_O_2(\pi_{xy}{}^*)$ and $d_{yz}\_O_2(\pi_{yz}{}^*)$, for the series of complexes **1 – 3**. As evident from the figure, all three complexes show the same δ and pseudo-σ bonds between iron and the peroxo ligand.

LUMO

SOMO

d$_{x2-y2}$**_N**$_{TMC}$**(p) σ***
85 % Fe
0 % O_2
-0.0 eV

d$_{yz}$**_O**$_2$**(π**$_{yz}$***) ps. σ***
74 % Fe
17 % O_2
-0.1 eV

d$_{xz}$
92 % Fe
3 % O_2
-1.0 eV

d$_{z2}$
90 % Fe
2 % O_2
-1.2 eV

O$_2$**(π**$_{xy}$***)_d**$_{xy}$ **δ***
32 % Fe
67 % O_2
-2.9 eV

HOMO

d$_{xy}$**_O**$_2$**(π**$_{xy}$***) δ**
66 % Fe
31 % O_2
-5.8 eV

O$_2$**(π**$_{yz}$***)_d**$_{yz}$ **ps. σ**
12 % Fe
62 % O_2
-7.2 eV
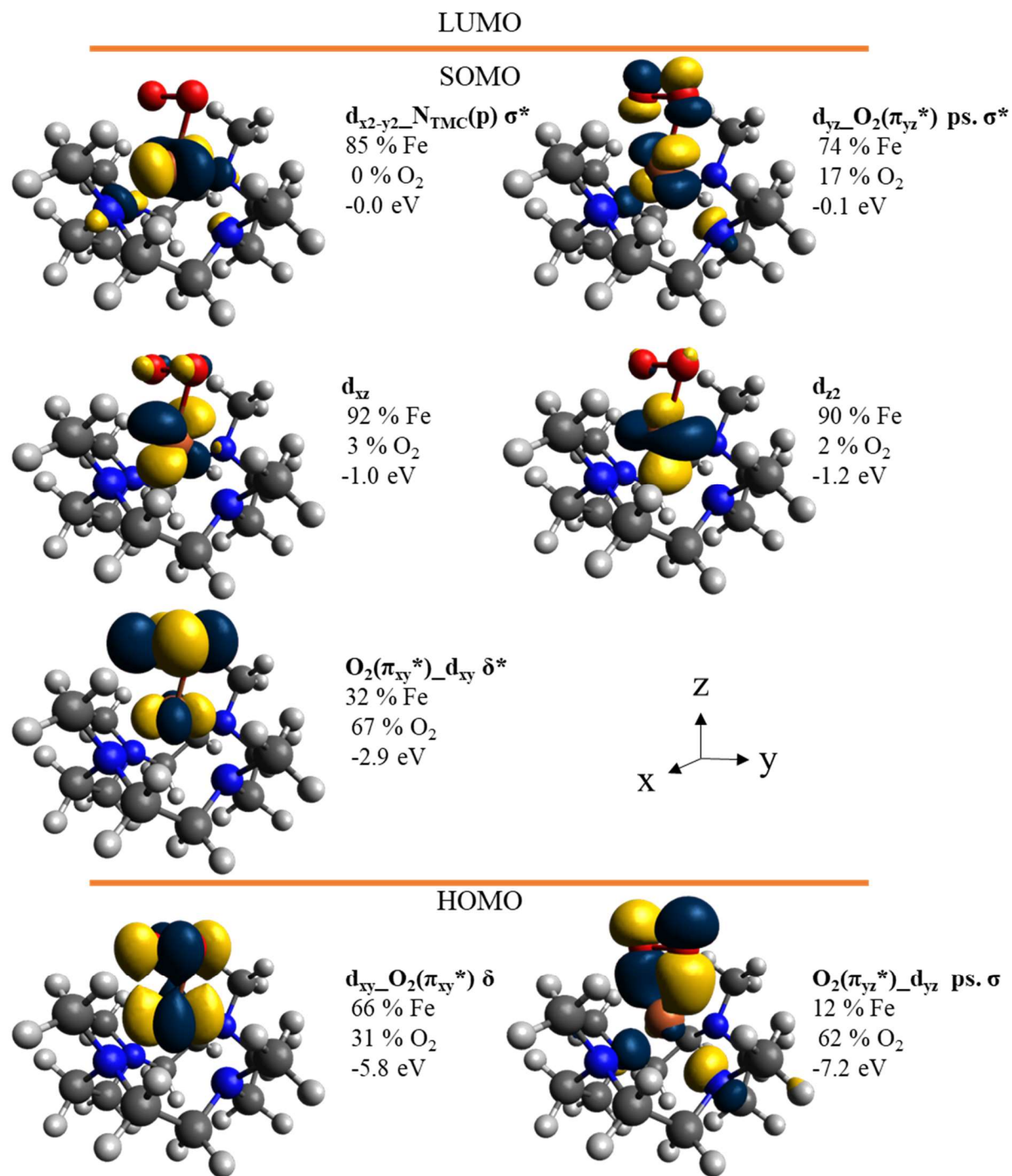
Figure 6.14. MO diagram of **1**. Molecular orbitals were calculated with PBE0/def2-SVP and imaged using Avogadro.

LUMO

SOMO

$d_{yz}\_O_2(\pi_{yz}{}^*)$ ps. σ^*
55 % Fe
37 % O_2
-1.2 eV

$d_{x2-y2}\_N_{TMC}(p)$ σ^*
81 % Fe
0 % O_2
-1.3 eV

d_{z2}
88 % Fe
4 % O_2
-1.8 eV

d_{xz}
90 % Fe
5 % O_2
-1.9 eV

$d_{xy}\_O_2(\pi_{xy}{}^*)$ δ^*
79 % Fe
18 % O_2
-2.4 eV

HOMO

$O_2(\pi_{xy}{}^*)\_d_{xy}$ δ
18 % Fe
80 % O_2
-5.8 eV

$O_2(\pi_{yz}{}^*)\_d_{yz}$ ps. σ
29 % Fe
52 % O_2
-7.2 eV
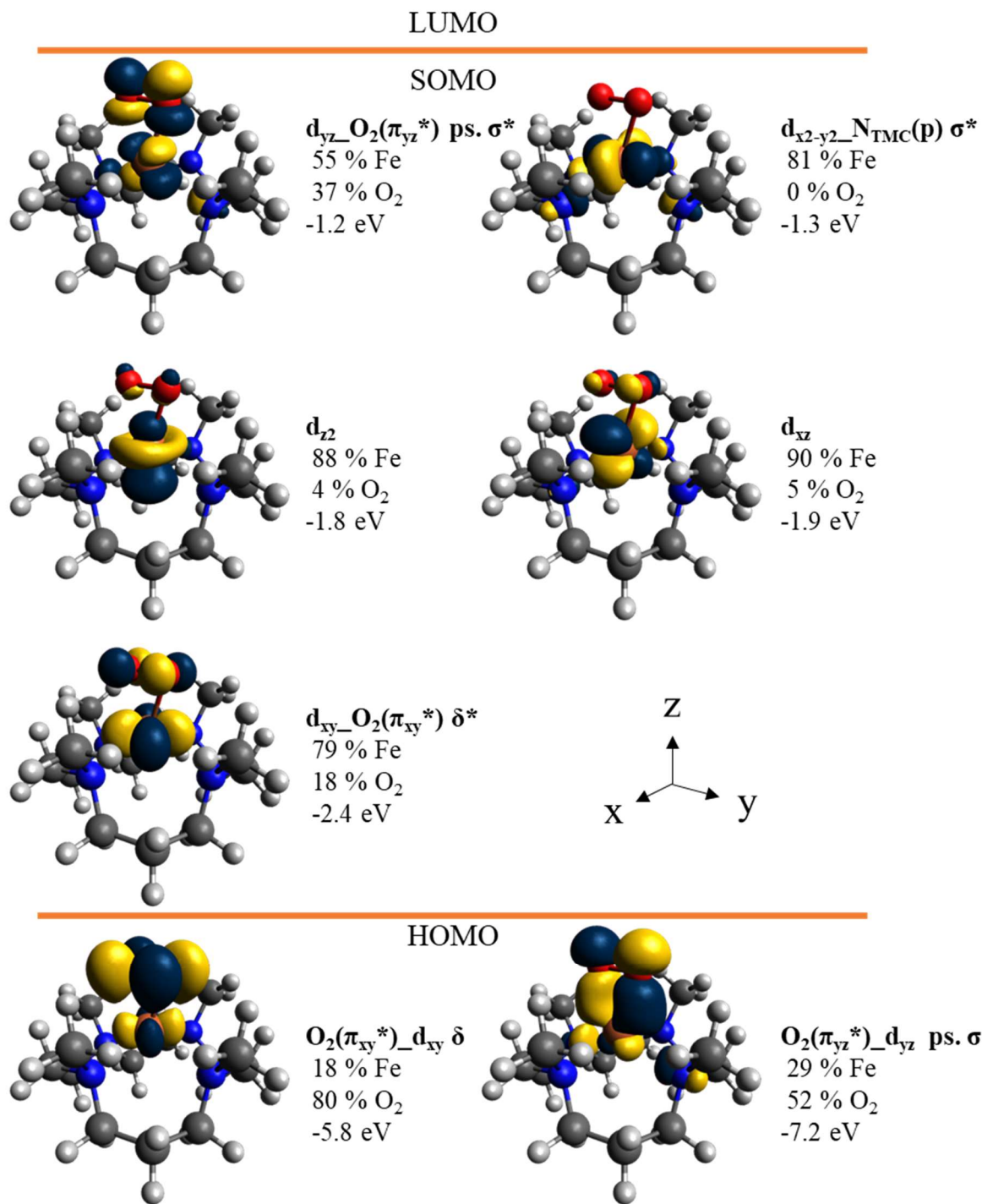
Figure 6.15. MO diagram of **2**. Molecular orbitals were calculated with PBE0/def2-SVP and imaged using Avogadro.
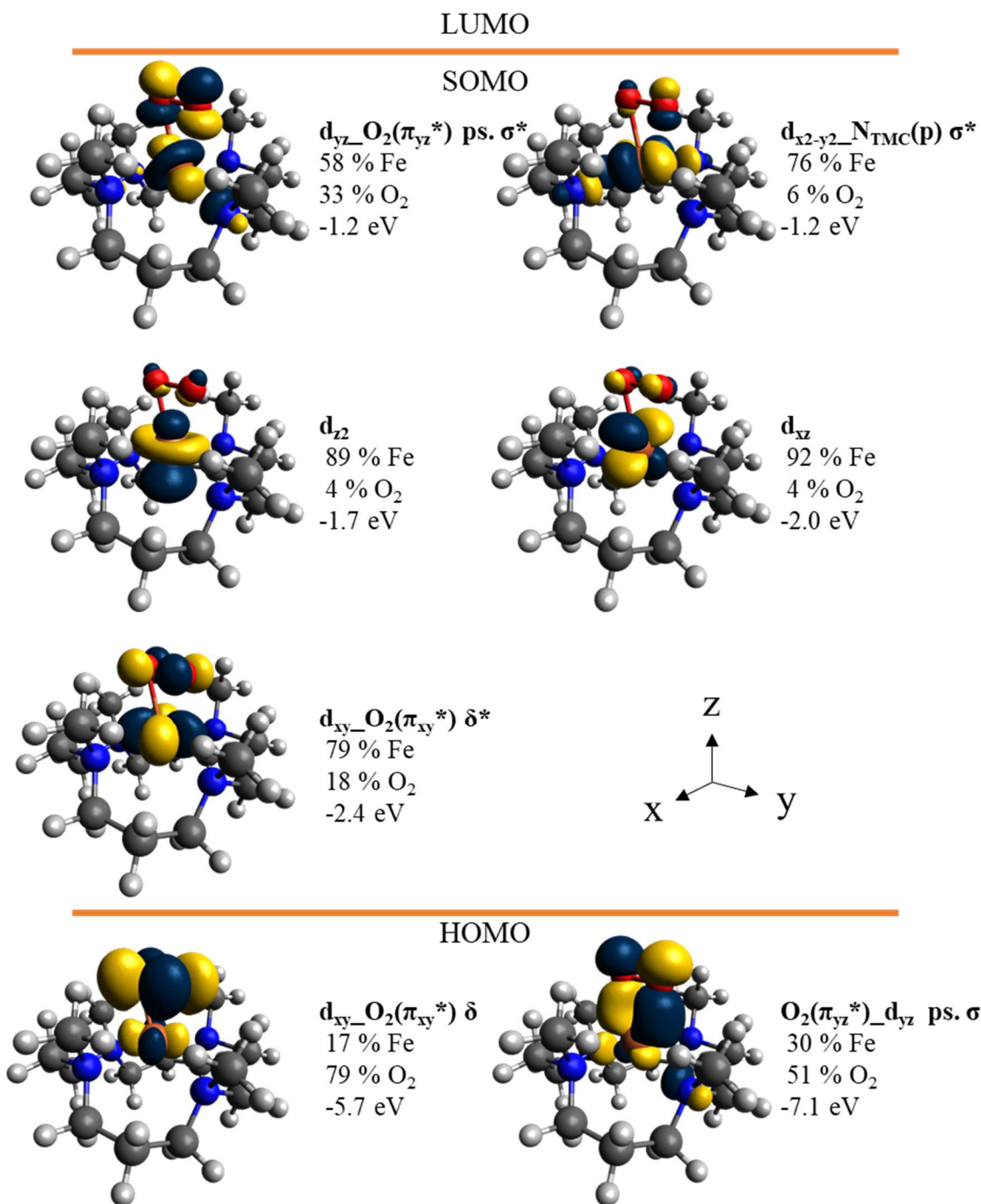
Figure 6.16. MO diagram of **3**. Molecular orbitals were calculated with PBE0/def2-SVP and imaged using Avogadro.

While the MO diagrams for **2** and **3** are very similar (Figure 6.15 and Figure 6.16), complex **1** shows some interesting differences (Figure 6.14). Here, the $O_2(\pi_{xz}^*)\_d_{xy}$ δ^* orbital is much lower in energy (see Figure 6.17), indicating that in the distorted coordination geometry of **1**, the d_{xy}

orbital experiences less interaction with the four nitrogen donors of the TMC ligand in the xy plane, causing a shift of d_{xy} to lower energy. This causes an inversion of the Fe-O_2 δ bond, with the bonding combination showing 66% Fe character, whereas the singly-occupied, antibonding combination has 67% O_2 character (see Figure 6.12 and Figure 6.14). This means that according to the DFT calculations, complex **1** has distinct Fe^{II}-superoxo character. This is supported by an increase in spin density on the O_2 ligand in **1** compared to **2** and **3** (see Table 6.5). At the same time, the pseudo-σ bond is predicted to be weaker in **1** compared to **2** and **3** (see Figure 6.12). While the $d_{yz}\_O_2(\pi_{yz}*)$ pseudo-$\sigma*$ and $d_{x^2-y^2}\_N_{TMC}(p)$ $\sigma*$ orbitals are close in energy in **2** and **3**, the weaker pseudo-σ bond combined with the altered ligand field (due to the distorted geometry) in **1** cause $d_{x^2-y^2}\_N_{TMC}(p)$ $\sigma*$ to be located higher in energy than $d_{yz}\_O_2(\pi_{yz}*)$ in **1** (see Figure 6.17). However, these DFT predictions must be taken with some skepticism. First, the DFT calculations overestimate the O–O stretching frequency of **1** (predicted at 928 cm^{-1}) compared to **2** and **3** (predicted around 860 cm^{-1}), indicating that the DFT calculations clearly overestimate the amount of superoxo character in complex **1**. Second, since complex **1** has the highest energy Fe-O stretch, we posit that the weaker pseudo-σ bond predicted by DFT for **1** is likely incorrect. Based on these considerations, we conclude that **1** still contains a strong Fe-O_2 pseudo-σ bond, and that the strength of the Fe-O_2 δ bond is increased, due to the weaker ligand field of **1** in the xy plane, and as evident from the UV–Vis data (see next), but not to a point where the bond is actually inverted (based on the EPR data for **1**, which are similar to **2** and **3** and show high-spin Fe^{III} complexes in all cases).
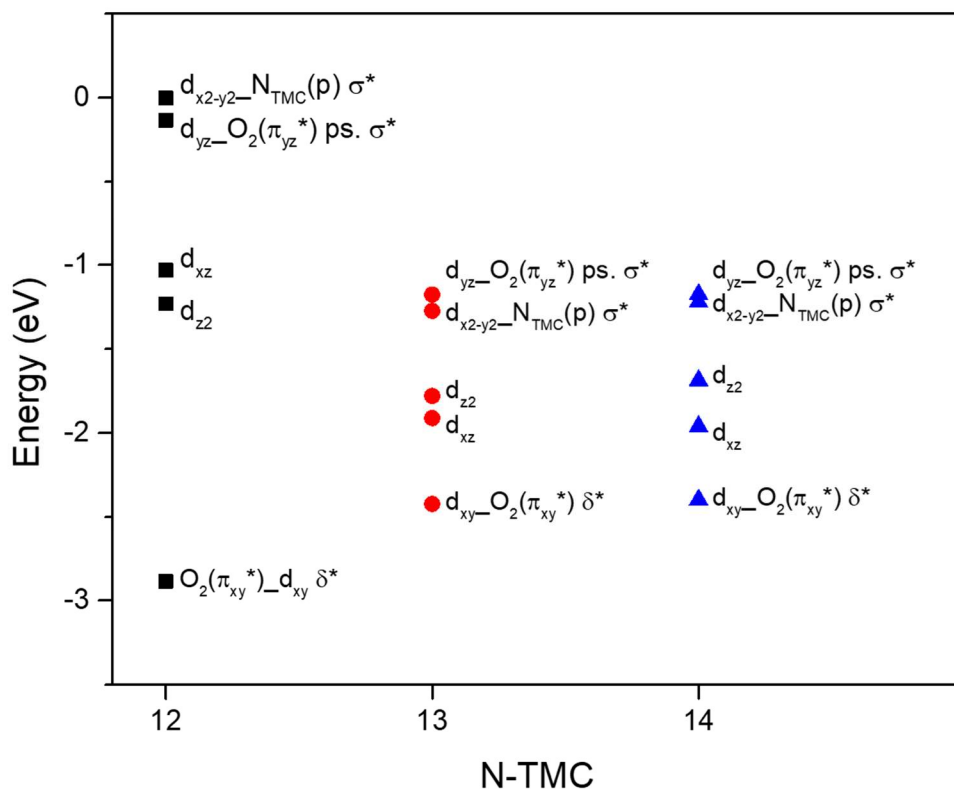
Figure 6.17. Relative energies of the SOMOs for **1** − **3**.

From the TD-DFT results, we can assign the electronic transitions observed by MCD and UV−Vis spectroscopies. We investigated four different functionals for TD-DFT using complex **3** as a test model, as it is the most well characterized and most stable complex in the series, to identify the functional that gives the best match to the experimental UV−Vis absorption spectrum of **3**. For each functional, the $[Fe^{III}(O_2)(14\text{-TMC})]^+$ structure and that with **3** TFE molecules were investigated. The results of these eight TD-DFT calculations are shown in Figure 6.18. B3LYP and PBE0 both give the best match with the experimental UV−Vis spectra of **3**. As shown in Table 6.1, H-bond donating solvents cause a significant shift in the low-energy absorption band of **3** to higher energy, and this shift is best reproduced by PBE0. Therefore, PBE0 was used for the MO analysis (see above) and the assignment of the optical spectra of **1** – **3**. TD-DFT calculated UV−Vis spectra for **1** and **2** are shown in Figure 6.19. In general, **2** and **3** give very similar predicted spectra, with only slight shifts in energy. In contrast, **1** is more distinct, which may reflect its more distorted

geometric structure and its somewhat increased superoxo character. Summary tables of the electronic transitions calculated by TD-DFT are provided in Table 6.6 – Table 6.8. Note the orientation of the coordinate system for **2** and **3** aligns well with the orientation of the d-tensors as calculated, see Figure 6.20, but for **1** the x and y directions of the D tensor are swapped. The polarizations listed are for the D tensor, but the MO names are kept consistent across the series.
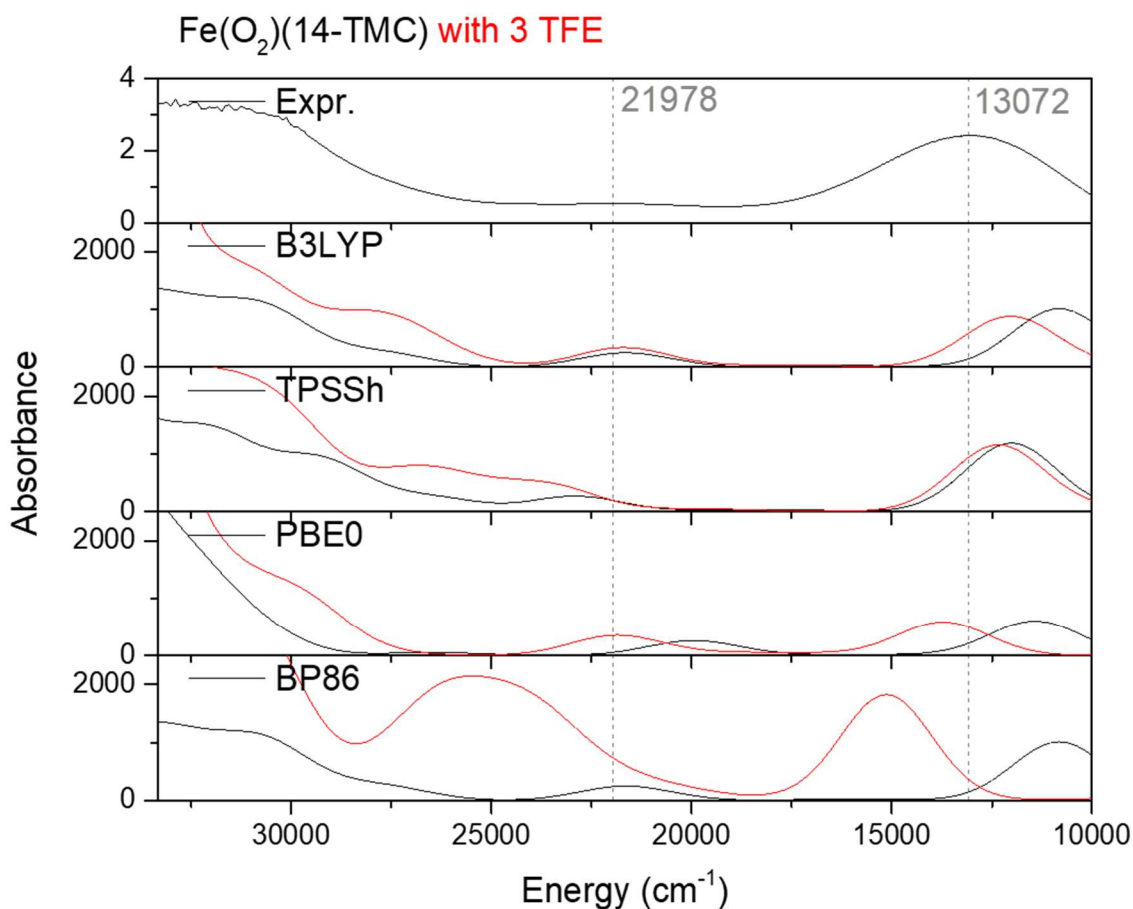
Figure 6.18. Comparison of TD-DFT predicted UV-Vis spectra for **3** and the experimental spectrum. The absorption spectra were calculated with def2-SVP and the functional listed. The λ_{max} of the experimental UV-Vis bands in $CH_3OH:CH_3CH_2OH$ (4:1 v/v) are shown to guide the eye.
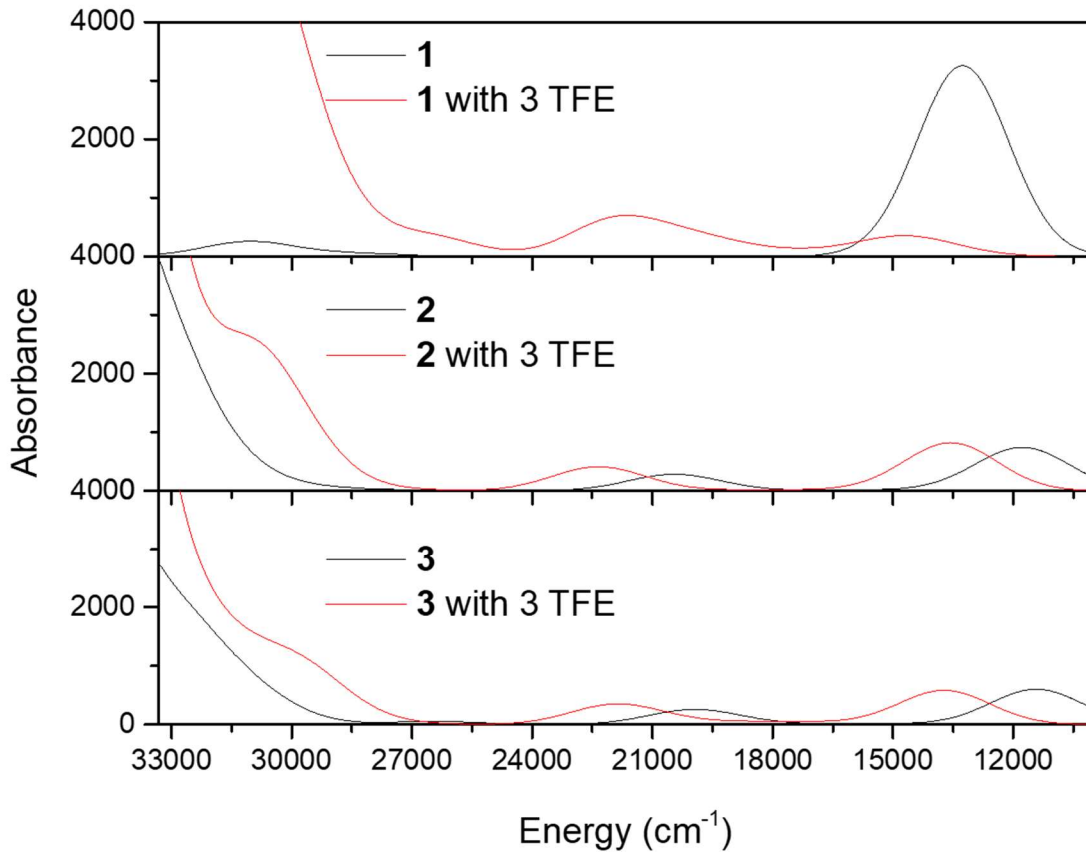
Figure 6.19. Comparison of TD-DFT predicted UV-Vis spectra for **1** – **3**. These absorption spectra were calculated with PBE0/def2-SVP.

$[Fe(O_2)(12\text{-TMC})]^+$ $[Fe(O_2)(13\text{-TMC})]^+$ $[Fe(O_2)(14\text{-TMC})]^+$
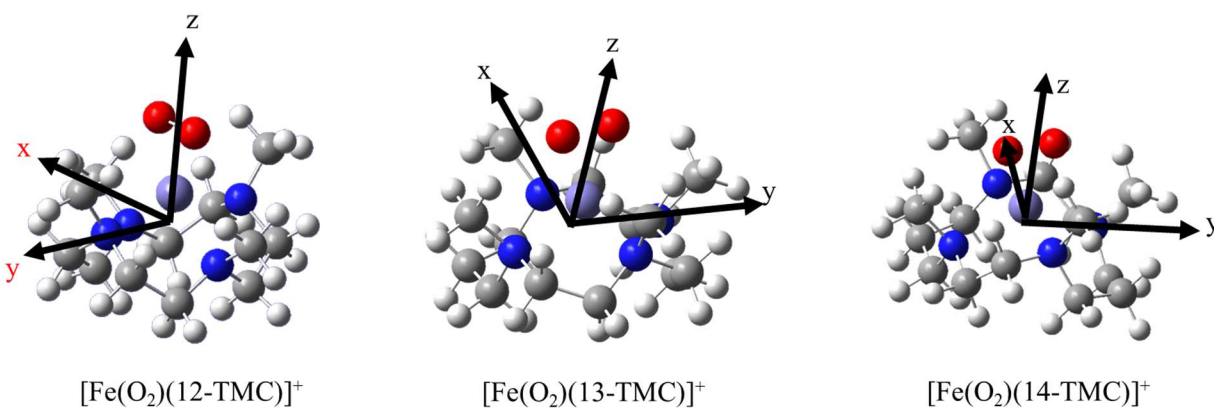
Figure 6.20. Calculated principal axes of the *D* tensors in **1** – **3**. Note how the *x* and *y* axes of **1** are swapped compared to those of **2** and **3**.

Table 6.6. Summary table of the TD-DFT (PBE0/def2-SVP) results for **1**. Select TD-DFT excitations and their energy/wavelength, oscillator strength, description of molecular orbitals in order of decreasing contribution to the excitation, and the calculated polarizations of the transitions are shown.

TD-DFT excitation #	Energy (cm^{-1})	Wavelength (nm)	Oscillator Strength	Molecular Orbital Transitions, in order of Decreasing Contribution	Polarization[a]		
					x	y	z
2	7077	1413	0.0002	$\delta \rightarrow d_{xz}$	100%	0%	0%
3	12692	788	0.0002	ps. σ, Fe-TMC $\sigma \rightarrow \delta^*$	0%	100%	0%
4	13262	754	0.0398	$\mathbf{\delta \rightarrow \delta^*}$	0%	0%	100%
5	13751	727	0.0002	$\delta \rightarrow$ Fe-TMC σ^*	0%	0%	100%
6	16018	624	0.0001	$\delta \rightarrow$ ps. σ^*	0%	100%	0%
7	28320	353	0.0006	$N_{TMC}(p) \rightarrow \delta^*$	99%	1%	0%
9	30414	329	0.0003	ps. $\sigma \rightarrow \delta^*$	0%	100%	0%
10	31115	321	0.0028	ps. $\sigma \rightarrow d_{z2}$	100%	0%	0%
13	38089	263	0.0001	Fe-TMC $\sigma \rightarrow d_{z2}$	0%	0%	100%
14	38798	258	0.0036	$N_{TMC}(p) \rightarrow d_{z2}$	0%	100%	0%
15	39020	256	0.0006	ps. $\sigma \rightarrow d_{z2}$	100%	0%	0%
16	39655	252	0.0339	Fe-TMC $\sigma \rightarrow d_{xz}$	0%	100%	0%
19	42151	237	0.0005	ps. $\sigma \rightarrow$ Fe-TMC σ^*	100%	0%	0%

Abbreviations used to denote MOs are as follows: $N_{TMC}(p)$ = p orbitals located on the Ns of the TMC co-ligand, Fe-TMC $\sigma = d_{x2-y2}\_N_{TMC}(p)$ σ, ps. $\sigma = O_2(\pi_{yz}^*)\_d_{yz}$ pseudo σ, $\delta = d_{xy}\_O_2(\pi_{xy}^*)$ δ, $\delta^* = O_2(\pi_{xy}^*)\_d_{xy}$ δ^*, Fe-TMC $\sigma^* = d_{x2-y2}\_N_{TMC}(p)$ σ^*, and ps. $\sigma^* = d_{yz}\_O_2(\pi_{yz}^*)$ pseudo σ^*.
[a] The polarizations listed here are with respect to the calculated principal axes of the D tensor for **1**, shown Figure 6.20. This is different than the orbital names, which are defined in the MO diagram in Figure 6.14. We chose to do this to keep the orbital names consistent for the whole series **1 – 3**. The difference between the two coordinate systems is the orientation of the *x* and *y* axes, which are roughly swapped between the two coordinate systems.

Table 6.7. Summary table of the TD-DFT (PBE0/def2-SVP) results for **2**. Select TD-DFT excitations and their energy/wavelength, oscillator strength, description of molecular orbitals in order of decreasing contribution to the excitation, and the calculated polarizations of the transitions are shown.

TD-DFT excitation #	Energy (cm^{-1})	Wavelength (nm)	Oscillator Strength	Molecular Orbital Transitions, in order of Decreasing Contribution	Polarization[a]		
					x	y	z
1	11677	856	0.0082	$\mathbf{\delta \rightarrow \delta^*}$; ps. $\sigma \rightarrow$ ps. σ^*	1%	2%	96%
2	12569	796	0.0013	$\delta \rightarrow d_{xz}$	1%	19%	80%
4	15073	663	0.00005	ps. $\sigma \rightarrow \delta^*$; $\delta \rightarrow$ ps. σ^*	56%	2%	42%
5	16212	617	0.0002	$\delta \rightarrow$ ps. σ^*; ps. $\sigma \rightarrow \delta^*$	77%	2%	22%
6	18206	549	0.00001	$\delta \rightarrow$ Fe-TMC σ^*	29%	6%	65%
7	19491	513	0.0002	ps. $\sigma \rightarrow d_{xz}$; $N_{TMC}(p) \rightarrow d_{xz}$	0%	100%	0%
8	20486	488	0.0033	ps. $\sigma \rightarrow d_{z2}$; $NTMC(p) \rightarrow d_{z2}$	0%	99%	0%
9	26316	380	0.0002	ps. σ, $N_{TMC}(p) \rightarrow$ Fe-TMC σ^*	0%	94%	6%

					x	y	z
10	29146	343	0.0006	$N_{TMC}(p)$, Fe-TMC $\sigma \rightarrow \delta^*$	32%	67%	1%
11	31244	320	0.0024	Fe-TMC σ, $N_{TMC}(p)$, ps. $\sigma \rightarrow \delta^*$	73%	27%	0%
12	32173	311	0.0040	$N_{TMC}(p)$, Fe-TMC $\sigma \rightarrow \delta^*$	53%	47%	0%
13	33262	301	0.0204	Fe-TMC $\sigma \rightarrow d_{xz}$	75%	0%	25%
16	35722	280	0.0362	$N_{TMC}(p) \rightarrow d_{xz}$; Fe-TMC $\sigma \rightarrow d_{z2}$;	5%	2%	92%
18	36468	274	0.0823	Fe-TMC $\sigma \rightarrow$ Fe-TMC σ^*; ps. $\sigma \rightarrow$ ps. σ^*; $N_{TMC}(p) \rightarrow d_{z2}$	1%	0%	99%
20	36940	271	0.0331	$N_{TMC}(p)$, Fe-TMC $\sigma \rightarrow d_{z2}$	54%	2%	44%

Abbreviations used to denote MOs are as follows: $N_{TMC}(p)$ = p orbitals located on the Ns of the TMC co-ligand, Fe-TMC $\sigma = d_{x2-y2}\_N_{TMC}(p)$ σ, ps. $\sigma = O_2(\pi_{yz}^*)\_d_{yz}$ pseudo σ, $\delta = O_2(\pi_{xy}^*)\_d_{xy}$ δ, $\delta^* = d_{xy}\_O_2(\pi_{xy}^*)$ δ^*, Fe-TMC $\sigma^* = d_{x2-y2}\_N_{TMC}(p)$ σ^*, and ps. $\sigma^* = d_{yz}\_O_2(\pi_{yz}^*)$ pseudo σ^*.

Table 6.8. Summary table of the TD-DFT (PBE0/def2-SVP) results for **3**. Select TD-DFT excitations and their energy/wavelength, oscillator strength, description of molecular orbitals in order of decreasing contribution to the excitation, and the calculated polarizations of the transitions are shown.

TD-DFT excitation #	Energy (cm⁻¹)	Wavelength (nm)	Oscillator Strength	Molecular Orbital Transitions, in order of Decreasing Contribution	Polarization[a]		
					x	y	z
1	11412	876	0.0067	$\delta \rightarrow \delta^*$	0%	0%	100%
2	11597	862	0.0007	$\delta \rightarrow d_{xz}$	26%	36%	38%
4	14494	690	0.0001	ps. $\sigma \rightarrow \delta^*$; $\delta \rightarrow$ ps. σ^*	60%	39%	1%
5	15658	639	0.0002	$\delta \rightarrow$ ps. σ^*; ps. $\sigma \rightarrow \delta^*$; $\delta \rightarrow$ Fe-TMC σ^*	53%	47%	0%
6	18174	550	0.0001	ps. $\sigma \rightarrow d_{xz}$	0%	2%	98%
7	18488	541	0.00003	$\delta \rightarrow$ Fe-TMC σ^*, ps. σ^*	6%	4%	89%
8	19960	501	0.0031	ps. $\sigma \rightarrow d_{z2}$; $N_{TMC}(p) \rightarrow d_{z2}$	26%	74%	0%
9	26465	378	0.0007	ps. $\sigma \rightarrow$ Fe-TMC σ^*, ps. σ^*	46%	52%	2%
11	30903	324	0.0047	$N_{TMC}(p)$, ps. $\sigma \rightarrow \delta^*$	95%	5%	0%
12	32348	309	0.0101	Fe-TMC $\sigma \rightarrow d_{xz}$	77%	21%	2%
14	33538	298	0.0147	$N_{TMC}(p) \rightarrow d_{xz}$; Fe-TMC $\sigma \rightarrow d_{z2}$;	1%	0%	99%
16	35884	279	0.0446	$N_{TMC}(p) \rightarrow d_{xz}$; Fe-TMC $\sigma \rightarrow d_{z2}$; ps. $\sigma \rightarrow$ ps. σ^*	1%	0%	99%
18	36635	273	0.0762	$N_{TMC}(p) \rightarrow d_{xz}$; Fe-TMC $\sigma \rightarrow$ Fe-TMC σ^*; ps. $\sigma \rightarrow$ ps. σ^*	0%	0%	100%
21	39662	252	0.0234	$N_{TMC}(p) \rightarrow d_{xz}$	61%	39%	0%

Abbreviations used to denote MOs are as follows: $N_{TMC}(p)$ = p orbitals located on the Ns of the TMC co-ligand, Fe-TMC $\sigma = d_{x2-y2}\_N_{TMC}(p)$ σ, ps. $\sigma = O_2(\pi_{yz}^*)\_d_{yz}$ pseudo σ, $\delta = O_2(\pi_{xy}^*)\_d_{xy}$ δ, $\delta^* = d_{xy}\_O_2(\pi_{xy}^*)$ δ^*, Fe-TMC $\sigma^* = d_{x2-y2}\_N_{TMC}(p)$ σ^*, and ps. $\sigma^* = d_{yz}\_O_2(\pi_{yz}^*)$ pseudo σ^*.

The TD-DFT results allow for the assignment of the main charge transfer band of **1 – 3**, observed in the 13,000 to 15,000 cm^{-1} range. This electronic transition, band 1 in our fit in Figure 6.4, is mainly comprised of the β-spin electron being promoted from the $O_2(\pi_{xy}*)\_d_{xy}$ δ to the $d_{xy}\_O_2(\pi_{xy}*)$ $\delta*$ orbital, and hence, corresponds to the $\delta \rightarrow \delta*$ ligand-to-metal charge-transfer (LMCT) transition of the Fe-O$_2$ unit. Experimentally, this band shifts to higher energy from **3** to **2** to **1**, and this is reproduced in the TD-DFT calculations (see Figure 6.19). In this way, the energy of the LMCT transition directly probes the strength of the Fe-O$_2$ δ bond, as indicated in Figure 6.12, right, with **3** having the weakest and **1** having the strongest δ bond. Correspondingly, complex **1** has the largest degree of Fe^{II}-superoxo character. The $\delta \rightarrow \delta*$ transition is calculated to be polarized along the z-axis. This agrees with the fitting of the VTVH saturation curves of this band for **2** and **3** (see Figure 6.8). Interestingly, the EPR spectra can be fit with either a small positive or negative D value. However, to obtain a z polarization for this transition, a small negative D value was necessary for the MCD VTVH fit (see Figure 6.21). This assignment of band 1 to a LMCT transition is further in agreement with the sensitivity of the energy of this band to H-bonding solvents, with the H-bonding solvents strongly interacting with the peroxo $\pi*$ orbitals. Here, a stabilization of the $O_2(\pi_{xy}*)$ orbital through H-bonding interactions causes a shift of the $\delta \rightarrow \delta*$ transition to higher energy, as a function of the strength of the hydrogen bond(s). In this way, the energy of the $\delta \rightarrow \delta*$ LMCT band is not only diagnostic for the strength of this interaction (comparing **1 – 3**), but for a given complex, it is also a sensitive probe for H-bonding with solvent.
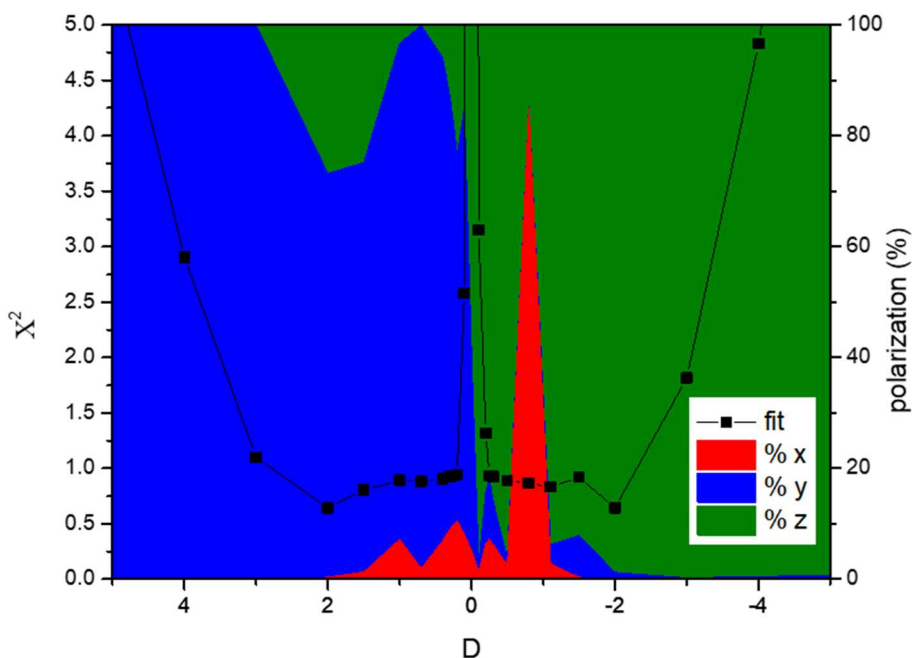
Figure 6.21. Goodness of fit and polarization for MCD VTVH saturation curves fit with varying *D* values. Here the VTVH saturation curves for **3** at 811 nm are fit with *E/D* = 0.3 and *g* = 2, 2, 2 while D was set to the value on the x-axis. The polarizations were allowed to optimize until a stable X^2 was achieved.

By MCD, we determined that the broad, low-energy absorption band of **1 – 3** is resolved into two transitions, bands 1 and 2 (see Figure 6.4), a potential pseudo **A**-term signal as discussed above. Band 2 is generally observed at $3,500 – 4,000$ cm^{-1} higher in energy compared to band 1. If the two excited states giving rise to bands 1 and 2 are spin-orbit coupled to give the pseudo **A**-term signal, as they appear to be, then band 2 cannot be polarized in the same direction as band 1. TD-DFT gives two probable transitions for band 2, both of which correspond to transitions originating from the $O_2(\pi_{xy}*)\_d_{xy}$ δ orbital, either into the $d_{yz}\_O_2(\pi_{yz}*)$ pseudo-σ* or the $d_{x2-y2}\_N_{TMC}(p)$ σ* orbital. The former is *x/y* polarized, and the latter is dominantly *z* polarized. Both transitions are calculated to have low intensity by UV–Vis; however, as they are d-d transitions, they would be stronger in the MCD spectrum. Experimentally, analysis of the VTVH saturation curves for band 2 shows *z* polarization (see Figure 6.9), although the data are not well fit, probably, due to the interference of the neighboring higher energy bands, which makes this assignment less certain. This indicates that band 2 corresponds to the $O_2(\pi_{xy}*)\_d_{xy}$ δ to $d_{x2-y2}\_N_{TMC}(p)$ σ* d-d transition and that the band 1/band 2 couple is not a true pseudo-**A** term signal. Nevertheless, since

both bands 1 and 2 correspond to transitions that originate from the same orbital, $O_2(\pi_{xy}*)\_d_{xy}\ \delta$, they are both sensitive to the size of the n-TMC ligand and show related shifts along the series **1** – **3**.

In the UV–Vis and MCD spectra of **3**, there is another band visible at 22,000 cm^{-1}, which is reproduced in the TD-DFT calculations. From the Gaussian fit, this region has a few contributing bands, bands 3 – 7. Bands 5 and 6 are the most prominent features, with band 5 matching best with the λ_{max} of the UV–Vis absorption band (see Figure 6.4). Band 5 is assigned to the relatively intense excitation 8 from the TD-DFT calculations (see Table 6.8), which is primarily a β-spin electron promotion from the $d_{yz}\_O_2(\pi_{yz}*)$ pseudo-σ bonding MO into the d_{z2} orbital. Excitation 8 is calculated to be y polarized. The VTVH data for band 5 are best fit with z polarization but can also be fit quite well with x or y polarization, as shown in Figure 6.10. For **2**, this transition is calculated at similar energy, and while not distinguishable in the UV–Vis spectra, it is observed by MCD. For **1**, the same transition is calculated 10,000 cm^{-1} higher in energy and is not observed by UV–Vis nor MCD spectroscopy.

6.6 C-H Bond Activation by 1-3. (Nam group)

The relative reactivities of **1** – **3** were studied by the Nam group. To understand how the ring size of n-TMC ligands affects the chemical properties of iron-peroxo complexes, the C–H bond activation of hydrocarbons by **1**, **2**, and **3** were systematically studied under identical reaction conditions. The most reactive species, 1, was measured to have a second-order rate constant (k_2) of 6.5×10^{-1} M^{-1} s^{-1} at –50 °C. The KIE of this reaction indicates that **1** reacts with xanthene by abstracting an H-atom, which is the rate determining step in the oxidation of xanthene by **1**.[348] The reactivity of **2** in H-atom transfer reactions was investigated in the same solvent. Due to the low reactivity of **2** at low temperature (e.g., −50 °C), temperature-dependent kinetic studies for **2** were performed to estimate its reactivity at −50 °C; the k_2 value at −50 °C was calculated to be 5.0×10^{-3} M^{-1} s^{-1}. By comparing the k_2 values of **1** and **2** at –50 °C, **1** was found to be ~130 times more reactive than **2** at −50 °C. Similar reactivity studies were carried out in the oxidation of xanthene by intermediate **3**. As **3** reacts less readily than **1** and **2**, for comparison with intermediates **1** and **2**, the k_2 value at −50 °C was determined by carrying out temperature-dependent kinetics study, giving the value of 3.7×10^{-5} M^{-1} s^{-1} at −50 °C. The above results clearly show that intermediate

3 is able to abstract an H-atom from hydrocarbon substrates, but the reactivity is about 130 times less than that of **2** and that **1** is about 18,000 times more reactive than **3**.

6.7 Mechanistic Insights into the Hydrogen Atom Transfer Reaction by Iron(III)-Peroxo Complexes (Wang Group)

The C-H activation mechanism was investigated theoretically by Peng Wu in the Wang Group. To understand the mechanism of the C–H activation by iron(III)-peroxo complexes and the ring size effect(s) of the macrocyclic *n*-TMC ligands in oxidation reactions, DFT calculations were performed for the reactions of **1**, **2**, and **3** with cyclohexadiene (CHD) that was used as a probe substrate. For the C–H bond activation reaction, we have considered two plausible mechanisms: The first is initiated by the homolytic O–O bond cleavage of the peroxo ligand, affording a dioxo (or a dioxyl) species. Then, one oxo ligand performs hydrogen atom abstraction (HAA) from CHD, which involves a small barrier of 4.4 kcal mol^{-1}. The second is initiated with the cleavage of one Fe-O bond, leading to the end-on Fe^{II}-superoxo species. The process is endothermic by ~4 kcal mol^{-1}, suggesting that such a transient species is challenging to be captured and identified by spectroscopy. Then, the end-on Fe^{II}-superoxo species can carry out HAA from substrate. The iron(II)-superoxo mediated HAA route is favored over the O–O bond cleavage mechanism. It is also noted that when we investigated the direct HAA of CHD by the side-on peroxo species, the reaction led to the end-on superoxo species. These results suggest that the Fe^{III}-peroxo complex is not reactive towards C–H bonds but is first activated by converting to the iron(II)-superoxo. The calculated HAA barriers were found to correlate well with the C–H activation rates determined experimentally. Interestingly, the HAA barriers are also well correlated with the Frontier Orbital energies of the end-on iron(II)-superoxo species for different *n*-TMC ligands. This is mainly because the singly-occupied π^* superoxo Frontier Orbital functions as the electron acceptor during the HAA reaction. The stronger the electron-donating ability is (e.g., 14-TMC > 13-TMC > 12-TMC), the higher in energy is the σ antibonding Fe-O(superoxo) π^* orbital, causing a higher barrier for the HAA reaction.

6.8 Discussion and Conclusions

In this study, we have analyzed the ring size effects of macrocyclic *n*-TMC ligands (*n* = 12, 13, and 14) on the physicochemical properties and reactivity of a series of synthetic

mononuclear nonheme iron(III)-peroxo complexes, such as $[Fe^{III}(O_2)(12\text{-TMC})]^+$ (**1**), $[Fe^{III}(O_2)(13\text{-TMC})]^+$ (**2**), and $[Fe^{III}(O_2)(14\text{-TMC})]^+$ (**3**), that show interesting co-ligand ring size dependent spectroscopic features, drastically different reactivities and model the corresponding Fe^{III}-peroxo intermediate in Rieske oxygenases. MCD and other spectroscopic methods along with DFT calculations were used to better understand the geometric and electronic structural differences in the Fe^{III}-peroxo complexes, **1 – 3**. First, all three Fe^{III}-peroxo complexes show the same δ and pseudo-σ bonds between iron and the peroxo ligand; however, the strength of these interactions varies depending on the ring size of the *n*-TMC ligands. It is important here to consider the experimental data along with the DFT calculations, as the DFT calculations can reproduce experimental spectroscopic trends, but not quantitatively. Experimentally, there is a gradual transition from **3** to **1**, indicated by the stepwise increase of the overall Fe-O bond strength, reflected by the increase in ν_s(Fe-O) (493-503-514 cm^{-1}), and the strength of the Fe-O$_2$ δ bond, reflected by a gradual shift of the low-energy δ → δ* LMCT band to higher energy (13605-14388-14925 cm^{-1}). In this regard, MCD spectroscopy played a key role in assigning the characteristic low-energy δ → δ* LMCT band, which provides direct insight into the strength of the Fe-O$_2$ δ bond along the series, and which is correlated with the amount of superoxo character of the complexes. The energy of this LMCT band is also a sensitive probe for hydrogen bonding between the peroxo unit and the solvent. Taken together, these results demonstrate that the ring size of *n*-TMC ligands affects the coordination geometry of the complexes in a way that reduces its overall donicity in the order of 14-TMC > 13-TMC > 12-TMC in a gradual way. Correspondingly, the Fe^{III}-peroxo interaction increases gradually in the order 14-TMC < 13-TMC < 12-TMC, with the 12-TMC complex featuring both the most exposed peroxo ligand and the compound with the largest amount of superoxo character. The DFT calculations can overall reproduce these trends, although they lack quantitative agreement with the experimental data.

Interestingly, our results demonstrate that the end-on Fe^{II}-superoxo form of the complexes is ultimately responsible for their reactivity towards the C–H bond activation. Importantly, in the case of the C–H bond activation, such as the HAT of xanthene, the reaction rate of **1** is ~10^2 and ~2×10^4 times greater than those of **2** and **3**, respectively. DFT calculations support the reactivity order of **1** > **2** > **3** in the C–H bond activation reaction, reproducing the experimental results well. The DFT calculations show that the HAA barriers in the reactions of **1 – 3** are well correlated with the Frontier Orbital energies of the end-on iron(II)-superoxo species bearing different *n*-TMC

ligands; the decrease of *n*-TMC ring size from 14-TMC to 13-TMC to 12-TMC lowers the energy barrier in the rate-determining HAA step by the end-on iron(II)-superoxo species, by lowering the singly-occupied π^* superoxo Frontier Orbital in energy that serves as the electron acceptor during the HAA reaction.

Besides elucidating the ring size effects of the *n*-TMC ligands on the properties of the corresponding Fe^{III}-peroxo complexes, we believe that the present study also provides valuable insight into the mechanism of the HAT reaction by Rieske (mono)oxygenases. Previous mechanistic studies have shown that a side-on Fe^{III}-peroxo complex is a likely intermediate of O_2 activation by Rieske oxygenases;[312] however, our DFT results demonstrate that these species are not reactive towards C–H bonds. Instead, we have shown that, with a suitable ligand environment and promoted by hydrogen bonding, the Fe^{III}-peroxo form can be easily transformed into the Fe^{II}-superoxo valence tautomer, which, as demonstrated for $[Fe^{III}(O_2)(12\text{-TMC})]^+$, is highly reactive towards aliphatic C–H bonds. The Fe^{II}-superoxo adduct is therefore a suitable intermediate in C–H bond activation by Rieske (mono)oxygenases, as demonstrated here for the first time. Previous work has also shown that the $[Fe^{III}(O_2)(12\text{-TMC})]^+$ complex is also able to mediate the *cis*-dihydroxylation of aromatic compounds.[315] Therefore, the $[Fe^{III}(O_2)(n\text{-TMC})]^+$ complex supports two key reactions of Rieske oxygenases, and more biomimetic studies for the reactions of Rieske oxygenases are underway with the mononuclear nonheme iron(III)-peroxo complexes bearing macrocyclic *n*-TMC ligands.

6.9 Experimental

6.9.1 Magnetic Circular Dichroism Spectroscopy

See Section 4.8.1 for description of Magnetic Circular Dichroism spectroscopy.

6.9.2 DFT Calculations

All calculations were performed with the Gaussian 16 software package.[349] The geometries of interested species were optimized by Peng Wu in the Wang group in conjunction with the SMD[350] continuum solvation model at the B3LYP[230,231,351]/def2-SVP[352] level of theory, in which the solvent of TFE was used. Gibbs energy corrections were obtained at 222.15K. The electronic energies were further refined with the larger basis set def2-TZVP[352] for all atoms. Dispersion corrections computed with Grimme's D3 method[353–355] were included. Electronic structure

calculations were performed on the structures optimized as described above by me. The same solvation model and dispersion corrections as listed above were included. TD-DFT calculations were performed by me in ORCA (version 5.0.3)[356] with the functionals B3LYP, PBE0,[233] BP86,[229,232] and TPSSh[234] and the basis set def2-SVP with auxiliary basis sets def2/J[357] and def2-SVP/C.[358] Molecular orbitals were calculated by me in Orca with PBE0/def2-SVP and visualized in Avogadro.[288]

6.9.3 Synthesis of Intermediates (Nam Group)

Synthesis of intermediates **1 – 3** were prepared by the Nam group, and have been reported previously.[315,335,336] Below, a brief preparation of the rRaman samples is provided here for the reader.

Generation of Intermediates 1 – 3 for rRaman measurements. Samples for resonance Raman were prepared as follows: a solution of $[Fe^{III}(O_2)(n\text{-TMC})]^+$ (n = 12, 13, and 14) was prepared by mixing 0.40 mL of MeOH solution containing $[Fe^{II}(n\text{-TMC})]^{2+}$ (32 mM for **1**, 16 mM for **2** and **3**) with H_2O_2 (5 eq for **1**, 10 eq for **2** and **3**) and TEA (5.0 eq) in MeOH at –80 °C. ^{18}O-labeled $[Fe^{III}(^{18}O_2)(n\text{-TMC})]^+$ were prepared by the same procedure from iron(II) starting, but in which $H_2^{16}O_2$ was replaced with $H_2^{18}O_2$ (2.7% $H_2^{18}O_2$ in water).

Chapter 7 Conclusions and Future Directions

7.1 Overall Summary

Understanding the water splitting reaction will ultimately allow for the clean production of hydrogen, a useful commodity chemical and promising clean fuel, aiding our transition to a sustainable society. Chapters 2 and 3 focus on the use of a family of molecular catalysts, cobalt bis(benzenedithiolate)s, for hydrogen production, the reductive side of water splitting. Chapters 4, 5, and 6 use spectroscopic techniques and density functional theory (DFT) calculations to investigate metal oxygen intermediates, which are relevant to the oxidative side of water splitting, the reverse reaction (O_2 reduction) in fuel cells, and oxidative reactions mediated by metalloenzymes in bioinorganic chemistry.

7.2 Co Bis(benzenedithiolate) Type Catalysts for Hydrogen Production: Summary and Future Directions

The first two data chapters of this thesis focus on the use of Co bis(benzenedithiolate) type catalysts for the hydrogen evolution reaction (HER). Chapter 2 describes the synthesis and characterization of a graphitic thin film material which has been covalently modified with Co bis(benzylaminedithiolate). The thin film material is highly active for electrocatalytic HER and the thermodynamic and kinetics of electrocatalysis are reported. This provides insight into the nature of the thin film, further adding to the scientific discussion of how immobilized catalysts interact with electrode surfaces electronically. Additionally, this thin film shows high Faradaic efficiency for HER even under an atmosphere of ambient air. However, the catalytic activity of the catalyst declines over the course of several hours. This led us to further investigate the mechanism of catalysis by this family of catalysts. In Chapter 3, the reaction of reduced Co(II) bis(benzenedichlorodithiolate) with protons was investigated in further detail. The reduced form of the complex was found to be reactive with protons, returning to the starting Co(III) complex.

7.2.1 Future Connections with Co Bis(benzylaminedithiolate) HER Catalyst

The first data chapter in this thesis describes the synthesis of an amine-modified benzenedithiolate ligand. This ligand provides a new and useful version of the traditional benzenedithiolate ligand, allowing it another moiety for reactivity. This ligand was metalated with Co, which gave a new version of the Co bis(benzenedithiolate) complex family of adept HER catalysts. In Chapter 2, the amine modified Co bis(benzenedithiolate) complex is shown to be attached to graphene oxide (GO), through the appended amine reacting with the epoxide groups of GO. However, amine moieties exhibit diverse reactivities and can be bound to many other useful substrates.
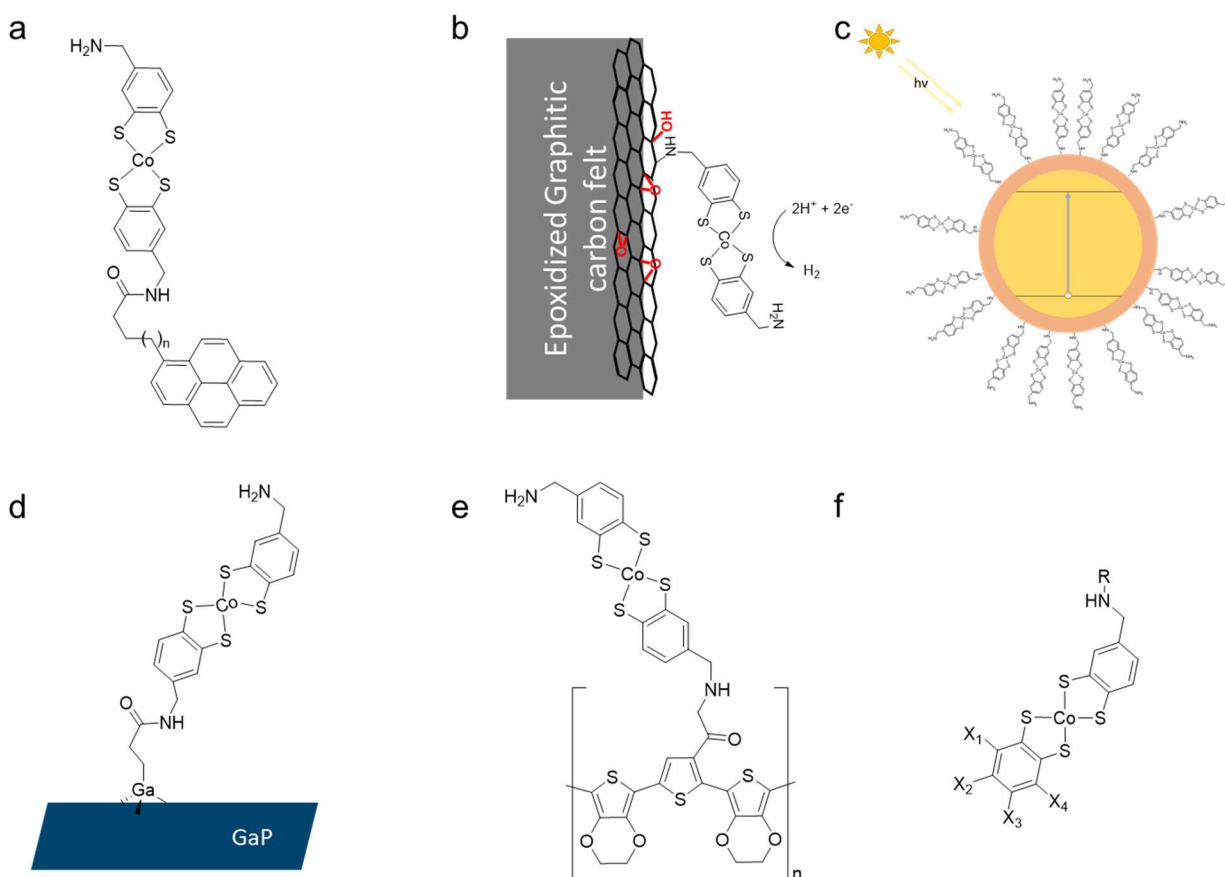
Figure 7.1. The amine-functionalized Co bis(benzenedithiolate) complex allows for advantageous attachment to (a) pyrene, (b) other graphitic electrode surfaces such as epoxidized carbon felt, (c) quantum dots, (d) modified GaP semiconductor surfaces, (e) monomers that could be incorporated into a polymer thin film, or (f) any of the above catalyst systems could be improved by modulating the non-covalently attached benzenedithiolate type ligand.

The amine functionality could be used to improve the attachment of the catalyst to other useful catalyst supports, as we are generally interested in immobilizing catalysts to electrode surfaces for HER. A few different options are depicted in Figure 7.1. First, in Figure 7.1a, physisorption to a

graphitic electrode surface could be improved by connecting the Co bis(benzylaminedithiolate) type complex to a carboxylic acid-modified pyrene. Pyrenes are well known to physisorb strongly to graphitic surfaces and can increase the catalyst loading and retention of the catalyst under catalytic conditions.[67,153] Another option to increase catalyst loading, per geometric area of the electrode, is to use graphitic carbon felt as a high surface area catalyst support. Graphitic carbon felt can be epoxidized to give epoxide functional groups on the surface that, as shown in Chapter 2, could be reacted with Co bis(benzylaminedithiolate) to yield a covalently modified electrode. This system is shown in Figure 7.1b.

Additionally, our group has been interested in expanding the use of these Co bis(benzenedithiolate) type catalysts from electrocatalytic HER to photo(electro)catalytic HER. As amines are common ligands for quantum dots and nanoparticle surfaces, there is an opportunity to use this catalyst to enhance the HER ability of quantum dots, as depicted in Figure 7.1c. The opportunities for photo(electro)catalytic HER with quantum dots is discussed further in Section 7.2.3. Another option for photoelectrocatalytic HER is the covalent attachment of Co bis(benzylaminedithiolate) to a modified gallium phosphide semiconductor surface, as illustrated in Figure 7.1d. Direct covalent attachment limits the electrode coverage to a monolayer of catalyst. Another option to increase the catalyst loading is to deposit a transparent, conducting, thin film material onto the electrode surface. Our group has developed reduced graphene oxide (RGO) thin films embedded with catalyst, but these need to be very thin, less than 200 nm, to ensure that they are transparent enough to allow light to pass through to the underlying semiconductor. Another option is to deposit a polymeric thin film with embedded catalyst. An option for such a film is shown in Figure 7.1e, where a primarily poly(3,4-ethylenedioxythiophene) (PEDOT) thin film is interspersed with thiophene monomers modified with Co bis(benzylaminedithiolate). The modified thiophene monomers could be synthesized from the commercially available 3-(bromoacetyl)thiophene through an S_N2 reaction with the amine moiety of Co bis(benzylaminedithiolate). Thin films that include these monomers could then be electropolymerized on a variety of electrode surfaces and characterized for electrochemical and photoelectrochemical HER.

Finally, when a highly active and durable variation of immobilized Co bis(benzylaminedithiolate) is found, one of the benzenedithiolate ligands could be modulated to optimize the catalytic activity and onset potential. Such a non-symmetric Co complex could be

prepared by mixing both ligands in the initial metalation phase and separating the statistical mix of complexes. It is also possible that these mixed-ligand complexes could be prepared after synthesis and purification by ligand exchange, as under specific conditions, the benzenedithiolate ligands appear to be labile, see discussion in the first paragraph of Section 3.3.1.

7.2.2 Further Thin Film Studies

The GO-Co bis(benzylaminedithiolate) catalyst system explored in Chapter 2 was shown to be highly active for HER. The electrochemical characterization of this system revealed that it shows some properties associated with an adsorbed species on the electrode surface and some properties associated with a metal-like catalyst. For example, the electrodes modified with the GO-Co bis(benzylaminedithiolate) thin film show a clear $Co^{III/II}$ couple. However, unlike molecular catalysts in solution, or attached to electrode surfaces outside of the electrochemical double layer, the onset potential of these catalysts changes with pH in a nearly Nernstian manner. This suggests very close electronic interaction between the catalyst and the RGO support. Further studies exploring the factors that control these interactions are recommended. It is possible that some of the catalyst is already within the electrochemical double layer at the beginning of catalysis, which would allow it to contribute to catalysis, without contributing to the $Co^{III/II}$ couple. Changing the degree of reduction of the RGO film while measuring how closely the $Co^{III/II}$ couple integration correlates with observed turnover frequency (TOF) could reveal whether this is the case. The active catalyst as given by the $Co^{III/II}$ couple could be compared with the amount of Co complex in the film as determined by the preparation of the film or by an independent measurement. A more reduced film would be expected to have more catalyst that does not contribute to the $Co^{III/II}$ couple, but that may contribute to catalysis. Additional studies by X-ray absorption spectroscopy could confirm if some catalyst remains Co^{III} under applied potentials more reducing than the $Co^{III/II}$ couple, and if so, this would suggest that the catalyst is merging with the electrode's band structure. We have previously assumed that any catalyst we know is on the electrode surface but does not contribute to the $Co^{III/II}$ couple is electronically insulated from the electrode and does not contribute to catalysis. Note that including this "silent" catalyst would not fully explain the interesting fact that Co bis(benzenedithiolate) complexes have a higher TOF when immobilized on electrode surfaces than when in solution, as in solution a TOF of 0.39 s^{-1} was reported,[47] while our group has reported immobilized Co bis(benzenedithiolate) type catalysts with TOFs four orders of

magnitude higher.[2,96] Also, the degree of reduction of GO may impact the change of onset potential with pH, with a more reduced GO becoming closer to Nernstian. The GO degree of reduction should be controllable via the amount of reducing charge passed electrochemically and can then be further assessed by Raman and X-ray photoelectron spectroscopy. However, if controlling the exact degree of GO reduction should turn out to be difficult, other conductive and nonconductive polymer mixtures could be utilized to provide similar conditions.

7.2.3 Photocatalytic HER: Preliminary Results and Future Directions

This thesis focuses on electrocatalytic HER, wherein electricity provides the energy necessary to drive the reaction. However, as electricity is being produced, stored, transferred, and used, there are small losses that add up. Ideally, the sun's energy could be used more efficiently to produce hydrogen directly through photochemical or photoelectrochemical HER. The relative efficiency of photocatalytic HER depends on the quantum yield of the photocatalytic HER, compared to the combined efficiency of solar electricity formation, storage, transportation, and Faradaic efficiency of electrocatalytic HER. As Co bis(benzenedithiolate) type catalysts are effective catalysts for HER, they can be useful in developing, testing, and characterizing the chemistry of molecular photo(electro)catalytic HER systems. Preliminary research on both Co bis(benzenedithiolate) type catalysts immobilized in thin films with photosensitizers for photoelectrocatalytic HER and in solution for homogeneous photocatalytic HER has been conducted. These two types of HER systems are visualized in Figure 1.1.
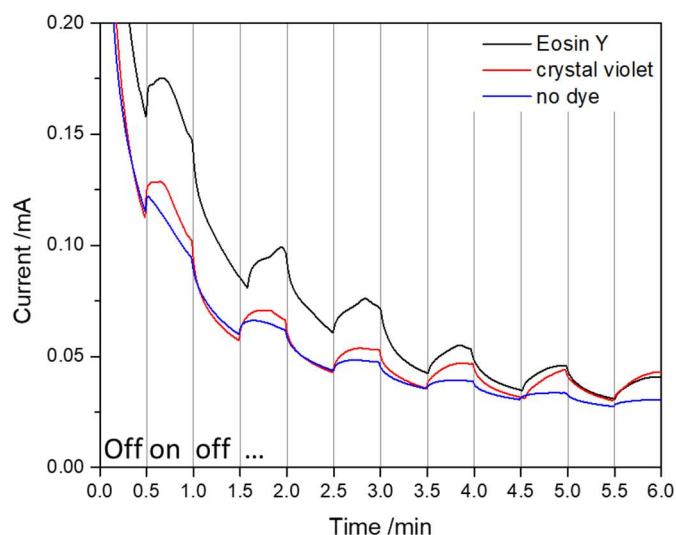
Figure 7.2. The photoelectrocatalytic current of a thin RGO film embedded with [TBA][Co(Cl$_2$bdt)$_2$] and with Eosin Y, crystal violet, or no dye as indicated. The thin films were made with 50 μL 0.5 mg/mL RGO, 10 μL 1 mM dye, 2 μL 1 mM [TBA][Co(Cl$_2$bdt)$_2$] mixed and drop-cast on a glassy carbon electrode. Once dried, the films were held at -0.4 V vs Ag|AgCl at pH 2.5, in 0.1 M KPF$_6$, with a Pt wire counter electrode, under N$_2$. The electrode was illuminated (on) and not illuminated (off) with a halogen light alternatingly every 30 s as indicated.

First, RGO thin films with embedded catalyst and photosensitizer were shown to have slight improvement in photocurrent. Here, crystal violet or Eosin Y dye was used as a photosensitizer, and [TBA][Co(Cl$_2$bdt)$_2$] was used as the catalyst, with both mixed into an RGO thin film. The electrode was held at a set potential, positive of electrocatalytic HER, so in the dark there was less than the necessary driving force for electrocatalytic HER. Upon illumination of the electrode surface, with a photosensitizer present in the film together with the catalyst, one would expect an increase in the current at a voltage positive of the electrocatalytic HER onset potential. Both the dyes show a moderate photocatalytic current, which is slightly improved over a film with no dye present, see Figure 7.2. This shows that the dyes are able to transfer some of the energy from the light to the catalyst to allow it to turn over protons to hydrogen at a potential that would otherwise be too positive for HER. The film with no dye also shows minor photocurrent, which might be due to the RGO itself being able to absorb light and act as a poor photosensitizer, or due to heating of the GC electrode from the IR radiation of the halogen lamp, thus facilitating the reaction. However, this observed photocurrent is a minor improvement over the background current, and subsequent

efforts were not able to further improve photocatalytic performance with these dyes. As discussed below, a more effective photosensitizer is likely necessary.
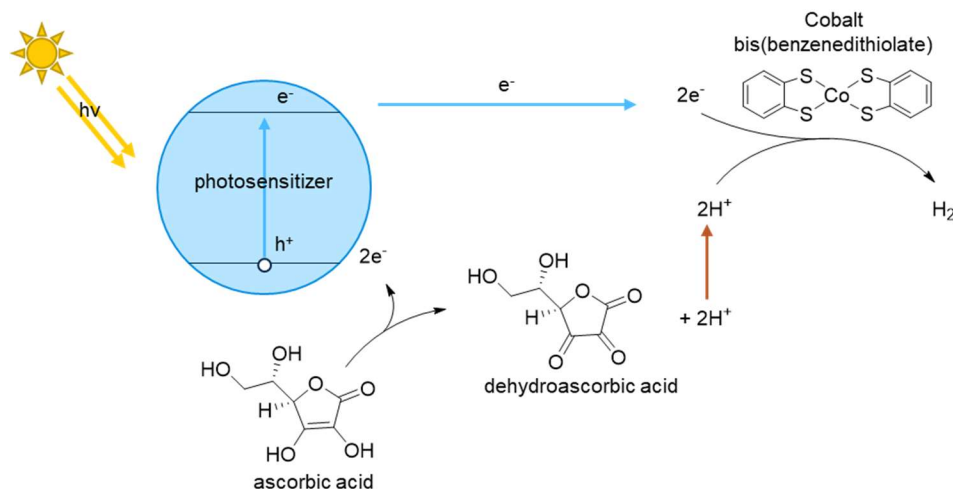
Figure 7.3. Scheme showing homogeneous photocatalytic HER with a photosensitizer, ascorbic acid as a sacrificial electron donor, and Co bis(benzenedithiolate) as the catalyst.

Second, homogeneous photocatalytic HER allows hydrogen to be generated in solution, without immobilizing the catalyst onto an electrode surface. For Co bis(benzenedithiolate) catalysts, there is precedent for this: Eisenberg and co-workers were able to generate hydrogen with $[Ru(bpy)_3]^{2+}$ and with CdSe nanoparticles acting as photosensitizers in homogeneous solution.[47,64] We are interested in finding a more sustainable yet still compatible photosensitizer, to improve on the literature precedent that relies on rare and toxic metals. To do this, screening tests were performed under halogen light, with $Co(bdtCl_2)_2$ as the catalyst, an organic dye or non-catalytic metalloporphyrin as the photosensitizer, and ascorbic acid as the sacrificial electron donor. This expected reaction scheme is illustrated in Figure 7.3. For these tests, any hydrogen produced was detected by H_2tape, a commercial tape that changes color to a darker gray in the presence of hydrogen gas. A control reaction with $[Ru(bpy)_3]^{2+}$ as the photosensitizer confirmed that hydrogen was produced and detected, repeating the results of Eisenberg et al.[47] However, upon testing Eosin Y, crystal violet, and ZnTPP, none of these photosensitizers were found to produce hydrogen at a comparable scale (TPP^{2-} = tetraphenylporphyrin dianion). Additionally, under this intensity of light, the Eosin Y showed significant photobleaching, see Figure 7.4. To be effective photosensitizers, dyes must be stable under the conditions used and compatible with both the

sacrificial electron donor and the catalyst. A screen of further organic dyes and other green photosensitizers is suggested, especially utilizing the photoreactor our group recently acquired.
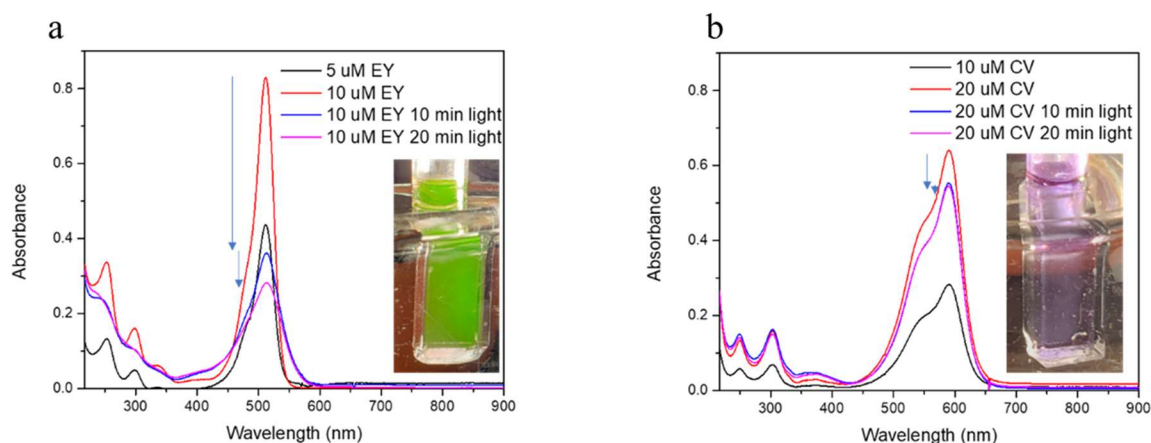
Figure 7.4. Change in UV-Vis absorption spectra of dyes after exposure to light. Left, 10 mM Eosin Y (EY) exposed to light shows a decrease in absorption after 10 and 20 minute light exposure. Right, 20 mM crystal violet shows less photobleaching under the same conditions. The inset shows a photo of the dye solution in a cuvette under halogen light illumination. The cuvette is submerged in a water bath to limit changes in temperature.

Quantum dots are a promising photosensitizer as well. They are often less susceptible to photobleaching than organic dye photosensitizers and can provide multiple high energy electrons. The amine groups on Co bis(benzylaminedithiolate) complexes could function as ligands for the commercially available ZnS/CdSe core-shell quantum dots. Ideally, the proximity of the Co catalyst to the quantum dot would yield higher HER activity than a non-bound catalyst in solution. Quantum dots could be useful as a homogeneous photosensitizer for HER with Co bis(benzenedithiolate) type catalysts. They could also be mixed with RGO to give thin films that could be tested for photoelectrochemical HER. ZnS/CdSe core-shell quantum dots are an ideal test system for this approach, and if this system proves promising, the new and quickly expanding field of quantum dots and nanocrystalline semiconductors could be further explored, to reduce the amount of heavy toxic metal in this system. Of particular interest and promise are carbon, CuInS, and InP quantum dots which feature less toxic elements and are already commercially available.

7.2.4 Non-HER Reductive Catalysis by Co Bis(benzenedithiolate) Type Catalysts

As Co bis(benzenedithiolate) complexes are adept proton reduction catalysts, they may be catalysts for other useful reductive reactions as well. Two features that suggest that this is the case

are the noninnocent dithiolate type ligands that the catalysts feature and their pH switchable HER activity. These catalysts show limited HER above pH 4, which provides conditions under which the Faradaic efficiency toward HER is limited. Such conditions are available by utilizing a higher pH in aqueous solution or using a weaker acid in organic solution. A few examples of such reductive reactions that Co bis(benzenedithiolate) type catalysts may be tested for include O_2 reduction, CO_2 reduction, nitrate reduction, and reduction of organic functional groups. If any reactivity is observed, the ligand and metal may be optimized as many related catalysts have been reported in the literature.[60,61,359,360]
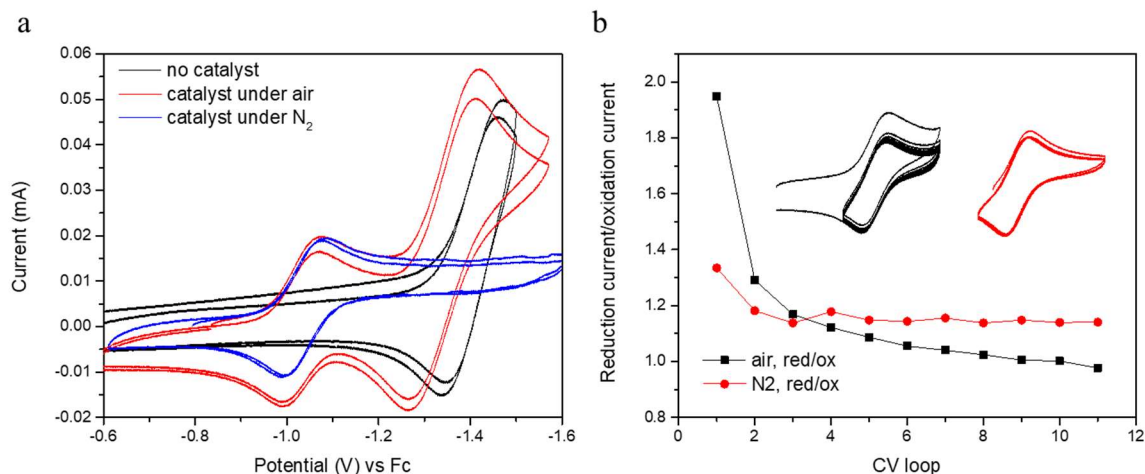
Figure 7.5. Changes observed in the cyclic voltammogram under air versus dinitrogen. Left, two consecutive CVs are shown for a GC electrode under air without catalyst present (black), for the catalyst under dinitrogen (blue), and the catalyst under air (red). Right, comparison of the ratio of the reductive current to the oxidative current, over multiple CV cycles, with the solution of catalyst under air (black) or nitrogen (red). The inset graphs show the corresponding CVs, offset for clarity. This experiment was conducted in a one-part cell with 1 mM [TBA][Co(bdtCl$_2$)$_2$] and 0.1 M [TBA](PF$_6$) in DMF. The solution was purged with air or dinitrogen as indicated. The working electrode was glassy carbon, the counter electrode was Pt wire, the pseudo-reference electrode was Ag, and the potentials were referenced to Fc^+/Fc after the experiment was complete.

Preliminary work shows that Co(Cl$_2$bdt)$_2$ is active for the O_2 reduction reaction. In Chapter 3, while studying the mechanism of this catalyst for HER, the reduced Co(II) species was found to be reactive with dioxygen, returning the Co(III) form of the catalyst upon exposure to ambient O_2 in air, see Figure 3.4. This suggests that the Co(II) form is capable of dioxygen reduction and this catalyst family could therefore be further developed into an O_2 reduction electrocatalyst. Initial studies show a 70 mV oxidative shift of the dioxygen reduction catalytic wave compared to bare glassy carbon. Additionally, the Co(III/II) couple is less reversible under exposure to O_2, which

suggests that dioxygen reduction is occurring on a small scale. The catalytic activity in this initial test may have been limited by the availability of protons in solution. Further trials titrating in weak acid sources and further optimization are recommended.

7.3 Summary of Investigations of Reactive Metal-Oxygen Intermediates

Chapters 3-6 of this thesis explore three metal-oxygen moieties. In general, for these studies, we used spectroscopy and density functional theory to define the species' identity and electronic structure. These species are very reactive and unusual, requiring careful study. Vibrational spectroscopies, like resonance Raman and nuclear resonance vibrational spectroscopy (NRVS) show the often-characteristic vibrations of the metal-oxygen species and reflect the subtle changes in bond strength due to ligand effects and hydrogen bonding. UV-Vis and magnetic circular dichroism spectroscopy characterize the electronic structure of the species. Magnetic circular dichroism offers many data points under temperature and magnetic field variation, which can determine the spin state of the complex and, with Time Dependent Density Functional Theory (TD-DFT) calculations, often allow assignment the observed electronic transitions. Combining the data from different spectroscopies gives us different views of the same species and the true chemical species explains all the experimental data. Density Functional Theory (DFT) allows us to corroborate that the proposed structure is a good model for the spectroscopic data and see if the trends we observe are explained by calculations. Further, when a good DFT model is obtained for a species of interest, its electronic structure and reactivity can be further understood and properties that were not measured can be predicted. The chemical knowledge gained in this way helps scientists understand fleeting intermediates in important reactions and recognize similar species.

First in Chapter 4, a high valent Ni-O intermediate is presented. By spectroscopic and DFT investigations, this complex is shown to be best described as a $S_t = 1$ Ni^{III}-oxyl species. The bonding inversion of the Ni-O π bond generates a hole primarily located in one of the p-orbitals of the oxyl ligand. This explains the electronic structure of a formally $Ni^{IV}=O$ species, which would otherwise not be expected to exist because of the "oxo wall". The next two chapters explore iron complexes, with cyclam derived ligands and oxygen containing ligands. The Fe(cyclam) precursors are known to react with O_2 and can support a variety of interesting Fe-oxygen derived moieties.[116,279,280,324] Chapter 5 examines the effect of changing a nitrogen for an oxygen donor atom in the cyclam scaffold on the reaction of the Fe^{II} complex with O_2, protons, and $NaBH_4$. This

allowed for the identification of a unique Fe^{II}-phenoxy radical intermediate. Careful DFT calculations ruled out the initially suspected structure, a Fe(II)-superoxide type species. Then magnetic circular dichroism (MCD) and resonance Raman spectroscopy, together with synthetic and spectroscopic efforts by our collaborators, showed the identity and characteristics of the intermediate in question as an Fe^{II}-phenoxy radical complex. Finally, Chapter 6 focuses on the characterization of Fe^{III}-peroxide complexes, elucidating how the electronic structure changes with the ring size of the co-ligand. The Fe-O_2 moieties in these complexes were found to exhibit consistent electronic structures across the series, which explains their similar spectroscopic properties. Their electronic structures feature two interesting bonding interactions: a Fe-O_2 δ and pseudo-σ bond. The electronic excitation of the electron in the δ bonding molecular orbital (MO) to the δ^* MO is responsible for the main band observed by UV-Vis and MCD spectroscopy. This band allowed us to track the strength of this bond, and we found that the CT band increases in energy as the ligand size decreases, showing a more tightly bound peroxide unit in the 12-TMC when compared to the 13- or 14-TMC species.

7.3.1 *Future Directions*

The studies conducted in this thesis have spectroscopically examined individual earth abundant transition metal intermediates in oxidation reactions. Our collaborators – the Nam group in Seoul, Korea and the Ray Group in Berlin, Germany – were able to trap these intermediates under careful synthetic conditions and to generally show stoichiometric reactivity. Future directions on this project could involve the study of intermediates that are capable of catalytic turnover. To do this, one must complete the cycle and return to the starting complex, which could then be re-oxidized to make the active intermediate. This could be accomplished by electrocatalysis. The cyclic voltammetry (CV) data of a few of the compounds with cyclic ligands that we study show clean $M^{n/n+1}$ couples, if not multiple clean oxidation couples. A good example is the Ni(TAML) species studied in Chapter 4.[150] This suggests that return to the starting oxidation state after catalysis should be possible. Our collaborator Dustin Kass has shown phenol electrooxidation by Fe(TMCO). Further in-depth titrations and controlled potential electrolysis experiments would be useful to quantify and optimize these types of reactions. Further, it would be interesting, now that we have identified the spectroscopic markers of these species, to see if they can be detected during catalysis. Already established molecular oxidation catalysts could be

examined to see if similar intermediates could be detected under catalytic conditions, and their electronic structures could be compared to those we found on the slightly more stable stoichiometric model complexes that our collaborators trapped.

These efforts to understand the electronic structures of reactive intermediates expand our understanding of what chemical species could occur in oxidative reactions, and how their nature determines reactivity. In turn, this helps chemists who are developing catalysts for oxidative reactions imagine and report accurate reaction mechanisms and tune the active site environments of their catalysts to optimize their reactions, as desired.

Bibliography

(1)   Larson, V. A.; Battistella, B.; Ray, K.; Lehnert, N.; Nam, W. Iron and Manganese Oxo Complexes, Oxo Wall and Beyond. *Nat. Chem. Rev.* **2020**, *4*, 404–419. https://doi.org/10.1038/s41570-020-0197-9.

(2)   Larson, V. A.; Lehnert, N. Covalent Attachment of Cobalt Bis(Benzylaminedithiolate) to Reduced Graphene Oxide as a Thin Film Electrocatalyst for Hydrogen Production with Remarkable Dioxygen Tolerance. *ACS Catal.* **2024**, *14* (1), 192–210. https://doi.org/10.1021/acscatal.3c03788.

(3)   Masson-Delmotte, V.; Zhai, P.; Chen, Y.; Goldfarb, L.; Gomis, M. I.; Matthews, J. B. R.; Berger, S.; Huang, M.; Yelekçi, O.; Yu, R.; Zhou, B.; Lonnoy, E.; Maycock, T. K.; Waterfield, T.; Leitzell, K.; Caud, N. *IPCC, 2021: Summary for Policymakers. Climate Change 2021: The Physical Science Basis. Contribution of Working Group I to the Sixth Assessment Report of the Intergovernmental Panel on Climate Change*; 2021.

(4)   Fontecave, M. Editorial: Sustainable Chemistry for Energizing the Planet. *Angew. Chemie Int. Ed.* **2015**, *54* (24), 6946–6947. https://doi.org/10.1002/ANIE.201502134.

(5)   Kron, W.; Löw, P.; Kundzewicz, Z. W. Changes in Risk of Extreme Weather Events in Europe. *Environ. Sci. Policy* **2019**, *100*, 74–83. https://doi.org/10.1016/J.ENVSCI.2019.06.007.

(6)   Ripple, W. J.; Wolf, C.; Gregg, J. W.; Levin, K.; Rockström, J.; Newsome, T. M.; Betts, M. G.; Huq, S.; Law, B. E.; Kemp, L.; Kalmus, P.; Lenton, T. M. World Scientists' Warning of a Climate Emergency 2022. *Bioscience* **2022**, *72* (12), 1149–1155. https://doi.org/10.1093/BIOSCI/BIAC083.

(7)   Anderson, R.; Bayer, P. E.; Edwards, D. Climate Change and the Need for Agricultural Adaptation. *Curr. Opin. Plant Biol.* **2020**, *56*, 197–202. https://doi.org/10.1016/J.PBI.2019.12.006.

(8)   Calvin, K.; Dasgupta, D.; Krinner, G.; Mukherji, A.; Thorne, P. W.; Trisos, C.; Romero, J.; Aldunce, P.; Barrett, K.; Blanco, G.; Cheung, W. W. L.; Connors, S.; Denton, F.; Diongue-Niang, A.; Dodman, D.; Garschagen, M.; Geden, O.; Hayward, B.; Jones, C.; Jotzo, F.; Krug, T.; Lasco, R.; Lee, Y.-Y.; Masson-Delmotte, V.; Meinshausen, M.; Mintenbeck, K.; Mokssit, A.; Otto, F. E. L.; Pathak, M.; Pirani, A.; Poloczanska, E.; Pörtner, H.-O.; Revi, A.; Roberts, D. C.; Roy, J.; Ruane, A. C.; Skea, J.; Shukla, P. R.; Slade, R.; Slangen, A.; Sokona, Y.; Sörensson, A. A.; Tignor, M.; van Vuuren, D.; Wei, Y.-M.; Winkler, H.; Zhai, P.; Zommers, Z.; Hourcade, J.-C.; Johnson, F. X.; Pachauri, S.; Simpson, N. P.; Singh, C.; Thomas, A.; Totin, E.; Alegría, A.; Armour, K.; Bednar-Friedl, B.; Blok, K.; Cissé, G.; Dentener, F.; Eriksen, S.; Fischer, E.; Garner, G.; Guivarch, C.; Haasnoot, M.; Hansen, G.; Hauser, M.; Hawkins, E.; Hermans, T.; Kopp, R.; Leprince-Ringuet, N.; Lewis, J.; Ley, D.; Ludden, C.; Niamir, L.; Nicholls, Z.; Some, S.; Szopa, S.; Trewin, B.; van der Wijst, K.-I.; Winter, G.; Witting, M.; Birt, A.; Ha, M. *IPCC, 2023: Summary for Policymakers. In: Climate Change 2023: Synthesis Report. Contribution of Working Groups I, II and III to*

the Sixth Assessment Report of the Intergovernmental Panel on Climate Change; Arias, P., Bustamante, M., Elgizouli, I., Flato, G., Howden, M., Méndez-Vallejo, C., Pereira, J. J., Pichs-Madruga, R., Rose, S. K., Saheb, Y., Sánchez Rodríguez, R., Ürge-Vorsatz, D., Xiao, C., Yassaa, N., Romero, J., Kim, J., Haites, E. F., Jung, Y., Stavins, R., Birt, A., Ha, M., Orendain, D. J. A., Ignon, L., Park, S., Park, Y., Reisinger, A., Cammaramo, D., Fischlin, A., Fuglestvedt, J. S., Hansen, G., Ludden, C., Masson-Delmotte, V., Matthews, J. B. R., Mintenbeck, K., Pirani, A., Poloczanska, E., Leprince-Ringuet, N., Péan, C., Eds.; Geneva, Switzerland., 2023. https://doi.org/10.59327/IPCC/AR6-9789291691647.

(9) Pörtner, H.-O.; Scholes, R. J.; Agard, J.; Archer, E.; Arneth, A.; Bai, X.; Barnes, D.; Burrows, M.; Chan, L.; Cheung, W. L. IPBES-IPCC Co-Sponsored Workshop Report on Biodiversity and Climate Change. *IPBES IPCC* **2021**, *10*.

(10) Chen, T. L.; Kim, H.; Pan, S. Y.; Tseng, P. C.; Lin, Y. P.; Chiang, P. C. Implementation of Green Chemistry Principles in Circular Economy System towards Sustainable Development Goals: Challenges and Perspectives. *Sci. Total Environ.* **2020**, *716*, 136998. https://doi.org/10.1016/J.SCITOTENV.2020.136998.

(11) Zimmerman, J. B.; Anastas, P. T.; Erythropel, H. C.; Leitner, W. Designing for a Green Chemistry Future. *Science.* **2020**, *367* (6476), 397–400. https://doi.org/10.1126/science.aay3060.

(12) Ziolkowska, J. R. Biofuels Technologies: An Overview of Feedstocks, Processes, and Technologies. *Biofuels a more Sustain. Futur.* **2020**, 1–19.

(13) PENN, I. California Invested Heavily in Solar Power. Now There's so Much That Other States Are Sometimes Paid to Take It. *Los Angeles Times* **2017**, 1–22.

(14) Kim, J. H.; Hansora, D.; Sharma, P.; Jang, J. W.; Lee, J. S. Toward Practical Solar Hydrogen Production – an Artificial Photosynthetic Leaf-to-Farm Challenge. *Chem. Soc. Rev.* **2019**, *48* (7), 1908–1971. https://doi.org/10.1039/C8CS00699G.

(15) IEA (2021), Hydrogen https://www.iea.org/reports/hydrogen (accessed Nov 11, 2021).

(16) Brandon, N. P.; Kurban, Z. Clean Energy and the Hydrogen Economy. *Philos. Trans. R. Soc. A Math. Phys. Eng. Sci.* **2017**, *375* (2098). https://doi.org/10.1098/RSTA.2016.0400.

(17) Turner, J. A. Sustainable Hydrogen Production. *Science.* **2004**, *305* (5686), 972–974. https://doi.org/10.1126/science.1103197.

(18) Esmieu, C.; Raleiras, P.; Berggren, G. From Protein Engineering to Artificial Enzymes – Biological and Biomimetic Approaches towards Sustainable Hydrogen Production. *Sustain. Energy Fuels* **2018**, *2* (4), 724–750. https://doi.org/10.1039/C7SE00582B.

(19) Ishaq, H.; Dincer, I.; Crawford, C. A Review on Hydrogen Production and Utilization: Challenges and Opportunities. *Int. J. Hydrogen Energy* **2022**, *47* (62), 26238–26264. https://doi.org/10.1016/j.ijhydene.2021.11.149.

(20) Hassan, Q.; Sameen, A. Z.; Salman, H. M.; Jaszczur, M.; Al-Jiboory, A. K. Hydrogen Energy Future: Advancements in Storage Technologies and Implications for Sustainability . *J. Energy Storage* **2023**, *72*, 2352–152. https://doi.org/10.1016/j.est.2023.108404.

(21) Oliveira, A. M.; Beswick, R. R.; Yan, Y. A Green Hydrogen Economy for a Renewable Energy Society. *Curr. Opin. Chem. Eng.* **2021**, *33*, 100701. https://doi.org/10.1016/J.COCHE.2021.100701.

(22) Hydrogen Shot | Department of Energy https://www.energy.gov/eere/fuelcells/hydrogen-shot (accessed Feb 8, 2023).

(23) Zhao, J.; Shi, R.; Li, Z.; Zhou, C.; Zhang, T. How to Make Use of Methanol in Green Catalytic Hydrogen Production? *Nano Sel.* **2020**, *1* (1), 12–29.

https://doi.org/10.1002/nano.202000010.

(24)   Zhou, H.; Li, Z.; Ma, L.; Duan, H. Electrocatalytic Oxidative Upgrading of Biomass Platform Chemicals: From the Aspect of Reaction Mechanism. *Chem. Commun.* **2022**, *58* (7), 897–907. https://doi.org/10.1039/d1cc06254a.

(25)   Wang, T.; Cao, X.; Jiao, L. Progress in Hydrogen Production Coupled with Electrochemical Oxidation of Small Molecules. *Angew. Chemie Int. Ed.* **2022**, *61* (51), e202213328. https://doi.org/10.1002/anie.202213328.

(26)   Dalle, K. E.; Warnan, J.; Leung, J. J.; Reuillard, B.; Karmel, I. S.; Reisner, E. Electro- and Solar-Driven Fuel Synthesis with First Row Transition Metal Complexes. *Chem. Rev.* **2019**, *119* (4), 2752–2875. https://doi.org/10.1021/acs.chemrev.8b00392.

(27)   Kärkäs, M. D.; Verho, O.; Johnston, E. V.; Åkermark, B. Artificial Photosynthesis: Molecular Systems for Catalytic Water Oxidation. *Chem. Rev.* **2014**, *114* (24), 11863–12001. https://doi.org/10.1021/cr400572f.

(28)   McKone, J. R.; Marinescu, S. C.; Brunschwig, B. S.; Winkler, J. R.; Gray, H. B. Earth-Abundant Hydrogen Evolution Electrocatalysts. *Chem. Sci.* **2014**, *5* (3), 865–878. https://doi.org/10.1039/c3sc51711j.

(29)   Eckenhoff, W. T. Molecular Catalysts of Co, Ni, Fe, and Mo for Hydrogen Generation in Artificial Photosynthetic Systems. *Coord. Chem. Rev.* **2018**, *373*, 295–316. https://doi.org/10.1016/J.CCR.2017.11.002.

(30)   Fukuzumi, S.; Lee, Y. M.; Nam, W. Thermal and Photocatalytic Production of Hydrogen with Earth-Abundant Metal Complexes. *Coord. Chem. Rev.* **2018**, *355*, 54–73. https://doi.org/10.1016/J.CCR.2017.07.014.

(31)   Razavet, M.; Artero, V.; Fontecave, M. Proton Electroreduction Catalyzed by Cobaloximes: Functional Models for Hydrogenases. *Inorg. Chem.* **2005**, *44* (13), 4786–4795. https://doi.org/10.1021/ic050167z.

(32)   Hu, X.; Cossairt, B. M.; Brunschwig, B. S.; Lewis, N. S.; Peters, J. C. Electrocatalytic Hydrogen Evolution by Cobalt Difluoroboryl-Diglyoximate Complexes. *Chem. Commun.* **2005**, No. 37, 4723–4725. https://doi.org/10.1039/B509188H.

(33)   Dempsey, J. L.; Brunschwig, B. S.; Winkler, J. R.; Gray, H. B. Hydrogen Evolution Catalyzed by Cobaloximes. *Acc. Chem. Res.* **2009**, *42* (12), 1995–2004. https://doi.org/10.1021/ar900253e.

(34)   Lakadamyali, F.; Kato, M.; Muresan, N. M.; Reisner, E. Selective Reduction of Aqueous Protons to Hydrogen with a Synthetic Cobaloxime Catalyst in the Presence of Atmospheric Oxygen. *Angew. Chemie Int. Ed.* **2012**, *51* (37), 9381–9384. https://doi.org/10.1002/anie.201204180.

(35)   Dolui, D.; Khandelwal, S.; Majumder, P.; Dutta, A. The Odyssey of Cobaloximes for Catalytic H 2 Production and Their Recent Revival with Enzyme-Inspired Design. *Chem. Commun.* **2020**, *56* (59), 8166–8181. https://doi.org/10.1039/D0CC03103H.

(36)   Sowmya, S.; Vijaikanth, V. Electrochemistry and Electrocatalytic Activity of Cobaloxime Complexes. *ChemistrySelect* **2022**, *7* (10), e202104044. https://doi.org/10.1002/SLCT.202104044.

(37)   Bullock, R. M.; Appel, A. M.; Helm, M. L. Production of Hydrogen by Electrocatalysis: Making the H–H Bond by Combining Protons and Hydrides. *Chem. Commun.* **2014**, *50* (24), 3125–3143. https://doi.org/10.1039/C3CC46135A.

(38)   Laureanti, J. A.; O'Hagan, M.; Shaw, W. J. Chicken Fat for Catalysis: A Scaffold Is as Important for Molecular Complexes for Energy Transformations as It Is for Enzymes in

Catalytic Function. *Sustain. Energy Fuels* **2019**, *3* (12), 3260–3278. https://doi.org/10.1039/C9SE00229D.

(39)   Wiedner, E. S.; Appel, A. M.; Raugei, S.; Shaw, W. J.; Morris Bullock, R. Molecular Catalysts with Diphosphine Ligands Containing Pendant Amines. *Chem. Rev.* **2022**, *122* (14), 12427–12474. https://doi.org/10.1021/acs.chemrev.1c01001.

(40)   Wang, J.-W.; Liu, W.-J.; Zhong, D.-C.; Lu, T.-B. Nickel Complexes as Molecular Catalysts for Water Splitting and CO2 Reduction. *Coord. Chem. Rev.* **2019**, *378*, 237–261. https://doi.org/10.1016/j.ccr.2017.12.009.

(41)   Li, X.; Lei, H.; Xie, L.; Wang, N.; Zhang, W.; Cao, R. Metalloporphyrins as Catalytic Models for Studying Hydrogen and Oxygen Evolution and Oxygen Reduction Reactions. *Acc. Chem. Res.* **2022**, *55* (6), 878–892. https://doi.org/10.1021/acs.accounts.1c00753.

(42)   Castro-Cruz, H. M.; Macías-Ruvalcaba, N. A. Porphyrin-Catalyzed Electrochemical Hydrogen Evolution Reaction. Metal-Centered and Ligand-Centered Mechanisms. *Coord. Chem. Rev.* **2022**, *458*, 214430. https://doi.org/10.1016/J.CCR.2022.214430.

(43)   Vlček, A.; Vlček, A. A. Metal-Localized Protonation of Mmnt3−2 (M = Rh, Co) Complexes. *Inorganica Chim. Acta* **1980**, *41* (C), 123–131. https://doi.org/10.1016/S0020-1693(00)88441-8.

(44)   Begum, A.; Moula, G.; Sarkar, S. A Nickel(II)–Sulfur-Based Radical-Ligand Complex as a Functional Model of Hydrogenase. *Chem. – A Eur. J.* **2010**, *16* (41), 12324–12327. https://doi.org/10.1002/CHEM.201001812.

(45)   Das, A.; Han, Z.; Brennessel, W. W.; Holland, P. L.; Eisenberg, R. Nickel Complexes for Robust Light-Driven and Electrocatalytic Hydrogen Production from Water. *ACS Catal.* **2015**, *5* (3), 1397–1406. https://doi.org/10.1021/ACSCATAL.5B00045.

(46)   McNamara, W. R.; Han, Z.; Alperin, P. J.; Brennessel, W. W.; Holland, P. L.; Eisenberg, R. A Cobalt–Dithiolene Complex for the Photocatalytic and Electrocatalytic Reduction of Protons. *J. Am. Chem. Soc.* **2011**, *133* (39), 15368–15371. https://doi.org/10.1021/ja207842r.

(47)   McNamara, W. R.; Han, Z.; Yin, C.-J. M.; Brennessel, W. W.; Holland, P. L.; Eisenberg, R.; By, E.; Meyer, T. J. Cobalt-Dithiolene Complexes for the Photocatalytic and Electrocatalytic Reduction of Protons in Aqueous Solutions. *Proc. Natl. Acad. Sci. U. S. A.* **2012**, *109* (39), 15594–15599. https://doi.org/10.1073/pnas.1120757109.

(48)   Drosou, M.; Kamatsos, F.; Mitsopoulou, C. A. Recent Advances in the Mechanisms of the Hydrogen Evolution Reaction by Non-Innocent Sulfur-Coordinating Metal Complexes. *Inorg. Chem. Front.* **2019**, *7* (1), 37–71. https://doi.org/10.1039/C9QI01113G.

(49)   Kleinhaus, J. T.; Wittkamp, F.; Yadav, S.; Siegmund, D.; Apfel, U. P. [FeFe]-Hydrogenases: Maturation and Reactivity of Enzymatic Systems and Overview of Biomimetic Models. *Chem. Soc. Rev.* **2021**, *50* (3), 1668–1784. https://doi.org/10.1039/D0CS01089H.

(50)   Simmons, T. R.; Berggren, G.; Bacchi, M.; Fontecave, M.; Artero, V. Mimicking Hydrogenases: From Biomimetics to Artificial Enzymes. *Coord. Chem. Rev.* **2014**, *270–271* (1), 127–150. https://doi.org/10.1016/J.CCR.2013.12.018.

(51)   Rauchfuss, T. B. Diiron Azadithiolates as Models for the [FeFe]-Hydrogenase Active Site and Paradigm for the Role of the Second Coordination Sphere. *Acc. Chem. Res.* **2015**, *48* (7), 2107–2116. https://doi.org/10.1021/acs.accounts.5b00177.

(52)   Chambers, G. M.; Huynh, M. T.; Li, Y.; Hammes-Schiffer, S.; Rauchfuss, T. B.; Reijerse, E.; Lubitz, W. Models of the Ni-L and Ni-SI$_a$ States of the [NiFe]-Hydrogenase Active Site.

Inorg. Chem. **2016**, *55* (2), 419–431. https://doi.org/10.1021/acs.inorgchem.5b01662.

(53) Shotonwa, I. O.; Ejeromedoghene, O.; Adesoji, A. O.; Alli, Y. A.; Akinremi, C.; Adewuyi, S. Electrochemistry, Electrocatalysis, and Mechanistic Details into Hydrogen Evolution Pathways of Hexacoordinated Iron Scaffolds in Hydrogenase Mimics. *J. Electroanal. Chem.* **2023**, *938*, 117446. https://doi.org/10.1016/J.JELECHEM.2023.117446.

(54) Gao, S.; Fan, W.; Liu, Y.; Jiang, D.; Duan, Q. Artificial Water-Soluble Systems Inspired by [FeFe]-Hydrogenases for Electro- and Photocatalytic Hydrogen Production. *Int. J. Hydrogen Energy* **2020**, *45* (7), 4305–4327. https://doi.org/10.1016/J.IJHYDENE.2019.11.206.

(55) Nayek, A.; Ahmed, M. E.; Samanta, S.; Dinda, S.; Patra, S.; Dey, S. G.; Dey, A. Bioinorganic Chemistry on Electrodes: Methods to Functional Modeling. *J. Am. Chem. Soc.* **2022**, *2022*, 8429. https://doi.org/10.1021/jacs.2c01842.

(56) Mills, W. H.; Clark, R. E. D. 35. Stereochemistry of Some New Complex Thio-Salts of Mercury, Cadmium, and Zinc. *J. Chem. Soc.* **1936**, 175–181.

(57) Clark, R. E. D. The Colorimetric Determination of Tin by Means of Toluene-3: 4-Dithiol ("Dithiol"). *Analyst* **1937**, *62* (738), 661–663.

(58) Clark, R. E. D. The Detection and Colorimetric Determination of Tin by Means of Substituted 1: 2-Dimercaptobenzenes. A Specific Reagent for Tin. *Analyst* **1936**, *61* (721), 242–245.

(59) Gray, H. B.; Billig, E. The Electronic Structures of Square-Planar Metal Complexes. III. High-Spin Planar Cobalt(I) and Iron(I). *J. Am. Chem. Soc.* **1963**, *85* (13), 2019–2020. https://doi.org/10.1021/ja00896a028.

(60) Eisenberg, R.; Gray, H. B. Noninnocence in Metal Complexes: A Dithiolene Dawn. *Inorg. Chem.* **2011**, *50* (20), 9741–9751. https://doi.org/10.1021/ic2011748.

(61) Baker-Hawkes, M. J.; Billig, E.; Gray, H. B. Characterization and Electronic Structures of Metal Complexes Containing Benzene-1,2-Dithiolate and Related Ligands. *J. Am. Chem. Soc.* **1966**, *88* (21), 4870–4875. https://doi.org/10.1021/ja00973a021.

(62) Ray, K.; Begum, A.; Weyhermüller, T.; Piligkos, S.; Van Slageren, J.; Neese, F.; Wieghardt, K. The Electronic Structure of the Isoelectronic, Square-Planar Complexes [FeII(L)2]2- and [CoIII(L Bu)2]- (L2- and (L Bu)2- = Benzene-1,2-Dithiolates): An Experimental and Density Functional Theoretical Study. *J. Am. Chem. Soc.* **2005**, *127* (12), 4403–4415. https://doi.org/10.1021/ja042803i.

(63) Benedito, F. L.; Petrenko, T.; Bill, E.; Weyhermüller, T.; Wieghardt, K. Square Planar Bis{3,6-Bis(Trimethylsilyl)Benzene-1,2-Dithiolato}metal Complexes of CrII, CoIII, and RhII: An Experimental and Density Functional Theoretical Study. *Inorg. Chem.* **2009**, *48* (23), 10913–10925. https://doi.org/10.1021/ic9008976.

(64) Das, A.; Han, Z.; Haghighi, M. G.; Eisenberg, R. Photogeneration of Hydrogen from Water Using CdSe Nanocrystals Demonstrating the Importance of Surface Exchange. *Proc. Natl. Acad. Sci. U. S. A.* **2013**, *110* (42), 16716–16723. https://doi.org/10.1073/pnas.1316755110.

(65) Solis, B. H.; Hammes-Schiffer, S. Computational Study of Anomalous Reduction Potentials for Hydrogen Evolution Catalyzed by Cobalt Dithiolene Complexes. *J. Am. Chem. Soc.* **2012**, *134* (37), 15253–15256. https://doi.org/10.1021/ja306857q.

(66) Zhang, B.; Fan, L.; Ambre, R. B.; Liu, T.; Meng, Q.; Timmer, B. J. J.; Sun, L. Advancing Proton Exchange Membrane Electrolyzers with Molecular Catalysts. *Joule* **2020**, *4* (7), 1408–1444. https://doi.org/10.1016/J.JOULE.2020.06.001.

(67) Bullock, R. M.; Das, A. K.; Appel, A. M. Surface Immobilization of Molecular

Electrocatalysts for Energy Conversion. *Chem. – A Eur. J.* **2017**, *23* (32), 7626–7641. https://doi.org/10.1002/CHEM.201605066.

(68) Kaeffer, N.; Morozan, A.; Fize, J.; Martinez, E.; Guetaz, L.; Artero, V. The Dark Side of Molecular Catalysis: Diimine-Dioxime Cobalt Complexes Are Not the Actual Hydrogen Evolution Electrocatalyst in Acidic Aqueous Solutions. *ACS Catal.* **2016**, *6* (6), 3727–3737. https://doi.org/10.1021/acscatal.6b00378.

(69) Zamader, A.; Reuillard, B.; Pécaut, J.; Billon, L.; Bousquet, A.; Berggren, G.; Artero, V. Non-Covalent Integration of a [FeFe]-Hydrogenase Mimic to Multiwalled Carbon Nanotubes for Electrocatalytic Hydrogen Evolution. *Chem. – A Eur. J.* **2022**, *28* (69), e202202260. https://doi.org/10.1002/CHEM.202202260.

(70) Zamader, A.; Reuillard, B.; Marcasuzaa, P.; Bousquet, A.; Billon, L.; Espí Gallart, J. J.; Berggren, G.; Artero, V. Electrode Integration of Synthetic Hydrogenase as Bioinspired and Noble Metal-Free Cathodes for Hydrogen Evolution. *ACS Catal.* **2023**, *13* (2), 1246–1256. https://doi.org/10.1021/acscatal.2c05175.

(71) Benazzi, E.; Begato, F.; Niorettini, A.; Destro, L.; Wurst, K.; Licini, G.; Agnoli, S.; Zonta, C.; Natali, M. Electrocatalytic Hydrogen Evolution Using Hybrid Electrodes Based on Single-Walled Carbon Nanohorns and Cobalt(II) Polypyridine Complexes. *J. Mater. Chem. A* **2021**, *9* (35), 20032–20039. https://doi.org/10.1039/D1TA03645A.

(72) Andreiadis, E. S.; Jacques, P. A.; Tran, P. D.; Leyris, A.; Chavarot-Kerlidou, M.; Jousselme, B.; Matheron, M.; Pécaut, J.; Palacin, S.; Fontecave, M.; Artero, V. Molecular Engineering of a Cobalt-Based Electrocatalytic Nanomaterial for H2 Evolution under Fully Aqueous Conditions. *Nat. Chem. 2012 51* **2012**, *5* (1), 48–53. https://doi.org/10.1038/nchem.1481.

(73) Eady, S. C.; MacInnes, M. M.; Lehnert, N. A Smorgasbord of Carbon: Electrochemical Analysis of Cobalt–Bis(Benzenedithiolate) Complex Adsorption and Electrocatalytic Activity on Diverse Graphitic Supports. *ACS Appl. Mater. Interfaces* **2016**, *8* (36), 23624–23634. https://doi.org/10.1021/acsami.6b05159.

(74) Tran, P. D.; Le Goff, A.; Heidkamp, J.; Jousselme, B.; Guillet, N.; Palacin, S.; Dau, H.; Fontecave, M.; Artero, V.; Tran, P. D.; Fontecave, M.; Artero, V.; Le Goff, A.; Jousselme, B.; Palacin, S.; Heidkamp, J.; Dau, H.; Guillet, N. Noncovalent Modification of Carbon Nanotubes with Pyrene-Functionalized Nickel Complexes: Carbon Monoxide Tolerant Catalysts for Hydrogen Evolution and Uptake. *Angew. Chemie* **2011**, *123* (6), 1407–1410. https://doi.org/10.1002/ANGE.201005427.

(75) Reuillard, B.; Warnan, J.; Leung, J. J.; Wakerley, D. W.; Reisner, E. A Poly(Cobaloxime)/Carbon Nanotube Electrode: Freestanding Buckypaper with Polymer-Enhanced H2-Evolution Performance. *Angew. Chemie Int. Ed.* **2016**, *55* (12), 3952–3957. https://doi.org/10.1002/ANIE.201511378.

(76) Zhang, C.; Prignot, E.; Jeannin, O.; Vacher, A.; Dragoe, D.; Camerel, F.; Halime, Z.; Gramage-Doria, R. Efficient Hydrogen Production at PH 7 in Water with a Heterogeneous Electrocatalyst Based on a Neutral Dimeric Cobalt-Dithiolene Complex. *ACS Catal.* **2023**, 2367–2373. https://doi.org/10.1021/ACSCATAL.2C04939.

(77) Ma, J.; Liu, L.; Chen, Q.; Yang, M.; Wang, D.; Tong, Z.; Chen, Z. A Facile Approach to Prepare Crumpled CoTMPyP/Electrochemically Reduced Graphene Oxide Nanohybrid as an Efficient Electrocatalyst for Hydrogen Evolution Reaction. *Appl. Surf. Sci.* **2017**, *399*, 535–541. https://doi.org/10.1016/J.APSUSC.2016.12.070.

(78) Macinnes, M. M. Materials for Electrochemical Energy Conversion and Storage, University of Michigan, 2020.

(79) Li, C. B.; Chu, Y.; Xie, P.; Xiong, L.; Wang, N.; Wang, H.; Tang, J. Molecular Cobalt Catalysts Grafted onto Polymers for Efficient Hydrogen Generation Cathodes. *Sol. RRL* **2021**, *5* (2), 2000281. https://doi.org/10.1002/SOLR.202000281.

(80) Goff, A. Le; Artero, V.; Jousselme, B.; Tran, P. D.; Guillet, N.; Métayé, R.; Fihri, A.; Palacin, S.; Fontecave, M. From Hydrogenases to Noble Metal-Free Catalytic Nanomaterials for H 2 Production and Uptake. *Science.* **2009**, *326* (5958), 1384–1387. https://doi.org/10.1126/science.1179773.

(81) Huan, T. N.; Jane, R. T.; Benayad, A.; Guetaz, L.; Tran, P. D.; Artero, V. Bio-Inspired Noble Metal-Free Nanomaterials Approaching Platinum Performances for H 2 Evolution and Uptake. *Energy Environ. Sci.* **2016**, *9* (3), 940–947. https://doi.org/10.1039/C5EE02739J.

(82) Ahmed, M. E.; Saha, D.; Wang, L.; Gennari, M.; Ghosh Dey, S.; Artero, V.; Dey, A.; Duboc, C. An [FeFe]-Hydrogenase Mimic Immobilized through Simple Physiadsorption and Active for Aqueous H2 Production. *ChemElectroChem* **2021**, *8* (9), 1674–1677. https://doi.org/10.1002/CELC.202100377.

(83) Ahmed, E.; Dey, S.; Mondal, B.; Dey, A.; Li, R.; Chemcomm, /; Communication, C. H 2 Evolution Catalyzed by a FeFe-Hydrogenase Synthetic Model Covalently Attached to Graphite Surfaces. *Chem. Commun.* **2017**, *53* (58), 8188–8191. https://doi.org/10.1039/C7CC04281G.

(84) Le Goff, A.; Artero, V.; Metayé, R.; Moggia, F.; Jousselme, B.; Razavet, M.; Tran, P. D.; Palacin, S.; Fontecave, M. Immobilization of FeFe Hydrogenase Mimics onto Carbon and Gold Electrodes by Controlled Aryldiazonium Salt Reduction: An Electrochemical, XPS and ATR-IR Study. *Int. J. Hydrogen Energy* **2010**, *35* (19), 10790–10796. https://doi.org/10.1016/J.IJHYDENE.2010.02.112.

(85) Kaminsky, C. J.; Weng, S.; Wright, J.; Surendranath, Y. Adsorbed Cobalt Porphyrins Act like Metal Surfaces in Electrocatalysis. *Nat. Catal. 2022 55* **2022**, *5* (5), 430–442. https://doi.org/10.1038/s41929-022-00791-6.

(86) Roy, S.; Huang, Z.; Bhunia, A.; Castner, A.; Gupta, A. K.; Zou, X.; Ott, S. Electrocatalytic Hydrogen Evolution from a Cobaloxime-Based Metal-Organic Framework Thin Film. *J. Am. Chem. Soc.* **2019**, *141* (40), 15942–15950. https://doi.org/10.1021/jacs.9b07084.

(87) Downes, C. A.; Marinescu, S. C. Electrocatalytic Metal–Organic Frameworks for Energy Applications. *ChemSusChem* **2017**, *10* (22), 4374–4392. https://doi.org/10.1002/CSSC.201701420.

(88) Clough, A. J.; Yoo, J. W.; Mecklenburg, M. H.; Marinescu, S. C. Two-Dimensional Metal-Organic Surfaces for Efficient Hydrogen Evolution from Water. *J. Am. Chem. Soc.* **2015**, *137* (1), 118–121. https://doi.org/10.1021/ja5116937.

(89) Downes, C. A.; Marinescu, S. C. Efficient Electrochemical and Photoelectrochemical H2 Production from Water by a Cobalt Dithiolene One-Dimensional Metal-Organic Surface. *J. Am. Chem. Soc.* **2015**, *137* (43), 13740–13743. https://doi.org/10.1021/jacs.5b07020.

(90) Downes, C. A.; Clough, A. J.; Chen, K.; Yoo, J. W.; Marinescu, S. C. Evaluation of the H2 Evolving Activity of Benzenehexathiolate Coordination Frameworks and the Effect of Film Thickness on H2 Production. *ACS Appl. Mater. Interfaces* **2018**, *10* (2), 1719–1727. https://doi.org/10.1021/acsami.7b15969.

(91) Downes, C. A.; Marinescu, S. C. Understanding Variability in the Hydrogen Evolution Activity of a Cobalt Anthracenetetrathiolate Coordination Polymer. *ACS Catal.* **2017**, *7* (12), 8605–8612. https://doi.org/10.1021/acscatal.7b02977.

(92) Nemiwal, M.; Gosu, V.; Zhang, T. C.; Kumar, D. Metal Organic Frameworks as Electrocatalysts: Hydrogen Evolution Reactions and Overall Water Splitting. *Int. J. Hydrogen Energy* **2021**, *46* (17), 10216–10238. https://doi.org/10.1016/J.IJHYDENE.2020.12.146.

(93) Micheroni, D.; Lan, G.; Lin, W. Efficient Electrocatalytic Proton Reduction with Carbon Nanotube-Supported Metal-Organic Frameworks. *J. Am. Chem. Soc.* **2018**, *140* (46), 15591–15595. https://doi.org/10.1021/jacs.8b09521.

(94) Jia, H.; Sun, Z.; Jiang, D.; Du, P. Covalent Cobalt Porphyrin Framework on Multiwalled Carbon Nanotubes for Efficient Water Oxidation at Low Overpotential. *Chem. Mater.* **2015**, *27* (13), 4586–4593. https://doi.org/10.1021/acs.chemmater.5b00882.

(95) Zhu, P.; Xiong, X.; Wang, D. Regulations of Active Moiety in Single Atom Catalysts for Electrochemical Hydrogen Evolution Reaction. *Nano Res.* **2022**, *15* (7), 5792–5815. https://doi.org/10.1007/s12274-022-4265-y.

(96) Eady, S. C.; Peczonczyk, S. L.; Maldonado, S.; Lehnert, N. Facile Heterogenization of a Cobalt Catalyst via Graphene Adsorption: Robust and Versatile Dihydrogen Production Systems. *Chem. Commun.* **2014**, *50* (59), 8065–8068. https://doi.org/10.1039/C4CC02920H.

(97) Eady, S. C.; MacInnes, M. M.; Lehnert, N. Immobilized Cobalt Bis(Benzenedithiolate) Complexes: Exceptionally Active Heterogeneous Electrocatalysts for Dihydrogen Production from Mildly Acidic Aqueous Solutions. *Inorg. Chem.* **2017**, *56* (19), 11654–11667. https://doi.org/10.1021/acs.inorgchem.7b01589.

(98) Macinnes, M. M.; Hlynchuk, S.; Acharya, S.; Lehnert, N.; Maldonado, S. Reduction of Graphene Oxide Thin Films by Cobaltocene and Decamethylcobaltocene. *ACS Appl. Mater. Interfaces* **2018**, *10*. https://doi.org/10.1021/acsami.7b15599.

(99) Downes, C. A.; Marinescu, S. C. One Dimensional Metal Dithiolene (M = Ni, Fe, Zn) Coordination Polymers for the Hydrogen Evolution Reaction. *Dalt. Trans.* **2016**, *45* (48), 19311–19321. https://doi.org/10.1039/C6DT03257E.

(100) Mersch, D.; Lee, C. Y.; Zhang, J. Z.; Brinkert, K.; Fontecilla-Camps, J. C.; Rutherford, A. W.; Reisner, E. Wiring of Photosystem II to Hydrogenase for Photoelectrochemical Water Splitting. *J. Am. Chem. Soc.* **2015**, *137* (26), 8541–8549. https://doi.org/10.1021/jacs.5b03737.

(101) Chen, Y.; Chen, H.; Tian, H. Immobilization of a Cobalt Catalyst on Fullerene in Molecular Devices for Water Reduction. *Chem. Commun.* **2015**, *51* (57), 11508–11511. https://doi.org/10.1039/C5CC03856A.

(102) Zhao, F.; Zhang, J.; Abe, T.; Wöhrle, D.; Kaneko, M. Electrocatalytic Proton Reduction by Phthalocyanine Cobalt Derivatives Incorporated in Poly(4-Vinylpyridine-Co-Styrene) Film. *J. Mol. Catal. A Chem.* **1999**, *145* (1–2), 245–256. https://doi.org/10.1016/S1381-1169(99)00013-8.

(103) Grätzel, M. Photoelectrochemical Cells. *Nature* **2001**, *414* (6861), 338–344. https://doi.org/10.1038/35104607.

(104) Lewis, N. S.; Nocera, D. G. Powering the Planet: Chemical Challenges in Solar Energy Utilization. *Proc. Natl. Acad. Sci. U. S. A.* **2006**, *103* (43), 15729–15735. https://doi.org/10.1073/pnas.0603395103.

(105) Gray, H. B.; Winkler, J. R. Living with Oxygen. *Acc. Chem. Res.* **2018**, *51* (8), 1850–1857. https://doi.org/10.1021/acs.accounts.8b00245.

(106) Borovik, A. S. Role of Metal-Oxo Complexes in the Cleavage of C-H Bonds. *Chem. Soc.*

Rev. **2011**, *40* (4), 1870–1874. https://doi.org/10.1039/c0cs00165a.

(107) Gunay, A.; Theopold, K. H. C-H Bond Activation by Metal-Oxo Compounds. *Chem. Rev.* **2010**, *110*, 1060–1081. https://doi.org/10.1021/cr900269x.

(108) Chen, Z.; Yin, G. The Reactivity of the Active Metal Oxo and Hydroxo Intermediates and Their Implications in Oxidations. *Chem. Soc. Rev.* **2015**, *44*, 1083–1100. https://doi.org/10.1039/C4CS00244J.

(109) Betley, T. A.; Wu, Q.; Van Voorhis, T.; Nocera, D. G. Electronic Design Criteria for O−O Bond Formation via Metal−Oxo Complexes. *Inorg. Chem.* **2008**, *47* (6), 1849–1861. https://doi.org/10.1021/ic701972n.

(110) McEvoy, J. P.; Brudvig, G. W. Water-Splitting Chemistry of Photosystem II. *Chem. Rev,* **2006**, *106* (11), 4455–4483. https://doi.org/10.1021/CR0204294.

(111) Nam, W. Dioxygen Activation by Metalloenzymes and Models. *Acc. Chem. Res.* **2007**, *40* (7), 465–465. https://doi.org/10.1021/ar700131d.

(112) Bollinger, J. M.; Krebs, C. Enzymatic C–H Activation by Metal–Superoxo Intermediates. *Curr. Opin. Chem. Biol.* **2007**, *11* (2), 151–158. https://doi.org/10.1016/J.CBPA.2007.02.037.

(113) Hohenberger, J.; Ray, K.; Meyer, K. The Biology and Chemistry of High-Valent Iron–Oxo and Iron–Nitrido Complexes. *Nat. Commun.* **2012**, *3* (1), 720. https://doi.org/10.1038/ncomms1718.

(114) Engelmann, X.; Monte-Pérez, I.; Ray, K. Oxidation Reactions with Bioinspired Mononuclear Non-Heme Metal-Oxo Complexes. *Angew. Chemie Int. Ed.* **2016**, *55* (27), 7632–7649. https://doi.org/10.1002/anie.201600507.

(115) Ray, K.; Pfaff, F. F.; Wang, B.; Nam, W. Status of Reactive Non-Heme Metal-Oxygen Intermediates in Chemical and Enzymatic Reactions. *J. Am. Chem. Soc.* **2014**, *136*, 13942–13958. https://doi.org/10.1021/ja507807v.

(116) Guo, M.; Corona, T.; Ray, K.; Nam, W. Heme and Nonheme High-Valent Iron and Manganese Oxo Cores in Biological and Abiological Oxidation Reactions. *ACS Cent. Sci.* **2019**, *5* (1), 13–28. https://doi.org/10.1021/acscentsci.8b00698.

(117) Kondo, M.; Tatewaki, H.; Masaoka, S. Design of Molecular Water Oxidation Catalysts with Earth-Abundant Metal Ions. *Chem. Soc. Rev.* **2021**, *50* (12), 6790–6831. https://doi.org/10.1039/D0CS01442G.

(118) Zhang, W.; Lai, W.; Cao, R. Energy-Related Small Molecule Activation Reactions: Oxygen Reduction and Hydrogen and Oxygen Evolution Reactions Catalyzed by Porphyrin- and Corrole-Based Systems. *Chem. Rev.* **2017**, *117* (4), 3717–3797. https://doi.org/10.1021/acs.chemrev.6b00299.

(119) Xiao, D.; Gregg, J.; Lakshmi, K. V; Bonitatibus, P. J.; Xiao, D. ; Gregg, J. ; Lakshmi, K. V. ;; Bonitatibus, P. J. Bio-Inspired Molecular Catalysts for Water Oxidation. *Catalysts* **2021**, *11*, 1068. https://doi.org/10.3390/catal11091068.

(120) Armstrong, F. A. Why Did Nature Choose Manganese to Make Oxygen? *Philos. Trans. R. Soc. B Biol. Sci.* **2008**, *363* (1494), 1263–1270. https://doi.org/10.1098/rstb.2007.2223.

(121) Cox, N.; Pantazis, D. A.; Neese, F.; Lubitz, W. Biological Water Oxidation. *Acc. Chem. Res.* **2013**, *46* (7), 1588–1596. https://doi.org/10.1021/ar3003249.

(122) Pantazis, D. A.; Orio, M.; Petrenko, T.; Zein, S.; Lubitz, W.; Messinger, J.; Neese, F. Structure of the Oxygen-Evolving Complex of Photosystem II: Information on the S2 State through Quantum Chemical Calculation of Its Magnetic Properties. *Phys. Chem. Chem. Phys.* **2009**, *11* (31), 6788–6798. https://doi.org/10.1039/b907038a.

(123) Cox, N.; Retegan, M.; Neese, F.; Pantazis, D. A.; Boussac, A.; Lubitz, W. Photosynthesis. Electronic Structure of the Oxygen-Evolving Complex in Photosystem II Prior to O-O Bond Formation. *Science* **2014**, *345* (6198), 804–808. https://doi.org/10.1126/science.1254910.

(124) Kundu, S.; Schwalbe, M.; Ray, K. Metal-Oxo-Mediated O-O Bond Formation Reactions in Chemistry and Biology. *Bioinorg. React. Mech.* **2012**, *8* (1–2), 41–57. https://doi.org/10.1515/irm-2012-0004.

(125) Yocum, C. F. The Calcium and Chloride Requirements of the O2 Evolving Complex. *Coord. Chem. Rev.* **2008**, *252* (3–4), 296–305. https://doi.org/10.1016/J.CCR.2007.08.010.

(126) Siegbahn, P. E. M. Theoretical Studies of O−O Bond Formation in Photosystem II. *Inorg. Chem.* **2008**, *47* (6), 1779–1786. https://doi.org/10.1021/ic7012057.

(127) Siegbahn, P. E. . Mechanism and Energy Diagram for O–O Bond Formation in the Oxygen-Evolving Complex in Photosystem II. *Philos. Trans. R. Soc. B Biol. Sci.* **2008**, *363* (1494), 1221–1228. https://doi.org/10.1098/rstb.2007.2218.

(128) Suga, M.; Akita, F.; Yamashita, K.; Nakajima, Y.; Ueno, G.; Li, H.; Yamane, T.; Hirata, K.; Umena, Y.; Yonekura, S.; Yu, L. J.; Murakami, H.; Nomura, T.; Kimura, T.; Kubo, M.; Baba, S.; Kumasaka, T.; Tono, K.; Yabashi, M.; Isobe, H.; Yamaguchi, K.; Yamamoto, M.; Ago, H.; Shen, J. R. An Oxyl/Oxo Mechanism for Oxygen-Oxygen Coupling in PSII Revealed by an x-Ray Free-Electron Laser. *Science.* **2019**, *366* (6463), 334–338. https://doi.org/10.1126/science.aax6998.

(129) Nam, W.; Lee, Y. M. Y.-M.; Fukuzumi, S. Tuning Reactivity and Mechanism in Oxidation Reactions by Mononuclear Nonheme Iron(IV)-Oxo Complexes. *Acc. Chem. Res.* **2014**, *47* (4), 1146–1154. https://doi.org/10.1021/ar400258p.

(130) Poulos, T. L. Heme Enzyme Structure and Function. *Chem. Rev.* **2014**, *114* (7), 3919–3962. https://doi.org/10.1021/cr400415k.

(131) Huang, X.; Groves, J. T. Oxygen Activation and Radical Transformations in Heme Proteins and Metalloporphyrins. *Chem. Rev.* **2018**, *118*, 2491–2553. https://doi.org/10.1021/acs.chemrev.7b00373.

(132) Banerjee, R.; Proshlyakov, Y.; Lipscomb, J. D.; Proshlyakov, D. A. Structure of the Key Species in the Enzymatic Oxidation of Methane to Methanol. *Nature* **2015**, *518* (7539), 431–434. https://doi.org/10.1038/nature14160.

(133) Castillo, R. G.; Banerjee, R.; Allpress, C. J.; Rohde, G. T.; Bill, E.; Que, L.; Lipscomb, J. D.; DeBeer, S. High-Energy-Resolution Fluorescence-Detected X-Ray Absorption of the Q Intermediate of Soluble Methane Monooxygenase. *J. Am. Chem. Soc.* **2017**, *139* (49), 18024–18033. https://doi.org/10.1021/jacs.7b09560.

(134) Kal, S.; Xu, S. N.; Que, L. R. Bio-Inspired Nonheme Iron Oxidation Catalysis: Involvement of Oxoiron(V) Oxidants in Cleaving Strong C-H Bonds. *Angew. Chemie-International Ed.* **2020**, *59* (19), 7332–7349. https://doi.org/10.1002/anie.201906551.

(135) Elwell, C. E.; Gagnon, N. L.; Neisen, B. D.; Dhar, D.; Spaeth, A. D.; Yee, G. M.; Tolman, W. B. Copper–Oxygen Complexes Revisited: Structures, Spectroscopy, and Reactivity. *Chem. Rev.* **2017**, *117* (3), 2059–2107. https://doi.org/10.1021/acs.chemrev.6b00636.

(136) Nam, W.; Lee, Y. M.; Fukuzumi, S. Hydrogen Atom Transfer Reactions of Mononuclear Nonheme Metal-Oxygen Intermediates. *Acc. Chem. Res.* **2018**, *51* (9), 2014–2022. https://doi.org/10.1021/acs.accounts.8b00299.

(137) Costas, M. Selective C-H Oxidation Catalyzed by Metalloporphyrins. *Coordination Chemistry Reviews.* December 2011, pp 2912–2932. https://doi.org/10.1016/j.ccr.2011.06.026.

(138) Ballhausen, C. J.; Gray, H. B. The Electronic Structure of the Vanadyl Ion. *Inorg. Chem.* **1962**, *1*, 111–122.

(139) Winkler, J. R.; Gray, H. B. Electronic Structures of Oxo-Metal Ions. *Struct. Bond.* **2012**, *142*, 17–28. https://doi.org/10.1007/430_2011_55.

(140) Gray, H. B. Elements of Life at the Oxo Wall. *Chem. Int.* **2019**, *41* (4), 16–19. https://doi.org/10.1515/ci-2019-0407.

(141) Wang, B.; Lee, Y.-M.; Tcho, W.-Y.; Tussupbayev, S.; Kim, S.-T. S. H.; Kim, Y.; Seo, M. S.; Cho, K.-B.; Dede, Y.; Keegan, B. C.; Ogura, T.; Kim, S.-T. S. H.; Ohta, T.; Baik, M.-H.; Ray, K.; Shearer, J.; Nam, W. Synthesis and Reactivity of a Mononuclear Non-Haem Cobalt(IV)-Oxo Complex. *Nat. Commun.* **2017**, *8*, 14839. https://doi.org/10.1038/ncomms14839.

(142) Scepaniak, J. J.; Fulton, M. D.; Bontchev, R. P.; Duesler, E. N.; Kirk, M. L.; Smith, J. M. Structural and Spectroscopic Characterization of an Electrophilic Iron Nitrido Complex. *J. Am. Chem. Soc.* **2008**, *130* (32), 10515–10517. https://doi.org/10.1021/ja8027372.

(143) Groysman, S.; Villagran, D.; Nocera, D. G. Pseudotetrahedral d^0, d^1, and d^2 Metal-Oxo Cores within a Tris(Alkoxide) Platform. *P. P. J. Organomet. Chem* **2010**, *49* (1), 10759–10761. https://doi.org/10.1021/ic101968s.

(144) Hay-Motherwell, R. S.; Wilkinson, G.; Hussain-Bates, B.; Hursthouse, M. B. Synthesis and X-Ray Crystal Structure of Oxotrimesityliridium(V). *Polyhedron* **1993**, *12* (16), 2009–2012. https://doi.org/10.1016/S0277-5387(00)81474-6.

(145) Yamaguchi, K.; Takahara, Y.; Fueno, T. Ab-Initio Molecular Orbital Studies of Structure and Reactivity of Transition Metal-OXO Compounds. In *Applied Quantum Chemistry*; Springer Netherlands: Dordrecht, 1986; pp 155–184. https://doi.org/10.1007/978-94-009-4746-7_11.

(146) Ray, K.; Heims, F.; Pfaff, F. F. Terminal Oxo and Imido Transition-Metal Complexes of Groups 9-11. *Eur. J. Inorg. Chem.* **2013**, *2013* (22–23), 3784–3807. https://doi.org/10.1002/ejic.201300223.

(147) Decker, A.; Solomon, E. I. Dioxygen Activation by Copper, Heme and Non-Heme Iron Enzymes: Comparison of Electronic Structures and Reactivities. *Curr. Opin. Chem. Biol.* **2005**, *9* (2), 152–163. https://doi.org/10.1016/J.CBPA.2005.02.012.

(148) Zhang, X. P.; Chandra, A.; Lee, Y.-M.; Cao, R.; Ray, K.; Nam, W. Transition Metal-Mediated O–O Bond Formation and Activation in Chemistry and Biology. *Chem. Soc. Rev.* **2021**, *50* (8), 4804–4811. https://doi.org/10.1039/D0CS01456G.

(149) Ray, K.; Heims, F.; Schwalbe, M.; Nam, W. High-Valent Metal-Oxo Intermediates in Energy Demanding Processes: From Dioxygen Reduction to Water Splitting. *Curr. Opin. Chem. Biol.* **2015**, *25*, 159–171. https://doi.org/10.1016/J.CBPA.2015.01.014.

(150) Karmalkar, D. G.; Larson, V. A.; Malik, D. D.; Lee, Y. M.; Seo, M. S.; Kim, J.; Vasiliauskas, D.; Shearer, J.; Lehnert, N.; Nam, W. Preparation and Characterization of a Formally NiIV–Oxo Complex with a Triplet Ground State and Application in Oxidation Reactions. *J. Am. Chem. Soc.* **2022**, *144* (49), 22698–22712. https://doi.org/10.1021/jacs.2c10196.

(151) Kass, D.; Larson, V. A.; Corona, T.; Kuhlmann, U.; Hildebrandt, P.; Schnegg, A.; Eckhard, B.; Lehnert, N.; Ray, K. Trapping of a Phenoxyl Radical at a Non-Heme High-Spin Iron(II) Center. *Nat. Chem.* **2024**. https://doi.org/s41557-023-01405-9.

(152) Zhu, W.; Wu, P.; Larson, V.; Kumar, A.; Li, X.-X.; Seo, M. S.; Lee, Y.-M.; Wang, B.; Lehnert, N.; Nam, W. Electronic Structure and Reactivity of Mononuclear Nonheme Iron-

Peroxo Complexes as a Biomimetic Model of Rieske Oxygenases: Ring Size Effects of Macrocyclic Ligands. *J. Am. Chem. Soc* **2024**, *146* (1), 250–262.

(153) Campisciano, V.; Gruttadauria, M.; Giacalone, F. Modified Nanocarbons for Catalysis. *ChemCatChem* **2019**, *11* (1), 90–133. https://doi.org/10.1002/cctc.201801414.

(154) Ray, K. Do S, S'-Coordinated o-Dithiobenzosemiquinonate(1-) Radicals Exist in Coordination Compounds? A Combined Experimental and Computational Study, Bochum, Univ., Diss., 2005.

(155) van der Put, P. J.; Schilperoord, A. A. Spin Delocalization in Square-Planar Spin-Triplet Benzene- and Toluenedithiolatecobaltate(III). *Inorg. Chem.* **1974**, *13* (10), 2476–2481. https://doi.org/10.1021/IC50140A034.

(156) Guo, H. L.; Wang, X. F.; Qian, Q. Y.; Wang, F. Bin; Xia, X. H. A Green Approach to the Synthesis of Graphene Nanosheets. *ACS Nano* **2009**, *3* (9), 2653–2659. https://doi.org/10.1021/nn900227d.

(157) Toh, S. Y.; Loh, K. S.; Kamarudin, S. K.; Daud, W. R. W. Graphene Production via Electrochemical Reduction of Graphene Oxide: Synthesis and Characterisation. *Chem. Eng. J.* **2014**, *251*, 422–434. https://doi.org/10.1016/J.CEJ.2014.04.004.

(158) Sadezky, A.; Muckenhuber, H.; Grothe, H.; Niessner, R.; Pöschl, U. Raman Microspectroscopy of Soot and Related Carbonaceous Materials: Spectral Analysis and Structural Information. *Carbon N. Y.* **2005**, *43* (8), 1731–1742. https://doi.org/10.1016/J.CARBON.2005.02.018.

(159) Ferrari, A.; Robertson, J. Interpretation of Raman Spectra of Disordered and Amorphous Carbon. *Phys. Rev. B* **2000**, *61* (20), 14095. https://doi.org/10.1103/PhysRevB.61.14095.

(160) Aoudi, B.; Khaligh, A.; Sheidaei, Y.; Tuncel, D. In Situ-Electrochemically Reduced Graphene Oxide Integrated with Cross-Linked Supramolecular Polymeric Network for Electrocatalytic Hydrogen Evaluation Reaction. *Polymer (Guildf).* **2021**, *231*, 124140. https://doi.org/10.1016/J.POLYMER.2021.124140.

(161) Huang, D.; Lu, J.; Li, S.; Luo, Y.; Zhao, C.; Hu, B.; Wang, M.; Shen, Y. Fabrication of Cobalt Porphyrin. Electrochemically Reduced Graphene Oxide Hybrid Films for Electrocatalytic Hydrogen Evolution in Aqueous Solution. *Langmuir* **2014**, *30* (23), 6990–6998. https://doi.org/10.1021/la501052m.

(162) Greczynski, G.; Hultman, L. A Step-by-Step Guide to Perform x-Ray Photoelectron Spectroscopy. *J. Appl. Phys.* **2022**, *132* (1), 11101. https://doi.org/10.1063/5.0086359.

(163) Costentin, C.; Saveant, J. M. Cyclic Voltammetry Analysis of Electrocatalytic Films. *J. Phys. Chem. C* **2015**, *119* (22), 12174–12182. https://doi.org/10.1021/acs.jpcc.5b02376.

(164) Elgrishi, N.; McCarthy, B. D.; Rountree, E. S.; Dempsey, J. L. Reaction Pathways of Hydrogen-Evolving Electrocatalysts: Electrochemical and Spectroscopic Studies of Proton-Coupled Electron Transfer Processes. *ACS Catal.* **2016**, *6* (6), 3644–3659. https://doi.org/10.1021/acscatal.6b00778.

(165) Elgrishi, N.; Kurtz, D. A.; Dempsey, J. L. Reaction Parameters Influencing Cobalt Hydride Formation Kinetics: Implications for Benchmarking H2-Evolution Catalysts. *J. Am. Chem. Soc.* **2017**, *139* (1), 239–244. https://doi.org/10.1021/jacs.6b10148.

(166) Queyriaux, N.; Sun, D.; Fize, J.; Pécaut, J.; J. Field, M.; Chavarot-Kerlidou, M.; Artero, V. Electrocatalytic Hydrogen Evolution with a Cobalt Complex Bearing Pendant Proton Relays: Acid Strength and Applied Potential Govern Mechanism and Stability. *J. Am. Chem. Soc.* **2019**, *142* (1), 274–282. https://doi.org/10.1021/jacs.9b10407.

(167) Costentin, C.; Drouet, S.; Robert, M.; Savéant, J. M. Turnover Numbers, Turnover

Frequencies, and Overpotential in Molecular Catalysis of Electrochemical Reactions. Cyclic Voltammetry and Preparative-Scale Electrolysis. *J. Am. Chem. Soc.* **2012**, *134* (27), 11235–11242. https://doi.org/10.1021/ja303560c.

(168) Lee, K. J.; Elgrishi, N.; Kandemir, B.; Dempsey, J. L. Electrochemical and Spectroscopic Methods for Evaluating Molecular Electrocatalysts. *Nat. Rev. Chem. 2017 15* **2017**, *1* (5), 1–14. https://doi.org/10.1038/s41570-017-0039.

(169) Hatakeyama, K.; Tateishi, H.; Taniguchi, T.; Koinuma, M.; Kida, T.; Hayami, S.; Yokoi, H.; Matsumoto, Y. Tunable Graphene Oxide Proton/Electron Mixed Conductor That Functions at Room Temperature. *Chem. Mater.* **2014**, *26* (19), 5598–5604. https://doi.org/10.1021/cm502098e.

(170) Shinagawa, T.; Garcia-Esparza, A. T.; Takanabe, K. Insight on Tafel Slopes from a Microkinetic Analysis of Aqueous Electrocatalysis for Energy Conversion. *Sci. Reports 2015 51* **2015**, *5* (1), 1–21. https://doi.org/10.1038/SREP13801.

(171) Mondal, B.; Dey, A. Development of Air-Stable Hydrogen Evolution Catalysts. *Chem. Commun.* **2017**, *53* (55), 7707–7715. https://doi.org/10.1039/c7cc02941a.

(172) Schechter, A.; Stanevsky, M.; Mahammed, A.; Gross, Z. Four-Electron Oxygen Reduction by Brominated Cobalt Corrole. *Inorg. Chem.* **2012**, *51* (1), 22–24. https://doi.org/10.1021/ic202139f.

(173) Plumeré, N.; Rüdiger, O.; Oughli, A. A.; Williams, R.; Vivekananthan, J.; Pöller, S.; Schuhmann, W.; Lubitz, W. A Redox Hydrogel Protects Hydrogenase from High-Potential Deactivation and Oxygen Damage. *Nat. Chem.* **2014**, *6* (9), 822–827. https://doi.org/10.1038/nchem.2022.

(174) Brezinski, W. P.; Karayilan, M.; Clary, K. E.; Pavlopoulos, N. G.; Li, S.; Fu, L.; Matyjaszewski, K.; Evans, D. H.; Glass, R. S.; Lichtenberger, D. L. [FeFe]-Hydrogenase Mimetic Metallopolymers with Enhanced Catalytic Activity for Hydrogen Production in Water. *Angew. Chemie Int. Ed.* **2018**, *57* (37), 11898–11902. https://doi.org/10.1002/anie.201804661.

(175) Brezinski, W. P.; Karayilan, M.; Clary, K. E.; McCleary-Petersen, K. C.; Fu, L.; Matyjaszewski, K.; Evans, D. H.; Lichtenberger, D. L.; Glass, R. S.; Pyun, J. Macromolecular Engineering of the Outer Coordination Sphere of [2Fe-2S] Metallopolymers to Enhance Catalytic Activity for H_2 Production. *ACS Macro Lett.* **2018**, *7* (11), 1383–1387. https://doi.org/10.1021/acsmacrolett.8b00765.

(176) Harriman, A. Electrochemical Catalysts to Meet the Challenge for Sustainable Fuel Production from Renewable Energy. *Curr. Opin. Green Sustain. Chem.* **2021**, *30*, 100492. https://doi.org/10.1016/J.COGSC.2021.100492.

(177) Audrieth, L. F. HEXAFLUOPHOSPHATES OF SODIUM, AMMONIUM, AND POTASSIUM. In *Inorganic synthesis, volume III*; ACS Publications, 1950; pp 111–117.

(178) Nishio, T. Direct Conversion of Alcohols into Thiols. *J. Chem. Soc. Perkin Trans. 1* **1993**, No. 10, 1113–1117. https://doi.org/10.1039/p19930001113.

(179) Ohno, M.; Miyamoto, M.; Hoshi, K.; Takeda, T.; Yamada, N.; Ohtake, A. Development of Dual-Acting Benzofurans for Thromboxane A $_2$ Receptor Antagonist and Prostacyclin Receptor Agonist: Synthesis, Structure−Activity Relationship, and Evaluation of Benzofuran Derivatives. *J. Med. Chem.* **2005**, *48* (16), 5279–5294. https://doi.org/10.1021/jm050194z.

(180) Nishio, T. A Novel Transformation of Alcohols to Thiols. *J. Chem. Soc. Chem. Commun.* **1989**, *4* (4), 205–206. https://doi.org/10.1039/C39890000205.

(181) Hunt, A. P. Synthesis and Spectroscopic Characterization of Ferric Heme-Thiolate Complexes and Their Reactivity with NO as Models for Cytochrome P450 Nitric Oxide Reductase, University of Michigan, 2019. https://doi.org/10.1017/CBO9781107415324.004.

(182) Sawyer, D. T.; Srivatsa, G. S.; Bodini, M. E.; Schaefer, W. P.; Wing, R. M. Redox Chemistry and Spectroscopy of Toluene-3, 4-Dithiol (TDTH2) and of Its M (TDT) 22-/- Complexes with Zinc (II), Copper (II), Nickel (II), Cobalt (II), Iron (II), and Manganese (II). Formation of a Stable Dn-(. Cntdot. SR) Bond upon Oxidation by One Ele. *J. Am. Chem. Soc.* **1986**, *108* (5), 936–942.

(183) Letko, C. S.; Panetier, J. A.; Head-Gordon, M.; Tilley, T. D. Mechanism of the Electrocatalytic Reduction of Protons with Diaryldithiolene Cobalt Complexes. *J. Am. Chem. Soc.* **2014**, *136* (26), 9364–9376. https://doi.org/10.1021/ja5019755.

(184) Tsukada, S.; Kondo, M.; Sato, H.; Gunji, T. Fine Electronic State Tuning of Cobaltadithiolene Complexes by Substituent Groups on the Benzene Ring. *Polyhedron* **2016**, *117*, 265–272. https://doi.org/10.1016/j.poly.2016.05.062.

(185) King, R. B.; Bisnette, M. B. Organosulfur Derivatives of the Metal Carbonyls. IX. Some Transtition Metal Derivatives Containing Both. Pi.-Cyclopentadienyl and Bis (Trifluoromethyl) Ethylene Dithiolate Ligands. *Inorg. Chem.* **1967**, *6* (3), 469–479.

(186) Chao, T.-H.; Espenson, J. H. Mechanism of Hydrogen Evolution from Hydridocobaloxime. *J. Am. Chem. Soc.* **1978**, *100* (1), 129–133.

(187) den boer, D.; Hetterscheid, D. G. H. Design Principles for Homogeneous Water Oxidation Catalysts Based on First–Row Transition Metals. *Curr. Opin. Electrochem.* **2022**, 101064. https://doi.org/10.1016/J.COELEC.2022.101064.

(188) Hocking, R. K. The Search for Intermediates Formed during Water-Oxidation Catalysis. *Chem Catal.* **2021**, *1* (2), 248–250. https://doi.org/10.1016/J.CHECAT.2021.06.004.

(189) Nocera, D. G. The Artificial Leaf. *Acc. Chem. Res.* **2012**, *45*, 767–776.

(190) Riggs-Gelasco, P. J.; Price, J. C.; Guyer, R. B.; Brehm, J. H.; Barr, E. W.; Bollinger, J. M.; Krebs, C. EXAFS Spectroscopic Evidence for an Fe═O Unit in the Fe(IV) Intermediate Observed during Oxygen Activation by Taurine:α-Ketoglutarate Dioxygenase. *J. Am. Chem. Soc.* **2004**, *126* (26), 8108–8109. https://doi.org/10.1021/ja048255q.

(191) Solomon, E. I.; Heppner, D. E.; Johnston, E. M.; Ginsbach, J. W.; Cirera, J.; Qayyum, M.; Kieber-Emmons, M. T.; Kjaergaard, C. H.; Hadt, R. G.; Tian, L. Copper Active Sites in Biology. *Chemical Reviews*. American Chemical Society April 9, 2014, pp 3659–3853. https://doi.org/10.1021/cr400327t.

(192) Solomon, E. I. Dioxygen Binding, Activation, and Reduction to H_2O by Cu Enzymes. *Inorg. Chem.* **2016**, *55* (13), 6364–6375. https://doi.org/10.1021/acs.inorgchem.6b01034.

(193) Quist, D. A.; Diaz, D. E.; Liu, J. J.; Karlin, K. D. Activation of Dioxygen by Copper Metalloproteins and Insights from Model Complexes. *Journal of Biological Inorganic Chemistry*. Springer Verlag April 1, 2017, pp 253–288. https://doi.org/10.1007/s00775-016-1415-2.

(194) Guo, M.; Lee, Y.-M.; Fukuzumi, S.; Nam, W. Biomimetic Metal-Oxidant Adducts as Active Oxidants in Oxidation Reactions. *Coordination Chemistry Reviews*. Elsevier May 15, 2021, p 213807. https://doi.org/10.1016/j.ccr.2021.213807.

(195) Paik, A.; Paul, S.; Bhowmik, S.; Das, R.; Naveen, T.; Rana, S. Recent Advances in First-Row Transition-Metal-Mediated C−H Halogenation of (Hetero)Arenes and Alkanes. *Asian J. Org. Chem.* **2022**, *11* (5), e202200060. https://doi.org/10.1002/AJOC.202200060.

(196) Li, X. X.; Cho, K. Bin; Nam, W. Electronic Properties and Reactivity Patterns of High-Valent Metal-Oxo Species of Mn, Fe, Co, and Ni. *Bull. Korean Chem. Soc.* **2021**, *42* (11), 1506–1512. https://doi.org/10.1002/BKCS.12389.

(197) Sen, A.; Rajaraman, G. Can You Break the Oxo-Wall? A Multiconfigurational Perspective. *Faraday Discuss.* **2022**, *234* (0), 175–194. https://doi.org/10.1039/D1FD00072A.

(198) Koola, J. D.; Kochi, J. K. Nickel Catalysis of Olefin Epoxidation. *Inorg. Chem.* **1987**, *26*, 908–916.

(199) Kinneary, J. F.; Albert, J. S.; Burrows, C. J. Mechanistic Studies of Alkene Epoxidation Catalyzed by Nickel(II) Cyclam Complexes. Oxygen-18 Labeling and Substituent Effects. *J. Am. Chem. Soc.* **1988**, *110*, 6124–6129.

(200) Nagataki, T.; Tachi, Y.; Itoh, S. NiII(TPA) as an Efficient Catalyst for Alkane Hydroxylation with m-CPBA. *Chem. Commun.* **2006**, *38*, 4016–4018. https://doi.org/10.1039/B608311K.

(201) Božović, A.; Feil, S.; Koyanagi, G. K.; Viggiano, A. A.; Zhang, X.; Schlangen, M.; Schwarz, H.; Bohme, D. K. Conversion of Methane to Methanol: Nickel, Palladium, and Platinum (d^9) Cations as Catalysts for the Oxidation of Methane by Ozone at Room Temperature. *Chem. - A Eur. J.* **2010**, *16* (38), 11605–11610. https://doi.org/10.1002/chem.201000627.

(202) Shiota, Y.; Yoshizawa, K. Methane-to-Methanol Conversion by First-Row Transition-Metal Oxide Ions: ScO^+, TiO^+, VO^+, CrO^+, MnO^+, FeO^+, CoO^+, NiO^+, and CuO^+. *J. Am. Chem. Soc.* **2000**, *122* (49), 12317–12326. https://doi.org/10.1021/ja0017965.

(203) Nagataki, T.; Ishii, K.; Tachi, Y.; Itoh, S. Ligand Effects on NiII-Catalysed Alkane-Hydroxylation with m-CPBA. *Dalt. Trans.* **2007**, 1120–1128. https://doi.org/10.1039/B615503K.

(204) Schröder, D.; Schwarz, H. C–H and C–C Bond Activation by Bare Transition-Metal Oxide Cations in the Gas Phase. *Angew. Chemie Int. Ed. English* **1995**, *34* (18), 1973–1995. https://doi.org/10.1002/anie.199519731.

(205) Roithova, J.; Schröder, D. Selective Activation of Alkanes by Gas-Phase Metal Lons. *Chem. Rev.* **2010**, *110* (2), 1170–1211. https://doi.org/10.1021/cr900183p.

(206) Qiu, Y.; Hartwig, J. F. Mechanism of Ni-Catalyzed Oxidations of Unactivated C(Sp3)-H Bonds. *J. Am. Chem. Soc.* **2020**, *142* (45), 19239–19248. https://doi.org/10.1021/JACS.0C09157.

(207) Nesterov, D. S.; Nesterova, O. V. Catalytic Oxidations with Meta-Chloroperoxybenzoic Acid (*m*-CPBA) and Mono-and Polynuclear Complexes of Nickel: A Mechanistic Outlook. **2021**. https://doi.org/10.3390/catal11101148.

(208) Fukuzumi, S.; Cho, K. Bin; Lee, Y.-M.; Hong, S.; Nam, W. Mechanistic Dichotomies in Redox Reactions of Mononuclear Metal–Oxygen Intermediates. *Chem. Soc. Rev.* **2020**, *49* (24), 8988–9027. https://doi.org/10.1039/D0CS01251C.

(209) Pfaff, F. F.; Heims, F.; Kundu, S.; Mebs, S.; Ray, K. Spectroscopic Capture and Reactivity of S = 1/2 Nickel(III)–Oxygen Intermediates in the Reaction of a NiII-Salt with MCPBA. *Chem. Commun.* **2012**, *48*, 3730–3732. https://doi.org/10.1039/C2CC30716B.

(210) Corona, T.; Pfaff, F. F.; Acuña-Parés, F.; Draksharapu, A.; Whiteoak, C. J.; Martin-Diaconescu, V.; Lloret-Fillol, J.; Browne, W. R.; Ray, K.; Company, A. Reactivity of a Nickel(II) Bis(Amidate) Complex with *Meta*-Chloroperbenzoic Acid: Formation of a Potent Oxidizing Species. *Chem. - A Eur. J.* **2015**, *21* (42), 15029–15038. https://doi.org/10.1002/chem.201501841.

(211) Bok, K. H.; Lee, M. M.; You, G. R.; Ahn, H. M.; Ryu, K. Y.; Kim, S.-J.; Kim, Y.; Kim, C. Synthesis, Characterization, and Catalytic Activities of A Nickel(II) Monoamido-Tetradentate Complex: Evidence For Ni^{III}-Oxo and Ni^{IV}-Oxo Species. *Chem. - A Eur. J.* **2017**, *23* (13), 3117–3125. https://doi.org/10.1002/chem.201605157.

(212) Cho, J. H.; Kim, S.; Lee, H. I. Peroxidase-like Activity of an Azamacrocyclic Ni(II) Complex. *Bull. Korean Chem. Soc.* **2022**, *43* (3), 417–420. https://doi.org/10.1002/BKCS.12493.

(213) Farhat, R.; Dhainy, J.; Halaoui, L. I. OER Catalysis at Activated and Codeposited NiFe-Oxo/Hydroxide Thin Films Is Due to Postdeposition Surface-Fe and Is Not Sustainable without Fe in Solution. *ACS Catal.* **2020**, *10* (1), 20–35. https://doi.org/10.1021/ACSCATAL.9B02580/SUPPL_FILE/CS9B02580_SI_002.CIF.

(214) Kim, S.; Jeong, H. Y.; Kim, S.; Kim, H.; Lee, S.; Cho, J.; Kim, C.; Lee, D. Proton Switch in the Secondary Coordination Sphere to Control Catalytic Events at the Metal Center: Biomimetic Oxo Transfer Chemistry of Nickel Amidate Complex. *Chem. – A Eur. J.* **2021**, *27* (14), 4700–4708. https://doi.org/10.1002/CHEM.202005183.

(215) Hu, J.; Li, Y.; Zou, Y.; Lin, L.; Li, B.; Li, X. Transition Metal Single-Atom Embedded on N-Doped Carbon as a Catalyst for Peroxymonosulfate Activation: A DFT Study. *Chem. Eng. J.* **2022**, *437*, 135428. https://doi.org/10.1016/J.CEJ.2022.135428.

(216) Li, L.; Beckers, H.; Stüker, T.; Lindič, T.; Schlöder, T.; Andrae, D.; Riedel, S. Molecular Oxofluorides OMF$_n$ of Nickel, Palladium and Platinum: Oxyl Radicals with Moderate Ligand Field Inversion. *Inorg. Chem. Front.* **2021**, *8* (5), 1215–1228. https://doi.org/10.1039/D0QI01151G.

(217) Stephens, P. J. Magnetic Circular Dichroism. *Adv. Chem. Phys.* **1976**, *35*, 197–264.

(218) Solomon, E. I.; Pavel, E. G.; Loeb, K. E.; Campochiaro, C. Magnetic Circular Dichroism Spectroscopy as a Probe of the Geometric and Electronic Structure of Non-Heme Ferrous Enzymes. *Coord. Chem. Rev.* **1995**, *144*, 369–460. https://doi.org/10.1016/0010-8545(95)01150-N.

(219) Neese, F.; Solomon, E. I. MCD C-Term Signs, Saturation Behavior, and Determination of Band Polarizations in Randomly Oriented Systems with Spin S > 1/2. Applications to S = 1/2 and S = 5/2. *Inorg. Chem.* **1999**, *38*, 1847–1865. https://doi.org/10.1021/ic981264d.

(220) Lehnert, N.; DeBeer George, S.; Solomon, E. I. Recent Advances in Bioinorganic Spectroscopy. *Curr. Opin. Chem. Biol.* **2001**, *5*, 176–187. https://doi.org/10.1016/S1367-5931(00)00188-5.

(221) Lehnert, N. Elucidating Second Coordination Sphere Effects in Heme Proteins Using Low-Temperature Magnetic Circular Dichroism Spectroscopy. *J. Inorg. Biochem.* **2012**, *110*, 83–93. https://doi.org/10.1016/j.jinorgbio.2012.02.033.

(222) Paulat, F.; Lehnert, N. Detailed Assignment of the Magnetic Circular Dichroism and UV-Vis Spectra of Five-Coordinate High-Spin Ferric [Fe(TPP)(Cl)]. **2008**, *47* (11), 4963–4976. https://doi.org/10.1021/ic8002838.

(223) Collins, T. J.; Powell, R. D.; Slebodnick, C.; Uffelman, E. S. Stable Highly Oxidizing Cobalt Complexes of Macrocyclic Ligands. *J. Am. Chem. Soc.* **1991**, *113* (22), 8419–8425. https://doi.org/10.1021/ja00022a033.

(224) Chanda, A.; Popescu, D. L.; de Oliveira, F. T.; Bominaar, E. L.; Ryabov, A. D.; Münck, E.; Collins, T. J. High-Valent Iron Complexes with Tetraamido Macrocyclic Ligands: Structures, Mössbauer Spectroscopy, and DFT Calculations. *J. Inorg. Biochem.* **2006**, *100* (4), 606–619. https://doi.org/10.1016/J.JINORGBIO.2005.12.016.

(225) Popescu, D.-L.; Chanda, A.; Stadler, M.; de Oliveira, F. T.; Ryabov, A. D.; Münck, E.; Bominaar, E. L.; Collins, T. J. High-Valent First-Row Transition-Metal Complexes of Tetraamido (4*N*) and Diamidodialkoxido or Diamidophenolato (2*N*/2*O*) Ligands: Synthesis, Structure, and Magnetochemistry. *Coord. Chem. Rev.* **2008**, *252* (18–20), 2050–2071. https://doi.org/10.1016/J.CCR.2007.11.006.

(226) Kwon, Y. M.; Lee, Y.; Schmautz, A. K.; Jackson, T. A.; Wang, D. C–H Bond Activation by a Mononuclear Nickel (IV)-Nitrate Complex. *J. Am. Chem. Soc.* **2022**, *144* (27), 12072–12080. https://doi.org/10.1021/jacs.2c02454.

(227) Wang, S.; Ma, P.; Shaik, S.; Chen, H. Valence-Inverted States of Nickel(II) Complexes Perform Facile C–H Bond Activation. *J. Am. Chem. Soc.* **2022**, *144* (32), 14607–14613. https://doi.org/10.1021/JACS.2C03835.

(228) M. J. Frisch H. B. Schlegel, G. E. Scuseria, M. A. Robb, J. R. Cheeseman, G. Scalmani, V. Barone, B. Mennucci, G. A. Petersson, H. Nakatsuji, M. Caricato, X. Li, H. P. Hratchian, A. F. Izmaylov, J. Bloino, G. Zheng, J. L. Sonnenberg, M. Hada, M. Ehara, K, G. W. T. Gaussian 09. *Gaussian*. Gaussian, Inc.: Wallingford CT 2009.

(229) Becke, A. D. Density-Functional Exchange-Energy Approximation with Correct Asymptotic-Behavior. *Phys. Rev. A* **1988**, *38* (6), 3098–3100. https://doi.org/DOI 10.1103/PhysRevA.38.3098.

(230) Becke, A. D. Density-Functional Thermochemistry. III. The Role of Exact Exchange. *J. Chem. Phys.* **1993**, *98* (7), 5648–5652. https://doi.org/10.1063/1.464913.

(231) Lee, C.; Yang, W.; Parr, R. G. Development of the Colle-Salvetti Correlation-Energy Formula into a Functional of the Electron Density. *Phys. Rev. B* **1988**, *37* (2), 785–789.

(232) Perdew, J. P. Density-Functional Approximation for the Correlation-Energy of the Inhomogeneous Electron-Gas. *Phys. Rev. B* **1986**, *33* (12), 8822–8824. https://doi.org/DOI 10.1103/PhysRevB.33.8822.

(233) Adamo, C.; Barone, V. Toward Reliable Density Functional Methods without Adjustable Parameters: The PBE0 Model. *J. Chem. Phys.* **1999**, *110* (13), 6158–6170. https://doi.org/10.1063/1.478522.

(234) Tao, J.; Perdew, J. P.; Staroverov, V. N.; Scuseria, G. E. Climbing the Density Functional Ladder: Nonempirical Meta–Generalized Gradient Approximation Designed for Molecules and Solids. *Phys. Rev. Lett.* **2003**, *91* (14), 146401. https://doi.org/ARTN 14640110.1103/PhysRevLett.91.146401.

(235) Staroverov, V. N.; Scuseria, G. E.; Tao, J.; Perdew, J. P. Comparative Assessment of a New Nonempirical Density Functional: Molecules and Hydrogen-Bonded Complexes. *J. Chem. Phys.* **2003**, *119* (23), 12129. https://doi.org/10.1063/1.1626543.

(236) Staroverov, V. N.; Scuseria, G. E.; Tao, J.; Perdew, J. P. Erratum: "Comparative Assessment of a New Nonempirical Density Functional: Molecules and Hydrogen-Bonded Complexes" [J. Chem. Phys. 119, 12129 (2003)]. *J. Chem. Phys.* **2004**, *121* (22), 11507. https://doi.org/10.1063/1.1795692.

(237) Neese, F. Software Update: The ORCA Program System, Version 4.0. *Wiley Interdiscip. Rev. Mol. Sci.* **2018**, *8* (1). https://doi.org/ARTN e132710.1002/wcms.1327.

(238) Nishida, Y.; Lee, Y.-M.; Nam, W.; Fukuzumi, S. Autocatalytic Formation of an Iron(IV)–Oxo Complex via Scandium Ion-Promoted Radical Chain Autoxidation of an Iron(II) Complex with Dioxygen and Tetraphenylborate. *J. Am. Chem. Soc.* **2014**, *136* (22), 8042–8049. https://doi.org/10.1021/ja502732p.

(239) Monte Pérez, I.; Engelmann, X.; Lee, Y.-M.; Yoo, M.; Kumaran, E.; Farquhar, E. R.; Bill,

E.; England, J.; Nam, W.; Swart, M.; Ray, K.; Monte Pérez, I.; Engelmann, X.; Lee, Y.-M.; Yoo, M.; Kumaran, E.; Farquhar, E. R.; Bill, E.; England, J.; Nam, W.; Swart, M.; Ray, K. A Highly Reactive Oxoiron(IV) Complex Supported by a Bioinspired N3O Macrocylic Ligand. *Angew. Chemie Int. Ed.* **2017**, *56* (46), 14384–14388. https://doi.org/10.1002/anie.201707872.

(240) Bren, K. L.; Eisenberg, R.; Gray, H. B. Discovery of the Magnetic Behavior of Hemoglobin: A Beginning of Bioinorganic Chemistry. *Proc Natl Acad Sci U S A* **2015**, *112* (43), 13123–13127. https://doi.org/10.1073/pnas.1515704112.

(241) Brunori, M. Hemoglobin Is an Honorary Enzyme. *Trends Biochem. Sci.* **1999**, *24* (4), 158–161. https://doi.org/10.1016/S0968-0004(99)01380-8.

(242) Ohta, T.; Liu, J.-G.; Nagaraju, P.; Ogura, T.; Naruta, Y. A Cryo-Generated Ferrous–Superoxo Porphyrin: EPR, Resonance Raman and DFT Studies. *Chem. Commun.* **2015**, *51* (62), 12407–12410. https://doi.org/10.1039/C5CC03520A.

(243) Kovaleva, E. G.; Lipscomb, J. D. Crystal Structures of Fe2+ Dioxygenase Superoxo, Alkylperoxo, and Bound Product Intermediates. *Science.* **2007**, *316* (5823), 453–457. https://doi.org/10.1126/science.1134697.

(244) DeFelippis, M. R.; Murthy, C. P.; Faraggi, M.; Klapper, M. H. Pulse Radiolytic Measurement of Redox Potentials: The Tyrosine and Tryptophan Radicals. *Biochemistry* **1989**, *28* (11), 4847–4853.

(245) Baldwin, J. E.; Bradley, M. Isopenicillin N Synthase: Mechanistic Studies. *Chem. Rev.* **1990**, *90* (7), 1079–1088. https://doi.org/10.1021/cr00105a001.

(246) Whittaker, J. W. The Free Radical-Coupled Copper. *Met. Ions Biol. Syst. Vol. 30 Met. Involv. Amin. Acid-residue Relat. Radicals* **1994**, *30*, 315.

(247) Whittaker, J. W. Free Radical Catalysis by Galactose Oxidase. *Chem. Rev.* **2003**, *103* (6), 2347–2364. https://doi.org/10.1021/cr020425z.

(248) Krüger, H.-J. What Can We Learn from Nature about the Reactivity of Coordinated Phenoxyl Radicals?—A Bioinorganic Success Story. *Angew. Chemie Int. Ed.* **1999**, *38* (5), 627–631. https://doi.org/10.1002/(SICI)1521-3773(19990301)38:5<627::AID-ANIE627>3.0.CO;2-8.

(249) Ray, K.; Petrenko, T.; Wieghardt, K.; Neese, F. Joint Spectroscopic and Theoretical Investigations of Transition Metal Complexes Involving Non-Innocent Ligands. *Dalt. Trans.* **2007**, No. 16, 1552–1566. https://doi.org/10.1039/B700096K.

(250) Shimazaki, Y. Recent Advances in X-Ray Structures of Metal-Phenoxyl Radical Complexes. *Adv. Mater. Phys. Chem.* **2013**, *3*, 60–71. https://doi.org/10.4236/ampc.2013.31A009.

(251) Stubbe, J.; van der Donk, W. A. Protein Radicals in Enzyme Catalysis. *Chem. Rev.* **1998**, *98* (2), 705–762. https://doi.org/10.1021/cr9400875.

(252) Greene, B. L.; Kang, G.; Cui, C.; Bennati, M.; Nocera, D. G.; Drennan, C. L.; Stubbe, J. Ribonucleotide Reductases: Structure, Chemistry, and Metabolism Suggest New Therapeutic Targets. *Annu Rev Biochem* **2020**, *89*, 45–75. https://doi.org/10.1146/annurev-biochem-013118-111843.

(253) Battistella, B.; Ray, K. O2 and H2O2 Activations at Dinuclear Mn and Fe Active Sites. *Coord. Chem. Rev.* **2020**, *408*, 213176. https://doi.org/10.1016/j.ccr.2019.213176.

(254) Ito, N.; Phillips, S. E.; Stevens, C.; Ogel, Z. B.; McPherson, M. J.; Keen, J. N.; Yadav, K. D.; Knowles, P. F. Novel Thioether Bond Revealed by a 1.7 A Crystal Structure of Galactose Oxidase. *Nature* **1991**, *350* (6313), 87–90. https://doi.org/10.1038/350087a0.

(255) Whittaker, M. M.; Whittaker, J. W. Cu(I)-Dependent Biogenesis of the Galactose Oxidase Redox Cofactor*. *J. Biol. Chem.* **2003**, *278* (24), 22090–22101. https://doi.org/10.1074/jbc.M300112200.

(256) Humphreys, K. J.; Mirica, L. M.; Wang, Y.; Klinman, J. P. Galactose Oxidase as a Model for Reactivity at a Copper Superoxide Center. *J. Am. Chem. Soc.* **2009**, *131* (13), 4657–4663. https://doi.org/10.1021/ja807963e.

(257) Itoh, S.; Taki, M.; Fukuzumi, S. Active Site Models for Galactose Oxidase and Related Enzymes. *Coord. Chem. Rev.* **2000**, *198* (1), 3–20. https://doi.org/10.1016/S0010-8545(99)00209-X.

(258) Daou, M.; Faulds, C. B. Glyoxal Oxidases: Their Nature and Properties. *World J Microbiol Biotechnol* **2017**, *33* (5), 87. https://doi.org/10.1007/s11274-017-2254-1.

(259) Koschorreck, K.; Alpdagtas, S.; Urlacher, V. B. Copper-Radical Oxidases: A Diverse Group of Biocatalysts with Distinct Properties and a Broad Range of Biotechnological Applications. *Eng. Microbiol.* **2022**, *2* (3), 100037. https://doi.org/10.1016/j.engmic.2022.100037.

(260) Whittaker, M. M.; Ballou, D. P.; Whittaker, J. W. Kinetic Isotope Effects as Probes of the Mechanism of Galactose Oxidase. *Biochemistry* **1998**, *37* (23), 8426–8436. https://doi.org/10.1021/bi980328t.

(261) Vaillancourt, F. H.; Bolin, J. T.; Eltis, L. D. The Ins and Outs of Ring-Cleaving Dioxygenases. *Crit Rev Biochem Mol Biol* **2006**, *41* (4), 241–267. https://doi.org/10.1080/10409230600817422.

(262) Lipscomb, J. D. Mechanism of Extradiol Aromatic Ring-Cleaving Dioxygenases. *Curr Opin Struct Biol* **2008**, *18* (6), 644–649. https://doi.org/10.1016/j.sbi.2008.11.001.

(263) Zhang, Y.; Colabroy, K. L.; Begley, T. P.; Ealick, S. E. Structural Studies on 3-Hydroxyanthranilate-3,4-Dioxygenase: The Catalytic Mechanism of a Complex Oxidation Involved in NAD Biosynthesis. *Biochemistry* **2005**, *44* (21), 7632–7643. https://doi.org/10.1021/bi047353l.

(264) Siegbahn, P. E. M.; Haeffner, F. Mechanism for Catechol Ring-Cleavage by Non-Heme Iron Extradiol Dioxygenases. *J. Am. Chem. Soc.* **2004**, *126* (29), 8919–8932. https://doi.org/10.1021/ja0493805.

(265) Deeth, R.; Bugg, T. A Density Functional Investigation of the Extradiol Cleavage Mechanism in Non-Heme Iron Catechol Dioxygenases. *J. Biol. Inorg. Chem.* **2003**, *8*, 409–418. https://doi.org/10.1007/s00775-002-0430-7.

(266) Spence, E. L.; Langley, G. J.; Bugg, T. D. H. Cis−Trans Isomerization of a Cyclopropyl Radical Trap Catalyzed by Extradiol Catechol Dioxygenases: Evidence for a Semiquinone Intermediate. *J. Am. Chem. Soc.* **1996**, *118* (35), 8336–8343. https://doi.org/10.1021/ja9607704.

(267) Chaudhuri, P.; Wieghardt, K. Phenoxyl Radical Complexes. *Prog. Inorg. Chem.* **2001**, *50*, 151–216. https://doi.org/10.1002/0471227110.ch2.

(268) Shimazaki, Y. Phenoxyl Radical–Metal Complexes. In *PATAI'S Chemistry of Functional Groups*. https://doi.org/10.1002/9780470682531.pat0603.

(269) Adam, B.; Bill, E.; Bothe, E.; Goerdt, B.; Haselhorst, G.; Hildenbrand, K.; Sokolowski, A.; Steenken, S.; Weyhermüller, T.; Wieghardt, K. Phenoxyl Radical Complexes of Gallium, Scandium, Iron and Manganese. *Chem. – A Eur. J.* **1997**, *3* (2), 308–319. https://doi.org/10.1002/chem.19970030221.

(270) Hockertz, J.; Steenken, S.; Wieghardt, K.; Hildebrandt, P. (Photo)Ionization of

Tris(Phenolato)Iron(III) Complexes: Generation of Phenoxyl Radical as Ligand. *J. Am. Chem. Soc.* **1993**, *115* (24), 11222–11230. https://doi.org/10.1021/ja00077a022.

(271) Allard, M. M.; Sonk, J. A.; Heeg, M. J.; McGarvey, B. R.; Schlegel, H. B.; Verani, C. N. Bioinspired Five-Coordinate Iron(III) Complexes for Stabilization of Phenoxyl Radicals. *Angew. Chemie Int. Ed.* **2012**, *51* (13), 3178–3182. https://doi.org/10.1002/anie.201103233.

(272) Shimazaki, Y.; Tani, F.; Fukui, K.; Naruta, Y.; Yamauchi, O. One-Electron Oxidized Nickel(II)−(Disalicylidene)Diamine Complex: Temperature-Dependent Tautomerism between Ni(III)−Phenolate and Ni(II)−Phenoxyl Radical States. *J. Am. Chem. Soc.* **2003**, *125* (35), 10512–10513. https://doi.org/10.1021/ja035806o.

(273) Chaudhuri, P.; Wieghardt, K.; Weyhermüller, T.; Paine, T. K.; Mukherjee, S.; Mukherjee, C. Biomimetic Metal-Radical Reactivity: Aerial Oxidation of Alcohols, Amines, Aminophenols and Catechols Catalyzed by Transition Metal Complexes. **2005**, *386* (10), 1023–1033. https://doi.org/10.1515/BC.2005.118.

(274) Chun, H.; Bill, E.; Bothe, E.; Weyhermüller, T.; Wieghardt, K. Octahedral (Cis-Cyclam)Iron(III) Complexes with O,N-Coordinated o-Iminosemiquinonate(1−) π Radicals and o-Imidophenolate(2−) Anions. *Inorg. Chem.* **2002**, *41* (20), 5091–5099. https://doi.org/10.1021/ic020329g.

(275) Sun, Y.; Hu, H. L.; Martell, A. E.; Clearfield, A. THE Fe(III) COMPLEX OF N,N′,N″-TRIS(3-HYDROXY-6 METHYL-2-PYRIDYLMETHYL)-1,4,7-TRIAZACYCLONONANE Fe(C27H33N6O3 · C6H6 · 2H2O). *J. Coord. Chem.* **1995**, *36* (1), 23–31. https://doi.org/10.1080/00958979508022216.

(276) Bittner, M. M.; Lindeman, S. V; Fiedler, A. T. A Synthetic Model of the Putative Fe(II)-Iminobenzosemiquinonate Intermediate in the Catalytic Cycle of o-Aminophenol Dioxygenases. *J. Am. Chem. Soc.* **2012**, *134* (12), 5460–5463. https://doi.org/10.1021/ja212163t.

(277) Trinh, T. K. H.; Morlet-Savary, F.; Pinaud, J.; Lacroix-Desmazes, P.; Reibel, C.; Joyeux, C.; Le Nouen, D.; Métivier, R.; Brosseau, A.; Héroguez, V.; Chemtob, A. Photoreduction of Triplet Thioxanthone Derivative by Azolium Tetraphenylborate: A Way to Photogenerate N-Heterocyclic Carbenes. *Phys. Chem. Chem. Phys.* **2019**, *21* (31), 17036–17046. https://doi.org/10.1039/C9CP03098K.

(278) Glaser, T. Mössbauer Spectroscopy and Transition Metal Chemistry. Fundamentals and Applications. Edited by Philipp Gütlich, Eckhard Bill and Alfred X. Trautwein. *Angew. Chemie Int. Ed.* **2011**, *50* (43), 10019–10020. https://doi.org/10.1002/anie.201104962.

(279) Kass, D.; Corona, T.; Warm, K.; Braun-Cula, B.; Kuhlmann, U.; Bill, E.; Mebs, S.; Swart, M.; Dau, H.; Haumann, M.; Hildebrandt, P.; Ray, K. Stoichiometric Formation of an Oxoiron(IV) Complex by a Soluble Methane Monooxygenase Type Activation of O2 at an Iron(II)-Cyclam Center. *J. Am. Chem. Soc.* **2020**, *142* (13), 5924–5928. https://doi.org/10.1021/jacs.9b13756.

(280) Hong, S.; So, H.; Yoon, H.; Cho, K. Bin; Lee, Y. M.; Fukuzumi, S.; Nam, W. Reactivity Comparison of High-Valent Iron(IV)-Oxo Complexes Bearing N-Tetramethylated Cyclam Ligands with Different Ring Size. *Dalt. Trans.* **2013**, *42* (22), 7842–7845. https://doi.org/10.1039/c3dt50750e.

(281) Zhang, S.; Jia, H.; Song, M.; Shen, H.; Dongfei, L.; Haibo, L. Raman Spectroscopy Study of Acetonitrile at Low Temperature. *Spectrochim. Acta Part A Mol. Biomol. Spectrosc.* **2021**, *246*, 119065. https://doi.org/10.1016/j.saa.2020.119065.

(282) Frisch, M. J.; Schlegel, H. B.; Scuseria, G. E.; Robb, M. A.; Cheeseman, J. R.; Scalmani,

G.; Barone, V.; Hratchian, H. P.; Mennucci, B.; Petersson, G. A.; Nakatsuji, H.; Li, X.; Caricato, M.; Bloino, J.; Izmaylov, A. F.; Zheng, G.; Sonnenberg, J. L.; Hada, M.; Ehara, M. G.W.T. Gaussian 09. Wallingford, CT 2009.

(283) Schäfer, A.; Horn, H.; Ahlrichs, R. Fully Optimized Contracted Gaussian-Basis Sets for Atoms Li to Kr. *J. Chem. Phys.* **1992**, *97* (4), 2571–2577. https://doi.org/10.1063/1.463096.

(284) Schäfer, A.; Huber, C.; Ahlrichs, R. Fully Optimized Contracted Gaussian Basis Sets of Triple Zeta Valence Quality for Atoms Li to Kr. *J. Chem. Phys.* **1994**, *100* (8), 5829–5835. https://doi.org/10.1063/1.467146.

(285) Neese, F. Prediction and Interpretation of the 57Fe Isomer Shift in Mössbauer Spectra by Density Functional Theory. *Inorganica Chim. Acta* **2002**, *337*, 181–192. https://doi.org/10.1016/S0020-1693(02)01031-9.

(286) Sinnecker, S.; Slep, L. D.; Bill, E.; Neese, F. Performance of Nonrelativistic and Quasi-Relativistic Hybrid DFT for the Prediction of Electric and Magnetic Hyperfine Parameters in 57Fe Mössbauer Spectra. *Inorg Chem* **2005**, *44* (7), 2245–2254. https://doi.org/10.1021/ic048609e.

(287) Römelt, M.; Ye, S.; Neese, F. Calibration of Modern Density Functional Theory Methods for the Prediction of 57Fe Mössbauer Isomer Shifts: Meta-GGA and Double-Hybrid Functionals. *Inorg Chem* **2009**, *48* (3), 784–785. https://doi.org/10.1021/ic801535v.

(288) Hanwell, M. D.; Curtis, D. E.; Lonie, D. C.; Vandermeersch, T.; Zurek, E.; Hutchison, G. R. Avogadro: An Advanced Semantic Chemical Editor, Visualization, and Analysis Platform. *J. Cheminform.* **2012**, *4* (1), 17. https://doi.org/10.1186/1758-2946-4-17.

(289) Bruijnincx, P. C. A.; van Koten, G.; Gebbink, R. J. M. K. Mononuclear Non-Heme Iron Enzymes with the 2-His-1-Carboxylate Facial Triad: Recent Developments in Enzymology and Modeling Studies. *Chem. Soc. Rev.* **2008**, *37* (12), 2716–2744.

(290) Que, L.; Tolman, W. B. Biologically Inspired Oxidation Catalysis. *Nature* **2008**, *455* (7211), 333–340. https://doi.org/10.1038/nature07371.

(291) Solomon, E. I.; Goudarzi, S.; Sutherlin, K. D. O₂ Activation by Non-Heme Iron Enzymes. *Biochemistry* **2016**, *55* (46), 6363–6374. https://doi.org/10.1021/acs.biochem.6b00635.

(292) Que, L. 60 Years of Dioxygen Activation. *JBIC J. Biol. Inorg. Chem.* **2017**, *22* (2–3), 171–173. https://doi.org/10.1007/s00775-017-1443-6.

(293) Nam, W. High-Valent Iron (IV)–Oxo Complexes of Heme and Non-Heme Ligands in Oxygenation Reactions. *Acc. Chem. Res.* **2007**, *40* (7), 522–531. https://doi.org/10.1021/ar700027f.

(294) Kovaleva, E. G.; Lipscomb, J. D. Versatility of Biological Non-Heme Fe(II) Centers in Oxygen Activation Reactions. *Nat. Chem. Biol.* **2008**, *4* (3), 186–193. https://doi.org/10.1038/nchembio.71.

(295) Dunham, N. P.; Chang, W.; Mitchell, A. J.; Martinie, R. J.; Zhang, B.; Bergman, J. A.; Rajakovich, L. J.; Wang, B.; Silakov, A.; Krebs, C. Two Distinct Mechanisms for C–C Desaturation by Iron (II)-and 2-(Oxo) Glutarate-Dependent Oxygenases: Importance of α-Heteroatom Assistance. *J. Am. Chem. Soc.* **2018**, *140* (23), 7116–7126. https://doi.org/10.1021/jacs.8b01933.

(296) Papadopoulou, A.; Meyer, F.; Buller, R. M. Engineering Fe (II)/α-Ketoglutarate-Dependent Halogenases and Desaturases. *Biochemistry* **2022**, *62* (2), 229–240. https://doi.org/10.1021/acs.biochem.2c00115.

(297) Barry, S. M.; Challis, G. L. Mechanism and Catalytic Diversity of Rieske Non-Heme Iron-Dependent Oxygenases. *ACS Catal.* **2013**, *3* (10), 2362–2370.

https://doi.org/10.1021/cs400087p.

(298) Guo, Y.; Chang, W.; Li, J.; Davidson, M. Non-Heme Mono-Iron Enzymes: Co-Substrate-Independent Dioxygen Activation. In *Comprehensive Coordination Chemistry III*; Constable, E. C., Parkin, G., Que, L., J., Eds.; Elsevier, 2021; pp 301–332.

(299) Wolfe, M. D.; Lipscomb, J. D. Hydrogen Peroxide-Coupled Cis-Diol Formation Catalyzed by Naphthalene 1, 2-Dioxygenase. *J. Biol. Chem.* **2003**, *278* (2), 829–835. https://doi.org/10.1074/jbc.M209604200.

(300) Neibergall, M. B.; Stubna, A.; Mekmouche, Y.; Münck, E.; Lipscomb, J. D. Hydrogen Peroxide Dependent Cis-Dihydroxylation of Benzoate by Fully Oxidized Benzoate 1, 2-Dioxygenase. *Biochemistry* **2007**, *46* (27), 8004–8016. https://doi.org/10.1021/bi700120j.

(301) Bugg, T. D. H.; Ramaswamy, S. Non-Heme Iron-Dependent Dioxygenases: Unravelling Catalytic Mechanisms for Complex Enzymatic Oxidations. *Curr. Opin. Chem. Biol.* **2008**, *12* (2), 134–140. https://doi.org/10.1016/j.cbpa.2007.12.007.

(302) Sydor, P. K.; Barry, S. M.; Odulate, O. M.; Barona-Gomez, F.; Haynes, S. W.; Corre, C.; Song, L.; Challis, G. L. Regio-and Stereodivergent Antibiotic Oxidative Carbocyclizations Catalysed by Rieske Oxygenase-like Enzymes. *Nat. Chem.* **2011**, *3* (5), 388–392. https://doi.org/10.1038/nchem.1024.

(303) Capyk, J. K.; Eltis, L. D. Phylogenetic Analysis Reveals the Surprising Diversity of an Oxygenase Class. *JBIC J. Biol. Inorg. Chem.* **2012**, *17*, 425–436. https://doi.org/10.1007/s00775-011-0865-9.

(304) Li, P.; Wang, L.; Feng, L. Characterization of a Novel Rieske-Type Alkane Monooxygenase System in Pusillimonas Sp. Strain T7-7. *J. Bacteriol.* **2013**, *195* (9), 1892–1901. https://doi.org/10.1128/jb.02107-12.

(305) Lukowski, A. L.; Ellinwood, D. C.; Hinze, M. E.; DeLuca, R. J.; Du Bois, J.; Hall, S.; Narayan, A. R. H. C–H Hydroxylation in Paralytic Shellfish Toxin Biosynthesis. *J. Am. Chem. Soc.* **2018**, *140* (37), 11863–11869. https://doi.org/10.1021/jacs.8b08901.

(306) Knapp, M.; Mendoza, J.; Bridwell-Rabb, J. An Aerobic Route for CH Bond Functionalization: The Rieske Non-Heme Iron Oxygenases. In *Encyclopedia of Biological Chemistry III*; Elsevier, 2021; pp 413–424.

(307) Liu, J.; Knapp, M.; Jo, M.; Dill, Z.; Bridwell-Rabb, J. Rieske Oxygenase Catalyzed C–H Bond Functionalization Reactions in Chlorophyll b Biosynthesis. *ACS Cent. Sci.* **2022**, *8* (10), 1393–1403. https://doi.org/10.1021/acscentsci.2c00058.

(308) Liu, J.; Tian, J.; Perry, C.; Lukowski, A. L.; Doukov, T. I.; Narayan, A. R. H.; Bridwell-Rabb, J. Design Principles for Site-Selective Hydroxylation by a Rieske Oxygenase. *Nat. Commun.* **2022**, *13* (1), 255. https://doi.org/10.1038/s41467-021-27822-3.

(309) Rogers, M. S.; Gordon, A. M.; Rappe, T. M.; Goodpaster, J. D.; Lipscomb, J. D. Contrasting Mechanisms of Aromatic and Aryl-Methyl Substituent Hydroxylation by the Rieske Monooxygenase Salicylate 5-Hydroxylase. *Biochemistry* **2022**, *62* (2), 507–523. https://doi.org/10.1021/acs.biochem.2c00610.

(310) Kauppi, B.; Lee, K.; Carredano, E.; Parales, R. E.; Gibson, D. T.; Eklund, H.; Ramaswamy, S. Structure of an Aromatic-Ring-Hydroxylating Dioxygenase–Naphthalene 1, 2-Dioxygenase. *Structure* **1998**, *6* (5), 571–586. https://doi.org/10.1016/S0969-2126(98)00059-8.

(311) Kovaleva, E. G.; Neibergall, M. B.; Chakrabarty, S.; Lipscomb, J. D. Finding Intermediates in the O2 Activation Pathways of Non-Heme Iron Oxygenases. *Acc. Chem. Res.* **2007**, *40*, 475–483. https://doi.org/10.1021/ar700052v.

(312) Karlsson, A.; Parales, J. V; Parales, R. E.; Gibson, D. T.; Eklund, H.; Ramaswamy, S. Crystal Structure of Naphthalene Dioxygenase: Side-on Binding of Dioxygen to Iron. *Science.* **2003**, *299* (5609), 1039–1042. https://doi.org/10.1126/science.1078020.

(313) Costas, M.; Mehn, M. P.; Jensen, M. P.; Que, L. J. Dioxygen Activation at Mononuclear Nonheme Iron Active Sites: Enzymes, Models, and Intermediates. *Chem. Rev.* **2004**, *104* (2), 939–986. https://doi.org/10.1021/CR020628N.

(314) Feng, Y.; Ke, C.; Xue, G.; Que, L. Bio-Inspired Arene Cis-Dihydroxylation by a Non-Haem Iron Catalyst Modeling the Action of Naphthalene Dioxygenase. *Chem. Commun.* **2008**, No. 1, 50–52. https://doi.org//10.1039/B817222F.

(315) Zhu, W.; Kumar, A.; Xiong, J.; Abernathy, M. J.; Li, X.-X.; Seo, M. S.; Lee, Y.-M.; Sarangi, R.; Guo, Y.; Nam, W. Seeing the Cis-Dihydroxylating Intermediate: A Mononuclear Nonheme Iron-Peroxo Complex in Cis-Dihydroxylation Reactions Modeling Rieske Dioxygenases. *J. Am. Chem. Soc.* **2023**, *145* (8), 4389–4393. https://doi.org/10.1021/jacs.2c13551.

(316) Nam, W. Synthetic Mononuclear Nonheme Iron–Oxygen Intermediates. *Acc. Chem. Res.* **2015**, *48*, 2415–2423. https://doi.org/10.1021/acs.accounts.5b00218.

(317) Wertz, D. L.; Valentine, J. S. Nucleophilicity of Iron-Peroxo Porphyrin Complexes. *Met. Met. Species Catal. Oxidations* **2000**, 37–60.

(318) Pirovano, P.; Magherusan, A. M.; McGlynn, C.; Ure, A.; Lynes, A.; McDonald, A. R. Nucleophilic Reactivity of a Copper (II)–Superoxide Complex. *Angew. Chemie* **2014**, *126* (23), 6056–6060. https://doi.org/10.1002/ange.201311152.

(319) Hong, S.; Sutherlin, K. D.; Park, J.; Kwon, E.; Siegler, M. A.; Solomon, E. I.; Nam, W. Crystallographic and Spectroscopic Characterization and Reactivities of a Mononuclear Non-Haem Iron (III)-Superoxo Complex. *Nat. Commun.* **2014**, *5* (1), 5440. https://doi.org/10.1038/ncomms6440.

(320) Panda, C.; Chandra, A.; Corona, T.; Andris, E.; Pandey, B.; Garai, S.; Lindenmaier, N.; Künstner, S.; Farquhar, E. R.; Roithová, J. Nucleophilic versus Electrophilic Reactivity of Bioinspired Superoxido Nickel (II) Complexes. *Angew. Chemie Int. Ed.* **2018**, *57* (45), 14883–14887. https://doi.org/10.1002/anie.201808085.

(321) Ure, A. D.; McDonald, A. R. Nucleophilic Reactivity of a Metal-Bound Superoxide Ligand. *Synlett* **2015**, *26* (15), 2060–2066. https://doi.org/10.1055/s-0034-1381023.

(322) Sankaralingam, M.; Lee, Y.-M.; Nam, W.; Fukuzumi, S. Amphoteric Reactivity of Metal–Oxygen Complexes in Oxidation Reactions. *Coord. Chem. Rev.* **2018**, *365*, 41–59. https://doi.org/10.1016/j.ccr.2018.03.003.

(323) Noh, H.; Cho, J. Synthesis, Characterization and Reactivity of Non-Heme 1st Row Transition Metal-Superoxo Intermediates. *Coord. Chem. Rev.* **2019**, *382*, 126–144. https://doi.org/10.1016/j.ccr.2018.12.006.

(324) Cho, J.; Sarangi, R.; Nam, W. Mononuclear Metal-O 2 Complexes Bearing Macrocyclic N-Tetramethylated Cyclam Ligands. *Acc. Chem. Res.* **2012**, *45* (8), 1321–1330. https://doi.org/10.1021/ar3000019.

(325) Jeong, D.; Valentine, J. S.; Cho, J. Bio-Inspired Mononuclear Nonheme Metal Peroxo Complexes: Synthesis, Structures and Mechanistic Studies toward Understanding Enzymatic Reactions. *Coord. Chem. Rev.* **2023**, *480*, 215021. https://doi.org/10.1016/j.ccr.2023.215021.

(326) Kieber-Emmons, M. T.; Annaraj, J.; Seo, M. S.; Van Heuvelen, K. M.; Tosha, T.; Kitagawa, T.; Brunold, T. C.; Nam, W.; Riordan, C. G. Identification of an "End-on" Nickel−

Superoxo Adduct,[Ni (TMC)(O2)]+. *J. Am. Chem. Soc.* **2006**, *128* (44), 14230–14231. https://doi.org/10.1021/ja0644879.

(327) Cho, J.; Sarangi, R.; Annaraj, J.; Kim, S. Y.; Kubo, M.; Ogura, T.; Solomon, E. I.; Nam, W. Geometric and Electronic Structure and Reactivity of a Mononuclear 'Side-on'Nickel (III)– Peroxo Complex. *Nat. Chem.* **2009**, *1* (7), 568–572. https://doi.org/10.1038/nchem.366.

(328) Cho, J.; Kang, H. Y.; Liu, L. V; Sarangi, R.; Solomon, E. I.; Nam, W. Mononuclear Nickel (II)-Superoxo and Nickel (III)-Peroxo Complexes Bearing a Common Macrocyclic TMC Ligand. *Chem. Sci.* **2013**, *4* (4), 1502–1508. https://doi.org/10.1039/C3SC22173C.

(329) Cho, J.; Woo, J.; Nam, W. An "End-On" Chromium(III)-Superoxo Complex: Crystallographic and Spectroscopic Characterization and Reactivity in C-H Bond Activation of Hydrocarbons. *J. Am. Chem. Soc.* **2010**, *132* (17), 5958-+. https://doi.org/10.1021/ja1015926.

(330) Yokoyama, A.; Han, J. E.; Cho, J.; Kubo, M.; Ogura, T.; Siegler, M. A.; Karlin, K. D.; Nam, W. Chromium (IV)–Peroxo Complex Formation and Its Nitric Oxide Dioxygenase Reactivity. *J. Am. Chem. Soc.* **2012**, *134* (37), 15269–15272. https://doi.org/10.1021/ja307384e.

(331) Seo, M. S.; Kim, J. Y.; Annaraj, J.; Kim, Y.; Lee, Y.; Kim, S.; Kim, J.; Nam, W. [Mn (Tmc)(O2)]+: A Side-On Peroxido Manganese (III) Complex Bearing a Non-Heme Ligand. *Angew. Chemie* **2007**, *119*, 381–384. https://doi.org/10.1002/ange.200603414.

(332) Annaraj, J.; Cho, J.; Lee, Y.; Kim, S. Y.; Latifi, R.; De Visser, S. P.; Nam, W. Structural Characterization and Remarkable Axial Ligand Effect on the Nucleophilic Reactivity of a Nonheme Manganese (III)–Peroxo Complex. *Angew. Chemie Int. Ed.* **2009**, *48* (23), 4150– 4153. https://doi.org/10.1002/anie.200900118.

(333) Kang, H.; Cho, J.; Cho, K.; Nomura, T.; Ogura, T.; Nam, W. Mononuclear Manganese– Peroxo and Bis (M-oxo) Dimanganese Complexes Bearing a Common N-Methylated Macrocyclic Ligand. *Chem. Eur. J.* **2013**, *19* (42), 14119–14125. https://doi.org/10.1002/chem.201301641.

(334) Annaraj, J.; Suh, Y.; Seo, M. S.; Kim, S. O.; Nam, W. Mononuclear Nonheme Ferric-Peroxo Complex in Aldehyde Deformylation. *Chem. Commun.* **2005**, No. 36, 4529–4531. https://doi.org/10.1039/b505562h.

(335) Cho, J.; Jeon, S.; Wilson, S. A.; Liu, L. V.; Kang, E. A.; Braymer, J. J.; Lim, M. H.; Hedman, B.; Hodgson, K. O.; Valentine, J. S.; Solomon, E. I.; Nam, W. Structure and Reactivity of a Mononuclear Non-Haem Iron(III)–Peroxo Complex. *Nat. 2011 4787370* **2011**, *478* (7370), 502–505. https://doi.org/10.1038/nature10535.

(336) Zhu, W.; Jang, S.; Xiong, J.; Ezhov, R.; Li, X.-X.; Kim, T.; Seo, M. S.; Lee, Y.-M.; Pushkar, Y.; Sarangi, R.; Guo, Y.; Nam, W. A Mononuclear Non-Heme Iron (III)–Peroxo Complex with an Unprecedented High O–O Stretch and Electrophilic Reactivity. *J. Am. Chem. Soc.* **2021**, *143* (38), 15556–15561. https://doi.org/10.1021/jacs.1c03358.

(337) Jo, Y.; Annaraj, J.; Seo, M. S.; Lee, Y.-M.; Kim, S. Y.; Cho, J.; Nam, W. Reactivity of a Cobalt (III)-Peroxo Complex in Oxidative Nucleophilic Reactions. *J. Inorg. Biochem.* **2008**, *102* (12), 2155–2159. https://doi.org/10.1016/j.jinorgbio.2008.08.008.

(338) Cho, J.; Sarangi, R.; Kang, H. Y.; Lee, J. Y.; Kubo, M.; Ogura, T.; Solomon, E. I.; Nam, W. Synthesis, Structural, and Spectroscopic Characterization and Reactivities of Mononuclear Cobalt (III)− Peroxo Complexes. *J. Am. Chem. Soc.* **2010**, *132* (47), 16977– 16986. https://doi.org/10.1021/ja107177m.

(339) Neese, F.; Solomon, E. I. Detailed Spectroscopic and Theoretical Studies on

[Fe(EDTA)(O2)]3-: Electronic Structure of the Side-on Ferric−Peroxide Bond and Its Relevance to Reactivity. *J. Am. Chem. Soc.* **1998**, *120* (49), 12829–12848. https://doi.org/10.1021/ja981561h.

(340) Simaan, A. J.; Döpner, S.; Banse, F.; Bourcier, S.; Bouchoux, G.; Boussac, A.; Hildebrandt, P.; Girerd, J.-J. Fe<sup>III<\sup>-Hydroperoxo and Peroxo Complexes with Aminopyridyl Ligands and the Resonance Raman Spectroscopic Identification of the Fe−O and O−O Stretching Modes. *Eur. J. Inorg. Chem.* **2000**, *2000* (7), 1627–1633. https://doi.org/10.1002/1099-0682(200007)2000:7<1627::AID-EJIC1627>3.0.CO;2-9.

(341) Simaan, A. J.; Banse, F.; Girerd, J.-J.; Wieghardt, K.; Bill, E. The Electronic Structure of Non-Heme Iron(III)−Hydroperoxo and Iron(III)−Peroxo Model Complexes Studied by Mössbauer and Electron Paramagnetic Resonance Spectroscopies. *Inorg. Chem.* **2001**, *40* (26), 6538–6540. https://doi.org/10.1021/ic010635e.

(342) Girerd, J.-J.; Banse, F.; Simaan, A. J. Characterization and Properties of Non-Heme Iron Peroxo Complexes BT - Metal-Oxo and Metal-Peroxo Species in Catalytic Oxidations; Meunier, B., Ed.; Springer Berlin Heidelberg: Berlin, Heidelberg, 2000; pp 145–177. https://doi.org/10.1007/3-540-46592-8_6.

(343) Sutherlin, K. D.; Liu, L. V; Lee, Y.-M.; Kwak, Y.; Yoda, Y.; Saito, M.; Kurokuzu, M.; Kobayashi, Y.; Seto, M.; Que, L. J.; Nam, W.; Solomon, E. I. Nuclear Resonance Vibrational Spectroscopic Definition of Peroxy Intermediates in Nonheme Iron Sites. *J. Am. Chem. Soc.* **2016**, *138* (43), 14294–14302. https://doi.org/10.1021/jacs.6b07227.

(344) Schenk, G.; Pau, M. Y. M.; Solomon, E. I. Comparison between the Geometric and Electronic Structures and Reactivities of {FeNO}7 and {FeO2}8 Complexes: A Density Functional Theory Study. *J. Am. Chem. Soc.* **2004**, *126* (2), 505–515. https://doi.org/10.1021/JA036715U.

(345) Bayot, D.; Devillers, M.; Peeters, D. Vibrational Spectra of Eight-Coordinate Niobium and Tantalum Complexes with Peroxo Ligands: A Theoretical Simulation. *Eur. J. Inorg. Chem.* **2005**, *2005* (20), 4118–4123. https://doi.org/10.1002/EJIC.200500428.

(346) Merrick, J. P.; Moran, D.; Radom, L. An Evaluation of Harmonic Vibrational Frequency Scale Factors. *J. Phys. Chem. A* **2007**, *111* (45), 11683–11700. https://doi.org/10.1021/jp073974n.

(347) Van Stappen, C.; Lehnert, N. Mechanism of N-N Bond Formation by Transition Metal-Nitrosyl Complexes: Modeling Flavodiiron Nitric Oxide Reductases. *Inorg. Chem.* **2018**, *57* (8), 4252–4269. https://doi.org/10.1021/acs.inorgchem.7b02333.

(348) Fukuzumi, S.; Lee, Y.; Nam, W. Deuterium Kinetic Isotope Effects as Redox Mechanistic Criterions. *Bull. Korean Chem. Soc.* **2021**, *42* (12), 1558–1568. https://doi.org/10.1002/bkcs.12417.

(349) Frisch, M. J.; Trucks, G. W.; Schlegel, H. B.; Scuseria, G. E.; Robb, M. A.; Cheeseman, J. R.; Scalmani, G.; Barone, V.; Petersson, G. A.; Nakatsuji, H.; Li, X.; Caricato, M.; Marenich, A. V.; Bloino, J.; Janesko, B. G.; Gomperts, R.; Mennucci, B.; Hratchian, H. P.; Ortiz, J. V.; Izmaylov, A. F.; Sonnenberg, J. L.; Williams-Young, D.; Ding, F.; Lipparini, F.; Egidi, F.; Goings, J.; Peng, B.; Petrone, A.; Henderson, T.; Ranasinghe, D.; Zakrzewski, V. G.; Gao, J.; Rega, N.; Zheng, G.; Liang, W.; Hada, M.; Ehara, M.; Toyota, K.; Fukuda, R.; Hasegawa, J.; Ishida, M.; Nakajima, T.; Honda, Y.; Kitao, O.; Nakai, H.; Vreven, T.; Throssell, K.; Montgomery, J. A., J.; Peralta, J. E.; Ogliaro, F.; Bearpark, M. J.; Heyd, J. J.; Brothers, E. N.; Kudin, K. N.; Staroverov, V. N.; Keith, T. A.; Kobayashi, R.; Normand, J.; Raghavachari, K.; Rendell, A. P.; Burant, J. C.; Iyengar, S. S.; Tomasi, J.; Cossi, M.;

Millam, J. M.; Klene, M.; Adamo, C.; Cammi, R.; Ochterski, J. W.; Martin, R. L.; Morokuma, K.; Farkas, O.; Foresman, J. B.; Fox, D. J. Gaussian 16. Gaussian, Inc.: Wallingford, CT 2016.

(350) Marenich, A. V; Cramer, C. J.; Truhlar, D. G. Universal Solvation Model Based on Solute Electron Density and on a Continuum Model of the Solvent Defined by the Bulk Dielectric Constant and Atomic Surface Tensions. *J. Phys. Chem. B* **2009**, *113* (18), 6378–6396. https://doi.org/10.1021/jp810292n.

(351) Becke, A. D. Density-functional Thermochemistry. II. The Effect of the Perdew–Wang Generalized-gradient Correlation Correction. *J. Chem. Phys.* **1992**, *97* (12), 9173–9177. https://doi.org/10.1063/1.463343.

(352) Weigend, F.; Ahlrichs, R. Balanced Basis Sets of Split Valence, Triple Zeta Valence and Quadruple Zeta Valence Quality for H to Rn: Design and Assessment of Accuracy. *Phys. Chem. Chem. Phys.* **2005**, *7* (18), 3297–3305. https://doi.org/DOI 10.1039/b508541a.

(353) Grimme, S.; Antony, J.; Ehrlich, S.; Krieg, H. A Consistent and Accurate Ab Initio Parametrization of Density Functional Dispersion Correction (DFT-D) for the 94 Elements H-Pu. *J. Chem. Phys.* **2010**, *132* (15). https://doi.org/10.1063/1.3382344.

(354) Grimme, S. Semiempirical GGA-type Density Functional Constructed with a Long-range Dispersion Correction. *J. Comput. Chem.* **2006**, *27* (15), 1787–1799. https://doi.org/10.1002/jcc.20495.

(355) Grimme, S.; Ehrlich, S.; Goerigk, L. Effect of the Damping Function in Dispersion Corrected Density Functional Theory. *J. Comput. Chem.* **2011**, *32* (7), 1456–1465. https://doi.org/10.1002/jcc.21759.

(356) Neese, F. Software Update: The ORCA Program System—Version 5.0. *Wiley Interdiscip. Rev. Comput. Mol. Sci.* **2022**, *12* (5), e1606.

(357) Weigend, F. Accurate Coulomb-Fitting Basis Sets for H to Rn. *Phys. Chem. Chem. Phys.* **2006**, *8* (9), 1057–1065. https://doi.org/10.1039/b515623h.

(358) Hellweg, A.; Hättig, C.; Höfener, S.; Klopper, W. Optimized Accurate Auxiliary Basis Sets for RI-MP2 and RI-CC2 Calculations for the Atoms Rb to Rn. *Theor. Chem. Acc.* **2007**, *117* (4), 587–597. https://doi.org/10.1007/s00214-007-0250-5.

(359) Holm, R. H.; Balch, A. L.; Davison, A.; Maki, A. H.; Berry, T. E. Electron-Transfer Complexes of the [M-N2S2] Type. The Existence of Cation-Stabilized Free-Radical Complexes. *J. Am. Chem. Soc.* **1967**, *89* (12), 2866–2874.

(360) Balch, A. L.; Holm, R. H. Complete Electron-Transfer Series of the [M-N4] Type. *J. Am. Chem. Soc.* **1966**, *88* (22), 5201–5209.